รายงานวิจัยฉบับสมบูรณ์

โครงการศึกษาเครื่องปฏิกรณ์แบบหลายหน้าที่สำหรับอุตสาหกรรมเคมีและปิโตรเคมี

โดย ศาสตราจารย์ ดร. สุทธิชัย อัสสะบำรุงรัตน์

กรกฎาคม 2554

สัญญาเลขที่ RTA5180001

รายงานวิจัยฉบับสมบูรณ์

โครงการศึกษาเครื่องปฏิกรณ์แบบหลายหน้าที่สำหรับ อุตสาหกรรมเคมีและปิโตรเคมี

ผู้วิจัย

ศาสตราจารย์ ดร. สุทธิชัย อัสสะบำรุงรัตน์

สังกัด

ภาควิชาวิศวกรรมเคมี

คณะวิศวกรรมศาสตร์

จุฬาลงกรณ์มหาวิทยาลัย

สนับสนุนโดยสำนักงานกองทุนสนับสนุนการวิจัย

(ความเห็นในรายงานนี้เป็นของผู้วิจัย สกว.ไม่จำเป็นต้องเห็นด้วยเสมอไป)

Abstract

This report summarizes the output from the project entitled “Study on Multifunctional Reactors for Chemical and Petrochemical Industries” which was supported by the Thailand Research Fund and Office of the Higher Education Commission. The project was aimed to develop new basic knowledge related to multifunctional reactors for chemical and petrochemical industries, to disseminate the knowledge via international publications, to graduate mater and Ph.D. students, and to establish strong research collaboration both national and international levels.

From this project, the overall outputs can be summarized as follows: 24 accepted international papers, 4 international papers under consideration, 3 reviews/book chapters, 4 Ph.D. and 20 MEng. The research team members have been academically promoted and received a number of important awards. Strong research collaborations have been established among the research team members and the other group of senior researcher scholar. The success of this project is certainly beneficial to the growth of Thailand economy.

Keywords: Multifunctional reactor, catalyst, catalysis, petrochemical

บทคัดย่อ

รายงานฉบับนี้สรุปผลการดำเนินงานของโครงการศึกษาเครื่องปฏิกรณ์แบบหลายหน้าที่สำหรับอุตสาหกรรมเคมีและปิโตรเคมี ซึ่งได้รับทุนส่งเสริมกลุ่มวิจัยจากสำนักงานกองทุนสนับสนุนการวิจัย (สกว.) และสำนักงานคณะกรรมการการอุดมศึกษา (สกอ.) โครงการนี้นอกจากมุ่งเน้นการสร้างองค์ความรู้ใหม่ที่มีความสำคัญต่อการพัฒนาอุตสาหกรรมปิโตรเคมีแล้ว ยังเน้นการเผยแพร่ผลงานวิจัยโดยการตีพิมพ์ผลงานในวารสารระดับนานาชาติที่มีการประเมินผลงานอย่างเข้มงวด การสร้างบุคลากรที่มีความสามารถทั้งในระดับปริญญาโทและปริญญาเอก และการสร้างความร่วมมือระหว่างนักวิจัยในประเทศไทยและต่างประเทศ

ผลที่ได้จากการดำเนินงานสามารถสรุปได้ดังนี้ คือ สามารถตีพิมพ์ผลงานในวารสารระดับนานาชาติจำนวน 24 บทความ และอยู่ในขั้นตอนการพิจารณาอีก 4 บทความ งาน Reviews/Book chapters จำนวน 3 หัวข้อ การผลิตดุษฎีบัณฑิตจำนวน 4 คน มหาบัณฑิตจำนวน 20 คน คณะผู้วิจัยได้เพิ่มความเชี่ยวชาญในงานวิจัยและมีความก้าวหน้าในตำแหน่งวิชาการ ตลอดจนได้รับการยกย่องจากหน่วยงานต่างๆ นอกจากนี้ยังสร้างความร่วมมือทางด้านงานวิจัยภายในคณะผู้วิจัยอย่างเข้มแข็งและกับทีมงานของเมธีวิจัยอาวุโสท่านอื่น ซึ่งผลสำเร็จที่ได้จากโครงการฯนี้นับเป็นประโยชน์ต่อการพัฒนาประเทศไทย

คำสำคัญ: เครื่องปฏิกรณ์แบบหลายหน้าที่ ตัวเร่งปฏิกิริยาเคมี คาตาไลซิส ปิโตรเคมี

กิตติกรรมประกาศ

โครงการวิจัยนี้ได้รับการสนับสนุนจากสำนักงานกองทุนสนับสนุนการวิจัย (สกว.) และสำนักงานคณะกรรมการการอุดมศึกษา (สกอ.) หัวหน้าโครงการขอขอบคุณความร่วมมืออย่างดีเยี่ยมจากผู้ร่วมวิจัยจากหน่วยงานต่างๆ ได้แก่ ผศ.ดร.อมรชัย อาภรณ์วิชานพ และอ.ดร.อภินันท์ สุทธิธารธวัช จากจุฬาลงกรณ์มหาวิทยาลัย รศ.ดร.นวดล เหล่าศิริพจน์ และอ.ดร.วิศิษฏ์ศรี วิยะรัตน์ จากมหาวิทยาลัยเทคโนโลยีพระจอมเกล้าธนบุรี ผศ.ดร.วรพล เกียรติกิตติพงษ์ จากมหาวิทยาลัยศิลปากร ที่มีความเอาใจใส่และการทำงานอย่างจริงจัง นอกจากนี้ขอขอบคุณผู้เชี่ยวชาญจากทั้งในประเทศและต่างประเทศ ได้แก่ Professor Shigeo Goto Professor Tomohiko Tagawa และ Assistant Professor Hiroshi Yamada จาก Nagoya University Professor Peter Douglas และ Professor Eric Croiset จาก University of Waterloo Professor Adesoji Adesina จาก University of New South Wales ดร.สุมิตรา จรสโรจน์กุล จาก MTEC นอกจากนี้คณะผู้วิจัยขอขอบพระคุณ ศ.ดร.ปิยะสาร ประเสริฐธรรม และคณาจารย์ใน Center of Excellence in Catalysis and Catalytic Reaction Engineering ที่ให้การสนับสนุนสถานที่ อุปกรณ์/เครื่องมือวิเคราะห์ ตลอดจนข้อแนะนำต่างๆ ที่เป็นประโยชน์ งานวิจัยโครงการนี้จะไม่สามารถสำเร็จได้หากขาดนิสิต/นักศึกษาทุกท่านในโครงการที่ตั้งใจทำงานด้วยความวิริยะอุตสาหะ

สัญญาเลขที่ RTA5180001

โครงการวิจัย: การศึกษาเครื่องปฏิกรณ์แบบหลายหน้าที่สำหรับอุตสาหกรรมเคมีและปิโตรเคมี

ชื่อหัวหน้าโครงการ ศ.ดร. สุทธิชัย อัสสะบำรุงรัตน์

รายงานผลงานโครงการในช่วงเวลาตั้งแต่วันที่ 1 สิงหาคม พ.ศ. 2551 **ถึง** 31 กรกฎาคม พ.ศ. 2554

1. กิจกรรมที่ได้ดำเนินการ

1.1 ด้านการประสานงานระหว่างผู้ดำเนินการ

เนื่องจากคณะผู้วิจัยประกอบด้วยนักวิจัยที่เป็นอาจารย์ประจำอยู่ที่ภาควิชาวิศวกรรมเคมี คณะวิศวกรรมศาสตร์ จุฬาลงกรณ์มหาวิทยาลัย จำนวน 3 ท่านแล้วยังประกอบด้วยนักวิจัยอีก 3 ท่านที่ทำงานประจำที่อื่นจึงได้มีการประชุมกลุ่มย่อยเป็นระยะๆ

2. ผลงาน

2.1 บทความวิจัยในวารสารระดับนานาชาติ

2.1.1 ผลงานที่ได้รับการตอบรับให้ตีพิมพ์แล้ว (ไม่รวมผลงานของทีมวิจัยที่ได้รับทุนอื่นๆ จากฝ่ายวิชาการ สำนักงานกองทุนสนับสนุนการวิจัย) จำนวน 24 ผลงาน

1) S. Assabumrungrat, N. Ruangrassamee, S. Vivanpatarakij, N. Laosiripojana and A. Arpornwichanop, “Influence of stack arrangement on performance of multiple-stack solid oxide fuel cells with non-uniform potential operation”, J. Power Sources, vol. 187 (2009) 1-7 (IF-2009 = 3.792). **(ภาคผนวก 1)**
2) W. Jamsak, P.L. Douglas, E. Croiset, R. Suwanwarangkul, N. Laosiripojana, S. Charojrochkul and S. Assabumrungrat, “Design of a Thermally Integrated Bioethanol-Fueled Solid Oxide Fuel Cell System Integrated with a Distillation Column”, J. Power Sources, vol. 187 (2009) 190-203 (IF-2009 = 3.792). **(ภาคผนวก 2)**
3) S. Vivanpatarakij, N. Laosiripojana, W. Kiatkittipong, A. Arpornwichanop, A. Soottitantawat and S. Assabumrungrat, “Simulation of solid oxide fuel cell systems integrated with sequential CaO–CO_2 capture unit”, Chem. Eng. J., vol. 147 (2009) 336-341 (IF-2009 = 2.816). **(ภาคผนวก 3)**
4) P. Dokamaingam, S. Assabumrungrat, A. Soottitantawat, I. Sramala, N. Laosiripojana, “Modeling of SOFC with Indirect Internal Reforming Operation: Comparison of

Conventional Packed-Bed and Catalytic Coated-Wall Internal Reformer", Int. J. Hydrogen Energy, vol. 34 (2009) 410-421 (IF-2009 = 3.945). **(ภาคผนวก 4)**

5) P. Piroonlerkgul, W. Kiatkittipong, A. Arpornwichanop, A. Soottitantawat, W. Wiyaratn, N. Laosiripojana, A.A. Adesina and S. Assabumrungrat, "Integration of solid oxide fuel cell and palladium membrane reactor: Technical and economic analysis", Int. J. Hydrogen Energy, 34 (2009) 3894-3907 (IF-2009 = 3.945). **(ภาคผนวก 5)**

6) Suttichai Assabumrungrat, Salinee Charoenseri, Navadol Laosiripojana, Worapon Kiatkittipong, and Piyasan Praserthdam, "Effect of oxygen addition on catalytic performance of carbon dioxide reforming of methane under periodic operation", Int. J. Hydrogen Energy, 34 (2009) 6211-6220 (IF-2009 = 3.945). **(ภาคผนวก 6)**

7) P. Dokmaingam, S. Assabumrungrat, A. Soottitantawat and N. Laosiripojana, "Effect of Operating Conditions and Gas Flow Patterns on the System Performances of IIR-SOFC Fueled by Methanol", Int. J. Hydrogen Energy, 34 (2009) 615-6424 (IF-2009 = 3.945). **(ภาคผนวก 7)**

8) P. Dokmaingam, S. Assabumrungrat, A. Soottitantawat and N. Laosiripojana, "Modeling of tubular-designed SOFC with Indirect Internal Reforming operation (IIR-SOFC) fed by different primary fuels", Journal of Power Sources, 195 (2010) 69-78 (IF-2009 = 3.792). **(ภาคผนวก 8)**

9) P. Piroonlerkgul, W. Wiyaratn, A. Soottitantawat, W. Kiatkittipong, A. Arpornwichanop, N. Laosiripojana, and S. Assabumrungrat, "Operation viability and performance of SOFC fuelled by different feeds", Chem. Eng. J., 155 (2009) 411-418 (IF-2009 = 2.816). **(ภาคผนวก 9)**

10) Nicha Tangchupong, Watcharapong Khaodee, Bunjerd Jongsomjit, Navadol Laosiripojana, Piyasan Praserthdam and Suttichai Assabumrungrat, "Effect of calcination temperature on characteristics of sulfated zirconia and its application as a catalyst for isosynthesis", Fuel Proc. Tech., 91 (2010) 121-126 (IF-2009 = 2.321). **(ภาคผนวก 10)**

11) P. Dokamaingam, S. Assabumrungrat, A. Soottitantawat and N. Laosiripojana, "Alternative concept for SOFC with direct internal reforming: Benefits from inserting catalyst rod", AIChE J., 56 (2010) 1639-1650 (IF-2009 = 1.955). **(ภาคผนวก 11)**

12) Garun Tanarungsun, Hiroshi Yamada, Tomohiko Tagawa, Worapon Kiatkittipong, Piyasan Praserthdam and Suttichai Assabumrungrat, "Reaction-Extraction-Regeneration System for

Highly Selective Oxidation of Benzene to Phenol" Chemical Engineering Communications, 197 (2010) 1140-1151 (IF-2009 = 0.586). **(ภาคผนวก 12)**

13) Watcharapong Khaodee, Nicha Tangchupong, Bunjerd Jongsomjit, Navadol Laosiripojana, Piyasan Praserthdam and Suttichai Assabumrungrat, "Isosynthesis via CO hydrogenation over SO_4-ZrO_2 catalysts", J. Ind. Eng. Chem., 16 (2010) 411-418 (IF-2009 = 1.752). **(ภาคผนวก 13)**

14) Issara Choedkiatsakul, Kanokporn Sintawarayan, Tanya Prawpipat, Apinan Soottitantawat, Wisitsree Wiyaratn, Worapon Kiatkittipong, Amornchai Arpornwichanop, Navadol Laosiripojana, Sumittra Charojrochkul and Suttichai Assabumrungrat, "Performance assessment of SOFC systems integrated with bio-ethanol production and purification processes", Engineering Journal, 13 (2010) 1-14 (IF-2009 = -). **(ภาคผนวก 14)**

15) P. Piroonlerkgul, W. Kiatkittipong, A. Arpornwichanop, W. Wiyaratn, A. Soottitantawat, N. Laosiripojana, A.A. Adesina and S. Assabumrungrat, "Technical and economic study of integrated system of solid oxide fuel cell, palladium membrane reactor, and CO_2 sorption enhancement unit", Chem. Eng. Process., 49 (2010) 1006-1016 (IF-2009 = 1.742).. **(ภาคผนวก 15)**

16) Thirasak Pairojpiriyakul, Worapon Kiatkittipong, Amornchai Arpornwichanop, Apinan Soottitantawat, Wisitsree Wiyaratn, Navadol Laosiripojana, Eric Coiset and Suttichai Assabumrungrat, "Effect of operation modes on hydrogen production from glycerol at energy self-sufficient conditions: Thermodynamic analysis", International Journal of Hydrogen Energy, 35 (2010) 10257-10270 (IF-2009 = 3.945) **(ภาคผนวก 16)**

17) Yaneeporn Patcharavorachot, N.P. Brandon, Woranee Paengjuntuek, Suttichai Assabumrungrat, Amornchai Arpornwichanop, "Analysis of Planar Solid Oxide Fuel Cells based on Proton-Conducting Electrolyte", Solid State Ionics, 181 (2010) 1568-1576 (IF-2009 = 2.162) **(ภาคผนวก 17)**

18) Lida Simasatitkul, Pimpatthar Siricharnsakunchai, Yaneeporn Patcharavorachot, Suttichai Assabumrungrat and Amornchai Arpornwichanop, "Reactive Distillation for Biodiesel Production from Soybean Oil" Korean Journal of Chemical Engineering, 28 (2011) 649-655 (IF-2009 = 0.893) **(ภาคผนวก 18)**

19) P. Dokmaingam, J.T.S. Irvine, S. Assabumrungrat, S. Charojrochkul, N. Laosiripojana, "Modeling of IT-SOFC with indirect internal reforming operation fueled by methane: Effect

of oxygen adding as autothermal reforming", International Journal of Hydrogen Energy, 35 (2010) 13271-13279 (IF-2009 = 3.945). **(ภาคผนวก 19)**

20) Garun Tanarungsun, Hiroshi Yamada, Tomohiko Tagawa, Worapon Kiatkittipong, Piyasan Praserthdam and Suttichai Assabumrungrat, "Partial Oxidation of Benzene Catalyzed by Vanadium Chloride in Novel Reaction-Extraction-Regeneration System" Chem. Eng. Proc., 50 (2011) 53–58 (IF-2009 = 1.742). **(ภาคผนวก 20)**

21) Shivanahalli K Rajesh, Navadol Laosiripojana, Suttichai Assabumrungrat, "Thermodynamic analysis for gasification of Thailand rice husk with air, steam, and mixed air/steam for hydrogen-rich gas production", International Journal of Chemical Reactor Engineering, 8 (2010) 1-27 (IF-2009 = 0.733). **(ภาคผนวก 21)**

22) Issara Choedkiatsakul, Worapon Kiatkittipong, Wisitsree Wiyaratn, Apinan Soottitantawat, Amornchai Arpornwichanop, Navadol Laosiripojana, Sumittra Charojrochkul and Suttichai Assabumrungrat, "Performance improvement of bioethanol fuelled solid oxide fuel cell system by using pervaporation", International Journal of Hydrogen Energy, 36 (2011) 5067-5075 (IF-2009 = 3.945). **(ภาคผนวก 22)**

23) S. Authayanun, A. Arpornwichanop, Y. Patcharavorachot, W. Wiyaratn, and S. Assabumrungrat, "Hydrogen Production from Glycerol Steam Reforming for Low and High-Temperature PEMFCs", International Journal of Hydrogen Energy, 36 (2011) 267-275. (IF-2009 = 3.945). **(ภาคผนวก 23)**

24) Thirasak Pairojpiriyakul, Worapon Kiatkittipong, Amornchai Arpornwichanop, Apinan Soottitantawat, Wisitsree Wiyaratn, Navadol Laosiripojana, Eric Coiset and Suttichai Assabumrungrat, "Thermodynamic analysis of hydrogen production from glycerol at energy self-sufficiency conditions", Can. J. Chem. Eng., accepted April 14, 2011 (IF-2009 = 0.63). **(ภาคผนวก 24)**

2.1.2 จำนวนผลงานที่อยู่ในขั้นตอนการแก้ไข จำนวน 3 ผลงาน

1) A. Arpornwichanop, W. Pothong, S. Assabumrungrat, and M. Tade, "Parametric Analysis of PEM Fuel Cells using Two-phase Flow Model", Chem. Eng. J., under revision (IF-2009 = 2.816).

2) L. Simasatitkul, P. Siricharnsakunchai, S. Assabumrungrat, and A. Arpornwichanop, “Reactive Distillation System for Biodiesel Production from Waste Cooking Oil”, Applied Energy, under revision (IF-2009 = 2.209).
3) Rajesh K Shivanahalli, Navadol Laosiripojana, Suttichai Assabumrungrat, “Cogeneration system configuration analysis of biomass gasification fueled SOFC for Thailand rice husk residues” International Journal of Energy Research, under revision (IF-2009 = 1.928).

2.1.3 ผลงานที่อยู่ระหว่างการพิจารณา จำนวน 1 ผลงาน

1) Rajesh K Shivanahalli, Navadol Laosiripojana, Suttichai Assabumrungrat, “System Efficiency Analysis of SOFC Coupling with Air, Mixed Air-Steam and Steam Gasification Fueled by Thailand Rice Husk” submitted to Energy conversion and management, December 2010 (IF-2009 = 1.944).

2.2 Book/reviews

1) Chapter “Fuels - Autothermal reforming” in Encyclopedia of Electrochemical Power Sources (S. Assabumrungrat and N. Laosiripojana) สำนักพิมพ์ Elsevier พิมพ์จำหน่าย 18 พฤศจิกายน 2552
2) N. Laosiripojana, W. Wiyaratn, W. Kiatkittipong, A. Arpornwichanop, A. Soottitantawat, and S. Assabumrungrat, “Reviews on Solid Oxide Fuel Cell Technology”, Engineering Journal, (2009), 13 (1), 73-90.
3) อภินันท์ สุทธิธารธวัช “การกักเก็บกลิ่นและรสชาติที่ไม่ละลายน้ำโดยการอบแห้งแบบพ่นฝอย” วารสารวิศวกรรมศาสตร์: 2552, 1 (3), 43-62

2.3 การประชุมทางวิชาการระดับนานาชาติ

1) P. Piroonlerkgul, W. Kiatkittipong, A. Arpornwichanop, A. Soottitantawat, W. Wiyratn, N. Laosiripojana, A.A. Adesina and S. Assabumrungrat, “Integration of solid oxide fuel cell and palladium membrane reactor: Technical and economic analysis”, Hydrogen + Fuel Cell 2009, May 31 – June 3, 2009, Vancouver, Canada (oral presentation)
2) P. Sonthisanga, P. Praserthdam, S. Assabumrungrat, N. Laosiripojana and W. Kiatkittipong “Hydrogen production by sorption-enhanced operation of combined carbon dioxide reforming and partial oxidation of biogas” The 2nd Thammasat University International

Conference on Chemical, Environmental and Energy Engineering, Swissotel Le Concorde Bangkok Hotel, Bangkok, 3-4 Mar, 2009 (oral presentation)

3) S. Vivanpatarakij, A. Arpornwichanop, A. Soottitantawat, S. Assabumrungrat, N. Laosiripojana and W. Kiatkittipong "Improvement of solid oxide fuel cell system performance by using CaO-CO_2 capture unit" The 2nd Thammasat University International Conference on Chemical, Environmental and Energy Engineering, Swissotel Le Concorde Bangkok Hotel, Bangkok, 3-4 Mar, 2009 (oral presentation)
4) Jirachotdaecho, G., Authayanun, S., Paengjuntuek, W., Assabumrungrat, S. and Arpornwichanop, A. "Analysis of Glycerol Autothermal Reforming for Hydrogen Production" The 3rd International Conference on Sustainable Energy and Environment (SEE 2009)- World Renewable Energy Congress 2009-Asia, May 18-23, 2009, Bangkok, Thailand.
5) Anchan Paethanom, Worapon Kiatkittipong, Amornchai Arpornwichanop, Piyasan Praserthdam and Suttichai Assabumrungrat, "Kinetic Behavior of Catalytic Esterification of Acetic Acid and Amyl Alcohol catalyzed by Zeolite-Hβ", Catalysis and Fine Chemicals 2009, Korea University, Korea, December 13-17, 2009. (oral presentation)
6) Worapon Kiatkittipong, Pichchapa Khongjarern, Suttichai Assabumrungrat, "Reduction of benzene in reformate by olefin alkylation", Pure and Applied Chemistry Conference (PACCON) 2010, Jan 21-23, 2010, Ubonratchathani, Thailand (oral presentation)
7) S. Boonkrue, W. Kiatkittipong, A. Arpornwichanop, N. Laosiripojana, Apinan Soottitantawat, Wisitsree Wiyaratn, S. Assabumrungrat, "Design of hydrogen production system for application in polymer electrolyte membrane fuel cell vehicle", Pure and Applied Chemistry Conference (PACCON) 2010, Jan 21-23, 2010, Ubonratchathani, Thailand (poster presentation)
8) Anchan Paethanom, Worapon Kiatkittipong, Piyasan Praserthdam and Suttichai Assabumrungrat, "Production of amyl acetate from amyl alcohol and acetic acid in reactive distillation: comparison between amberlyst-15 and dowex50wx8-100 catalysts", Pure and Applied Chemistry Conference (PACCON) 2010, Jan 21-23, 2010, Ubonratchathani, Thailand (oral presentation).
9) W. Kiatkittipong, P. Khongjarern and S. Assabumrungrat "Reduction of Benzene in Reformate by Olefin Alkylation" International Conference on Chemical & Biomolecular Engineering, National University of Singapore, Singapore, 28-29 Jan, 2010 (oral presentation)

10) P. Intaracharoen, P. Ratanakarn, W. Kiatkittipong, C. Chaisuk, N. Laosiripojana and S. Assabumrungrat "Production of Ether from glycerol: Kinetic Study" International Conference on Chemical & Biomolecular Engineering, National University of Singapore, Singapore, 28-29 Jan, 2010 (oral presentation)
11) Simasatitkul, L., Siricharnsakunchai, P., Assabumrungrat, S. and Arpornwichanop, S. (2010). Reactive Distillation System for Biodiesel Production from Waste Cooking Oil. Proceedings of International Conference on Applied Energy (ICAE 2010), April 21-23, 2010, Singapore. (oral presentation)
12) S. Ratchahat, N. Viriya-empikul, K. Faungnawakij, T. Charinpanitkul, and A. Soottitantawat, Synthesis of carbon microspheres from starch by hydrothermal process, Pure and Applied Chemistry International Conference 2010 (PACCON 2010), Thailand on January 21-23, 2010
13) H. Khoomkhainum, N. Viriya-empikul, K. Faungnawakij, T. Charinpanitkul, and A. Soottitantawat, Synthesis of Ni-Doped mesoporous carbon by direct addition of Ni-salt to resorcinol/formaldehyde gel, Pure and Applied Chemistry International Conference 2010 (PACCON 2010), Thailand on January 21-23, 2010
14) T. Jarunglumlert, N. Viriya-empikul, K. Faungnawakij, K. Fukaya, T. Charinpanitkul, and A. Soottitantawat, Synthesis and structure characterization of polyoxometalates supported on titania, 6th Asian Aerosol Conference 2009 (AAC 2009), Thailand on November 24-27, 2009
15) S. Parinyataramas, N. Viriya-empikul, K. Faungnawakij, T. Charinpanitkul and A. Soottitantawat, Spray drying of mesoporous carbon particles prepared from resorcinol/formaldehyde/triblock copolymer, 6th Asian Aerosol Conference 2009 (AAC 2009), Thailand on November 24-27, 2009
16) A Soottitantawat, T. Jarunglumlert, N. Viriya-empikul, K. Faungnawakij, K. Fukaya and T. Charinpanitkul, Photocatalytic properties of polyoxometalate supported on titanate nanotubes, the 21st International Symposium on Chemical Reaction Engineering (ISCRE 21), Philadelphia, USA, June 13-16, 2010.

2.4 การเสนอผลงานในที่ประชุมวิชาการในประเทศไทย

1) Suttichai Assabumrungrat (2009). Multifunctional Reactors: A Promising Concept for Process Intensification. *The 19th Thailand Chemical Engineering and Applied Chemistry Conference*, October 26-27, 2009, Kanchanaburi, Thailand. (Keynote speaker).

2) Navadol Laosiripojana (2009). Overview of biofuel productions. *The 19th Thailand Chemical Engineering and Applied Chemistry Conference*, October 26-27, 2009, Kanchanaburi, Thailand. (Keynote speaker).

3) I. Choedkiatsakul, K. Sintawarayan, W. Prawpipat, A. Soottitantawat, W. Wiyaratn, W. Kiatkittipong, A. Arpornwichanop, N. Laosiripojana, S. Charojrochkul and S. Assabumrungrat (2009). Performance Assessment of SOFC System integrated with Bio-ethanol Production and Purification Processes. *The 19th Thailand Chemical Engineering and Applied Chemistry Conference*, October 26-27, 2009, Kanchanaburi, Thailand. (oral presentation).

4) T. Pairojpiriyakul, W. Kiatkittipong, A. Arpornwichanop, A. Soottitantawat, W. Wiyaratn, N. Laosiripojana, and S. Assabumrungrat (2009). Equilibrium simulation study of hydrogen production from glycerol reforming. *The 19th Thailand Chemical Engineering and Applied Chemistry Conference*, October 26-27, 2009, Kanchanaburi, Thailand. (oral presentation).

5) Simasatitkul, L., Paengjuntuek, W., Assabumrungrat, S. and Arpornwichanop, A. (2009). Preliminary Design of Reactive Distillation for Biodiesel Production from Waste Cooking Oil. *The 19th Thailand Chemical Engineering and Applied Chemistry Conference*, October 26-27, 2009, Kanchanaburi, Thailand. (oral presentation).

6) พอตา บวรสถิตธรรม, สุทธิชัย อัสสะบำรุงรัตน์ (2009) อิทธิพลของอุณหภูมิและค่าความเป็นกรด-ด่างต่อการย่อยสลายของเลือดบนผ้าฝ้ายโดยการฟอกด้วย เปอร์อะซิติก แอซิด. *The 19th Thailand Chemical Engineering and Applied Chemistry Conference*, October 26-27, 2009, Kanchanaburi, Thailand. (poster presentation).

7) ปริญญา อินทรเจริญ, วรพล เกียรติกิตติพงษ์, นวดล เหล่าศิริพจน์, ปิยะสาร ประเสริฐธรรม, สุทธิชัย อัสสะบำรุงรัตน์ (2009) การผลิตสารเพิ่มค่าซีเทนจากกลีเซอรอล: การศึกษาจลนพลศาสตร์ด้วยตัวเร่งปฏิกิริยา Amberlyst 15. *The 19th Thailand Chemical Engineering and Applied Chemistry Conference*, October 26-27, 2009, Kanchanaburi, Thailand. (oral presentation).

8) ปริญญา อินทรเจริญ, วรพล เกียรติกิตติพงษ์, นวดล เหล่าศิริพจน์, ปิยะสาร ประเสริฐธรรม, สุทธิชัย อัสสะบำรุงรัตน์ (2009) การผลิตสารเพิ่มค่าซีเทนจากกลีเซอรอล: การประยุกต์ใช้หอกลั่นแบบมีปฏิกิริยา. *The 19th Thailand Chemical Engineering and Applied Chemistry Conference*, October 26-27, 2009, Kanchanaburi, Thailand. (poster presentation).

2.5 จำนวนนิสิตที่จบ

2.5.1 ดุษฎีบัณฑิต สำเร็จการศึกษา 4 คน

1) นายปกรณ์ พิรุณฤกษ์กุล จุฬาลงกรณ์มหาวิทยาลัย
2) นางสาวพรรณิภา ดอกไม้งาม มหาวิทยาลัยเทคโนโลยีพระจอมเกล้าธนบุรี
3) Mr. Rajesh Shivanahalli Kempegowda มหาวิทยาลัยเทคโนโลยีพระจอมเกล้าธนบุรี
4) นางสาวญาณีพร พัชรวรโชติ จุฬาลงกรณ์มหาวิทยาลัย

2.5.2 มหาบัณฑิต สำเร็จการศึกษาแล้ว 20 คน

1) นางสาวพรนิภา สนธิสง่า จุฬาลงกรณ์มหาวิทยาลัย
2) นางสาวศิริมา สุวรรณมณี จุฬาลงกรณ์มหาวิทยาลัย
3) นายคำรณ หยู่ทองคำ จุฬาลงกรณ์มหาวิทยาลัย
4) นางสาวลิดา สิมะสาธิตกุล จุฬาลงกรณ์มหาวิทยาลัย
5) นางสาวกิดาการ แสงเดือน จุฬาลงกรณ์มหาวิทยาลัย
6) นาย ไกรฤกษ์ รักสม มหาวิทยาลัยเทคโนโลยีพระจอมเกล้าธนบุรี
7) นาย ประวุฒิ ศรีมโนธรรม มหาวิทยาลัยเทคโนโลยีพระจอมเกล้าธนบุรี
8) น.ส. วราภรณ์ นวลแปง มหาวิทยาลัยเทคโนโลยีพระจอมเกล้าธนบุรี
9) นายปริญญา อินทรเจริญ มหาวิทยาลัยศิลปากร
10) น.ส.พิชชภา คงเจริญ จุฬาลงกรณ์มหาวิทยาลัย
11) น.ส. ศิริพร บุญเครือ จุฬาลงกรณ์มหาวิทยาลัย
12) น.ส. อิสสรา เชิดเกียรติสกุล จุฬาลงกรณ์มหาวิทยาลัย
13) น.ส. อัญชัญ แพถนอม จุฬาลงกรณ์มหาวิทยาลัย
14) น.ส. วาสนา เดชสุขโสภณ มหาวิทยาลัยเทคโนโลยีพระจอมเกล้าธนบุรี
15) น.ส. ฟาติมา ปริยากร มหาวิทยาลัยเทคโนโลยีพระจอมเกล้าธนบุรี
16) น.ส. มยุรี สรรเสริญนิเวศ มหาวิทยาลัยเทคโนโลยีพระจอมเกล้าธนบุรี
17) น.ส. มาริษา ไร่ทะ มหาวิทยาลัยเทคโนโลยีพระจอมเกล้าธนบุรี
18) นาย วรฉัตร สุขวัฒนจรูญ จุฬาลงกรณ์มหาวิทยาลัย
19) นาย ชัยยศ คงวัฒนกุล จุฬาลงกรณ์มหาวิทยาลัย
20) น.ส. นริศรา ไตรภพ จุฬาลงกรณ์มหาวิทยาลัย

2.6 การขอตำแหน่งทางวิชาการ

1) ผศ.ดร.นวดล เหล่าศิริพจน์ ได้ยื่นขอตำแหน่งรองศาสตราจารย์ เมื่อเดือนตุลาคม พ.ศ. 2551 และได้รับอนุมัติให้ดำรงตำแหน่งรองศาสตราจารย์ เมื่อเดือนพฤษภาคม พ.ศ. 2552
2) ดร.อภินันท์ สุทธิธารธวัช ได้ยื่นขอตำแหน่งผู้ช่วยศาสตราจารย์ เมื่อเดือนมิถุนายน พ.ศ. 2554

3) ดร.วิศิษฏ์ศรี วิยะรัตน์ กำลังแก้เอกสารที่ใช้ยื่นขอตำแหน่งผู้ช่วยศาสตราจารย์

4) รศ.ดร.นวดล เหล่าศิริพจน์ ได้ยื่นขอตำแหน่งศาสตราจารย์ เมื่อเดือนมกราคม พ.ศ. 2554

2.7 การจัดสัมมนาทางวิชาการ

<u>ปีที่ 1</u>

ได้ร่วมกับศาสตราจารย์ ดร.รัตนา จิระรัตนานนท์ ภาควิชาวิศวกรรมเคมี คณะวิศวกรรมศาสตร์ มหาวิทยาลัยเทคโนโลยีพระจอมเกล้าธนบุรี จัดสัมมนาขึ้นในหัวข้อ “การสัมมนาวิชาการในสาขาวิศวกรรมเคมี” ในวันศุกร์ที่ 17 กรกฎาคม พ.ศ.2552 เวลา 8.00 – 16.30 น. ณ อาคารสัมมนา ศูนย์การศึกษาต่อเนื่อง มหาวิทยาลัยเทคโนโลยีพระจอมเกล้าธนบุรี

<u>ปีที่ 2</u>

ได้ร่วมกับศาสตราจารย์ ดร.รัตนา จิระรัตนานนท์ ภาควิชาวิศวกรรมเคมี คณะวิศวกรรมศาสตร์ มหาวิทยาลัยเทคโนโลยีพระจอมเกล้าธนบุรี จัดสัมมนาขึ้นในหัวข้อ “การสัมมนาวิชาการในสาขาวิศวกรรมเคมี” ในวันจันทร์ที่ 19 กรกฎาคม พ.ศ.2553 เวลา 8.00 – 16.30 น. ณ ห้องประชุมชั้น 2 อาคาร 4 คณะวิศวกรรมศาสตร์ จุฬาลงกรณ์มหาวิทยาลัย มีผู้เข้าร่วมงานสัมมนาจำนวน 127 คน

<u>ปีที่ 3</u>

ได้ร่วมกับศาสตราจารย์ ดร.ปิยะสาร ประเสริฐธรรม ภาควิชาวิศวกรรมเคมี คณะวิศวกรรมศาสตร์ จุฬาลงกรณ์มหาวิทยาลัย จัดสัมมนาขึ้นในหัวข้อ “Recent Progress in Catalysis & Catalytic Reaction Engineering” ในวันศุกร์ที่ 29 กรกฎาคม พ.ศ. 2554 เวลา 8.00 – 16.00 น. ณ อาคาร 50 ปี (ห้องประชุมชั้น 7) มหาวิทยาลัยศิลปากร จังหวัด นครปฐมผู้เข้าร่วมงานสัมมนาจำนวน 70 คน

3. อื่นๆ

3.1 รางวัลที่ทีมวิจัยได้รับ

1) ผศ.ดร.อมรชัย อาภรณ์วิชานพ ได้รับรางวัลนักวิทยาศาสตร์รุ่นใหม่ ประจำปี 2552 จากมูลนิธิส่งเสริมวิทยาศาสตร์และเทคโนโลยีในพระบรมราชูปถัมภ์
2) รศ.ดร.นวดล เหล่าศิริพจน์ ได้รับรางวัล PTIT AWARD (PTIT SCHOLAR) ประจำปี 2552 จากสถาบันปิโตรเลียมแห่งประเทศไทย
3) ศ.ดร.สุทธิชัย อัสสะบำรุงรัตน์ ได้รับรางวัล ศักดิ์อินทาเนีย (บุคคลผู้ทำชื่อเสียง) จากคณะวิศวกรรมศาสตร์ จุฬาลงกรณ์มหาวิทยาลัย ประจำปี 2552

4) อ.ดร.อภินันท์ สุทธิธารธวัช ได้รับรางวัลการนำเสนอแบบโปสเตอร์ดีเด่นในการประชุมนักวิจัยใหม่พบเมธีวิจัยอาวุโส ตุลาคม 2552

5) นายธีรศักดิ์ ไพโรจน์พิริยะกุล ได้รับรางวัลการนำเสนอแบบบรรยายดีเด่นในการประชุมทางวิชาการ The 19th Thailand Chemical Engineering and Applied Chemistry Conference, October 26-27, 2009, Kanchanaburi, Thailand

6) นายปริญญา อินทรเจริญ ได้รับรางวัลการนำเสนอแบบโปสเตอร์ดีเด่นในการประชุมทางวิชาการ The 19th Thailand Chemical Engineering and Applied Chemistry Conference, October 26-27, 2009, Kanchanaburi, Thailand

7) นางสาววาสนา แจ่มศักดิ์ รางวัลวิทยานิพนธ์ประจำปี 2552 (ประเภทดี) สำนักงานคณะกรรมการการวิจัยแห่งชาติ (ศ.ดร.สุทธิชัย อัสสะบำรุงรัตน์ เป็นอาจารย์ที่ปรึกษาวิทยานิพนธ์)

8) ศ.ดร.สุทธิชัย อัสสะบำรุงรัตน์ ได้รับรางวัล ศักดิ์อินทาเนีย (งานวิจัยอ้างอิงสูงสุด) จากคณะวิศวกรรมศาสตร์ จุฬาลงกรณ์มหาวิทยาลัย ประจำปี 2553

9) ผศ.ดร.วรพล เกียรติกิตติพงษ์ ได้รับรางวัลนักวิจัยดีเด่น (นักวิจัยที่มีผลงานตีพิมพ์ในวารสารทางวิชาการมากที่สุด) จากคณะวิศวกรรมศาสตร์และเทคโนโลยีอุตสาหกรรม มหาวิทยาลัย ศิลปากร ประจำปี 2553

10) รศ.ดร.นวดล เหล่าศิริพจน์ ได้รับรางวัล TRF-SCOPUS ประจำปี 2553 จากสำนักงานกองทุนสนับสนุนการวิจัย

11) ผศ.ดร.อมรชัย อาภรณ์วิชานพ ได้รับรางวัลการนำเสนอโปสเตอร์ดีเด่น จากการประชุมนักวิจัยรุ่นใหม่พบเมธีวิจัยอาวุโส ตุลาคม 2553

12) ศ.ดร.สุทธิชัย อัสสะบำรุงรัตน์ ได้รับรางวัล PTIT AWARD (PTIT FELLOW) ประจำปี 2554 จากสถาบันปิโตรเลียมแห่งประเทศไทย

13) น.ส. เนตรชนก ยุทธศักดิ์สุนทร รางวัลชนะเลิศประเภทบุคคล การประกวดโครงงานของนักวิทยาศาสตร์รุ่นเยาว์ (YSC) จากสำนักงานพัฒนาวิทยาศาสตร์และเทคโนโลยีแห่งประเทศไทย พ.ศ. 2554 (ศ.ดร.สุทธิชัย อัสสะบำรุงรัตน์ เป็นอาจารย์ที่ปรึกษาโครงการ)

3.2 กิจกรรมการเยี่ยมชม

- ทีมวิจัยจากบริษัท UBE Industries Ltd. นำโดย Dr. Morihisa Yokota จากประเทศญี่ปุ่น และคณะ จำนวน 6 คน ได้มาเยี่ยมกลุ่มวิจัยที่ภาควิชาวิศวกรรมเคมี คณะวิศวกรรมศาสตร์ จุฬาลงกรณ์มหาวิทยาลัย เมื่อวันที่ 11 พฤศจิกายน 2552
- ศ.ดร.สุทธิชัย อัสสะบำรุงรัตน์ และรศ.ดร.นวดล เหล่าศิริพจน์ ได้ไปเยี่ยมนักวิจัยใหม่ 2 ท่าน (ดร. อุณาโลม เวทย์วัฒนะ และ ดร.สุขสันต์ อมรรักษา) ที่ บัณฑิตวิทยาลัยวิศวกรรมศาสตร์นานาชาติสิ

รินธร ไทย-เยอรมัน (TGGS) สถาบันเทคโนโลยี พระจอมเกล้าพระนครเหนือ เมื่อวันที่ 13 กรกฎาคม 2553

3.3 การสร้างความร่วมมือกับนักวิจัยใหม่

ได้มีการสร้างความร่วมมือทางด้านงานวิจัยกับนักวิจัยใหม่ดังต่อไปนี้

- ดร.สุภวัฒน์ วิวรรธ์ภัทรกิจ นักวิจัยประจำสถาบันวิจัยพลังงาน จุฬาลงกรณ์มหาวิทยาลัย ในหัวข้องานวิจัยด้าน Gasification of biomass/municipal waste
- อ. สาธิต ปิยนลินมาศ อาจารย์ประจำภาควิชาเคมีอุตสาหกรรม คณะวิทยาศาสตร์ มหาวิทยาลัยเชียงใหม่ ในหัวข้อการใช้ประโยชน์กลีเซอรอลเพื่อผลิตสารเคมี

3.4 การสร้างความร่วมมือกับเมธีวิจัยอาวุโส

ได้มีงานวิจัยร่วมกันกับศ.ดร.รัตนา จิระรัตนานนท์ (เมธีวิจัยอาวุโส สกว.) ในหัวข้อเกี่ยวกับการแยกคาร์บอนไดออกไซด์จากแก๊สธรรมชาติโดยใช้เทคโนโลยี Membrane contactor โดยมีผลงานวิจัยที่ตีพิมพ์ในวารสารระดับนานาชาติ 2 ฉบับคือ

1) Somnuk Boributh, Suttichai Assabumrungrat, Navadol Laosiripojana, Ratana Jiraratananon, "Effect of membrane module arrangement of gas–liquid membrane contacting process on CO_2 absorption performance: A modeling study", Journal of Membrane Science, 372 (2011) 75-86. (IF-2009 = 3.203)
2) Somnuk Boributh, Suttichai Assabumrungrat, Navadol Laosiripojana and Ratana Jiraratananon, "A modeling study on the effects of membrane characteristics and operating parameters on physical absorption of CO_2 by hollow fiber membrane contactor", J. Mem. Sci., accepted June 20, 2011 (IF 2009 = 3.203)

3.5 กรรมการในงานประชุมวิชาการระดับนานาชาติ

- ศ.ดร.สุทธิชัย อัสสะบำรุงรัตน์ ทำหน้าที่เป็น Organizing Committee of The 4th Asian Polyolefin Workshop 2011 (APO2011) จัดโดยจุฬาลงกรณ์มหาวิทยาลัย ระหว่างวันที่ 24 – 27 กรกฎาคม 2554
- ศ.ดร.สุทธิชัย อัสสะบำรุงรัตน์ ทำหน้าที่เป็น Scientific committee ของงานประชุมทางวิชาการ The 6th Asia Pacific Chemical Reaction Engineering Symposium จัดที่ Beijing, China, ระหว่างวันที่ 18-21 กันยายน 2554

- ศ.ดร.สุทธิชัย อัสสะบำรุงรัตน์ ทำหน้าที่เป็น Scientific committee ของงานประชุมทางวิชาการ International Symposium in Chemical Reaction Engineering (ISCRE 22) จัดที่ Maastricht, The Netherlands, ระหว่างวันที่ 2-5 กันยายน 2555

3.6 วิทยากรบรรยาย

1. ศ.ดร.สุทธิชัย อัสสะบำรุงรัตน์ เป็นวิทยากรบรรยายในหัวข้อ “เรื่องราวของงานวิจัยที่มีทั้งการสร้างความรู้และการแปลงความรู้” การประชุมนักวิจัยใหม่พบเมธีวิจัยอาวุโส สกว. ครั้งที่ 8 โรงแรมฮอลิเดอินน์ รีสอร์ท รีเจนท์ บีชชะอำ จังหวัดเพชรบุรี วันที่ 16-18 ตุลาคม 2551
2. ศ.ดร.สุทธิชัย อัสสะบำรุงรัตน์ เป็นวิทยากรบรรยายในหัวข้อ “How to be a professor before 40?” การประชุมนักวิจัยใหม่พบเมธีวิจัยอาวุโส สกว. ครั้งที่ 8 โรงแรมฮอลิเดอินน์ รีสอร์ท รีเจนท์ บีชชะอำ จังหวัดเพชรบุรี วันที่ 16-18 ตุลาคม 2551
3. ศ.ดร.สุทธิชัย อัสสะบำรุงรัตน์ เป็นวิทยากรรับเชิญบรรยายในหัวข้อ “Multifunctional Reactor: A Tool for Process Intensification” ในการประชุมทางวิชาการ The 19th Thailand Chemical Engineering and Applied Chemistry Conference, October 26-27, 2009, Kanchanaburi, Thailand
4. ศ.ดร.สุทธิชัย อัสสะบำรุงรัตน์ เป็นวิทยากรในการประชุมเชิงปฏิบัติการ เรื่อง เทคนิคการเขียนบทความวิจัยเพื่อการตีพิมพ์ในวารสารระดับนานาชาติ วันที่ 28 กรกฎาคม 2552 จัดโดยส่วนส่งเสริมและพัฒนาวิจัย สำนักบริหารวิชาการ จุฬาลงกรณ์มหาวิทยาลัย
5. ศ.ดร.สุทธิชัย อัสสะบำรุงรัตน์ เป็นวิทยากรรับเชิญบรรยายในหัวข้อ “Hydrogen Production and Solid Oxide Fuel Cell” Society of Chemical Engineers Japan, Tokai branch seminar" Department of Chemical Engineering, Nagoya University 22 ตุลาคม 2553
6. ศ.ดร.สุทธิชัย อัสสะบำรุงรัตน์ เป็นวิทยากรบรรยายในหัวข้อ “How to be a professor before 40?” การประชุมสัมมนาอาจารย์ใหม่คณะวิศวกรรมศาสตร์และเทคโนโลยีอุตสาหกรรม มหาวิทยาลัยศิลปากร จังหวัดสมุทรสาคร วันที่ 28 ตุลาคม 2553

4. สรุปผลงาน

ตารางที่ 1 สรุปผลงานตามข้อเสนอโครงการและผลงานรวมจนถึงปัจจุบัน

ผลงาน	ปีที่ 1	ปีที่ 2	ปีที่ 3	รวม	ผลงานที่ได้จนถึงปัจจุบัน (3 ปี)
1. บทความในวารสารนานาชาติ	8	8	8	**24**	**24+ (3)[1] + (1)[2]**
2. Book chapter/reviews	-	-	-	**-**	**3**
3. การเสนอผลงานในที่ประชุมทางวิชาการระดับนานาชาติ	-	-	-	**-**	**16**
4. การเสนอผลงานในที่ประชุมวิชาการในประเทศไทย	-	-	-	**-**	**8**
5. ดุษฎีบัณฑิต	-	1	2	**3**	**4**
6. มหาบัณฑิต	6	6	6	**18**	**20**
7. ผู้ช่วยศาสตราจารย์	-	-	2	**2**	**2**[3]
8. รองศาสตราจารย์	-	1	2	**3**	**1**
9. ศาสตราจารย์	-	-	-	**-**	**1**[4]
10. สัมมนา	1	1	1	**3**	**3**

หมายเหตุ [1] บทความที่อยู่ระหว่างการแก้ไขตามคำแนะนำของ Reviewers

[2] บทความที่อยู่ระหว่างการพิจารณา

[3] อยู่ระหว่างการพิจารณา (ได้ยื่นเอกสารในเดือนมิถุนายน 2554)

[4] อยู่ระหว่างการพิจารณา (ได้ยื่นเอกสารในเดือนมกราคม 2554)

ลงนาม .....

(ศ.ดร. สุทธิชัย อัสสะบำรุงรัตน์)

หัวหน้าโครงการ

ภาคผนวก

ภาคผนวก 1	“Influence of stack arrangement on performance of multiple-stack solid oxide fuel cells with non-uniform potential operation” J. Power Sources, vol. 187 (2009) 1-7.
ภาคผนวก 2	“Design of a Thermally Integrated Bioethanol-Fueled Solid Oxide Fuel Cell System Integrated with a Distillation Column”, J. Power Sources, vol. 187 (2009) 190-203.
ภาคผนวก 3	“Simulation of solid oxide fuel cell systems integrated with sequential CaO–CO_2 capture unit”, Chem. Eng. J., vol. 147 (2009) 336-341.
ภาคผนวก 4	“Modeling of SOFC with Indirect Internal Reforming Operation: Comparison of Conventional Packed-Bed and Catalytic Coated-Wall Internal Reformer”, Int. J. Hydrogen Energy, vol. 34 (2009) 410-421.
ภาคผนวก 5	“Integration of solid oxide fuel cell and palladium membrane reactor: Technical and economic analysis”, Int. J. Hydrogen Energy, 34 (2009) 3894-3907.
ภาคผนวก 6	“Effect of oxygen addition on catalytic performance of carbon dioxide reforming of methane under periodic operation” Int. J. Hydrogen Energy, 34 (2009) 6211-6220.
ภาคผนวก 7	“Effect of Operating Conditions and Gas Flow Patterns on the System Performances of IIR-SOFC Fueled by Methanol” Int. J. Hydrogen Energy, 34 (2009) 615-6424.
ภาคผนวก 8	P. Dokmaingam, S. Assabumrungrat, A. Soottitantawat and N. Laosiripojana, “Modeling of tubular-designed SOFC with Indirect Internal Reforming operation (IIR-SOFC) fed by different primary fuels”, Journal of Power Sources, 195 (2010) 69-78.
ภาคผนวก 9	“Operation viability and performance of SOFC fuelled by different feeds”, Chem. Eng. J., 155 (2009) 411-418.
ภาคผนวก 10	“Effect of calcination temperature on characteristics of sulfated zirconia and its application as a catalyst for isosynthesis”, Fuel Proc. Tech., 91 (2010) 121-126.
ภาคผนวก 11	“Alternative concept for SOFC with direct internal reforming: Benefits from inserting catalyst rod”, AIChE J., 56 (2010) 1639-1650.

ภาคผนวก 12	“Reaction-Extraction-Regeneration System for Highly Selective Oxidation of Benzene to Phenol” Chemical Engineering Communications, 197 (2010) 1140-1151.
ภาคผนวก 13	“Isosynthesis via CO hydrogenation over SO_4-ZrO_2 catalysts”, J. Ind. Eng. Chem., 16 (2010) 411-418.
ภาคผนวก 14	“Performance assessment of SOFC systems integrated with bio-ethanol production and purification processes”, Engineering Journal, 13 (2010) 1-14.
ภาคผนวก 15	“Technical and economic study of integrated system of solid oxide fuel cell, palladium membrane reactor, and CO_2 sorption enhancement unit”, Chem. Eng. Process., 49 (2010) 1006-1016
ภาคผนวก 16	“Effect of operation modes on hydrogen production from glycerol at energy self-sufficient conditions: Thermodynamic analysis”, International Journal of Hydrogen Energy, 35 (2010) 10257-10270.
ภาคผนวก 17	“Analysis of Planar Solid Oxide Fuel Cells based on Proton-Conducting Electrolyte”, Solid State Ionics, 181 (2010) 1568-1576.
ภาคผนวก 18	“Reactive Distillation for Biodiesel Production from Soybean Oil” Korean Journal of Chemical Engineering, 28 (2011) 649-655.
ภาคผนวก 19	“Modeling of IT-SOFC with indirect internal reforming operation fueled by methane: Effect of oxygen adding as autothermal reforming”, International Journal of Hydrogen Energy, 35 (2010) 13271-13279.
ภาคผนวก 20	“Partial Oxidation of Benzene Catalyzed by Vanadium Chloride in Novel Reaction-Extraction-Regeneration System” Chem. Eng. Proc., in press.
ภาคผนวก 21	“Thermodynamic analysis for gasification of Thailand rice husk with air, steam, and mixed air/steam for hydrogen-rich gas production”, International Journal of Chemical Reactor Engineering, 8 (2010) 1-27.
ภาคผนวก 22	“Performance improvement of bioethanol fuelled solid oxide fuel cell system by using pervaporation”, International Journal of Hydrogen Energy, accepted January, 2011 (IF-2009 = 3.945).
ภาคผนวก 23	“Hydrogen Production from Glycerol Steam Reforming for Low and High-Temperature PEMFCs”, International Journal of Hydrogen Energy, 36 (2011) 267-275. (IF-2009 = 3.945).

ภาคผนวก 24	“Thermodynamic analysis of hydrogen production from glycerol at energy self-sufficiency conditions”, Can. J. Chem. Eng., accepted April 14, 2011 (IF-2009 = 0.63).

ภาคผนวก 1

Journal of Power Sources 187 (2009) 1–7

Contents lists available at ScienceDirect

Journal of Power Sources

journal homepage: www.elsevier.com/locate/jpowsour

Influence of stack arrangement on performance of multiple-stack solid oxide fuel cells with non-uniform potential operation

S. Assabumrungrat[a,*], N. Ruangrassamee[a], S. Vivanpatarakij[a], N. Laosiripojana[b], A. Arpornwichanop[c]

[a] Center of Excellence in Catalysis and Catalytic Reaction Engineering, Department of Chemical Engineering, Faculty of Engineering, Chulalongkorn University, Bangkok 10330, Thailand
[b] The Joint Graduate School of Energy and Environment, King Mongkut's University of Technology Thonburi, Bangkok 10140, Thailand
[c] Control and Systems Engineering, Department of Chemical Engineering, Faculty of Engineering, Chulalongkorn University, Bangkok 10330, Thailand

ARTICLE INFO

Article history:
Received 15 June 2008
Received in revised form 8 September 2008
Accepted 20 October 2008
Available online 7 November 2008

Keywords:
Non-uniform potential
Pressure drop
Solid oxide fuel cell
Series/parallel
Multi-stack

ABSTRACT

The performance of multiple-stack solid oxide fuel cells (SOFCs) with different stack arrangements is compared with respect to the presence of an in-stack pressure drop. It was demonstrated in our previous work that when a multiple-stack SOFC is arranged in series and the operating voltages are allowed to vary among the different stacks, an improved performance over a conventional SOFC (stacks arranged in parallel and operated under the same operating voltage) can be realized. Nevertheless, the differences in pressure drop and the required power for compression among the different operations were not taken into account. In the study reported here, it is demonstrated that the pressure drop in the stack depends not only on the feed rate and operating voltage, but also on the stack arrangement. The pressure drop in the anode channels is about half that in the cathode channels. The configuration of stacks in series with compressors installed only at the inlets of the first stack is the best option as it shows the highest electrical power generation. The pressure drops in the anode and cathode channels are about 4.7 and 3.75 times those in the corresponding channels of the conventional case with the stacks arranged in parallel. In addition, when considering the net obtained electrical power, it appears that multiple-stack SOFCs with stacks arranged in series are not as attractive as the conventional SOFC because they require much higher compression power. Therefore, it is suggested that a new stack design with a low pressure drop is required for the concept of multiple-stack SOFC with non-uniform potential operation to become practical.

1. Introduction

Fuel cells are considered to be an attractive technology for energy conversion because of their better environmental friendliness, practically noise-free operation, and higher efficiency. Nevertheless, the use of fuel cell is still limited due to the high cost of cell stacks. Consequently, much effort has been made to improve the performance fuel cells and their systems. For example, stack cell components with better characteristics have been explored [1–3]. Some researchers have focused on integrating a fuel cell with other units such as a gas turbine (GT) [4]. Among the several procedures aimed at improving fuel cell performance, non-uniform potential operation (NUP) or multiple-stack operation, whose concept is based on arranging stacks in series and allowing operating voltages to be varied stack-by-stack, is an interesting approach. Under such operation, the cell is run close to its theoretical potential, and therefore results in lower overpotential losses and thus higher efficiency.

The concept of multiple-stack operation has been studied by some researchers. George and Lames [5] stated that the United States Department of Energy (DOE) proposed a multiple-stack fuel cell system with five serial stages of cells in order to reduce the regenerative heat for fuel and air, and to extend the operating temperature range. Moreover, Senn and Poulikakos [6] investigated the performance of polymer electrolyte membrane fuel cells (PEMFCs) that were divided into many stages of equal stage size. It was found that the non-uniform potential operation offers enhanced maximum electrical power densities compared with the traditional concept involving uniform potential operation. An improvement in maximum power density of 6.5% was reported. For a molten carbonate fuel cell (MCFC), it was reported that an improvement in electrical efficiency of about 1% could be achieved by splitting the cell area into two segments [7]. This conclusion was based on both analytical mathematical modelling and simplified flowsheet calculations. Multiple-stack operations of a MCFC with a different flow arrangement have been studied [8]. When both

* Corresponding author. Fax: +66 2 218 6877.
E-mail address: Suttichai.A@chula.ac.th (S. Assabumrungrat).

0378-7753/$ – see front matter © 2008 Elsevier B.V. All rights reserved.
doi:10.1016/j.jpowsour.2008.10.114

Nomenclature

a	first ohmic resistance constant as shown in Eq. (12) (Ω m)
b	second ohmic resistant constant as shown in Eq. (12) (K)
C_p	specific heat capacity at constant pressure (J mol^{-1} K^{-1})
C_V	specific heat capacity at constant volume (J mol^{-1} K^{-1})
D	hydraulic diameter (m)
E_0	open-circuit voltage (V)
f	friction factor
F	Faraday constant (96485.34 C mol^{-1})
g_c	proportionality factor (kg m N^{-1} s^{-2})
i	current density (A m^{-2})
L	cell length (m)
m	constant polarization parameters
$\dot{m}$	molar flow rate of gas (mol s^{-1})
p	partial pressure (atm)
P	power (kW)
R	universal gas constant (8.31447×10^{-3}) (kJ mol^{-1} K^{-1})
T	absolute temperature (K)
T_1	feed temperature to compressor (K)
T_2	isentropic temperature (K)
u	gas velocity (m s^{-1})
U_f	fuel utilization (%)
V	operating voltage (V)

Greeks letters

η	overpotential (Ω m^2)
η_c	isentropic efficiency
γ	ratio of specific heat capacities of a gas, C_p/C_V
δ	thickness (m)
ρ	specific ohmic resistance (Ω m)
φ	potential (V)

Subscripts

A	anode
Act	activation
C	cathode
Conc	concentration
Ohm	ohmic

the anode and cathode streams were passed in series along the stacks, the improvement in performance was about 0.6%. Additionally, when the anode stream flowed in series while the cathode streams were flowed in parallel, an improved performance up to 0.3% was achieved. Liebhafsky and Cairns [9] and Selimovic and Palsson [10] applied the concept of multiple-stack operation to a solid oxide fuel cell (SOFC). It was found that an improvement in power output of about 5% could be obtained from their systems. Our previous work [11] determined suitable operating voltages and the number of cell sections for an SOFC system. The cell was divided into equal sections in term of fuel utilization (U_f) and no pressure drop was assumed. It was reported that no significant improvement was obtained when the cell was divided into more than two sections and the increase in electrical efficiency was within 10%.

The concept of non-uniform potential operation is not practically implemented for single stack operation because the design of current-collectors becomes very complicated. It is generally carried out by arranging the multiple stacks in series and operating the voltages at different values among the stacks. Under this operation, as each stack is operated under a small value of fuel utilization, higher flow rates of fuel and air in each stack and thus a higher pressure drop and a higher power consumption for operating compressors are inevitable. Therefore, it is the aim of this work to determine whether the gained electrical power from such operation can compensate the attendant higher demands in energy. Two configurations of multiple-stack SOFCs arranged in series with non-uniform potential operation (one with compressors installed only at the inlets of the first stack and the other with compressors installed at the inlets of each stack) are considered. The performances in terms of pressure drop, power consumption at compressors, generated electrical power and net electrical power are calculated and compared with those of a conventional SOFC with multiple stacks arranged in parallel and operated at the same operating voltage.

2. Theory

2.1. Mathematical model

A planar-type SOFC with co-flow configuration is considered as it has been reported to offer a higher power density than a tubular-type SOFC [12]. The higher power density of the planar-type SOFC is due to the shorter current paths that result in low ohmic overpotential. Moreover, the planar-type SOFC is simple to fabricate and can be manufactured in various configurations [13]. A schematic diagram of the planar-type SOFC stack is given in Fig. 1. Typical information on the system has been given by Iwata et al. [14] and Pasaogullari and Wang [15]. The typical SOFC dimensions [16,17] adopted for this study are given in Fig. 2. In a single cell, the interconnects are in the form of ribs with twenty air channels for the air-side interconnect and 20 fuel channels for the fuel-side interconnect corresponding to the location of the rib roots, and the gas channel locations to the rib tips. The stack module is a column of 100 cells (30 cm × 30 cm × 60 cm) joined with interconnects. Thus, one standard stack in this work has a total cell area of 1.2 m^2. The multiple stacks are connected in different configurations, as will be described in the next section. It should be noted that as the cell channels of the planar-type SOFC usually have slimmer cross-sectional area than those of the tubular-type SOFC, the planar-type SOFC is likely to encounter greater influence of generated pressure drop in the cell channels. This effect is taken into account in this work. The pressure drop and required compression power can be calculated using the following equations (refer to list of

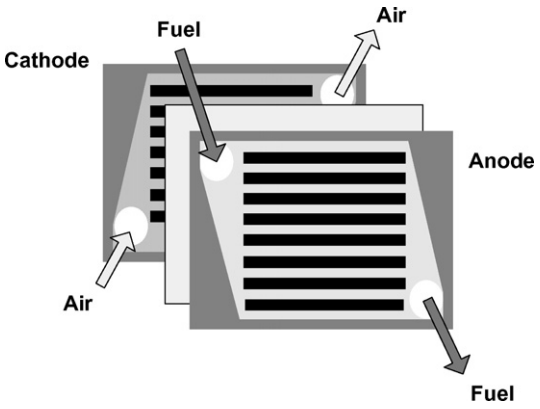

Fig. 1. Schematic diagram of planar-type SOFC stack.

nomenclature):

$$\Delta P = fp\frac{L}{D}\frac{u^2}{2g_c} \quad (1)$$

$$\text{Power} = \dot{m}C_p\frac{T_1}{\eta_c}\left(\left(\frac{P_2}{P_1}\right)^{\gamma-1/\gamma} - 1\right) \quad (2)$$

$$\eta_c = \frac{T_1}{T_2 - T_1}\left(\left(\frac{P_2}{P_1}\right)^{\gamma-1/\gamma} - 1\right) \quad (3)$$

$$\frac{T_2'}{T_1} = \left(\frac{P_2}{P_1}\right)^{\gamma-1/\gamma} \quad (4)$$

The SOFC can be operated with a non-hydrogen fuel such as methane, which is the fuel used in this work. A reformer is generally required to process the fuel with a reforming agent (e.g., steam) to a hydrogen-rich stream before feeding to the SOFC stack. Methane steam reforming is followed by the water–gas shift reaction. It is assumed that the equilibrium reactions take place at 973 K, to yield an outlet gas composition of 1.50% CH_4, 12.77% CO, 5.93% CO_2, 62.01% H_2 and 17.79% H_2O. In the SOFC stack, it is assumed that only hydrogen reacts electrochemically with oxygen. The equilibrium water–gas shift reaction takes place along the stack channel to convert CO to hydrogen in the anode stream.

2.2. Electrochemical model

The electrochemical reactions of hydrogen and oxygen taking place in the cell are as follows:

$$\text{anode}: H_2 + O^{2-} = H_2O + 2e^- \quad (5)$$

$$\text{cathode}: O_2 + 4e^- = 2O^{2-} \quad (6)$$

The cell is divided into small cell elements in calculations of the electrochemical performance. The actual SOFC voltage is always lower than its open-circuit value because of the presence of various irreversible losses, i.e., activation overpotential (η_{Act}), ohmic overpotential (η_{Ohm}) and concentration overpotential (η_{Conc}). The activation overpotential Eqs. (7)–(10) can be determined from the Butler–Volmer equation [18]. The ohmic overpotential (Eqs. (11) and (12)) is calculated from the resistivity and an equivalent area corresponding to the thickness of the electrodes or electrolyte. The resistivity for the SOFC materials (Table 1) is based on the values reported by Bessette et al. [19].

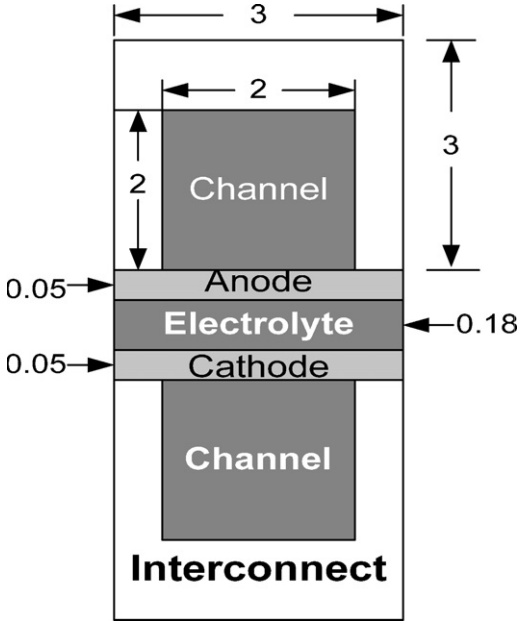

Fig. 2. Dimensions of fuel/air channels in SOFC stack (units in mm).

Table 1
Summary of cell components and their resistivities.

Materials (anode/electrolyte/cathode)	Ni–YSZ/YSZ/LSM–YSZ
Anode ohmic resistance constant	$a = 0.0000298$, $b = -1392$
Cathode ohmic resistance constant	$a = 0.0000811$, $b = 600$
Electrolyte ohmic resistance constant	$a = 0.0000294$, $b = 10350$
Interconnect ohmic resistance constant	$a = 0.0001256$, $b = 4690$

Activation overpotential:

$$i = i_0\left[\exp\left(\frac{\alpha n_e F\eta_{Act}}{RT}\right) - \exp\left(-\frac{(1-\alpha)n_e F\eta_{Act}}{RT}\right)\right] \quad (7)$$

$$\eta_{Act} = \frac{2RT}{n_e F}\ \sinh^{-1}\left(\frac{i}{i_0}\right);\quad \text{where } \alpha = 0.5 \quad (8)$$

$$i_{0,A} = 5.5\times 10^8\left(\frac{p_{H_2}}{p}\right)\left(\frac{p_{H_2O}}{p}\right)\ \exp\left(\frac{-100\times 10^3}{RT}\right) \quad (9)$$

$$i_{0,C} = 7.0\times 10^8\left(\frac{p_{O_2}}{p}\right)^m\ \exp\left(\frac{-120\times 10^3}{RT}\right) \quad (10)$$

Ohmic overpotential:

$$\eta_{Ohm} = \sum \rho_j\delta_j \quad (11)$$

$$\rho_j = a_j\ \exp(b_jT) \quad (12)$$

It is assumed that the SOFC stacks are operated under steady-state and isothermal conditions. In this case, the operating temperature is maintained at 1173 K. To simplify calculations of the SOFC performance, the concentration overpotential due to the mass transport effect is neglected. Such overpotential becomes important at low concentration of the reactant gases and high values of current density. Therefore, the calculations in this study are performed only within moderate ranges of current density (<8000 A m^{-2}).

2.3. System configurations

The following three configurations of multiple-stack SOFC are considered:

(1) *Configuration A*: Multiple-stack SOFC with stacks arranged in parallel. There is only one set of compressors installed at the feed inlets (Fig. 3a). The outlet pressure of each stack is at atmospheric pressure. This configuration is a conventional SOFC system.
(2) *Configuration B*: Multiple-stack SOFC with stacks arranged in series with only one set of compressors installed at the inlets of the first stack (Fig. 3b). The outlet pressure of the last stack is at atmospheric pressure.
(3) *Configuration C*: Multiple-stack SOFC with stacks arranged in series with compressors installed at the inlets of each stack. The outlet pressure of each stack is at atmospheric pressure (Fig. 3c).

In this study, only two stacks are considered according to the previous report [11] indicating that the performance improvement of the multiple stacks arranged in series with non-uniform potential operation becomes less significant when the number of stacks is more than two.

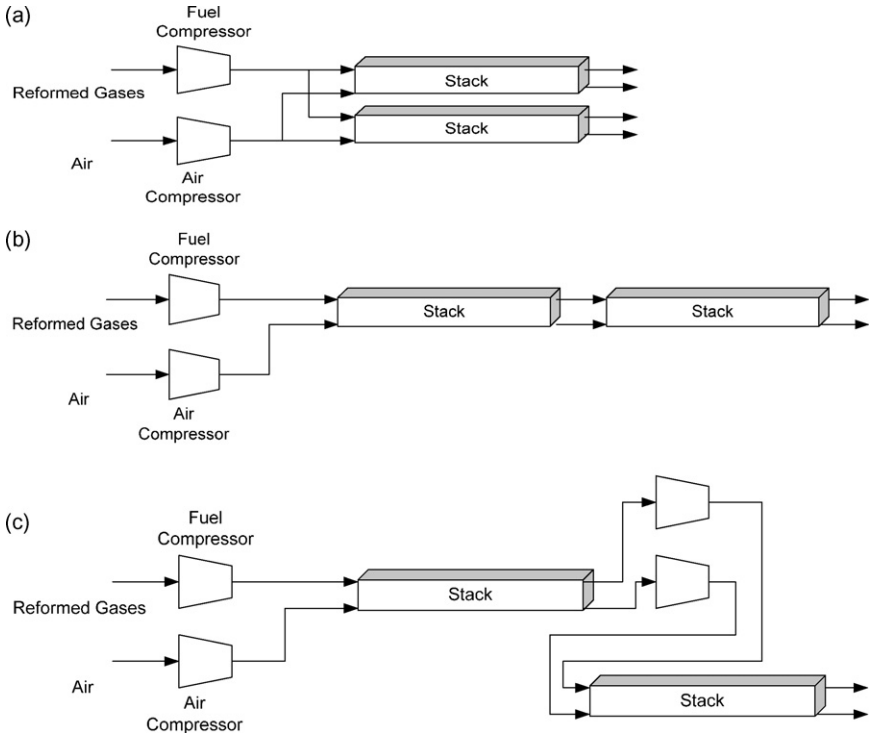

Fig. 3. Different configurations of multiple-stack SOFC: (a) parallel stacks with one set of compressors inlets of SOFC stack; (b) stacks in series with compressors at inlets of first SOFC stack; (c) stack in series with compressors at inlets of each stack.

3. Results and discussion

3.1. Model validation

The developed model was validated with results from the previous literature [20]. Fig. 4 shows the characteristic *I–P* and *I–V* curves for the system fed by pure hydrogen as the fuel and air as the oxidant. The cell was operated at 1173 K and a fuel utilization (U_f) of 80%. The continuous lines show the simulation results from this study while symbols show those from the previous work. Based on the same operating condition, the comparison shows good agreement between those data with small deviation within 4.6%, indicating that our model is capable of predicting the performance of a planar SOFC. It should be noted that the discrepancy may be arisen from our assumption that neglects the effect of concentration overpotential due to the mass transport effect, unlike the reference work. It was reported that concentration overpotential becomes an important loss when the system is operated at low concentrations of the reactant gases and high values of current density [21]. Therefore, to ensure the reliability of our model, the simulations in this study are performed within the range of moderate current density (<8000 A m^{-2}).

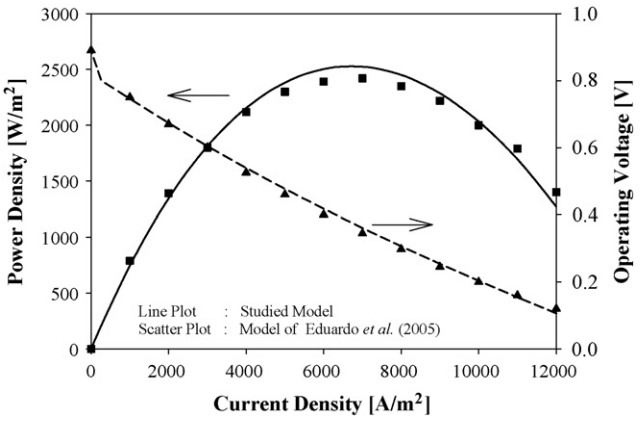

Fig. 4. Characteristic curves of SOFC (anode feed = pure H_2, cathode feed = air, U_f = 80% and T = 1173 K).

3.2. Generated pressure drop in single-stack SOFC

In practical operation, as the stack is divided into many small cell channels, particularly for a planar-type stack, compressors are required to feed the fuel and air into the anode and cathode channels, respectively. Fig. 5 shows the pressure drop at the anode and cathode channels at different methane feed rates and operating voltages. In all calculations, the pressures at the channel exits are always maintained at atmospheric pressure. It is obvious that both methane feed rate and operating voltage influence the pressure drop. In addition, the anode pressure drop is much lower than the cathode pressure drop, i.e., by about a half. The observed results agree well with numerical simulation results of Koh et al. [22] who calculated the generated pressure drop in both anode and cathode channels by varying the channel depth [19]. It was found that the anode pressure drop is approximately 45–60% of the cathode pressure drop. In this work, it was found that the maximum calculated pressure drops in the anode and cathode channels are not higher than 4% and 6% of inlet pressure, respectively. Moreover, it is clear that when the methane feed rate increases, a higher pressure drop is observed. In addition, the pressure drop also varies with operating voltage. When the stack is run at a higher operating voltage and the methane feed rate is kept constant, less oxygen is transferred to the anode according to the characteristic *I–V* curve (Fig. 4) and thus the pressure drop in the cathode increases. The pressure drop in the anode channel also varies due to the difference in the anode gas compositions (especially H_2 and H_2O) that arises from the change of operating voltage. It should be noted that the operat-

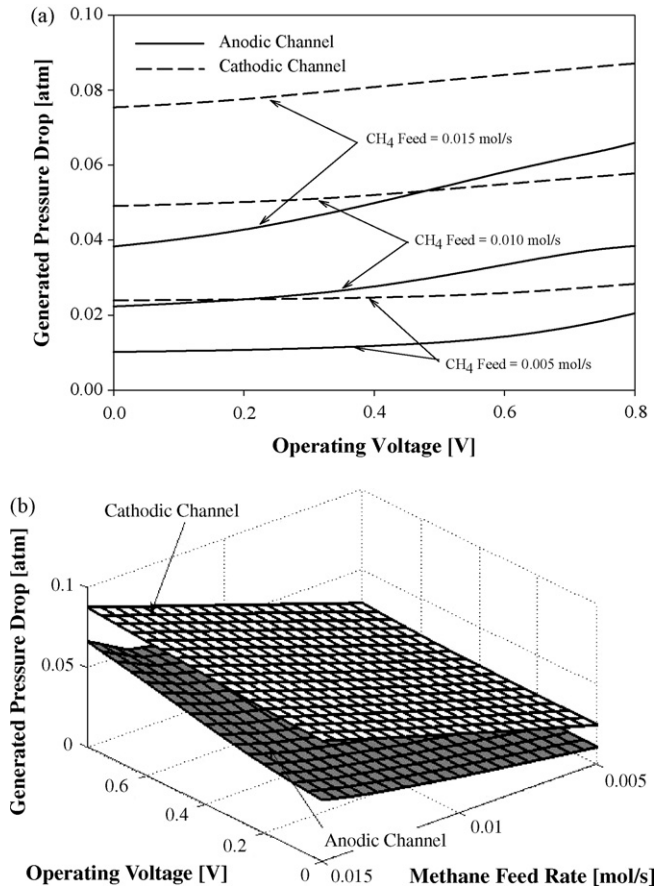

Fig. 5. Effects of operating voltage and methane feed rate on pressure drop in anode and cathode channels of single-stack SOFC.

ing voltage is closely related to the current density according to the *I–V* characteristic curve, whereas the methane feed rate is closely related to fuel utilization (U_f) (Fig. 5).

In SOFC operation, part of the electrical power obtained from the SOFC is consumed by the compressors that elevate the pressures of both fuel and air to the desired values. The effects of operating voltage and methane feed rate on the power generated from the SOFC and the power consumption by the compressors in a single-stack SOFC are shown in Fig. 6. Considering the solid lines, it is found that the generated power follows the form of an upturned curve. By contrast, the percentage of power consumption at the compressor shows an inverse tendency to the generated power, that is, percentage of power consumption increases rapidly at the lowest and highest operating voltages. This obviously shows that the presence of a pressure drop influences the performance of SOFC, depending on the levels of the operating voltage and methane feed rate. In particular, the fraction of energy required for the compressor depends significantly on these two parameters. At maximum generated power, the compression power is within the range of 10% of the generated power. This shows that the power consumption by the compressor is not pronounced as long as the power obtained from the SOFC is high. It should be noted that when the multiple-stack SOFC is arranged in series, the flow rates in each stack become much higher and thus the pressure drop and power consumption for operating the compressors should become more significant.

3.3. Performance of multiple-stack SOFCs with different stack arrangements

The performance of three configurations of multiple-stack SOFCs have been compared with respect to the effect of the generated pressure drop. The influence of operating voltage in the first stack on the generated electrical power is demonstrated in Fig. 7. Three values of the operating voltage of the second stack (0.55, 0.65 and 0.75 V) are considered. The solid line represents the results for the conventional SOFC whose stacks are arranged in parallel and operated at the same operating voltage. It is clear that there are some ranges of operating voltages in which the arrangement in series offers higher generated electrical power than that in parallel. For the series arrangement with two different configurations of stacks and compressors, however, the configuration with one set of compressors installed at the inlets of the first stack always offers slightly higher power than that with compressors at the inlets of each SOFC stack. For the former system, it is necessary to compress the fuel and air at higher inlet pressures at the first stack in order to guarantee that the outlet pressure at the last stack is at atmospheric pressure. Due to this pressurized condition, the electrochemical performance becomes better. Thus the configuration in series with one set of compressors installed at the inlets of the first stack is a preferable choice in terms of generated power (Fig. 7). Nevertheless, due to high inlet pressure, it is essential to consider the additional power consumption by the compressors so as to calculate the net electrical power generation, which is an important

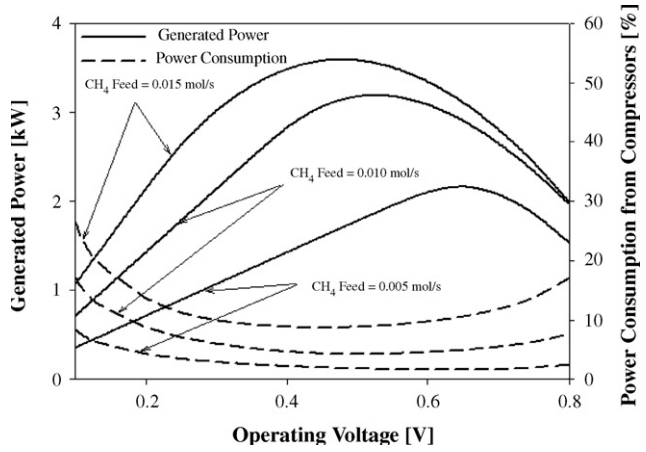

Fig. 6. Effects of operating voltage and methane feed rate on electrical power generation and power requirement for compressors in single-stack SOFC.

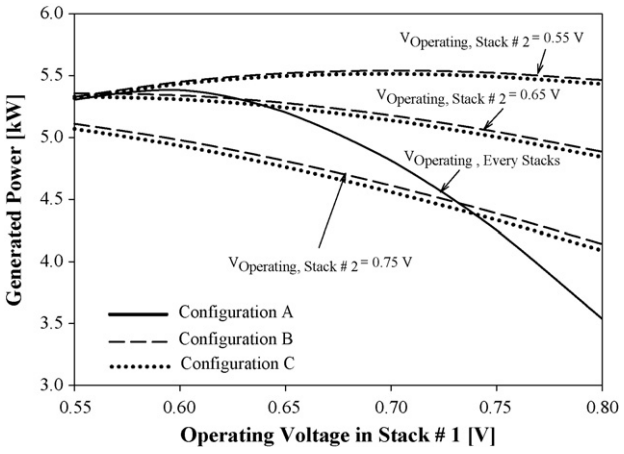

Fig. 7. Effects of operating voltages and configuration of multiple-stack SOFC on electrical power generation.

indicator of the practical feasibility of the use of the best configuration of multiple-stack SOFC.

Among the three configurations, it is important to understand that the flow rates of the fuel and air streams through stacks networked in series are much larger than those through stacks connected in parallel even though the same initial feed streams are used. For the SOFC configuration in parallel, the initial feed streams are divided into many streams corresponding to the number of stacks arranged in parallel. For stacks arranged in series, however, the initial feed streams are not divided but fed directly into the first stack and others in the series of many stacks. From the results discussed in Section 3.2, it is obvious that an increased flow rate creates larger pressure drops. Thus, it is certain that both configurations in series should encounter larger generated pressure drop than the configuration in parallel. As shown in Fig. 8, pressure drops in series configurations are higher by about 4.7 and 3.75 times in the anode and cathode channels, respectively, compared with the parallel configuration. The pressure drop also depends on the operating voltage as mentioned earlier in Section 3.2. Considering the power consumption by the compressors, Fig. 9 shows that multiple stacks arranged in series with one set of compressors installed at the inlets of the first stack consume less power for operating the compressors than the arrangement in which the staged compressors are installed at the inlets of each SOFC stack. Compared with the conventional SOFC with stacks arranged in parallel, it is clear that the power consumption by series multiple-stack SOFCs are about 5–6 times higher.

As reduced from the above results there are some contrasts between the results for generated power from a SOFC and power consumption of the compressors. To propose the best configuration among the different stack arrangements, it is necessary to examine the net obtained electrical power. The data given in Fig. 10, indicate that the maximum net electrical power from the series multiple-stack SOFC is still less than that of the conventional parallel multiple-stack SOFC although the generated electrical power could be higher, as shown in Fig. 7. This is due to the presence of a higher pressure drop when the stacks are arranged in series. Thus, for the conventional planar-type stack, the use of non-uniform potential operation is not attractive in items of practical operation. It is necessary to develop a new stack design with a low pressure drop in order to make the concept of a multiple-stack SOFC with non-uniform potential operation become practical. A tubular-type stack could be a possible choice; but, various aspects such as cell performance and stack power density need to be taken into account. It should again noted that the electrical performance and stack pressure drop are also dependent on operating temperature. In general, increasing the operating temperature improves the electrical performance; but choices of materials and seal problem then become critical issues. A higher operating temperature also increases the pressure drop in the stack. This selection of cell components could also influence the performance of multiple-stack SOFCs. A number of efforts have addressed the search for better cell components, that would allow stack size, and consequently stack pressure drop, to become smaller. The influence works on the effects of cell components and operating temperature should be further investigated.

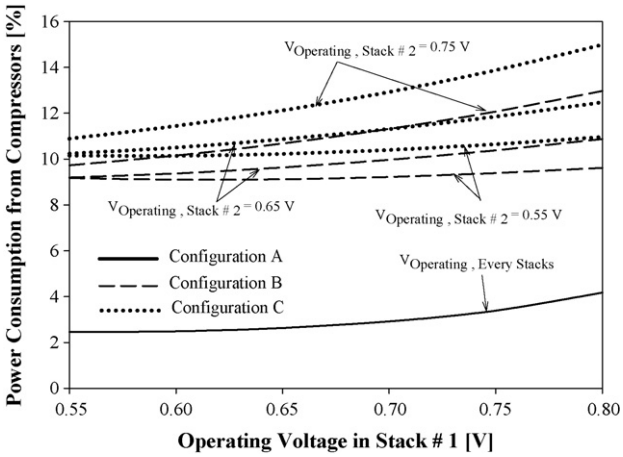

Fig. 9. Effects of operating voltages and configuration of multiple-stack SOFC on power requirement for compressors.

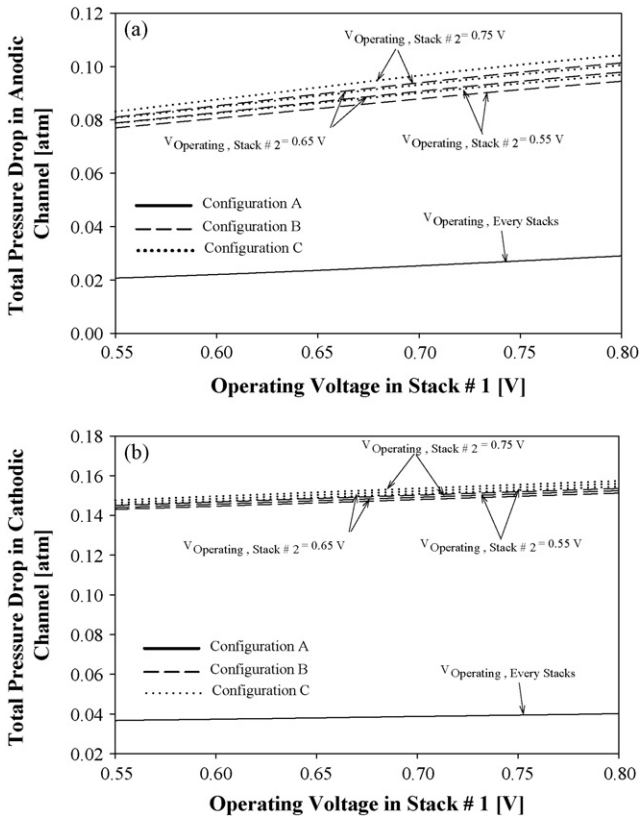

Fig. 8. Effects of operating voltages and configuration of multiple-stack SOFC on total pressure drop in anode and cathode channels.

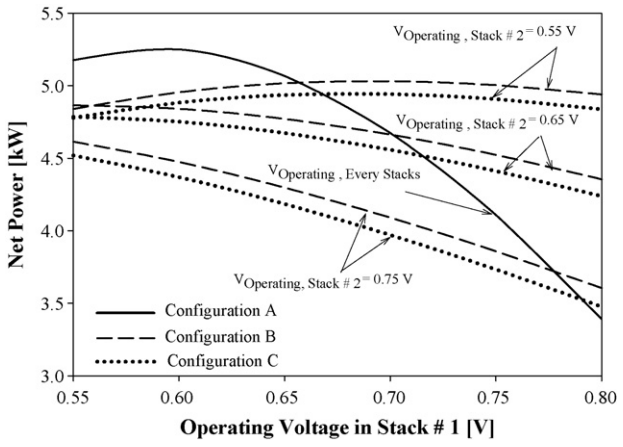

Fig. 10. Effects of operating voltages and configuration of multiple-stack SOFC on net electrical power generation.

4. Conclusions

The performance of multiple-stack SOFCs with different stack arrangements has been evaluated. Both configurations of series multiple-stack SOFCs can offer higher generated electrical power than conventional parallel multi-stack counterparts when operating voltages of the stacks are carefully selected. Nevertheless, due to the higher in-stack pressure drop, and thus higher power consumption on compressors, it appears that the conventional SOFC is the best configuration in terms of net power generation. It is therefore suggested that a new stack design with a low pressure drop is required for a multiple-stack SOFC with non-uniform potential operation to prove practical.

Acknowledgement

The support from the Thailand Research Fund and Commission on Higher Education is gratefully acknowledged.

References

[1] S.P. Yoon, J. Han, S.W. Nam, T.H. Lim, S.A. Hong, J. Power Sources 136 (2004) 30–36.
[2] S.D. Kim, S.H. Hyun, J. Moon, J.H. Kim, R.H. Song, J. Power Sources 139 (2005) 67–72.
[3] S.P. Simner, J.F. Bonnett, N.L. Canfield, K.D. Meinhardt, J.P. Shelton, V.L. Sprenkle, J.W. Stevenson, J. Power Sources 113 (2003) 1–10.
[4] P. Kuchonthara, S. Bhattacharya, A. Tsutsumi, J. Power Sources 124 (2003) 65–75.
[5] T.J. George, R.J. Lames, Multi-stage Solid Stage Fuel Cell Power Plant Concept, National Energy Technology Laboratory, 1998.
[6] S.M. Senn, D. Poulikakos, Electrochem. Commun. 7 (2005) 773–780.
[7] F. Standeart, Analytical fuel cell modelling and energy analysis of fuel cells, Ph.D. Thesis, Delft University of Technology, 1998.
[8] S.F. Au, N. Woudstra, K. Hemmes, J. Power Sources 122 (2003) 28–36.
[9] H.A. Liebhafsky, E.J. Cairns, Fuel Cells and Fuel Batteries, Wiley, 1968.
[10] A. Selimovic, J. Palsson, J. Power Sources 106 (2002) 76–82.
[11] S. Vivanpatarakij, S. Assabumrungrat, N. Laosiripojana, J. Power Sources 167 (2007) 139–144.
[12] M.A. Khaleel, Z. Lin, P. Singh, W. Surdoval, D. Collin, J. Power Sources 130 (2004) 136–148.
[13] H. Yakabe, T. Ogiwara, M. Hishinuma, I. Yasuda, J. Power Sources 93 (2001) 1–7.
[14] M. Iwata, T. Hikosaka, M. Morita, T. Iwanari, K. Ito, K. Onda, Y. Esaki, Y. Sakaki, S. Nagata, Solid State Ionics 132 (2000) 297–308.
[15] U. Pasaogullari, C.Y. Wang, Electrochemical Society Proceeding, 2003.
[16] P. Costamagna, K. Honegger, J. Electrochem. Soc. 145 (1998) 3995–4007.
[17] J.D.J. Van Der Steen, B. Kenny, J.G. Pharoah, K. Karan, Proceedings of Hydrogen and Fuel Cells, 2004.
[18] J. Newman, A.K. Thomas, Electrochemical Systems, Wiley, 2004.
[19] N.F. Bessette, W.J. Wepfer, J.A. Winick, J. Electrochem. Soc. 142 (1995) 3792–3800.
[20] E. Hernandez-Pacheco, M.D. Mann, P.N. Hutton, D. Singh, K.E. Martin, Int. J. Hydrogen Energy 30 (2005) 1221–1233.
[21] S.H. Chan, K.A. Khor, X.T. Xia, J. Power Sources 93 (2001) 130–140.
[22] J.H. Koh, H.K. Seo, Y.S. Yoo, H.C. Lim, Chem. Eng. J. 87 (2002) 367–379.

ภาคผนวก 2

Journal of Power Sources 187 (2009) 190–203

Contents lists available at ScienceDirect

Journal of Power Sources

journal homepage: www.elsevier.com/locate/jpowsour

Design of a thermally integrated bioethanol-fueled solid oxide fuel cell system integrated with a distillation column

W. Jamsak[a], P.L. Douglas[b,*], E. Croiset[b], R. Suwanwarangkul[c], N. Laosiripojana[d], S. Charojrochkul[e], S. Assabumrungrat[a]

[a] Center of Excellence in Catalysis and Catalytic Reaction Engineering, Department of Chemical Engineering, Faculty of Engineering, Chulalongkorn University, Thailand
[b] Department of Chemical Engineering, University of Waterloo, Canada
[c] School of Bio-Chemical Engineering and Technology, Sirindhorn International Institute of Technology, Thammasart University-Rangsit Campus, Patum Thani 12121, Thailand
[d] The Joint Graduate School of Energy and Environment, King Mongkut's University of Technology, Thonburi, Thailand
[e] National Metal and Materials Technology Center (MTEC), Thailand

ARTICLE INFO

Article history:
Received 21 May 2008
Received in revised form 1 September 2008
Accepted 2 September 2008
Available online 20 September 2008

Keywords:
Solid oxide fuel cell
Integration
Bioethanol
Distillation unit
Heat exchanger network

ABSTRACT

Solid oxide fuel cell systems integrated with a distillation column (SOFC-DIS) have been investigated in this study. The MER (maximum energy recovery) network for SOFC-DIS system under the base conditions (C_{EtOH} = 25%, EtOH recovery = 80%, V = 0.7 V, fuel utilization = 80%, T_{SOFC} = 1200 K) yields Q_{Cmin} = 73.4 and Q_{Hmin} = 0 kW. To enhance the performance of SOFC-DIS, utilization of internal useful heat sources from within the system (e.g. condenser duty and hot water from the bottom of the distillation column) and a cathode recirculation have been considered in this study. The utilization of condenser duty for preheating the incoming bioethanol and cathode recirculation for SOFC-DIS system were chosen and implemented to the SOFC-DIS (CondBio-CathRec). Different MER designs were investigated. The obtained MER network of CondBio-CathRec configuration shows the lower minimum cold utility (Q_{Cmin}) of 55.9 kW and total cost index than that of the base case. A heat exchanger loop and utility path were also investigated. It was found that eliminate the high temperature distillate heat exchanger can lower the total cost index. The recommended network is that the hot effluent gas is heat exchanged with the anode heat exchanger, the external reformer, the air heat exchanger, the distillate heat exchanger and the reboiler, respectively. The corresponding performances of this design are 40.8%, 54.3%, 0.221 W cm^{-2} for overall electrical efficiency, Combine Heat and Power (CHP) efficiency and power density, respectively. The effect of operating conditions on composite curves on the design of heat exchanger network was investigated. The obtained composite curves can be divided into two groups: the threshold case and the pinch case. It was found that the pinch case which T_{SOFC} = 1173 K yields higher total cost index than the CondBio-CathRec at the base conditions. It was also found that the pinch case can become a threshold case by adjusting split fraction or operating at lower fuel utilization. The total cost index of the threshold cases is lower than that of the pinch case. Moreover, it was found that some conditions can give lower total cost index than that of the CondBio-CathRec at the base conditions.

1. Introduction

A Solid Oxide Fuel Cell (SOFC) is known as one of potential power generator because of its high systematic efficiency, wide range of applications, and fuel flexibility. Typically, due to the high operating temperature of SOFC and the remain of unreacted fuels from the SOFC stack, the high temperature effluent and the combustion heat of unreacted fuels can be thermally utilized to other parts of the system. In general, there are two possible options to utilize high temperature effluent and enhance high SOFC system performance, i.e. Solid Oxide Fuel Cell with Gas Turbine system (SOFC-GT) and Solid Oxide Fuel Cell with Combined Heat and Power system (SOFC-CHP). It should be noted that SOFC-CHP is the main focus in the present work.

Typically, SOFC-CHP system consists of preheaters, an SOFC stack and an afterburner. A reformer is also required when other compounds apart from hydrogen were used as the primary feed. According to the operation, the unreacted fuels and excess air from the stack are burnt in the afterburner to generate more heat. Until now, several configurations of the SOFC system have been proposed. Fontell et al. [1] and Zhang et al. [3] studied natural gas-fed system integrated with a desulfurization unit. According

* Corresponding author. Tel.: +1 519 888 4601; fax: +1 519 888 4365.
E-mail address: pdouglas@uwaterloo.ca (P.L. Douglas).

0378-7753/$ – see front matter © 2008 Elsevier B.V. All rights reserved.
doi:10.1016/j.jpowsour.2008.09.036

Nomenclature

C_{EtOH}	ethanol concentration [mol%]
E	electromotive force of a cell [V]
E_a	activation energy [J mol^{-1}]
F	Faraday constant [C mol^{-1}]
i	current density [A cm^{-2}]
I	current [A]
LHV_{EtOH}	lower heating value of ethanol [J mol^{-1}]
n_{EtOH}	total ethanol flow rate fed to the distillation column [mol s^{-1}]
p_i	partial pressure of component i [kPa]
P	pressure [kPa]
P_{den}	power density [A cm^{-2}]
Q_1	energy required for Preheater 1 [kW]
Q_2	energy required for Preheater 2 [kW]
Q_3	energy required for a reformer [kW]
Q_4	energy required for Preheater 4 [kW]
Q_5	energy left in a bottom stream of the distillation column [kW]
Q_6	energy involved with the combustion of exhausted gases after being cooled to the exit temperature [kW]
Q_{Con}	condenser duty [kW]
Q_{Net}	net useful heat [kW]
Q_{Reb}	reboiler duty [kW]
$Q_{SOFC,Net}$	net exothermic from SOFC [kW]
r	area specific resistance [Ω cm^2]
r_{act}	activation polarization area specific resistance [Ω cm^2]
r_{ohm}	ohmic polarization area specific resistance [Ω cm^2]
$r_{H_2,cons}$	rate of hydrogen consumed by the electrochemical reaction [mol s^{-1}]
R	gas constant [J mol^{-1} K^{-1}]
Sp	split faction
$T_{anode,in}$	anode inlet temperature [K]
$T_{cath,in}$	cathode inlet temperature [K]
T_{RF}	reforming temperature [K]
T_{SOFC}	SOFC temperature [K]
U_f	fuel utilization [%]
V	operating voltage [V]
W_e	electrical power [kW]

Greek letters

η_{CHP}	CHP efficiency [%]
$\eta_{elec,ov}$	overall electrical efficiency [%]
ρ	resistivity [Ω cm]

Subscripts

a	anode
c	cathode

to the configuration in Fontell's work, the anode effluent provided heat to the anode incoming stream and was then split into two streams; the first stream was burnt with the air effluent from the cathode in the afterburner, whereas the second one was recirculated and mixed with the inlet stream before being fed to the pre-reformer. The exhaust gas from the afterburner preheated both water stream and the sulfur-free stream. Regarding Zhang's work, the split of anode outlet stream was also applied but it was not used for preheating the incoming anode stream; the exhaust gas from the afterburner was only used to heat the air inlet stream and the pre-reformer was operated under adiabatic condition. Omosun et al. [2] studied biomass-fueled SOFC system and compared between hot and cold processes. According to the cold process, the anode and cathode effluent preheated the incoming anode and cathode stream, respectively, before being burnt in the afterburner. On the contrary, there is no use of anode effluent to heat the incoming anode stream for the hot process. They reported that the heat management of hot process gave the superior electrical and overall efficiency to that of the cold process; however, the cost of the hot process is higher than that of the cold process due to the fluidized bed gasifier and the hot ceramic filter. Braun et al. [4] studied an anode supported SOFC with micro CHP for residential applications. The effect of fuel types (hydrogen/methane), mode of methane reforming (internal/external reforming), fuel processing with anode recirculation, oxidant processing with cathode recirculation and the combination of recycle and internal reforming on the system performance were investigated. The results showed that the methane-fueled system with cathode and anode recirculation with internal reforming yielded the highest efficiency among all designs. System electrical efficiency and CHP efficiency are 40% (HHV) and 79% (HHV), respectively.

A few investigations on ethanol-fed SOFC system have previously been published. Generally, ethanol-fed SOFC system consists of a vaporizer, preheaters, a reformer, an SOFC stack and an afterburner. Douvartzides et al. [5] used exergy analysis and optimization strategy to investigate the system performance and reported that the exergy loss of SOFC can be minimized by matching the appropriate reforming temperature and air preheating temperature. With the same system configuration, Douvartzides et al. [6] also compared the performance of SOFC system fed by methane with that fueled by ethanol. The exergy analysis indicated that the efficiency of the methane-fed system is higher than that of the ethanol-fed one. Arteaga et al. [7] studied ethanol-fed SOFC system consisting of a mixer, a vaporizer, an ethanol/water mixture heater, a compressor, a reformer, a fuel cell stack and a furnace by using pseudo-homogenous model. They reported that the heating consumption for vaporizing the H_2O/EtOH mixture increases with increasing the steam to EtOH ratio (H_2O:EtOH) and H_2 production initially increases but decreases when the H_2O:EtOH ratio is higher than 8. In addition, the increase of reforming temperature promoted the fuel cell efficiency and decreases energy required for heating up the synthesis gas before reaching SOFC stack; however, the higher energy consumption for the external reformer is also required.

Most of the previous studies on the ethanol-fed SOFC system have been carried out by using pure ethanol mixed with water. From an energy point of view, it is not efficient and necessary to purify bioethanol to highly pure ethanol as some water is usually required for the steam reforming reaction. Therefore, purifying bioethanol just to reach a desired ethanol concentration needed for the steam reforming is adequate. The SOFC system implemented with a distillation column (SOFC-DIS) has been considered in our previous work [8]. The hot effluent from the afterburner was used for heating all heaters, an external reformer and a boiler of a distillation column. The possibility to operate the SOFC-DIS as a self energy-sufficient system was examined. It was found that the SOFC-DIS system can operate without an external heat source. Nevertheless, the calculation in our previous study was based on the direct subtraction between net supply energy and net consumption energy in the system, and no details on heat transfer arrangement were considered. Moreover, other useful heat in the system (e.g. condenser duty and hot water at the bottom of the distillation column) were not utilized. Also, the high temperature of air coming out from the cathode should also be considered as the SOFC stack is usually operated under excess air.

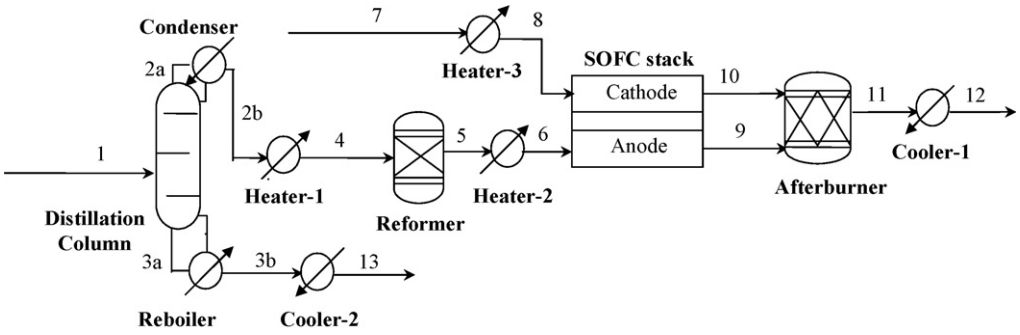

Fig. 1. Schematic diagram of base case SOFC-DIS systems at the base conditions (C_{EtOH} = 25%, EtOH recovery = 80%, U_f = 80%, V = 0.7 V, T_{SOFC} = 1200 K, $T_{anode,in}$ = 1100 K, $T_{cath,in}$ = 1000 K, T_{RF} = 1023 K and P = 101.3 kPa).

The main objective of this work is to study the performance of the SOFC-DIS when all heat transfer is considered. Moreover, other useful heat, e.g. condenser duty and hot water from the bottom of the column and the cathode recirculation are taking into account to enhance the performance of SOFC-DIS. In addition, the effect of operating conditions on composite curve is also examined and lastly the designs of the heat exchanger network for the SOFC-DIS system are further investigated.

2. SOFC-DIS process system modelling using Aspen Plus™

Fig. 1 shows the simplified process flow diagram of the SOFC-DIS system; the SOFC-DIS system was simulated using Aspen Plus™ 2006.

The SOFC-DIS system consists of a distillation column, an external reformer, heaters, coolers, an SOFC stack and an afterburner. Bioethanol containing 5 mol% ethanol (C_2H_5OH) is introduced to the distillation column at atmospheric pressure and 298 K and purified to a desired concentration. Thereafter, the concentrated ethanol is fed to the Heater-1 prior to entering the external reformer in order to reform ethanol to H_2. The synthesis gas from an external reformer is further heated by Heater-2 and fed to an anode side of the SOFC stack for producing electricity. The air stream is heated in Heater-3 and then fed to the cathode side of the SOFC stack. The exhaust gas from the SOFC stack containing small amount of unused fuel enters the afterburner where excess fuel is combusted to produce additional heat for use in the system. The heat recovery from the post-combustion stream can be calculated by cooling the hot effluent from the afterburner to 403 K before emitting to the surrounding.

The *Peng–Robinson* thermodynamic option set, suitable for non-polar light components, was used for all units except the distillation column; the *UNIFAC* activity coefficient model was used in the distillation column.

One design-spec was used in simulation. *Design-spec*-1 was used to adjust incoming bioethanol flow rate (stream 1) to reach the fuel utilization target. In addition, the stack area also keeps constant by using calculated current density and the operation of *Design-spec-1*. The target fuel utilization and voltage was set. The calculations of mass balance, energy balance and performances were performed inside the user-subroutine SOFC. The calculated mass, enthalpy and other physical properties (i.e. density, molecular weight) of anode and cathode stream were sent through material stream numbers 9 and 10, respectively. The details of modelling for each unit in the system are described below.

2.1. Distillation column

The distillation column is modelled using Aspen Plus™ rigorous distillation model, *RadFrac*. A partial condenser and a kettle reboiler are used in this study. Four stages are sufficient to purify bioethanol until it reaches the concentration of 41 mol% with 99% recovery. It should be noted that 41 mol% is the maximum ethanol concentration that can be fed to the external reformer without carbon formation [9]. *UNIFAC* which is suitable for polar systems, in this case the mixture of ethanol and water, at atmospheric pressure is used as a thermodynamics equation for the distillation column. A *RadFrac* built-in *Design-spec* was used to adjust the distillate rate and reflux ratio to obtain the desired ethanol concentration and recovery.

2.2. Ethanol reformer

In this study, an *RGibbs* reactor model was used for simulating the external reformer. Previous experimental results confirmed that a gas mixture at thermodynamic equilibrium contains only five components with noticeable concentration: i.e. carbon monoxide, carbon dioxide, hydrogen, steam, and methane [10,11]. Therefore, these five components and one more ethanol component are modelled in the reactor.

2.3. SOFC stack

The SOFC stack is simulated by using a user-subroutine named *USRUSR*. The subroutine contains mass and energy balance equations and SOFC performance equations. For the mass balance, the synthesis gas which contains CO, CO_2, H_2, CH_4 and H_2O is fed to the SOFC stack. Only water gas shift reaction and electrochemical reactions take place inside the SOFC stack as shown in the following equations.

$$CO + H_2O = H_2 + CO_2 \quad (1)$$

$$H_2 + \tfrac{1}{2}O_2 \rightarrow H_2O \quad (2)$$

It should be bear in mind that water gas shift reaction is fast equilibrium reaction. Ethanol reforming is not considered in the stack as trace amount of ethanol is present in the product stream for the reformer. In addition, methanation hardly takes place at high temperature. Therefore, both reactions can be neglected in calculations. The components inside the SOFC stack were calculated based on thermodynamics calculation. The performance of the SOFC was calculated by equilibrium components inside the stack and based on one-dimensional calculation. Details of SOFC model including

Table 1
Parameters for activation loss [12].

r_{act} (Ω cm^2)	k ($\times 10^{-13}$ A cm^2)	E_a (kJ mol^{-1} K^{-1})	m
$r_{act,c}$	14.9	160	0.25
$r_{act,a}$	0.213	110	0.25

Table 2
Parameters of ohmic loss in SOFC cell components [13].

Materials	Parameters		Thickness (μm)
	α (Ω cm)	β (K)	
Anode (40% Ni/YSZ cermet)	2.98×10^{-5}	−1392	150
Cathode (Sr-doped $LaMnO_3$:LSM)	8.11×10^{-5}	600	2000
Electrolyte (Y_2O_3-doped ZrO_2:YSZ)	2094×10^{-5}	10350	40
Interconnect (Mg-doped $LaCrO_3$)	1.256×10^{-3}	4690	100

performance calculations are presented in Tables 1 and 2 and in our previous work [8]. The energy balance equation, the SOFC stack operates under steady state and adiabatic condition. The energy equation can be calculated by enthalpy change and power around the SOFC stack as presented in Eq. (3).

$$0 = H_{fuel,in} + H_{air,in} - H_{fuel,out} - H_{air,out} - W_e \quad (3)$$

Because the inlet and outlet temperature of the streams was set, the required amount of air was then calculated.

2.4. Afterburner

The afterburner was modelled using the *Rstoic*, stoichiometric reactor model. All unreacted products from an SOFC stack (e.g. CH_4, CO, and H_2) are reacted with the unreacted O_2 as shown in Eqs. (4)–(6). The complete combustion is assumed. It should be noted that ethanol is not present in the afterburner due to complete ethanol reforming [8]. In this study, N_2 is assumed to be inert and no NO_X is produced.

$$CH_4 + 2O_2 \rightarrow CO_2 + 2H_2O \quad (4)$$

$$CO + \tfrac{1}{2}O_2 \rightarrow CO_2 \quad (5)$$

$$H_2 + \tfrac{1}{2}O_2 \rightarrow H_2O \quad (6)$$

2.5. Heaters and coolers

Heaters and coolers were modelled using the *Heater* model in Aspen Plus™. One only needs to supply the desired exit temperature and the model calculates the heat duty resulting from the change in enthalpy between the inlet and the specified outlet.

2.6. Performance definition

In this study, overall electrical efficiency and CHP efficiency can be calculated as

$$\eta_{elec,ov} = \frac{W_e}{(n_{EtOH} \times LHV_{EtOH}) + Q_{ext}} \quad (7)$$

$$\eta_{CHP} = \frac{W_e + Q_U}{(n_{EtOH} \times LHV_{EtOH}) + Q_{ext}} \quad (8)$$

where W_e represents the electrical power, LHV_{EtOH} the low heating value of ethanol, $\eta_{elec,ov}$ the overall electrical efficiency, η_{CHP} the Combine Heat and Power (CHP) efficiency, Q_U the net heat produced by the SOFC-DIS system after heat exchanging with heaters and a reboiler, Q_{ext} the external heat from an external heat source, Q_k the energy consumption at Heater k, Q_{Reb} the reboiler duty.

2.7. Heat exchanger network

The obtained information from Aspen Plus™ was used to design heat exchanger network by using Aspen Plus™ HX-NET module (version 2006). The input data for HX-Net is initial temperature, temperature target and enthalpy change. The effect of operating conditions (i.e. ethanol concentration, ethanol recovery, fuel utilization, voltage and split fraction) on the composite curves and the design of heat exchanger network was also investigated. Hot utility and cold utility used in this work are fired heat and cooling water, respectively. For costing, five year was used for the operating period.

2.8. System configuration study

In this work, condenser duty, hot water from the bottom of the column and cathode recirculation were also considered to enhance the performance of SOFC-DIS. Since hot water at the bottom and condenser duty is low-temperature heat source, the application of these types of heat is to preheat incoming low-temperature reactants, in this case, incoming air or bioethanol. Four additional configurations are listed as below.

- Case a: No thermal heat integration (No-HX).
- Case b: Utilization of heat from the condenser to incoming bioethanol (CondBio).
- Case c: Utilization of heat from hot water at the bottom of the column to incoming bioethanol (HW-Cond).
- Case d: Utilization of heat from the condenser to incoming air (Cond-Air).
- Case e: Implementation of cathode recirculation (CathRec).

All options were compared and a suitable configuration was chosen for further design of heat exchanger network of SOFC-DIS. The discussion will be presented in the following section.

3. Results and discussion

3.1. Heat exchanger network for base case SOFC-DIS

The base case of the SOFC-DIS is illustrated by Fig. 1. All cold process streams, which need to be heated, were heated using a hot utility to reach the target temperatures. Likewise, all hot process streams, which need to be cooled, were cooled using a cold utility. The minimum temperature difference for heat exchange was fixed at 10 K and it was assumed that the heat capacity of all streams was constant during heat exchanging process. Cooling water at 293.2 K and fired heat at 1273.2 K were selected as cold and hot utilities

Table 3
Operating parameters at base conditions.

Parameter	Value/quality
Fuel option	Bioethanol with 5 mol%
C_{EtOH}	25 mol%
Ethanol recovery	80%
U_f	80%
Voltage	0.7 V
T_{SOFC}	1200 K
T_{RF}	1023 K
$T_{anode,in}$	1100 K
$T_{cath,in}$	1000 K
P	101.3 kPa

Table 4
Information of hot and cold streams at the base case SOFC-DIS (No-HX).

Stream no.	Stream label	T_{in} (K)	T_{out} (K)	Load (kW)	MC_p (kW K^{-1})
Hot stream					
Cooler-1 (11–12)	H1	1304.9	403.0	847.3	0.940
Condenser (2a–2b)	H2	365.9	365.9	48.8	Large
Cooler-2 (3b–13)	H3	369.3	303.2	45.4	0.687
Cold stream					
Air stream (7b–8)	C1	298.2	1000.0	580.7	0.827
BioEtOH stream (1)	C2	298.2	–	–	–
Anode heater (5–6)	C3	1023.0	1100.0	7.3	0.095
Distillate stream (2–4)	C4	365.9	1023.0	50.9	0.078
Reboiler (3a–3b)	C5	298.2	369.3	149.1	2.097
Reformer (4–5)	C6	1023.0	1023.0	85.4	Large

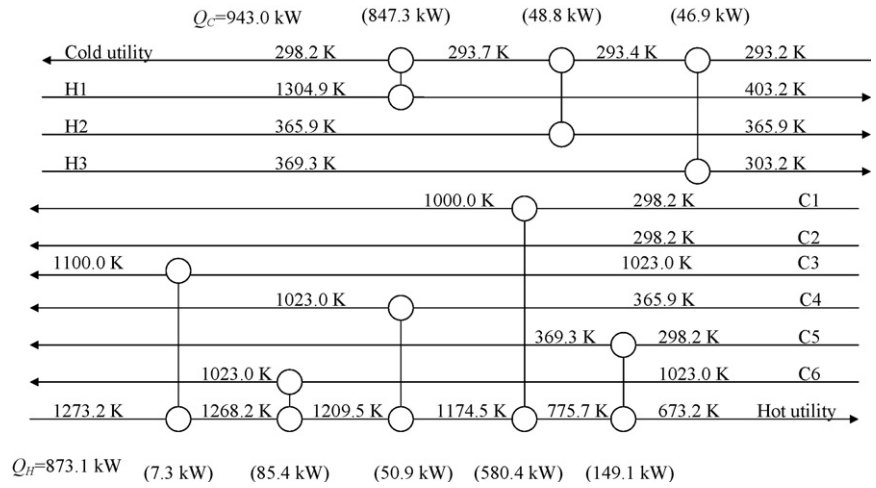

Fig. 2. Heat exchanger network of base case SOFC-DIS (No-HX) at the base conditions (C_{EtOH} = 25%, EtOH recovery = 80%, U_f = 80%, V = 0.7 V, T_{SOFC} = 1200 K, $T_{anode,in}$ = 1100 K, $T_{cath,in}$ = 1000 K, T_{RF} = 1023 K and P = 101.3 kPa).

respectively. The base operating conditions, shown in Table 3, are C_{EtOH} = 25 mol%, EtOH recovery = 80%, V = 0.7 V, U_f = 80%, T_{RF} = 1023 K and T_{SOFC} = 1200 K. The starting temperature, target temperature, heat load and heat capacity of all hot and cold streams for the base case are presented in Table 4. The heat exchanger network involving only utility heaters and coolers for the base case is presented in Fig. 2. It can be seen that the major energy consumers are *Heater-2*, the air preheater (580.4 kW or 66.5% of the overall energy consumption) and the reboiler (149.1 kW or 17.1% of the overall energy consumption); the net energy consumption is 873.1 kW which is supplied by the hot utility. It can be seen that the hot stream from the afterburner is the major energy supplier and contains 847.3 kW of thermal energy which, in this case, corresponds to the cooling energy by the cold utility. Electrical power of 220.5 kW is produced. The overall electrical efficiency, CHP efficiency and corresponding power density of SOFC-DIS are 15.8%, 76.5% and 0.229 W cm^{-2}, respectively.

The composite curves at the base conditions, when the minimum temperature difference (ΔT_{min}) is set at 10 K, are shown in Fig. 3. The cold composite curve move closely until it reaches ΔT_{min} so as to yield the maximum energy recovery. As shown in Fig. 3, the composite curves become the threshold case where no pinch point occurred; in other words, the composite curves were adjusted to reduce the hot and cold utilities and the need for a hot utility was eliminated before the curves pinched. From the composite curve results, the minimum heating utility required is Q_{Hmin} = 0 and the minimum cooling utility required is Q_{Cmin} = 73.4 kW. In practical terms, this means that we can eliminate entirely the need for a hot utility of 873.1 kW shown in Fig. 2, by appropriate heat exchange; we will, however, still need to buy a small amount of cooling utility. The next step is to design an appropriate MER (maximum energy recovery) network, i.e. one that results in $Q_H = Q_{Hmin}$ and $Q_C = Q_{Cmin}$. Note that it is impossible to find a network that will result in $Q_H < Q_{Hmin}$ or $Q_C < Q_{Cmin}$ at the current design and operating conditions. An example of MER network of the base conditions is shown in Fig. 4. Obviously, the utility can be reduced to $Q_c = Q_{Hmin} = 0$ and $Q_c = Q_{Cmin}$ = 73.4 kW. It can be seen that the hot effluent gas after the afterburner (stream no. 11) is heat exchanged with the anode inlet stream (C3) first and then the reformer (C6), the distillate stream (C4), the air stream (C1) and finally the reboiler

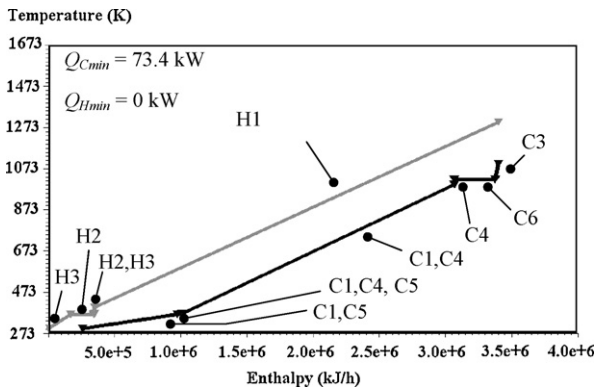

Fig. 3. Composite curves of SOFC-DIS at base conditions (C_{EtOH} = 25%, EtOH recovery = 80%, U_f = 80%, V = 0.7 V, T_{SOFC} = 1200 K, $T_{anode,in}$ = 1100 K, $T_{cath,in}$ = 1000 K, T_{RF} = 1023 K and P = 101.3 kPa).

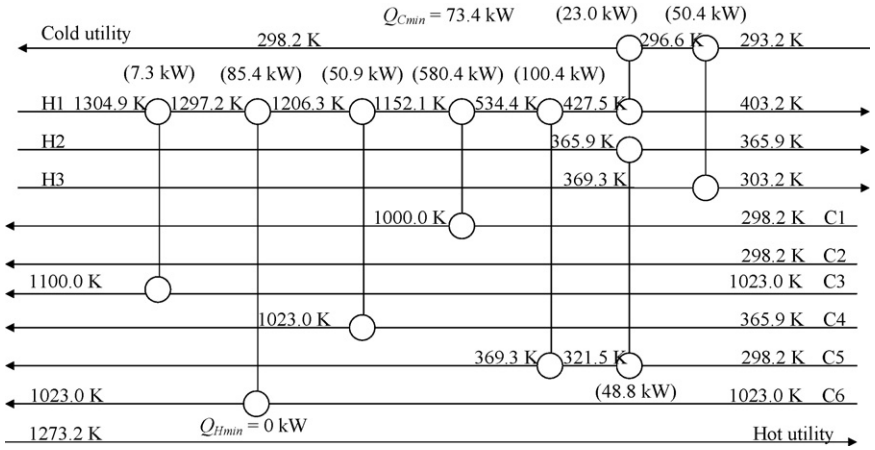

Fig. 4. MER network of SOFC-DIS at the base conditions (C_{EtOH} = 25%, EtOH recovery = 80%, U_f = 80%, V = 0.7 V, T_{SOFC} = 1200 K, $T_{anode,in}$ = 1100 K, $T_{cath,in}$ = 1000 K, T_{RF} = 1023 K and P = 101.3 kPa).

(C5). However, the hot effluent gases cannot supply heat sufficiently to the reboiler. Some heat from the condenser need to supply heat to the reboiler before the reboiler is heated by the hot effluent gases. This is because if the reboiler is heat exchanged with the effluent gases and afterwards by other hot streams (i.e. the heat from the condenser and the hot water of the bottom of the column), the temperature of the reboiler after heat exchanged with the hot effluent gases will be higher than the starting temperature of the other hot streams. Therefore, the heat cannot be transferred and the hot utility is required. The MER network cannot be obtained. However, it should be noted that providing heat to the reboiler requires two hot streams and causes in the high complexity in operation.

3.2. Effect of process structure and operating conditions

3.2.1. Utilizing internal heat and adjusting process flowsheet

To lower the requirement of cold utility for No-HX case used for cooling down the other hot streams, the useful heat from the overhead vapour stream going to the condenser and the useful heat from hot water from the bottom of the distillation column are used for providing heat to other parts of the system. As mentioned earlier, the heat from the vapour stream going to the condenser and from hot water are low-temperature heat streams. To utilize this heat, preheating incoming reactants (air or bioethanol) is reasonable. Moreover, a large amount of air is introduced to the system in order to cool down the SOFC stack. However, the amount of air is more than that needed for burning unreacted fuels from the anode. Therefore, it appears that some benefits could be gained from thermal integration of the heat from the hot streams (that need to be cooled) to the cool streams (that need to be heated). An investigation of the performance of SOFC-DIS when the cathode recirculation is implemented into the system will be performed. Four different configurations of the system are shown in Fig. 5 with different lines. In this study, the utilization of the heat recovery from the condenser for preheating incoming bioethanol (CondBio) representing by dashed line, the heat recovery from condenser for preheating incoming air (Cond-Air) representing by dotted line, the heat recovery from the hot water from the distillation column for preheating bioethanol (HW-Bio) represented by dash dot line and the implementation of cathode recirculation (CathRec) represented by long dash line are considered. It should be noted that the heat from the vapour stream going to the condenser and from hot water are low-temperature heat streams which are suitable for preheating incoming reactants (air or bioethanol). Moreover, a large amount of cooling air introduced to the SOFC in order to cool down the stack is more than that needed for burning unreacted fuels from the anode. Therefore, some air outlet from the SOFC stack should be split and recycled in the system. Heat exchanger networks of different configurations are presented in Figs. 6–10. The performances (e.g. overall electrical efficiency, CHP efficiency and total cost index) of all configurations have been summarized in Table 5. It should be noted that the total cost index is calculated from the total cost of each configuration divided by the total cost of the base case in which no heat integration is considered. In addition, the total cost is a summation of operating cost from hot utility and cold utility and capital cost of heat exchangers, heaters and a cooler in the system.

Since the bioethanol feed stream is available to the system at 298 K it is sub-cooled and needs heating either in the column (increasing the reboiler heat duty) or prior to entering column via heat exchange with a process stream (reducing the energy consumption in the reboiler). Two options, CondBio and HW-Bio are considered to be logical choices for preheating the bioethanol feed stream. From Table 5, the results show that the CondBio yields a slightly higher CHP efficiency and lower total cost index than does the HW-Bio case. Hot water from the bottom of the distillation column yields 46.9 kW for preheating incoming bioethanol in the HW-Bio case. The heat recovery from the condenser (48.8 kW) is fully utilized for preheating bioethanol because the temperature at the condenser remains constant during heat exchange as shown in Fig. 6. On the other hand, the temperature of the hot water drops while exchanging heat as presented in Fig. 7. Due to higher overall electrical efficiency, high CHP efficiency and lower total cost index, the CondBio configuration is selected for preheating bioethanol.

To preheat the incoming air, the performance of the Bio-Air and the CathRec configurations were compared. For the CathRec, the SOFC-DIS operates at split fraction of 0.5 which means that half of the cathode outlet stream is recycled and mixed with fresh air while the rest of cathode stream is fed to the afterburner. It

Table 5
System performance and total cost index of the SOFC-DIS with different configurations.

	Overall electrical efficiency (%)	CHP efficiency (%)	Total cost index
No-HX (base case)	15.79	76.45	1.000
CondBio	16.26	78.73	0.965
HW-Bio	16.21	78.48	0.969
Cond-Air	16.95	81.74	0.948
CathRec	21.67	79.87	0.662
CondBio-CathRec	22.53	74.71	0.641

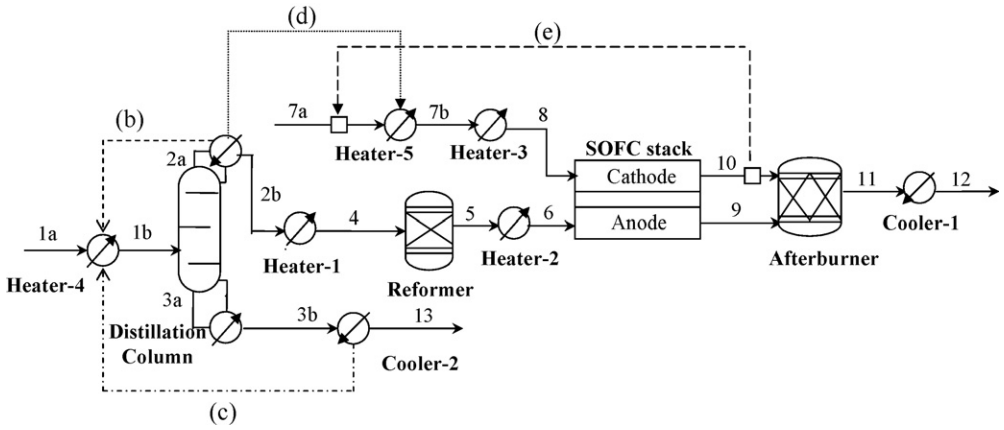

Fig. 5. Schematic diagram of SOFC-DIS systems: (a) No-HX, (b) CondBio, (c) HW-Bio, (d) Cond-Air and (e) CathRec at the base conditions (C_{EtOH} = 25%, EtOH recovery = 80%, U_f = 80%, V = 0.7 V, T_{SOFC} = 1200 K, $T_{anode,in}$ = 1100 K, $T_{cath,in}$ = 1000 K, T_{RF} = 1023 K and P = 101.3 kPa).

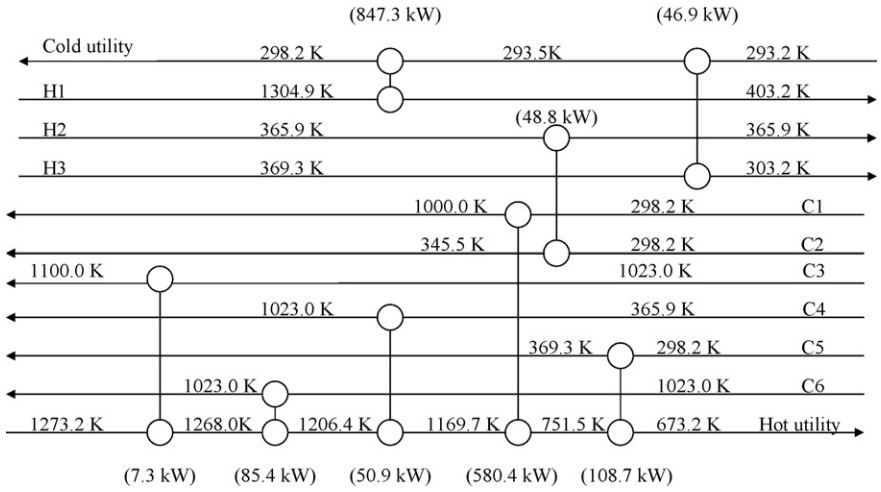

Fig. 6. Heat exchanger network of SOFC-DIS (CondBio) at the base conditions (C_{EtOH} = 25%, EtOH recovery = 80%, U_f = 80%, V = 0.7 V, T_{SOFC} = 1200 K, $T_{anode,in}$ = 1100 K, $T_{cath,in}$ = 1000 K, T_{RF} = 1023 K and P = 101.3 kPa).

should be noted that the heat recovery from hot water to preheat incoming air has not been studied because the heat cannot be fully transferred as mentioned earlier in the previous section. From the results, Table 5, the CHP efficiency for both the Bio-Air configuration and the CathRec configuration shows similar potential. However, the overall electrical efficiency of the CathRec configuration is 5% higher than that of the Bio-Air. In addition, the total cost index of the CathRec configuration is 28% lower than that of the Bio-Air config-

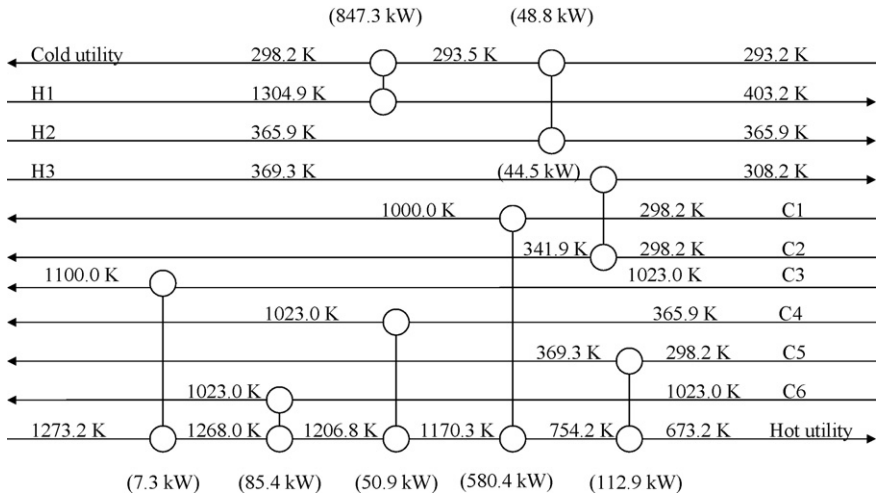

Fig. 7. Heat exchanger network of SOFC-DIS (HW-Bio) at the base conditions (C_{EtOH} = 25%, EtOH recovery = 80%, U_f = 80%, V = 0.7 V, T_{SOFC} = 1200 K, $T_{anode,in}$ = 1100 K, $T_{cath,in}$ = 1000 K, T_{RF} = 1023 K and P = 101.3 kPa).

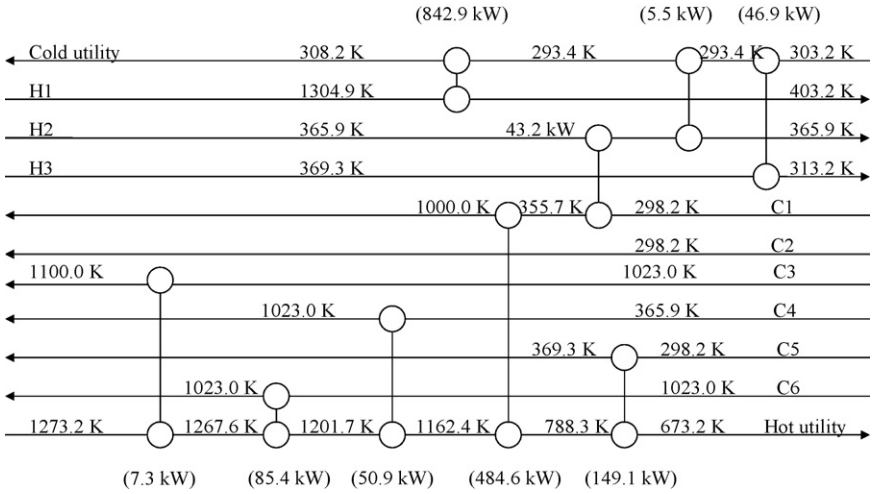

Fig. 8. Heat exchanger network of SOFC-DIS (Cond-Air) at the base conditions (C_{EtOH} = 25%, EtOH recovery = 80%, U_f = 80%, V = 0.7 V, T_{SOFC} = 1200 K, $T_{anode,in}$ = 1100 K, $T_{cath,in}$ = 1000 K, T_{RF} = 1023 K and P = 101.3 kPa).

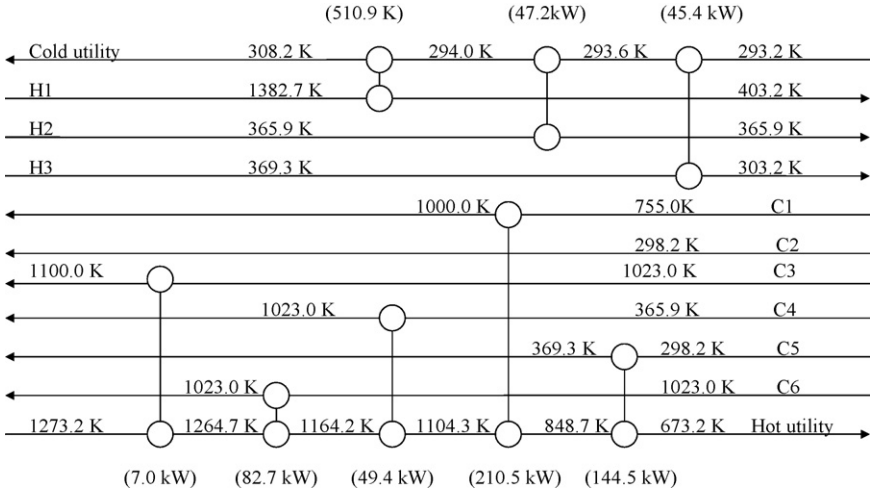

Fig. 9. Heat exchanger network of SOFC-DIS (CathRec) at the base conditions with Sp = 0.5 (C_{EtOH} = 25%, EtOH recovery = 80%, U_f = 80%, V = 0.7 V, T_{SOFC} = 1200 K, $T_{anode,in}$ = 1100 K, $T_{cath,in}$ = 1000 K, T_{RF} = 1023 K and P = 101.3 kPa).

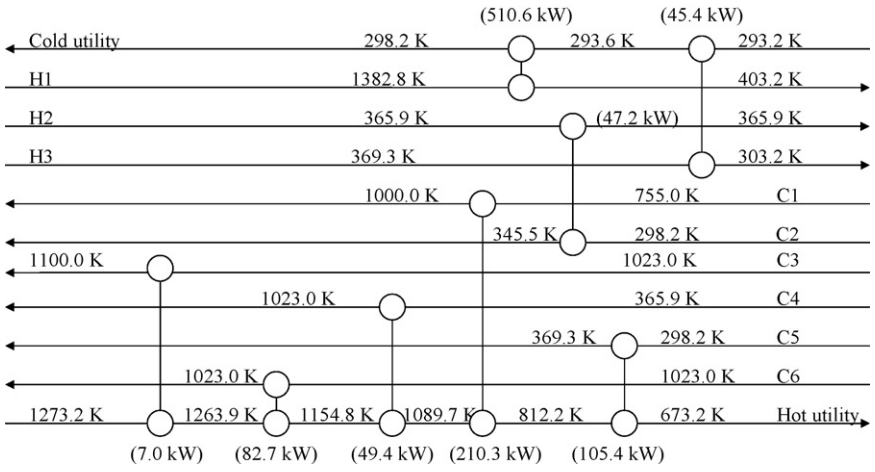

Fig. 10. Heat exchanger network of SOFC-DIS (CondBio-CathRec) at the base conditions with Sp = 0.5 (C_{EtOH} = 25%, EtOH recovery = 80%, U_f = 80%, V = 0.7 V, T_{SOFC} = 1200 K, $T_{anode,in}$ = 1100 K, $T_{cath,in}$ = 1000 K, T_{RF} = 1023 K and P = 101.3 kPa).

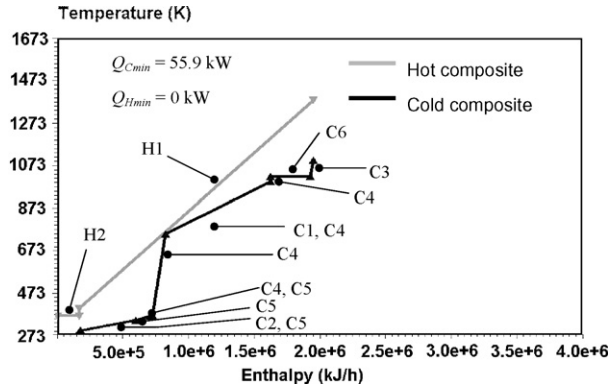

Fig. 11. Composite curves of SOFC-DIS (CondBio-CathRec) at base conditions with $Sp = 0.5$ (C_{EtOH} = 25%, EtOH recovery = 80%, U_f = 80%, V = 0.7 V, T_{SOFC} = 1200 K, $T_{anode,in}$ = 1100 K, $T_{cath,in}$ = 1000 K, T_{RF} = 1023 K and P = 101.3 kPa).

uration, therefore, the CathRec configuration is selected to preheat the incoming SOFC air. The Bio-Cond and the CathRec configurations are then combined, so-called CondBio-CathRec, and chosen to be further designed for a process-to-process heat exchanger network. It can be noticed that the CondBio-CathRec configuration yields the highest overall electrical efficiency and the lowest total cost index as shown in Table 5. The heat exchanger network for the CondBio-CathRec configuration is also presented in Fig. 10. The amount of utility for Q_C = 566.0 kW and Q_H = 454.8 kW are required. Noticeably, high amount of hot and cold utility are still needed. The composite curve of the CondBio-CathRec configuration at the base conditions with $Sp = 0.5$ when ΔT_{Min} is set at 10 K is presented in Fig. 11. The narrowest gap in the threshold problem is so called 'pseudo-pinch' and in this case, it is located at the air inlet temperature. The base conditions with $Sp = 0.5$ is still a threshold problem with Q_{Cmin} = 55.9 and Q_{Hmin} are 0 kW, respectively. Clearly, the heat exchanger network for the CondBio-CathRec in Fig. 10 needs more work to be done to reach an MER network.

The design of the threshold case follows the same rules as that of the pinch case. To design a MER network, it is necessary to design the heat exchanger network above and below the pseudo-pinch point separately because the pseudo-pinch is in the middle of the composite curves. The following rules for the MER design are required [14].

(1) No cold utility is used above the pinch point.
(2) No hot utility is used below the pinch point.
(3) No heat transfer across the pinch point.

The heat capacity (MC_p) of each stream at the base conditions with $Sp = 0.5$ are presented in Table 6. Overall, there are two hot streams (a hot flue gas from the afterburner (H1) and heat recovery from the condenser (H2)) and six cold streams (e.g. a syngas stream (C3), a reformer (C6), a distillate stream (C4), an air stream (C1), a reboiler (C5) and a bioethanol inlet (C2)). However, it should be noted that the heat recovery from the condenser has to be matched with the bioethanol inlet as the CondBio is selected for preheating the incoming bioethanol. For the design above pseudo-pinch, the MC_p of the hot stream has to be lower than the cold stream near the pseudo-pinch point in order to avoid the temperature crossover [14]. The possible cold streams that can be matched with the hot stream near the pinch point are the reformer and the air stream. However, when the reformer is the last unit which is near the pseudo-pinch point, the hot flue gas cannot supply heat to the reformer due to low inlet temperature for heat exchange. Consequently, the hot flue gas cannot be cooled down to the pseudo-pinch temperature using process streams. Cold utility is required above the pseudo-pinch and this violates the rule for MER design. Therefore, the only configuration which ends with the air heat exchanger is considered for the above pseudo-pinch design. Below the pseudo-pinch, one hot stream and two cold streams (e.g. a distillate stream (C4) and a reboiler (C5) are considered. It is known that the MC_p of the hot stream must be higher than that of the cold stream near the low-temperature pinch point [14]. From Table 6, only the MC_p of the distillate is higher than that of the hot flue gas. Therefore, only one match is possible. The hot stream has to exchange heat with the distillate and then with the reboiler. From these preliminary considerations, there are six possible MER designs, D1 through D6, for the pinch case. The sequences of heat exchanging for MER designs are listed as follows. The first stream label is the first cold stream to be heat exchanged with hot stream and so on.

- D1: C3–C4–C6–C1–C4–C5
- D2: C3–C6–C4–C1–C4–C5
- D3: C4–C3–C6–C1–C4–C5
- D4: C4–C6–C3–C1–C4–C5
- D5: C6–C3–C4–C1–C4–C5
- D6: C6–C4–C3–C1–C4–C5

The total cost index of all six designs is presented in Table 7. All six MER designs have the target energy of 21.2 and 62.5 kW for hot utility and cold utility, respectively. From the results, it can be seen that the total cost index for all six designs are similar but Design D2, C3–C6–C4–C1–C4–C5 shows the lowest total cost index from the six considered among other designs and is then chosen for a further design. The heat exchanger network of D2 MER design is next presented in Fig. 12. The utility meets the utility targets at Q_{Cmin} = 55.9 and Q_{Hmin} = 0. Obviously, changing process structure by implementing cathode recirculation and adding one more heat exchanger to preheat incoming bioethanol can reduce Q_{Cmin} from 73.4 kW (for the No-HX case) to 55.9 kW. It should be noted that although all six MER configurations (D1–D6) are somewhat complex from operability point of view and one should the tradeoff between annualised cost and complexity; one maybe able to simplify the design how-

Table 6
Information of each unit operated at the base condition (threshold problem).

Stream no.	Stream label	T_{in} (K)	T_{out} (K)	Load (kW)	MC_p (kW K^{-1})
Hot stream					
Cooler-1 (11–12)	H1	1382.9	403.0	510.6	0.521
Condenser (2a–2b)	H2	366.0	366.0	47.2	Large
Cold stream					
Air stream (7b–8)	C1	755.0	1000.0	210.3	0.858
BioEtOH stream (1a–1b)	C2	298.2	345.7	47.2	0.994
Syngas stream (5–6)	C3	1023.0	1100.0	7.0	0.091
Distillate stream (2–4)	C4	366.0	1023.0	49.4	0.075
Reboiler (3a–3b)	C5	298.2	369.3	105.4	1.482
Reformer (4–5)	C6	1023.0	1023.0	82.7	Large

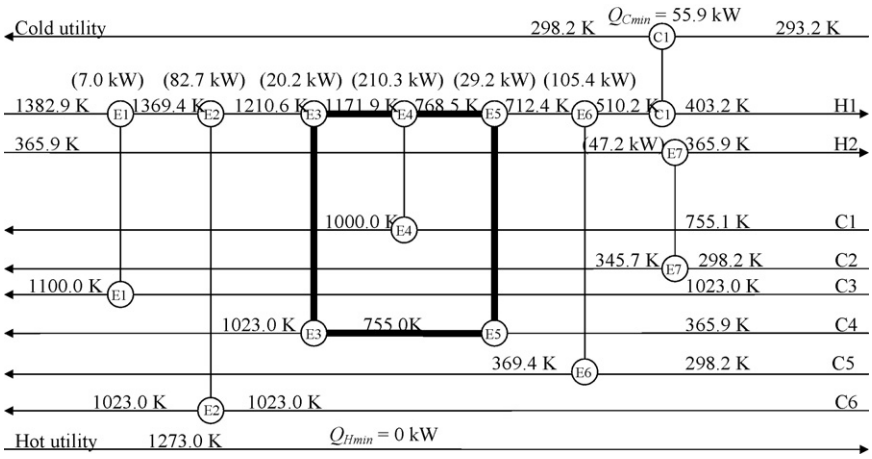

Fig. 12. The MER design of SOFC-DIS (CondBio-CathRec) at the base conditions with $Sp = 0.5$ (C_{EtOH} = 25%, EtOH recovery = 80%, U_f = 80%, V = 0.7 V, T_{SOFC} = 1200 K, $T_{anode,in}$ = 1100 K, T_{RF} = 1023 K and P = 101.3 kPa).

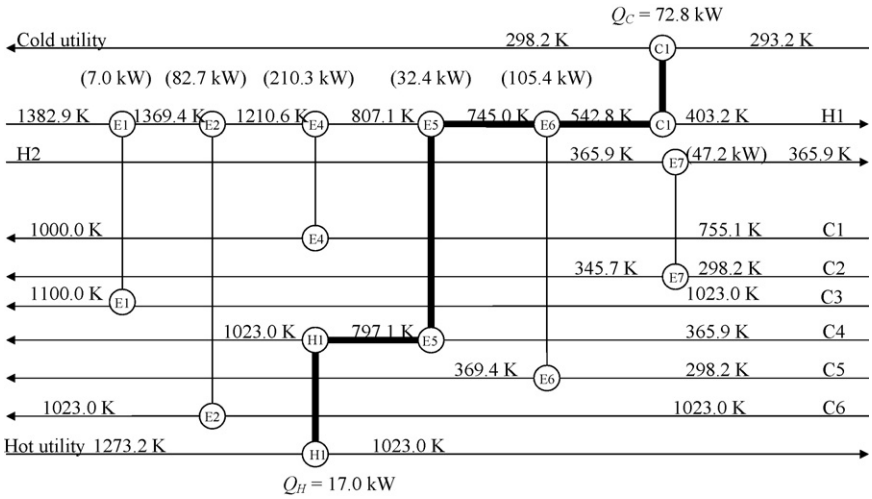

Fig. 13. The design of SOFC-DIS (CondBio-CathRec) without E3 at the base conditions with $Sp = 0.5$ (C_{EtOH} = 25%, EtOH recovery = 80%, U_f = 80%, V = 0.7 V, T_{SOFC} = 1200 K, $T_{anode,in}$ = 1100 K, T_{RF} = 1023 K and P = 101.3 kPa).

ever it will no longer be an MER design and will cost more. Clearly, the distillate stream requires two heat exchangers for heating up to the target temperature, one high temperature heat exchanger (E3) and one low-temperature heat exchanger (E5) and results in an E3–E5–E5–E3 loop in all configurations as shown by the dark line in Fig. 12. Two heat exchanges are present on the distillate stream and this loop results in the complexity of the design and operability difficulties. In an attempt to simplify the network we removed one of the heat exchangers on the distillate stream; however, it is not obvious which ones of the distillate heat exchangers should be eliminated. Table 8 shows the operating cost index, capital cost index and total cost index for different cases. In this section, the total cost index can be calculated by the ratio of total cost of each design to the total cost of the MER design at the base conditions with $Sp = 0.5$. The total costs index follow the sequence of C3–C6–C1–C4–C5 (base-no E3 case) ≈ C3–C6–C4–C1–C5 (base-no E5 case) < MER case. The operating cost index of the base-no E3 case is lower than that of the base-no E5 case because large amount of heating utility

Table 7
Total cost index for different designs.

Configuration	Total cost index[a]
No-HX CondBio-CathRec (base case)	1.000
D1 (C3–C4–C6–C1–C4–C5)	0.3559
D2 (C3–C6–C4–C1–C4–C5)	**0.3556**
D3 (C4–C3–C6–C1–C4–C5)	0.3559
D4 (C4–C6–C3–C1–C4–C5)	0.3565
D5 (C6–C3–C4–C1–C4–C5)	0.3559
D6 (C6–C4–C3–C1–C4–C5)	0.3562

[a] Operate at the base condition (C_{EtOH} = 25%, EtOH recovery = 80%, U_f = 80%, V = 0.7 V, T_{SOFC} = 1200 K, $T_{anode,in}$ = 1100 K, T_{RF} = 1023 K and P = 101.3 kPa).

Table 8
Cost estimation of the SOFC-DIS of different scenarios.

	Operating cost index	Capital cost index	Total cost index
Threshold problem			
Base condition-MER	1.000	1.000	1.000
Base-no E3	7.381	0.930	0.996
Base-no E5	11.31	1.018	1.124
Base-no E3-no path	19.55	0.826	1.020
Avoiding pinch (based on MER design)			
1173 K	8.719	1.102	1.181
1173 K–Uf75	2.093	0.848	0.860
1173 K–Sp0.3	0.442	1.077	1.071
1173 K–Sp0.7	1.407	0.836	0.841

is required to heat up air stream to meet the target temperature for the case of base-no E5. However, the base-no E3 case requires two heaters to heat up both distillate stream and air stream and results in higher capital cost index but still lower than that of the MER case.

The benefit of eliminating path of utility is also investigated. As shown in Fig. 13, there is a path connecting the cold and hot utilities via the distillate heater shown by the dark line. The total cost index of the case of no path (base-no E3-no path) and the base-no E3 are compared and presented in Table 8. It was found that the total cost index of the case without path way is higher than that of the base-no E3. This is because the operating cost of the base-no E3-no path is almost three times higher than that of with path. Therefore, it can be concluded that the base-no E3 is the most preferable. One heater has to be located after the distillate heat exchanger. The corresponding performances of this design are 40.8%, 54.3%, 0.221 W cm^{-2} for overall electrical efficiency, CHP efficiency and power density, respectively.

3.2.2. Effect of operating conditions

The effect of operating conditions (e.g. ethanol recovery, ethanol concentration, fuel utilization, voltage, split fraction, SOFC temperature, cathode inlet temperature) on the composite curves was first investigated. The EtOH recovery and C_{EtOH} are in the range

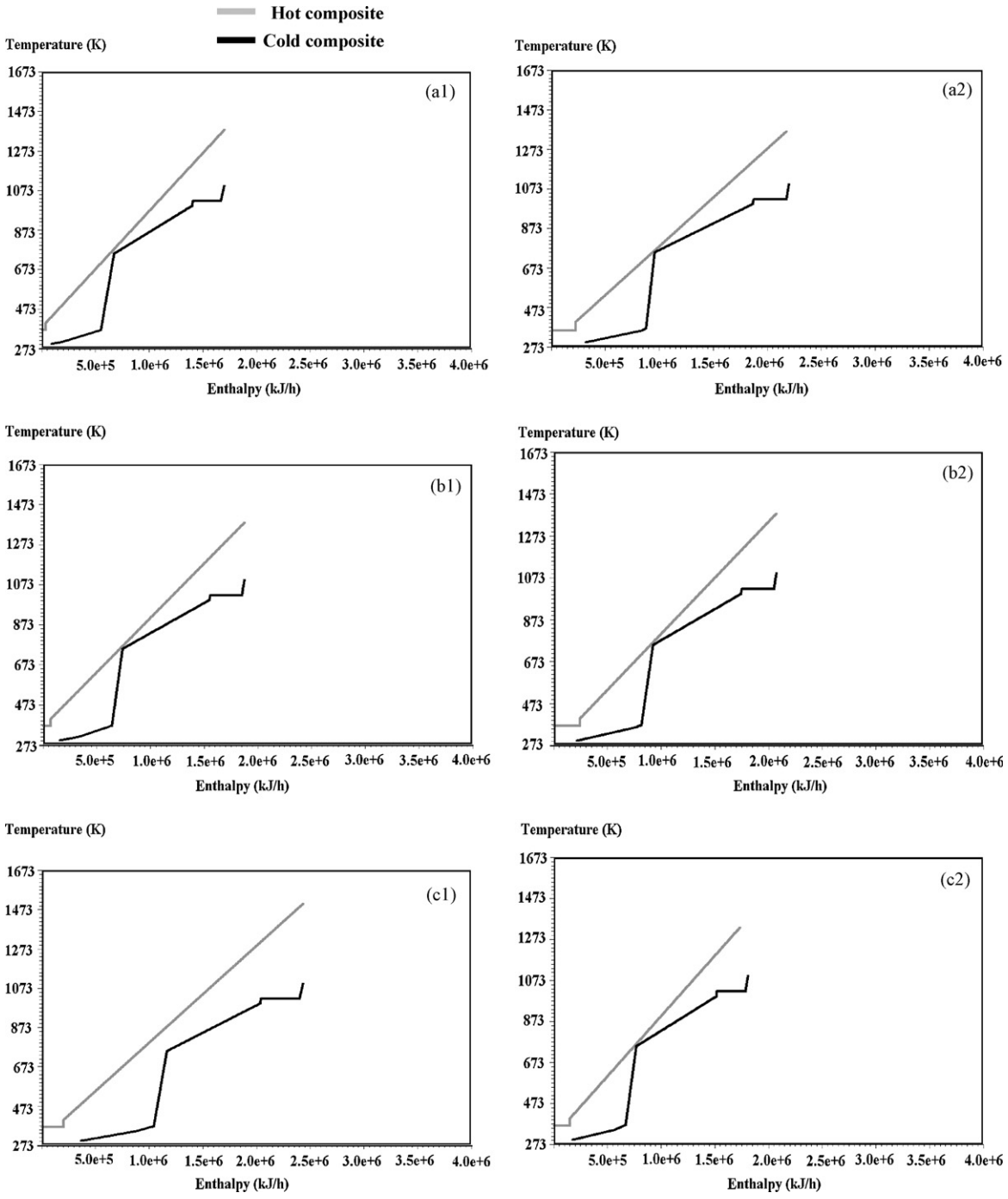

Fig. 14. Composite curves of SOFC-DIS at different operating conditions: (a1) C_{EtOH}, = 17 mol%, (a2) C_{EtOH}, = 41 mol%, (b1) EtOH recovery = 70%, (b2) EtOH recovery = 90%, (c1) V = 0.65 V, (c2) V = 0.75 V, (d1) U_f = 75%, (d2) U_f = 85%, (e1) Sp = 0.3, (e2) Sp = 0.7, (f) T_{SOFC} = 1173 K, (g) $T_{cath,in}$ = 1100 K.

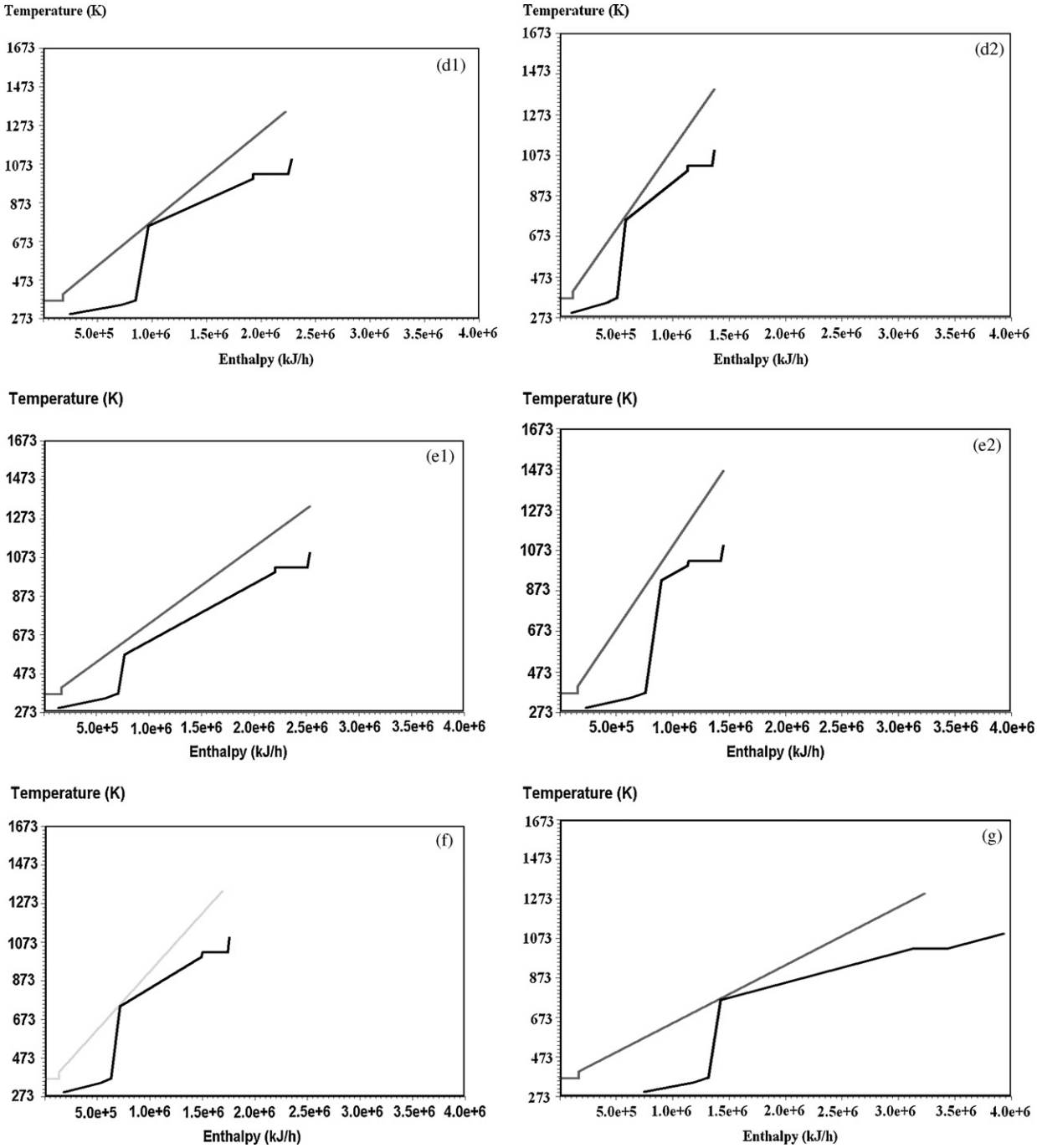

Fig. 14. (*Continued*).

of 70–90% and 17–41 mol%, respectively. It should be noted that the maximum ethanol concentration that can be fed to the external reformer without carbon formation is 41 mol% [9]. Also, in this study, only high ethanol recovery is considered due to high SOFC efficiency. Fuel utilization and voltage were varied from 70 to 85% and 0.65 to 0.75 V, respectively and the split fraction was varied from 0.3 to 0.7. The SOFC temperature of 1173 K and the cathode inlet temperature of 1100 K were examined. Fig. 14 shows the composite curves at these different conditions. Noticeably, it can be seen that the distillation parameters (e.g. ethanol concentration and recovery) does not have significant effect on the composite curves. For SOFC operating conditions, voltage, fuel utilization and split fraction have a strong effect on the composite curves. For the effect of voltage, the higher the voltage, the steeper the composite curves. This can be explained that the lower voltage relates to higher amount of heat loss within the SOFC stack. Therefore, to maintain the temperature inside the stack, more air is required, resulting in lower outlet temperature from the afterburner and higher heat capacity of hot stream. It should be noted that the slope of composite curve is inverse with heat capacity of the streams. Hence, the less steep slope of the hot composite curve is obtained. Moreover, because more air is required for cooling the stack, more heat is needed at the air heater and results in less steep slope of the cold composite curve as illustrated in Fig. 14(c1). In addition, for a lower U_f, more unreacted fuel is burnt in the afterburner and this results in a higher outlet temperature of the hot flue gas and

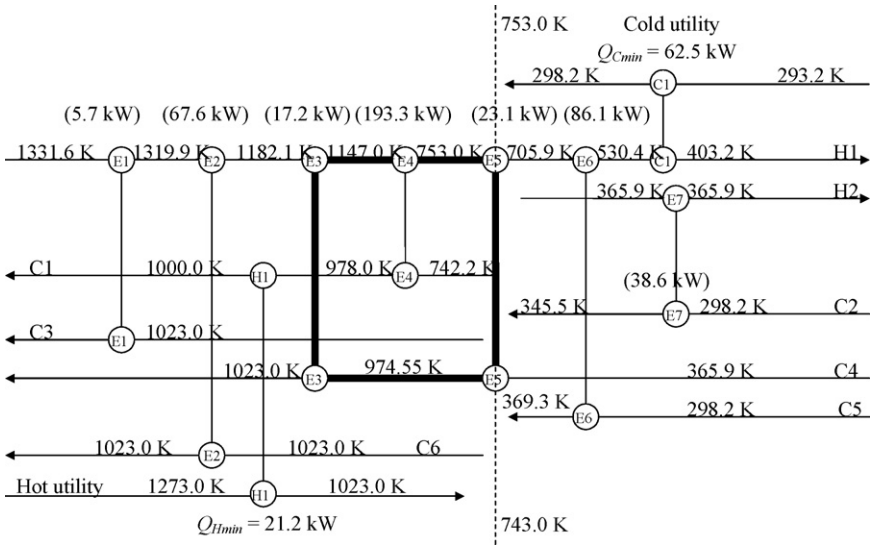

Fig. 15. MER design of SOFC-DIS (CondBio-CathRec) (C_{EtOH} = 25 mol%, EtOH recovery = 80%, U_f = 80%, V = 0.7 V, Sp = 0.5, T_{SOFC} = 1173 K, $T_{anode,in}$ = 1100 K, $T_{cath,in}$ = 1000 K, T_{RF} = 1023 K and P = 101.3 kPa).

more heat recovered from the afterburner as shown in Fig. 14(d1). Consequently, the cold composite curve moves horizontally toward the hot composite curve until it reaches the threshold case in which no hot utility is required. For the higher U_f (in this case, U_f = 85%), the lower temperature of the hot flue gas is obtained. The cold composite curve moves horizontally to the hot composite curve and reaches the pinch point before it meets the threshold condition.

The effect of split fraction was investigated. At low split fractions, a lower amount of high temperature air from the cathode is mixed with the fresh air; therefore, lower air inlet temperature and more energy is consumed in the air heater. Consequently, the slope of the cold stream, especially that of the air heater, decreases and the location of the kink on the cold stream changes. Noticeably, the outlet temperature of hot flue gas from the afterburner is lower because more air, heat carrier, is burnt inside the afterburner. The less steep hot stream can be detected due to higher amount of air in the hot flue gas stream. Higher split fractions result in a larger amount of air to be mixed with the fresh air. A higher air inlet temperature and the lower energy consumption at the air heater were observed. However, when the amount of air fed to the afterburner is reduced, the outlet temperature of the hot stream is higher. Also, lower amount of air in the hot flue gas results in a steeper slope of the hot stream.

From the results, the composite curves can be divided into two groups: (1) the pinch problem and (2) the threshold problem. For the pinch case, the conditions that were found to cause a pinch point in the composite curves are: C_{EtOH} of 41 mol%, operating voltage of 0.65 V, cathode inlet temperature of 1100 K, SOFC temperature of 1173 K and U_f of 85%. Other conditions resulted in the threshold case. The MER design for the pinch case when T_{SOFC} = 1173 K are presented in Fig. 15. The heat capacity and heat load for each stream are presented in Table 9. It can be noticed that Q_{Cmin} = 62.5 and Q_{Hmin} = 21.2 kW. The total cost index is compared to that of the threshold case at the base conditions with Sp = 0.5 in Table 8. It should be noted that the total cost indexes for the pinch case are calculated based on the total cost of the base-MER cases; therefore, the total cost index of the pinch case can be directly compared to that of the threshold cases. Table 8 shows that operating at T_{SOFC} = 1173 K yields higher operating cost, capital cost and total cost than the base-no E3 case.

3.2.3. Avoiding a pinch point by operating at different conditions

As mentioned earlier, the pinch point was found when operating at C_{EtOH} = 41 mol%, T_{SOFC} = 1173 K, $T_{cath,in}$ = 1100 K, U_f = 85% or V = 0.65 V. It can be noticed that the pinch point occurs at the air inlet temperature; therefore, we investigated the effect of the SOFC-DIS operating conditions on the pinch point. As shown in Fig. 14, the shape of composite curves changes dramatically when U_f, split fraction or voltage change. In this case, only split fraction and fuel utilization are considered. It should be noted that adjusting voltage is not considered in this study because it directly affects the SOFC stack performance. In addition, lower split fraction, higher split fraction and lower fuel

Table 9
Information of each unit operated under pinch problem.

Stream no.	Stream label	T_{in} (K)	T_{out} (K)	Load (kW)	MC_p (kW K^{-1})
Hot stream					
Cooler-1 (11–12)	H1	1331.6	403.0	455.5	0.486
Condenser (2a–ab)	H2	365.9	365.9	38.6	Large
Cold stream					
Air stream (7b–8)	C1	742.1	1000.0	214.5	0.832
BioEtOH stream (1a–1b)	C2	298.2	345.5	48.4	1.023
Syngas stream (5–6)	C3	1023.0	1100.0	5.7	0.074
Distillate stream (2–4)	C4	365.9	1023.0	40.3	0.061
Reboiler (3a–3b)	C5	298.2	369.4	86.1	1.209
Reformer (4–5)	C6	1023.0	1023.0	67.6	Large

utilization are examined. As mentioned in the preceding section, lower split fraction reduces the slope of the cold stream and the kink at the air heater occurs at a lower temperature; this could eliminate the pinch point. For higher split fractions, steeper hot composite curves could also help avoiding the pinch point as shown in the wider gap between the hot and cold composite curves in Fig. 14(e). Lastly, operating at lower fuel utilization can make the hot composite curve have higher outlet temperature and probably affect the gap between the composite curves.

For T_{SOFC} = 1173 K, the results show that when the SOFC-DIS operates at a higher split ratio (Sp = 0.7) or lower value (Sp = 0.3) or lower U_f = 75%, the pinch point disappears and a threshold problem is obtained. At U_f = 85%, operating SOFC-DIS at Sp = 0.7 or 0.3 the pinch point disappears. The total cost index of the pinch case and the threshold case are compared and shown in Table 8. When the SOFC-DIS operates at threshold conditions, lower total cost index is obtained for all cases. The total cost index are in the sequence of 1173 K–Sp = 0.7 < 1173 K–U_f = 75% < 1173 K–Sp = 0.3. In addition, it can be seen that the 1173 K–Sp = 0.7 and 1173 K–U_f = 75% yield lower total cost index than that of base-no E3 case. This can be implied that adjusting operating conditions can lower the total cost index at the base conditions.

4. Conclusions

The performance of a thermally integrated SOFC system integrated with a distillation column (SOFC-DIS) was presented in this study. The heat exchanger network of the SOFC-DIS without thermal integration (No-HX SOFC-DIS) at the base conditions was first investigated. Q_{Cmin} of 73.4 kW and Q_{Hmin} of 0 kW were required. The improvement of SOFC-DIS by changing process structure and utilizing internal heat sources (e.g. condenser duty and hot water from the bottom of the distillation column) was then examined. It was found that a utilization of condenser duty to preheat an incoming bioethanol and a cathode recirculation significantly helped reducing an energy demand for the reboiler and the air heater, respectively and resulted in higher overall electrical efficiency and lower total cost index. The system configuration is so-called 'CondBio-CathRec'. The MER network for the CondBio-CathRec was then obtained. It was found that the MER network can reduce Q_{Cmin} of 73.4 kW in No-HX case to 55.9 kW. The heat exchanger loop and utility path in MER network were further studied. It was found that eliminating high temperature distillate heat exchanger (E3) yields the lowest total cost index. Conclusively, the recommended network for SOFC-DIS at the base condition is C3–C6–C1–C4–C5 that means the hot effluent from the afterburner was designed to provide heat to an anode heat exchanger first and then an external reformer, an air heat exchanger, a distillate downstream heat exchanger and finally a reboiler. The effect of operating conditions on the network was then investigated. The results were found that no pinch point occurs except for C_{EtOH} = 41 mol% or the cathode inlet temperature of 1100 K or T_{SOFC} = 1173 K or U_f = 85%. The MER network for the pinch case when T_{SOFC} = 1173 K was investigated and found the higher total cost index. Lastly, the results showed that T_{SOFC} = 1173 K can become a threshold case when operating at lower/higher split fraction or lower fuel utilization. The results found that the obtained threshold problem yields lower total cost indexes than that of the pinch case (T_{SOFC} = 1173 K). Moreover, it can be noticed that changing operating conditions (e.g. lower fuel utilization or higher split fraction) can achieve the lower total cost index than that of the base conditions. Suitable operating conditions which yield the lowest total cost index should be further investigated.

Acknowledgements

The support from the Thailand Research Fund, Commission of High Education and National Metal and Materials Technology Center (MTEC) are gratefully acknowledged.

References

[1] E. Fontell, T. Kivisaari, N. Christiansen, J.B. Hansen, J. Pålsson, J. Power Sources 131 (2004) 49–56.
[2] A.O. Omosun, A. Bauen, N.P. Brandon, C.S. Adjiman, D. Hart, J. Power Sources 131 (2004) 96–106.
[3] W. Zhang, E. Croiset, P.L. Douglas, M.W. Fowler, E. Entchev, Energy Convers. Manage. 46 (2005) 181–196.
[4] R.J. Braun, S.A. Klein, D.T. Reindl, J. Power Sources 158 (2006) 1290–1305.
[5] S. Douvartzides, F.A. Coutelieris, P.E. Tsiakaras, J. Power Sources 114 (2003) 203–212.
[6] S. Douvartzides, F. Coutelieris, P. Tsiakaras, J. Power Sources 131 (2004) 224–230.
[7] L.E. Arteaga, L.M. Peralta, V. Kafarov, Y. Casas, E. Gonzales, Chem. Eng. J. 136 (2008) 256–266.
[8] W. Jamsak, S. Assabumrungrat, P.L. Douglas, N. Laosiripojana, R. Suwanwarangkul, S. Charojrochkul, ECS Trans. 7 (2007) 1475–1482.
[9] S. Assabumrungrat, V. Pavarajarn, S. Charojrochkul, N. Laosiripojana, Chem. Eng. Sci. 59 (2004) 6015–6020.
[10] E.Y. Garcia, M.A. Laborde, Int. J. Hydrogen Energy 16 (1991) 307–312.
[11] K. Vasudeva, N. Mitra, P. Umasankar, S.C. Dhinggra, Int. J. Hydrogen Energy 21 (1996) 13–18.
[12] E. Achenbach, J. Power Sources 49 (1994) 333–348.
[13] S.H. Chan, C.F. Low, O.L. Ding, J. Power Sources 103 (2002) 188–200.
[14] B. Linnhoff, D.W. Townsend, D. Boland, G.F. Hewitt, B.E.A. Thomas, A.R. Guy, R.H. Marsland, User Guide on Process Integration for the Efficient Use of Energy, 1st edition, Institution of Chemical Engineering, UK, 1982.

ภาคผนวก 3

Chemical Engineering Journal 147 (2009) 336–341

Contents lists available at ScienceDirect

Chemical Engineering Journal

journal homepage: www.elsevier.com/locate/cej

Simulation of solid oxide fuel cell systems integrated with sequential CaO–CO_2 capture unit

S. Vivanpatarakij[a], N. Laosiripojana[b], W. Kiatkittipong[c], A. Arpornwichanop[a], A. Soottitantawat[a], S. Assabumrungrat[a,*]

[a] Department of Chemical Engineering, Faculty of Engineering, Chulalongkorn University, Bangkok 10330, Thailand
[b] The Joint Graduate School of Energy and Environment, King Mongkut's University of Technology Thonburi, Bangkok 10140, Thailand
[c] Department of Chemical Engineering, Faculty of Engineering and Industrial Technology, Silpakorn University, Nakhon Pathom 73000, Thailand

ARTICLE INFO

Article history:
Received 17 July 2008
Received in revised form
14 November 2008
Accepted 25 November 2008

Keywords:
Adsorption
CO_2 capture
Fuel cell system
SOFC

ABSTRACT

This paper presents preliminary simulation results from the performance analysis of the integrated systems of calcium oxide (CaO)–carbon dioxide (CO_2) capture unit and solid oxide fuel cell (SOFC). The CO_2 was extracted for further sequestration in the CaO–CO_2 capture unit. Three configurations of the integrated systems (CaO-Before-SOFC: CBS, CaO-After-SOFC: CAS and CaO-After-Burner: CAB) were considered. It was found that the CO_2 capture efficiency (E_c) is dependent on CaO fresh feed rate (F_0) and CaO recycle rate (F_R). The improvement of SOFC performance was only realized for the CBS system. The SOFC performance increases with increasing CO_2 E_c. The preliminary economic analysis was carried out considering total additional cost per mole of CO_2 captured. At a low percentage of CO_2 capture (<42.5%), the CBS system is the most suitable configuration while the CAS system becomes an attractive choice at higher values. However, only the CAB system could be possible at a very high range of CO_2 capture (>94%).

1. Introduction

Nowadays, global warming is considered to be an important problem of the world. A major cause is arisen from a large emission of carbon dioxide to the environment which has been particularly driven by the growth of economics. Therefore, low-CO_2-emission processes are desired. Fuel cell is one of the novel processes for electrical power generation via an electrochemical reaction of hydrogen. Small amount of CO_2 is emitted from the fuel cell. Among a various type of fuel cell, solid oxide fuel cell (SOFC) is the most promising process. Due to high electrical efficiency of SOFC, lower amount of fuel is consumed, resulting in a lower amount of generated CO_2. At present, a number of efforts have been carried out to improve its efficiency. An integration of an SOFC with a CaO–CO_2 capture unit is one of an attractive choice for electrical power generation. The use of the CaO–CO_2 capture unit for CO_2 sequestration could further reduce the amount of CO_2 emitted to the environment.

The in situ CaO–CO_2 capture for shifting equilibrium of reaction was studied [1–6]. A coal/H_2O/CaO gasification system offers a higher yield of hydrogen production compared to a conventional coal/H_2O gasification system [1]. Methane steam reforming reaction (MSR) combined with CaO-carbonation showed a potential benefit on CO_2 acceptor and hydrogen production at 1023 K [2]. The simulation of in situ carbonation of CaO in MSR was studied [3,4] and the kinetics of the carbonation of CaO were proposed. The addition of CaO in a methane steam reforming system can increase the purity of hydrogen to be higher than 95% in a laboratory-scale operation [5]. The similar result was also reported in an ethanol steam reforming with addition of CaO [6].

Although CaO is a good candidate for CO_2 capture, the main problem of CaO–CO_2 capture is the generation of $CaCO_3$. Therefore, a carbonation–calcination cycle of CaO was considered as reported in many researches [7–10]. Gupta and Fan [7] used the reaction based on the cycle of separated CO_2 with CaO from flue gas. Sintering of CaO sorbent was not observed within 2–3 cycles of carbonation–calcination at 973 K. However, carbonation conversion decreased with increasing the number of cycles [8,9]. Abanades [10] proposed an expression for calculating the maximum CO_2 capture efficiency of CaO.

Some researchers have investigated the combined system of fuel cell and CO_2 capture unit to improve the system efficiency and reduce the global warming gas. Amorelli et al. [11] reported that a 1.6 MW MCFC-gas turbine (MCFC/GT) incorporated with a CO_2 capture unit could reduce the CO_2 emission by 50% from the conventional MCFC/GT system. Moreover, Fredriksson Möller et al. [12] showed that an SOFC/GT system can be operated at an electrical efficiency close to 65% when incorporating with a CO_2 capture unit.

* Corresponding author. Tel.: +66 2 218 6868; fax: +66 2 218 6877.
E-mail address: Suttichai.A@chula.ac.th (S. Assabumrungrat).

1385-8947/$ – see front matter © 2008 Elsevier B.V. All rights reserved.
doi:10.1016/j.cej.2008.11.040

Nomenclature

a_j	constant in Eq. (11) (Ω m)
b	constant in Eq. (4) (0.174)
b_j	constant in Eq. (11) (K)
d_p	particle diameter (m)
D	diameter of reactor (m)
E	open circuit voltage (OCV) (V)
E_c	CO_2 capture efficiency (%)
E_0	reversible potential (V)
f	constant in Eq. (4) (0.782)
f_g	gas friction factor [14]
f_s	solid friction factor [14]
F	Faraday constant (96,485.34) (C mol^{-1})
F_0	fresh feed rate of CaO (mol s^{-1})
F_{CO_2}	molar flow rate of CO_2 (mol s^{-1})
F_R	recycle rate of CaO (mol s^{-1})
g	gravity acceleration (m s^{-2})
i	current density (A m^{-2})
i_0	exchange current density (A m^{-2})
L	length of reactor (m)
m	exponent parameter in Eq. (15)
n_e	number of electron transfer
P	total pressure (atm)
P_i	partial pressure (atm)
R	universal gas constant (8.31447×10^{-3}) (kJ mol^{-1} K^{-1})
T	absolute temperature (K)
u	velocity (m s^{-1})
U_f	fuel utilization (%)
v_t	gas terminal velocity (m s^{-1})
V	operating voltage (V)

Greeks letters

α	electron transfer coefficient
δ	thickness (m)
ε	bed void fraction
η_i	overpotential (Ω m^2)
μ	viscosity of fluid (Pa s)
ρ	density (kg m^{-3})
ρ_ι	specific ohmic resistance (Ω m)

Subscript

A	anode
C	cathode
f	fluid
p	particle

In this study, performances of various systems of SOFC integrated with carbonation–calcination systems (SOFC–CaO system) were simulated. The effects of location of CaO–CO_2 acceptor in the SOFC system, the CaO fresh feed rate, the CaO recycle rate and the fuel utilization were studied in terms of amount of CO_2 captured and SOFC performance. Finally, preliminary economic analysis was also considered.

2. Theory

2.1. Methane steam reforming

Methane steam reforming is the conventional route for hydrogen production. The major reactions taking place in the reactor are methane steam reforming (MSR, Eq. (1)) and water gas shift reaction (WGSR, Eq. (2)).

$$CH_4 + H_2O \leftrightarrows CO + 3H_2 \quad (1)$$

$$CO + H_2O \leftrightarrows CO_2 + H_2 \quad (2)$$

$$CH_4 + 2H_2O \leftrightarrows CO_2 + 4H_2 \quad (3)$$

In order to avoid a carbon formation problem, the molar ratio of H_2O:CH_4 in the feed stream should be higher than 2.5 [13]. In this work, it was assumed that the gas exiting the reformer is at its equilibrium composition.

2.2. CaO–CO_2 acceptor systems

Carbonation reaction of calcium oxide (CaO) can convert carbon dioxide (CO_2) to calcium carbonate ($CaCO_3$) whereas $CaCO_3$ can reverse to CaO at high temperature calcinations. The carbonation–calcination cycle for CO_2 separation is illustrated in Fig. 1. The maximum efficiency of CO_2 capture can be expressed as follows [10]:

$$E_c = \frac{F_R + F_0}{F_0 + F_{CO_2}} \cdot \left(\frac{f \cdot F_0}{F_0 + F_R(1-f)} + b \right) \quad (4)$$

where $b = 0.174$, $f = 0.782$, F_0 is fresh feed rate of CaO, F_R is feed recycle rate of CaO and F_{CO_2} is feed rate of CO_2.

The circulating fluidized bed was chosen for the CaO carbonation–calcination operation. The constraint of circulating fluidized bed is that gas velocity (v) must be higher than gas terminal velocity (v_t), ($v > v_t$) (Eq. (5)). Pressure drop along the reactor can be calculated by Eq. (6) [14].

$$v_t = \frac{g(\rho_p - \rho_f)d_p^2}{18\mu} \quad (5)$$

$$\frac{\Delta P}{L} = \rho_p(1-\varepsilon)g + \rho_f \varepsilon g + \frac{2f_g \rho_f u_f^2}{D} + \frac{2f_s \rho_p (1-\varepsilon) u_p^2}{D} \quad (6)$$

2.3. SOFC

An SOFC unit consists of two porous ceramic electrodes (i.e., an anode and a cathode) and a solid ceramic electrolyte. In theory, both hydrogen and CO can react electrochemically with oxygen ions at the anode of the SOFC cells. However, it was reported that about 98% of current is produced via H_2 oxidation in common situations [15]. Therefore it was assumed in this study that the CO electro-oxidation is neglected. The theoretical open-circuit voltage of the cell (E), which is the maximum voltage under specific operating conditions, can be calculated from the following equations [16]:

$$E = E_0 + \frac{RT}{2F} \ln \left(\frac{P_{H_2} P_{O_2}^{0.5}}{P_{H_2O}} \right) \quad (7)$$

$$E_0 = 1.253 - 2.4516 \times 10^{-4} T \quad (8)$$

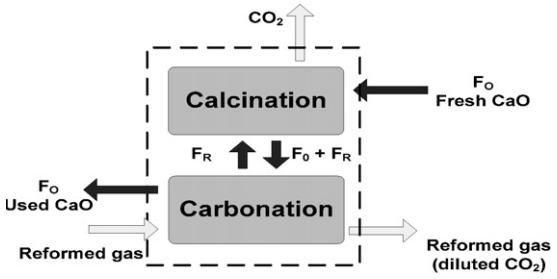

Fig. 1. Schematic diagram of a CaO–CO_2 acceptor system.

The actual voltage (Eq. (9)) is usually lower than the theoretical open-circuit voltage due to the presence of polarization losses: ohmic polarization, activation polarization and concentration polarization [17].

$$V = E - (\eta_{Ohm} + \eta_{Act} + \eta_{Conc}) \quad (9)$$

The ohmic polarization (Eqs. (10) and (11)) is the resistance of electrons through electrolyte and that of ions through electrodes. The activation polarization (Eqs. (12)–(15)) is mostly illustration of a loss for driving the electrochemical reaction to completion. The concentration polarization occurs due to the mass transfer limitation through the porous electrodes.

Ohmic polarization:

$$\eta_{Ohm} = \sum \rho_j \delta_j \quad (10)$$

$$\rho_j = a_j \exp(b_j T) \quad (11)$$

Activation polarization:

$$i = i_0 \left[\exp\left(\frac{\alpha n_e F \eta_{Act}}{RT}\right) - \exp\left(-\frac{(1-\alpha) n_e F \eta_{Act}}{RT}\right)\right] \quad (12)$$

$$\eta_{Act} = \frac{2RT}{n_e F} sinh^{-1}\left(\frac{i}{i_0}\right); \quad \text{where } \alpha = 0.5 \quad (13)$$

$$i_{0,A} = 5.5 \times 10^8 \left(\frac{p_{H_2}}{p}\right)\left(\frac{p_{H_2O}}{p}\right) \exp\left(\frac{-100 \times 10^3}{RT}\right) \quad (14)$$

$$i_{0,C} = 7.0 \times 10^8 \left(\frac{p_{O_2}}{p}\right)^m \exp\left(\frac{-120 \times 10^3}{RT}\right) \quad (15)$$

To simplify the calculation of the SOFC performance, it was assumed that both fuel and oxidant are well-diffused through the electrodes. Therefore, the concentration polarization losses ($\eta_{Conc,A}$ and $\eta_{Conc,C}$) are neglected. This assumption is valid when the current density is not very high [18]. Table 1 summarizes the ohmic polarization parameters of the cell components employed in this work. It was also assumed that the gas composition in the anode is always at its equilibrium as the rate of WGSR is fast particularly at high operating temperatures of SOFC [15]. The model validations of methane steam reformer and fuel cell performance were performed and good agreements with previous literatures [16,19] were observed.

Table 1
Ohmic polarization constants of Eqs. (10) and (11).

	a	b	δ (μm)
Anode (Ni–YSZ)	2.98×10^{-5}	−1,392	50
Cathode (LSM–YSZ)	8.11×10^{-5}	600	50
Electrolyte (YSZ)	2.94×10^{-5}	10,350	140

2.4. CaO–SOFC configurations

The conventional SOFC system is composed of a reformer, an SOFC and an afterburner. First, methane and water are fed to the reformer where methane steam reforming reaction and water gas shift reaction take place. Then, the reformed gas, a mixture of hydrogen, carbon monoxide, carbon dioxide and unreacted reagents, are fed to the SOFC unit. Oxygen is reduced, permeated through an electrolyte and then reacted with hydrogen at the anode. After that, the exhaust gas is fed to the afterburner where residual fuels are combusted, providing heat to other parts of the system. Fig. 2(a–c) shows the SOFC systems with different configurations: (a) the SOFC system incorporated with a CaO–CO_2 acceptor before the SOFC unit (CaO-Before-SOFC: CBS), (b) the SOFC system incorporated with a CaO–CO_2 acceptor after the SOFC unit (CaO-After-SOFC: CAS) and (c) the SOFC system incorporated with a CaO–CO_2 acceptor after the afterburner unit (CaO-After-Burner: CAB). Because the amount of CO_2 produced varies among the different streams in the system, the location of the CaO–CO_2 capture unit could affect the performance of the SOFC system. Table 2 summarizes the standard operating condition of the SOFC with the CaO–CO_2 acceptor.

2.5. Economic analysis

Economic analysis was carried out to compare the costs of different SOFC systems incorporated with a sequential CaO–CO_2 capture unit. The total capital cost includes the costs of compressor, SOFC stack (1500 \$/m^2) [18] and CaO (60 \$/ton). The compressor cost was

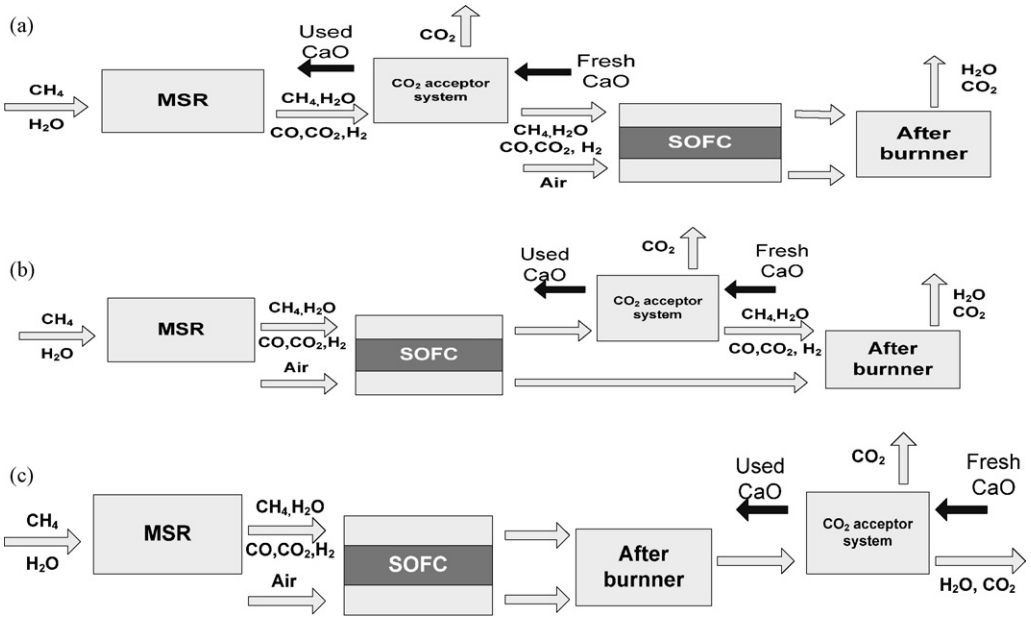

Fig. 2. Schematic diagrams of (a) CBS system, (b) CAS system and (c) CAB system.

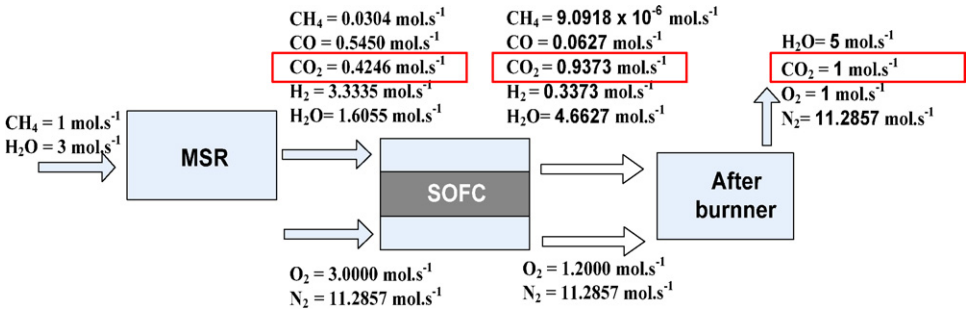

Fig. 3. Molar flow rates of different gases in the conventional SOFC system (U_f = 90%, T_R = 973 K and T_{SOFC} = 1073 K).

estimated from the following expression [20]:

$$\text{Cost of compressor (\$)} = 1.49 \cdot \text{HP}^{0.71} \times 10^3 \quad (16)$$

where 10 < HP < 800.

3. Results and discussion

Fig. 3 shows molar flow rates of different gases in the conventional SOFC system operated at U_f = 90%, T_R = 973 K and T_{SOFC} = 1073 K. Methane of 1 mol s^{-1} and water of 3 mol s^{-1} were fed to the system. The CO_2 flow rates of the streams before SOFC, after SOFC and after the burner are 0.4246, 0.9373 and 1.0 mol s^{-1}, respectively. Therefore, different amount of CO_2 can be captured when the CaO–CO_2 acceptor is installed at different places in the system. The flow rate of CO_2 after the reformer (before the SOFC) is still low as the WGSR is a mildly exothermic and therefore CO is not favorably converted to CO_2 at this high reforming temperature (973 K). The flow rate of CO_2 increases in the SOFC as hydrogen is consumed, generating H_2O which can further convert CO to CO_2 by WGSR in the anode channel. Finally, the flow rate of CO_2 becomes the highest after all spent fuels are completely combusted in the afterburner.

The effects of fresh CaO feed (F_0) and recycle rate of CaO (F_R) on maximum CO_2 capture efficiency (E_c) for the CBS, CAS and CAB systems are shown in Fig. 4(a–c). As indicated in Eq. (4), the maximum CO_2 capture efficiency (E_c) depends on the flow rate of fresh CaO feed (F_0), the recycle rate of CaO (F_R) and the concentration of CO_2 in the stream inlet. All figures show that the CO_2 capture efficiency increases with increasing fresh CaO feed (F_0) and recycle rate of used CaO (F_R). Therefore, a higher E_c can be achieved by increasing F_0 and/or F_R.

The SOFC performance in the case of CBS at various values of fuel utilization (U_f) and CO_2 capture efficiency (E_c) is illustrated in Fig. 5. Solid lines represent the obtained power density of the conventional SOFC system while dashed lines represent the power density at different values of E_c ranging from 50 to 90%. It is obvious that the CBS can improve the SOFC performance. This is particularly pronounced at a higher efficiency of CO_2 capture. It should be noted that the SOFC performance improvement is not realized in the CAS and CAB systems as the feed composition of the SOFC is not

Table 2
Standard condition.

Parameter	Value
CH_4 feed rate	1 (mol s^{-1})
H_2O:CH_4 feed ratio	3 (–)
Temperature of SOFC (T_{SOFC})	1073 (K)
Temperature of reformer (T_R)	973 (K)
Temperature of carbonation of CaO	873 (K)
Temperature of calcination of $CaCO_3$	1173 (K)
Air:CH_4 feed ratio	15 (–)
Temperature of reformer (T_R)	973 (K)
Density of CaO (ρ_{CaO})	1503 (kg m^{-3})
Bed void fraction (ε)	0.45 (–)
Particle size of CaO	0.5 (mm)
Length:diameter ratio of CaO acceptor (L/D)	10 (–)

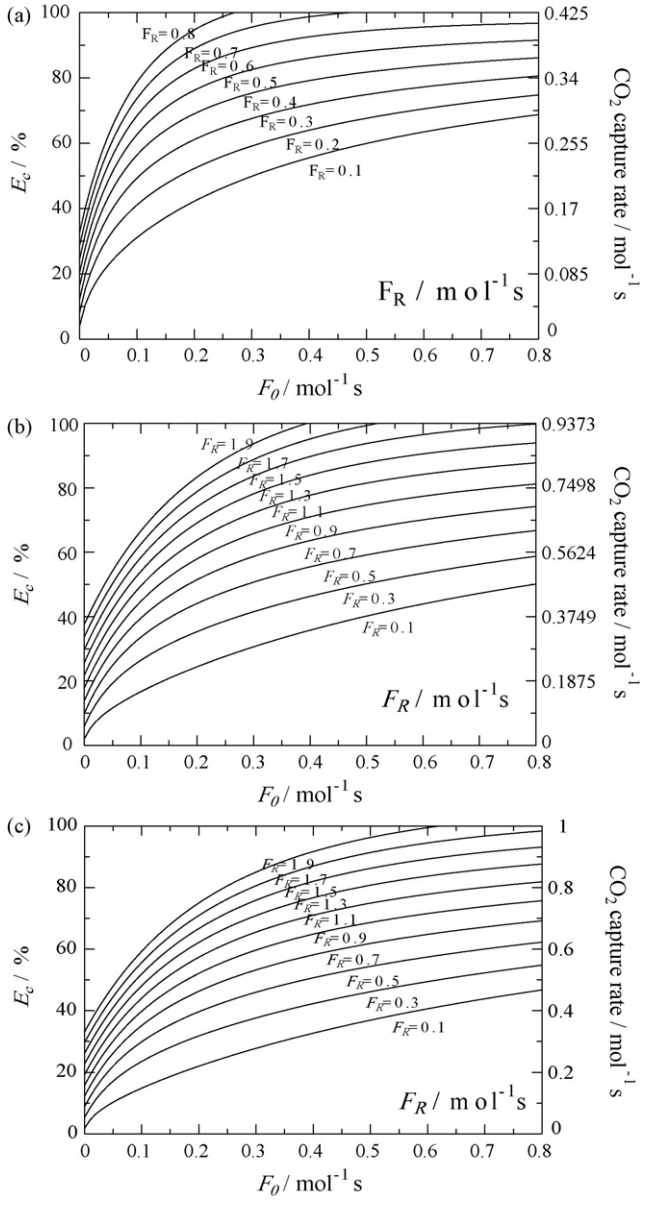

Fig. 4. Effects of CaO fresh feed rate (F_0) and CaO recycle rate (F_R) on CO_2 capture efficiency (E_c): (a) CBS, (b) CAS and (c) CAB (T_R = 973 K).

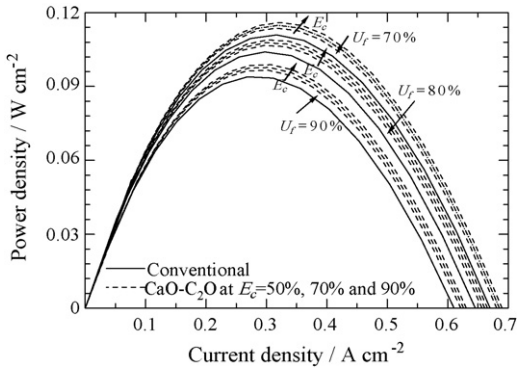

Fig. 5. Comparison of SOFC performance between CBS and conventional SOFC systems at various values of CO_2 capture efficiency (E_c) and fuel utilization (U_f) (T_R = 973 K, T_{SOFC} = 1073 K).

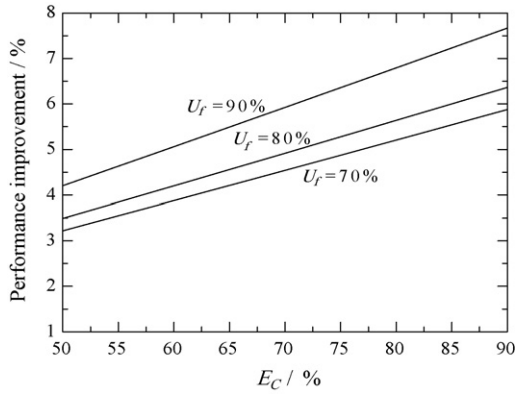

Fig. 6. Performance improvement of CBS system (V = 0.56 V, T_R = 973 K, T_{SOFC} = 1073 K).

influenced by the presence of the CaO–CO_2 acceptor. Therefore, the SOFC performance of CAS and CAB system is not different from the conventional system without the CaO–CO_2 acceptor. Fig. 6 shows the SOFC performance improvement for the CBS system in term of power density compared to that of the conventional system. The SOFC performance increases with increasing the fuel utilization and efficiency of CO_2 capture. With E_c = 90% and U_f = 90%, the CBS can increase the performance of SOFC by 8%.

A preliminary economic analysis of different SOFC–CaO systems was carried out to determine a suitable place of the CaO–CO_2 capture unit to be integrated in the SOFC system. With the presence of the capture unit, some electrical power is required to operate the compressor for fluidizing the CaO adsorbent. Furthermore, there is the additional operating cost on the use of fresh CaO. In order to achieve a minimum cost on compressor and compressor power, it is desired to operate the CaO–CO_2 capture unit at the condition in which the total flow rate of CaO in the capture unit ($F_0 + F_R$) is at minimum. Fig. 7 shows an example for determining a suitable F_0 for the case of CBS. It is observed that the optimum F_0 increases with the increasing CO_2 capture efficiency (E_c). The other systems were also calculated on the same procedure. For comparison among the different systems, total additional cost from the use of CaO–CO_2 capture unit, which was assumed to be operated for 5 years, was calculated taking into account the capital cost (extra SOFC area and compressor) and the operating cost (cost of CaO). Table 3 shows an example of the economic analysis for the systems with net electrical power of about 400 kW (electrical efficiency = 45.9%) and %CO_2 capture of 38.2%. It is observed that additional electrical power required for operating the compressor in CAB systems is higher than the CBS and CAS systems about 5 times. As the CO_2 composition in the exhaust gas from the afterburner is much lower than that of the reformed gas and the anode gas from the SOFC, much higher electrical power is required. Furthermore, the CAB system also showed the highest requirement of SOFC area which is about twice of the other systems. This is corresponding well with the required electrical power. It should be noted that for the CBS system, a lower SOFC area compared to that of the conventional SOFC system is observed due to the improved SOFC performance as discussed earlier. From

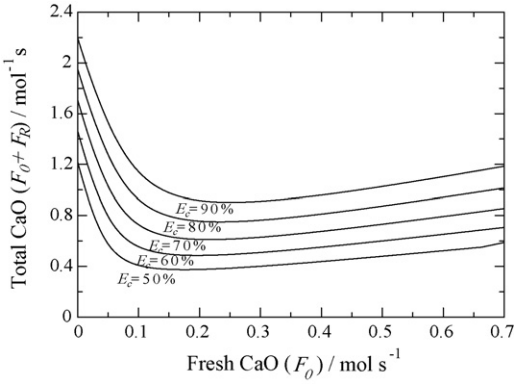

Fig. 7. Effect of CaO fresh feed rate on total in-process CaO flow rate ($F_0 + F_R$) for the CAS system (T_R = 973 K).

Table 3
Economic analysis of CaO–SOFC system and conventional SOFC system.

	Conventional	CBS	CAS	CAB
CO_2 reduction (%)	–	38.2	38.2	38.2
Fuel utilization (U_f) (%)	90	90	90	90
Total electrical power production (kW)	401.39	401.39	401.39	401.39
Total electrical efficiency (%)	45.9	45.9	45.9	45.9
Electrical power (kW)	401.39	408.53	409.5	440.07
SOFC area (m^2)	723.86	719.24	794.59	1,406.06
Compressor power (kW)	–	7.14	8.11	38.69
Operating voltage (V)	0.58	0.59	0.59	0.63
Cost of SOFC area/\$ (1500 \$ m^{-2})	1,085,784	1,078,860	1,191,882	2,109,086
Compressor cost (\$)	–	6,018.95	6,585.89	19,969.23
Additional SOFC cost (\$)	–	−6,924	106,097	1,023,301
F_R of CaO (mol s^{-1})	–	0.65269	0.29982	0.28209
F_0 of CaO (mol s^{-1})	–	0.25	0.335	0.34
Total CaO at start up (mol)	–	0.90269	0.63482	0.62209
Operating cost of capture unit: 5 years/\$	–	132,639	177,736	180,389
Total additional cost (\$)	–	125,715	283,833	1,203,690
CO_2 reduction: 5 years/mol	–	66.9×10^6	66.9×10^6	66.9×10^6
Total additional cost:mol of CO_2 captured (\$ mol^{-1})	NA	0.0019	0.0042	0.0180

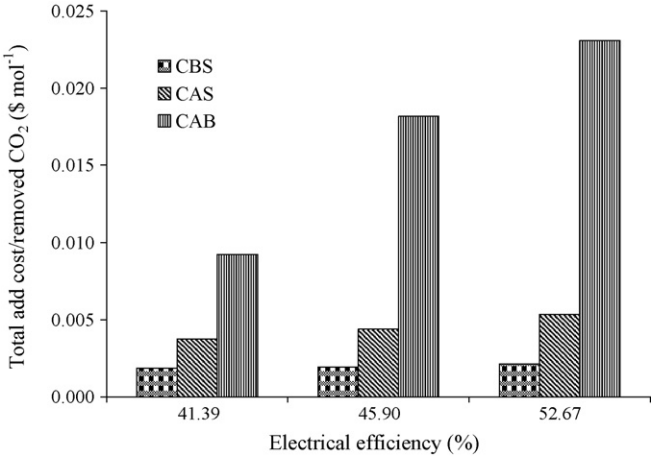

Fig. 8. Effect of electrical efficiency on total additional cost per mole of CO_2 captured (U_f = 90%, T_{SOFC} = 1073 K, CO_2 capture rate = 0.382 mol s^{-1}).

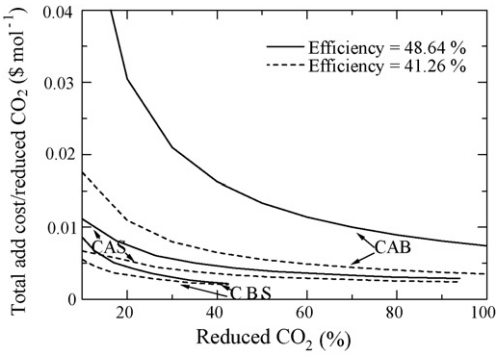

Fig. 9. Economic analysis of CBS, CAS and CAB system (T_R = 973 K, T_{SOFC} = 1073 K).

the comparison, it is observed that at 38.2% CO_2 capture the CBS system is the most attractive system due to the lowest total additional cost and total additional cost per mole of CO_2 captured.

Fig. 8 shows the total additional cost per mole of CO_2 captured at various values of electrical efficiency (41.4, 45.9 and 52.7%). It is obvious that the cost per mole of CO_2 captured increases when the overall system is operated at a higher electrical efficiency. However, the increase is much less pronounced for the CBS system having improved SOFC performance.

Fig. 9 shows the total additional cost per mole of CO_2 captured at various levels of CO_2 capture. The solid lines represent the case with an electrical efficiency of 48.6% while dash lines represent that with an electrical efficiency of 41.3%. It is obvious that for each level of %CO_2 capture, the additional cost per mole of CO_2 captured is in the order: CBS < CAS < CAB. However, the maximum %CO_2 capture varies among the systems. From the study it is suggested that at a low range of %CO_2 capture (<42.5%) the CBS system is the best configuration. At a higher range, the CAS system is recommended. However, at a very high value (>94%) the CAB system is the only possible configuration for operation. It should be noted that although the energy balance has not been considered in this study, our calculations indicate that the exothermic energy from the SOFC stack, the after-burner and the carbonation reaction is sufficient to provide the heat to the heat-consuming units in the integrated system such as the feed preheaters, the reformer and calcination reaction. In addition, for practical operation, design of a heat exchanger network for the integrated system of CaO–CO_2 capture unit and SOFC is required. The design needs to take into account the periodic operation nature of the CaO–CO_2 capture unit.

4. Conclusions

The SOFC system integrated with a CaO–CO_2 capture unit was investigated in this study. The effect of location of the CaO–CO_2 capture unit in the SOFC system (i.e., CaO-Before-SOFC; CBS, CaO-After-SOFC; CAS and CaO-After-Burner; CAB) and other operating parameters on the amount of CO_2 captured, SOFC performance and economic analysis was considered. It was found that all SOFC–CaO systems can reduce the CO_2 emission; however, only the CBS system can improve performance of SOFC. Economic analysis was carried out to compare the different systems. It was indicated that the additional cost per mole of CO_2 captured follows the order: CBS < CAS < CAB. However, the selection of a suitable system significantly depends on the level of CO_2 capture.

Acknowledgement

The support from The Thailand Research Fund and Commission on Higher Education is gratefully acknowledged.

References

[1] Z. Wang, J. Zhou, Q. Wang, J. Fan, K. Cen, Int. J. Hydrogen Energy 31 (2006) 945–952.
[2] D.K. Lee, I.H. Baek, W.L. Yoon, Chem. Eng. Sci. 59 (2004) 931–942.
[3] D.K. Lee, I.H. Baek, W.L. Yoon, Int. J. Hydrogen Energy 31 (2006) 649–657.
[4] D.K. Lee, Chem. Eng. J. 100 (2004) 71–77.
[5] B. Balasubramanian, A. Lopez Ortiz, S. Kaytakoglu, D.P. Harrison, Chem. Eng. Sci. 54 (1999) 3543–3552.
[6] J. Comas, M. Laborde, N. Amadeo, J. Power Sources 138 (2004) 61–67.
[7] H. Gupta, L.S. Fan, Ind. Eng. Chem. Res. 41 (2002) 4035–4042.
[8] M.V. Iyer, H. Gupta, B.B. Sakadjian, L.S. Fan, Ind. Eng. Chem. Res. 43 (2004) 3939–3947.
[9] G.S. Grasa, J.C. Abanades, M. Alonso, B. Gonzalez, Chem. Eng. J. 137 (2008) 561–567.
[10] J.C. Abanades, Chem. Eng. J. 90 (2002) 303–306.
[11] A. Amorelli, M.B. Wilkinson, P. Bedont, P. Capobianco, B. Marcenaro, F. Parodi, A. Torazza, Energy 29 (2004) 1279–1284.
[12] B. Fredriksson Möller, J. Arriagada, M. Assadi, I. Potts, J. Power Sources 131 (2004) 320–326.
[13] H.J. Renner, R. Marschner, Catalytic reforming of natural gas and other hydrocarbon Ullmann's Encyclopedia of Industrial Chemistry, vol. A2, fifth ed., VCH Verlagsgesellschaft, Weinheim, Germany, 1985, pp. 186–204.
[14] S.M. Walas, Chemical Process Equipment Selection and Design, Butterworth, Inc., 1988.
[15] M.A. Khaleel, Z. Lin, P. Singh, W. Surdoval, D. Collin, J. Power Sources 130 (2004) 136–148.
[16] E. Hernandez-Pacheco, M.D. Mann, P.N. Hutton, D. Singh, K.E. Martin, Int. J. Hydrogen Energy 30 (2005) 1221–1233.
[17] M. Pfafferodt, P. Heidebrecht, M. Stelter, K. Sundmacher, J. Power Sources 149 (2005) 53–62.
[18] E. Riensche, U. Stimming, G. Unverzagt, J. Power Sources 73 (1998) 251–256.
[19] J. Shu, B.P.A. Grandjean, S. Kaliaguine, Appl. Catal. A 119 (1994) 305–325.
[20] S.M. Walas, Chemical Process Equipment Selection and Design, Butterworth, Inc., 1988, pp. 665–668.

ภาคผนวก 4

Available at www.sciencedirect.com

ScienceDirect

journal homepage: www.elsevier.com/locate/he

Modeling of SOFC with indirect internal reforming operation: Comparison of conventional packed-bed and catalytic coated-wall internal reformer

P. Dokamaingam[a], *S. Assabumrungrat*[b], *A. Soottitantawat*[b], *I. Sramala*[c], *N. Laosiripojana*[a,*]

[a]*The Joint Graduate School of Energy and Environment, King Mongkut's University of Technology Thonburi, Bangkok, Thailand*
[b]*Department of Chemical Engineering, Faculty of Engineering, Chulalongkorn University, Bangkok, Thailand*
[c]*National Nanotechnology Center, National Science and Technology Development Agency, Pathumthani, Thailand*

ARTICLE INFO

Article history:
Received 6 June 2008
Received in revised form
1 October 2008
Accepted 1 October 2008
Available online 26 November 2008

Keywords:
Indirect internal reforming
Solid oxide fuel cell
Coated-wall reformer

ABSTRACT

In the present work, mathematical models of indirect internal reforming solid oxide fuel cells (IIR-SOFC) fueled by methane were developed to analyze the thermal coupling of an internal endothermic reforming with exothermic electrochemical reactions and determine the system performance. The models are based on steady-state, heterogeneous, two-dimensional reformer and annular design SOFC models. Two types of internal reformer i.e. conventional packed-bed and catalytic coated-wall reformers were considered here. The simulations indicated that IIR-SOFC with packed-bed internal reformer leads to the rapid methane consumption and undesirable local cooling at the entrance of internal reformer due to the mismatch between thermal load associated with rapid reforming rate and local amount of heat available from electrochemical reactions. The simulation then revealed that IIR-SOFC with coated-wall internal reformer provides smoother methane conversion with significant lower local cooling at the entrance of internal reformer.

Sensitivity analysis of three important parameters (i.e. flow direction, fuel inlet temperature and operating pressure) was then performed. IIR-SOFC with conventional counter-flow pattern (counter-flow of air and fuel streams through fuel cell) was compared to that with co-flow pattern. It was found that IIR-SOFC with co-flow pattern provides higher voltage and smoother temperature gradient along the system. Lowering the fuel inlet temperature results in smoother temperature profile at the entrance of the reformer, but leads to the increase in cell overpotentials and consequently reduces the cell voltage. Lastly, by increasing operating pressure, the system efficiency increases; in addition, the temperature dropping at the entrance of internal reformer is minimized.

1. Introduction

Solid Oxide Fuel Cell (SOFC) with an indirect internal reforming operation, as called IIR-SOFC, is expected to be an important technology for energy generation in the near future [1–3]. Regarding this operation, endothermic reforming reaction takes place at reformer, which is in close thermal contact with anode side of SOFC where exothermic electrochemical

* *Corresponding author.*
E-mail address: navadol_l@jgsee.kmutt.ac.th (N. Laosiripojana).
0360-3199/$ – see front matter © 2008 International Association for Hydrogen Energy. Published by Elsevier Ltd. All rights reserved.
doi:10.1016/j.ijhydene.2008.10.055

reaction occurs. IIR-SOFC gives advantage in terms of eliminating the requirement of separate fuel reformer, providing good heat transfer between reformer and fuel cell, and preventing anode material from carbon deposition. IIR-SOFC can be designed like an annular configuration as illustrated schematically in Fig. 1 [4,5]. According to this design, the primary fuel (e.g. methane) and steam firstly introduce through an internal reformer, located in the middle of SOFC system, where endothermic steam reforming takes place. At the end of this internal reformer, all product gases flow backward through the anode side of SOFC, where exothermic electrochemical reaction occurs. Heat generated from electrochemical reaction and from ohmic losses at actual operation [2,6] is efficiently consumed by reforming reaction and expected to provide autothermal operation. Typically, the internal reformer is designed as packed-bed configuration [7] containing of pellet or powder shape of Ni-based catalysts (e.g. Ni/Al_2O_3 and Ni/YSZ). Previously, several works on the reactivity toward methane steam reforming and the kinetic models of Ni-based catalyst have widely been reported [8–12]. Among them, one of the well-known methane steam reforming kinetic model and reaction mechanism over $Ni/MgAl_2O_4$ catalyst were reported by Xu and Froment [8]; their equations are applied in the present work.

It is well established that the main drawback of IIR-SOFC is possible mismatch between rates of endothermic and exothermic reactions, which leads to significant local temperature reduction particularly near the entrance of internal reformer and consequently results in mechanical failure due to thermal induced stresses [3,4]. It was also reported that the endothermic steam reforming over conventional Ni-based reforming catalyst is predicted to be too fast for indirect internal reforming operation [13]. Previously, there have been several attempts to minimize this problem e.g. by applying catalyst with lower reforming reactivity [13] or by introducing some oxygen at the feed as autothermal reforming [14]. Here, we present another alternative procedure by applying catalytic coated-wall reformer instead of the conventional packed-bed configuration. The benefits of coated-wall reformer with catalyst wash-coated at inside surface are its excellent heat transfer characteristics and low pressure drop across the reactor. In addition, as the amount of catalyst per volume for the catalytic coated-wall reactor is much lower than that for the catalytic packed-bed reactor, this could be a great benefit for the application in IIR-SOFC, where only low methane steam reforming activity is required [15,16].

In the present work, a set of mathematical modeling was developed in order to predict the behaviors (in terms of cell performance and temperature gradient along the cell) of tubular IIR-SOFC with typical packed-bed and coated-wall internal reformers and fueled by methane. The developed model was coded in COMSOL® program within 2-D axial dimension application with an aim to determine the effect of operating conditions (i.e. inlet fuel temperature, operating pressure, and gas flow pattern) on cell performance and temperature profile along each section of IIR-SOFC system (i.e. reformer channel, fuel channel, and air channel). From this study, the suitable operating conditions of IIR-SOFC system fueled by methane were identified.

2. Mathematical models

2.1. Model geometry

Schematic diagrams of IIR-SOFC with either internal packed-bed or coated-wall reformer are shown in Fig. 1(a) and (b), respectively. According to both configurations, methane and steam are converted to hydrogen-rich gas at internal reformer before introduced to fuel channel of tubular SOFC. Simultaneously, air is fed with opposite flow direction through air channel. It is noted that all dimensions and physical properties of SOFC system in the present work, which are summarized in Table 1, are based on previous reports from literatures [17–20].

2.2. Model assumption and equations

The model was developed as the smallest single unit cell taking into account the effect of temperature on gas

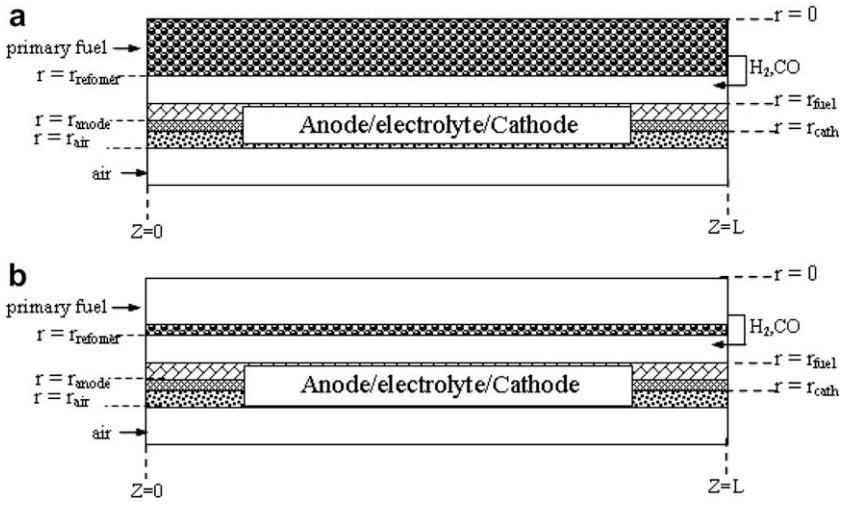

Fig. 1 – Schematic view of IIR-SOFC with an indirect internal reforming ((a) packed-bed reformer and (b) coated-wall reformer).

Table 1 – Steady-state 2-D dimensional model for tubular packed-bed reformer and coated-wall reformer. Q6

Packed–bed reforming model	
Mass Balance	$\nabla(-D_i\nabla c_i + c_i\vec{v}) - \rho_B\sum \nu_i R_{refrom} = 0$ (16)
Energy Balance	$\nabla(\vec{v}\rho c_p T) - \nabla(\lambda_i\nabla T) + \sum \Delta H_{reform} R_{reform} = 0$ (17)
Boundary	$z=0;\ r\geq 0;\ u_r=0,\ v_r=v_{r,in},\ c_{i,r}=c_{r,in},\ T_r=T_{r,in}$
	$r=r_r;\ z\geq 0;\ \mathbf{n}\cdot(k\nabla T)=\lambda_{r,f}(T_r-T_f)+\frac{\sigma A_s(T_r^4-T_s^4)}{\frac{1}{\varepsilon_r}+\frac{A_r}{A_s}(\frac{1}{\varepsilon_s}-1)}$
Coated-wall reforming model	
Mass Balance	$\nabla(-D_i\nabla c_i + c_i\vec{v}) = 0$ (18)
Energy Balance	$\nabla(\vec{v}\rho c_p T) - \nabla(\lambda_i\nabla T) = 0$ (19)
Boundary	$z=0;\ r\geq 0;\ u_r=0,\ v_r=v_{r,in},\ c_{i,r}=c_{r,in},\ T_r=T_{r,in}$
	$r=r_r;\ z\geq 0;\ \mathbf{n}\cdot N_i=\frac{1}{S_{act}A_{act}}\sum \nu_i R_j$
	$\mathbf{n}\cdot(k\nabla T)=\lambda_{rf}(T_r-T_f)+\sum \Delta H_{reform}R_{reform}+\frac{\sigma A_s(T_r^4-T_s^4)}{\frac{1}{\varepsilon_r}+\frac{A_r}{A_s}(\frac{1}{\varepsilon_s}-1)}$

distribution, reactant conversion, and charge transfer. All assumptions made are:

- Each section is considered as non-isothermal steady-state conditions.
- Ideal gas behavior is applied for all gas components.
- Pressure drop in SOFC stack and coated-wall reformer are neglected.
- Fuel utilization was fixed constantly at 80% along the cell coordinate.

A number of equations were applied to predict concentration and temperature gradients along this tubular IIR-SOFC system. Details for these set of equations are presented below:

2.2.1. *Gas distribution*

Brinkman equation (Eq. (1)) was applied to calculate gas distribution in catalytic packed-bed and electrodes (considering the effect of porous media on gas flow character and velocity gradient), while incompressible Navier–Stokes equation (Eq. (2)) [21] was used to predict gas flow pattern in all gas channels.

$$\nabla p = -\frac{\mu}{k_p}\vec{v} + \tilde{\mu}\nabla^2\vec{v} \tag{1}$$

$$\vec{v}\nabla(\rho\vec{v}) = -\nabla p + \mu\nabla^2\vec{v} + S \tag{2}$$

where $\vec{v}$ is fluid velocity, ρ is density, p is pressure, $\tilde{\mu}$ is effective viscosity, k_p is permeability, and S is source term (which is neglected). It is noted that the influences of pressure and velocity gradient on gas diffusion properties were taken into account by applying molecular diffusion and binary diffusion equations (Eqs. (3) and (4), respectively) [22].

$$D_{i,mix} = (1-y_i)\Big/\sum_{j,j\neq 1}\left(y_j/D_{ij}\right) \tag{3}$$

$$D_{i,j} = (0.00143)T^{1.75}/pM_{i,j}^{1/2}\left[\gamma_i^{1/3}+\gamma_j^{1/3}\right]^2 \tag{4}$$

where $D_{i,mix}$ and $D_{i,j}$ are molecular diffusion and binary diffusion flux of species i in mixed gas (m^2/s), y_i is the mole fraction of species i, p is pressure, $M_{i,j}=2/(1/M_i+1/M_j)$ and M_i is molecular weight of component i, and γ is the special diffusion volume (reported by Fuller et al. [23]). It is noted that, in the case of porous media, the diffusion behavior was corrected by applying porosity (ε) and tortuosity (τ); as called effective diffusivity coefficient, $D_{i,pmix}{}^e$ (Eq. (5)). Furthermore, gas diffusion through porous media, $D_{i,pmix}$, was explained by two mechanisms i.e. molecular diffusion ($D_{i,mix}$) (from Eq. (6)), and Knudsen diffusion ($D_{i,ku}$) [24] (from Eq. (7)) depending on the relation between pore diameter (d_p) and mean free path of molecular species.

$$D_{i,pmix}^e = \frac{\varepsilon}{\tau}D_{i,pmix} \tag{5}$$

$$\frac{1}{D_{i,pmix}} = \frac{1}{D_{i,mix}} + \frac{1}{D_{i,ku}} \tag{6}$$

$$D_{i,ku} = \frac{1}{3}d_p\sqrt{\frac{8RT}{\pi M_i}} \tag{7}$$

where R is universal gas constant.

2.2.2. *Energy transfer*

Heat transfer phenomena considered in this system involves the conduction along stack materials, convection from heat flow though the system. Furthermore, it has to concern the radiation between the reformer and the SOFC [25,26]. The calculated gas properties were referred as function of temperature; thus momentum, mass and energy balances were linked to each others. It should be noted that, in all gas flow channels, both conduction and convection heat transfer

Table 2 – Resistivity of cell components, Ni-YSZ/YSZ/LSM-, (S.H. Chan 2001).

Anode resistance constant	$a=0.0000298,\ b=-1392$
Cathode resistance constant	$a=0.0000811,\ b=600$
Electrolyte resistance constant	$a=0.0000294,\ b=10\,350$

Table 3 – steady-state 2 D dimensional model for tubular SOFC.

Fuel Channel		
Mass balance	$\nabla(-D_i\nabla c_i + c_i\vec{v}) - \sum \nu_i R_{elec} = 0$	(20)
Energy balance	$\nabla(\vec{v}\rho c_p T) - \sum \nabla(\lambda_i \nabla T) = 0$	(21)
Boundary	$z = L$; $r \geq 0$; $u_f = u_r$, $v_f = v_r$, $p_f = p_r$, $c_{i,f} = c_{i,r}$, $T_f = T_r$ $r = r_r$; $z \geq 0$; $\mathbf{n}\cdot(k\nabla T) = h_{rf}(T_f - T_r)$ $r = r_f$; $z \geq 0$; $\mathbf{n}\cdot N_{H_2,f} = -J_{H_2}/2F$, $\mathbf{n}\cdot N_{H_2O,f} = J_{H_2}/2F$ $\mathbf{n}\cdot N_{CO,f} = -J_{CO}/2F$, $\mathbf{n}\cdot N_{CO_2,f} = J_{CO}/2F$ $\mathbf{n}\cdot(k\nabla T) = h_{fs}(T_s - T_f)$	
Solid Cell		
Energy balance	$\nabla(\vec{v}\rho c_p T) - \nabla(\lambda_s \nabla T) + \sum \Delta H_{elec} + \frac{\sigma A_s (T_r^4 - T_s^4)}{\frac{1}{\varepsilon_r} + \frac{A_r}{A_s}\left(\frac{1}{\varepsilon_s} - 1\right)} = 0$	(22)
Boundary	Anode/electrolyte interface; $\mathbf{n}\cdot(k\nabla T) = \sum \Delta H_{elec} R_{elec} + J\eta_{total}$ $r = r_f$; $z \geq 0$; $\mathbf{n}\cdot(k\nabla T) = h_{fs}(T_s - T_f)$ $r = r_s$; $z \geq 0$; $\mathbf{n}\cdot(k_{sa}\nabla T) = \lambda_{sa}(T_a - T_s)$	
Air channel		
Mass balance	$\nabla(-D_i\nabla c_i + c_i\vec{v}) = 0$	(23)
Energy balance	$\nabla(\vec{v}\rho c_p T) - \sum \nabla(\lambda_i \nabla T) = 0$	(24)
Boundary	$z = 0$; $r \geq 0$; $u_a = 0$, $v_a = v_{a,in}$, $c_{i,a} = c_{a,in}$, $T_a = T_{a,in}$ $r = r_a$; $z \geq 0$; $\mathbf{n}\cdot N_{O_2,f} = -J_{O_2}/2F$ $\mathbf{n}\cdot(k\nabla T) = \lambda_{fs}(T_s - T_f)$ $r = r_a$; $z \geq 0$ $\mathbf{n}\cdot(k\nabla T) = 0$	

were considered; and the heat capacity and conductivity of gas species were set as function of temperature [22].

2.2.3. *Reforming model*

As mentioned earlier, methane steam reforming reaction in the present work was simulated based on intrinsic rate equations and parameters reported by Xu and Froment [8]. The content of gas species in reformer is mainly related to catalyst density, catalyst active area and the thickness of coated catalyst layer (for coated-wall configuration). Furthermore, according to literatures [16,27], pressure drop in coated-wall reactor is considered negligible. Here, we considered that the temperature of reformer is affected by heat transfer convection in gas stream, heat of reactions, conductive heat

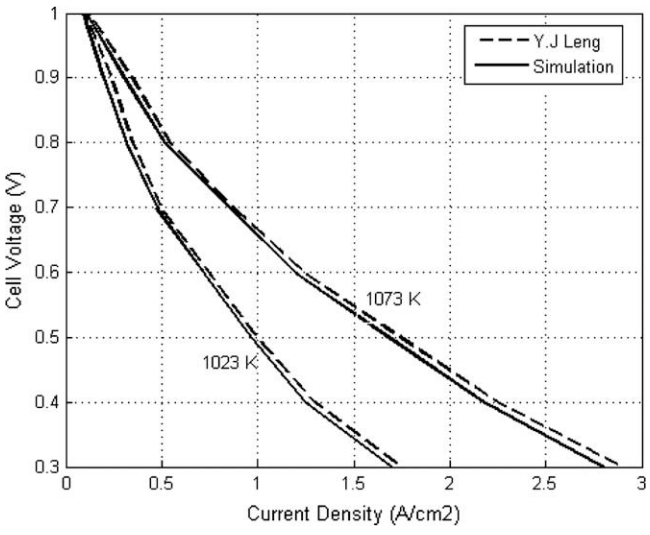

Fig. 2 – I–V curve validation between the simulation results in the present work with the experimental results from literature [28].

Table 4 – Constant parameter values of a tubular IIR-SOFC system.

Parameter	Value	Reference
Fuel cell Length	0.60 m	Zhu et al. [20]
Reformer radius	2×10^{-3} m	Zhu et al. [20]
Inside radius of the cell	5.4×10^{-3} m	Zhu et al. [20]
Anode thickness	1×10^{-3} m	Zhu et al. [20]
Electrolyte thickness	4×10^{-5} m	Zhu et al. [20]
Cathode thickness	5×10^{-5} m	Zhu et al. [20]
Anode permeability	1×10^{-12}	Costamagna et al. [28]
Cathode permeability	1×10^{-12}	Costamagna et al. [28]
Average density of triple phase	633.73 kg/m^3	Xue et al. [19]
Average specific heat of triple phase	574.3 J/kg/K	Xue et al. [19]
Anode thermal conductivity	6.23 W/m/K	Xue et al. [19]
Electrolyte conductivity	2.7 W/m/K	Xue et al. [19]
Cathode thermal conductivity	9.6 W/m/K	Xue et al. [19]
Convection coefficienct in the fuel channel	2987 W/m^2/K	Xue et al. [19]
Convection coefficienct in the air channel	1322.8 W/m^2/K	Xue et al. [19]

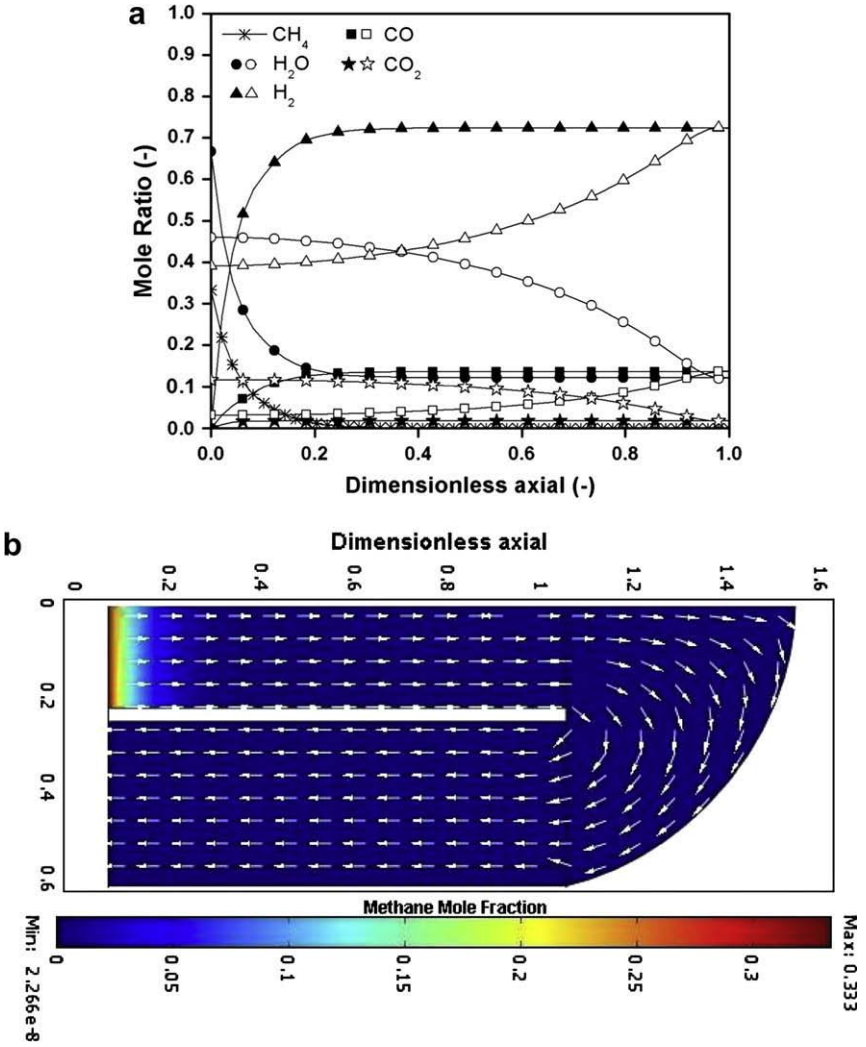

Fig. 3 – (a) Concentration profiles in the reformer (white symbols) and fuel channel (black symbols) of IIR-SOFC with packed-bed reformer (at base case conditions). (b) Results from COMSOL® represented mole fraction of CH_4 in the reformer and fuel channel of IIR-SOFC with packed-bed reformer (at base case conditions).

transfers from fuel channel, and also radiation from the solid cell. All mass and heat balance equations for IIR-SOFC system in the present work are given in Table 1.

2.2.4. *SOFC model*

Typically, all electrochemical reactions take place at electrodes and electrolyte interface to generate electricity from both hydrogen and carbon monoxide. Here, the cell voltage is theoretically calculated from Nernst Equation. It is noted that actual voltage is always less than the theoretical value due to the presence of activation loss and the concentration and ohmic overpotentials [2,6]:

2.2.4.1. *Activation loss*. Activation loss, η_{act}, is the activation barrier of electrochemical reaction at electrode, which is significant at low current density [2]. This overpotential is determined from Butler–Volmer equation, Eq. (8). The relations of current density with hydrogen and oxygen concentrations at electrodes are given in Eqs. (9) and (10) [28]. Since the expression of activation loss from carbon monoxide oxidation is not well ascertained, the current density from CO is assumed to be 3 times lower than that from H_2 (Eq. (11)) [29].

$$j = j_0\left[\exp\left(\alpha\frac{n_eF}{RT}\eta_{act}\right) - \exp\left((-(1-\alpha)\frac{n_eF}{RT}\eta_{act}\right)\right] \tag{8}$$

$$j_{0,H_2} = \vartheta_{anode}\left(\frac{p_{H_2}}{p_{ref}}\right)\left(\frac{p_{H_2O}}{p_{ref}}\right)\exp\left(-\frac{E_{act,anode}}{RT}\right) \tag{9}$$

$$j_{0,O_2} = \vartheta_{cathode}\left(\frac{p_{O_2}}{p_{ref}}\right)^{0.25}\exp\left(-\frac{E_{act,cathode}}{RT}\right) \tag{10}$$

$$j_{0,CO} = \frac{1}{3}j_{0,H_2} \tag{11}$$

where j_0 is exchange current density, j is current density, ϑ is exchange current density constant, α is charge transfer

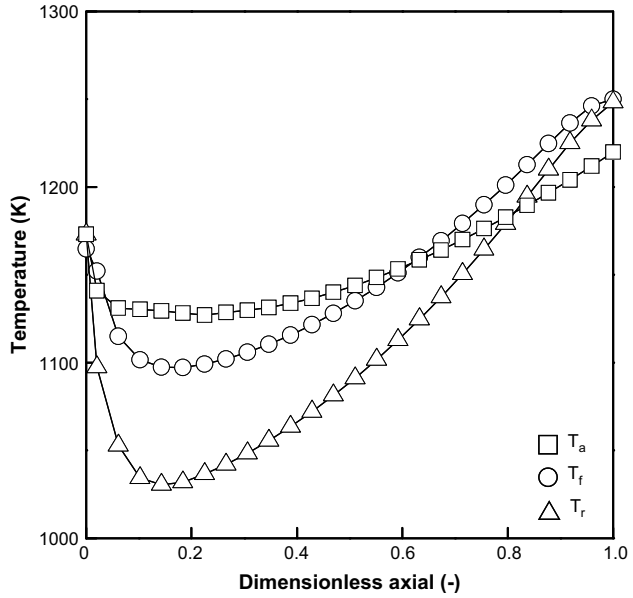

Fig. 4 – Temperature profiles of the reformer, fuel and air channels (T_r, T_f and T_a respectively) for IIR-SOFC with packed-bed reformer (at base case conditions).

coefficient, n_e is number of electron, F is Faraday's constant and E_{act} is activation energy.

2.2.4.2. *Concentration overpotential*. This overpotential, η_{con}, is caused by the dropping of pressure or partial pressure of reactant gases along porous electrodes at reaction sites [2]. The diffusion at bulk zone as defined in term of concentration overpotential is given in Eq. (12) [30,31]. This overpotential is normally reduced at high current density. According to the works from Suwanwarangkul et al. [32] and Hernández-Pacheco et al [33], the dusty gas model was applied to calculate concentration at active site.

$$\eta_{con} = \frac{RT}{2F}\ln\left(\frac{p^*_{H_2}p_{H_2O}}{p_{H_2}p^*_{H_2O}}\right) + \frac{RT}{2F}\ln\left(\frac{p^*_{CO}p_{CO_2}}{p_{CO}p^*_{CO_2}}\right) + \frac{RT}{4F}\ln\left(\frac{p^*_{O_2}}{p_{O_2}}\right) \quad (12)$$

where * represent gases partial pressure at active site.

2.2.4.3. *Ohmic overpotential*. This overpotential, η_{ohm}, occurs from the ion transport across the cell, which mainly depends on ionic conductivity of cell material [2]. By applying ohm's law, the relation of ohmic overpotential and material resistivity is given in Eqs. (13)–(14) [17], in which the resistivity is determined from Eq. (15) based on the data in Table 2.

$$\eta_{ohm} = jR_{ohm} \quad (13)$$

$$R_{ohm} = \frac{\omega\delta}{A_{elec}} \quad (14)$$

$$\omega = a\exp(b/T) \quad (15)$$

where R_{ohm} is ohmic resistance, ω is ionic conductivity, δ is thickness of electrode or electrolyte layer, and a, b are constant properties of material. The governing equation of mass and heat transfers for anode SOFC are summarized in Table 3. It should be noted that the I–V curve obtained from the developed model in the present work was validated with the work from Leng et al. [18], as shown in Fig. 2. Clearly, the results are in good agreement.

3. Results and discussion

3.1. *Modeling of IIR-SOFC as base case*

IIR-SOFC model was firstly simulated at 1173 K and 1 bar. The inlet fuel (methane and steam) with carbon to steam ratio of 1/3 was fed to internal reformer with the total flow rate of 14.2 $cm^3 s^{-1}$, whereas the inlet air flow rate to the cathode was 94.24 $cm^3 s^{-1}$ (theoretical oxygen ratio). It is noted that the requirement of high air flow rate for internal stack cooling becomes less demanding under IIR-SOFC operation [14]. In addition, the fuel utilization was always kept at 80%. Based on the same rate of electrochemical reactions of H_2 and CO at the anode, the obtained electrical power can be directly used to compare the electrical efficiency among different operations. Table 4 presents all related parameters of IIR-SOFC system applied in the present work. Under these conditions, characteristic results of this IIR-SOFC system i.e. methane conversion, product gas distribution and temperature gradient along internal reformer (either packed-bed or coated-wall reformer) and SOFC channels (both fuel and air channels) are shown in Figs. 3–6.

Fig. 3 presents the profiles of methane, steam, hydrogen, carbon monoxide, and carbon dioxide mole fraction in reformer and fuel channel of SOFC for IIR-SOFC with packed-bed internal reformer. It can be seen that, due to the high reforming reactivity, methane is completely consumed at the first one fourth of the reformer; therefore, hydrogen and carbon monoxide mole fractions increase rapidly in this region while methane and water decrease dramatically. At the outlet of the reformer, the product gas (consisting of 72% H_2, 14% CO, 12% H_2O, and 2% CO_2) flows backward into fuel channel of SOFC where H_2 and CO are electrochemically converted to H_2O and CO_2. At the outlet of fuel channel, the stream consists of 47% H_2O, 40% H_2, 11% CO_2, and 2% CO; and under these base case conditions, the terminal cell voltage is 0.682 V.

Fig. 4 presents temperature profiles of reformer, fuel and air channels for this IIR-SOFC system (with packed-bed internal reformer). It can be seen that the heat generated from fuel cell side is sufficient for internal reforming operation [34]. Nevertheless, a significant local cooling associated with indirect internal reforming operation takes place, and the reformer temperature decreases rapidly (from 1173 K to the lowest 1030 K) at the first half of the reformer length. This local cooling is not compatible with ceramic components of SOFC and therefore requires an alternative procedure for operation i.e. applying a coated-wall internal reformer.

3.2. *Coated-wall internal reformer vs. packed-bed internal reformer*

Fig. 5 shows the mole fraction profiles of all gas presenting in the reformer and SOFC fuel channel for IIR-SOFC with

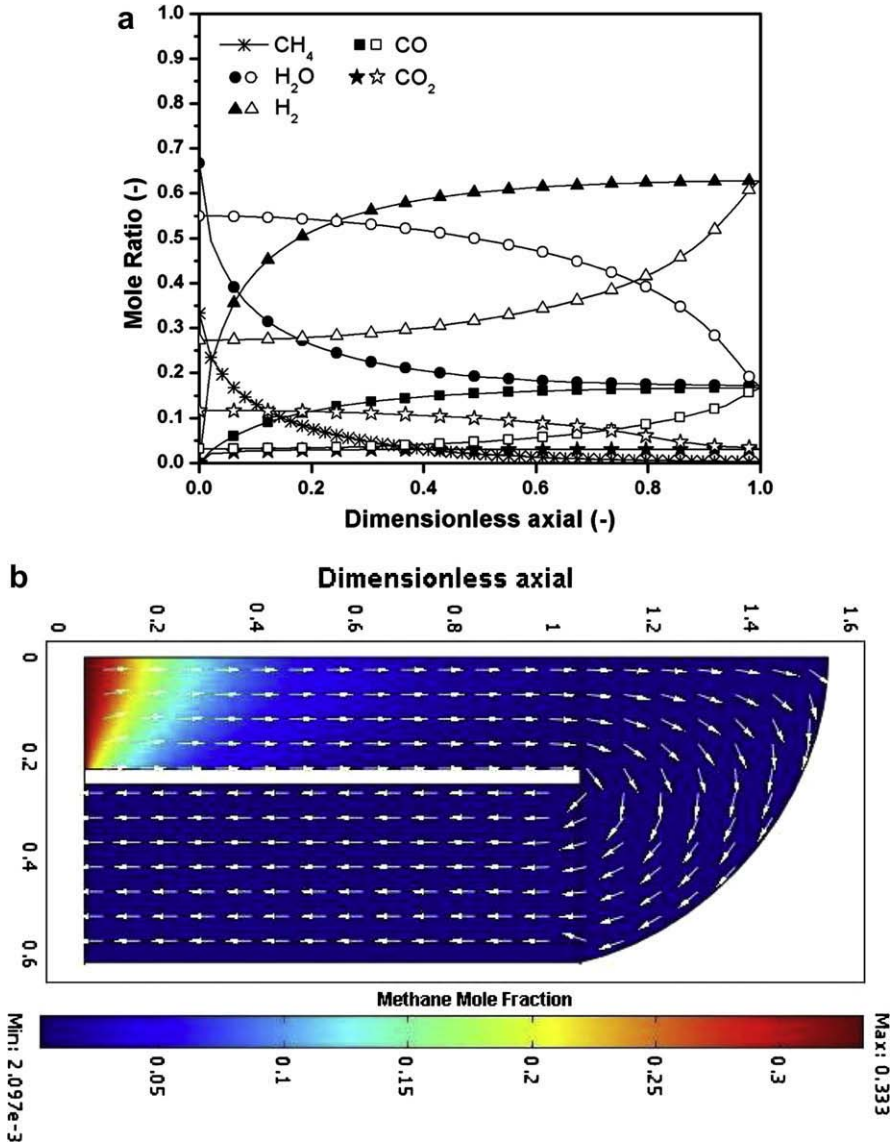

Fig. 5 – (a) Concentration profiles in the reformer (white symbols) and fuel channel (black symbols) of IIR-SOFC with coated-wall reformer (at base case conditions). (b) Results from COMSOL® represented mole fraction of CH_4 in the reformer and fuel channel of IIR-SOFC with coated-wall reformer (at base case conditions).

coated-wall internal reformer. Unlike the result in Fig. 3, methane conversion profile is smoother than that observed from the IIR-SOFC with packed-bed reformer; and all inlet methane is completely converted at approximately 80% of the reformer length (the outlet stream from the reformer consists of 62% H_2, 18% CO, 18% H_2O, and 2% CO_2). Slightly lower content of hydrogen and higher content of carbon monoxide are generated compared to IIR-SOFC with packed-bed internal reformer; these differences could be related to the level of water–gas shift reaction taking place in the reformer.

The product gas from reformer flows backward into fuel channel of SOFC, where electrochemical reaction occurs. Fig. 6 presents temperature profiles of reformer, fuel and air channels for this IIR-SOFC system (with coated-wall internal reformer). Clearly, lower local cooling takes place, and the reformer temperature decreases only 89 K from the inlet temperature (compared to 143 K in the case of IIR-SOFC with packed-bed internal reformer). Therefore, IIR-SOFC with coated-wall internal reformer is more compatible with ceramic components of SOFC than IIR-SOFC with packed-bed internal reformer. It is also noted that, under these inlet conditions, the terminal cell voltage from IIR-SOFC with coated-wall internal reformer is 0.664 V, which is close to 0.682 V observed from IIR-SOFC with packed-bed internal reformer. Importantly, Fig. 7 compares the power density and electrical efficiency achieved from both configurations; it can be seen that IIR-SOFC with coated-wall internal reformer provides significantly greater power density with higher electrical efficiency at the same operating conditions.

3.3. *Effect of flow direction*

According to the simulation results in Sections 3.1 and 3.2, it can be noticed that IIR-SOFC with catalytic coated-wall

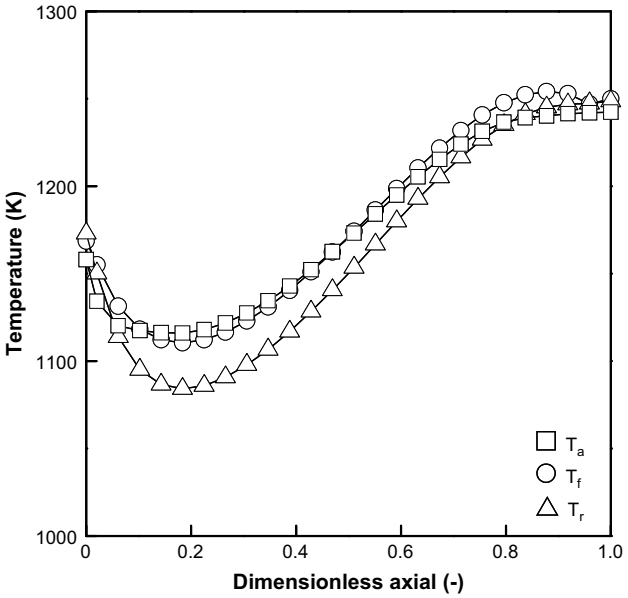

Fig. 6 – Temperature profiles of the reformer, fuel and air channels (T_r, T_f and T_a respectively) for IIR-SOFC with coated-wall reformer (at base case conditions).

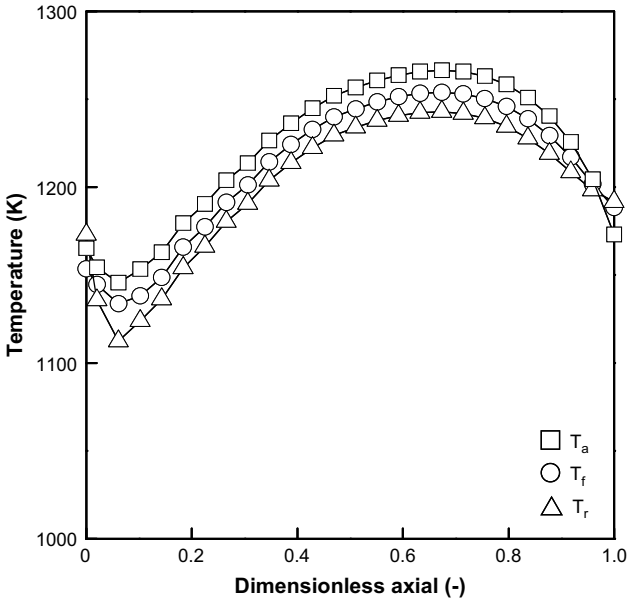

Fig. 8 – Temperature profiles of the reformer, fuel and air channels (T_r, T_f and T_a respectively) for IIR-SOFC with packed-bed reformer (operated with co-flow pattern).

reformer is more appropriate than that with packed-bed reformer in terms of power density, electrical efficiency and temperature gradient along the system. As next step, the effects of several operating parameters on the system performance were studied in order to optimize the suitable operating conditions for this IIR-SOFC system.

Theoretically, as for a typical heat exchanging system, flow direction of exchanged fluids strongly affects the heat transfer and reaction behavior in the fluid stream, thus the effect of fuel and oxidant flow direction on the IIR-SOFC performance was firstly considered. In Sections 3.1 and 3.2, air flow is counter-flow to fuel flow in SOFC fuel channel. As an alternative option, the system behavior was analyzed as co-flow pattern by changing mass and energy balances in air channel along with their corresponding boundary conditions while keeping all other operating conditions identical to those of counter-flow pattern.

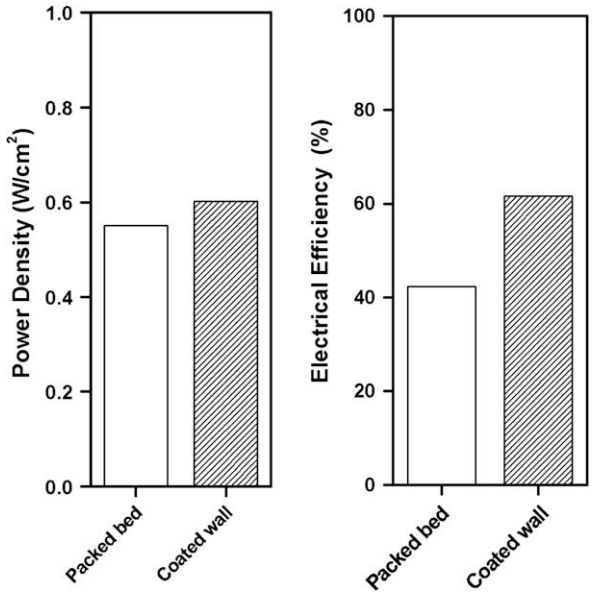

Fig. 7 – Power density and electrical efficiency achieved from IIR-SOFC with packed-bed and coated-wall internal reformer (at base case conditions).

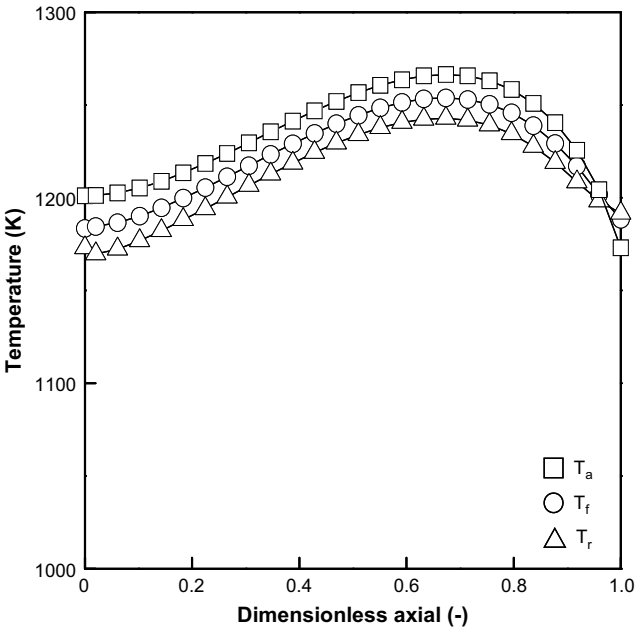

Fig. 9 – Temperature profiles of the reformer, fuel and air channels (T_r, T_f and T_a respectively) for IIR-SOFC with coated-wall reformer (operated with co-flow pattern).

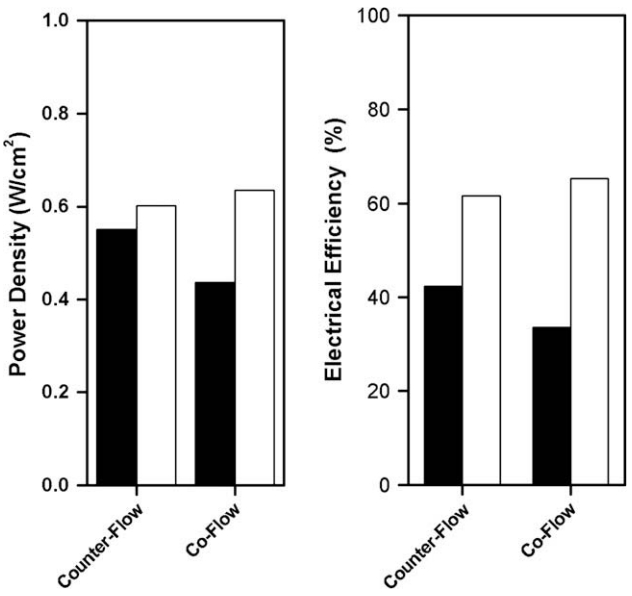

Fig. 10 – Power density and electrical efficiency achieved from IIR-SOFC with packed-bed (black column) and coated-wall internal reformer (white column) operated under counter-flow and co-flow patterns.

Figs. 8 and 9 present the temperature profiles of reformer, fuel and air channels for IIR-SOFC with packed-bed internal reformer (Fig. 8) and coated-wall internal reformer (Fig. 9) and operated under co-flow pattern. It can be seen that while in the case of counter-flow pattern, the temperature profiles increase along the system and the maximum temperature occurs at the outlet of air channel (Figs. 4 and 6); in the case of co-flow pattern, the maximum temperature occurs at approximate center of the system. Under counter-flow pattern, the increasing of temperature along air flow direction is mainly due to heat accumulation along SOFC system. For co-flow pattern, heat is firstly generated at the end of the system ($z = 1$) and then accumulated along air stream until reaching the entrance of reforming regime ($z = 0$), where great amount of energy is consumed, thus the temperature at approximate center of the system is higher than the two ends. It should be noted that the average temperatures in reformer, fuel and air channels of IIR-SOFC with co-flow pattern is higher than those of IIR-SOFC with counter-flow pattern; this consequently leads to the greater amount of mean cell temperature, lower overpotentials and thus higher efficiency for IIR-SOFC with co-flow pattern.

Furthermore, according to simulation results for co-flow pattern, the terminal voltage is 0.701 V (for IIR-SOFC with packed-bed internal reformer) and 0.716 V (for IIR-SOFC with coated-wall internal reformer), which are clearly higher than those for IIR-SOFC with counter-flow pattern. In addition, the comparison of power density and electrical efficiency achieved from IIR-SOFC system with counter-flow and co-flow patterns (as shown in Fig. 10) indicates that the co-flow pattern provides higher power density and electrical efficiency. We therefore concluded here that IIR-SOFC with co-flow pattern is more satisfactory, thus the effects of further parameters on system performance are investigated based on IIR-SOFC with co-flow pattern.

3.4. *Effect of fuel inlet temperature*

It was reported in the literature that another alternative procedure to reduce temperature gradient along the system is to decrease the reforming reactivity at the reformer [2], which can be done by reducing the reformer temperature since the rate equations of methane steam reforming reaction are expressed as a function of temperature. Typically, the

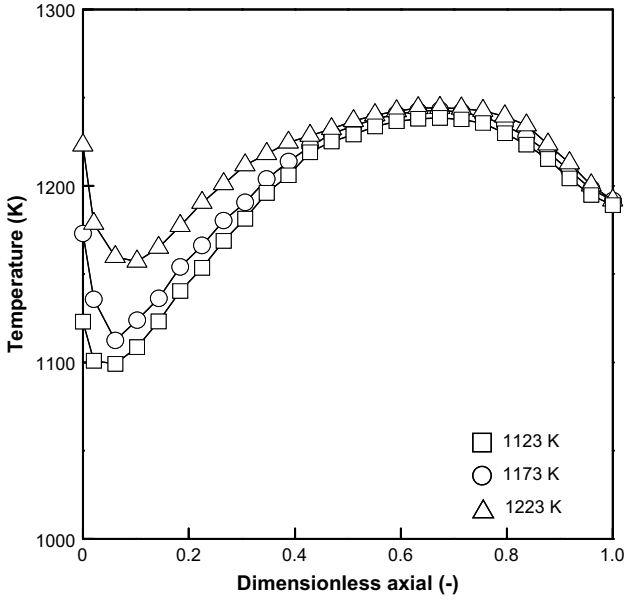

Fig. 11 – Effect of inlet fuel temperature on the temperature profile of reformer for IIR-SOFC with packed-bed reformer and operated under co-flow pattern.

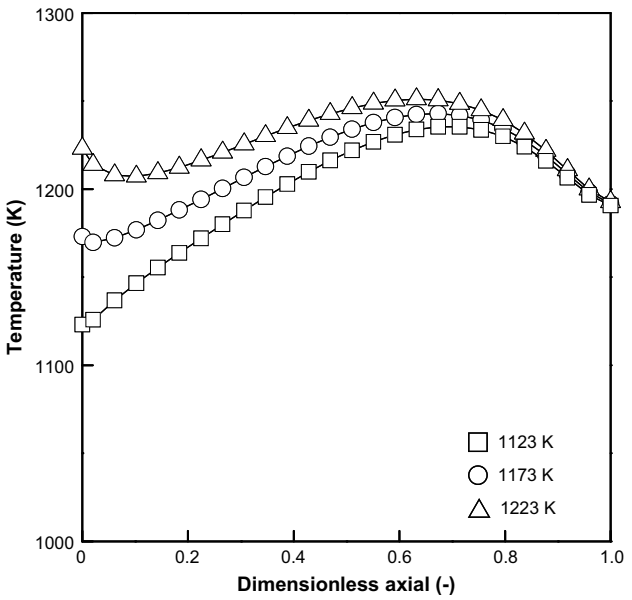

Fig. 12 – Effect of inlet fuel temperature on the temperature profile of reformer for IIR-SOFC with coated-wall reformer and operated under co-flow pattern.

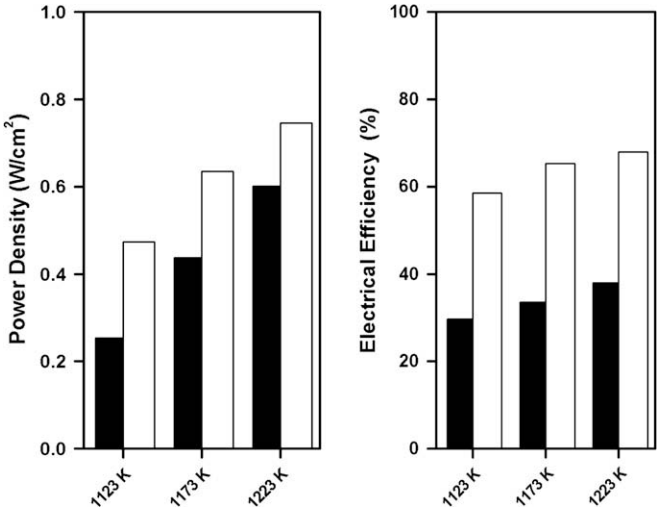

Fig. 13 – Effect of inlet fuel temperature on power density and electrical efficiency achieved from IIR-SOFC with packed-bed (black column) and coated-wall internal reformer (white column), operated under co-flow pattern.

reformer temperature is controlled by several variables; one of them is the fuel inlet temperature. Therefore, in the present work, we investigated the effect of the fuel inlet temperature on temperature gradient and cell performance by varying the fuel inlet temperature from 1173 K to 1123 K and 1223 K. Figs. 11 and 12 show the influence of this parameter on temperature profile along IIR-SOFC with packed-bed and coated-wall reformers, respectively. It can be seen that for both configurations the dropping of temperature at the entrance of the reformer reduced when the inlet temperature decreased. Nevertheless, it was also found from the simulation that the use of low fuel inlet temperature reduces the heat accumulated in the system and consequently increases cell overpotentials. For IIR-SOFC with packed-bed and reformer, the cell voltage reduces from 0.729 V at the fuel inlet temperature of 1223 K to 0.682 V at 1173 K and 0.651 V at 1123 K, while it decreases from 0.736 V at 1223 K to 0.664 V at 1173 K and 0.638 V at 1123 K for IIR-SOFC with and coated-wall reformer. Fig. 13 also indicates that the power density and electrical efficiency also decrease with reducing the fuel inlet temperature. Therefore, the use of lower fuel inlet temperature should not be a practical option for IIR-SOFC operation.

3.5. *Effect of operating pressure*

As the last parameter studied in the present work, the effect of operating pressure on temperature gradient and cell performance was determined. Figs. 14–16 present the influence of operating pressure (1 (base case), 5, and 10 bar) on temperature profiles of IIR-SOFC with packed-bed and coated-wall

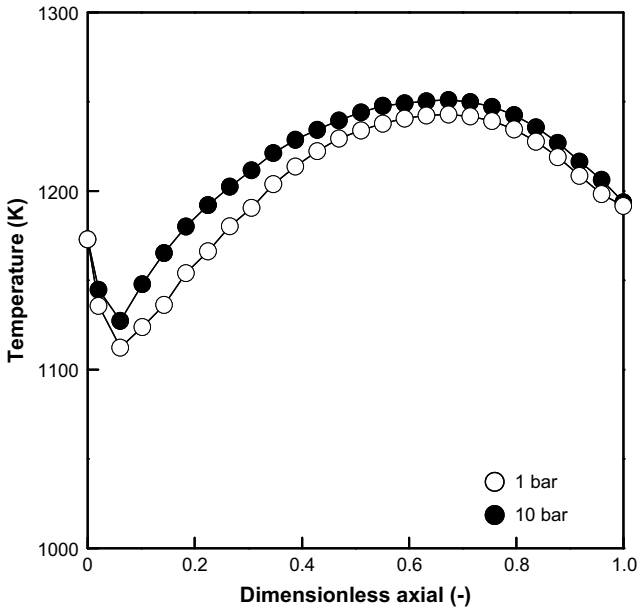

Fig. 14 – Effect of operating pressure on the temperature profile of reformer for IIR-SOFC with packed-bed reformer and operated under co-flow pattern.

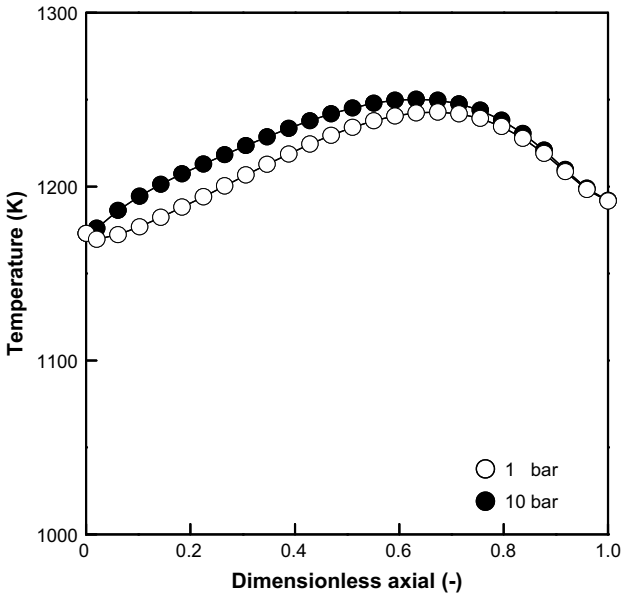

Fig. 15 – Effect of operating pressure on the temperature profile of reformer for IIR-SOFC with coated-wall reformer and operated under co-flow pattern.

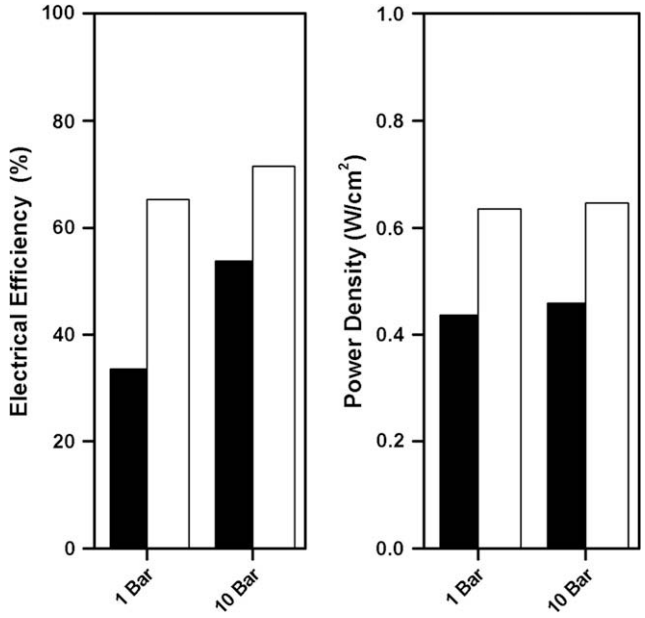

Fig. 16 – Effect of operating pressure on power density and electrical efficiency achieved from IIR-SOFC with packed-bed (black column) and coated-wall internal reformer (white column), operated under co-flow pattern at the inlet fuel temperature of 1173 K and with 80% fuel utilization.

reformer, respectively. It can be seen that the increase of pressure significantly reduces the dropping of temperature at the entrance of reformer for both configurations. This could be due to the influence of pressure on gas diffusion (as explained in Eq. (7)) and partial pressure of gas species in steam reforming and electrochemical reactions since the extent of steam reforming rate reaction decreases with increasing pressure due to the thermodynamic restrictions and the kinetic expressions in use [4].

It was also found that the increase of pressure results in the higher open-circuit potential and consequently lower over-potentials, which leads to the achievement of higher voltages. At 10 bar, the cell voltage increased to 0.732 V (for IIR-SOFC with packed-bed internal reformer) and to 0.741 V (for IIR-SOFC with coated-wall internal reformer). Thus, the increasing of operating pressure is an effective way of reducing the temperature gradient as well as increasing the cell performance.

4. Conclusion

The simulations indicated that IIR-SOFC with conventional packed-bed internal reformer leads to the rapid methane consumption and undesirable local cooling at the entrance of reformer due to the mismatch between the rapid reforming rate and the amount of heat available from electrochemical reaction. In contrast, it was revealed that IIR-SOFC with coated-wall internal reformer provides smoother methane conversion and significant lower local cooling at the entrance of internal reformer. According to above results, it seems that IIR-SOFC with coated-wall internal reformer is more compatible than that with packed-bed internal reformer.

Sensitivity analysis of several parameters was then performed. IIR-SOFC with co-flow pattern (co-flow of air and fuel streams through fuel cell) provides higher voltage and smoother temperature gradient along the system than that with counter-flow pattern. The reducing of fuel inlet temperature results in smoother temperature profile at the entrance of the reformer, but also leads to the increase in cell over-potentials and consequently reduces cell voltage. Lastly, by increase operating pressure, the system efficiency increases and the degree of temperature dropping at the entrance of internal reformer significantly reduces. Therefore, we concluded here that the performance of IIR-SOFC fueled by methane can be maximized by applying catalytic coated-wall internal reformer with co-flow pattern and operated with high operating pressure.

Acknowledgment

The financial support from the Thailand Research Fund (TRF), the Joint Graduate School of Energy and Environment (JGSEE), and the Thailand Graduate Institute of Science and Technology (TGIST) program, Thailand's National Science and Technology Development Agency (NSTDA), grant no. TG-55-20-50-058D are gratefully acknowledged.

REFERENCES

[1] Vielstich W, Gasteiger HA, Lamm A. Internal reforming. In: Eguchi K, editor. Handbook of fuel cells. John Wiley and Sons; 2003. p. 1059–69.
[2] Larminie J, Dicks A. Fuel cell systems explained. John Wiley and Sons; 2000.
[3] Park HK, Lee YR, Kim MH, Chung GY, Nam SW, Hong SA, et al. Studies of the effects of the reforming in an internal-reforming molten carbonate fuel cell by mathematical modeling. J Power Sources 2002;104:140–7.
[4] Aguiar P, Chadwick D, Kershenbaum L. Modelling of an internal reforming solid oxide fuel cell. Chem Eng Sci 2002; 57:1665–77.
[5] Sánchez D, Chacartegui R, Munoz A, Sánchez T. Thermal and electrochemical model of internal reforming solid oxide fuel cells with tubular geometry. J Power Sources 2006;160:1074–87.
[6] Kakaç S, Pramuanjaroenkij A, Zhou XY. A review of numerical modeling of solid oxide fuel cells. Int J Hydrogen Energy 2007;32:761–86.
[7] Fogler HS. Elements of chemical reaction engineering. 3rd ed. Prentice-Hall International; 1999.
[8] Xu J, Froment GF. Methane steam reforming, methanation and water–gas shift: I intrinsic kinetics. AIChE J 1989;35:88–96.
[9] Dicks AL, Pointon KD, Siddle A. Intrinsic reaction kinetics of methane steam reforming on a nickel/zirconia anode. J Power Sources 2000;86:523–30.
[10] Ahmed K, Foger K. Kinetics of internal steam reforming of methane on Ni/YSZ-based anodes for solid oxide fuel cells. Catal Today 2000;63:479–87.
[11] Hou K, Hughes RR. The kinetics of methane steam reforming over a Ni/α-Al_2O catalyst. Chem Eng J 2001;82:311–28.
[12] Hoang DL, Chan SH, Ding OL. Kinetic and modelling study of methane steam reforming over sulfide nickel catalyst on a gamma alumina support. Chem Eng J 2005;112:1–11.

[13] Aguiar P, Chadwick D, Kershenbaum L. Effect of methane slippage on an indirect internal reforming solid oxide fuel cell. Chem Eng Sci 2004;59:87–97.
[14] Lim LT, Chadwick D, Kershenbaum L. Achieving autothermal operation in internally reforming solid oxide fuel cells: simulation studies. Ind Eng Chem Res 2005;44: 9609–18.
[15] Fukuhara C, Kamata Y, Igarashi A. Catalytic performance of microtube-type copper-based catalyst for methanol steam reforming, prepared on the inner wall of an aluminum tube by electroless plating. Appl Catal A General 2005;296:100–7.
[16] Fukuhara C, Igarashi A. Performance simulation of a wall-type reactor in which exothermic and endothermic reactions proceed simultaneously, comparing with that of a fixed-bed reactor. Chem Eng Sci 2005;60:6824–34.
[17] Chan SH, Khor KA, Xia ZT. A complete polarization model of a solid oxide fuel cell and its sensitivity to the change of cell component thickness. J Power Sources 2001;93:130–40.
[18] Leng YJ, Chan SH, Khor KA, Jiang SP. Performance evaluation of anode-supported solid oxide fuel cells with thin film YSZ electrolyte. Int J Hydrogen Energy 2004;29:1025–33.
[19] Xue X, Tang J. Dynamic modeling of single tubular SOFC combining heat/mass transfer and electrochemical reaction effects. J Power Sources 2005;142(1–2):211–22.
[20] Zhu H, Colclasure AM, Kee RJ, Lin Y, Barnett SA. Anode barrier layers for tubular solid-oxide fuel cells with methane fuel streams. J Power Sources 2006;161:413–9.
[21] Mauri R. A new application of the reciprocity relations to the study of fluid flows through fixed beds. J Eng Math 1998;33: 103–12.
[22] Todd B, Young JB. Thermodynamic and transport properties of gases for use in solid oxide fuel cell modeling. J Power Sources 2002;110:186–200.
[23] Fuller EN, Schettler PD, Giddings JC. A new method for prediction of binary gas-phase diffusion coefficients. Ind Eng Chem 1966;58:19–27.
[24] Arnost D, Schneider P. Dynamic transport of multicomponent mixtures of gases in porous solids. Chem Eng J 1995;57:91–9.
[25] Haynes C, Wepfer WJ. Characterizing heat transfer within a commercial-grade tubular solid oxide fuel cell for enhanced thermal management. Int J Hydrogen Energy 2001;26:369–79.
[26] Calise F, Accadia MD, Restuccia G. Simulation of a tubular solid oxide fuel cell through finite volume analysis: effects of the radiative heat transfer and exergy analysis. Int J Hydrogen Energy 2007;32:4575–90.
[27] Karim A, Bravo J, Datye A. Nonisothermality in packed bed reactors for steam reforming of methanol. Appl Catal A General 2005;282(1–2):101–9.
[28] Costamagna P, Selimovic A, Borghi MD, Agnew G. Electrochemical model of the integrated planar solid oxide fuel cell (IP-SOFC). Chem Eng J 2004;102:61–9.
[29] Matsuzaki Y, Yasuda I. Relationship between the steady-state polarization of the SOFC air electrode, $La_{0.6}Sr_{0.4}MnO_{3+\delta}$/YSZ, and its complex impedance measured at the equilibrium potential. Solid State Ionics 1999;126(3–4):307–13.
[30] Zhu H, Kee RJ. A general mathematical model for analyzing the performance of fuel-cell membrane-electrode assemblies. J Power Sources 2003;117(1–2):61–74.
[31] Zhao F, Virkar AV. Dependence of polarization in anode-supported solid oxide fuel cells on various cell parameters. J Power Sources 2005;141:79–95.
[32] Suwanwarangkul R, Croiset E, Fowler MW, Douglas PL, Entche E, Douglas MA. Performance comparison of Fick's, dusty-gas and Stefan–Maxwell models to predict the concentration overpotential of a SOFC anode. J Power Sources 2003;122:9–18.
[33] Pacheco EH, Singha D, Huttonb PN, Patelb N, Manna MD. A macro-level model for determining the performance characteristics of solid oxide fuel cells. J Power Sources 2004; 138:174–86.
[34] Sanchez D, Chacartegui R, Munoz A, Sanchez T. On the effect of methane internal reforming modelling in solid oxide fuel cell. Int J Hydrogen Energy 2008;33:1834–44.

List of nomenclatures

C_P: specific heat of the gas streams, kJ/mol/K
A_{act}: external catalyst surface area $= \pi(d_r - 2\tau_{cat})L/\pi(d_r^2 - (d_r - 2\tau_{cat})^2)L$
c_i: concentration, mol/m^3
$D_{i,j}$: binary diffusion, m^2/s
$D_{i,mix}^{e}$: the effective molecular diffusivity, m^2/s
$D_{i,ku}$: the Kundsen diffusivity, m^2/s
d_p: pore diameter, m
E_{act}: activation energy, kJ/mol
F: Faraday's constant, 5,96,484 C/mol
ΔH: the change of heat of reaction, kJ/mol
j_0: exchange current density, mA/cm^2
j: current density, mA/cm^2
j_{H_2}: current density from hydrogen oxidation reaction, mA/cm^2
h: thermal conductivity, W/m^2 K
N_i^D: the bulk molar diffusive flux of gas component, mol/m s
p^o: standard partial pressure, bar
p_i: partial pressure of species i,
R: universal gas constant; 8.414 kJ/mol K
R_{elect}: the hydrogen oxidation reaction rate, mol/m^2 s
q_{rad}: the heat flux from radiation,W/m^2
S_{act}: specific surface area of catalyst
T: temperature, K
$\vec{v}$: fluid velocity, m/s
y_i: the mole fraction of gas

Greek letters
ρ: density (kg/m^3)
γ: special Fuller et al. diffusion volume
ϑ: exchange current density constant, (mA/cm^2)
$\alpha_{a,c}$: charge transfer coefficient of anode and cathode
σ: Stefan–Boltzmann coefficient
ε: porosity
τ: tortuosity
η_{cell}: voltage drop of the whole cell, Volts
λ: thermal conductivity (kJ/m/s/K)

Superscripts
*: active site

Subscripts
a: air channel
i: component (methanol, water, hydrogen, etc.)
j: reaction (SRM, WGS, etc.)
f: fuel channel
r: reformer
s: solid oxide fuel cell
Act: activation losses
Cell: cell stack
Con: concentration losses
ohm: ohmic losses
elec: electrochemical reactions

ภาคผนวก 5

Available at www.sciencedirect.com

ScienceDirect

journal homepage: www.elsevier.com/locate/he

Integration of solid oxide fuel cell and palladium membrane reactor: Technical and economic analysis

P. Piroonlerkgul[a], W. Kiatkittipong[b], A. Arpornwichanop[a], A. Soottitantawat[a], W. Wiyaratn[c], N. Laosiripojana[d], A.A. Adesina[e], S. Assabumrungrat[a,*]

[a]Department of Chemical Engineering, Faculty of Engineering, Chulalongkorn University, Bangkok 10330, Thailand
[b]Department of Chemical Engineering, Faculty of Engineering and Industrial Technology, Silpakorn University, Nakhon Pathom 73000, Thailand
[c]Department of Production Technology Education, Faculty of Industrial Education and Technology, King Mongkut's University of Technology Thonburi, Bangkok 10140, Thailand
[d]The Joint Graduate School of Energy and Environment, King Mongkut's University of Technology Thonburi, Bangkok 10140, Thailand
[e]Reactor Engineering & Technology Group, School of Chemical Sciences & Engineering, University of New South Wales, Sydney, NSW 2052, Australia

ARTICLE INFO

Article history:
Received 19 January 2009
Received in revised form
16 February 2009
Accepted 16 February 2009
Available online 1 April 2009

Keywords:
Biogas
Palladium membrane
Solid oxide fuel cell
Economic analysis

ABSTRACT

This paper presents a technical and economic analysis of a solid oxide fuel cell system equipped with a palladium membrane reactor (PMR–SOFC) with the aim of determining the benefits of such an integrated unit over the conventional reformer module (CON-SOFC). The performance of both SOFC systems under the conditions for energetically self-sustaining operation ($Q_{NET} = 0$) was achieved by varying the fuel utilization for each operating voltage. Two types of fuels, i.e., methane and desulphurized biogas, are considered. The simulation results show that the maximum power density of the CON-SOFC fuelled by methane (0.423 W/cm^2) is higher than that of the CON-SOFC fuelled by biogas (0.399 W/cm^2) due to the presence of CO_2 in biogas. For the PMR–SOFC, it is found that the operation at a higher permeation pressure offers higher power density because lower fuel utilization is required when operating the SOFC at the energy self-sustained condition. When the membrane reactor is operated at the permeation pressure of 1 bar, the methane-fuelled and biogas-fuelled PMR–SOFCs can achieve the maximum power density of 0.4398 and 0.4213 W/cm^2, respectively. Although the PMR–SOFC can offer higher power density, compared with the CON-SOFC, the capital costs of supporting units, i.e., palladium membrane reactor, high-pressure compressor, and vacuum pump, for PMR–SOFC need to be taken into account. The economic analysis shows that the PMR–SOFC is not a good choice from an economic viewpoint because of the requirement of a large high-pressure compressor for feeding gas to the membrane reactor.

1. Introduction

Due to increasing concerns on energy shortage and environmental crisis, a number of researchers have focused on new electricity generation technologies with high electrical efficiency and environmental-friendly operation. A solid oxide fuel cell (SOFC) is one of the promising technologies since it directly transforms chemical energy into electrical energy. Specifically, energy loss in an SOFC is lower when compared with conventional power generation processes. In general, the

* Corresponding author. Fax: +66 2 218 6877.
E-mail address: suttichai.a@chula.ac.th (S. Assabumrungrat).
0360-3199/$ – see front matter © 2009 International Association for Hydrogen Energy. Published by Elsevier Ltd. All rights reserved.
doi:10.1016/j.ijhydene.2009.02.049

performance of SOFC depends on the composition of fuel gas fed to the anode chamber of SOFC. Baron et al. [1] have reported that the presence of methane in the SOFC feed decreased the SOFC performance due to carbon deposition and partial blocking of anode pores. Likewise, the SOFC performance also decreases as the amount of carbon monoxide in anode feed gas increases due to an increase in activation and concentration polarizations [1,2]. The presence of carbon dioxide could also lower the SOFC performance via the reverse water gas shift reaction (RWGS) [3]. For this reason, pure hydrogen seems to be an ideal fuel for SOFC; however, it is not available in natural resources.

Various types of fuels such as alcohols, natural gas, coal and petroleum-based compounds may be used to produce hydrogen. Biogas is one of the attractive fuels for hydrogen generation since it contains a large amount of methane (40–65 mol%) [4]. Compared to fossil fuels, biogas offers advantages of being renewable and free of non-methane hydrocarbons. Considering the conventional hydrogen generator fuelled by biogas, the presence of carbon dioxide (30–40 mol%) in biogas inhibits the production of H_2 due to the effect of the RWGS. Effendi et al. [5] proposed the installation of high-temperature and low-temperature shift reactors with the biogas-fed reformer. They showed that hydrogen product with the purity of 68 mol% can be achieved. To remove carbon dioxide, an adsorption unit can be employed but requires high running costs.

The use of a hydrogen-selective membrane reactor can offer pure hydrogen with high methane conversion. A suitable membrane is chosen based on its ability to offer high hydrogen permeability and selectivity. Although some polymeric membranes can offer high hydrogen selectivity, they cannot be operated at high temperatures necessary for steam reforming reaction. An inorganic membrane particularly a palladium membrane is a preferred choice due to its high selectivity of hydrogen [6]. The use of palladium membrane reactors for hydrogen-generating reactions has been widely investigated [7–9]. Under this operation, hydrogen gas produced in the reaction side permeates through the palladium membrane to the permeation side where pure hydrogen is collected. The simultaneous removal of hydrogen from the reaction side helps improve the reaction conversion.

When pure hydrogen instead of a conventional reformed gas is fed to an SOFC, a superior SOFC performance is reported [3]. Our previous work [10] analyzed performance of methanol-fuelled solid oxide fuel cell system incorporated with a palladium membrane reactor. It was demonstrated that when the membrane reactor (operated under high-pressure compressor mode) is employed, the maximum power density was about 13% higher than that from the system with the conventional reformer. Comparison between the two SOFC systems which provide the same net electrical efficiency indicates that the SOFC system with the membrane reactor requires a smaller SOFC stack than the conventional SOFC system. However, the former requires an extra cost on palladium membranes and extra electrical power for operating the compressor for the membrane reactor. Preliminary economic analysis reveals that the use of the membrane reactor to the SOFC system is not cost-effective due to high cost of palladium membranes. A further study was carried out for methane-fed SOFC systems considering three operation modes of membrane reactors; i.e., high-pressure compressor, combined low pressure compressor and vacuum pump and combined high-pressure compressor and vacuum pump [11]. Their overall SOFC system characteristics are compared with those of the SOFC system with the conventional reformer. The economic analysis reveals that the total capital cost/net electrical power is dependent on hydrogen recovery, net electrical efficiency and operation mode. At high electrical efficiency, the replacement of the conventional reformer with the membrane reactor becomes attractive. It was also demonstrated that the combined high-pressure compressor and vacuum pump is the best operation mode for integration with the SOFC system. However, this work did not take into account the thermal management within the integrated systems.

In the present study, a comprehensive analysis of two SOFC systems (one coupled to a membrane reactor and the other fitted with a conventional reformer) was carried out. Evaluation of the system performance was based on energetically self-sustaining operation. The effects of the type of feed gas (methane and desulphurized biogas) and operating pressures in the permeate side on the system performance were investigated. Finally, the economic analysis was carried out to determine 'best' operating conditions for the SOFC system coupled to the membrane reactor when fed by different fuels.

2. Modeling

2.1. Palladium membrane reactor

Our recent work [12] indicated that steam is the most suitable reforming agent for the SOFC system. Given that methane (or biogas) is the feedstock, the major reactions taking place in the reactors are methane steam reforming (Eq. (1)), water gas shift reaction (Eq. (2)) and carbon dioxide methanation (Eq. (3)).

$$CH_4 + H_2O \leftrightarrow 3H_2 + CO \tag{1}$$

$$CO + H_2O \leftrightarrow H_2 + CO_2 \tag{2}$$

$$4H_2 + CO_2 \leftrightarrow CH_4 + 2\,H_2O \tag{3}$$

The addition of excess reforming agent can inhibit the carbon formation [13]; hence, the molar ratio of H_2O to CH_4 in the fuel processor feed was always set to 2.5 in this study. The kinetic rates derived from the experimental results on $Ni/MgAl_2O_4$ catalyst [13] were used in the calculation. The rate expressions for the reactions shown in Eqs. (1)–(3) are given by;

$$r_1 = \frac{\frac{k_1}{p_{H_2}^{2.5}}\left(p_{CH_4}p_{H_2O} - \frac{p_{H_2}^3 p_{CO}}{K_1}\right)}{(DEN)^2} \tag{4}$$

$$r_2 = \frac{\frac{k_2}{p_{H_2}}\left(p_{CO}p_{H_2O} - \frac{p_{H_2}p_{CO_2}}{K_2}\right)}{(DEN)^2} \tag{5}$$

Table 1 – Kinetic parameters for methane steam reforming [13].

Parameter	Pre-exponential factor (A or B)	E or ΔH (kJ mol^{-1})
k_1	4.225×10^{15} (mol atm$^{0.5}$ g h)$^{-1}$)	240.10
k_2	1.955×10^{6} (mol g h^{-1})	67.13
k_2	1.020×10^{15} (mol atm$^{0.5}$ g h^{-1})	243.9
K_{CH_4}	6.65×10^{-4} (atm^{-1})	−38.28
K_{H_2O}	1.77×10^{5} (–)	88.68
K_{H_2}	6.12×10^{-9} (atm^{-1})	−82.90
K_{CO}	8.23×10^{-5} (atm^{-1})	−70.65

$$r_3 = \frac{\frac{k_3}{p_{H_2}^{3.5}}\left(p_{CH_4}p_{H_2O}^2 - \frac{p_{H_2}^4 p_{CO_2}}{K_3}\right)}{(DEN)^2} \quad (6)$$

$$DEN = 1 + K_{CO}p_{CO} + K_{H_2}p_{H_2} + K_{CH_4}p_{CH_4} + \frac{K_{H_2O}p_{H_2O}}{p_{H_2}} \quad (7)$$

$$k_i = A_i \exp\left(\frac{-E_i}{RT}\right);\ i = 1,\ 2,\ 3 \quad (8)$$

$$K_k = B_k \exp\left(\frac{-\Delta H_k}{RT}\right);\ k = CO,\ H_2,\ CH_4,\ H_2O \quad (9)$$

The parameters used in the rate equations are summarized in Table 1.

A palladium membrane reactor (PMR) can be divided into two main sections, i.e., a permeate side and a retentate side. Methane (or biogas) and reforming agent are compressed and fed into the retentate side of PMR where three major chemical reactions (Eqs. (1)–(3)) take place to generate H_2. Due to the difference in partial pressure, H_2 in the retentate side can permeate through the palladium membrane to the permeate side. Therefore, pure H_2 can be derived from the permeate side of PMR. Generally, hydrogen flux is inversely proportional to the membrane thickness and also varies with the operating temperature. The expression used for the hydrogen flux calculation is given in Eq. (10).

$$N_{H_2} = \frac{Q_0}{\delta}\exp\left(\frac{-E_P}{RT}\right)\left(p_{H_2,\,R}^{0.5} - p_{H_2,\,P}^{0.5}\right) \quad (10)$$

The values of the pre-exponential factor (Q_0) and the activation energy (E_P) are 6.33×10^{-7} mol/(m Pa$^{1/2}$ s) and 15,700 J/mol, respectively [8]. The membrane thickness (δ) is set to be 4.5 μm [8].

For the calculations, the pressure drop in the reactor was assumed to be negligible and the reactor was divided into several small volumes (cf. Fig. 1). The finite difference method was employed in the numerical algorithm. The mass balances for the retentate side and permeate side of the membrane reactor are given in Eqs. (11) and (12), respectively.

$$R_k^{j+1} = R_k^j + \frac{\rho_c \pi d^2 \Delta x}{4}\sum_i \upsilon_{ki} r_i^j - N_k^j \pi d \Delta x \quad (11)$$

$$PE_k^{j+1} = PE_k^j + N_k^j \pi d \Delta x \quad (12)$$

Computations were carried out until a desired value of hydrogen recovery (ζ) defined as the mole of hydrogen extracted by the membrane divided by the mole of hydrogen theoretically produced based on the mole of methane feed (4 mol of H_2: 1 mol of CH_4) was achieved. This was then used to obtain the palladium membrane area.

2.2. SOFC stack model

Eqs. (13) and (14) constitute the key electrochemical reactions involving the reduction of molecular O_2 at the cathode to oxygen anions. The latter species permeate through the solid electrolyte to the anode where it reacts with H_2 to produce steam. In this study, CO electro-oxidation is neglected due to the fact that its reaction rate is significantly slower compared with that of H_2 electro-oxidation [14]. Since the rate of WGS reaction is fast at high temperatures [15–17], the anode section would experience an equilibrium conversion of CO (via WGS reaction). It was also assumed that methane remaining from the fuel processor is consumed via the steam reforming and that gas composition at the anode channel is always at equilibrium along the cell length due to the fast kinetics at high-temperature. Ni–YSZ, YSZ and LSM–YSZ were chosen as the materials in the anode, electrolyte and cathode, respectively.

$$\frac{1}{2}O_2 + 2e^- \rightarrow O^{2-} \quad (13)$$

$$H_2 + O^{2-} \rightarrow H_2O + 2e^- \quad (14)$$

The theoretical open-circuit voltage of the cell (E) can be calculated from the Nernst equation as:

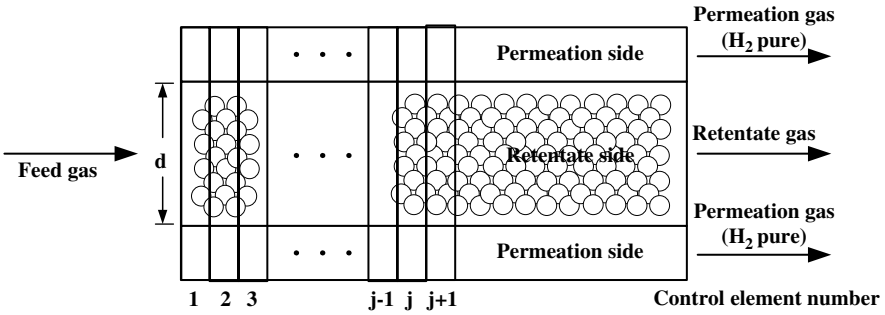

Fig. 1 – The scheme showing the basic working of the membrane reactor.

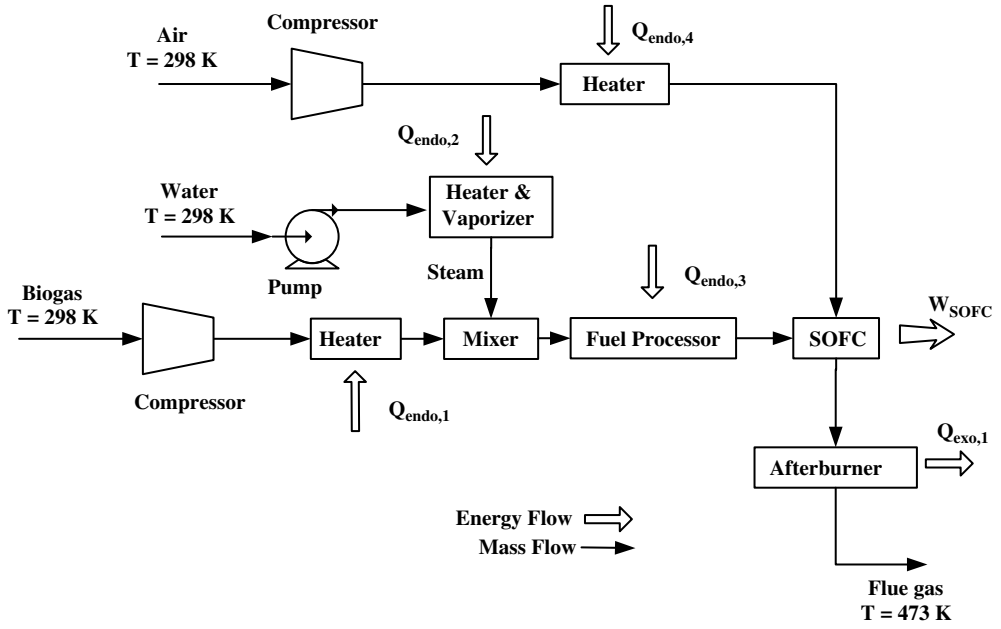

Fig. 2 – The plant configuration of the CON-SOFC.

$$E = E^0 + \frac{RT}{2F}\ln\left(\frac{p_{H_2}p_{O_2}^{1/2}}{p_{H_2O}}\right) \quad (15)$$

In real operation, the actual cell potential (V) at closed-circuit condition is less than the theoretical open-circuit voltage of the cell (E) due to the existence of overpotentials as shown in Eq. (16). The overpotentials can arise from three main sources, namely: ohmic over-potential (η_{ohm}), activation over-potential (η_{act}) and concentration over-potential (η_{conc}).

$$V = E - \eta_{act} - \eta_{ohm} - \eta_{conc} \quad (16)$$

Activation overpotential is controlled by the kinetics at the electrode surface. It can be expressed by the Butler–Volmer equation

$$i = i_{0,z}\left[\exp\left(\frac{\alpha z F \eta_{act,\,z}}{RT}\right) - \exp\left(-\frac{(1-\alpha)zF\eta_{act,\,z}}{RT}\right)\right] \quad (17)$$

In case of SOFC, α and z are set to 0.5 and 2 [18]. Therefore, the activation potential at the anode and cathode can be explicitly written as:

$$\eta_{act,\,z} = \frac{RT}{F}\sinh^{-1}\left(\frac{i}{2i_{0,z}}\right) \quad (18)$$

It should be noted that the exchange current density (i_0) for the cathode side depends on partial pressure of both hydrogen and water as well as the operating temperature [19,20]. For the anode side, i_0 depends on oxygen partial pressure and operating temperature as expressed in Eqs. (19)–(20) [21].

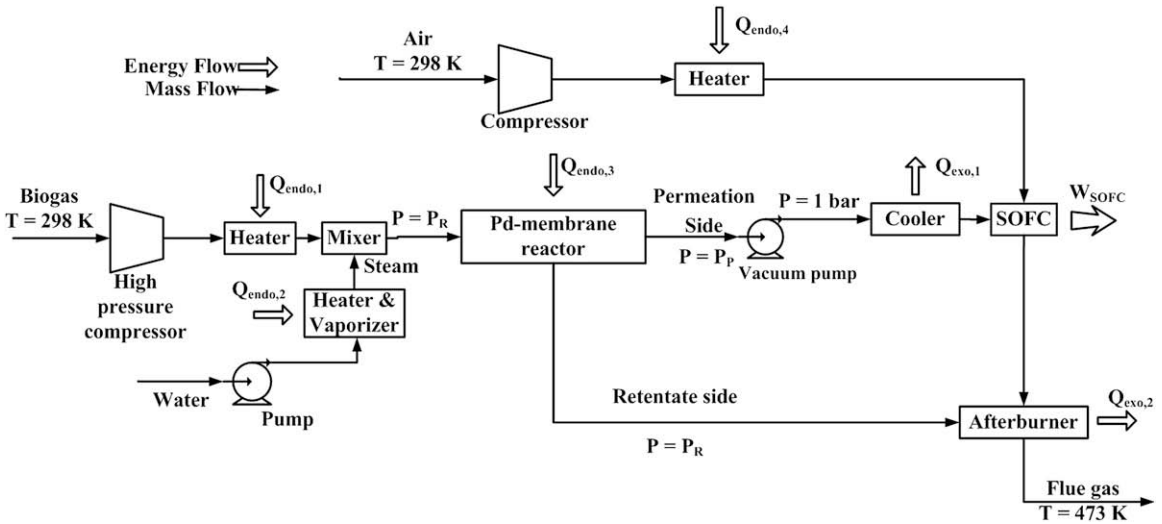

Fig. 3 – The plant configuration of the PMR–SOFC.

Table 2 – Summary of model parameters [29].

Parameters	Value
SOFC stack	
n	0.48
ξ	5.4
D_p	3 μm
l_a	750 μm
l_c	50 μm
L	50 μm
T	1073 K
P	1 bar
Palladium membrane reactor	
T	823 K
P	1 bar
ρ_c	1177.6 kg/m^3
d	10 mm
Reactor tube length	0.15 m
Number of reactor tube	1000
Conventional reformer	
T	973 K
P	1 bar

$$i_{0,a} = \gamma_a \left(\frac{p_{H_2}}{p_{ref}}\right)\left(\frac{p_{H_2O}}{p_{ref}}\right)\exp\left(-\frac{E_{act,\,a}}{RT}\right) \tag{19}$$

$$i_{0,\,c} = \gamma_c \left(\frac{p_{O_2}}{p_{ref}}\right)^{0.25}\exp\left(-\frac{E_{act,\,c}}{RT}\right) \tag{20}$$

The ohmic loss is the resistance to flow of electron through the electrodes and the interconnectors as well as resistance to the flow of ions through electrolyte. It is linearly proportional to current density (i) and also varies with the electrical conductivity (σ) as expressed in Eq. (21). Due to the higher electrical conductivity of the electrodes and interconnectors compared to the electrolyte, only ohmic loss in the electrolyte is considered. The electrical conductivity increases with the cell operating temperature as expressed in Eq. (22) [22].

$$\eta_{ohmic} = \frac{iL}{\sigma} \tag{21}$$

$$\sigma = 3.34 \times 10^4 \exp\left(-\frac{10300}{T}\right) \tag{22}$$

Considering the concentration loss, it is the electrical loss arising from the difference between the reactant concentration on the reaction site and that in the bulk of the gas stream. It may be calculated from Eqs. (23) and (24):

$$\eta_{conc,\,a} = \frac{RT}{2F}\ln\left[\frac{\left(1+\left(\frac{RT}{2F}\right)\left(\frac{l_a}{D_{a(eff)}p^l_{H_2O}}\right)i\right)}{\left(1-\left(\frac{RT}{2F}\right)\left(\frac{l_a}{D_{a(eff)}p^l_{H_2}}\right)i\right)}\right] \tag{23}$$

$$\eta_{conc,\,c} = \frac{RT}{4F}\ln\left[\frac{p^l_{O_2}}{(p_c-\delta_{O_2})-\left((p_c-\delta_{O_2})-p^l_{O_2}\right)\exp\left[\left(\frac{RT}{4F}\right)\left(\frac{\delta_{O_2}l_c}{D_{c(eff)}p_c}\right)i\right]}\right] \tag{24}$$

More details and the values of the parameters used in calculating these over-potentials were given in our recent paper [23].

2.3. *Afterburner and heat exchanger*

At the exit of the SOFC stack, the anode and cathode outlet gases are mixed for post combustion. Complete combustion was assumed in the afterburner; hence, the composition of methane, carbon monoxide and hydrogen in the flue gas were deemed to be zero. The heat exchanger was also assumed to operate adiabatically.

2.4. *Vacuum pump and compressor*

For the calculation of vacuum pump and compressor, their outlet gas temperature and power consumption can be estimated by using Eqs. (25) and (26), respectively [24]. In this study, the efficiency of both the vacuum pump and compressor was determined to be 75% [24].

$$T_{out} = T_{in}\left(1+\frac{1}{\eta_{comp}}\left(\left(\frac{P_{out}}{P_{in}}\right)^{\frac{\gamma-1}{\gamma}}-1\right)\right) \tag{25}$$

$$\dot{W}_{comp} = -\dot{m}\int_{T_{in}}^{T_{out}} C_p dT \tag{26}$$

where

$$\gamma = \frac{C_p}{C_p - R} \tag{27}$$

2.5. *Calculation procedure for determining SOFC stack performance*

For the SOFC operation, a constant operating voltage along the cell length was assumed as the current collector usually has high electrical conductivity. The flow rate of methane in fuel feed is 1 mol/s whereas the flow rate of air fed into the SOFC cathode as the oxidant is always set to 5 times the theoretical amount of air required to combust the methane fuel (biogas). The current density inside the stack varies with the distance from the stack entrance owing to the changes in gas composition in the cathode and anode sections and therefore the open-circuit voltage is also different. Hence, the average current density and power density of the SOFC stack can be calculated. Calculations were performed for each small fuel utilization region employing the mathematical model given in Section 2.2. In each region, the open-circuit voltage, overpotentials, equilibrium composition of anode fuel, stack area and current density were computed. The stack areas obtained in each region were added up to determine the total stack area. Finally, the current calculated from the fuel utilized in the stack was divided by the total stack area to obtain the average current density and hence, the average power

$$\text{SOFC plant efficiency} = \frac{\text{net electrical power generated}}{(\text{LHV of methane})(\text{methane or biogas feed rate})(\text{mole fraction of methane in feed})} \times 100 \quad (28)$$

$$\text{Fuel utilization} = \frac{\text{H}_2 \text{ consumption in electrochemical reaction in SOFC stack}}{\text{SOFC feed rate of H}_2 + \text{SOFC feed rate of CO}} \quad (29)$$

density. The electrical efficiency and the fuel utilization may be estimated from Eqs. (28) and (29), as.

2.6. SOFC system configurations

The SOFC system equipped with a palladium membrane reactor (PMR–SOFC) is considered in this study. The performance was compared with that of the typical SOFC with a conventional reformer (CON-SOFC). The plant configuration for the CON-SOFC is illustrated in Fig. 2. Several units are included, which consist of a pre-reformer, an SOFC stack, an afterburner, a mixer, a vaporizer and pre-heaters. Steam generated via the vaporizer is preheated and then mixed with methane (biogas). The mixture gas is then fed into the fuel processor. In the fuel processor, several chemical reactions (Eqs. (1)–(3)) take place to produce H_2-rich gas. Chemical equilibrium was assumed in the calculations for the conventional reformer. The H_2-rich gas produced in the fuel processor is fed into the SOFC stack where the electrical energy is generated. Isothermal condition was assumed for the SOFC stack to simplify the computation. The heat generated in the SOFC stack is utilized for air and H_2-rich gas preheating to ensure isothermal operation of the SOFC stack. To achieve a desired temperature of the SOFC stack, an oxidizing agent (air) temperature is tuned up based on the energy balance in the SOFC stack. The residue fuel gas exiting the SOFC stack is burned up in the afterburner in order to supply heat to the pre-heaters, pre-reformer and vaporizer. The flue gas is set to be released from the system at 473 K. For energetically self-sustained operation, the total heat requirement for the SOFC system is computed via a trial-and-error by tuning the fuel utilization until the total heat requirement for the system is equal to the total heat generation from the system.

In the PMR–SOFC (cf. Fig. 3), the conventional fuel processor is replaced by PMR. The mixture of methane (biogas) and steam is compressed and then fed into the retentate side of membrane reactor. The set of chemical reactions (Eqs. (1)–(3)) takes place in the retentate side and H_2 generated permeates through the palladium membrane to the permeate side. The permeate gas (H_2-pure) is compressed to atmospheric pressure and then fed into the SOFC stack to generate the electricity, while high-pressure retentate gas is fed into the afterburner. The pressure drop in PMR is neglected and the hydrogen recovery (ζ) was fixed at 95% as it is a suitable value for the SOFC system that can be operated at an energy self-sustained condition. If the hydrogen recovery is lower than this value, large amount of H_2 and CO is released from the PMR at the retentate side and fed to the afterburner. This causes the generation of over-demand heat in the burner. As a result, the energy self-sufficient operation is difficult to be achieved under the operation at low hydrogen recovery (<0.95). With too

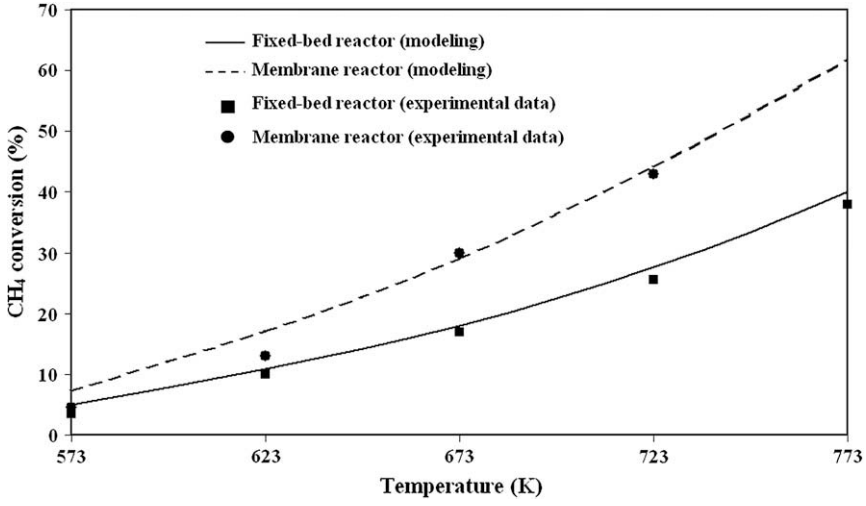

Fig. 4 – The comparison of the methane conversion in the fuel processor between the modeling results and the experimental results. (sweep gas flow rate = 3.62×10^{-5} mol/s, P_R = 1.22 bar, P_P = 1.1 bar, H_2O/CH_4 = 3).

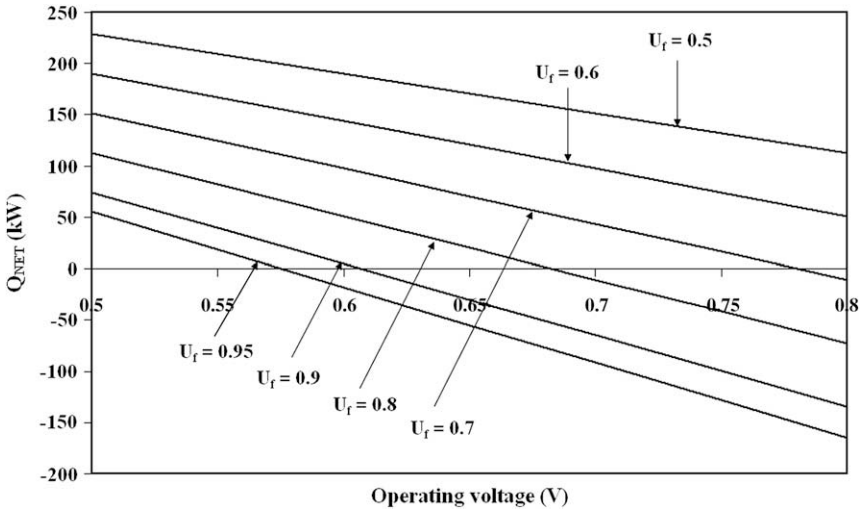

Fig. 5 – Q_{NET} at different operating voltage and fuel utilization for methane-fuelled CON-SOFC.

high hydrogen recovery, high retentate pressure and thus high additional cost of compressor is required.

3. Results and discussion

The numerical algorithms to the models used in this study were written in Visual Basic and the values of all parameters utilized in the computation are summarized in Table 2. As described in our previous investigation [12], the SOFC model developed adequately predicted the experimental results of Zhao and Virkar [25] for the feed of a mixture of hydrogen (97%) and water (3%) and the simulation results of Petruzzi et al. [26] for the feed of gas containing a low concentration of hydrogen [23]. The kinetic model and H_2 permeation model for the membrane reactor were also verified. Again, our modeling results are in good agreement with the experimental results reported in the literature [9,27] as illustrated in Fig. 4.

Based on an earlier study [28], the CON-SOFC system can stand alone without requirement of external heat sources (the energy self-sustained operation, $Q_{NET} > 0$) when it operates at suitable operating conditions. It is noted that Q_{NET} is the difference between heat generated and heat demanded within the SOFC system. Fig. 5 shows that at different operating voltage, Q_{NET} can become zero when the appropriate fuel utilization (U_f) is chosen. At a higher operating voltage where the cell efficiency is high, the SOFC needs to be operated at lower fuel utilization so that the residual fuel can provide sufficient heat to the overall SOFC system after burning. It should be noted that a very low operating voltage is not recommended for practical operation due to the possible large in-stack temperature gradient arising from the difficulty in heat removal from the SOFC stack. In addition, the condition with $Q_{NET} = 0$ may not be possible. Two types of feed, i.e., pure methane and biogas were considered in this study. Generally, the composition of biogas varies depending on its source. It mainly contains methane (40–65%) and CO_2 (30–40%). In this

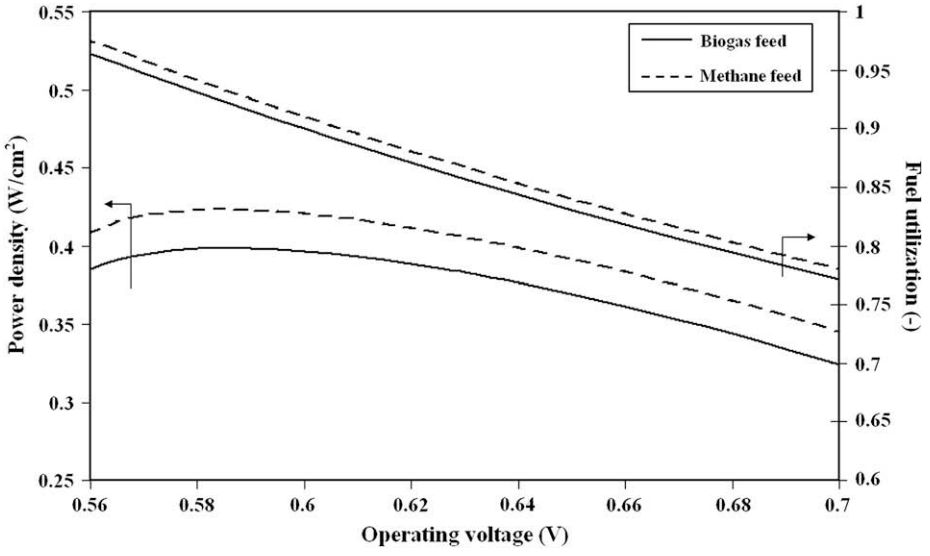

Fig. 6 – Power density and fuel utilization at different operating voltage in case that $Q_{NET} = 0$.

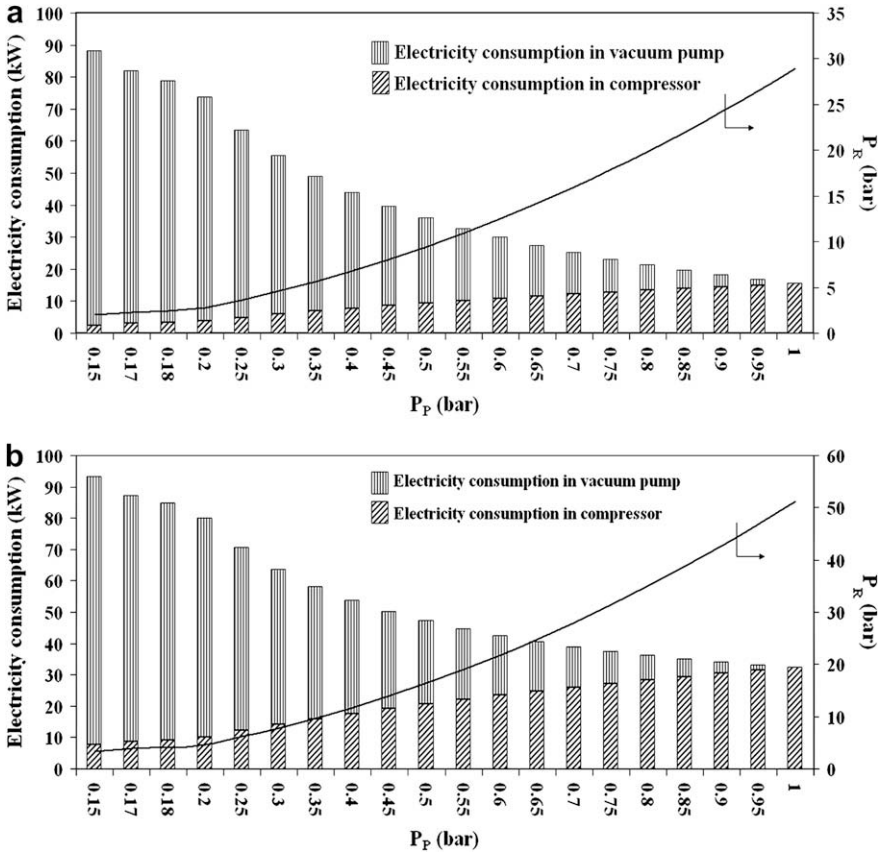

Fig. 7 – Electrical power consumed in HPC and vacuum pump at different retentate pressure (P_R) and permeate pressure (P_P) in case that $\zeta = 0.95$ for (a) methane feed and (b) biogas feed.

work, the value of CH_4:CO_2 in biogas was set at 60:40. It should be noted that biogas usually contains a small amount of H_2S which can cause poisoning to catalysts and Pd membrane. In this study, it was assumed that H_2S is removed from biogas by a desulphurization process. Fig. 6 shows the effects of operating voltage on the power density and the fuel utilization of the CON-SOFC fed by methane and biogas for the case of $Q_{NET} = 0$. For both types of feed, it is clear that at a higher operating voltage, the SOFC system needs to operate at a lower value of fuel utilization. There exists an optimum operating voltage which offers the maximum power density for each type of feed. The maximum power density and the corresponding voltage are 0.423 W/cm^2 and 0.585 V, and 0.399 W/cm^2 and 0.585 V for the methane and biogas feeds, respectively. The lower methane concentration in biogas results in the lower achievable power density.

It should be noted that for the case of $Q_{NET} = 0$, the decrease in operating voltage can initially improve the power density of the SOFC; however, the resulting higher fuel utilization for achieving the energetically self-sustaining condition results in the poorer cell performance particularly near the exit of the SOFC stack where concentration of fuel is low, and, consequently the power density later decreases at much lower operating voltages.

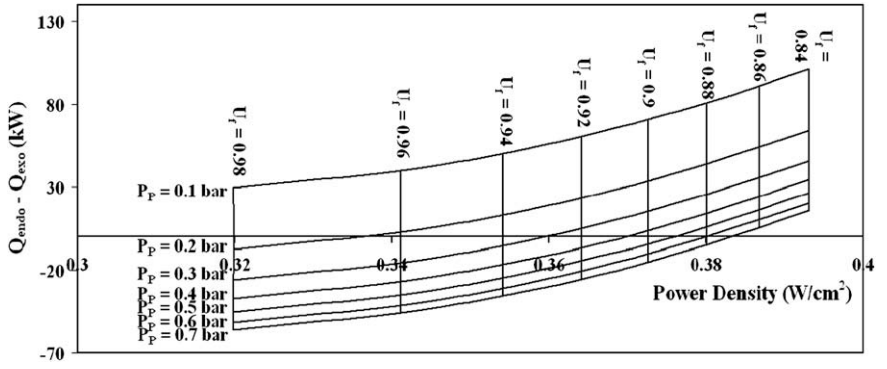

Fig. 8 – Q_{NET} and power density at different permeate pressure and fuel utilization (U_f) for PMR–SOFC in the case of methane feed.

For PMR–SOFC, a part of electrical energy produced in SOFC stack is supplied to a high-pressure compressor (HPC) and a vacuum pump. The electrical power consumption in these equipments varies with the operating pressures of the HPC (retentate pressure, P_R) and vacuum pump (permeation pressure, P_P). The sum of the electrical power consumed in the HPC and the vacuum pump to obtain the hydrogen recovery of 0.95 is illustrated in Fig. 7 a and b for pure methane and biogas feeds, respectively. The electrical consumption decreases as P_P increases and the minimum electricity load can be found when P_P equals to 1 bar (vacuum pump does not operate). The results also indicate that the electrical power consumption in the PMR for the pure methane feed is lower than that for the biogas feed which contains 40% CO_2. It should be noted that even if an operation at the permeation pressure of 1 bar can offer the minimum electricity load, P_R is extremely high and the structure of PMR may be damaged. Therefore, the limitation of PMR structure should also be carefully considered.

The change in P_P also affects the heat management in the PMR–SOFC system. Operation at a lower P_P causes higher heat generation during vacuum pump compression. Some heat removal may be required to reduce the temperature of gas discharged from the vacuum pump prior to being fed into SOFC anode. Therefore, for the operation at low P_P, the SOFC system requires an operation at a higher fuel utilization to achieve energetically self-sustained operation, resulting in a lower power density. As illustrated in Fig. 8, operation of the PMR–SOFC fed by pure methane at P_P of 0.1 bar cannot be self-sustained, whilst U_f should be set to be 0.965 for the operation at P_P of 0.2 bar. Hence, operation at high P_P is preferable since the condition with $Q_{NET} = 0$ can be achieved and the corresponding power density is higher.

The performance of PMR–SOFC and CON-SOFC under energetically self-sustained operation ($Q_{NET} = 0$) are compared as seen in Fig. 9. It is clear that the PMR–SOFC can offer higher power density compared with the CON-SOFC when the operating voltage and P_P are judiciously chosen. Fig. 9 a and b show that the power density of the PMR–SOFC fuelled by methane and biogas is improved as P_P increases. Maximum power density may be achieved when P_P is 1 bar. An optimum operating voltage that provides a maximum power density is observed. The effect of variation in P_P on the power density and the SOFC area at the optimum operating voltage is

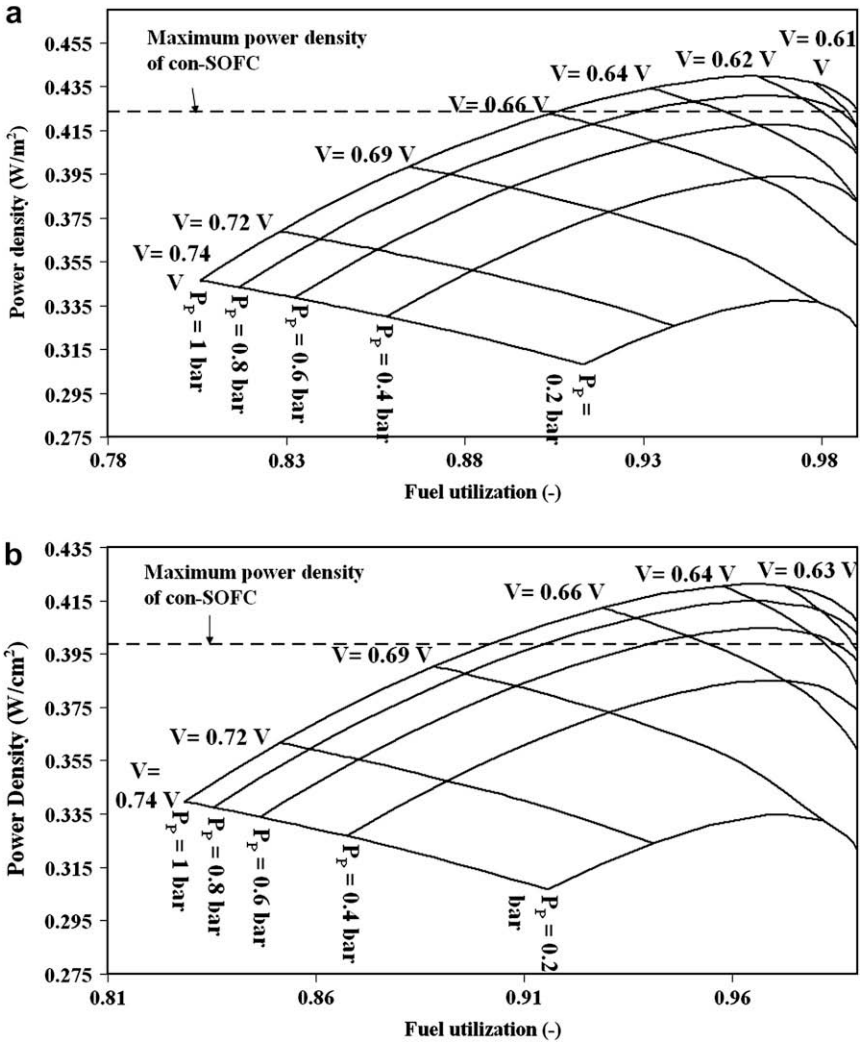

Fig. 9 – Power density and fuel utilization at different permeate pressure and operating voltage in case that $Q_{NET} = 0$ for (a) methane-fuelled PMR–SOFC and (b) biogas-fuelled PMR–SOFC.

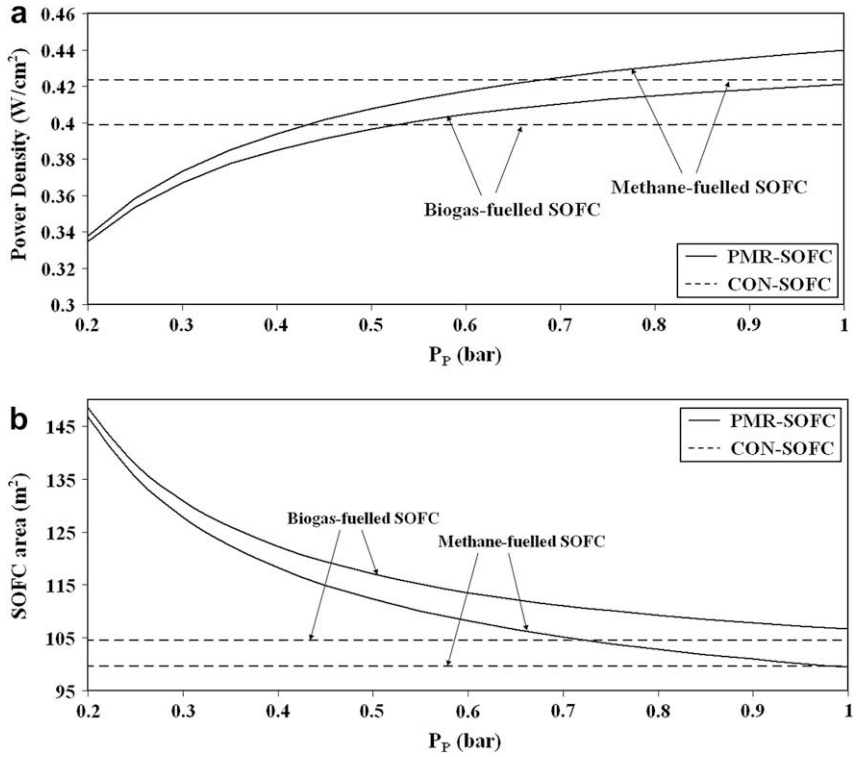

Fig. 10 – The effect of change in permeate pressure on (a) power density and (b) SOFC area at optimum operating voltage in case that $Q_{NET} = 0$.

summarized in Fig. 10 a and b, respectively. The power density of the PMR–SOFC fed by pure methane and biogas is higher than that of the CON-SOFC when P_P is higher than 0.67 and 0.52 bar, respectively, and the benefit gained from the reduction in SOFC stack area of the PMR–SOFC over the CON-SOFC can be found when P_P is higher than 0.98 bar for methane feed. Nevertheless, the reduction in SOFC stack area over the CON-SOFC is not achieved for PMR–SOFC fuelled by biogas.

Even if the use of PMR in the SOFC system can reduce the SOFC stack size in case of methane feed, the additional capital costs from the supporting units, i.e., PMR, HPC, and vacuum pump, need to be taken into account. Therefore, an economic analysis is employed to examine the potential benefit of the use of PMR in the SOFC system for both methane and biogas feeds. In the following analysis, the methane feed rate was kept at 1 mol/s for all scenarios to achieve negligible fuel feed cost. Furthermore, since the SOFC system under the energetically self-sustained operation was considered, additional energy or electricity from the outside of the system is not necessary. Therefore, only the capital costs of SOFC stack, PMR, HPC, and vacuum pump were taken into account. It should be noted that when the PMR is operated at high pressure, it may cause an additional cost on reinforcing the palladium membrane structure; however, this cost is not taken into account for the economic analysis in this study.

The parameters used in the capital cost estimation for these equipment items are listed in Table 3. Net cost saving was calculated as an economic index, viz;

$$\text{Net cost saving} = \text{Saving in capital cost of SOFC stack} - \text{Additional capital cost of PMR, HPC and vacuum pump} \quad (30)$$

Fig. 11 a and b indicate that the replacement of a conventional reformer with a membrane reactor in the SOFC system is not advantageous in economic point of view as the saving stack cost is always lower than the additional capital costs of PMR,

Table 3 – Costing models of SOFC [30], palladium membrane [31], compressor [17] and vacuum pump [32].

Costing model	
Cell cost ($)	$C_{cell} = A_{single\ cell} \times 0.1442$[a]
Number of cells	$N_{cell} = A_{cell}/A_{single\ cell}$
Number of stacks	$N_{stack} = N_{cell}/100$
Fuel cell stacks cost ($)	$C_{stack} = 2.7 \times (C_{cell} \times N_{cell} + 2 \times N_{stack} \times A_{single\ cell} \times 0.46425)$
Palladium membrane cost ($/kg)	6700
Compressor ($)	$C_{comp} = 1.49 \times HP^{0.71} \times 10^3$
Vacuum pump ($)	$C_{vacuum\ pump} = 2.59 \times X^{1.03} \times 10^5$ where: $0.01 < X < 0.52$ (lbs h suction Torr)

a A single cell area is fixed at 200 cm^2.

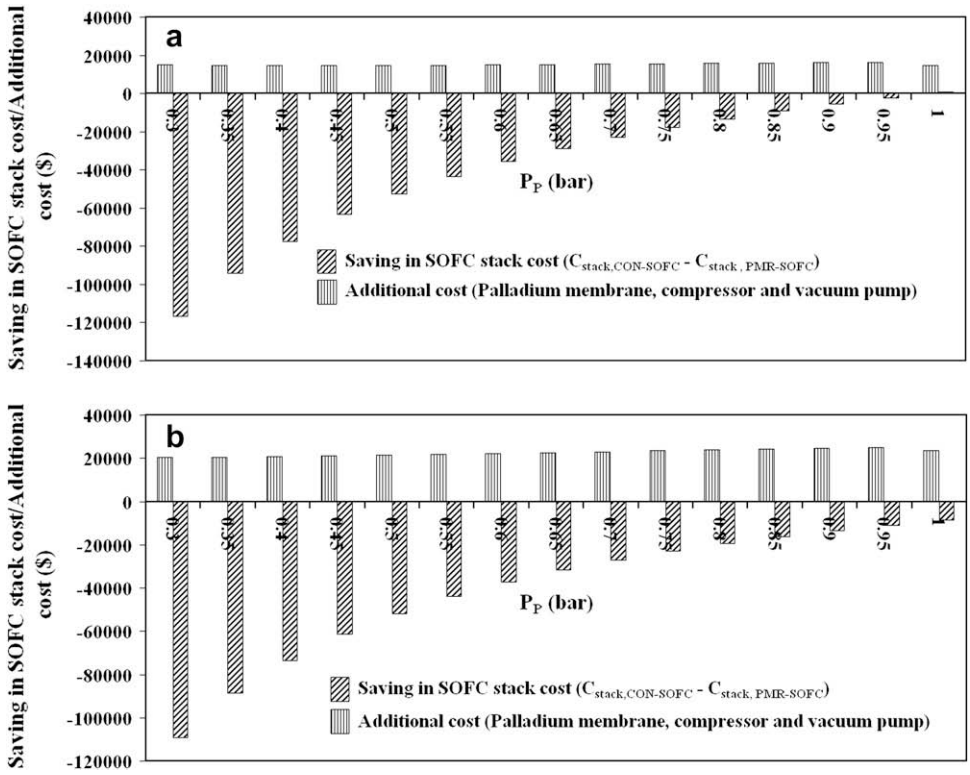

Fig. 11 – Saving in SOFC stack cost/additional cost at different permeate pressure (optimum operating voltage and $Q_{NET} = 0$) for (a) methane-fuelled PMR–SOFC and (b) biogas-fuelled PMR–SOFC.

Table 4 – The technical and economical comparison of four scenarios.

	Methane-fuelled		Biogas-fuelled	
	CON-SOFC	PMR–SOFC	CON-SOFC	PMR–SOFC
Feed rate (mol/s)	1	1	1.667	1.667
% Methane in feed	100	100	60	60
Retentate pressure (bar)	–	28.94	–	51.27
Permeate pressure (bar)	–	1	–	1
Operating voltage (V)	0.585	0.62	0.585	0.635
Power density (W/cm^2)	0.4233	0.4398	0.3986	0.4213
% Improvement in power density	–	3.90	–	5.69
Electricity produced in SOFC (kW)	421.68	437.34	416.79	449.30
Net electricity produced (kW)	421.68	421.68	416.79	416.79
Electricity consumed in compressor (kW)	–	15.53	–	32.46
SOFC active area (m^2)	99.62	99.45	104.57	106.66
% Improvement in SOFC area	–	0.17	–	−2.00
Palladium membrane area (m^2)	–	4.71	–	4.71
Capital cost of SOFC ($)	412,814.40	412,114.22	433,358.34	442,000.46
Capital cost of Pd membrane ($)	–	1716.52	–	1716.52
Capital cost of compressor ($)	–	12866.86	–	21,712.86
Saving cost on SOFC ($)	–	700.18	–	−8642.13
Net cost saving ($)	–	−13,883.20	–	−32,071.51

HPC and vacuum pump. The saving stack cost increases as permeate pressure increases due to the improvement of the power density. The saving stack cost is always negative for PMR–SOFC fuelled by biogas since SOFC stack area reduction over the CON-SOFC is not achieved. The additional cost of PMR–SOFC system in case of biogas feed is always higher than that in case of methane feed since higher retentate pressure and thus higher compressor load are required for the former one. All technical and economic analyses of four scenarios are summarized in Table 4. The optimum condition is chosen for each scenario. With the use of PMR in the SOFC system (PMR–SOFC), the power density improvement of 3.9% and 5.69% can be observed, compared with the CON-SOFC, for methane and biogas feeds, respectively. Although the replacement of CON-SOFC by PMR–SOFC can improve the power density, higher electrical power is generated in SOFC stack for the latter one to supply the demand of electricity in HPC. This is the reason why the SOFC stack area reduction over CON-SOFC is not achieved for PMR–SOFC fed by biogas feed and the required SOFC stack area of PMR–SOFC fed by methane is only decreased by 0.17%. From this economic consideration, it seems that both methane-fuelled PMR–SOFC and biogas-fuelled PMR–SOFC offer negative net cost saving (−$13,883.20 and −$32,071.51). The operation at high retentate pressure of both methane-fuelled PMR–SOFC (28.94 bar) and biogas-fuelled PMR–SOFC (51.27 bar) extremely affects their HPC cost and electricity load in HPC. The HPC cost of $12,886.86 and $21,712.86 is paid for the methane and biogas feeds, respectively, whereas the electrical power of 15.53 kW and 32.46 kW is consumed in HPC for the methane and biogas feeds, respectively. These results imply that the improvement in the permeability of palladium membrane can reduce retentate pressure, the electricity load and thus the profitability of PMR–SOFC. Finally, it may be concluded that the PMR–SOFC fed by either methane or biogas is attractive for its technical benefits, however, the economic benefit is not found in these operations.

4. Conclusions

The performance improvement of SOFC system by replacing a conventional reformer (CON-SOFC) by a palladium membrane reactor (PMR–SOFC) is investigated. Methane and desulphurized biogas are used as feed streams for SOFC system. The energetically self-sustained operation ($Q_{NET} = 0$) for each mode may be obtained by tuning up the fuel utilization (U_f). The decrease in operating voltage can improve the power density; however, when it is too low, a high U_f is required to achieve the condition for $Q_{NET} = 0$ and no power density improvement is obtained. For the PMR–SOFC, the change in permeate pressure (P_P) also affects the SOFC power density and energy self-sufficiency point. Increase in P_P can improve the power density due to the decrease in U_f which offers zero Q_{NET}. It is found that the values of power density of the PMR–SOFC are 3.9% and 5.69% higher than those of the CON-SOFC for methane feed and biogas feed, respectively. The use of PMR in the methane-fuelled SOFC can reduce the SOFC area by 0.17%, however, SOFC stack area reduction over CON-SOFC is not achieved for biogas feed. For economic study, it was found that both methane-fuelled PMR–SOFC and biogas-fuelled PMR–SOFC always offer the negative net cost saving. It may be concluded from this study that both of the methane-fuelled and biogas-fuelled PMR–SOFCs are technically interesting operation modes, however, both of them cannot offer economic benefits over conventional SOFC.

Acknowledgement

This research is financially supported by the Thailand Research Fund and Commission on Higher Education.

REFERENCES

[1] Baron S, Brandon N, Atkinson A, Steele B, Rudkin R. The impact of wood-derived gasification gases on Ni–CGO anodes in intermediate temperature solid oxide fuel cells. J Power Sources 2004;126:58–66.
[2] Eguchi K, Kojo H, Takeguchi T, Kikuchi R, Sasaki K. Fuel flexibility in power generation by solid oxide fuel cells. Solid State Ionics 2002;152–153:411–6.
[3] Suwanwarangkul R, Croiset E, Entchev E, Charojrochkul S, Pritzker MD, Fowler MW, et al. Experimental and modeling study of solid oxide fuel cell operating with syngas fuel. J Power Sources 2006;161:308–22.
[4] Dayton DC. Fuel cell integration-a study of the impacts of gas quality and impurities. NREL final report; 2001.
[5] Effendi A, Hellgardt K, Zhang ZG, Yoshida T. Optimising H_2 production from model biogas via combined steam reforming and CO shift reactions. Fuel 2005;84:869–74.
[6] Lu GQ, Diniz da Costa JC, Duke M, Giessler S, Socolow R, Williams RH, et al. Inorganic membranes for hydrogen production and purification: a critical review and perspective. J Colloid Interface Sci 2007;314:589–603.
[7] Basile A, Paturzo L, Gallucci F. Co-current and counter-current modes for water gas shift membrane reactor. Catal Today 2003;82:275–81.
[8] Patel KS, Sunol AK. Modeling and simulation of methane steam reforming in a thermally coupled membrane reactor. Int J Hydrogen Energy 2007;32:2344–58.
[9] Gallucci F, Paturzo L, Basile A. A simulation study of the steam reforming of methane in a dense tubular membrane reactor. Int J Hydrogen Energy 2004;29:611–7.
[10] Sangtongkitcharoen W, Vivanpatarakij S, Laosiripojana N, Arpornwichanop A, Assabumrungrat S. Performance analysis of methanol-fueled solid oxide fuel cell system incorporated with palladium membrane reactor. Chem Eng J 2008;138:436–41.
[11] Vivanpatarakij S, Laosiripojana N, Arpornwichanop A, Assabumrungrat S. Performance improvement of solid oxide fuel cell system using palladium membrane reactor with different operation modes. Chem Eng J 2009;146:112–9.
[12] Piroonlerkgul P, Assabumrungrat S, Laosiripojana N, Adesina AA. Selection of appropriate fuel processor for biogas-fuelled SOFC system. Chem Eng J 2008;140:341–51.
[13] Xu J, Froment GF. Methane steam reforming, methanation and water–gas shift: I. Intrinsic kinetics. AIChE J 1989;35:88–96.
[14] Khaleel MA, Lin Z, Singh P, Surdoval W, Collin D. A finite element analysis modeling tool for solid oxide fuel cell development: coupled electrochemistry, thermal and flow analysis in MARC(R). J Power Sources 2004;130:136–48.
[15] Blom R, Dahl IM, Slagtem A, Sortland B, Spjelkavik A, Tangstad E. Carbon dioxide reforming of methane over

lanthanum-modified catalysts in a fluidized-bed reactor. Catal Today 1994;21:535–43.
[16] Bradford MCJ, Vannice MA. Catalytic reforming of methane with carbon dioxide over nickel catalysts II. Reaction kinetics. Appl Catal A: Gen 1996;142:97–122.
[17] Swaan HM, Kroll VCH, Martin GA, Mirodatos C. Deactivation of supported nickel catalysts during the reforming of methane by carbon dioxide. Catal Today 1994;21:571–8.
[18] Chan SH, Khor KA, Xia ZT. A complete polarization model of a solid oxide fuel cell and its sensitivity to the change of cell component thickness. J Power Sources 2001;93: 130–40.
[19] Jiang SP, Badwal SPS. Hydrogen oxidation at the nickel and platinum electrodes on yttria-tetragonal zirconia electrolyte. J Electrochem Soc 1997;144:3777–84.
[20] Jiang SP, Badwal SPS. An electrode kinetics study of H_2 oxidation on Ni/Y_2O_3–ZrO_2 cermet electrode of the solid oxide fuel cell. Solid State Ionics 1999;123:209–24.
[21] Fleig J. Solid oxide fuel cell cathodes: polarization mechanisms and modeling of the electrochemical performance. Annu Rev Mater Res 2003;33:361–82.
[22] Ferguson JR, Fiard JM, Herbin R. Three-dimensional numerical simulation for various geometries of solid oxide fuel cells. J Power Sources 1996;58:109–22.
[23] Piroonlerkgul P, Assabumrungrat S, Laosiripojana N, Adesina AA. Performance of biogas-fed solid oxide fuel cell system integrated with membrane module for CO_2 removal. Chemical Engineering and Processing: Process Intensification 2009;48:672–82.
[24] Kaneko T, Brouwer J, Samuelsen GS. Power and temperature control of fluctuating biomass gas fueled solid oxide fuel cell and micro gas turbine hybrid system. J Power Sources 2006; 160:316–25.
[25] Zhao F, Virkar AV. Dependence of polarization in anode-supported solid oxide fuel cells on various cell parameters. J Power Sources 2005;141:79–95.
[26] Petruzzi L, Cocchi S, Fineschi F. A global thermo-electrochemical model for SOFC systems design and engineering. J Power Sources 2003;118:96–107.
[27] Shu J, Grandjean BPA, Kaliaguine S. Asymmetric Pd–Ag/ stainless steel catalytic membranes for methane steam reforming. Catal Today 1995;25:327–32.
[28] Jamsak W, Assabumrungrat S, Douglas PL, Croiset E, Laosiripojana N, Suwanwarangkul R, et al. Thermodynamic assessment of solid oxide fuel cell system integrated with bioethanol purification unit. J Power Sources 2007;174: 191–8.
[29] Ni M, Leung MKH, Leung DYC. Parametric study of solid oxide fuel cell performance. Energy Convers Manage 2007;48: 1525–35.
[30] Palazzi F, Autissier N, Marechal FMA, Favrat D. A methodology for thermo-economic modeling and optimization of solid oxide fuel cell systems. Appl Therm Eng 2007;27:2703–12.
[31] Amelio M, Morrone P, Gallucci F, Basile A. Integrated gasification gas combined cycle plant with membrane reactors: technological and economical analysis. Energy Convers Manage 2007;48:2680–93.
[32] Walas SM. Chemical process equipment selection and design. Butterworth, Inc.; 1988.

Nomenclature

$A_{single\ cell}$: active area of SOFC single cell, m^2
A_{cell}: total active area of SOFC, m^2
A_i: pre-exponential factor for i^{th} reaction, various units
B_k: pre-exponential factor for component k, various units
C_{cell}: capital cost of SOFC single cell, $
C_{comp}: capital cost of compressor, $
C_p: heat capacity, $J\,mol^{-1}\,K^{-1}$
C_{stack}: capital cost of SOFC stack, $
$C_{vacuum\ pump}$: capital cost of vacuum pump, $
d: diameter of inner tube of membrane reactor, mm
DEN: term given for the reforming kinetics, dimensionless
D_p: catalyst pore diameter, μm
$D_{z(eff)}$: effective diffusion coefficient of z (z = anode, cathode), $cm^2\,s^{-1}$
E: theoretical open-circuit voltage of the cell, V
E0: theoretical open-circuit voltage of the cell at standard pressure, V
$E_{act,z}$: apparent activation energy of exchange current density of z (z = anode, cathode), $J\,mol^{-1}$
E_i: activation energy for ith reaction, $J\,mol^{-1}$
E_p: activation energy for hydrogen permeation, $J\,mol^{-1}$
F: Faraday constant (9.6495×10^4), $C\,mol^{-1}$
ΔH_i: heat of reaction for reaction i, $J\,mol^{-1}$
ΔH_k: heat of adsorption for component k, $J\,mol^{-1}$
i: current density, $A\,cm^{-2}$
$i_{0,z}$: exchange current density of z (z = anode, cathode), $A\,cm^{-2}$
k_i: reaction rate constant for ith reaction, various units
K_i: equilibrium constant for ith reaction, various units
K_k: adsorption constant for component k, various units
l_a: thickness of anode, μm
l_c: thickness of cathode, μm
L: thickness of electrolyte, μm
LHV: lower heating value, $kJ\,mol^{-1}$
$\dot{m}$: molar flow rate, $mol\,s^{-1}$
n: electrode porosity, dimensionless
N_k: permeation flux of component k, $mol\,m^{-2}\,s^{-1}$
N_{cell}: number of SOFC single cell, dimensionless
N_{stack}: number of SOFC stack, dimensionless
P: pressure, Pa
p_c: operating pressure at the SOFC cathode, Pa
p_k: partial pressure of component k, Pa
p_kI: inlet pressure of component k, Pa
$P_{H_2,\,P}$: partial pressure of hydrogen in permeate side of membrane reactor, Pa
$p_{H_2,R}$: partial pressure of hydrogen in retentate side of membrane reactor, Pa
p_{ref}: reference pressure (10^5), Pa
PE_k: molar flow rate of component k at permeate side of membrane, $mol\,s^{-1}$
Q_0: pre-exponential factor for hydrogen permeation, $mol\,m^{-1}\,Pa^{-0.5}\,s^{-1}$
Q_{NET}: difference between heat demand and heat generated in SOFC system, kW
r_i: reaction rate for ith reaction, $mol\,s^{-1}$
R: gas constant (8.3145), $J\,mol^{-1}\,K^{-1}$
R_k: molar flow rate of component k at retentate side of membrane, $mol\,s^{-1}$
T: temperature, K
U_f: fuel utilization, dimensionless
V: cell voltage, V
$\dot{W}_{comp}$: electricity consumed in the compressor, kW
Δx: length of control volume in membrane reactor, m
X: parameter used in vacuum pump cost estimation, $lbs\,H_2\,h^{-1}$ suction $Torr^{-1}$
z: the number of electrons involved per reaction, dimensionless

Greek letters
α: symmetrical factor, dimensionless
ξ: electrode tortuosity, dimensionless

δ: membrane thickness, μm
ζ: hydrogen recovery, dimensionless
$\eta_{act,z}$: activation loss of z (z = anode, cathode), V
$\eta_{conc,z}$: concentration loss of z (z = anode, cathode), V
η_{comp}: compressor or pump efficiency, dimensionless
η_{ohm}: ohmic loss, V
σ: electrical conductivity, $\Omega^{-1}\,m^{-1}$
ρ_c: catalyst density, $kg\,m^{-3}$
$v_{k,i}$: stoichiometric coefficient of component k in chemical reaction i
γ_z: pre-exponential factor for exchange current density of z (z = anode, cathode), $A\,m^{-2}$

Superscripts
j: j-th control volume

Subscripts
a: anode
c: cathode
i: i-th reaction
in: input
k: component
out: output
P: permeate side of membrane
R: retentate side of membrane

ภาคผนวก 6

Available at www.sciencedirect.com

ScienceDirect

journal homepage: www.elsevier.com/locate/he

Effect of oxygen addition on catalytic performance of $Ni/SiO_2 \cdot MgO$ toward carbon dioxide reforming of methane under periodic operation

S. Assabumrungrat[a,*], S. Charoenseri[a], N. Laosiripojana[b], W. Kiatkittipong[c], P. Praserthdam[a]

[a]Center of Excellence in Catalysis and Catalytic Reaction Engineering, Department of Chemical Engineering, Faculty of Engineering, Chulalongkorn University, Bangkok 10330, Thailand
[b]The Joint Graduate School of Energy and Environment, King Mongkut's University of Technology Thonburi, Bangkok 10140, Thailand
[c]Department of Chemical Engineering, Faculty of Engineering and Industrial Technology, Silpakorn University, Nakhon Pathom 73000, Thailand

ARTICLE INFO

Article history:
Received 31 January 2009
Received in revised form
25 May 2009
Accepted 29 May 2009
Available online 27 June 2009

Keywords:
Coke
Dry reforming
Hydrogen production
Periodic operation

ABSTRACT

This work investigates the catalytic performance of an industrial steam reforming $Ni/SiO_2 \cdot MgO$ catalyst toward dry reforming of CH_4 under periodic operation. The effects of cracking/regeneration temperatures and O_2 addition during regeneration on the catalyst stability and activity were determined and various characterizations i.e. BET, SEM, XRD, and TPO were employed to relate the catalyst performance with its physical properties. It was found that, without O_2 addition, the catalyst showed good stability at 650 °C but observed high deactivation at 750 °C due to the formation of encapsulating carbon. The addition of O_2 along with CO_2 can eliminate all deactivation at 750 °C and no significant loss of catalyst activity was observed for at least 12 cracking/regeneration cycles. The optimal performance for periodic operation was found at the condition with 5 min of the cracking step followed by 5 min of the regeneration step at 750 °C with CO_2/O_2 ratio of 7/3.

1. Introduction

Carbon dioxide reforming (or dry reforming) of CH_4 (Eq. (1)) is an interesting route for synthesis gas (as called syngas) production because both reactants known as major green house gases can be efficiently consumed in the reaction providing useful syngas with low H_2/CO ratio, which is suitable for later production of valuable chemicals such as alcohol, aldehyde and isobutene.

$$CH_4 + CO_2 \leftrightarrow 2CO + 2\,H_2 \quad (1)$$

Several supported transition metal catalysts (e.g., Ni, Ru, Rh and Pd) have been tested for the CO_2 reforming of CH_4 [1–8]; among them, nickel is the most practical catalyst due to its low cost [9–14]. It is noted that the typical problem found for this reaction is catalyst deactivation due to the carbonaceous deposition, which is mainly generated from the following catalytic cracking of methane (Eq. (2)) [15]. Importantly, the presence of CO_2 theoretically helps remove deposited carbon according to the following reverse Boudouard reaction (Eq. (3)) [16].

$$CH_4 \rightarrow C + 2H_2 \quad (2)$$

* *Corresponding author*. Fax: +66 2 218 6877.
E-mail address: suttichai.a@chula.ac.th (S. Assabumrungrat).
0360-3199/$ – see front matter
doi:10.1016/j.ijhydene.2009.05.128

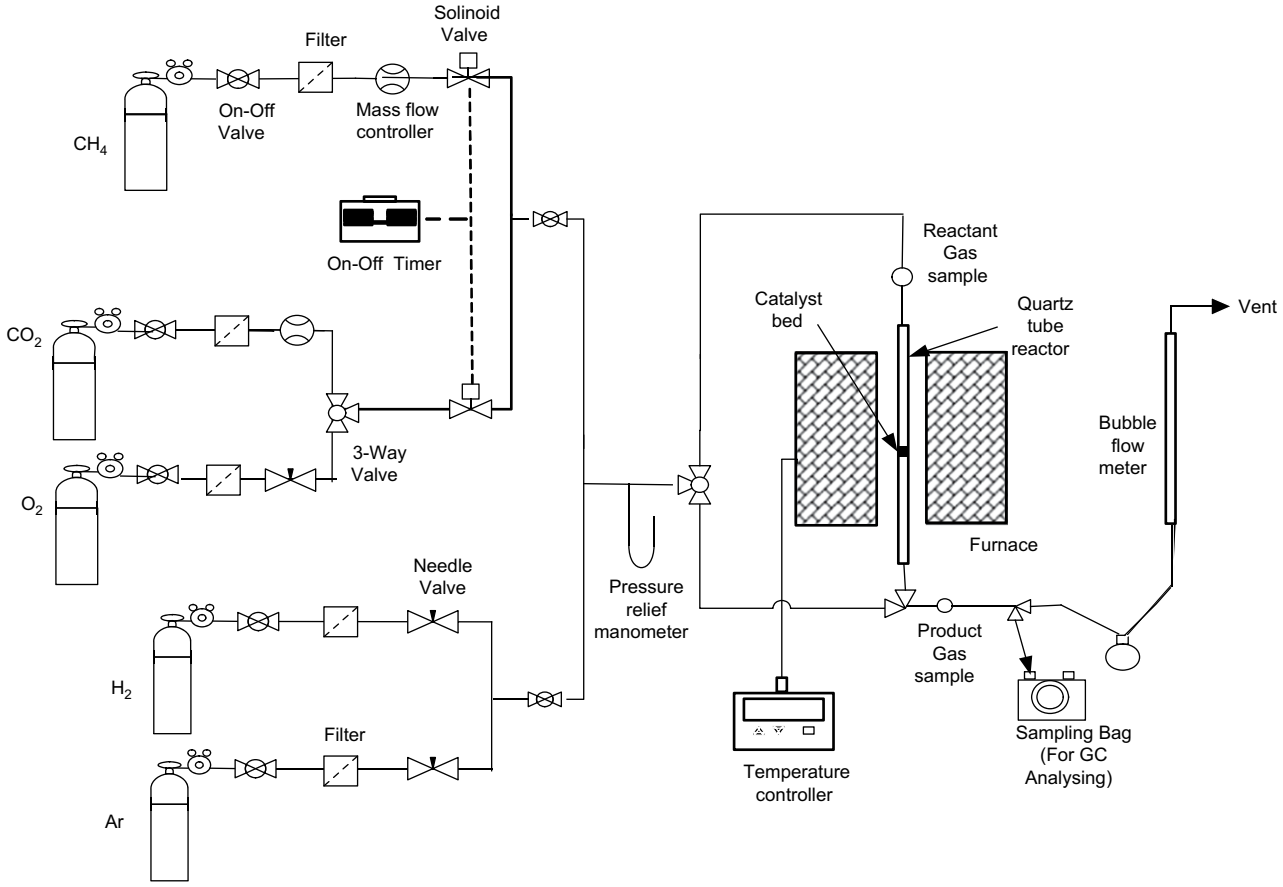

Fig. 1 – Schematic diagram of the experimental setup.

$$C + CO_2 \rightarrow 2CO \quad (3)$$

From the above reactions, it is obvious that the CO_2 reforming of CH_4 can be operated periodically by feeding CH_4 and CO_2 alternately. Based on this periodic operation, hydrogen and carbon monoxide are generated separately at different intervals, and consequently, these products can be directly separated without requirement of further purification units. This operation is particularly attractive for some applications where pure hydrogen is required, e.g. for proton-exchange membrane (PEM) fuel cell.

Recently, several researchers have employed the periodic operation for hydrogen production. Most of the studies have used O_2 and/or steam for removing deposited coke on catalysts. Both reactions with O_2 and steam were reported to be able to restore the catalytic activity of Ni-based catalyst after deactivation by carbon formation [17]. It was reported that Ni/SiO_2 catalyst could be fully regenerated at 650 °C with steam for up to 10 successive cracking/regeneration cycles without significant loss of catalytic activity [18]. In our previous work [19], we studied the performance of periodic operation for the CO_2 reforming of CH_4 over an industrial steam reforming Ni/SiO_2·MgO catalyst. It was found that the catalytic reactivity of periodic operation was significantly lower than that of steady-state operation over all ranges of reaction time for both reaction temperatures of 650 and 750 °C due to incomplete removal of deposited carbon by CO_2 in the regeneration step.

In this work, the further works were carried out based on the same reaction system but some O_2 was added along with CO_2 for helping regenerate the deactivated catalyst. It is worthy to note that if a catalyst possesses an excellent anti-sintering property, the elimination of the carbon deposited may be realized by CO_2 or steam. However, oxidation with O_2 could be faster for coke removal than that of CO_2 or steam [17]. According to this operation, the system can also gain benefit from the potential heat integration since the exothermic heat from the catalyst regeneration particularly from oxidation by O_2 can supply for the endothermic catalytic cracking of CH_4. In details, the effect of O_2 contents on catalytic performance of the reaction under periodic operation was investigated and compared to those of steady state operation. In addition, spent catalysts after exposure in reaction at different

Table 1 – The molar flow rates of reactant gases used for steady state operation.

Reactants	Flow rate (cm^3/min)		
	CH_4:CO_2:O_2 = 1:0.9:0.1	CH_4:CO_2:O_2 = 1:0.8:0.2	CH_4:CO_2:O_2 = 1:0.7:0.3
CH_4	12.5	12.5	12.5
CO_2	11.25	10	8.75
O_2	1.25	2.5	3.75

Table 2 – The molar flow rates of reactant gases used for periodic operation.

Reactants	Flow rate (cm^3/min)		
	CH_4:CO_2: O_2 = 1:0.9:0.1	CH_4:CO_2: O_2 = 1:0.8:0.2	CH_4:CO_2: O_2 = 1:0.7:0.3
CH_4	25	25	25
CO_2	22.5	20	17.5
O_2	2.5	5	7.5

conditions were characterized by using various analytical methods including BET, SEM, XRD, and TPO. Additionally, their performance under periodic operation at different cycle periods and cycle splits were also determined and compared with those from the steady state operation.

2. Experimental method

2.1. *Reaction procedure*

A commercial-grade reforming catalyst, $Ni/SiO_2 \cdot MgO$, containing 55 wt% of nickel supplied from Japan was employed in this study. The catalyst was solid cylindrical extrudate with a diameter of 3 mm and a length of 3 mm. Silicon carbide supplied from Fluka with an average size of 40–100 mesh was used as a dilution material. The schematic diagram of the experimental setup, as shown in Fig. 1, consists of a gas feeding section, a fixed-bed reactor and an analytical section. High purity CH_4 (99.999 %), CO_2 (99.999%) and O_2 (99.99%) were used as the reactant gases. Argon was used for purging the system, and hydrogen was used for reducing catalyst before the experiment.

The reaction was carried out in a quartz tube fixed-bed reactor (internal diameter = 0.011 m, length = 0.5 m) heated by a temperature controlled electric oven. A thermocouple was placed in the furnace, at the level of the catalyst bed, to monitor temperature. Experiments were performed using $Ni/SiO_2 \cdot MgO$ catalyst (0.1314 g), diluted with silicon carbide (0.438 g). The catalyst was reduced in a hydrogen flow (30 cm^3/min) at 650 °C for 1 h before use. The reaction was conducted at atmospheric pressure. For steady state operation, all gas mixtures were continuously fed to the catalyst bed. The composition of exit gas effluent was analyzed by a TCD gas chromatograph (Shimadzu GC-8A, Japan) equipped with a Porapak-Q and Molecular Sieve 5A column. For periodic operation, the feeds were switched alternately between opening and closing by solenoid valves (Flon industry, Japan), which were controlled by on-off timers (Sibata BT-3). For a based condition with a cycle split of 0.5, CH_4 (25 cm^3/min) was switched to the catalyst bed for 10 min and then followed by a mixture of CO_2 and O_2 (total flow rate = 25 cm^3/min) for 10 min. Between the cracking/regeneration steps, the system was purged with argon for 10 min. The operation occurred repeatedly until the end of experiment. Tables 1 and 2 summarize the gas feed flow rates for steady-state operation and periodic operation, respectively. The composition in gas product of each cracking/regeneration step

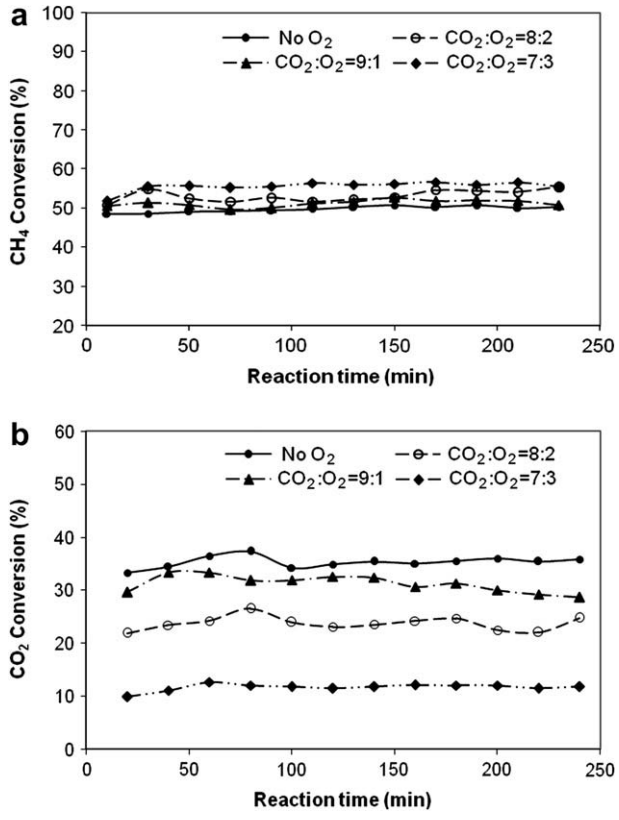

Fig. 2 – (a) Methane conversion and (b) carbon dioxide conversion under cracking/regeneration periodic operation at 650 °C with different feed oxygen contents.

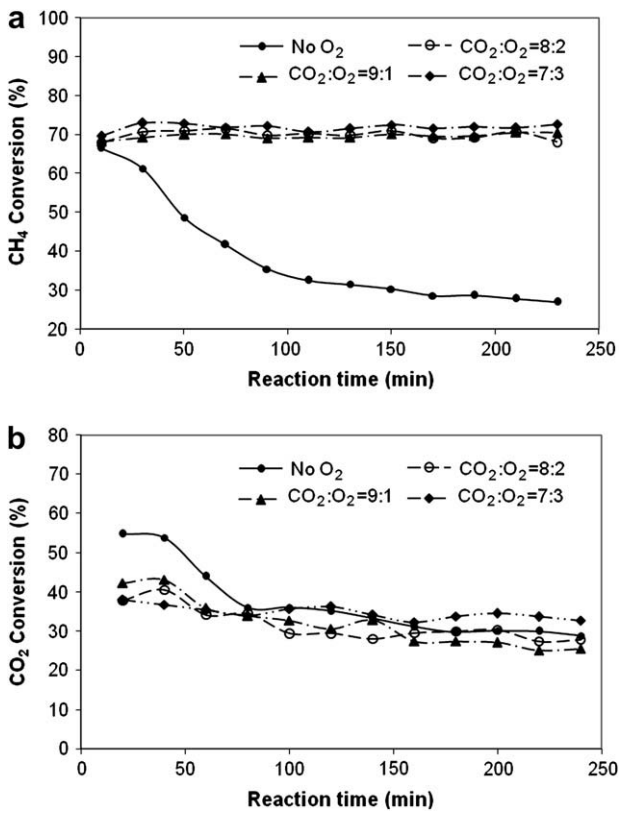

Fig. 3 – (a) Methane conversion and (b) carbon dioxide conversions under cracking/regeneration periodic operation at 750 °C with different feed oxygen contents.

was also analyzed by the GC-TCD. It should be noted that, additionally, the effects of cycle period (10, 20 and 40 min) and cycle split (0.25, 0.5 and 0.75) on catalytic performance of reaction were also investigated.

2.2. *Catalyst characterization*

In order to study the physical properties, both fresh and spent catalysts (after the reaction at 90, 100, 190 and 200 min) were characterized by several methods as follows:

2.2.1. *BET surface area measurement*

The total surface area, pore volume and pore size of catalysts were determined using a Micromeritrics model ASAP 2020. The sample cell packed with 0.3 g of sample was placed into the unit. After degassing step, N_2 physisorption was carried out for measuring the surface area and pore volume of catalyst.

2.2.2. *X-ray diffraction (XRD)*

The crystallinity and X-ray diffraction patterns of the fresh and spent catalysts were performed by an X-ray diffractometer, SIEMENS D5000, using Cu Kα radiation with Ni filter.

2.2.3. *Scanning electron microscopy (SEM)*

Scanning electron microscopy (SEM) was used to determine the catalyst granule morphology, using a JEOL JSM-35CF scanning electron microscope. The SEM was operated using the back scattering electron (BSE) mode at 15 kV.

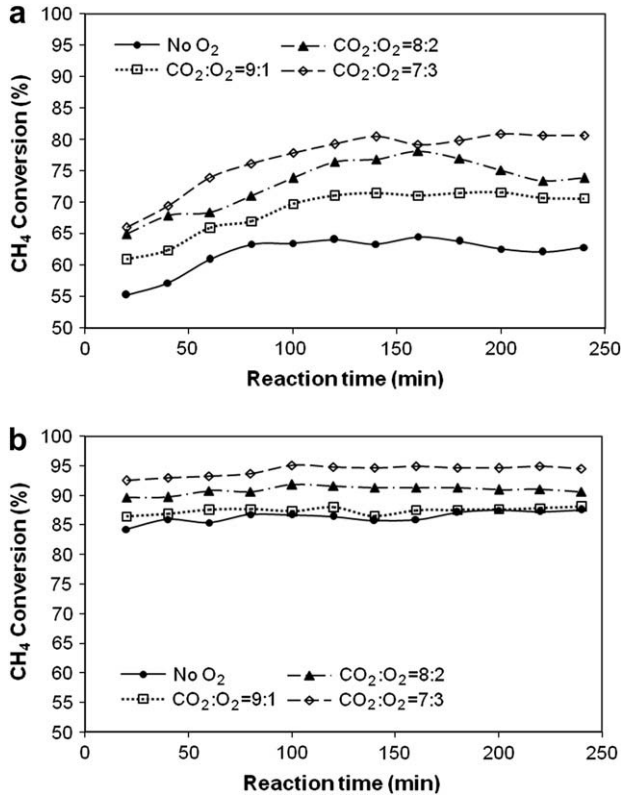

Fig. 4 – Methane conversions from combined carbon dioxide reforming and partial oxidation of methane under steady state operation with different oxygen contents at (a) 650 °C and (b) 750 °C.

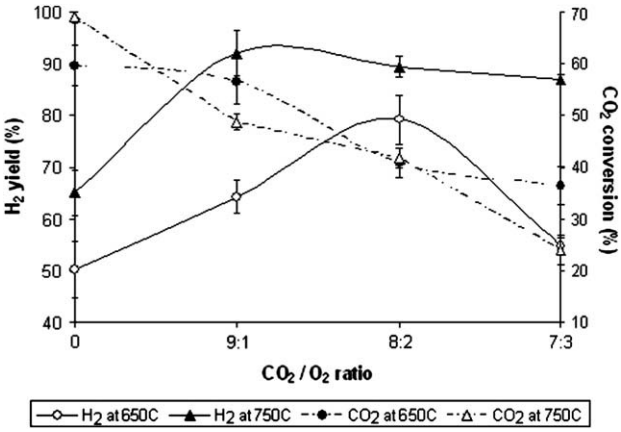

Fig. 5 – CO_2 conversions and hydrogen yields from combined carbon dioxide reforming and partial oxidation of methane under steady state operation at 650 and 750 °C with different oxygen contents.

2.2.4. *Temperature-programmed oxidation (TPO)*

Temperature-programmed oxidation was used to characterize the coke deposited on the catalysts. The operation was performed by using Micromeritrics Chemisorb 2750. Most amount of sample after the reaction was pre-treated in He (25 cm^3/min) at 250 °C for 1 h to eliminate moisture from the catalyst and cooled down to room temperature. Then 1 vol% O_2 in helium (15 cm^3/min) was switched into the sample while the system was heated at a rate of 10 °C/min to 1000 °C and the exit gas was detected by a TCD detector. The calculation of amount of CO_2 in the effluent gas was analyzed and reported by Chemisorp TPx software.

3. Results & discussion

3.1. *Catalytic reactivity toward the carbon dioxide reforming of methane in the presence of oxygen (steady-state vs. periodic operations)*

The catalytic reactivity in terms of activity and stability toward the CO_2 reforming of CH_4 in the presence of O_2 under steady

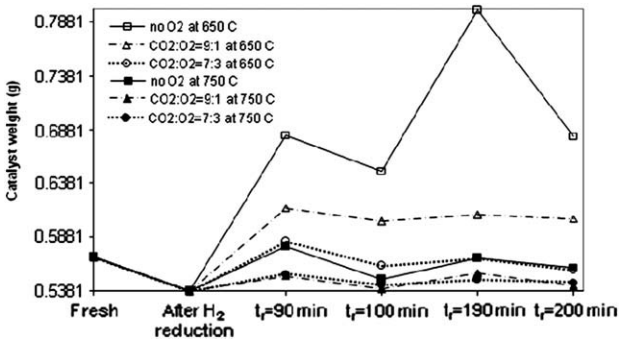

Fig. 6 – The effects of oxygen content and reaction temperature on change in catalyst weight at various reaction times of periodic operation.

Table 3 – BET surface areas of catalysts at different conditions.

Catalysts	Surface area (m^2/g)
Fresh	104.6
After reduction with H_2 at 650 °C 1 h	47.0
After calcination in air at 750 °C 3 h	34.7
After calcination and reduction with H_2 at 750 °C 1 h	20.4

Rxn.Temp.	Oxidant ratio	Operation	Reaction time			
			90 min	100 min	190 min	200 min
650 °C	no O_2	Periodic	66.9	60.5	76.6	65.7
	CO_2:O_2 = 9:1	Steady state	–	–	–	42.4
		Periodic	52.7	25.2	81.9	33.9
	CO_2:O_2 = 7:3	Steady state	–	–	–	16.5
		Periodic	31.8	27.1	47.2	14.5
750 °C	no O_2	Periodic	20.7	19.4	20.4	14.1
	CO_2:O_2 = 9:1	Steady state	–	–	–	36.0
		Periodic	10.1	5.3	22.3	6.4
	CO_2:O_2 = 7:3	Steady state	–	–	–	16.3
		Periodic	11.8	4.5	14.1	3.5

state and periodic conditions was studied at different CO_2/O_2 ratios (10/0, 9/1, 8/2 and 7/3) and two reaction temperatures (650 and 750 °C). For periodic operation, the reaction was started by alternately feeding CH_4 in the cracking step ($CH_4 \rightarrow C + H_2$) and combined CO_2 with O_2 in the regeneration step ($C + CO_2 \leftrightarrow 2CO$, $C + 1/2O_2 \rightarrow CO$, $CO + 1/2O_2 \rightarrow CO_2$). For steady state operation, the reaction was carried out by feeding CH_4, CO_2 and O_2 simultaneously. It should be noted that the average total flow rates of feeds for both operations were identical. The results of activities under periodic operation were shown in Figs. 2, 3 whereas those under steady state operation were shown in Figs. 4, 5.

As shown in Fig. 2 (a), at 650 °C under periodic operation, the O_2 addition (for all CO_2/O_2 ratios) slightly affects the catalytic reactivity by increasing the CH_4 conversion from about 49% to the maximum value of about 56%. It is noted that the catalyst stability seems to be unaffected by O_2 adding, as the CH_4 conversions were almost constant for at least 12 cracking/regeneration cycles either with or without O_2 feed. At 750 °C, the addition of O_2 showed greater impact on catalyst activity and stability. Significant decrease in CH_4 conversion was observed in the case without O_2 addition (Fig. 3 (a)), whereas no considerable deactivation was found when O_2 was co-fed with CO_2 in the regeneration step. After 12 cracking/regeneration cycles, the CH_4 conversion increased from 27% (without O_2 addition) to maximum 72% (O_2 addition with CO_2/O_2 ratio of 7/3). Thus, this result indicated that CO_2 alone is not appropriate to regenerate the catalyst for high temperature cracking/regeneration periodic operation due to the incomplete reaction of carbon deposited from the cracking of CH_4. The addition of O_2 during regeneration period could overcome this problem since it acted as a co-oxidant of CO_2 to accelerate the coke removal in the regeneration step. Considering the apparent CO_2 conversion, it decreased with increasing O_2 content from about 35% to the minimum value of 12% at 650 °C and from 29% to 25% at 750 °C as shown in Figs. 2 (b) and 3 (b), respectively. It is noted that an error analysis was checked for some experimental results. It was found that that the errors were within a range of ±5%.

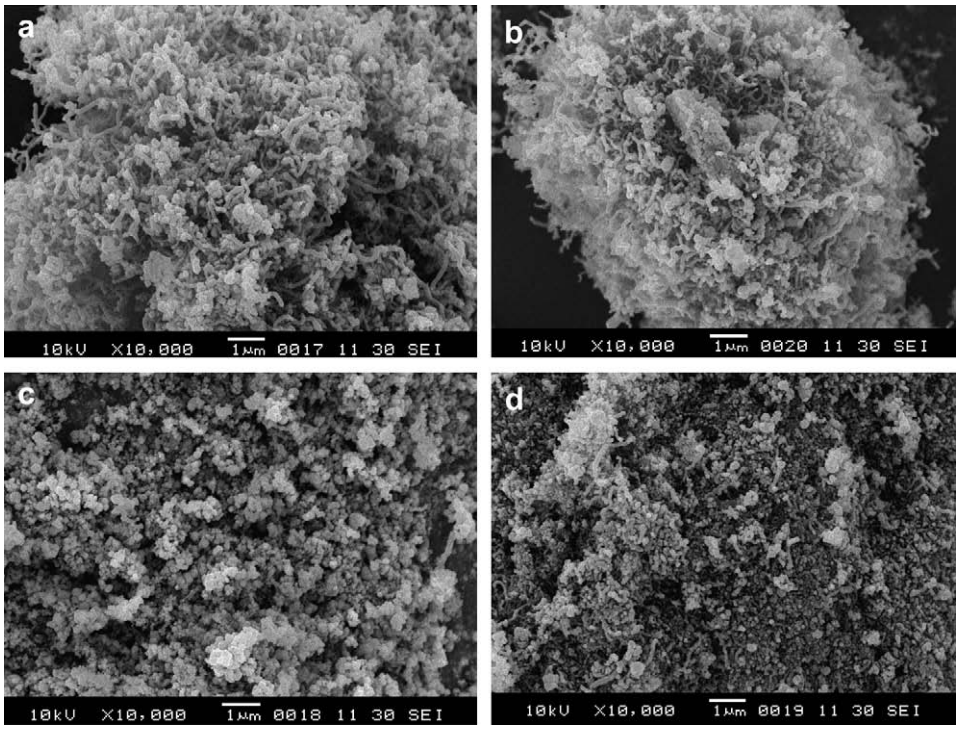

Fig. 7 – SEM micrographs of spent catalysts after exposure in the reaction for 190 minutes at 650 and 750 °C with different reactant ratios; (a) CO_2:O_2 = 9:1 at 650 °C, (b) CO_2:O_2 = 7:3 at 650 °C, (c) CO_2:O_2 = 9:1 at 750 °C and (d) CO_2:O_2 = 7:3 at 750 °C.

In the absence of O_2 in feed, CH_4 and CO_2 conversions in both temperatures of this study were corresponding well with our previous studies which were performed at a different feed flow rate to catalyst ratio [19,20]. Aiello et al. [18] investigated periodic operation of direct cracking of CH_4 reaction over Ni/SiO_2 and catalyst regeneration in steam atmosphere. At the operating temperature of 650 °C, CH_4 conversions ranged from 24% to 34% and slightly decreased during each cracking cycle. Monnerat et al. [21] studied CH_4 cracking over nickel gauze under periodic operation by regeneration with O_2. The operating temperatures were in a range of 410–550 °C. Hydrogen was produced efficiently at temperatures of 540–550 °C but hot spot temperature during the regeneration step occurred at temperatures higher than 500 °C. The suitable operating temperature of 500 °C for the system was suggested [21]. In the presence of O_2, the decrease in CO_2 conversion was due to the fact that O_2 is a stronger oxidizing agent than CO_2; moreover, C atom and CO produced could be oxidized by O_2 to CO_2. As for hydrogen yield, the selectivity of CH_4 to hydrogen production was considered to be equal to 100% as it is likely that the decomposition of CH_4 is the only reaction taking place in the cracking step which was previously proven in our study [19], thus hydrogen yield is equal to the CH_4 conversion in this operation.

Under steady state operation, the CH_4 conversion tended to increase with increasing O_2 content and reaction temperature. It increased from 62% to maximum 80% at 650 °C (with CO_2/O_2 ratio of 7/3) and reached 95% at 750 °C as shown in Fig. 4 (a) and (b), respectively. It should be noted that the improvement of CH_4 conversion was accompanied with the changing of CO_2 conversion and hydrogen yield as shown in Fig. 5. Similar to the periodic operation, the O_2 addition significantly reduced CO_2 conversion due to the partial consumption of CH_4 with added O_2 (partial oxidation reaction) and the possible oxidation of CO with added O_2 to CO_2. The O_2 addition also improved the hydrogen yield. By adding O_2 with CO_2/O_2 ratio of 8/2 at 650 °C and 9/1 at 750 °C, hydrogen yield increased from 50% to 79% and from 65% to 92%, respectively. It should be noted that the addition of higher O_2 content in the reaction caused slight decrease in hydrogen yield for both reaction temperatures. This could be affected by the occurrence of the complete combustion of CH_4 (Eq. (4)), resulting in the reduction of hydrogen yield. In addition, hydrogen product can directly react with O_2 to water (Eq. (5))

$$CH_4 + 2O_2 \rightarrow CO_2 + H_2O \quad (4)$$

$$2H_2 + O_2 \rightarrow 2H_2O \quad (5)$$

Comparison between periodic and steady state operations for combined CO_2 reforming and partial oxidation of CH_4 at reaction temperatures of 650 and 750 °C revealed that the periodic operation showed lower performance in term of CH_4 conversion than the steady state operation. Nevertheless, considering the benefit in term of separated product stream achievement, the periodic operation that combined CO_2 reforming and partial oxidation of CH_4 could be a great option for some specific applications.

3.2. *Characterization of spent catalysts*

In order to investigate the accumulated coke and understand the behavior of coke formation on surface of catalyst, the used catalysts after exposure in the reaction with different O_2 contents in each cracking/regeneration cycle under periodic and steady state operations were characterized by various techniques i.e. BET surface area measurement, SEM, XRD and TPO. All spent catalysts were exposed to the reactions at total reaction time of 200 min. The different CO_2/O_2 flow rate ratios (10/0, 9/1 and 7/3) and reaction temperatures (650 and 750 °C) were varied. Under periodic operation, the experiments were performed using a constant cycle time (τ) of 20 min and cycle split (s) of 0.5. Thus, reactants were fed alternately between CH_4 and combined CO_2 with O_2 every 10 min. Four values of reaction time at 90, 100, 190, and 200 min were considered. The reaction times of 90 and 190 min stand for the used catalyst after cracking step at the cycle number of 5 and 10 respectively, whereas the reaction

Table 4 – Coke amount obtained from TPO profiles of spent catalysts at different conditions.

Catalysts			Coke amount		
Rxn. Temp. (°C)	Oxidant ratio	Operation	Rxn. Time (min)	Oxidizing Temp. (°C)	Amount (mg)
650 °C	no O_2	Periodic	90	514.7	5.38
			100	510.1	5.30
			190	529.3	3.88
			200	511.5	4.81
	CO_2:O_2 = 9:1	Steady-state	200	519.2	4.74
		Periodic	90	518.6	2.54
			100	551.2	1.33
			190	520.4	5.15
			200	550.3	1.96
	CO_2:O_2 = 7:3	Steady-state	200	520.1	2.90
		Periodic	90	524.1	4.73
			100	551.5	3.54
			190	520.8	5.28
			200	546.7	2.88
750 °C	no O_2	Periodic	90	516.2	2.04
			100	538.5	5.30
			190	518.6	1.60
			200	530.4	1.43
	CO_2:O_2 = 9:1	Steady-state	200	498.4	2.14
		Periodic	90	503.8	1.02
			100	555.3	0.88
			190	504.2	3.64
			200	523.5	1.15
	CO_2:O_2 = 7:3	Steady-state	200	–	–
		Periodic	90	517.8	1.82
			100	546.1	0.85
			190	483.2	3.56
			200	540.4	0.93

times of 100 and 200 min stand for the used catalyst after regeneration step at the cycle number of 5 and 10 respectively. For steady state operation, a mixture of CH_4, CO_2 and O_2 was fed simultaneously and reaction time of 200 min was considered.

Fig. 6 shows the effects of O_2 content and reaction temperature on the changes in catalyst weight at various reaction times. After the catalyst was reduced with hydrogen to form an active metallic phase for the reforming reaction, the periodic operation was started. During the cracking step, the increase in catalyst weight by the coke formation on the catalyst surface was observed. While during the regeneration step, deposited coke was removed and its weight decreased. However, the change in catalyst weight decreased with increasing the number of cycle. The results also indicate that lower amount of coke was formed in the system at higher reaction temperature and O_2 content; similar tendency was also found under the steady state operation. These results are in good agreement with the observed results in Section 3.1 i.e. catalytic reactivity increased with increasing O_2 content and reaction temperature.

The BET surface area measurements of spent catalyst are summarized in Table 3. These results were corresponding to the results of catalyst weight; BET surface area increased during cracking step due to coke formation but decreased by coke oxidation during the regeneration step. At higher temperature, the lower of BET surface area was observed, indicating that accumulated coke is lessened because filamentous carbon can be removed easily at high temperature [16]. This result is in good agreement with previous study by Pholjaroen et al. [20] that there are 2 types of coke forming on the surface of catalyst at different temperatures. At low temperature, coke mostly formed in filamentous carbon that appears the growing length with higher surface area and accelerates the rate of carbon deposition. At high temperature, a lesser amount of total coke was obtained, however, most of them were encapsulating carbon that covers the catalyst surface and can block active sites of the reactions; the lower surface area was achieved. Importantly, the addition of O_2 as an efficient oxidizing agent can improve the stability of the reaction by accelerating coke removal.

BET surface area of the spent catalyst was found to be lower than that of the reduced catalyst. Ito et al. [22] explained that when the filamentous carbons having nickel cores on the growing top were oxidized during the regeneration step, the nickel cores fell on the surface and became inactive particles. Coalescence of inactive nickel cores on the bulk nickel surface to the larger size especially at high temperature caused the BET surface area to be decreased. Additionally, inactive nickel cores can suppress the active site for coke deposition without participation of active site for reforming reaction. It is noted that the O_2 addition into the regeneration step also affected the BET surface area of catalyst. At higher O_2 content, lower surface area was obtained due to higher coke removal. Additionally, the BET study of spent catalysts under the steady-

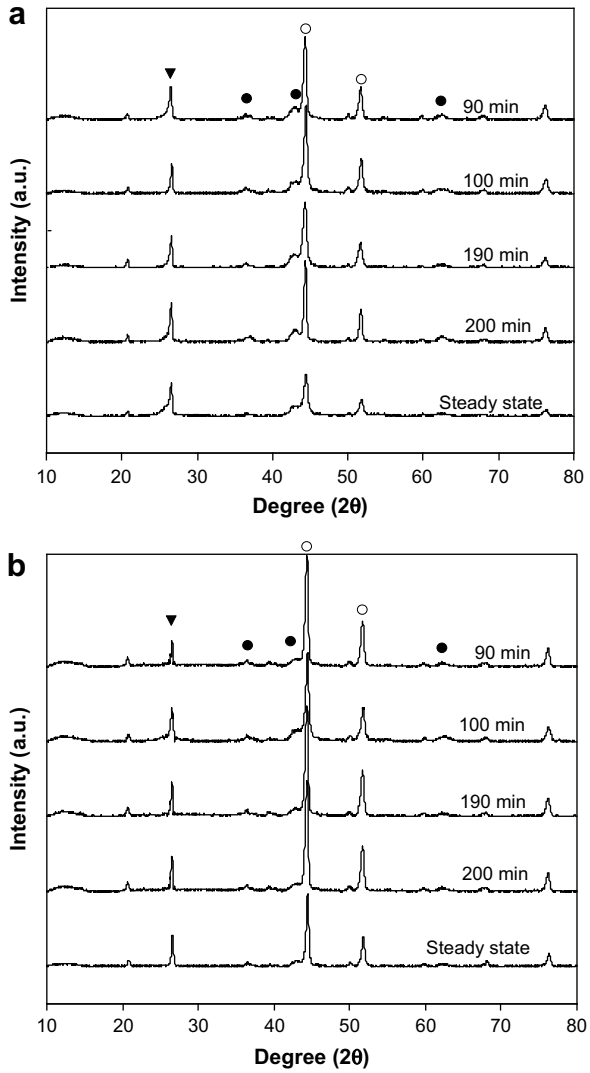

Fig. 8 – XRD patterns of spent catalysts after exposure in the reaction under periodic and steady state operations with CO_2:O_2 = 7:3; (a) at 650 °C and (b) at 750 °C (▼Coke, ○ Ni, and ● NiO).

Table 5 – The crystalline sizes of nickel on catalysts at different conditions.

Catalysts			d-spacing of nickel (nm)			
Fresh			4.83			
After calcination in air at 750 °C 3 h			25.45			
After calcination and reduction with H_2 at 750 °C 1 h			21.11			
Rxn.Temp.	Oxidant ratio	Operation	Rxn. time			
			90 min	100 min	190 min	200 min
650 °C	No O_2	Periodic	18.23	14.96	14.9	13.86
	CO_2:O_2 = 9:1	Steady state	–	–	–	15.67
		Periodic	14.76	16.23	14.93	17.34
	CO_2:O_2 = 7:3	Steady state	–	–	–	18.55
		Periodic	15.53	13.65	12.65	12.82
750 °C	No O_2	Periodic	26.88	28.25	20.9	27.92
	CO_2:O_2 = 9:1	Steady state	–	–	–	30.45
		Periodic	27.45	30.02	27.49	28.76
	CO_2:O_2 = 7:3	Steady state	–	–	–	26.84
		Periodic	30.51	27.34	26.47	28.84

Table 6 – The crystalline sizes of coke deposited on catalysts at different conditions.

Catalysts			d-spacing of coke (nm)			
Rxn.Temp.	Oxidant ratio	Operation	Rxn. time			
			90 min	100 min	190 min	200 min
650 °C	No O_2	Periodic	9.82	15.69	17.66	5.73
	CO_2:O_2 = 9:1	Steady state	–	–	–	14.39
		Periodic	17.43	20.83	19.53	15.6
	CO_2:O_2 = 7:3	Steady state	–	–	–	17.25
		Periodic	18.38	22.14	16.78	20.44
750 °C	No O_2	Periodic	35.75	39.34	27.36	26.1
	CO_2:O_2 = 9:1	Steady state	–	–	–	35.84
		Periodic	30.88	35.76	33.76	36.74
	CO_2:O_2 = 7:3	Steady state	–	–	–	39.64
		Periodic	37.55	39.85	36.94	38.34

state operation at different conditions was also measured; the results indicate similar trend as the periodic operation.

Scanning electron microscopy (SEM) technique was applied to observe the catalyst samples that were conducted under periodic operation at CO_2/O_2 flow rate ratios of 9/1 and 7/3 and reaction temperatures of 650 and 750 °C (Fig. 7 (a)–(d)). All samples were tested after exposure in the reaction for 190 min, which was the ending time of CH_4 cracking period. At low temperature, deposited cokes are in form of filamentous carbon structure. Contrary at high temperature, no visible filamentous carbon was observed. It was also found that with higher O_2 content employed, less amount of coke was seen. Temperature-programmed oxidation (TPO) technique was then applied to measure the certain amount of coke on catalyst; the calculated amounts of deposited coke on catalyst surface are given in Table 4. It can be seen that, in the presence of O_2 during the regeneration, the amounts of coke after cracking period tend to increase with increasing reaction time (e.g. comparing between 90 and 190 or 100 and 200 min). In contrast, when without O_2 addition during the regeneration, the amount of coke after cracking period was found to decrease with increasing reaction time; this could be due to the inactive cracking of CH_4 since carbon could not be removed effectively. This characterization results are well supported with the catalyst testing results in Figs. 2(a) and 3(a).

Spent catalysts were further studied by X-Ray diffraction (XRD). This technique was chosen to identify the crystal structure of Ni metallic and other metal forms on the catalysts. Fig. 8 shows the XRD patterns of the spent catalysts under periodic operation (after cracking and regeneration steps at 650 and 750 °C with CO_2:O_2 of 7:3); the results under steady state operation was also given for comparison. Under periodic operation, it was found that the presence of accumulated coke of graphitic nature on the catalyst surface was evident during the cracking step. After the regeneration step, the intensity of this peak was considerably lower due to the removal of carbon from the catalyst surface, whereas the metallic Ni peaks (detected at $2\theta = 44.5$, 51.8, and 76.4°) were unchanged. However, higher and sharper intensity peak of metallic Ni was found with increasing temperature and O_2 content in feed. XRD results also indicated that the intensity peak of coke was weaker and broader by increasing temperature and O_2 content. Tables 5 and 6 show the crystalline sizes of nickel and deposited coke, respectively, calculated by using Scherrer's equation for different conditions. It was found that at higher temperature, larger crystalline size of both nickel and coke were observed. These results were corresponding to those from BET surface area; larger crystalline size of particle induced to be lessened BET surface area.

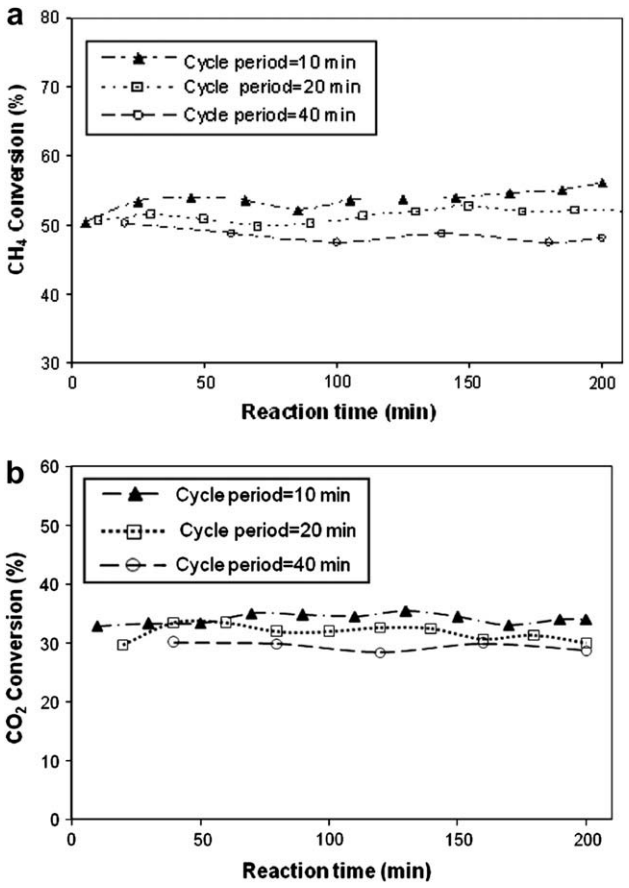

Fig. 9 – (a) Methane conversion and (b) CO_2 conversions comparison between periodic and steady state operation at different cycle periods.

Table 7 – The molar flow rates of reactant gases at various cycle splits.

Reactants	Flow rate (cm^3/min)		
	$S_{CH_4} = 0.25$	$S_{CH_4} = 0.5$	$S_{CH_4} = 0.75$
CH_4	50	25	16.67
CO_2	15.00	22.5	45
O_2	1.67	2.5	5

3.3. *Effects of cycle period and cycle split on reaction performance*

As the next step, performances of combined CO_2 reforming and partial oxidation of CH_4 under periodic operation were investigated using various cycle periods (τ) and cycle splits (s) (cycle split is defined as duration of cracking step to cycle period). All experiments were performed using CO_2/O_2 flow rate ratio of 9/1 at 650 °C. In order to investigate the effect of cycle period, the constant cycle split of 0.5 was conducted. According to our previous study [19], the cracking step was limited at 20 min for preventing complete deactivation of catalyst. Therefore, the cycle period was varied at 40 min (5 cycles), 20 min (10 cycles), and 10 min (20 cycles). The results were shown in Fig. 9 for (a) CH_4 conversion and (b) CO_2 conversion. It was found that their performances tend to decrease as the cycle period increased; CH_4 conversions and CO_2 conversions were slightly decreased from 55% to 47% and from 34% to 29% respectively, when the cycle period increased from 10 min to 40 min. This could be due to the higher coke deposition at the extended period.

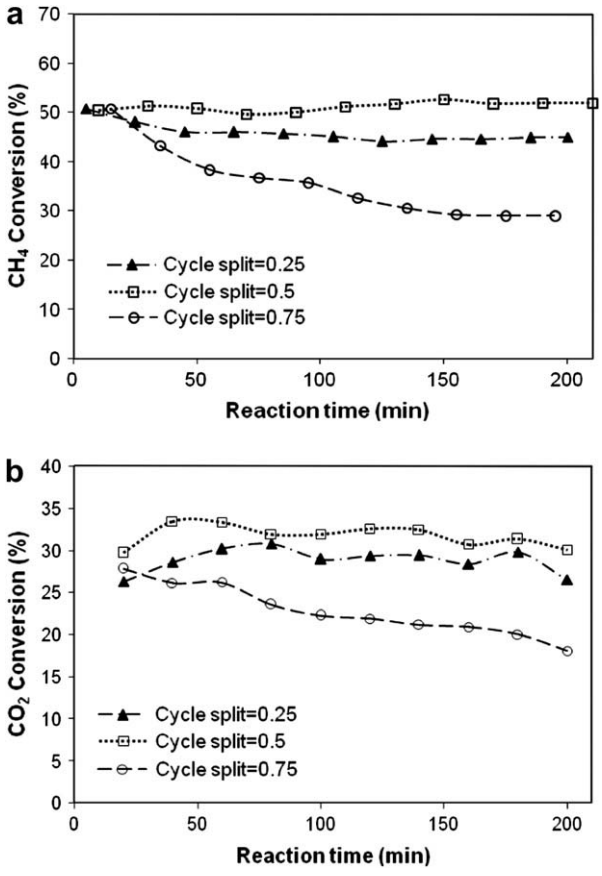

Fig. 10 – (a) Methane conversion and (b) CO_2 conversions under period operation at different cycle splits.

Another set of experiments were carried out at the constant cycle period of 20 min, three values of cycle split at 0.25, 0.5 and 0.75 were considered (the molar flow rates at various cycle splits were summarized in Table 7). The results in Fig. 10 show that, by decreasing the cycle split value from 0.5 to 0.25, both CH_4 and CO_2 conversions slightly decreased from 51% to 44% and from 29% to 26% respectively as a result of the shorter residence time during the CH_4 cracking, which caused the lower CH_4 conversion and carbon deposition. The decrease of CO_2 conversion could be due to the lower amount of carbon to be reacted with the oxidants and the higher effect of mass transfer resistance at low reactant flow rate. At the cycle split value of 0.75, CH_4 and CO_2 conversions were initially 50% and 27% respectively, however, the conversions later decreased rapidly to 29% and 18%, as shown in Fig. 10. This high deactivation could be due to the higher amount of coke accumulation and the incomplete re-oxidization of catalyst surface caused by the decrease in amount of O_2 and CO_2 adsorbed on the surface. This study indicated that the suitable split value was 0.5; corresponding to a symmetric period when the time of cracking is equal to the time of regeneration due to the same reaction rate of CH_4 cracking and coke oxidation.

4. Conclusion

- For periodic operation, the addition of oxygen during the regeneration (with the CO_2/O_2 ratio of 7/3) at 750 °C significantly improves the reaction performance in terms of catalyst stability and activity.
- For steady state operation, the catalytic performance of $Ni/SiO_2{\cdot}MgO$ toward the carbon dioxide reforming of methane in the presence of oxygen increased with increasing oxygen content and reaction temperature. However, the higher oxygen contents caused a slight decrease in hydrogen yield for both temperatures.
- Although it was revealed that the periodic operation shows lower performance in term of methane conversion than that from the steady state operation at the same condition, considering the benefit in term of separated product stream achievement, the periodic operation that combins carbon dioxide reforming and partial oxidation of methane could be a great option for some specific applications where pure hydrogen is required e.g. for proton-exchange membrane (PEM) fuel cell.

Acknowledgement

The support from the Thailand Research Fund and Commission on Higher Education is gratefully acknowledged.

REFERENCES

[1] Gadalla AM, Bower B. The role of catalyst support on the activity of nickel for reforming methane with CO_2. Chemical Engineering Science 1988;11:3049–62.

[2] Rostrup-Nielsen JR. Production of synthesis gas. Catalysis Today 1993;4:305–24.
[3] Edwards JH, Maitra AM. The chemistry of methane reforming with carbon dioxide and its current and potential applications. Fuel Processing Technology 1995;42:269–89.
[4] Inui T, Ichino K, Matsuoka I, Takeguchi T, Iwamoto S, Pu SB, et al. Ultra-rapid synthesis of syngas by the catalytic reforming of methane enhanced by in-situ heat supply through combustion. Korean Journal of Chemical Engineering 1997;14:441–4.
[5] Chen X, Honda K, Zhang Z-G. CO_2–CH_4 reforming over NiO/γ-Al_2O_3 in fixed-bed/fluidized-bed switching mode. Catalysis Today 2004;93–95:87–93.
[6] Diaz K, Garcia V, Matos J. Activated carbon supported Ni–Ca: influence of reaction parameters on activity and stability of catalyst on methane reformation. Fuel 2007;86:1337–44.
[7] Jing Q, Lou H, Fei J, Hou Z, Zheng X. Syngas production from reforming of methane with CO_2 and O_2 over Ni/SrO–SiO_2 catalysts in a fluidized bed reactor. International Journal of Hydrogen Energy 2004;29:1245–51.
[8] Pompeo F, Nichio NN, Ferretti OA, Resasco D. Study of Ni catalysts on different supports to obtain synthesis gas. International Journal of Hydrogen Energy 2005;30:1399–405.
[9] Xu S, Wang XL. Highly active and coking resistant Ni/CeO_2–ZrO_2 catalyst for partial oxidation of methane. Fuel 2005;84:563–7.
[10] Xu S, Yan X, Wang X. Catalytic performances of NiO–CeO_2 for the reforming of methane with CO_2 and O_2. Fuel 2006;85:2243–7.
[11] Guo J, Hou Z, Gao J, Zheng X. Syngas production via combined oxy-CO_2 reforming of methane over Gd_2O_3-modified Ni/SiO_2 catalysts in a fluidized-bed reactor. Fuel 2008;87:1348–54.
[12] Pompeo F, Gazzoli D, Nichio NN. Stability improvements of Ni/α-Al_2O_3 catalysts to obtain hydrogen from methane reforming. International Journal of Hydrogen Energy 2009;34:2260–8.
[13] Therdthianwong S, Therdthianwong A, Siangchin C, Yongprapat S. Synthesis gas production from dry reforming of methane over Ni/Al_2O_3 stabilized by ZrO_2. International Journal of Hydrogen Energy 2008;33:991–9.
[14] Nimwattanakul W, Luengnaruemitchai A, Jitkarnka S. Potential of Ni supported on clinoptilolite catalysts for carbon dioxide reforming of methane. International Journal of Hydrogen Energy 2006;31:93–100.
[15] Kim MH, Lee EK, Jun JH, Han GY, Kong SJ, Lee BK, et al. Hydrogen production by catalytic decomposition of methane over activated carbons: deactivation study. Korean Journal of Chemical Engineering 2003;20:835–9.
[16] Takano A, Tagawa T, Goto S. Carbon deposition on supported nickel catalysts for carbon dioxide reforming of methane. Journal of the Japan Petroleum Institute 1996;39:144–50.
[17] Zhang T, Amiridis MD. Hydrogen production via the direct cracking of methane over silica-supported nickel catalysts. Applied Catalysis A-General 1998;167:161–72.
[18] Aiello R, Fiscus JE, Loye H-C, Amiridis MD. Hydrogen production via the direct cracking of methane over Ni/SiO_2: catalyst deactivation and regeneration. Applied Catalysis A-General 2000;192:227–34.
[19] Promaros E, Assabumrungrat S, Laosiripojana N, Praserthdam P, Tagawa T, Goto S. Carbon dioxide reforming of methane under periodic operation. Korean Journal of Chemical Engineering 2007;24:44–50.
[20] Pholjaroen B, Assabumrungrat S, Laosiripojana N, Praserthdam P. Reactivity of Ni/SiO2·MgO toward carbon dioxide reforming of methane under steady state and periodic operations. Journal of Industrial and Engineering Chemistry, in press.
[21] Monnerat B, Kiwi-Minsker L, Renken A. Hydrogen production by catalytic cracking of methane over nickel gauze under periodic reactor operation. Chemical Engineering Science 2001;56:633–9.
[22] Ito M, Tagawa T, Goto S. Suppression of carbonaceous depositions on nickel catalyst for the carbon dioxide reforming of methane. Applied Catalysis A-General 1999;177:15–23.

ภาคผนวก 7

INTERNATIONAL JOURNAL OF HYDROGEN ENERGY 34 (2009) 6415–6424

Available at www.sciencedirect.com

ScienceDirect

journal homepage: www.elsevier.com/locate/he

Effect of operating conditions and gas flow patterns on the system performances of IIR-SOFC fueled by methanol

P. Dokamaingam[a], S. Assabumrungrat[b], A. Soottitantawat[b], N. Laosiripojana[a,*]

[a]The Joint Graduate School of Energy and Environment, King Mongkut's University of Technology Thonburi, Bangkok 10140, Thailand
[b]Department of Chemical Engineering, Faculty of Engineering, Chulalongkorn University, Bangkok 10330, Thailand

ARTICLE INFO

Article history:
Received 30 March 2009
Received in revised form
17 May 2009
Accepted 23 May 2009
Available online 24 June 2009

Keywords:
Indirect internal reforming
Solid oxide fuel cell
Methanol

ABSTRACT

Mathematical models of an indirect internal reforming solid oxide fuel cells (IIR-SOFC) fueled by methanol were developed to analyze the thermal coupling of the internal endothermic steam reforming with exothermic electrochemical reactions and predict the system performance. The simulations indicated that IIR-SOFC fueled by methanol can be well performed as autothermal operation, although slight temperature gradient occurred at the entrance of the reformer chamber. Sensitivity analysis of five important parameters (i.e. operating voltage, reforming catalyst reactivity, inlet steam to carbon ratio, operating pressure and flow direction) was then performed. The increase of operating voltage lowered the average temperature along the reformer chamber and improved the electrical efficiency, but it oppositely reduced the average current density. Greater temperature profile along the system can be obtained by applying the catalyst with lower reforming reactivity; nevertheless, the current density and electrical efficiency slightly decreased. By using high inlet steam to carbon ratio, the cooling spot at the entrance of the reformer can be reduced but both current density and electrical efficiency were decreased. Lastly, with increasing operating pressure, the system efficiency increased and the temperature dropping at the reformer chamber was minimized.

It was also found that IIR-SOFC with co-flow pattern (co-flow of air and fuel streams through fuel cell) provides higher voltage and smoother temperature gradient along the system compared to that with counter-flow pattern due to the better matching between the heat supplied from the electrochemical reaction and the heat required for the steam reforming reaction. Hence, the performance of IIR-SOFC fueled by methanol can be maximized by applying co-flow pattern and operated with high operating pressure.

1. Introduction

Solid Oxide Fuel Cell (SOFC) is an electrochemical device typically fueled by hydrogen-rich gas and operated at high temperature (973–1373 K). It offers several advantages e.g. the ability to use CO (along with H_2) as fuel and the high level of exhaust heat which can be efficiently utilized in combined heat and power and combined cycle gas turbine applications [1,2]. Importantly, due to the high operating temperature of SOFC, hydrocarbon fuels (e.g. methane) could be applied as

* Corresponding author.
E-mail address: navadol_l@jgsee.kmutt.ac.th (N. Laosiripojana).
0360-3199/$ – see front matter © 2009 International Association for Hydrogen Energy. Published by Elsevier Ltd. All rights reserved.
doi:10.1016/j.ijhydene.2009.05.105

the primary fuels when it is operated as internal reforming (IR-SOFC). This operation is referred to as the utilization of heat generated from the exothermic electrochemical reaction to the endothermic (steam) reforming of hydrocarbons [3–5]. Theoretically, there are 2 main approaches for IR-SOFC i.e. direct internal reforming (DIR-SOFC) and indirect internal reforming (IIR-SOFC). For DIR-SOFC approach, along with the electrochemical reaction, the reforming reaction occurred simultaneously at the anode side of SOFC. Thus, high heat transfer rate can be achieved from this operation, nevertheless, anode material must be optimized for both reactions and could be easily poisoned by carbon deposition from the reforming of hydrocarbons. As for IIR-SOFC, the endothermic reforming reaction takes place at reformer, which is in close thermal contact with the anode side of SOFC where exothermic electrochemical reaction occurs. IIR-SOFC offers advantages in terms of eliminating the requirement of separate fuel reformer, providing good heat transfer between reformer and fuel cell, and preventing anode material from carbon deposition. However, the main drawback of IIR-SOFC is possible mismatch between rates of endothermic and exothermic reactions, which leads to significant local temperature reduction particularly near the entrance of reformer and consequently results in mechanical failure due to thermal induced stresses [3–5]. Hence, IIR-SOFC generally requires intensive coupling operation of both reforming and SOFC sections.

Focusing on the primary fuels for IR-SOFC, several hydrocarbons e.g. methane, methanol, or ethanol can theoretically be applied since these hydrocarbons can be efficiently reformed to H_2 and CO at SOFC operating temperature (700–1100 °C). Among them, methanol is one of an interesting candidate due to its ready availability, high-specific energy, sulfur free and storage transportation convenience [5,6]; moreover, it can be produced from both chemical and biological processes. Thus, methanol was selected as the primary fuel in this study. Theoretically, according to the steam reforming of methanol, hydrogen can be produced from three reactions [6] i.e. methanol decomposition (1), methanol steam reforming (2) and Water-Gas Shift (WGS) (3) reactions.

$$CH_3OH \leftrightarrow CO + 2H_2 \quad (1)$$

$$CH_3OH + H_2O \leftrightarrow CO_2 + 3H_2 \quad (2)$$

$$CO + H_2O \leftrightarrow CO_2 + H_2 \quad (3)$$

Previously, several works on the kinetic models and the rate expressions of methanol steam reforming have been reported [7–11]. Peppy et al. [7] proposed the kinetic rate expressions of methanol steam reforming along with WGS and methanol decomposition reactions based on Langmuir–Hinshelwood approach. Recently, Choi et al. [9] proposed more simplified methanol steam reforming rate expressions with three more involved reactions, which are DME formation (4), formaldehyde formation (5) and methane formation (6) reactions. They indicated that these rate equations were reliable to predict the methanol steam reforming behavior, thus their equations were applied in the present work.

$$2CH_3OH + H_2O \rightarrow CH_3CH_3 + H_2O \quad (4)$$

$$2CH_3OH \rightarrow CH_3OCHO + 2H_2 \quad (5)$$

$$CH_3OCHO \rightarrow CO_2 \quad (6)$$

In this study, a set of mathematical modeling was developed in order to predict the behaviors (in terms of cell performance and temperature gradient along the cell) of tubular IIR-SOFC fueled by methanol. The model was developed by using bvp4c routine in MATLAB program. This routine is generally applied for solving the boundary condition equation with finite element method. Number of mesh in each investigation was optimized between accuracy of results and time for calculation, (relative error tolerance is 1e-5). The effects of operating conditions (i.e. inlet fuel temperature, operating voltage, catalytic reforming reactivity, inlet steam to methanol ratio, operating pressure, and gas flow pattern) on cell performance and temperature profile along each section of IIR-SOFC system i.e. reformer channel, fuel channel, and air channel were determined. From this study, the suitable operating conditions of IIR-SOFC system fueled by methanol were identified.

2. Mathematical models

2.1. Model geometry

Schematic diagram of tubular-designed IIR-SOFC applied in the present work is shown in Fig. 1. According to this configuration, methanol and steam are converted to hydrogen-rich gas at the internal catalytic packed-bed reformer before being introduced to the fuel channel of tubular SOFC. Simultaneously, air is fed with the opposite flow direction through the air channel. It is noted that all dimensions and physical properties of the SOFC system in the present work, which are summarized in Table 1, are based on previous report from literature [4].

It should be noted that the effect of gas (i.e. fuel and air) flow directions on the system performance was also

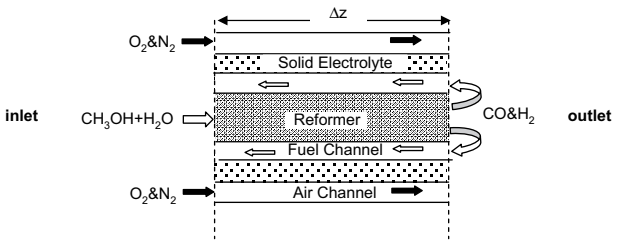

Fig. 1 – Schematic design of tubular-designed IIR-SOFC with counter-flow configuration.

Table 1 – Important parameter values of IIR-SOFC system studied in this work.

Parameter	Value	Parameter	Value
r_r	2.26×10^{-3} m	r_f	3.19×10^{-3} m
r_{ss}	4.09×10^{-3} m	r_a	4.67×10^{-3} m
$\varepsilon_1,\varepsilon_2$	0.9	R_{ohm}	3×10^{-5} Ω/m^2
α_R,h_f,h_a	0.1 kJ/m s K	λ_{ss}	2×10^{-3} kJ/m s K

considered. As shown in Fig. 1, the air flow is counter-flowed to the fuel flow in the fuel channel of SOFC, thus it is called ''counter-flow'' configuration. Alternatively, the fuel and air streams can also be flowed in the same direction, so called ''co-flow'' configuration. There are two possible configurations for co-flow operation i.e. ''conventional co-flow'' and ''alternative co-flow'' operations as shown in Fig. 2(a) and (b). For both conventional and alternative co-flow operations, the fuel and air streams are flowed in the same direction; the different is that for the alternative co-flow operation the reforming gas of the internal reformer is fed back to the other side of the fuel channel via an external insulation channel. The effect of these flow patterns on the temperature profiles along the system and cell performance was identified.

2.2. Model assumptions

The model was developed as the smallest single unit cell taking into account the effect of temperature on gas distribution, reactant conversion, and charge transfer. Two main sets of equations i.e. for the steam reformer, and for SOFC stack – including electrodes and solid electrolyte were applied to predict the concentration and temperature gradients along the system. The developed models were based on the following assumptions.

- Each section is considered as non-isothermal steady-state conditions.
- Ideal gas behavior is applied for all gas components.
- Diffusion in gas phase and pressure drop in SOFC stack and reformer are neglected.
- Operating cell potential is constant along the cell coordinate.
- Fuel utilization is fixed constant at 80% along the cell coordinate.

2.3. Reforming model

One-dimensional steam reformer model was developed to investigate the temperature and the concentration profiles along the internal reformer in the present work. Importantly, the gas components in the reformer were kinetically controlled by the rate of methanol steam reforming. As mentioned earlier, methanol steam reforming reaction in the present work was simulated based on the reaction pathways with six rate expressions proposed by Choi et al. [9] (details of these rate expressions with all related parameters are given in Tables 2 and 3). Since the internal reformer was adjacent to the solid stack, energy flux was accounted from heat convection in the fuel flow along the reformer, heat conduction between the fuel channel and the reformer, and the radiation from the solid stack to the reformer. The temperature profile could be predicted by Eq. (7), whereas the mass flux along the reformer was determined by Eq. (8).

$$\sum_i F_i C_{p,i} \frac{dT_r}{dz} - \alpha_R (A_r/V_f)\,(T_r - T_f) + \sum_j \Delta H_j R_j - \frac{(A_r/V_{ss})\,(T_r^4 - T_{ss}^4)}{1/\varepsilon_1 + A_r/A_f((1/\varepsilon_2) - 1)} = 0 \quad (7)$$

$$\frac{-dF_i}{dz} + \rho_B A_r \sum \nu_i R_i = 0 \quad (8)$$

Boundary conditions: $z = 0,\ F_i = F_i^o,\ T_r = T^o$

where i and j stand for components and reactions involved in the system. As methanol steam reforming was selected for studying in this work.

2.4. Solid oxide fuel cell model

A steady-state one-dimensional model of SOFC was developed. It composes of the models for fuel and air channels as well as for the electrochemical active tri-layer region represented by the anode, electrolyte, and cathode. The electrochemical rate is corresponded to amount of the electric current that is drawn according to Faraday's law (Eq. (9)), whereas the conversions of fuel and air stream are determined by Eqs. (10) and (11), respectively.

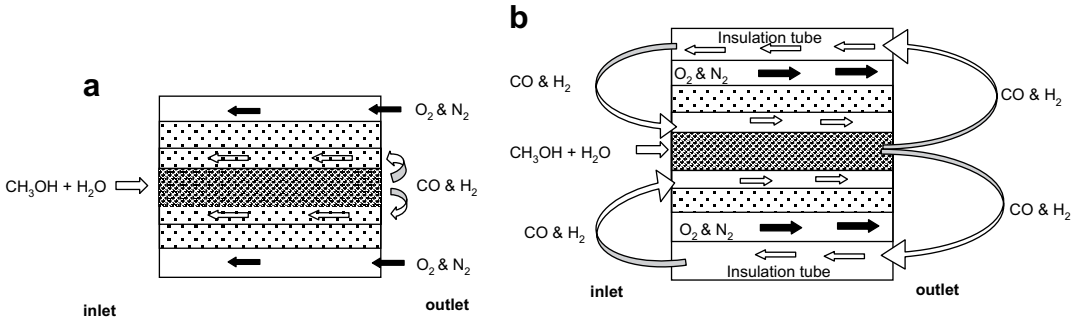

Fig. 2 – IIR-SOFC with (a) conventional co-flow and (b) alternative co-flow configurations.

Table 2 – Involved reactions and their rate expressions for methanol steam reforming reaction [9].

Reaction	Formula	Rate law
(1) Methanol decomposition	$CH_3OH \leftrightarrow CO + 2H_2$	$-r_1 = k_1(P_{CH_3OH} - K_1^{-1}P_{H_2}P_{CO})$
(2) DME formation	$2CH_3OH \rightarrow CH_3OCH_3 + H_2O$	$-r_2 = k_2(P_{CH_3OH})^2$
(3) WGS reaction	$CO + H_3O \leftrightarrow CO_2 + H_2$	$-r_3 = k_3(P_{CO}P_{H_2O} - K_3^{-1}P_{H_2}P_{CO_2})$
(4) MF formation	$2CH_3OH \rightarrow CH_3OCHO + 2H_2$	$-r_4 = k_4(P_{CH_3OH})^2$
(5) Methane formation	$CH_3OCHO \rightarrow CO_2 + CH_4$	$-r_5 = k_5P_{MF}$
(6) Methanol steam reforming	$CH_3OH + H_2O \leftrightarrow CO_2 + 3H_4$	$-r_6 = k_6(P_{CH_3OH}P_{H_2O})$

$$R_{k,elec} = j/2F \tag{9}$$

$$\frac{-d}{dz}\left(\frac{F_i}{A_f}\right) + \sum \nu_i R_{k,elec}(A_{act}/V_f) = 0 \tag{10}$$

$$\frac{-d}{dz}\left(\frac{F_i}{A_a}\right) + \sum \nu_i R_{k,elec}(A_{act}/V_a) = 0 \tag{11}$$

As for the thermal flux in each channel, due to the thermal contact between the internal reformer and the SOFC stack, the thermal flux in the fuel channel was affected by the convective heat transfer from the fuel flowed through the channel and the conductive heat transfer between the reformer and fuel channels, whereas the thermal flux at the air channel was influenced by the convective heat transfer of air flowed and the conductive heat transfer between the air channel and SOFC solid stacks. It should be noted that, in the present work, the outer layer of air channel was concerned as adiabatic. The thermal behaviors of the fuel and air channels can be calculated from Eqs. (12) and (13), respectively.

$$\text{Fuel channel: } \sum_i F_i C_{p_i}\frac{dT_f}{dz} - \alpha_R(A_r/V_f)\,(T_r - T_f) - h_f(A_f/V_f)\,(T_s - T_f) = 0 \tag{12}$$

$$\text{Boundary condition: } z = L,\ T_f = T_r$$

$$\text{Air channel: } \sum F_i C_{p_i}\frac{dT_a}{dz} - h_a(A_a/V_a)\,(T_s - T_a) = 0 \tag{13}$$

In the part of solid electrolyte, the effect of electrochemical reaction at the active tri-layer located between the fuel and the air channel was considered. The thermal flux was calculated by taking into account the conductive heat transfer from both channels and also radiation from the reformer; it is noted that several literatures suggested that the radiation heat transfer is one major influence for the non-isothermal SOFC simulation [12,13]. Importantly, the heat is also generated from the electrochemical reaction. Thus, the overall thermal flux for solid electrolyte can be determined by Eq. (14):

$$\lambda_s\frac{d^2T_s}{dz^2} - h_f(A_f/V_s)\,(T_s - T_f) - h_a(A_a/V_s)\,(T_s - T_a) - \frac{\sigma(A_r/V_s)(T_r^4 - T_s^4)}{1/\varepsilon_1 + A_r/A_f((1/\varepsilon_2) - 1)} = 0 + \Delta H_k R_k(A_{act}/V_s) + jE(A_{act}/V_s) \tag{14}$$

$$\text{Boundary condition: } z = 0,\ \frac{dT_s}{dz} = 0;\ \ z = L,\ \frac{dT_s}{dz} = 0$$

According to the electrochemical model for SOFC, the theoretical and actual voltage can be calculated from Eqs. (15) and (16). It is noted that the actual potential is always lower than theoretical value due to the occurring activation, concentration and ohmic overpotentials.

$$\text{Theoretical voltage: } E_{H_2}^{OCP} = E_{H_2}^{o} - RT_f/2F\ln\left(p_{H_2}p_{O_2}^{1/2}/p_{H_2O}\right) \tag{15}$$

$$\text{Operating potential: } E = E_{H_2}^{OCP} - \left(R_{ohm}j + R_{A,H_2}j_{H_2} + R_c j\right) \tag{16}$$

Activation loss is the activation barrier of electrochemical reaction at electrode. This overpotential was here determined using Butler–Volmer equation [14] since several literatures suggested that this equation is suitable to explain the activation behavior with insignificant error [15]. As for the concentration overpotential, it occurs due to the resistance of gas diffusion through the porous media. Generally, gas diffusion behavior can be predicted by three mathematical models i.e. Fick's model, Dusty gas model (DGM), and Stefan–Maxwell models [16]; the DGM was chosen in the present work. Importantly, Achenbach [17] proposed that the activation and concentration polarizations, taking place at the electrode/electrolyte interface, were dependent on the reactivity of reactants, the properties of SOFC materials and the electric resistance polarizations at the electrode. Hence, three overpotential correlations were established to simplify the model calculation; these correlations were also accounted in the present work, as expressed in Eqs. (17)–(19).

$$\text{Anode polarization: } 1/R_{A,H_2} = RT_f/2Fk_{A,H_2}\left(p_{H_2}/p^o\right)^m \exp - E_A/RT_f \tag{17}$$

$$\text{Anode polarization: } 1/R_{A,CO} = RT_f/2Fk_{A,CO}\left(p_{CO}/p^o\right)^m \exp - E_A/RT_f \tag{18}$$

Table 3 – Activation energy and frequency factors for methanol reforming reaction [9].

Reaction	E_a (kJ/mol)	k_i (mol/gcat. s. atm)
(1) Methanol decomposition	91.8	5854
(2) DME formation	88.9	125
(3) WGS reaction	43.7	17.973
(4) MF formation	82.2	1650
(5) Methane formation	45.6	1.174
(6) Methanol steam reforming	2670	70358

Cathode polarization: $1/R_c = RT_a/4Fk_C\left(p_{O_2}/p^o\right)^m \exp -E_C/RT_a$ (19)

As for the ohmic overpotential, it occurs from the ion transport across the cell, which mainly depends on ionic conductivity of SOFC material. By applying ohm's law, the relation of ohmic overpotential and material resistivity can be determined. Considering all polarizations, the cell performance was determined in terms of the average current density and system efficiency. It is noted that the anodic current was calculated from both H_2 and CO conversion rates, whereas the system efficiency, η_{elec}, was defined as a ratio between energy output from generated electricity and energy input into the reformer. The output energy was calculated from power density (P), whereas the input energy was determined from the energies of all input fluids, Eq. (20).

$$\eta_{elec} = \frac{PA_{act}}{\sum y_i^{in} LHV_{i,1173\ K}} \quad (20)$$

where A_{act} is the activation area (m^2), y_i^{in} is the mole fraction of the inlet fluid, and LHV is lower heating value at 1173 K.

3. Results and discussion

3.1. *Modeling of IIR-SOFC as base case*

The model of IIR-SOFC fueled by methanol was firstly simulated at 1173 K and 1 bar. The inlet fuel (methanol and steam) with steam to carbon ratio of 2 was fed to the internal reformer, while SOFC load voltage was constant at 0.7 V. Table 1 presents all related parameters of IIR-SOFC system applied in the present work (i.e. mass and heat transfer coefficients, thermal conductivities and SOFC physical properties); as reported by Aguiar et al. [4]. Under these conditions, characteristic results of this IIR-SOFC system i.e. methanol conversion, product gas distribution and temperature gradient along internal reformer and SOFC channels (both fuel and air channels) were determined as shown in Figs. 3 and 4.

Fig. 3 presents the profiles of methanol, hydrogen, carbon monoxide, and carbon dioxide mole fraction in reformer and fuel channel of SOFC. It can be seen that, due to the high reforming reactivity, methanol was completely consumed at the first one-fourth of the reformer chamber; therefore, hydrogen and carbon monoxide mole fractions increased rapidly in this region. It is noted that insignificant amount of methane from the decomposition of methanol was also observed at the first half of the reformer. At the outlet of the reformer, the product gas flows backward into fuel channel of SOFC where H_2 and CO are electrochemically converted to H_2O and CO_2. Under these conditions, the average current density and fuel efficiency were 2891.78 A m^{-2} and 32.48%, respectively. It is noted that, based on the size of cell stack and operating conditions studied, the values of current density observed in the present work are in the same range as the current densities that were previously reported [17–20].

Fig. 4 shows the temperature profiles of reformer, fuel and air channels for this IIR-SOFC system. It can be seen that the heat generated from fuel cell side is sufficient for internal reforming operation; nevertheless, a noticeable temperature gradient associated with indirect internal reforming operation was also observed (as also reported by several previous researchers [4,12]). The reformer temperature decreased from 1173 K to the lowest 1148 K at the first half of the reformer length; and this local cooling may affect the cell performance as well as the ceramic components of SOFC. It is noted that the temperature distribution is mainly corresponded to the level of methanol conversion along the reformer. At the entrance of the reformer where the conversion of methanol is extremely high, large amount of heat is required for endothermic steam reforming reaction; thus the cooling effect occurs. Oppositely, when methanol is converted along the length of the reformer, the required heat is relatively lower than the generated heat from electrochemical reaction; thus the rising in temperature profile is observed. Importantly, significant temperature difference along the reformer could affect several properties of stack material i.e. thermal expression and electrical resistance as well as damage the ceramic components of SOFC.

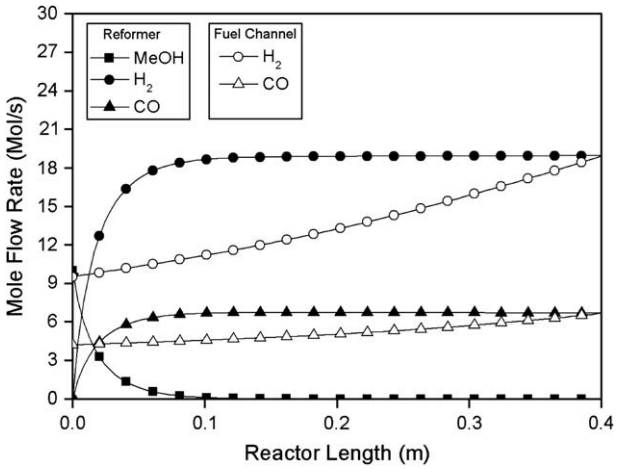

Fig. 3 – Concentration profiles in the reformer and fuel channels of IIR-SOFC (at base case condition).

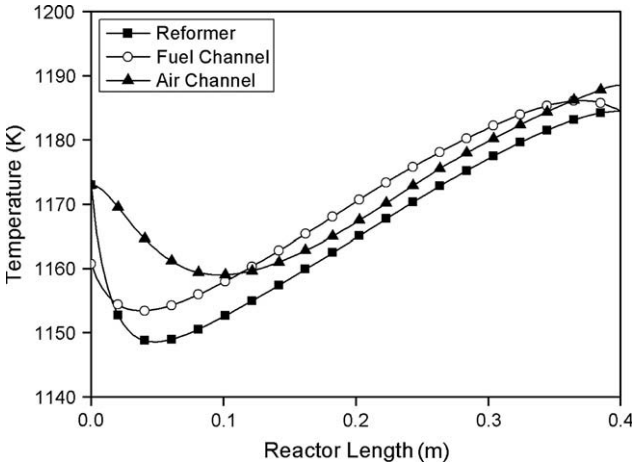

Fig. 4 – Temperature gradients in the reformer and fuel channels of IIR-SOFC (at base case condition).

Hence, as the major aim of this work, several operating conditions i.e. operating voltage, catalytic reforming reactivity, inlet steam to methanol ratio, operating pressure and gas flow pattern were varied in order to minimize this temperature gradient as well as maximize the outputs (i.e. current density and fuel efficiency) from this SOFC system.

3.2. *Effect of operating voltage*

The effect of operating voltage on the system performance was investigated by varying the operating voltage from 0.6 V to 0.8 V. Fig. 5 shows the temperature distribution in the reformer chamber at different operating voltages; it can be seen that the increase of operating voltage reduced the average temperature along the length of reformer and the temperature at the exit of the reformer was relatively lower than that operated at low operating voltage. The decreasing of average temperature leads to the higher ohmic loss, which eventually results in lower current density generated and less electrical efficiency achieved, as shown in Fig. 6 (a) and (b). In detail, when the operating voltage increased from 0.6 V to 0.8 V, the efficiency appeared to increase from 27.9% to 50.4%; however, the average current density oppositely reduces from 4286 A m^{-2} to 1249 A m^{-2}.

It is noted that the decrease in current density with increasing operating voltage comes from the relation between the potential, current density and cell polarizations in Eq. (16), whereas the increase in system efficiency with increasing operating voltage is due to the relation of system efficiency with power density in Eq. (20). The increase of efficiency with increasing operating voltage was also related to the decrease of cell polarization with increasing output voltage, whereas the decrease of current density with increasing output voltage was previously reported to due with the low hydrogen consumption at high output voltage [21].

3.3. *Effect of reforming reactivity*

According to the literatures [4,12], the use of catalyst with too high reforming reactivity could lead to the rapid endothermic steam reforming and high hydrocarbon conversion at the beginning of the reformer, then results in the significant cooling spot at the entrance of the reformer chamber. Here, we studied the effect of reforming reactivity on the system performance by applying catalyst with various reforming reactivities (25%, 50% and 80% compared to the base case) and determining the potential to reduce the rapid endothermic steam reforming rate at the beginning state, which could result in the smoother temperature profile along the chamber.

Fig. 7 shows the effect of catalyst reactivity on the conversion profiles along the reformer chamber. It was observed that the complete conversion of methanol shifted to the exit of the reformer chamber with decreasing catalyst reactivity; and methanol was completely reformed at the end of the reforming chamber when the 50% catalyst reactivity was applied. Importantly, it must be aware that the catalyst reactivity must not too low, which could result in the incomplete reforming at the exit of the reformer chamber and allow the slippage of unreacted methanol into the fuel chamber. By applying 25% catalyst reactivity, the incomplete reforming

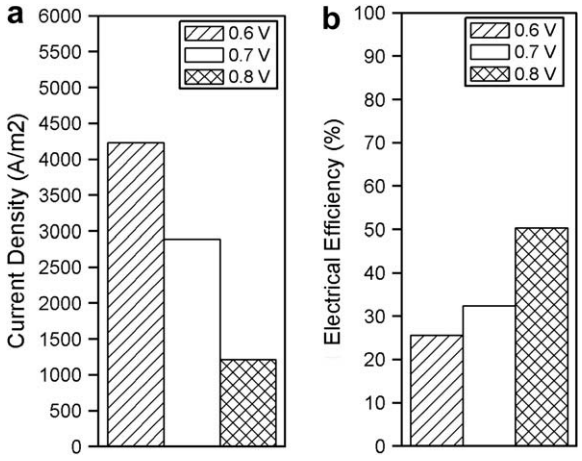

Fig. 6 – Effect of operating voltage on (a) current density and (b) electrical efficiency achieved from IIR-SOFC system.

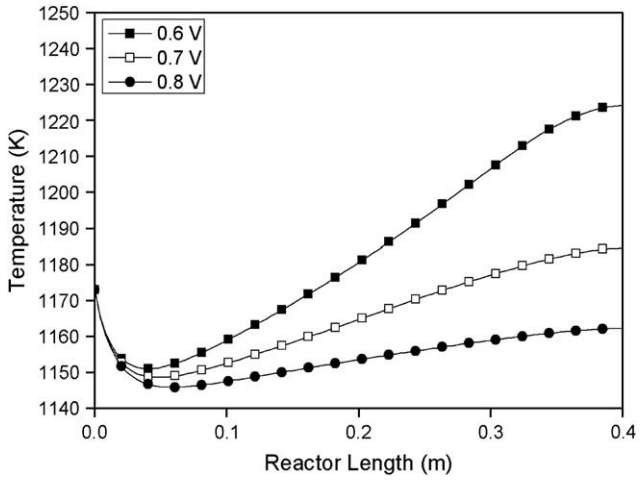

Fig. 5 – Effect of operating voltage on the temperature gradient in the reformer channel of IIR-SOFC system.

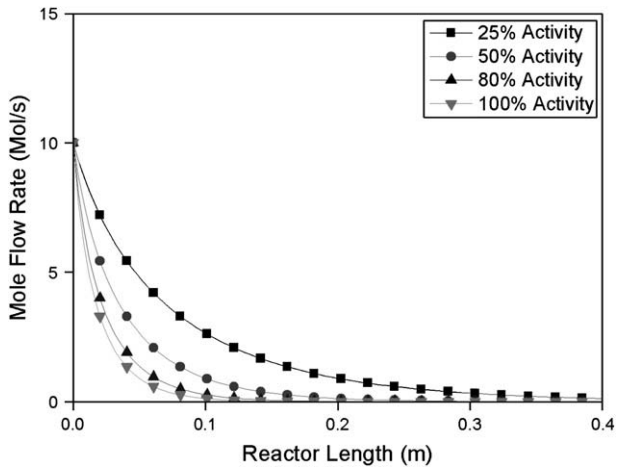

Fig. 7 – Effect of catalyst activity on the methane conversion in the reformer channel of IIR-SOFC system.

occurred and noticeable amount of methanol remains observed at the exit of the reformer chamber, thus the system performance with this condition was not considered.

Fig. 8 presents the effect of catalyst reactivity on the temperature profiles along the reformer chamber. Clearly, the temperature gradient of the system becomes smoother and the exit temperature was lower when less reactivity catalysts (50% and 80% catalyst reactivity) were applied. The use of lower reactivity catalyst results in the decrease of endothermic steam reforming rate, thus the cooling spot at the entrance of the reformer eventually reduces and the temperature gradient along the chamber becomes smoother. Nevertheless, it was found that the current density and electrical efficiency slightly decreased with decreasing catalyst reactivity (from 32.48% to 31.06% and 30.29% at 80% and 50% catalyst reactivity, Fig. 9). This slight decreasing could be due to the increase in cell resistances since the accumulated heat in the system was reduced by using low catalyst reactivity.

3.4. *Effect of steam to carbon ratio*

As the thermodynamic properties of inlet fluids are important factor that could influence the thermal behavior of SOFC system, the effect of inlet steam content on the temperature gradient along the system and the system performance was investigated by varying the inlet steam to carbon (S/C) ratios from 2.0 to 3.0 and 4.0. Fig. 10 presents the effect of inlet S/C ratio on the temperature gradient along the reformer chamber. As shown from the figure, the cooling spot at the entrance of the reformer reduced when the inlet S/C increased. This improvement could be caused by the increase of heat accumulated from the excess steam fed into the system, which could be efficiently used for the endothermic steam reforming reaction.

Nevertheless, it was found that both current density and electrical efficiency decreased with increasing inlet S/C ratio (Fig. 11 (a) and (b)). The decrease in current density could be due to the higher cell polarizations with increasing inlet S/C ratio, while the decrease in electrical efficiency comes from the higher energy requirement to vaporize steam when excess steam was introduced to the system [22].

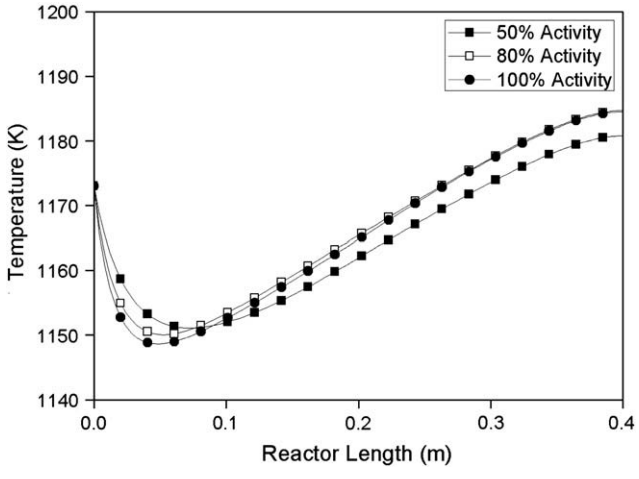

Fig. 8 – Effect of catalyst activity on the temperature gradient in the reformer channel of IIR-SOFC system.

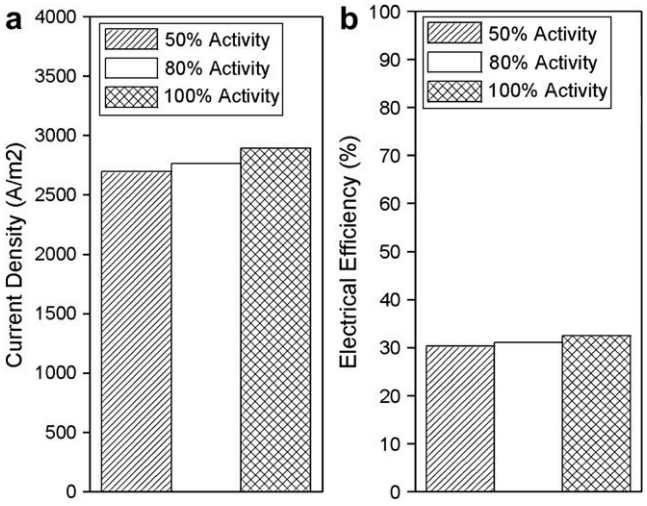

Fig. 9 – Effect of catalyst activity on (a) current density and (b) electrical efficiency achieved from IIR-SOFC system.

3.5. *Effect of operation pressure*

Fig. 12 shows the influence of operating pressure (1 (base case), 5, and 10 bar) on temperature profiles of this IIR-SOFC system. It can be seen that the increase of pressure significantly reduces the dropping of temperature at the entrance of reformer chamber. This could be due to the effect of partial pressure of gas species in steam reforming and electrochemical reactions since the extent of steam reforming rate reaction decreases with increasing pressure due to the thermodynamic restrictions and the kinetic expressions in use [4].

It was also found that the increase of operating pressure results in the higher open-circuit potential and consequently lower polarizations, which leads to the achievement of higher current density and eventually electrical efficiency. The current density increased from 2891.78 A m^{-2} to 4132.20 A m^{-2} and 4274.02 A m^{-2} at 1, 5, and 10 bar

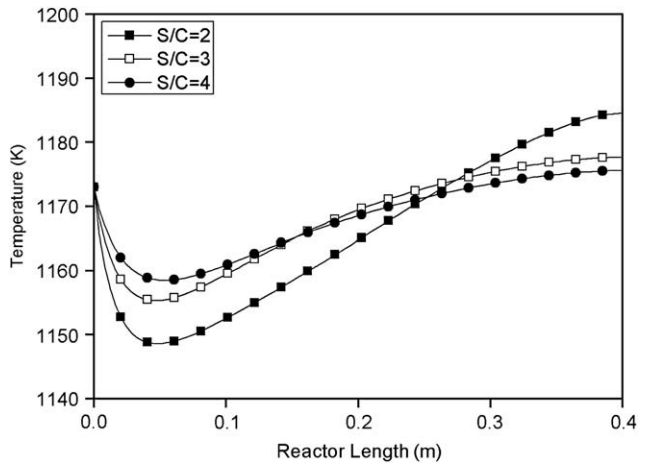

Fig. 10 – Effect of inlet steam to carbon (S/C) ratio on the temperature gradient in the reformer channel of IIR-SOFC system.

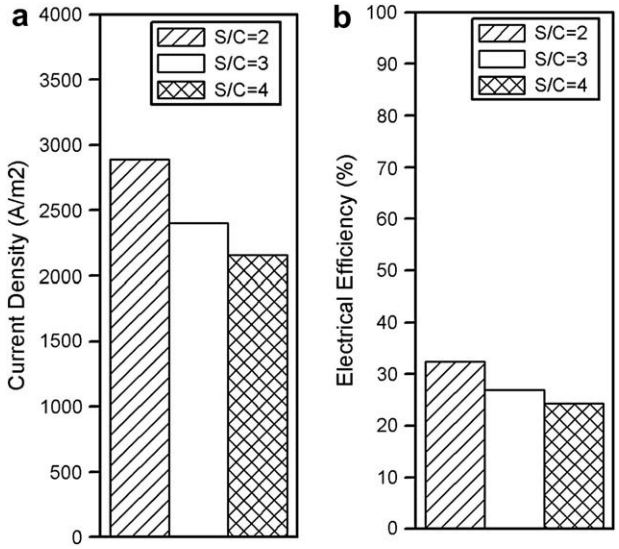

Fig. 11 – Effect of inlet steam to carbon (S/C) ratio on (a) current density and (b) electrical efficiency achieved from IIR-SOFC system.

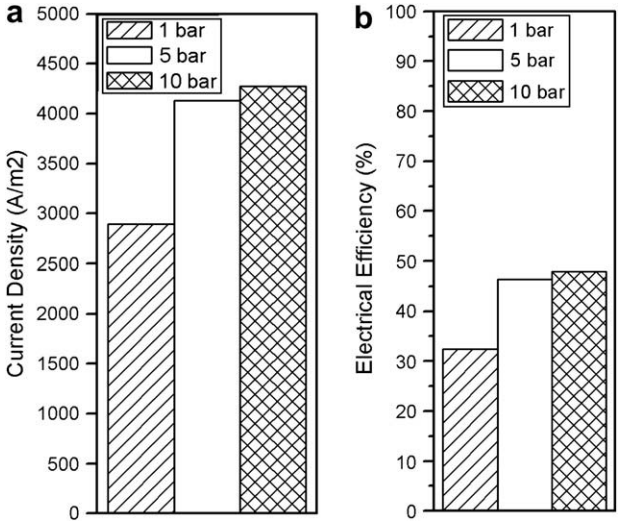

Fig. 13 – Effect of pressure on (a) current density and (b) electrical efficiency achieved from IIR-SOFC system.

respectively, Fig. 13 (a). Thus, the increasing of operating pressure is an effective way of reducing the temperature gradient as well as increasing the cell performance. Nevertheless, it must be aware that the operating pressure should not be too high, which could affect the strength of system materials.

3.6. *Effect of gas flow patterns*

Theoretically, as for a typical heat exchanging system, flow direction of exchanged fluids strongly affects the heat transfer and reaction behavior in the fluid stream, thus the effect of fuel and oxidant flow direction on the IIR-SOFC performance was also considered. In the previous sections, air flow is counter-flow to fuel flow in SOFC fuel channel. As an alternative option, the system behavior was analyzed as co-flow pattern by changing mass and energy balances in air channel along with their corresponding boundary conditions while keeping all other operating conditions identical to those of counter-flow pattern. As described earlier, the co-flow configuration can be divided in 2 patterns i.e. conventional co-flow and alternative co-flow. The effect of these two gas flow patterns on the temperature profiles along the reformer, fuel and air channels was simulated and showed in Fig. 14(a) and (b).

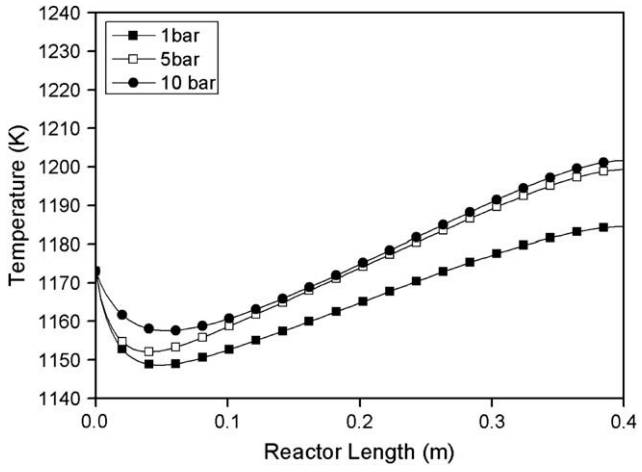

Fig. 12 – Effect of pressure on the temperature gradient in the reformer channel of IIR-SOFC system.

Interestingly, it was found that the flow directions of fuel gases and air strongly affect the temperature gradient along the system. Compared to the counter-flow pattern as previously shown in Fig. 4, the alternative co-flow pattern can provide the smoothest temperature gradient and lowest average temperature along the system; nevertheless, it also gives the lowest current density and electrical efficiency as shown in Fig. 15 due to its high polarization with low system temperature. Compared between the counter-flow and conventional co-flow patterns, it can be seen that while in the case of counter-flow pattern the temperature profiles increase along the system and the maximum temperature occurs at the outlet of air channel (Fig. 4); in the case of co-flow pattern, the maximum temperature occurs at approximate the third quadrant of the system. Under counter-flow pattern, the increasing of temperature along air flow direction is mainly due to heat accumulation along SOFC system. For co-flow pattern, heat is firstly generated at the end of the system ($z = 1$) and then accumulated along air stream until reaching the entrance of reforming regime ($z = 0$), where great amount of energy is consumed, thus the temperature along the system is higher than the two ends. It should be noted that the temperature dropping at the entrance of the reformer chamber for IIR-SOFC with co-flow pattern was slightly better than that with counter-flow pattern (the reformer temperature decreased to the lowest 1153 K for co-flow pattern compared to 1148 K for counter-flow pattern). In addition, the average temperatures in reformer, fuel and air channels of

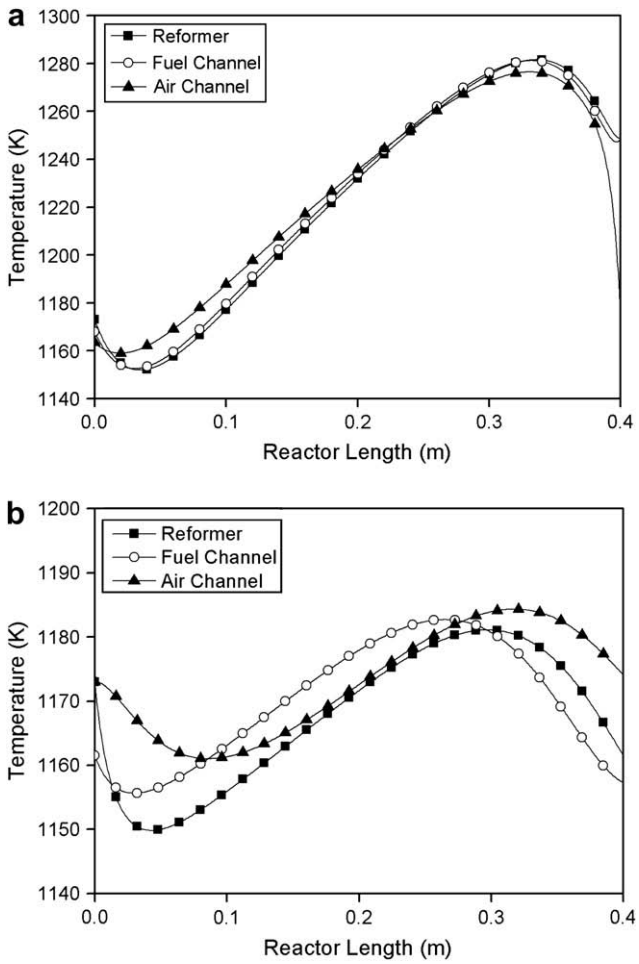

Fig. 14 – Effect of fuel/air flow pattern ((a) co-flow and (b) alternative co-flow) on the temperature gradient in the reformer channel of IIR-SOFC system.

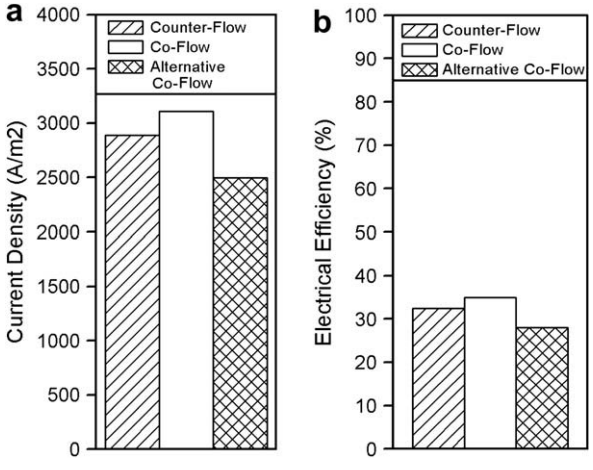

Fig. 15 – Effect of fuel/air flow pattern on (a) current density and (b) electrical efficiency achieved from IIR-SOFC system.

IIR-SOFC with co-flow pattern is higher than those of IIR-SOFC with counter-flow pattern; this consequently leads to the higher current density and electrical efficiency for IIR-SOFC with co-flow pattern. We summarized that the high efficiency of IIR-SOFC with conventional co-flow pattern is due to the good matching between the heat exothermically supplied from the electrochemical reaction and the heat required for the endothermic steam reforming reaction along the fuel cell system, thus concluded here that IIR-SOFC with co-flow pattern is more satisfactory than that with counter-flow pattern.

4. Conclusion

The simulations indicated that IIR-SOFC fueled by methanol can be well performed as autothermal operation, although slight temperature gradient occurred at the entrance of the reformer chamber. The increase of operating voltage lowered the average temperature along the reformer chamber and improved the electrical efficiency, but it oppositely reduced the average current density achievement. Greater temperature profile along the system can be obtained by applying the catalyst with low reforming reactivity; nevertheless, the current density and electrical efficiency slightly decreased due to the increase in cell resistances because the accumulated heat in the system was reduced by using low catalyst reactivity. By using high inlet steam to carbon ratio, the cooling spot at the entrance of the reformer can be reduced but again both current density and electrical efficiency decreased due to the higher cell polarizations and energy requirement to vaporize steam when excess steam was introduced. By increase operating pressure, the system efficiency significantly improved due to the higher open-circuit potential and lower polarizations with increasing pressure, which leads to the achievement of higher current density and electrical efficiency. In addition, the degree of temperature dropping at the entrance of internal reformer significantly reduces with increasing operating pressure.

We also found from this work that IIR-SOFC with co-flow pattern (co-flow of air and fuel streams through fuel cell) provides higher voltage and smoother temperature gradient along the system than that with counter-flow pattern due to the better matching between the heat exothermically supplied from the electrochemical reaction and the heat required for the endothermic steam reforming reaction along the fuel cell system. Therefore, we concluded here that the performance of IIR-SOFC fueled by methanol can be maximized by applying co-flow pattern and operated with high operating pressure.

Acknowledgment

The financial support from the Thailand Research Fund (TRF) and Commission on Higher Education, and the Thailand Graduate Institute of Science and Technology (TGIST): grant no. TG-55-20-50-058D throughout this project is gratefully acknowledged.

REFERENCES

[1] Haseli Y, Dincer I, Naterer GF. Thermodynamic modeling of a gas turbine cycle combined with a solid oxide fuel cell. Int J Hydrogen Energy 2008;33:5811–22.
[2] Motahar S, Alemrajabi AA. Exergy based performance analysis of a solid oxide fuel cell and steam injected gas turbine hybrid power system. Int J Hydrogen Energy 2009;34: 2396–407.
[3] Park HK, Lee YR, Kim MH, Chung GY, Nam SW, Hong SA, et al. Studies of the effects of the reformer in an internal-reforming molten carbonate fuel cell by mathematical modeling. J Power Sources 2002;104:140–7.
[4] Aguiar P, Chadwick D, Kershenbaum L. Modelling of an indirect internal reforming solid oxide fuel cell. Chem Eng Sci 2002;57:1665–77.
[5] Dokamaingam P, Assabumrungrat S, Soottitantawat A, Sramala I, Laosiripojana N. Modeling of SOFC with indirect internal reforming operation: comparison of conventional packed-bed and catalytic coated-wall internal reformer. Int J Hydrogen Energy 2009;34:410–21.
[6] Samms SR, Savinell RE. Kinetics of methanol-steam reformation in an internal reforming fuel cell. J Power Sources 2002;112:13–29.
[7] Peppley BA, Amphlett JC, Kearns LM, Mann RF. Kinetics of methanol-steam reforming in an internal reforming fuel cell. Appl Catal A 1999;179:21–9.
[8] Bichon P, Asheim M, Jordal A, Sperle T, Fathi M, Holmen A, et al. Hydrogen from methanol steam-reforming over Cu-based catalysts with and without Pd promotion. Int J Hydrogen Energy 2007;32:1799–805.
[9] Choi Y, Stenger H. Fuel cell grade hydrogen from methanol on a commercial $Cu/ZnO/Al_2O_3$ catalyst. Appl Catal B 2002; 38:259–69.
[10] Liwei P, Shudong W. Methanol steam reforming in a compact plate-fin reformer for fuel-cell systems. Int J Hydrogen Energy 2005;30:973–9.
[11] Mastalir A, Frank B, Szizybalski A, Soerijanto H, Deshpanda A, Niederberger M, et al. Steam reforming of methanol over $Cu/ZnO_2/CeO_2$. J Catal 2005;230:464–75.
[12] Sánchez D, Chacartegui R, Munoz A, Sánchez T. Thermal and electrochemical model of internal reforming solid oxide fuel cells with tubular geometry. J Power Sources 2006;160:1074–87.
[13] Calise F, d'Accadia MD, Restuccia G. Simulation of a tubular solid oxide fuel cell through finite volume analysis: effects of the radiative heat transfer and exergy analysis. Int J Hydrogen Energy 2007;32:4575–90.
[14] Larminie J, Dicks A. Fuel cell systems explained. Chichester: John Wiley & Sons, Ltd. 2000.
[15] H-Pacheco E, Singha D, Huttonb PN, Patelb N, Manna MD. A macro-level model for determining the performance characteristics of solid oxide fuel cells. J Power Sources 2004; 138:174–86.
[16] Suwanwarangkul R, Croiset E, Fowler MW, Douglas PL, Entche E, Douglas MA. Performance comparison of Fick's, dusty-gas and Stefan–Maxwell models to predict the concentration overpotential of a SOFC anode. J Power Sources 2003;122:9–18.
[17] Achenbach E. Three-dimensional and time-dependent simulation of a planar solid oxide fuel cell stack. J Power Sources 1994;49:333–48.
[18] Ferguson JR, Fiard JM, Herbin R. Three-dimensional numerical simulation for various geometries of solid oxide fuel cells. J Power Sources 1996;58:109–22.
[19] Costamagna P, Honegger K. Modeling of solid oxide heat exchanger integrated stacks and simulation at high fuel utilization. J Electrochem Soc 1998;145:3995–4007.
[20] Chan SH, Khor KA, Xia ZT. A complete polarization model of a solid oxide fuel cell and its sensitivity to the change of cell component thickness. J Power Sources 2001;93: 130–40.
[21] Campanari S, Iora P. Definition and sensitivity analysis of a finite volume SOFC model for tubular cell geometry. J Power Sources 2004;132:113–26.
[22] Lutz AE, Bradshaw RW, Keller JO, Witmer DE. Thermodynamic analysis of hydrogen production by steam reforming. Int J Hydrogen Energy 2003;28:159–67.

List of nomenclatures

Symbols

$(-\Delta H)_{elect,k}$: heat of the electrochemical reaction k, kJ/mol
$(-\Delta H)_j$: heat of reaction j in the reformer, kJ/mol
A_{act}: anode active surface area ($2\pi r_f L$), m^2
A_f: fuel channel outer surface area ($2\pi r_f L$), m^2
A_r: reformer outer surface area ($2\pi r_R L$), m^2
A_s: solid electrolyte outer surface area ($2\pi r_s L$), m^2
E_a: activation energy, kJ/mol
E: potential, V
$E_{H_2}^{OCP}$: open-circuit potential (OCP), V
$E_{H_2}^{\infty}$: potential for standard temperature and pressure and pure reactants, V
F: Faraday's constant 96,485 C/mol
F_i: molar flow rate of species i, mol/s
h: heat transfer coefficient, kJ/m^2 s K
j: current density, A/m^2
k_i: frequency factor of reaction i, mol/gcat s atm
L: system length, m
P: power density, W/cm^2
p^o: standard partial pressure, atm
p_i: partial pressure of species i, atm
R: universal gas constant; 8.414 J/K mol
$R_{elect,k}$: rate of the electrochemical reaction k, mol/m^2 s
R_j: rate of reaction j in the reformer, mol/kg_{cat} s
R: polarization, $\Omega\,m^2$
T: temperature, K
V_a: air channel volume ($\pi(r^2 - r_s^2)L$), m^3
V_f: fuel channel volume ($\pi(r^2 - r_f^2)L$), m^3
V_p: catalyst particle volume, m^3
V_s: solid electrolyte volume ($\pi(r^2 - r_f^2)L$), m^3

Greek symbols

α_R: overall heat transfer coefficient, kJ/m^2 s K
λ_s: thermal conductivity of the solid structure, kJ/m s K
$\nu_{i,k}$: stoichiometric coefficient of component i in electrochemical reaction k
$\nu_{i,j}$: stoichiometric coefficient of component i in reforming reaction j
ρ_B: catalyst bulk density, kg_{cat}/m^3
η_{elec}: electrical efficiency

Subscripts

i: reaction (SRM, WGS, etc.)
j: component (methanol, water, hydrogen, etc.)
Ohm: ohmic losses
a: air channel
A: anode
C: cathode
elect: electrochemical reactions
f: fuel channel
i: component
j, k: reaction
r: reformer
s: solid electrolyte

ภาคผนวก 8

Journal of Power Sources 195 (2010) 69–78

Contents lists available at ScienceDirect

Journal of Power Sources

journal homepage: www.elsevier.com/locate/jpowsour

Modelling of tubular-designed solid oxide fuel cell with indirect internal reforming operation fed by different primary fuels

P. Dokmaingam[a], S. Assabumrungrat[b], A. Soottitantawat[b], N. Laosiripojana[a,*]

[a] The Joint Graduate School of Energy and Environment, King Mongkut's University of Technology Thonburi, 126 Prachauthit Rd., Bangmod, Tungkru, Bangkok 10140, Thailand
[b] Department of Chemical Engineering, Faculty of Engineering, Chulalongkorn University, Bangkok 10330, Thailand

ARTICLE INFO

Article history:
Received 25 March 2009
Received in revised form 10 June 2009
Accepted 23 June 2009
Available online 10 July 2009

Keywords:
Indirect internal reforming
Solid oxide fuel cell
Methane
Methanol
Ethanol
Biogas

ABSTRACT

Mathematical models of an indirect internal reforming solid oxide fuel cell (IIR-SOFC) fed by four different primary fuels, i.e., methane, biogas, methanol and ethanol, are developed based on steady-state, heterogeneous, two-dimensional and tubular-design SOFC models. The effect of fuel type on the thermal coupling between internal endothermic reforming with exothermic electrochemical reactions and system performance are determined. The simulation reveals that an IIR-SOFC fuelled by methanol provides the smoothest temperature gradient with high electrochemical efficiency. Furthermore, the content of CO_2 in biogas plays an important role on system performance since electrical efficiency is improved by the removal of some CO_2 from biogas but a larger temperature gradient is expected.

Sensitivity analysis of three parameters, namely, a operating pressure, inlet steam to carbon (S:C) ratio and flow direction is then performed. By increasing the operating pressure up to 10 bar, the system efficiency increases and the temperature gradient can be minimized. The use of a high inlet S:C ratio reduces the cooling spot at the entrance of reformer channel but the electrical efficiency is considerably decreased. An IIR-SOFC with a counter-flow pattern (as based case) is compared with that with co-flow pattern (co-flow of air and fuel streams through fuel cell). The IIR-SOFC with co-flow pattern provides higher voltage and a smoother temperature gradient along the system due to superior matching between heat supplied from electrochemical reaction and heat required for steam reforming reaction; thus it is expected to be a better option for practical applications.

1. Introduction

During the past two decades, several types of fuel cell have been continuously developed and modified. Among them, the solid oxide fuel cell (SOFC) has attracted much interest for stationary power generation since it provides high efficiency with low pollutant emission [1]. Generally, SOFC is operated at high temperatures (1073–1473 K), thus hydrocarbon fuels (e.g., methane) can be applied as a primary fuel when the system is operated with internal reforming (IR-SOFC). This operation uses the heat generated from the exothermic electrochemical reaction to conduct the endothermic (steam) reforming of hydrocarbons [2–5].

Theoretically, there are two main designs of a IR-SOFC namely, direct internal reforming (DIR-SOFC) and indirect internal reforming (IIR-SOFC). In the DIR-SOFC approach, together with electrochemical reaction, the reforming reaction occurs simultaneously at the anode side of SOFC. Thus, a high heat transfer rate can be achieved from this operation; nevertheless, the anode material must be optimized for both reactions and can be easily poisoned by deposition of carbon produced from the reforming of hydrocarbons. In an IIR-SOFC, the endothermic reforming reaction takes place at a reformer, which is in close thermal contact with the anode side of the SOFC where exothermic electrochemical reaction occurs. The great advantage of an IIR-SOFC is that the released heat can be utilized efficiently and the anode material is not subject to coke deposition occurring from the cracking and reforming of hydrocarbons, thus the primary fuels for IIR-SOFC are more flexible than DIR-SOFC. It is noted that the main drawback of IIR-SOFC is the mismatch between the rates of endothermic and exothermic reactions. This problem leads to significant local temperature reduction, particularly near the entrance of the internal reformer [3,4,6], which can result in mechanical failure due to thermally induced stresses. Importantly, the temperature gradient along the SOFC system is affected by several operating parameters, namely, inlet temperature, pressure and drawn current [4,6], as well as the type of primary inlet fuel.

Focusing on the primary fuel selection, methane (or natural gas) is accepted to be the most applicable fuel for IR-SOFC due to its abundance and well-developed supply infrastructure. Among other

* Corresponding author. Tel.: +66 2 4708309; fax: +66 2 8726736.
E-mail address: navadol_l@jgsee.kmutt.ac.th (N. Laosiripojana).

0378-7753/$ – see front matter © 2009 Elsevier B.V. All rights reserved.
doi:10.1016/j.jpowsour.2009.06.102

Nomenclature

A_{act}	area (m^2)
A_{act}	active area $= \frac{\pi(d_r - 2\Gamma_{cat})L}{\pi(d_r^2 - (d_r - 2\Gamma_{cat})^2 L)}$ (m^2)
C_P	specific heat of the gas streams ($kJ\,mol^{-1}\,K^{-1}$)
c_i	concentration of component i ($mol\,m^{-3}$)
$D_{i,j}$	binary diffusion of component i and j ($m^2\,s^{-1}$)
$D^e_{i,mix}$	effective molecular diffusivity ($m^2\,s^{-1}$)
d	diameter (m)
Eff	efficiency
F	Faraday's constant (96,484 C mol^{-1})
$F_{r,s}$	gray-body transfer factor from reformer surface to solid oxide surface
ΔH	heat of reaction ($kJ\,mol^{-1}$)
J_0	Exchange current density ($A\,m^{-2}$)
J	current density ($A\,m^{-2}$)
k_p	permeability
LHV_i	lower heating value of component i
M_i	molecular weight of component i ($kg\,kJ^{-1}$)
n_i	number of mole of component i
p^0	standard partial pressure (Pa)
p_i	partial pressure of species i
P_{SOFC}	power density ($W\,m^{-2}$)
Q_{elec}	local generated heat ($W\,m^{-2}$)
R_k	rate of reaction k
R_g	universal gas constant: 8.414 $kJ\,mol^{-1}\,K^{-1}$.
R_{ohm}	ohmic resistant ($k\Omega\,m^{-2}$)
T	temperature (K)
$\vec{v}$	fluid velocity ($m\,s^{-1}$)
y_i	the mole fraction of gas

Greek letters

ρ	density ($kg\,m^{-3}$)
ε_m	emittance
$\tilde{\mu}$	effect of viscosity (Pa s)
γ	special Fuller et al. diffusion volume [13]
$\alpha_{a,c}$	charge transfer coefficient of anode and cathode
σ	Stefan–Boltzmann coefficient
ε	porosity
τ	tortuosity
λ	thermal conductivity ($kJ\,m^{-1}\,s^{-1}K^{-1}$)
η	voltage drop (V)
Γ	thickness (m)

Subscripts

a	air channel
i	component (methane, water, hydrogen, etc.)
j	reaction (SRM, WGS, etc.)
f	fuel channel
p	particle
r	reformer
s	solid oxide fuel cell
Act	activation losses
Cat	catalyst
Cell	cell stack
Con	concentration losses
Elec	electrical
Thermal	thermal

potential primary fuels, ethanol and methanol are also interesting candidates due to their ready availability, high specific energy, sulfur-free content and storage transportation convenience [5]; moreover, they can be produced renewably from both chemical and biological processes. In addition to these three types of fuel, biogas is another attractive candidate—particularly for agricultural countries since it is a promising renewable fuel that can be produced biologically from the waste residues. Normally, after desulfurization, biogas is composed of approximately 60–65 vol.% of methane and 35–40 vol.% of CO_2.

In the present study, a set of mathematical models has been developed to predict and compare the behaviour of a tubular IIR-SOFC fuelled by methane, methanol, ethanol, and biogas. The models are coded in the COMSOL® program within 2D axisymmetric application. From the simulation, the performance of an IIR-SOFC (i.e., electrical efficiency and temperature gradient along the system) fuelled by these four types of primary fuels are determined; in addition, the effects of inlet steam to carbon (S:C) ratio, operating pressure and gas flow patterns on the performance of the IIR-SOFC are also investigated. Finally, a suitable type of primary fuel and suitable operating conditions for an IIR-SOFC system are identified.

2. Mathematical models

2.1. Kinetic equations for steam reforming of primary fuels

A steam reforming reaction was chosen to convert methane, methanol, ethanol and biogas to hydrogen-rich gas. The kinetic equations for each reaction were based on previous reports in the literature [7–10]. For methane reforming, the well-known kinetic models and reaction mechanisms proposed by Xu and Froment [7] were applied. For methanol reforming, the rate expressions reported by Peppley et al. [8] were selected, whereas the simulation of ethanol reforming was based on the rate expressions proposed by Sahoo et al. [10]. For biogas, the rate expressions of methane steam reforming with coupling of carbon dioxide reforming reported by Abashar [9] were applied.

2.2. Model geometry and assumptions

A tubular-designed IIR-SOFC was selected, as shown schematically in Fig. 1. According to this configuration, primary fuels (e.g., methane, methanol, ethanol, or biogas) and steam are converted to hydrogen-rich gas in an internal catalytic packed-bed reformer before being introduced to the fuel channel of the SOFC. Simultaneously, air is fed in an opposite flow direction through the air channel. It is noted that all dimensions and physical properties of SOFC system in the present work, which are summarized in Table 1, are based on the work of Aguiar et al. [4].

The mathematical model was developed as the smallest, single, unit cell taking into account the effect of temperature on gas distribution, reactant conversion and charge transfer. Two main sets of equations, namely, for the internal reformer and the SOFC stack (including electrodes and solid electrolyte) were applied to predict the concentration and temperature gradients along the system based on the following assumptions:

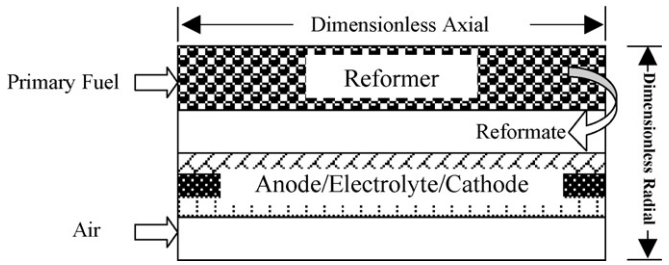

Fig. 1. Schematic diagram of tubular-designed SOFC with indirect internal reforming operation.

Table 1
Dimensional parameter for modelling.

Parameters	Value
Reformer diameter	0.6 cm
Gap between reformer to fuel channel	0.24 cm
Anode thickness	0.07 cm
Electrolyte thickness	20 μm
Cathode thickness	50 μm
Gap between cathode to air channel	0.3 cm
Length	60 cm
Anode	
Porosity (ε)	0.35
Tortuosity (τ)	4.80
Pore radius (r_p)	0.20 μm
Particle diameter (dp)	1.00 μm
Cathode	
Porosity (ε)	0.35
Tortuosity (τ)	4.00
Pore radius (r_p)	0.25 μm
Particle diameter (dp)	1.25 μm

- Each section is considered to be under non-isothermal, steady-state conditions.
- Ideal gas behaviour is applied for all gas components.
- Diffusion in the gas phase and pressure drop in the SOFC stack and reformer are ignored.
- The operating cell potential is constant along the cell coordinate.
- Final fuel utilization is fixed constantly at 80%.

By adopting a non-isothermal state, the calculated gas properties are derived as the function of temperature; thus, momentum, mass and energy balances are integrated under the conditions of interest. According to the tubular IIR-SOFC design (as shown in Fig. 1), the system structure consists of two main parts, i.e., porous and bulk gas channels. The transport behaviour of both parts is treated differently, as explained in the following sections.

2.2.1. Gas transport

Gas transport behaviour in the porous media, reformer and cell layer was calculated by means of the Brinkmen equation (Eq. (1)), whereas the Navier–Stokes equation (Eq. (2)) was applied to predict the momentum transfer in gas channels [11].

$$\nabla p = -\frac{\mu}{k_p} v + \tilde{\mu} \nabla^2 v \tag{1}$$

$$v\,\nabla(\rho v) = -\nabla p + \tilde{\mu} \nabla^2 v \tag{2}$$

where v is the fluid velocity; ρ is the density (kg m^{-3}); p is the pressure (Pa); $\tilde{\mu}$ is the effect of viscosity (as function of temperature), and k_p is the permeability. In this system, the diffusion properties of several gas species were investigated by using the binary diffusion flux, as given by [12]:

$$D_{i,j} = \frac{(0.00143)T^{1.75}}{pM_{i,j}^{1/2}[\gamma_i^{1/3} + \gamma_j^{1/3}]} \tag{3}$$

where $D_{i,j}$ is the binary diffusion of component i (mol m^{-1} s^{-1}); T is the temperature (K); p is the pressure (Pa); $M_{i,j} = 2/(1/M_i + 1/M_j)$; M_i is the molecular weight of component i; γ is a special diffusion volume (reported by Fuller et al. [13]); p_i is the partial pressure of component i. In the case of transportation through porous media, the diffusion behaviour is corrected by taking into account the porosity, ε, and the tortuosity, τ, namely, the effective diffusivity coefficiency (m^2 s^{-1}), $D^e_{i,mix}$:

$$D^e_{i,mix} = \frac{\varepsilon}{\tau} \sum D_{i,j} \tag{4}$$

Generally, gas diffusion through electrode layers can be explained by the coupling of two diffusion mechanisms, namely, molecular and Knudsen diffusions. This is known as the dusty gas model (DGM) [14]. If the mean free path of gas molecular species is larger than the pore diameter, Knudsen diffusion is the main mechanism; otherwise, molecular diffusion will dominate.

2.2.2. Ionic transport

The electricity generation was calculated from the relation between polarization and the activated area of SOFC. Activation, concentration and ohmic polarization are known as major losses for high-temperature fuel cells like SOFCs. Activation loss arises from an activation barrier to the electrochemical reaction at the electrode. In this work, the activation polarization, η_{act}, was computed by [15]:

$$J_i = J_0 \left[\exp\left(\frac{\alpha_a F \eta_{act}}{R_g T}\right) - \exp\left(\frac{-(1-\alpha_c) F \eta_{act}}{R_g T}\right) \right] \tag{5}$$

where J_i is the current density (A m^{-2}); J_0 is the exchange current density (A m^{-2}); R_g is the universal gas constant (kJ mol^{-1} K^{-1}); F is the Faraday constant. All relevant parameters were reported by Zhu et al. [16]. The concentration polarization occurs due to the resistance to gas diffusion through the porous media. Generally, gas diffusion behaviour can be predicted by three mathematical models: Fick's model, Dusty gas model (DGM), and Stefan–Maxwell model; the DGM was chosen in the present work. Ohmic polarization arises from the ion transport across the cell, which mainly depends on the ionic conductivity of the SOFC material. By applying ohm's law, the relation of ohmic polarization and material resistivity can be determined. It is noted that, in the present work, the material properties reported by Zhu et al. [16] were used. This voltage drop was computed by the simplified equation:

$$\eta_{ohmic} = J.R_{ohm} \tag{6}$$

where η_{ohmic} is the voltage drop caused by ohmic losses (V); J is the current density (A m^{-2}), and R_{ohm} is the ohmic resistant per unit area (kΩ m^2). It is noted that although both H_2 and CO can be electrochemically consumed in a SOFC, it has been reported that the

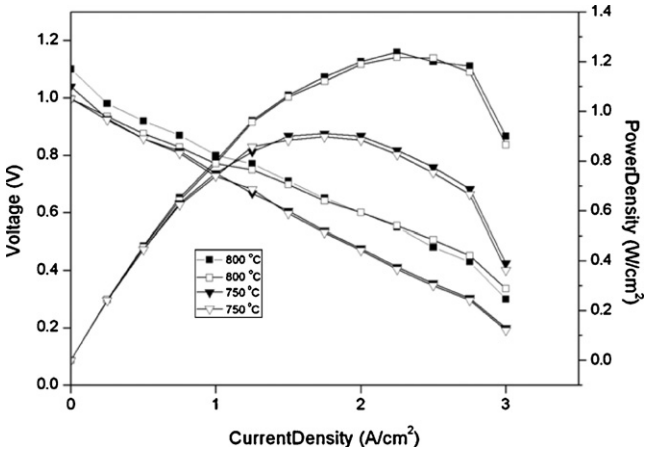

Fig. 2. *I–V* curve validation between simulation results of present work (blank symbols) with those from Lin et al. [16] (solid symbols).

Table 2
Thermal properties of each fuel under isothermal condition (1173 K and 1 bar).

Fuel	Thermal properties	
	LHV	Thermal efficiency (%)
Methane	744.7	49.4
Biogas	466.8	39.5
Methanol	631.5	76.3
Ethanol	1194.3	69.7

rate of electricity generation from CO is three times lower than that of H_2 [17]; thus the rate of CO oxidation in SOFC has been neglected in this study. At the anode|electrolyte interface, H_2 is electrochemically oxidized whereas O_2 is consumed at the cathode|electrolyte interface. The conversion rate of H_2, R_{elec,H_2}, and O_2, R_{elec,O_2}, at the indicated boundary was simulated from Eqs. (7) and (8), respectively:

$$R_{elec,H_2} = \frac{J_{H_2}}{2F} \tag{7}$$

$$R_{elec,O_2} = \frac{J_{O_2}}{4F} \tag{8}$$

The reliability of these electrochemical equations, coded in COMSOL® program, was validated by comparison with the results from the work of Lin et al. [18], as shown in Fig. 2. Clearly, the results are in good agreement.

2.2.3. Heat transfer

Conduction heat transfer along stack materials, convection heat transfer from fluid flow though the system and radiation between the reformer and the solid electrolyte were considered to predict the temperature distribution of the IIR-SOFC system. In the bulk gas channel, both conduction and convection heat transfer were calculated by:

$$\nabla \cdot (v\rho c_p T) - \nabla \cdot (\lambda \cdot \nabla T) = 0 \tag{9}$$

where v is the fluid velocity ($m\,s^{-1}$); ρ is the gas density ($kg\,m^{-3}$); c_p is the specific heat ($kJ\,kg^{-1}\,K^{-1}$); λ is the thermal conductivity ($kJ\,m^{-1}\,s^{-1}\,K^{-1}$); T is the temperature (K). It is noted that the influence of the radiation between the reformer and the solid electrolyte was also taken into account by considering the heat required for steam reforming in the reformer (Eq. (10)) and the heat of electrochemical reaction at the anode|electrolyte layer (Eq. (11)) [19].

$$\nabla \cdot (v\rho c_p T) - \nabla \cdot (\lambda \cdot \nabla T) + (-\Delta H_{reform}) R_{reform} + \frac{\sigma(T_r^4 - T_s^4)}{(1-\varepsilon_m/\varepsilon_m A)_r + 1/A_r F_{r,s} + (1-\varepsilon_m/\varepsilon_m A)_s} = 0 \tag{10}$$

$$\nabla \cdot (v\rho c_p T) - \nabla \cdot (\lambda \cdot \nabla T) + Q_{elec} + \frac{\sigma(T_s^4 - T_r^4)}{(1-\varepsilon_m/\varepsilon_m A)_s + 1/A_s F_{r,s} + (1-\varepsilon_m/\varepsilon_m A)_r} = 0 \tag{11}$$

where $Q_{elec} = (-\Delta H_{elec}) R_{elec} - P_{SOFC}$ is the local generated heat ($W\,m^{-2}$); $(-\Delta H_k)$ is the heat of reaction k; A is the area (m^2); $F_{r,s}$ is the gray-body transfer factor from the reformer surface to the solid oxide surface; σ is the Stefan–Boltzmann coefficient; ε_m is the emittance; P_{SOFC} is the local power density of the SOFC ($W\,m^{-2}$).

2.3. Calculation of thermal and electrical efficiencies

Base on the assumption that most of the generated hydrogen was combusted to supply heat for the steam reforming reaction, some heat generated was used as the heat source. The thermal efficiency, $Eff_{thermal}$, of an IIR-SOFC fuelled by different primary fuels was defined as the ratio between the heating value of hydrogen

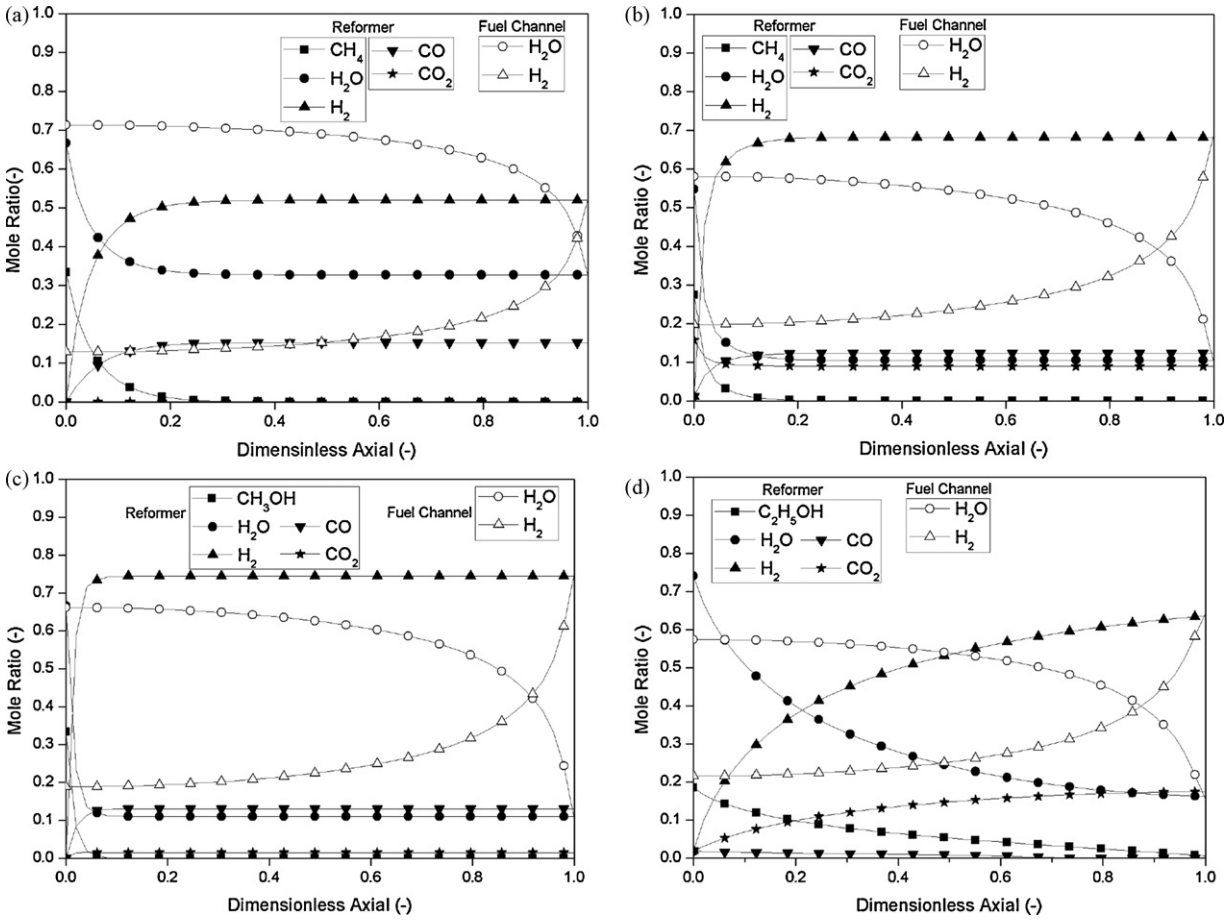

Fig. 3. Concentration profiles in reformer (black symbols) and fuel channel (white symbols) of IIR-SOFC fuelled by (a) methane, (b) biogas, (c) methanol and (d) ethanol (at base case conditions).

leftover from combustion with that of the inlet fuel, i.e.:

$$Eff_{thermal} = \frac{n_{H_2}^{out} LHV_{H_2,1173\ K} - \sum\left(-\Delta H_{reform}\right)}{\sum n_i^{in} LHV_{i,1173\ K}} \quad (12)$$

where n_i is number of moles for component i, and $LHV_{i,1173\,K}$ is the lower heating value of component i at 1173 K. In order to investigate the electrical efficiency, Eff_{elec}, outlet reformats were fed into SOFC and the electrical efficiency was defined as:

$$Eff_{elec} = \frac{P_{SOFC}.A_{act}}{\sum y_i^{in} LHV_{i,1173K}} \quad (13)$$

where A_{act} is the active area (m^2) and y_{fuel}^{in} is the mole fraction of the primary fuel.

3. Result and discussion

3.1. Thermodynamic property comparison

Before undertaking a thermodynamic analysis of an IIR-SOFC fuelled by different primary fuels, the thermodynamic properties of each fuel, i.e., methane, methanol, ethanol, and biogas (60% CH_4 and 40% CO_2) were identified in terms of lower heating value (LHV) and thermal efficiency. According to the thermal efficiency calculation, a steady-state operation was assumed and the inlet fuel was kinetically converted to hydrogen in the packed-bed reformer, which was eventually combusted to predict the thermal efficiency. It is noted that the simulation was carried out at 1173 K and 1 bar with the inlet steam to carbon (S/C) ratio of 2.0. Importantly, the limitation of gases transport through the packed catalyst was also

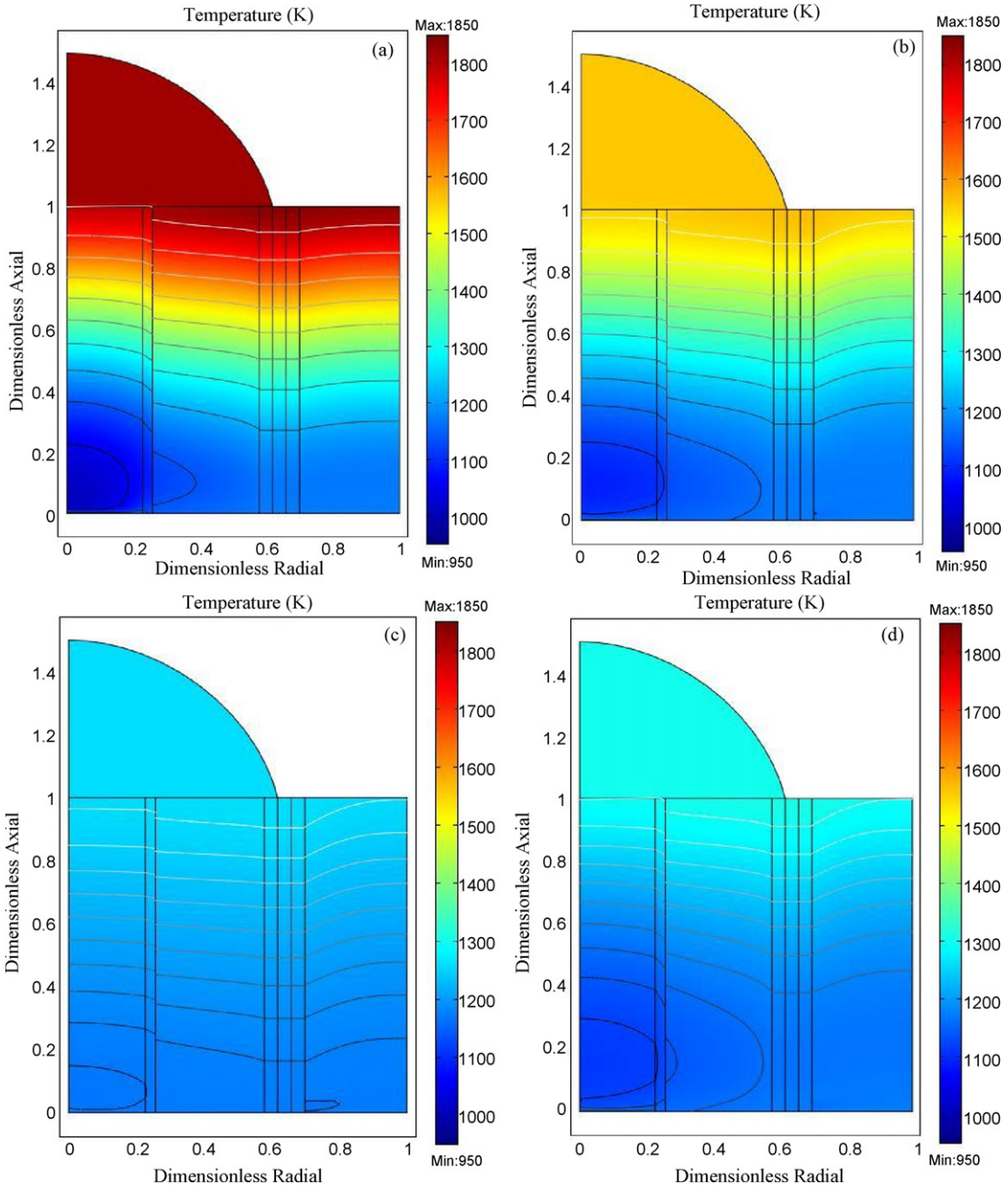

Fig. 4. Results from COMSOL® represented temperature gradients in reformer and fuel channel of IIR-SOFC fuelled by (a) methane, (b) biogas, (c) methanol and (d) ethanol (at base case conditions).

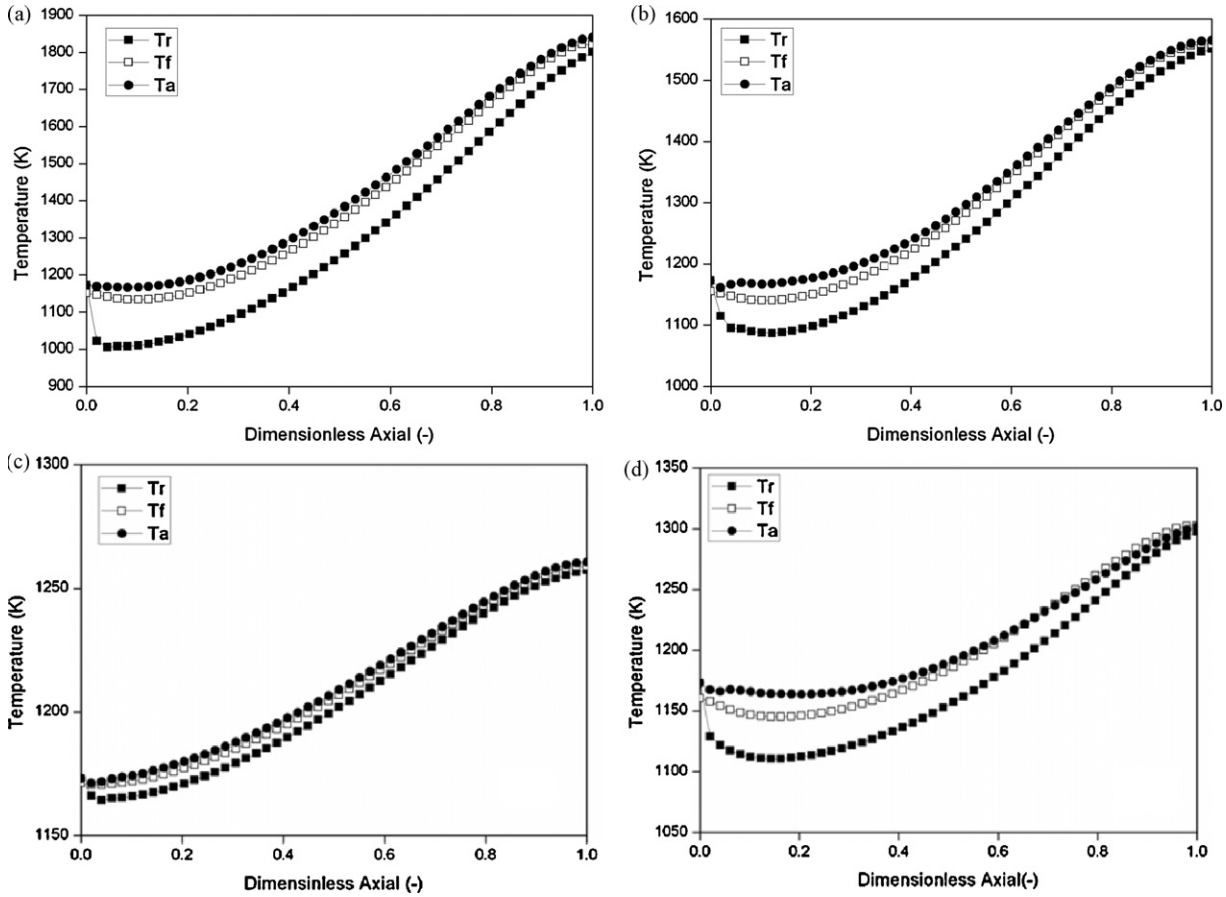

Fig. 5. Temperature profiles of reformer, fuel and air channels (T_r, T_f and T_a, respectively) for IIR-SOFC fuelled by (a) methane, (b) biogas, (c) methanol and (d) ethanol (at base case conditions).

taken into account. The dimensions of the system configuration are listed in Table 1, while the LHV and thermal efficiencies of each primary fuel are compared in Table 2. Among these primary fuels, alcohol-based fuels (methanol and ethanol) provide significantly higher thermal efficiency than methane-based fuels. Furthermore, the LHV of ethanol is considerably higher than those of other fuels, while that of methanol is close to that of methane. Hence, alcohol would be a promising candidate fuel for IIR-SOFC, IIR-SOFCs. The performance of an IIR-SOFC fuelled by these primary fuels in terms of electrical efficiency and temperature gradient along the system was then compared as presented in the following sections.

3.2. Modelling of IIR-SOFC fuelled by different fuels as based case

The non-isothermal model of IIR-SOFC was first simulated at 1 bar by introducing inlet fuels and steam at a S:C ratio of 2.0. A SOFC load voltage of 0.7 V and a fuel utilization of 80% were applied. Under these conditions, characteristic results, i.e., primary fuel conversion, product gas distribution and temperature gradient along the internal reformer and SOFC channels (both fuel and air channels) are shown in Figs. 3–5. The mole fraction profiles of primary fuels, hydrogen, steam, carbon monoxide, and carbon dioxide in reformer and fuel channel of SOFC, are presented in Fig. 3(a)–(d). Among these primary fuels, ethanol provides the slowest conversion rate along the reformer channel. At the outlet of the internal reformer, the product gas flows backward into fuel channel where hydrogen and carbon monoxide are electrochemically converted to steam and carbon dioxide.

Fig. 4(a)–(d) shows the results from COMSOL software representing temperature distributions in reformer, fuel and air channels for the IIR-SOFC system fuelled by different fuels, while Fig. 5(a)–(d) summarizes the temperature profiles in each channel. It can be seen that the heat generated from fuel cell side is sufficient for the internal reforming operation; nevertheless, a noticeable temperature gradient associated with indirect internal reforming operation is also observed for all types of fuel (as also reported by other researchers [4,6]). Among them, IIR-SOFC fuelled by methane shows the largest cooling spot at the first half of the reformer channel (reformer temperature decreases from 1173 to 1000 K), whereas IIR-SOFC fuelled by methanol presents the smoothest temperature profile (reformer temperature decreases from 1173 to 1163 K). It is noted that although the rate of the methanol conversion is faster than that of ethanol (Fig. 3(b) and (c)), the heat of the methanol steam reforming reaction is considerably lower, thus the temperature gradient for IIR-SOFC fuelled by methanol is smoother. The electrical efficiencies achieved from the IIR-SOFC with different fuels are compared in Table 3. It can be seen that methanol provides the greatest electrical efficiency; nevertheless, the system also requires the largest amount of inlet fuel compared with other fuels.

Table 3
Comparison of required volumetric flow rate and electrical efficiency achieved from IIR-SOFC fuelled different fuels.

Fuel	Properties	
	Volumetric flow rate	Electrical efficiency (%)
Methane	0.15	61.1
Biogas	0.18	46.7
Methanol	0.22	85.6
Ethanol	0.096	32.0

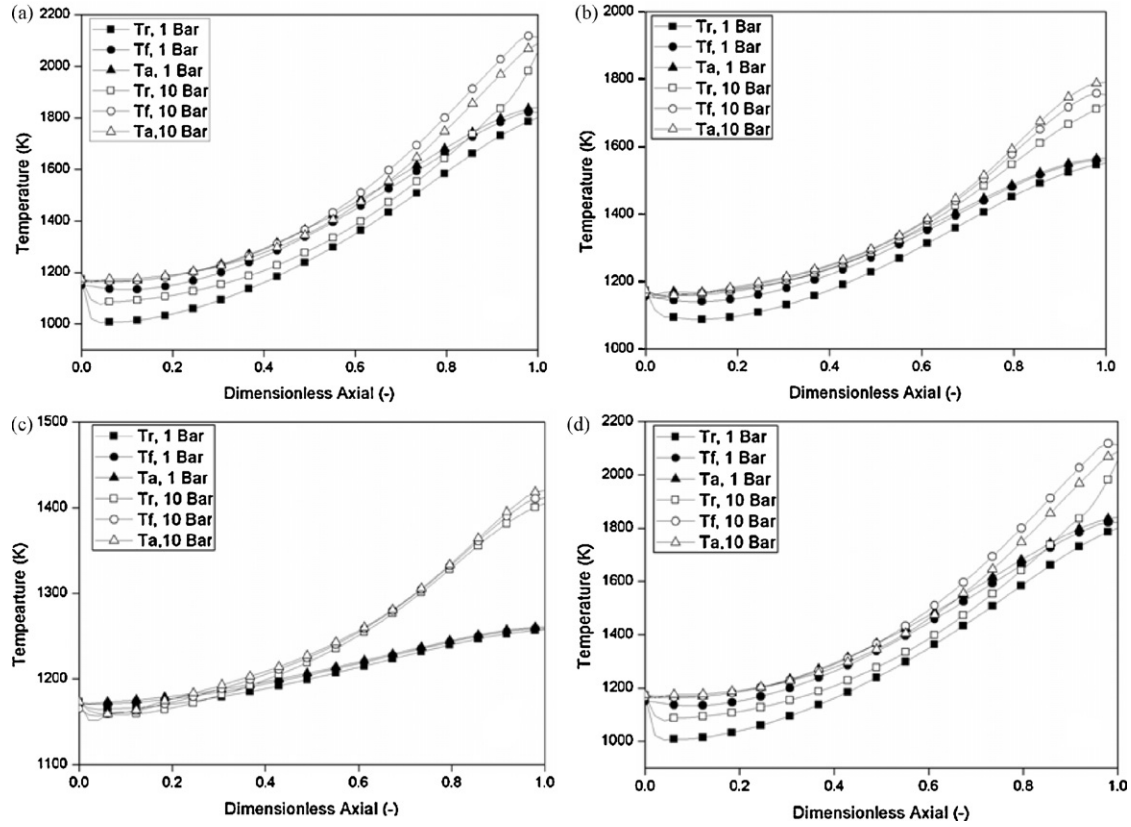

Fig. 6. Effect of operating pressure on temperature profile of IIR-SOFC fuelled by (a) methane, (b) biogas, (c) methanol and (d) ethanol.

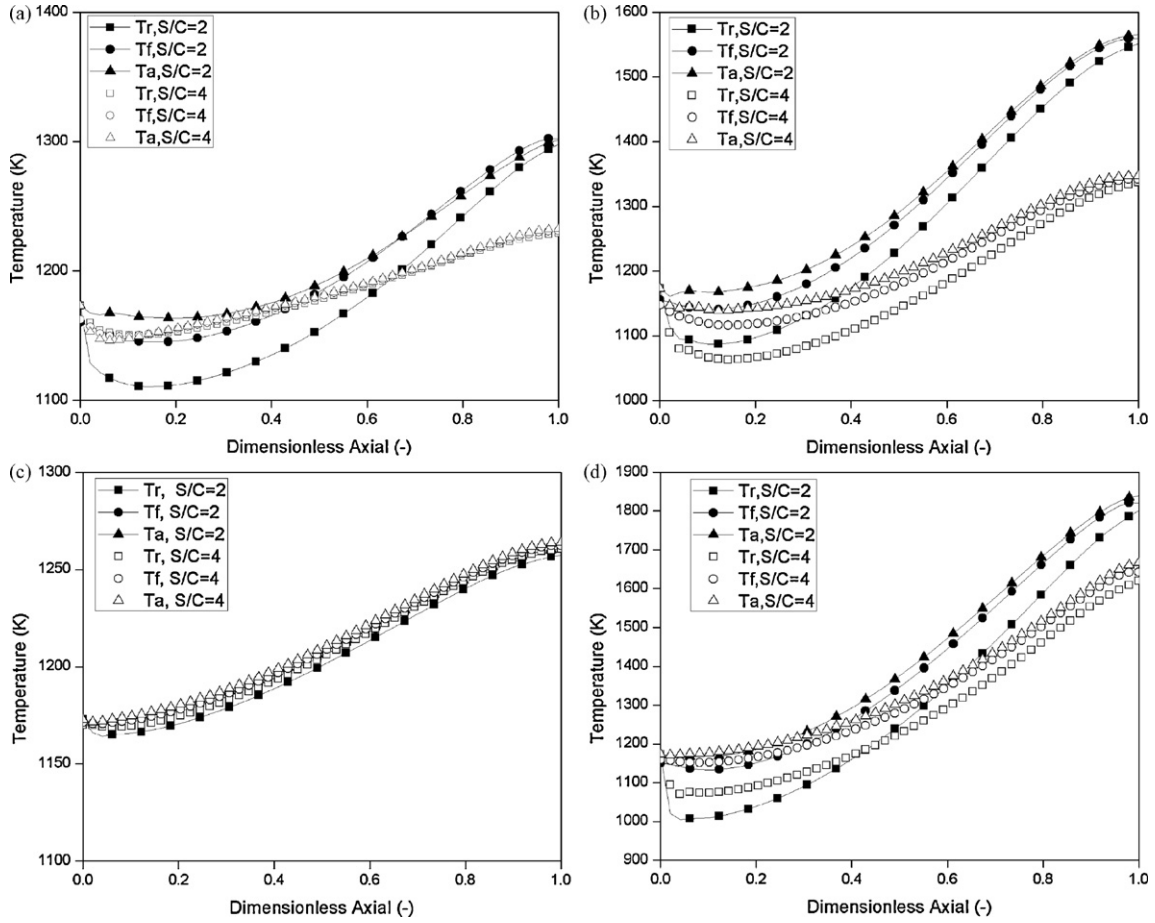

Fig. 7. Effect of S:C ratio on temperature profile of IIR-SOFC fuelled by (a) methane, (b) biogas, (c) methanol and (d) ethanol.

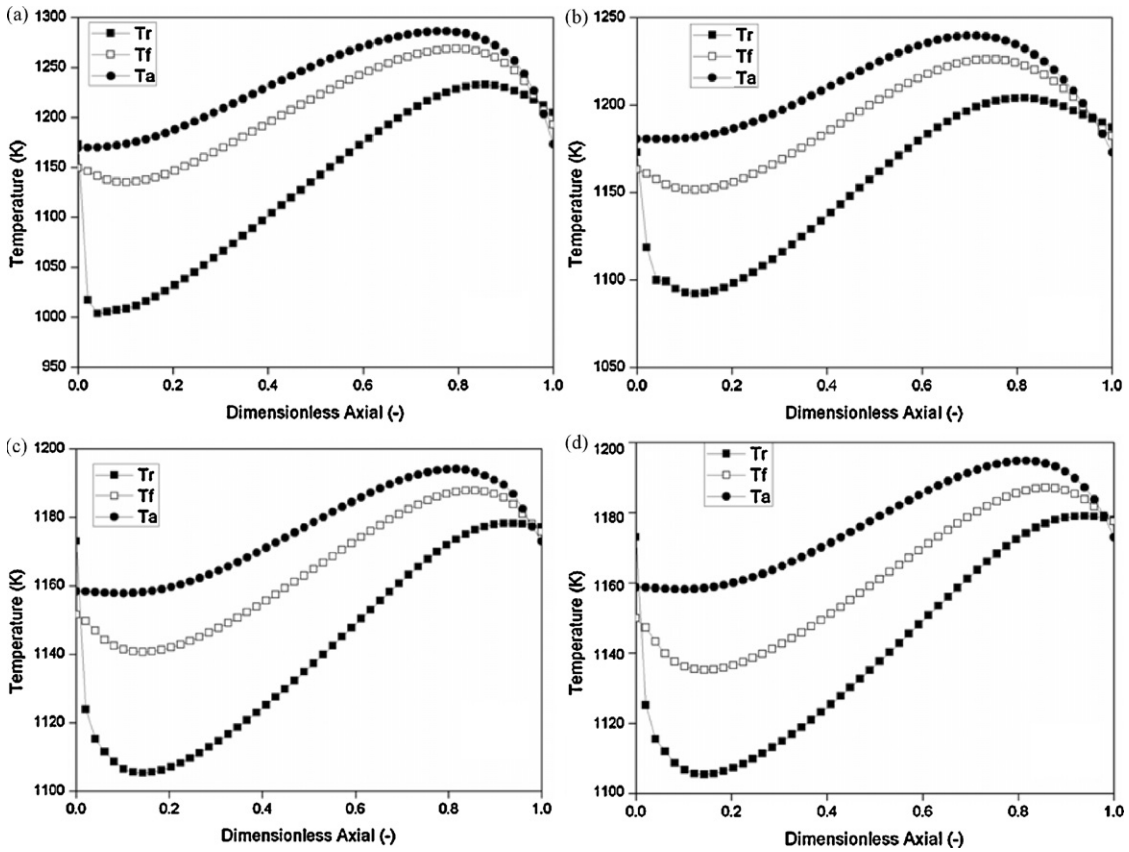

Fig. 8. Temperature profiles of reformer, fuel and air channels (T_r, T_f and T_a) for IIR-SOFC with co-flow pattern fuelled by (a) methane, (b) biogas, (c) methanol and (d) ethanol.

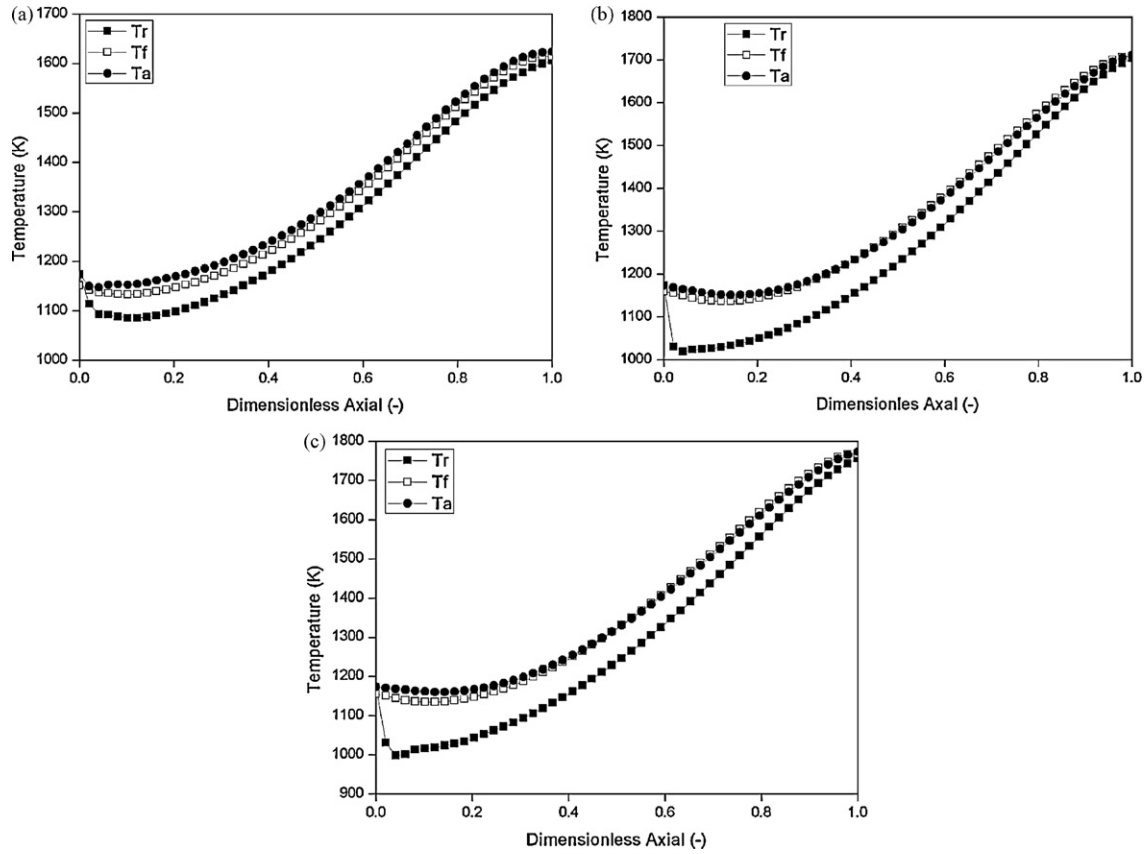

Fig. 9. Effect of CO_2 content in biogas ((a) 30%, (b) 20% and (c) 10%) on the temperature profiles of reformer, fuel and air channels (T_r, T_f and T_a) of IIR-SOFC system.

From the literature, the temperature gradient along the system can affect the cell performance and the properties of the ceramic component; the temperature difference along the SOFC system should be less than 10 K cm^{-1} [20]. According to the present analysis, only an IIR-SOFC fuelled with methanol can meet this criterion. Thus, as another aim of this study, several operating conditions, i.e., operating pressure, inlet S:C ratio and gas flow pattern are varied in order to minimize the temperature gradient as well as maximize the outputs (i.e., electrical efficiency) from an IIR-SOFC fuelled by these fuels.

3.3. Effect of pressure

According to the kinetic expressions for steam reforming of selected fuels, the operating pressure plays an important role on gas conversion behaviour as well as product selectivity. Thus, the effect of operating pressure on the system performance was determined by varying the operating pressure from 1 to 10 bar. As seen in Fig. 6(a)–(d), an increase in pressure significantly reduces the temperature drop at the entrance of reformer channel. This could be due to the effect of the partial pressure of gas species in the steam reforming and electrochemical reactions since the extent of the steam reforming rate reaction decreases with increasing pressure due to the thermodynamic restrictions and the kinetic expressions in use. It is also found that an increase of operating pressure results in a higher open-circuit potential and consequently lower polarization, which leads to higher electrical efficiency. According to simulation, the electrical efficiency of IIR-SOFC fuelled by methane, biogas, methanol and ethanol increases to 58.3, 44.8, 69.46, and 34.2%, respectively, when the operating pressure is increased from 1 to 10 bar. Thus, an increase in operating pressure is an effective way for reducing the temperature gradient, as well as enhancing cell performance.

3.4. Effect of steam to carbon (S/C) ratio

As the thermodynamic properties of inlet fluids are important factors that could influence the thermal behaviour of SOFC system, the effect of inlet steam content on the temperature gradient along the system and the system performance was investigated by varying the inlet steam to carbon (S:C) ratio from 2.0 to 4.0. Fig. 7(a)–(d) presents the effect of inlet S:C ratio on the temperature gradient along the reformer channel of an IIR-SOFC fuelled by different primary fuels. It can be seen that the cooling spot reduces when the ratio is increased for all types of fuel, particularly in the case of ethanol. This improvement could be caused by an increase in heat accumulated from excess steam fed into the system, which could be efficiently used for the endothermic steam reforming reaction. Nevertheless, it is also found that the electrical efficiency considerably decreases with increasing inlet S:C ratio (decreases to 33.3, 29.3, 54.6 and 15.4% for IIR-SOFC fuelled by methane, biogas, methanol and ethanol, respectively, when the inlet S:C ratio increases from 2.0 to 4.0). The decrease could be due to the higher cell polarization with increasing inlet S:C ratio and the higher energy requirement to vaporize steam when excess steam is introduced to the system [20].

3.5. Effect of flow direction

For typical autothermal application, e.g., a heat exchanging system, the flow direction of exchanged fluids strongly affects the heat transfer and reaction behaviour in the fluid stream; thus the effect of the fuel and oxidant flow direction on the IIR-SOFC performance was also considered in the present work. In previous sections, air flow is counter-flow to fuel flow in the fuel channel of SOFC (a so-called 'counter-flow' pattern). Alternatively, fuel and air streams can be passed in the same direction, a so-called "co-flow" pattern. The system behaviour of with co-flow pattern was analyzed by changing mass and energy balances in the air channel along with their corresponding boundary conditions, while keeping all other operating conditions identical to those of the counter-flow pattern. Fig. 8(a)–(d) shows the temperature profiles along all channels of an IIR-SOFC with co-flow pattern. Compared with the data in Fig. 5, it can be seen that the flow direction of fuel gases and air strongly affects the temperature gradient along the system. The IIR-SOFC with a co-flow pattern provides smoother temperature distribution with a higher average cell temperature, which leads to a reduction in cell overpotentials and consequently yields a higher electrical efficiency (increases to 55.8, 46.6, 67.1 and 39.8% for methane, biogas, methanol and ethanol, respectively). The high efficiency of an IIR-SOFC with a co-flow pattern is due to the good matching between the heat exothermically supplied from electrochemical reaction and the heat required for endothermic steam reforming along the SOFC system, thus it is concluded that an IIR-SOFC with co-flow pattern is more satisfactory than that with counter-flow pattern.

3.6. Effect of CO_2 content in biogas

According to the above study, the electrical efficiency of IIR-SOFC fuelled by biogas is relatively low due to the high content of CO_2 in biogas. It is well known that the presence of a high CO_2 content is a major problem with biogas in terms of several energy aspects, e.g., combust for power generation or compress and use as fuel in vehicle; thus the removal of CO_2 from biogas, which can be done by means of several techniques, e.g., water scrubbing, pressure swing adsorption or membrane technology, has been proposed and widely applied recently. In the present work, the effect of CO_2 content in biogas on system performance was also studied by varying the CO_2 content from 40 to 30, 20 and 10%. It is found that the electrical efficiency increases with decreasing CO_2 content (from 34.5 to 35.9, 38.2 and 39.2%, respectively); nevertheless, it can be seen from Fig. 9(a)–(c) that the content of CO_2 also affects the temperature gradient along the system. The temperature difference increases from 28.1 to 30.4, 42.8 and 47.6 K cm^{-1} when the CO_2 content is decreased from 40 to 30, 20 and 10%, respectively, thus it could affect the ceramic component of the SOFC and result in mechanical failure due to thermally induced stresses.

4. Conclusions

The simulation indicates that, among the four types of fuel studied, an IIR-SOFC fuelled by methanol provides the greatest performance in terms of electrical efficiency and temperature gradient along the system. It is also found that the content of CO_2 in biogas strongly affects the system performance; by removal of some CO_2 from biogas, the electrical efficiency can be improved but a larger temperature gradient is expected. By increasing the operating pressure, the system efficiency increases and the temperature gradient can be minimized. The use of a high inlet S:C ratio can reduce the cooling spot at the entrance of the internal reformer channel but the electrical efficiency considerably decreases due to the higher cell polarization and higher energy requirement to vaporize steam when excess steam is introduced to the system. An IIR-SOFC with a counter-flow pattern is also compared with an IIR-SOFC that has a co-flow pattern. It is found that a co-flow pattern provides higher voltage a and smoother temperature gradient along the system due to better matching between the heat supplied from the electrochemical reaction and the heat required for the steam reforming reaction.

Acknowledgements

The financial support from the Thailand Research Fund (TRF) and Commission on Higher Education, and the Thailand Graduate Institute of Science and Technology (TGIST) program, Thailand's National Science and Technology Development Agency (NSTDA), grant no. TG-55-20-50-058D throughout this project is gratefully acknowledged.

References

[1] G. Hoogers (Ed.), Fuel Cell Technology, 1st edition, 2003.
[2] P. Dokamaingam, S. Assabumrungrat, A. Soottitantawat, I. Sramala, N. Laosiripojana, Int. J. Hydrogen Energy 34 (2009) 410–421.
[3] H.-K. Park, Y.-R. Lee, M.-H. Kim, G.-Y. Chung, S.-W. Nam, S.-A. Hong, T.-H. Lim, H.-C. Lim, J. Power Sources 104 (2002) 140–147.
[4] P. Aguiar, D. Chadwick, L. Kershenbaum, Chem. Eng. Sci. 57 (2002) 1665–1677.
[5] K. Eguchi, Handbook of Fuel Cells 4 (2003) 1057–1069.
[6] D. Sánchez, R. Chacartegui, A. Munoz, T. Sánchez, J. Power Sources 60 (2006) 1074–1087.
[7] J. Xu, G.F. Froment, AIChE J. 35 (1989) 88–96.
[8] B.A. Peppley, J.C. Amphlett, L.M. Kearns, R.F. Mann, Appl. Catal. A: Gen. 179 (1999) 31–49.
[9] M.E.E. Abashar, Int. J. Hydrogen Energy 29 (2004) 799–808.
[10] D.R. Sahoo, S. Vajpai, S.P.K. Pant, Chem. Eng. Sci. 125 (2007) 139–147.
[11] R. Mauri, J. Eng. Math. 33 (1998) 103–112.
[12] B. Todd, J.B. Young, J. Power Sources 110 (2002) 186–200.
[13] E.N. Fuller, P.D. Schettler, J.C. Giddings, Ind. Eng. Chem. 58 (1966) 19–27.
[14] R. Suwanwarangkul, E. Croiset, M.W. Fowler, P.L. Douglas, E. Entche, M.A. Douglas, J. Power Sources 122 (2003) 9–18.
[15] H. Zhu, R. Kee, V. Janardhanan, O. Deutschmann, D. Goodwin, J. Electrochem. Soc. 152 (2005) A2427–A2440.
[16] H. Zhu, A.M. Colclasure, R.J. Kee, Y. Lin, S.A. Barnett, J. Power Sources 161 (2006) 413–419.
[17] Y. Matsuzaki, I. Yasuda, Solid State Ionics 126 (1999) 307–313.
[18] Y. Lin, Z. Zhan, S.A. Barnett, J. Power Sources 158 (2006) 1313–1316.
[19] D.L. Damm, A.G. Fedorov, J. Power Sources 143 (1–2) (2005) 158–1653.
[20] A.E. Lutz, R.W. Bradshaw, J.O. Keller, D.E. Witmer, Int. J. Hydrogen Energy 28 (2003) 159–167.

ภาคผนวก 9

Chemical Engineering Journal 155 (2009) 411–418

Contents lists available at ScienceDirect

Chemical Engineering Journal

journal homepage: www.elsevier.com/locate/cej

Operation viability and performance of solid oxide fuel cell fuelled by different feeds

P. Piroonlerkgul[a], W. Wiyaratn[b], A. Soottitantawat[a], W. Kiatkittipong[c], A. Arpornwichanop[a], N. Laosiripojana[d], S. Assabumrungrat[a,*]

[a] Department of Chemical Engineering, Faculty of Engineering, Chulalongkorn University, Phyathai Road, Wang Mai, Phatumwan, Bangkok 10330, Thailand
[b] Department of Production Technology Education, Faculty of Industrial Education and Technology, King Mongkut's University of Technology Thonburi, Bangkok 10140, Thailand
[c] Department of Chemical Engineering, Faculty of Engineering and Industrial Technology, Silpakorn University, Nakhon Pathom 73000, Thailand
[d] The Joint Graduate School of Energy and Environment, King Mongkut's University of Technology Thonburi, Bangkok 10140, Thailand

ARTICLE INFO

Article history:
Received 5 March 2009
Received in revised form 31 July 2009
Accepted 4 August 2009

Keywords:
Biogas
Solid oxide fuel cell
Non-isothermal
Operation viability
Modeling

ABSTRACT

The performances of solid oxide fuel cells (SOFCs) fed by different types of feed, i.e. biogas, biogas-reformed feed, methane-reformed feed and pure hydrogen, are simulated in this work. Maximum temperature gradient and maximum cell temperature are regarded as indicators for operation viability investigation whereas power density and electrical efficiency are considered as performance indicators. The change in operating parameters, i.e. excess air, fuel feed rate and operating voltage, affects both the performance and operation viability of SOFC, and therefore, these operating parameters should be carefully selected to obtain best possible power density and reasonable temperature and temperature gradient. Pure hydrogen feed offers the highest SOFC performance among the other feeds. Extremely high excess air is required for SOFC fed by biogas to become operation viable and, in addition, its power density is much lower than those of SOFCs fed by the other feeds. Methane-reformed feed offers higher power density than biogas-reformed feed since H_2 concentration of the former one is higher.

1. Introduction

With the increasing concern on environmental problems, many countries are pursuing efforts to develop more sustainable energy systems to replace conventional combustion heat engines. Solid oxide fuel cell (SOFC) power generation shows great promise to serve as an alternative in the near future. For SOFC, the chemical energy can be transformed directly into the electrical energy. Therefore, the energy loss in an SOFC is lower than that in the conventional heat engines. Furthermore, additional efficiency can be gained by incorporating a steam/gas turbine cycle to recover heat from the hot gas exhausted from the SOFC which is typically operated at high temperatures between 1073 and 1273 K. By the same reason, various types of fuel, e.g. methane, methanol, ethanol, natural gas, oil derivatives, can be directly used as fuel in SOFC. Biogas is also one of the interesting alternatives. It can be derived from an anaerobic digestion process. In this process, organic matter present in the variety of sources, e.g. wastewater, animal waste, is microbial consumed in the absence of oxygen. The composition of biogas derived from this process varies with its source. It mainly contains, on a dry basis, methane (55–65%), carbon dioxide (30–40%), nitrogen (1–10%), oxygen (<5%) and trace of sulfur [1]. By using biogas in power generation, zero greenhouse gas emission can be achieved since CO_2 released from the process could be consumed in the photo-synthesis of plant.

The presence of CH_4 in the feed gas (biogas) at the anode side of SOFC decreases the SOFC performance due to the carbon deposition and partial blocking of anode pore [2]. Pre-reformer should be installed to resolve this problem. According to the literature, pre-reforming of methane before feeding to SOFC can improve the power density [3]. The removal of CO_2 from biogas before feeding can also improve the power density of biogas-fuelled SOFC [4]. The presence of CO_2 in SOFC feed dwindles its performance owing to the effect of reverse water gas shift reaction (RWGS) [5]. Our recent works also reported that SOFC fed by pure H_2 derived from using a palladium membrane reactor can offer higher power density compared with SOFC fed by reformed gas [6]. Even if the power density is a vital technical term used in evaluating SOFC performance, heat generation in SOFC stack should also receive closer attention. With inappropriate operating conditions, some solid parts in an SOFC stack may be damaged due to extreme increase in its temperature. At the present state-of-the-art of SOFC, YSZ typically used as an electrolyte material, the maximum allowable temperature gradient is around 10 K cm^{-1} [7]. A selection of suitable feedstock for SOFC is also an interesting issue in thermal consideration. Although the use of pure H_2 as SOFC feed can offer high power density, its rapid

* Corresponding author. Tel.: +66 2 218 6868; fax: +66 2 218 6877.
E-mail address: Suttichai.A@chula.ac.th (S. Assabumrungrat).

1385-8947/$ – see front matter © 2009 Elsevier B.V. All rights reserved.
doi:10.1016/j.cej.2009.08.001

Nomenclature

A	SOFC stack active area (m^2)
E	electromotive force (V)
E_0	electromotive force at standard pressure (V)
F	Faraday constant (9.6495×10^4) ($C\,mol^{-1}$)
$F_{CH_4,eq}$	methane equivalent flow ($mol\,s^{-1}$)
h	heat transfer coefficient ($W\,m^{-2}\,K^{-1}$)
ΔH_i	heat of reaction for ith reaction ($J\,mol^{-1}$)
ΔH_{elec}	heat of reaction for electrochemical reaction ($J\,mol^{-1}$)
H	energy rate ($J\,s^{-1}$)
i	current density ($A\,cm^{-2}$)
K_{ref}	equilibrium constant for steam reforming reaction (Pa^2)
l_a	thickness of anode (μm)
l_c	thickness of cathode (μm)
L	thickness of electrolyte (μm)
N_k	molar flow rate of component k ($mol\,s^{-1}$)
p_k	partial pressure of component k (Pa)
r_i	reaction rate for ith reaction ($mol\,s^{-1}$)
r_{ref}	reaction rate for steam reforming reaction ($mol\,s^{-1}$)
R	gas constant (8.3145) ($J\,mol^{-1}\,K^{-1}$)
T	temperature (K)
U_f	fuel utilization
V	cell voltage (V)

Greek letters

η_{act}	activation loss (V)
η_{conc}	concentration loss (V)
η_{ohm}	ohmic loss (V)
$\nu_{k,i}$	stoichiometric coefficient of component k in ith reaction
$\nu_{k,elec}$	stoichiometric coefficient of component k in electrochemical reaction

Superscript

j	jth control volume

Subscripts

a	anode channel
ave	average
c	cathode channel
$elec$	electrochemical reaction
i	ith reaction
k	component
ref	reforming reaction
s	solid trilayer

electrochemical reaction may cause high temperature gradient in solid parts of SOFC.

One-dimensional analysis (1D analysis) is an attractive technique to investigate the thermal behavior of an SOFC stack. Sorrentino et al. [8] employed 1D analysis for investigating temperature and current density profiles along the flow direction of a planar SOFC fed by reformed gas. The results obtained from the simulation shows good agreement with the experimental results. The investigation on the operation of indirect internal reforming SOFC (IIR-SOFC) fed by methane employing 1D analysis is performed by Lim et al. [7]. The results indicated that the temperature gradient of SOFC is extremely high near the exit of the anode section (entrance of reforming section) due to high extent of endothermic steam reforming reaction. Several methods were proposed in this literature to minimize the temperature gradient of SOFC, i.e. reduction of catalyst activity, use of non-uniform distributed catalyst and operation under autothermal reforming.

Aguiar et al. [9] studied the thermal behavior of IIR-SOFC towards the change in catalyst activity, fuel inlet temperature, current density and operating pressure utilizing 1D analysis. It was concluded that the increase in operating pressure can diminish both temperature gradient and overall temperature of IIR-SOFC due to the inhibition in reforming reaction rate and the improvement of electrochemical reaction rate. The reduction of the SOFC temperature gradient by minimizing the catalyst activity was also given by Aguiar et al. [10]. With this idea, less active catalyst is used in the reforming chamber of IIR-SOFC and, therefore, the local cooling effect caused from the reforming reaction is inhibited. However, the local cooling also generates, causing from the reforming reaction of unreacted methane at the entrance of the anode chamber. The results indicated that considerable decrease in temperature gradient can be achieved by reducing reforming activity of catalyst in both reforming chamber and anode chamber.

As described above, the performance and thermal behavior of SOFC depend on the type of feedstock and operating conditions. In this study, the performance of SOFC is analyzed employing 1D analysis. The effect of operating voltage, inlet fuel flow rate and inlet air flow rate (in term of excess air) on maximum temperature gradient and maximum temperature of solid part in the SOFC stack, power density and electrical efficiency are investigated for four types of SOFC feedstock, i.e. biogas, biogas-reformed feed, methane-reformed feed and pure H_2. To consider the viability of the operation of SOFC, maximum acceptable temperature gradient and maximum acceptable cell temperature are set to 10 $K\,cm^{-1}$ and 1273 K, respectively.

2. Modeling

2.1. SOFC stack model

Electrochemical reaction is the reaction between fuel (H_2 and CO) and oxidizing agent (air or O_2). At the cathode section, oxygen is reduced to oxygen ions (Eq. (1)) which permeate via the solid electrolyte to react with the hydrogen fuel (Eq. (2)) at the anode section. Only hydrogen is assumed to react electrochemically with oxygen ions due to the fact that the H_2 electro-oxidation is much faster than the CO electro-oxidation [11] and the rate of WGS reaction is fast at high temperatures [12–14]. Ni–Yttria Stabilized Zirconia (YSZ), YSZ and LSM–YSZ are chosen as the materials in the anode, electrolyte and cathode, respectively, of the SOFC stack:

$$\tfrac{1}{2}O_2 + 2e^- \rightarrow O^{2-} \quad (1)$$

$$H_2 + 2O^{2-} \rightarrow H_2O + 2e^- \quad (2)$$

The calculations take place for each control volume in the flow direction of SOFC stack as described in Fig. 1. The open circuit voltage (E^j) of the cell can be calculated from the Nernst equation which is expressed as:

$$E^j = E_0^j + \frac{RT_s^j}{2F} \ln\left(\frac{p_{H_2}^j (p_{O_2}^j)^{1/2}}{p_{H_2O}^j}\right) \quad (3)$$

The actual cell potential (V) is always less than the open circuit voltage (E^j) due to the existence of overpotentials as shown in Eq. (4). The overpotentials can be categorized into three main sources: ohmic overpotential (η_{ohm}^j), activation overpotential (η_{act}^j) and concentration overpotential (η_{conc}^j). The details on the calculation of these three overpotentials given in our recent work [4] are also

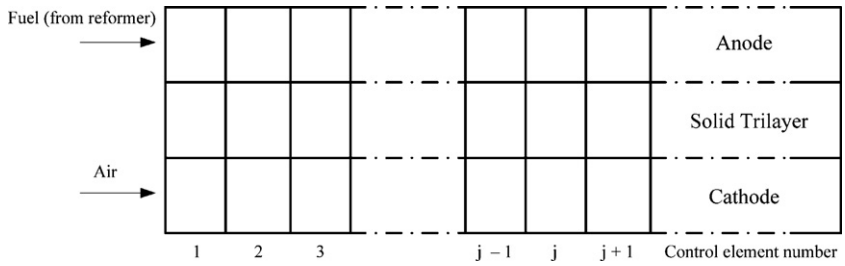

Fig. 1. A small element divided for the calculation in SOFC cell.

used in the present work:

$$V = E^j - \eta^j_{act} - \eta^j_{ohm} - \eta^j_{conc} \tag{4}$$

2.2. Mass and energy balance in SOFC stack

Mass and energy balance computations take place for each control volume (1 mm distance) in the flow direction of the SOFC stack. To simplify the problem, the following assumptions are made: (i) the pressure drop across the cell is neglected; (ii) heat radiation between solid components of the cell is negligible [8]; (iii) heat conduction in the solid electrolyte of the cell is neglected [8]. For pure-H_2 feed, only the electrochemical reaction (Eq. (2)) takes place in the cell anode side. However, for biogas, methane and reformed gas feed, steam reforming reaction (Eq. (5)) and WGS reaction (Eq. (6)) also occur in the anode side of the cell. Thermodynamic equilibrium is assumed for the WGS reaction in each region since its reaction rate is very fast at high temperature as described in Section 2.1. The rate of the reforming reaction in the SOFC stack [15] can be calculated employing Eq. (7) and the mass balance equations for each component in the anode and cathode sides are given in Eqs. (8) and (9), respectively:

$$CH_4 + H_2O \rightarrow CO + 3H_2 \tag{5}$$

$$CO + H_2O \rightarrow CO_2 + H_2 \tag{6}$$

$$r^j_{ref} = 4274A^j\, e^{-(82000/RT^j_s)} p^j_{CH_4} \left(1 - \frac{p^j_{CO}(p^j_{H_2})^3}{p^j_{CH_4} p^j_{H_2O} K^j_{ref}}\right) \tag{7}$$

$$N^{j+1}_{a,k} = N^j_{a,k} + \sum_i \nu_{k,i} r^j_i + \frac{\nu_{k,elec} i^j A^j}{2F} \tag{8}$$

$$N^{j+1}_{c,k} = N^j_{c,k} + \frac{\nu_{k,elec} i^j A^j}{2F} \tag{9}$$

A constant operating voltage along the cell length is assumed as the current collector usually has high electrical conductivity. For the energy calculation, excess heat produced in the solid trilayer caused from reactions (1) and (2) and the irreversibility of the electrochemical reaction is transferred to the anode and cathode channels. Energy balance equations for each small element in anode, cathode and solid trilayer are given in Eqs. (10)–(12), respectively:

$$H^{j+1}_a = H^j_a + h_a A^j (T^j_s - T^j_a) \tag{10}$$

$$H^{j+1}_c = H^j_c + h_c A^j (T^j_s - T^j_c) \tag{11}$$

$$-h_a A^j (T^j_s - T^j_a) - h_c A^j (T^j_s - T^j_c) + \left[\frac{(-\Delta H)^j_{elec}}{2F} - V\right] i^j A^j + \sum_i r^j_i (-\Delta H)^j_i = 0 \tag{12}$$

In the consideration, maximum temperature gradient and maximum temperature in the solid trilayer are determined and compared with maximum acceptable temperature gradient and maximum acceptable cell temperature. Also, the technical terms, i.e. average current density (i_{ave}), fuel utilization (U_f), electrical efficiency and excess air, are defined as follows:

$$i_{ave} = \frac{\sum_j i^j A^j}{\sum_j A^j} \tag{13}$$

$$U_f = \frac{(\sum_j i^j A^j / 2F)}{4F_{CH_4,eq}} \tag{14}$$

$$\%\text{electrical efficiency} = \frac{\text{electrical power}}{\text{LHV of SOFC anode feed} \times \text{anode feed rate}} \times 100 \tag{15}$$

$$\%\text{excess air} = \frac{0.21 \times \text{air feed rate}}{4F_{CH_4,eq}} \times 100 \tag{16}$$

It should be noted that for different types of feed, the feed rates are based on the same "methane equivalent flow ($F_{CH_4,eq}$)" as defined in Section 2.3. The term "excess air" stands for the flow rate of air fed into the SOFC system relative to the stoichiometric flow rate of air required for complete combustion of methane equivalent flow.

2.3. Type of feed in consideration

Four feed types, i.e. biogas, reformed-biogas, reformed-methane and pure-H_2, are considered in this study. Their compositions are determined by the following hypotheses:

Biogas: In this study, the quantity of methane and carbon dioxide in biogas is assumed to be fixed at 60 and 40%, respectively (biogas feed rate = $F_{CH_4,eq}/0.6$). Steam is fed together with biogas into the SOFC cell. The amount of steam is 2.5 times of methane in biogas.

Biogas-reformed feed: Biogas (biogas feed rate = $F_{CH_4,eq}/0.6$) and steam is fed into the reformer prior to be fed to SOFC cell. The quantity of steam fed is equal to that in case of biogas feed. Two chemical reactions, i.e. steam reforming (Eq. (5)) and WGS (Eq. (6)), take place in the reformer. Thermodynamic equilibrium is assumed for the calculation of reformer.

Methane-reformed feed: The calculation of SOFC feed composition for methane-reformed feed is identical to that for biogas-reformed feed; however, the reformer feed is changed from biogas to methane (methane feed rate = $F_{CH_4,eq}$).

Pure-H_2: H_2 is fed directly into SOFC cell. Its feed rate is equal to 4 times of $F_{CH_4,eq}$ (H_2 feed rate = $4 \times F_{CH_4,eq}$).

3. Results and discussion

All models used in this study are written in Visual Basic and the values of all parameters utilized in the computation are summa-

Table 1
Summary of model parameters [18,19].

Parameters	Value
SOFC cell	
l_a	750 μm
l_c	50 μm
L	50 μm
Cell length	400 mm
Cell width	100 mm
Anode channel height	1 mm
Cathode channel height	1 mm
$h_a = h_c$	0.2 kJ m^{-2} s^{-1} K^{-1}
Operating pressure	1 bar
SOFC feed temperature	998 K
Reformer	
Operating temperature	998 K
Operating pressure	1 bar

rized in Table 1. As described in our previous work [16], the SOFC model used in the calculation can well predict the experimental results of Zhao and Virkar [17] for the mixture of hydrogen (97%) and water (3%).

Temperature profiles of the solid part in SOFC fed by different feeds are first investigated. A base case is determined as given in Table 2. The operating voltage for each case is tuned up to achieve U_f = 80% at constant excess air and $F_{CH_4,eq}$. As described in Table 2, SOFC fed by pure-H_2 offers higher power density than the other feed types since it operates at higher operating voltage. Moreover, the maximum temperature gradient and maximum cell temperature of the pure-H_2 feed are much lower than those of the other feed types.

As illustrated in Fig. 2a, excluding SOFC fed by biogas, temperature of the solid part of SOFC increases along the flow direction due to the release of heat generated from irreversibility of the electrochemical reaction. The increase in temperature of the solid part of SOFC with the cell distance is more severe for the biogas-reformed feed and the methane-reformed feed compared with that of the pure-H_2 feed. It is obvious that the operation at high operating voltage can reduce irreversibility loss and also temperature gradient of solid part in the SOFC cell. For the SOFC fed by biogas, the decrease in cell temperature with cell distance is found at the inlet of the cell. This is due to the effect of the endothermic steam reforming reaction. Considering power density profile, power density increases with cell distance as shown in Fig. 2b. The increase in cell temperature along the cell distance causes the reduction of ohmic loss and consequently the power density increases. The increase in power density inside the SOFC cell fed by biogas-reformed feed and methane-reformed feed is more severe than in the case of pure-H_2 feed which is conformed to the increase of temperature with distance in Fig. 2a. However, near the gas outlet of the SOFC cell, the decrease in power density with cell distance is observed even if the increase in cell temperature with cell distance is observed. This implies that the effect of the depletion of H_2 concentration

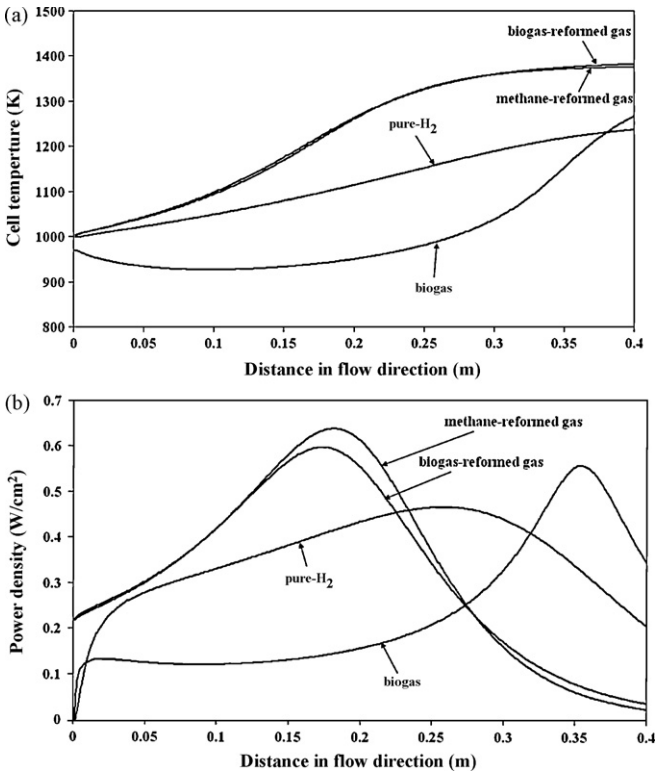

Fig. 2. The variation of (a) cell temperature and (b) power density with cell distance in SOFC cell fed by different types of feed. ($F_{CH_4,eq} = 3 \times 10^{-4}$ mol s^{-1}, excess air = 400%, U_f = 0.8).

with cell distance dominates the effect of the increase in cell temperature near the gas outlet of SOFC. Similar to the change in cell temperature in the flow direction, the decrease in power density of SOFC fed by biogas with cell distance is observed at the gas inlet of the SOFC cell.

The effect of the change in excess air on the maximum temperature gradient and maximum cell temperature of the solid part of SOFC fed by different types of feed is investigated as illustrated in Fig. 3a. As excess air increases, maximum temperature gradient and maximum temperature of the solid part in SOFC cell decrease, implying that SOFC is more feasible to operate at high excess air. However, using large amount of oxidizing agent (air), massive air compressor is required and much of electricity generated in SOFC must be supplied to it. Hence, the appropriate excess air value should be carefully selected. Even if the operation with high excess air can improve the operation viability (lower temperature gradient) of SOFC, the power density and fuel utilization are inhibited for SOFC fed by pure-H_2 as shown in Fig. 3b. This is due to the decrease in cell temperature which results in the increase in ohmic loss as excess air increases. Inversely, the power density and fuel utiliza-

Table 2
Base case in consideration for different feed (U_f = 0.8).

Type of feed	Biogas	Biogas-reformed feed	Methane-reformed feed	Pure-H_2
$F_{CH_4,eq}$ (mol s^{-1})	0.0003	0.0003	0.0003	0.0003
Excess air (%)	400	400	400	400
Operating voltage (V)	0.511	0.695	0.714	0.769
Power density (W cm^{-1})	0.234	0.322	0.33	0.357
Current density (A cm^{-1})	0.457	0.463	0.463	0.464
Electrical efficiency (%)	38.86	42.74	44.51	49.14
U_f	0.8	0.8	0.8	0.8
Electricity produced (W)	93.53	128.67	132.12	142.61
Maximum temperature gradient (K cm^{-1})	28.75	18.08	18.65	7.68
Maximum cell temperature (K)	1267.5	1381.5	1375.7	1236.6

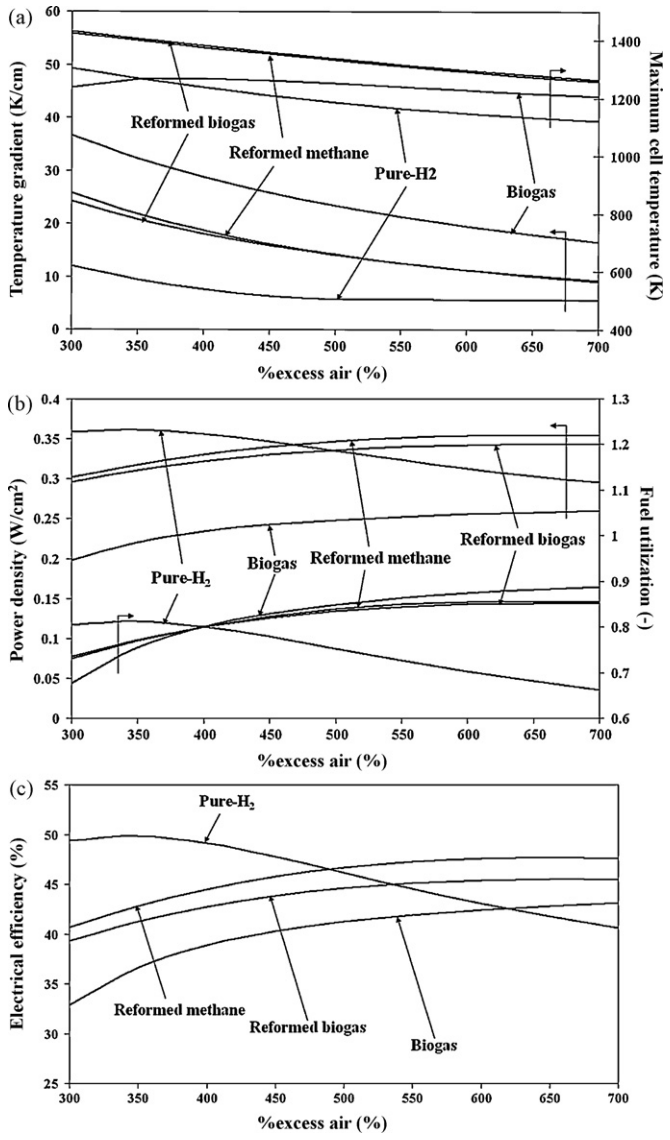

Fig. 3. The effect of the change in excess air on (a) the maximum temperature gradient, maximum cell temperature, (b) power density, fuel utilization and (c) electrical efficiency for SOFC fed by different types of feed. ($F_{CH_4,eq}$ and operating voltage are equal to base case values.)

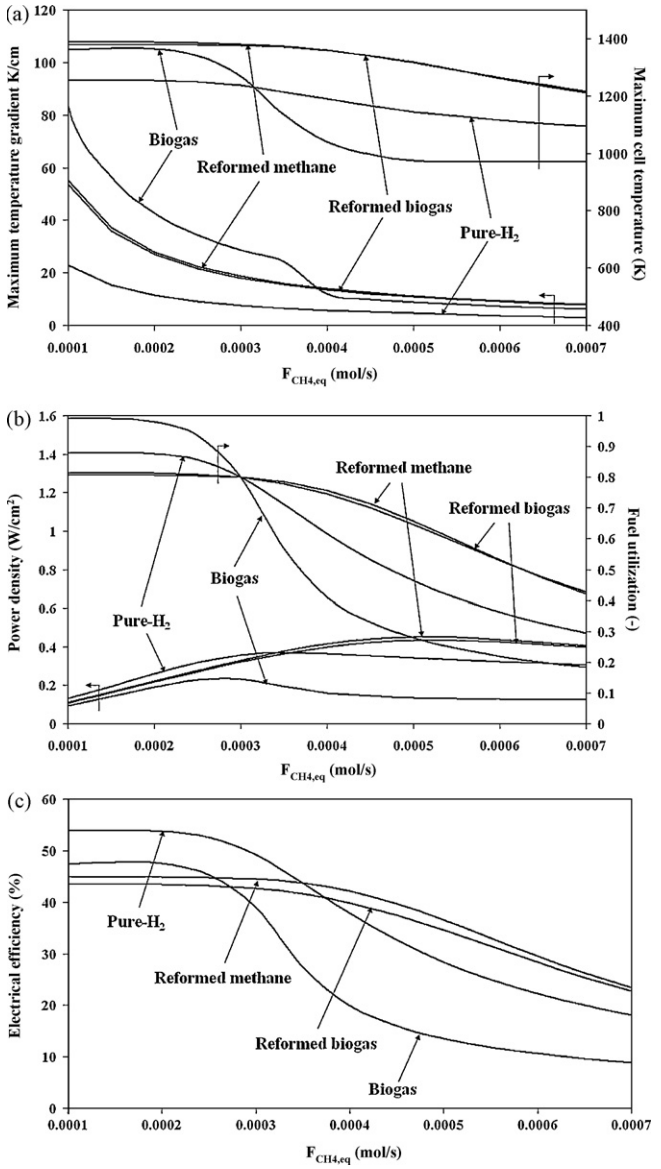

Fig. 4. The effect of the change in $F_{CH_4,eq}$ on (a) the maximum temperature gradient, maximum cell temperature, (b) power density, fuel utilization and (c) electrical efficiency for SOFC fed by different types of feed. (Excess air and operating voltage are equal to base case values.)

tion obtained from biogas-reformed feed, methane-reformed feed and biogas increases with the increase in excess air. This is due to the effect of the increase in electromotive force as the cell temperature decreases could defeat the effect of the increase in ohmic loss. The influence of excess air on the electrical efficiency of SOFC stack is also studied as illustrated in Fig. 3c. Similar to power density and fuel utilization, optimum electrical efficiency is found at low % excess air for SOFC fed by pure-H_2 and the electrical efficiency increases with excess air for SOFC fed by the other feeds.

Fig. 4a shows effect of the change in $F_{CH_4,eq}$ on maximum temperature gradient and maximum cell temperature of the solid part in SOFC fed by different types of feed. The increase in $F_{CH_4,eq}$ can decrease both maximum temperature gradient and maximum temperature in SOFC cell. This is due to the fact that fuel utilization and also the irreversibility are very high for SOFC with low feed rate and they decrease as $F_{CH_4,eq}$ increases as illustrated in Fig. 4b. However, for SOFC fed by biogas, severe decrease in fuel utilization, maximum temperature gradient and maximum cell temperature with the increase in $F_{CH_4,eq}$ can be found at around 3×10^{-4}–4×10^{-4} mol s^{-1}. It can be explained by the fact that CH_4 in biogas cannot be entirely reformed when $F_{CH_4,eq}$ is higher than 3×10^{-4} mol s^{-1}. The optimum power density can be obtained when $F_{CH_4,eq}$ is well tuned up. When the feed rate is low, the increase in feed rate can improve the power density because the fuel utilization does not significantly decrease with the feed velocity. However, for SOFC with high feed rate, the fuel utilization significantly drops as the feed velocity increases while the power density does not significantly decrease with the increase of feed rate. These results imply that $F_{CH_4,eq}$ should be carefully considered to achieve a suitable value. With low $F_{CH_4,eq}$, the solid part in SOFC cell may be damaged due to extremely high temperature. However, with excessively high $F_{CH_4,eq}$, fuel utilization and power density of SOFC may be inhibited. The study on the effect of the change in feed flow rate on the electrical efficiency (Fig. 4c) also indicates that the intermediate fuel flow rate is preferred. Optimum electrical efficiency is found and does not change with feed velocity at low to intermediate fuel feed rates, however, when operating at high fuel velocities, it decreases as the fuel feed rate increases.

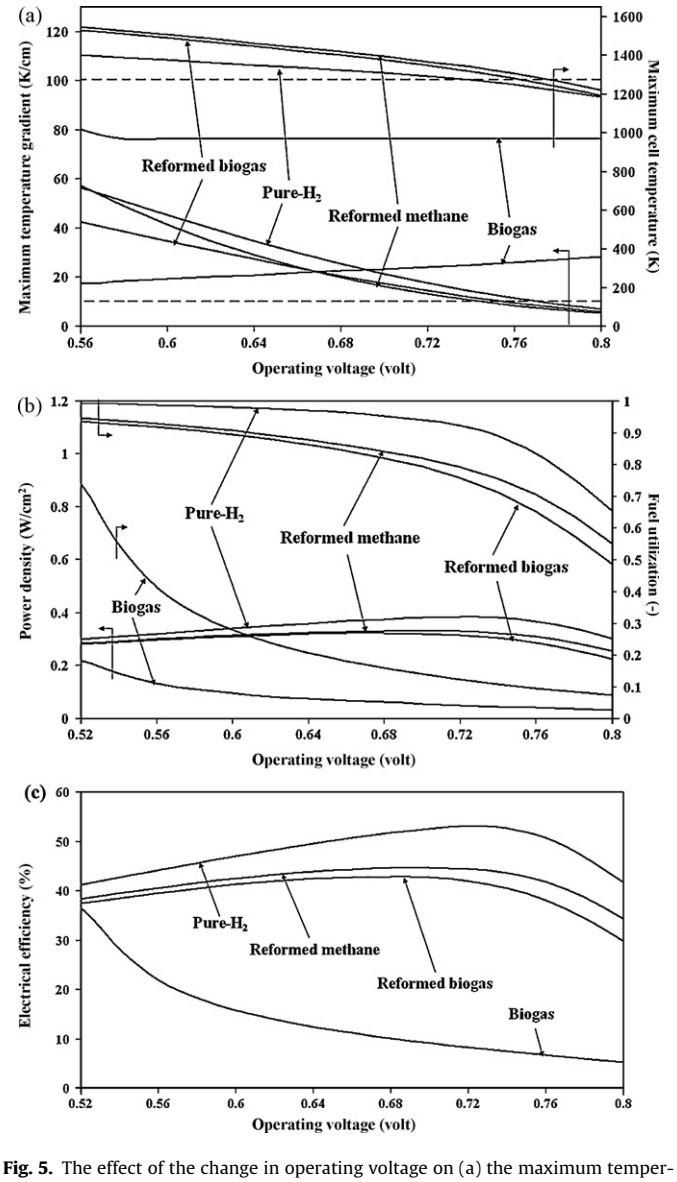

Fig. 5. The effect of the change in operating voltage on (a) the maximum temperature gradient, maximum cell temperature, (b) power density, fuel utilization and (c) electrical efficiency for SOFC fed by different types of feed in case that $F_{CH_4,eq}$ is equal to 3×10^{-4} mol s^{-1}. (Excess air is equal to base case values.)

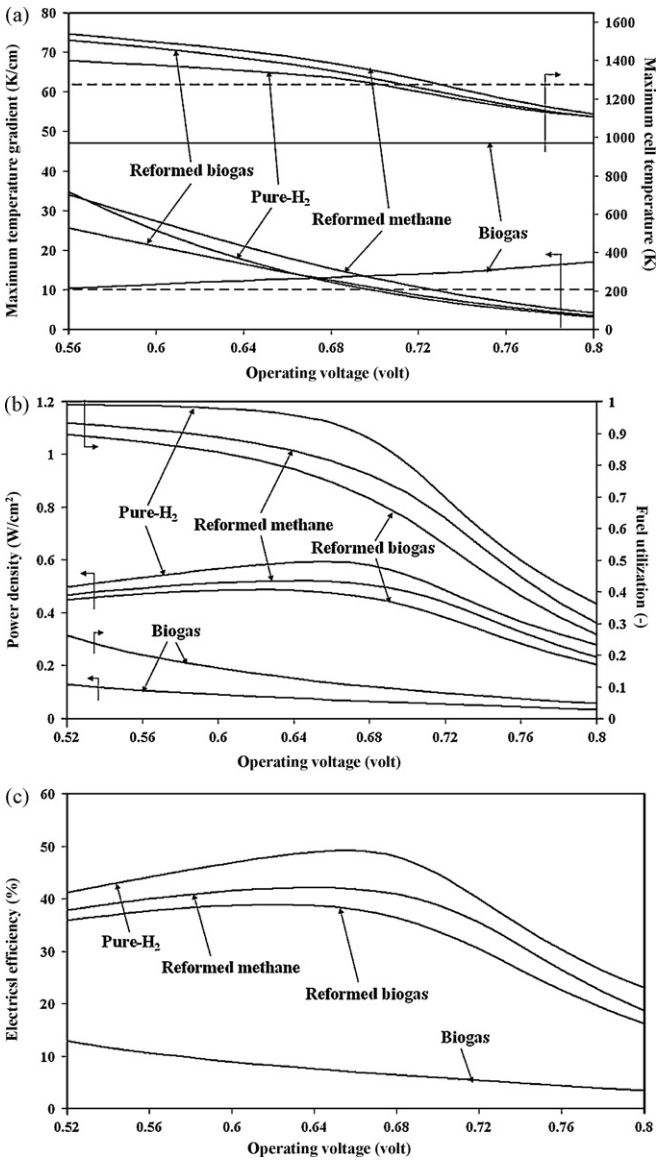

Fig. 6. The effect of the change in operating voltage on (a) the maximum temperature gradient, maximum cell temperature, (b) power density, fuel utilization and (c) electrical efficiency for SOFC fed by different types of feed in case that $F_{CH_4,eq}$ is equal to 5×10^{-4} mol s^{-1}. (Excess air is equal to base case values).

To compare the performance of SOFC fed by different feed, the effects of the operating voltage on the maximum temperature gradient, maximum cell temperature, power density, fuel utilization and electrical efficiency were investigated as shown in Figs. 5 and 6 for $F_{CH_4,eq}$ of 3×10^{-4} and 5×10^{-4} mol s^{-1}, respectively. The excess air is kept to be constant at the base case of 400% excess. The dash lines in Figs. 5a and 6a represent the maximum acceptable temperature gradient (MATG), 10 K cm^{-1}, and maximum acceptable cell temperature (MACT), 1273 K. As shown in Figs. 5a and 6a, excluding SOFC fed by biogas, the increase in operating voltage can improve the operation viability of SOFC. As the operating voltage increases, heat generation caused from the irreversibility is reduced and the cell temperature drops. Inversely, for SOFC fed by biogas, the operation at low operating voltage is preferred since large amount of heating energy generated from the irreversibility can be used in endothermic methane steam reforming and the decreasing rate of cell temperature in the flow direction is reduced. The results in Figs. 5a and 6a also imply that it is difficult to operate SOFC fed by biogas at excess air lower than 400% since the maximum temperature gradient and maximum cell temperature would increase. Moreover, as illustrated in Figs. 5b, 5c, 6b and 6c, the fuel utilization, power density and electrical efficiency of SOFC fed by biogas are significantly lower than those of SOFC fed by the other feeds. Therefore, it can be concluded that direct biogas feed is not a recommended feedstock for SOFC. The operation at high operating voltage is desired to minimize the temperature and temperature gradient of solid part in SOFC. However, the fuel utilization obtained at this condition is not satisfied, as shown in Figs. 5b and 6b, the fuel utilization decreases as the operating voltage increases. When operating at the same operating voltage, SOFC fed by pure-H_2 offers higher fuel utilization compared with SOFC fed by the other feed types. This implies that H_2 concentration is the important factor which affects the rate of electrochemical reaction. The optimum operating voltage which offers maximum power density can be observed as illustrated in Figs. 5b and 6b. When the operating voltage is lower than the optimum value, the increase in operating voltage can improve the power density since fuel utilization does not significantly decrease. The pronounced decrease in fuel utilization with the increase in operating voltage can be found as the operating volt-

Table 3
Summary of SOFC fed by different feed operating at the optimum operating condition in case that $F_{CH_4,eq}$ and excess air are equal to 3×10^{-4} mol s^{-1} and 400%, respectively.

Type of feed	Biogas	Biogas-reformed feed	Methane-reformed feed	Pure-H_2
$F_{CH_4,eq}$ (mol s^{-1})	0.0003	0.0003	0.0003	0.0003
Excess air (%)	400	400	400	400
Operating voltage (V)	n.a.	0.764	0.778	0.746
Power density (W cm^{-1})	n.a.	0.282	0.29	0.379
Current density (A cm^{-1})	n.a.	0.369	0.373	0.508
Electrical efficiency (%)	n.a.	37.48	39.13	52.20
U_f	n.a.	0.638	0.645	0.877
Electricity produced (W)	n.a.	112.82	116.14	151.48
Maximum temperature gradient (K cm^{-1})	n.a.	9.09	9.21	9.95
Maximum cell temperature (K)	n.a.	1272.06	1271.71	1267.26

Table 4
Summary of SOFC fed by different feed operating at the optimum operating condition in case that $F_{CH_4,eq}$ and excess air are equal to 5×10^{-4} mol s^{-1} and 400%, respectively.

Type of feed	Biogas	Biogas-reformed feed	Methane-reformed feed	Pure-H_2
$F_{CH_4,eq}$ (mol s^{-1})	0.0005	0.0005	0.0005	0.0005
Excess air (%)	400	400	400	400
Operating voltage (V)	0.48	0.715	0.732	0.704
Power density (W cm^{-1})	0.167	0.393	0.407	0.532
Current density (A cm^{-1})	0.349	0.55	0.556	0.755
Electrical efficiency (%)	16.69	31.35	32.91	43.97
U_f	0.366	0.57	0.577	0.783
Electricity produced (W)	66.97	157.27	162.79	212.69
Maximum temperature gradient (K cm^{-1})	9.74	9.09	9.35	9.38
Maximum cell temperature (K)	1030.88	1271.67	1271.80	1272.52

age is higher than the optimum value; hence, power density also decreases. The change in electrical efficiency with the operating voltage is in the same tendency as the change in power density as shown in Figs. 5c and 6c.

Tables 3 and 4 summarize the optimum operating condition of SOFC fuelled by each feed type for $F_{CH_4,eq} = 3 \times 10^{-4}$ and 5×10^{-4} mol s^{-1}, respectively. These results imply that, with the same cell dimension, excess air and $F_{CH_4,eq}$, SOFC fed by pure-H_2 feed offers higher power density than SOFC fed by the other fuel types. For $F_{CH_4,eq}$ of 3×10^{-4} and 5×10^{-4} mol s^{-1}, power density of SOFC fuelled by pure-H_2 is 0.379 and 0.532 W cm^{-2}, respectively. Also, the values of electrical efficiency of 52.20 and 43.97% are achieved for SOFC fed by pure-H_2 with $F_{CH_4,eq}$ of 3×10^{-4} and 5×10^{-4} mol s^{-1}, respectively. Methane-reformed feed is fairly better than biogas-reformed feed due to its higher hydrogen concentration. With excess air of 400%, biogas-fed SOFC is not viable to operate when $F_{CH_4,eq}$ is equal to 3×10^{-4} mol s^{-1}. On the other hand, at 5×10^{-4} mol s^{-1} of $F_{CH_4,eq}$ the SOFC fed by biogas offers extremely lower power density (0.167 W cm^{-2}) compared with the other feeds.

4. Conclusion

Mathematical model of SOFC has been developed for investigating operation viability and performance of SOFC fed by different feeds. Four types of fuel feed, i.e. biogas, biogas-reformed feed, methane-reformed feed and pure-H_2, are considered in this study. In operation viability investigation, maximum temperature gradient and maximum cell temperature are employed as the indicators. Additionally, power density and electrical efficiency are considered as performance indicators. The effect of the change in operating conditions, i.e. excess air, fuel feed rate and operating voltage, are also investigated. The increase in excess air can improve the operation viability of SOFC; however, with surplus excess air, its power density is inhibited. Also, the operation of SOFC is viable at high fuel feed rate. Nevertheless, excess high fuel feed rate is not favored since the SOFC cell could be saturated with current, resulting in the dropping of the fuel utilization. Excluding SOFC fed by biogas, SOFC becomes operation viable as it operates at high operating voltage. Inversely, for biogas-fuelled SOFC, the operation at low operating voltage is preferred in thermal management point of view. The optimum operating voltage which offers utmost power density can be observed. Conclusively, the value of excess air, fuel feed rate and operating voltage should be carefully adjusted to obtain best possible power density and reasonable temperature and temperature gradient. SOFC fed by pure-H_2 offers highest power density compared with that fed by the other feeds. Biogas-fed SOFC can become operation viable as it operates at high excess air; nevertheless, its power density is extremely lower than SOFC fuelled by the other feeds. Methane-reformed feed offers higher SOFC power density compared with biogas-reformed feed since its H_2 concentration is higher. Although pure-H_2 is an attractive fuel for SOFC, the transformation process of a primary fuel to H_2 should also be received the attention.

Acknowledgement

The support from The Thailand Research Fund and Commission on Higher Education is gratefully acknowledged.

References

[1] R.J. Spiegel, J.L. Preston, Test results for fuel cell operation on anaerobic digester gas, J. Power Sources 86 (2000) 283–288.
[2] S. Baron, N. Brandon, A. Atkinson, B. Steele, R. Rudkin, The impact of wood-derived gasification gases on Ni-CGO anodes in intermediate temperature solid oxide fuel cells, J. Power Sources 126 (2004) 58–66.
[3] V.M. Janardhanan, V. Heuveline, O. Deutschmann, Performance analysis of a SOFC under direct internal reforming conditions, J. Power Sources 172 (2007) 296–307.
[4] P. Piroonlerkgul, S. Assabumrungrat, N. Laosiripojana, A.A. Adesina, Performance of biogas-fed solid oxide fuel cell system integrated with membrane module for CO_2 removal, Chem. Eng. Process.: Process Intensification 48 (2009) 672–682.
[5] R. Suwanwarangkul, E. Croiset, E. Entchev, S. Charojrochkul, M.D. Pritzker, M.W. Fowler, P.L. Douglas, S. Chewathanakup, H. Mahaudom, Experimental and modeling study of solid oxide fuel cell operating with syngas fuel, J. Power Sources 161 (2006) 308–322.
[6] W. Sangtongkitcharoen, S. Vivanpatarakij, N. Laosiripojana, A. Arpornwichanop, S. Assabumrungrat, Performance analysis of methanol-fueled solid oxide fuel cell system incorporated with palladium membrane reactor, Chem. Eng. J. 138 (2008) 436–441.

[7] L.T. Lim, D. Chadwick, L. Kershenbaum, Achieving autothermal operation in internally reformed solid oxide fuel cells: simulation studies, Ind. Eng. Chem. Res. 44 (2005) 9609–9618.
[8] M. Sorrentino, C. Pianese, Y.G. Guezennec, A hierarchical modeling approach to the simulation and control of planar solid oxide fuel cells, J. Power Sources 180 (2008) 380–392.
[9] P. Aguiar, D. Chadwick, L. Kershenbaum, Modelling of an indirect internal reforming solid oxide fuel cell, Chem. Eng. Sci. 57 (2002) 1665–1677.
[10] P. Aguiar, D. Chadwick, L. Kershenbaum, Effect of methane slippage on an indirect internal reforming solid oxide fuel cell, Chem. Eng. Sci. 59 (2004) 87–97.
[11] M.A. Khaleel, Z. Lin, P. Singh, W. Surdoval, D. Collin, A finite element analysis modeling tool for solid oxide fuel cell development: coupled electrochemistry, thermal and flow analysis in MARC(R), J. Power Sources 130 (2004) 136–148.
[12] R. Blom, I.M. Dahl, A. Slagtem, B. Sortland, A. Spjelkavik, E. Tangstad, Carbon dioxide reforming of methane over lanthanum-modified catalysts in a fluidized-bed reactor, Catal. Today 21 (1994) 535–543.
[13] M.C.J. Bradford, M.A. Vannice, Catalytic reforming of methane with carbon dioxide over nickel catalysts. II. Reaction kinetics, Appl. Catal. A: Gen. 142 (1996) 97–122.
[14] H.M. Swaan, V.C.H. Kroll, G.A. Martin, C. Mirodatos, Deactivation of supported nickel catalysts during the reforming of methane by carbon dioxide, Catal. Today 21 (1994) 571–578.
[15] E. Achenbach, E. Riensche, Methane/steam reforming kinetics for solid oxide fuel cells, J. Power Sources 52 (1994) 283–288.
[16] P. Piroonlerkgul, S. Assabumrungrat, N. Laosiripojana, A.A. Adesina, Selection of appropriate fuel processor for biogas-fuelled SOFC system, Chem. Eng. J. 140 (2008) 341–351.
[17] F. Zhao, A.V. Virkar, Dependence of polarization in anode-supported solid oxide fuel cells on various cell parameters, J. Power Sources 141 (2005) 79–95.
[18] P. Aguiar, C.S. Adjiman, N.P. Brandon, Anode-supported intermediate temperature direct internal reforming solid oxide fuel cell. I. Model-based steady-state performance, J. Power Sources 138 (2004) 120–136.
[19] M. Ni, M.K.H. Leung, D.Y.C. Leung, Parametric study of solid oxide fuel cell performance, Energy Convers. Manage. 48 (2007) 1525–1535.

ภาคผนวก 10

Fuel Processing Technology 91 (2010) 121–126

Contents lists available at ScienceDirect

Fuel Processing Technology

journal homepage: www.elsevier.com/locate/fuproc

Effect of calcination temperature on characteristics of sulfated zirconia and its application as catalyst for isosynthesis

Nicha Tangchupong [a], Watcharapong Khaodee [a], Bunjerd Jongsomjit [a], Navadol Laosiripojana [b], Piyasan Praserthdam [a], Suttichai Assabumrungrat [a,*]

[a] Center of Excellence in Catalysis and Catalytic Reaction Engineering, Department of Chemical Engineering, Faculty of Engineering, Chulalongkorn University, Bangkok 10330, Thailand
[b] The Joint Graduate School of Energy and Environment, King Mongkut's University of Technology Thonburi, Bangkok 10140, Thailand

ARTICLE INFO

Article history:
Received 11 April 2009
Received in revised form 29 July 2009
Accepted 4 September 2009

Keywords:
CO hydrogenation
Isobutene
Isosynthesis
Sulfated zirconia
Synthesis gas

ABSTRACT

The effect of catalyst calcination temperature (450 °C, 600 °C, and 750 °C) on catalytic performance of synthesized and commercial grade sulfated zirconia catalysts towards isosynthesis was studied. The characteristics of these catalysts were determined by using various techniques including BET surface area, XRD, NH_3- and CO_2-TPD, ESR, and XPS in order to relate the catalytic reactivity with their physical, chemical, and surface properties. It was found that, for both synthesized and commercial sulfated zirconia catalysts, the increase of calcination temperature resulted in the increase of monoclinic phase in sulfated zirconia, and the decrease of acid sites. According to the catalytic reactivity, at high calcination temperature, lower CO conversion, but higher isobutene production selectivity was observed from commercial sulfated zirconia. As for synthesized sulfated zirconia, the isobutene production selectivity slightly decreased with increasing calcination temperature, whereas the CO conversion was maximized at the calcination temperature of 600 °C. We concluded from the study that the difference in the calcination temperatures influenced the catalytic performance, sulfur content, specific surface area, phase composition, the relative intensity of Zr^{3+}, and acid–base properties of the catalysts.

1. Introduction

Isosynthesis via carbon monoxide hydrogenation is an attractive route for producing isobutene which is an important raw material for the production of important octane enhancers such as methyl *tert*-butyl ether (MTBE) and ethyl *tert*-butyl ether (ETBE). Currently, isobutene is extracted from the C_4 stream in petroleum refining process. However, the supply of isobutene from the petroleum products is likely inadequate in the near future. Syngas derived from a renewable resource such as biomass is expected to be an alternative source for the production of isobutene. This route shows potential benefits, for examples, (i) the chosen resource of isobutene production is renewable, (ii) carbon dioxide, a byproduct of fermentation process, is substantially consumed to produce syngas, thus reducing the CO_2 emission to the atmosphere, and (iii) the ratio of carbon monoxide to hydrogen of 1:1 for the syngas from fermentation of biomass is suitable for the isosynthesis reaction.

Since the first report by Pichler and Ziesecke in 1950s [1], some research groups have focused on developing suitable catalysts for the isosynthesis. Difficult reducible oxides such as thoria (ThO_2) and zirconia (ZrO_2) have been reported to be suitable catalysts for isosynthesis reaction rather than other reduced transition metals [2]. Most studies [3–7] have demonstrated that zirconia is a selective catalyst for isosynthesis. Then, various mixed metal oxides such as Sm_2O_3–ZrO_2 [8] and CeO_2–TiO_2 [9] and Ca-promoted zirconia [10] have been tested. In our previous works, micron- and nanoscale zirconia and ceria were tested for the isosynthesis [11,12]. It was reported that the acid–base properties, the crystallite size and crystal phase essentially influence the catalytic performance. At the same crystallite size, ceria shows higher activity than zirconia [11]. The temperature ramping rate during calcination also has an effect on characteristics of nanoscale zirconia and its catalytic performance for isosynthesis [12]. It was shown that both tetragonal phase in zirconia and intensity of Zr^{3+} influence the selectivity to isobutene. ZrO_2–CeO_2 mixed oxide catalysts synthesized by coprecipitation and physical mixing methods with various contents of CeO_2 were also investigated [13]. It was reported that the catalysts prepared by the physical mixing method offer higher catalytic activity than those prepared by the coprecipitation method. The change in the selectivity of isobutene in hydrocarbons of the catalysts was well-correlated with the change in intensity of Zr^{3+}. The isosynthesis of sulfated zirconia catalysts with various contents of sulfur (from 0.1 to 0.75 wt.%) were studied [14]. It was observed that the catalytic reactivity and selectivity significantly improved by sulfur loading. This can be related to the acid–base properties, specific surface area and phase composition.

* Corresponding author. Tel.: +66 2 218 6868: fax: +66 2 218 6877.
E-mail address: Suttichai.A@chula.ac.th (S. Assabumrungrat).

0378-3820/$ – see front matter © 2009 Elsevier B.V. All rights reserved.
doi:10.1016/j.fuproc.2009.09.003

In this work, the effect of calcination temperature on characteristics of sulfated zirconia and its reactivity toward isosynthesis reaction were investigated. Both synthesized and commercial sulfated zirconias were applied and various characterization techniques i.e. XRD, TPD, ESR and XPS were employed to relate the physical characteristics with its catalytic performance.

2. Experimental

2.1. Preparation of synthesized sulfated zirconia

Zirconia (ZrO_2) was initially prepared by the precipitation method. A solution of 0.15 M zirconyl nitrate ($ZrO(NO_3)_2$) was slowly dropped into a well-stirred precipitating solution of 2.5 wt.% ammonium hydroxide (NH_4OH) at room temperature. The pH of the solution was controlled at 10. The resulting precipitate was removed, and then washed with deionized water. The obtained sample was then dried overnight at 110 °C and calcined at 450 °C for 3 h with a temperature ramping rate of 5 °C/min. Sulfated zirconia was then prepared by the incipient wetness impregnation method. Sulfuric acid was doped on zirconia with a sulfur content of 0.75 wt.% at room temperature. The obtained sample was then dried overnight at 110 °C and calcined at 450, 600, or 750 °C for 3 h with a temperature ramping rate of 5 °C/min. These catalysts were named as 0.75% SZ (N-450), 0.75% SZ (N-600), and 0.75% SZ (N-750), respectively.

For commercial sulfated zirconia obtained from Aldrich, the catalysts were also calcined at 450, 600, and 750 °C for 3 h with a temperature ramping rate of 5 °C/min. These catalysts were denoted as SZ(450), SZ(600), and SZ(750), respectively.

2.2. Catalyst characterization

2.2.1. N_2 physisorption

The measurement of BET surface area, cumulative pore volume and average pore diameter were performed by the N_2 physisorption using a Micromeritics ASAP 2020 surface area and porosity analyzer.

2.2.2. X-ray diffraction (XRD)

The XRD spectra of catalysts were measured by a SIEMENS D5000 X-ray diffractometer using Cu K_α radiation with a nickel filter over the 2θ ranging from 20 to 80°. The crystal sizes of the prepared catalysts were obtained by XRD line broadening using the Scherrer's equation. The characteristic peaks at $2\theta = 28.2°$ and 31.5° for (-111) and (111) reflexes, respectively, were assigned to the monoclinic phase in ZrO_2. The characteristic peak at $2\theta = 30.2°$ for the (111) reflex in the XRD patterns represented the tetragonal phase in ZrO_2.

The percents of tetragonal and monoclinic phases in ZrO_2 were calculated by a comparison of the areas for the characteristic peaks of the monoclinic phase and the tetragonal phase. The percent of each phase was determined by means of the Gaussian areas $h \times w$, where h and w are the height and half-height width of the corresponding XRD characteristic peak as follows [5]:

$$\%\ monoclinic\ phase = \frac{\sum (h \times w)\, monoclinic\ phase}{\sum (h \times w) monoclinic\ and\ tetragonal\ phase}$$

$$\%\ tetragonal\ phase = \frac{\sum (h \times w)\, tetragonal\ phase}{\sum (h \times w)\, monoclinic\ and\ tetragonal\ phase}$$

2.2.3. Temperature-programmed desorption (TPD)

The acid–base properties of catalysts were measured by using temperature-programmed desorption of ammonia and carbon dioxide (NH_3- and CO_2-TPD) techniques. The experiments were carried out using a flow apparatus. The catalyst sample (0.1 g) was treated at 450 °C in a helium flow for 1 h and then saturated with a 15% NH_3/He mixture or a pure CO_2 flow after cooling to 100 °C. After purging with the helium at 100 °C for 1 h to remove weakly physisorbed NH_3 or CO_2, the sample was heated to 450 °C at a rate of 20 °C/min in a helium flow (50 cm^3/min). The desorption amounts of NH_3 and CO_2 were used to calculate the amounts of acid and base sites on the catalyst surface, respectively.

2.2.4. Electron spin resonance spectroscopy (ESR)

Electron spin configuration was detected by using electron spin resonance spectroscopy (ESR) (JEOL model JES-RE2X). The sample was degassed before measurement at room temperature. This technique typically detects a spin of unpaired electron, which is related to the existence of Zr^{3+} sites. Based on equal weight of each catalyst tested with ESR, the peak height of Zr^{3+} signal can be assigned to the quantity of Zr^{3+}.

2.2.5. X-ray photoelectron spectroscopy (XPS)

The XPS spectra and the binding energy of sulfated zirconia catalysts were determined using a Kratos Amicus X-ray photoelectron spectrometer. The analyses were carried out with Mg K_α X-ray source under a working pressure of 1×10^{-6} Pa at current of 20 mA and 12 kV, resolution of 0.1 eV/step, and pass energy at 75 eV. The catalyst samples were mounted on a carbon tape. The binding energy was calibrated using the C 1s peak at 285.0 eV as reference. This technique was mainly quantified the sulfur content on the catalyst surface.

2.3. Reaction study

Isosynthesis was carried out at 400 °C and atmospheric pressure in a fixed-bed quartz reactor. An inlet mixture of $CO/H_2/N_2$ with the flow rate of 10/10/5 cm^3/min was fed to the reactor packed with 2 g of catalyst. The reactor effluent samples were taken at intervals of 1.5 h and analyzed using the gas chromatography technique. Thermal conductivity detectors (TCD) with molecular sieve 5A and Porapak-Q columns were applied to detect the CO and CO_2, respectively. A flame ionization detector (FID) with a VZ-10 column was used to detect the light hydrocarbons such as C_1–C_4 hydrocarbons. The steady-state rate for all catalysts was obtained after 20 h.

3. Results and discussion

Two types of sulfated zirconia catalysts; i.e., synthesized 0.75%SO_4/ZrO_2 and commercial sulfated zirconia were used in the study. The calcination temperatures were at 450, 600 and 750 °C. The differences in physical, chemical, and surface properties for both types of catalysts were provided in Section 3.1. The relationships between those properties and catalytic performances were described in Section 3.2.

3.1. Catalyst characterization

The XRD patterns of synthesized and commercial sulfated zirconia catalysts are illustrated in Figs. 1 and 2. As seen from these figures, the calcination temperature shows significant impact on both crystallite size and crystal phase. Considering the characteristic peak areas of monoclinic and tetragonal phases (Fig. 1), it was observed that the former was more dominant than the latter upon increasing in calcination temperature. In addition, the phase composition of each 0.75% SO_4/ZrO_2–N catalyst can be calculated as shown in Table 1. The results from that table indicate that the crystal size in monoclinic phase and the fraction of monoclinic phase increase with increasing the calcination temperature. It should be noted that the calcination temperature also affected the phase structure of commercial SZ as shown in Fig. 2. The XRD patterns of catalyst exhibited tetragonal–monoclinic phase transformation. The tetragonal phase decreased with increased calcination temperature. Most published studies agree that sulfation retards crystallization of zirconia support and then the

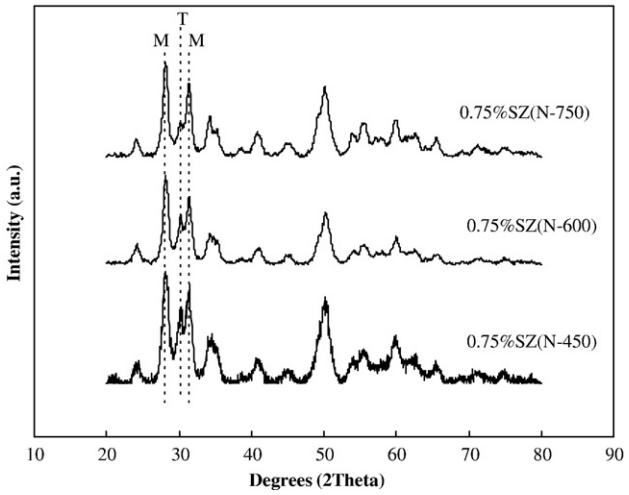

Fig. 1. XRD patterns of 0.75% SZ (N) at various calcination temperatures.

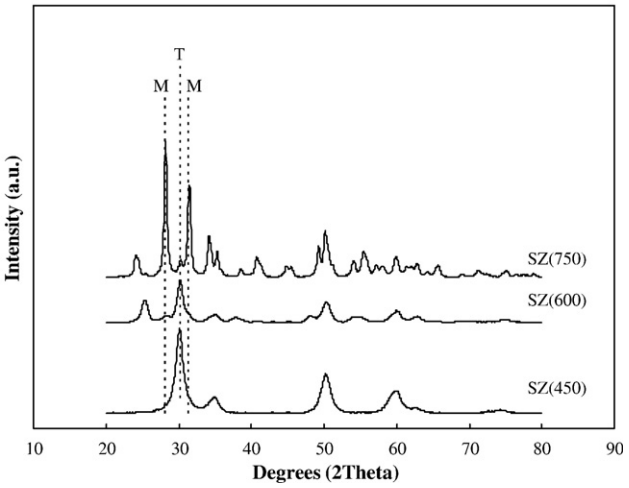

Fig. 2. XRD patterns of commercial SO_4/ZrO_2 at various calcination temperatures.

transition from the tetragonal phase to the monoclinic phase occurs [15]. According to monoclinic–tetragonal phase transformation of zirconia, the tetragonal phase should be formed above 1170 °C, but the zirconia prepared by precipitation from aqueous salt solution can be occurred as a metastable tetragonal phase at lower temperature. Moreover, the transformation of the metastable tetragonal phase into the monoclinic phase was probably due to the lower surface energy of the tetragonal phase compared to monoclinic phase [16,17]. In fact, phase transformation of catalyst can be occurred by varying the calcination temperature. In this case, increased calcination temperature would correlate with the alteration of crystal structure.

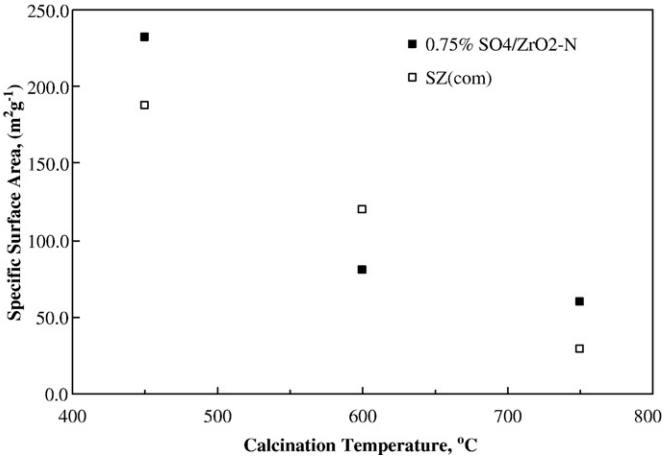

Fig. 3. Surface areas of the catalysts as a function of calcination temperature.

Fig. 3 shows the effect of calcination temperature on the specific surface areas of both synthesized and commercial sulfated zirconia. It is clear that the specific surface area of all catalysts immediately decreases with increased calcination temperature and the decreases in surface area with temperature are almost linear. Due to the effect of crystal growth, the catalyst exhibited the larger crystallite size with increased calcination temperature, leading to lower surface area. The physical properties of ZrO_2 catalysts characterized by means of N_2 physisorption such as BET surface area, cumulative pore volume and average pore diameter are summarized in Table 2. The surface area calculated from adsorption isotherm using BET equation was in the range of 29–232 m^2/g. These sulfated zirconia catalysts that were calcined at the lowest temperature exhibited higher specific surface area, furthermore, average pore diameter was dramatically increased with increased calcination temperature. Considering, pore size distribution of catalysts as shown in Fig. 4, these peaks of 0.75%SO_4/ZrO_2–N were shifted to higher pore diameter whereas the SZ commercial peaks decreased. Nevertheless, similar distribution trends were observed for all catalysts.

Based on the XPS measurement, the atomic concentrations of O 1s, Zr 3d, and S 2p present on the surface of sulfated zirconia catalysts are summarized in Table 3. It reveals that the catalyst has binding energies of 533.2 eV for O 1s, 183.4 eV for Zr 3d, and 169.5 eV for S 2p. The XPS results indicate less sulfur contents on the catalyst surface of synthesized and commercial sulfated zirconia catalysts upon higher calcination temperature. These results are similar to those reported by Fărcaşiu and Li [18]. In addition, the sulfated group on the sulfated zirconia was labile sulfates, which can be reduced by washing with water, increasing the calcination temperature, and duration during calcination step [19].

NH_3-TPD profiles of 0.75%SO_4/ZrO_2–N and commercial sulfated zirconia catalysts calcined at different temperatures are illustrated in Fig. 5. As seen in that figure, the calcination temperature apparently

Table 1
Characteristics of ZrO_2 at various calcination temperatures.

Catalysts	Phase	Crystal size (nm)[a]		% Tetragonal phase[a]
		M[b]	T[c]	
0.75% SZ (N-450)	M, T	9.1	8.1	28.9
0.75% SZ (N-600)	M, T	9.7	8.1	27.5
0.75% SZ (N-750)	M, T	11.0	6.5	25.6
SZ(450)	T	n.d.	7.1	100.0
SZ(600)	M, T	5.4	8.5	78.3
SZ(750)	M, T	19.5	10.7	11.3

[a] Based on XRD line broadening.
[b] Monoclinic phase in ZrO_2.
[c] Tetragonal phase in ZrO_2.

Table 2
N_2 physisorption results.

Catalysts	BET surface area[a] (m^2/g)	Cumulative pore volume[b] (cm^3/g)	Average pore diameter[c] (nm)
0.75% SZ (N-450)	232.2	0.351	4.8
0.75% SZ (N-600)	80.5	0.171	5.1
0.75% SZ (N-750)	60.0	0.157	6.3
SZ(450)	187.1	0.172	3.1
SZ(600)	119.3	0.180	3.7
SZ(750)	29.4	0.067	7.0

[a] Error of measurement = ±5%.
[b] BJH desorption cumulative volume of pores between 1.7 and 300 nm diameter.
[c] BJH desorption average pore diameter.

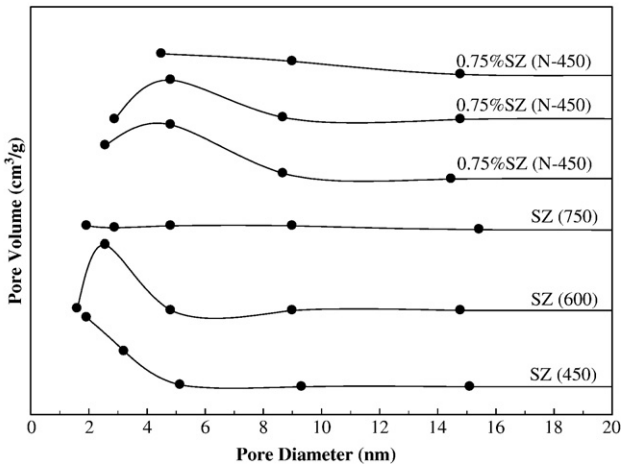

Fig. 4. Pore size distribution of sulfated zirconia catalysts.

Table 3
Results from XPS.

Catalysts	Atomic concentration (%)		
	O 1s	Zr 3d	S 2p
0.75% SZ (N-450)	79.03	20.43	0.54
0.75% SZ (N-600)	79.22	20.49	0.29
0.75% SZ (N-750)	78.85	20.92	0.23
SZ(450)	71.29	28.06	0.65
SZ(600)	71.23	28.28	0.49
SZ(750)	73.55	26.16	0.29

affects the acid–base properties of catalysts. From the calculation of acid and base sites, the presence of weak and moderate acid sites is related to the characteristic peaks of desorption temperature. With increased calcination temperature, the profiles did not change, but the amount of acid sites significantly decreased. The amounts of acid and base sites of sulfated zirconia catalysts are listed in Table 4. As mentioned by Hino et al. [20], the structural model of sulfate species contained mainly three or four S atoms with two ionic bonds of S–O–Zr in addition to coordination bonds of S O, acting as Lewis acid sites on the S atoms. The results showed that the acidity of sulfated zirconia commercial catalyst was higher than another one. The acid sites at lower calcination temperature of catalysts were higher than other catalysts because sulfated groups were still remained on surface of catalysts.

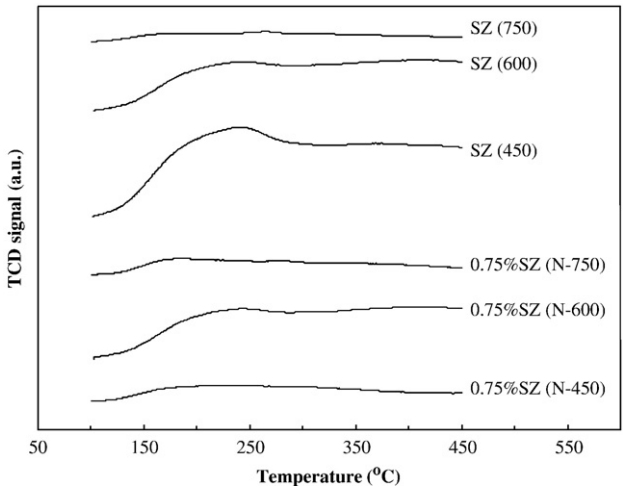

Fig. 5. NH_3-TPD profiles of SO_4–ZrO_2 catalysts.

Table 4
Results from NH_3- and CO_2-TPD.

Catalysts	Total sites (μmol/g)	
	Acid sites[a]	Base sites[b]
0.75% SZ (N-450)	917	39
0.75% SZ (N-600)	712	46
0.75% SZ (N-750)	432	53
SZ(450)	1881	n.d.
SZ(600)	1032	n.d.
SZ(750)	58	n.d.

n.d., not determined.
[a] From NH_3-TPD.
[b] From CO_2-TPD.

The CO_2-TPD profiles for synthesized 0.75%SO_4/ZrO_2–N calcined at different temperatures are shown in Fig. 6. Clearly, the pattern changed with the calcination temperature, indicating higher amount of moderate base sites along with the disappearance of weak base sites. Table 4 indicates that base sites increased with increased calcination temperature, whereas the acid sites decreased. The results showed that the percentage of monoclinic phase related linearly with the base sites on the synthesized catalyst as shown in Fig. 7. As described in Li et al. [19], the monoclinic phase is able to retain more sulfur than tetragonal phase, suggesting that the monoclinic form is more basic than the tetragonal one.

Fig. 8 showed the relative ESR intensity at various calcination temperatures of sulfated zirconia. It was found that increased calcination temperatures resulted in the increase of Zr^{3+} intensity.

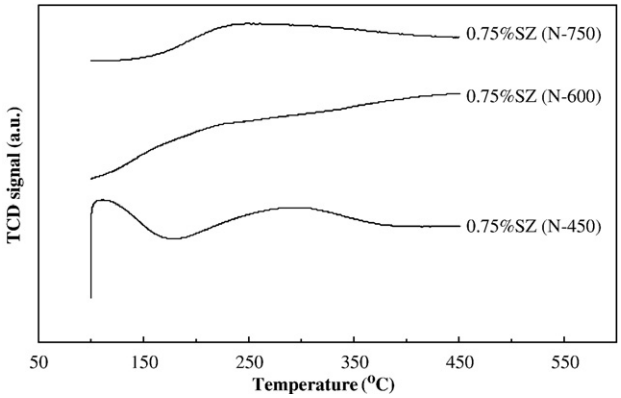

Fig. 6. CO_2-TPD profiles of SO_4–ZrO_2 catalysts.

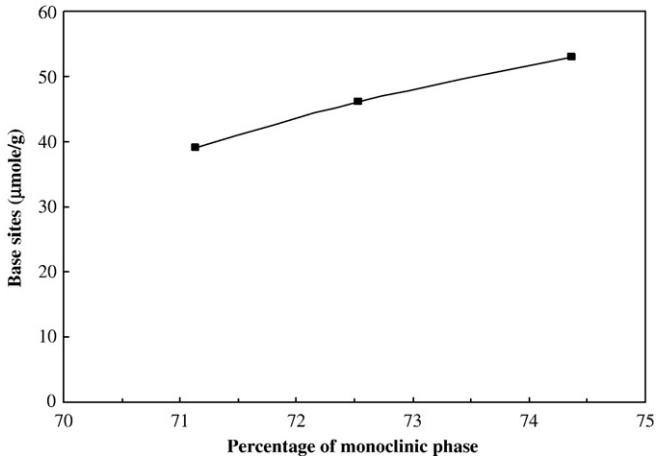

Fig. 7. Relationship between percentage of monoclinic phase and base sites on 0.75% SZ (ZrO_2–N).

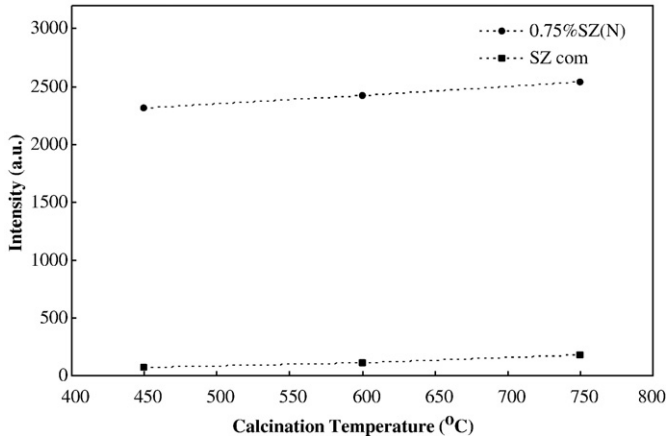

Fig. 8. Relative ESR intensity of various calcination temperatures in sulfated zirconia catalysts.

Considering commercial sulfated zirconia and 0.75% SZ (ZrO_2–N), it indicates that the 0.75% SZ (ZrO_2–N) samples with various calcination temperatures have higher intensity of Zr^{3+} than that of the commercial one. As mentioned above, the amount of sulfated retained decreased with the increased calcination temperature. Thus, sulfate group has to be removed from the catalyst surface. Elimination of sulfate group on the surface could generate the coordinately unsaturated zirconium sites on the sulfated zirconia surface [18]. Therefore, sulfur content on the surface decreased with increasing calcination temperature, whereas the quantity of Zr^{3+} increased.

3.2. Catalytic performance of sulfated zirconia catalysts toward isosynthesis

Tables 5 and 6 show the results of CO conversion, reaction rate, and selectivity of the isosynthesis over SO_4–ZrO_2 catalysts. The reaction was operated at 400 °C, atmospheric pressure and CO/H_2 of 1. It was found that commercial sulfated zirconia catalysts exhibited higher CO conversion and reaction rate than those of synthesized SO_4–ZrO_2 catalysts. According to the effect of calcination temperature, for commercial sulfated zirconia, CO conversion and reaction rate decreased with increasing calcination temperatures, whereas the isobutene selectivity increased. As for synthesized 0.75% SZ (ZrO_2–N), the isobutene selectivity decreased with increasing calcination temperature, while the CO conversion and reaction rate firstly increased when the calcination temperature increased from 450 °C to 600 °C. Then they decreased at higher calcination temperature (750 °C).

The fact that catalytic activities depend strongly on the calcination temperature suggested that the calcination temperature affects the crystalline structure, acid and base sites, and surface properties. The concentration of the sulfated groups was a function of percentages of monoclinic phase because monoclinic form may be more basic than the tetragonal [19]. The trend is also seen in the acid sites of sulfated zirconia at various calcination temperatures. The uptake of acid sites decreased with increasing concentration of monoclinic phase (Fig. 9). A previous study suggests that stronger basic sites allow binding sulfated group more effectively on monoclinic zirconia than on tetragonal zirconia.

As seen in Table 6, the SZ(450) sample exhibited the highest activity among other catalysts and produced paraffin more than olefin with the absence of isobutene. This catalyst also had the highest acidity and pure tetragonal phase. From the previous work [21,22], it was reported that the acidity of catalyst was responsible for the activation of reactant molecules and formation of linear C_4 hydrocarbons. In addition, the percentage of tetragonal phase related with the amount of acid sites on the catalyst linearly. Therefore, the acidity and tetragonal phase were major factors affected the catalytic activity. Moreover, the catalytic activity of isosynthesis was also dependent on sulfur content on the surface. From the results shown in Tables 3 and 5, the activities of the commercial sulfated zirconia catalysts were higher than those of the synthesized ones due to higher content of sulfur on the surface. However, the acidity from sulfate groups on the surface of catalyst was a portion of total acidity on surface, which can also affect the catalytic activity.

Besides the SZ(450) sample, other catalysts mainly achieved olefin with high isobutene selectivity. It was found that the presence of monoclinic phase on the catalyst can result in high selectivity of isobutene. As mentioned above, there was a relationship between monoclinic phase and the base sites on the catalyst. As reported by Li et al. [21,22], the base sites on the zirconia catalyst were responsible for the formation of isobutene. Therefore, it can be concluded that the selectivity of isobutene depended on both properties. However, the isobutene selectivities of synthesized sulfated zirconia catalysts were higher than those of the commercial ones. This was probably due to the quantity of Zr^{3+} on the surface of the former was higher than the latter.

Now turn our attention to the role of calcination temperature that affects to specific surface areas, the increase of calcination

Table 5
The catalytic activity results from isosynthesis.

Catalysts	CO conversion (%)	Reaction rate (μmol kg $cat^{-1}s^{-1}$)
0.75% SZ (N-450)	2.70	90.5
0.75% SZ (N-600)	3.60	120.7
0.75% SZ (N-750)	2.67	89.5
SZ(450)	43.39	1454.3
SZ(600)	9.24	309.9
SZ(750)	4.76	159.6

Table 6
Product selectivity results from isosynthesis.

Catalysts	Product selectivity in hydrocarbons[a] (mol%)			
	C_1	C_2	C_3	i-C_4H_8
0.75% SZ (N-450)	0.7	0.5 (78.5)	8.1 (99.5)	90.6
0.75% SZ (N-600)	1.11	0.8 (81.1)	8.0 (99.4)	90.1
0.75% SZ (N-750)	4.21	3.2 (88.1)	9.7 (98.2)	82.9
SZ(450)	77.32	19.3 (57.9)	3.3 (0.0)	0
SZ(600)	17.87	7.9 (80.9)	12.1 (94.5)	62.1
SZ(750)	1.69	2.3 (94.0)	9.3 (99.29)	86.7

[a] Parentheses are the selectivity of olefin.

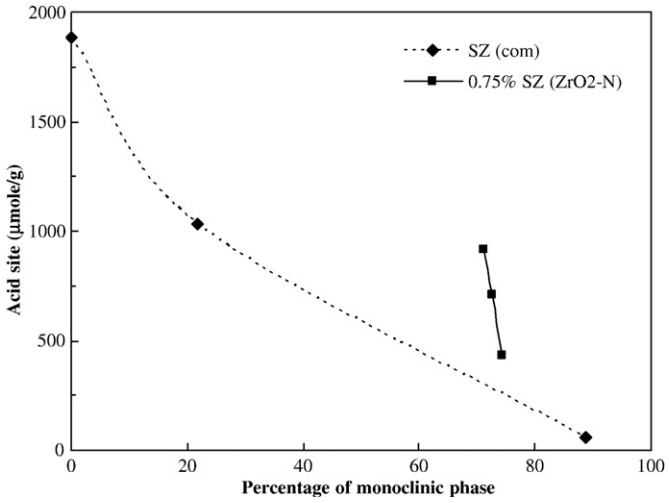

Fig. 9. Relationship between percentage of monoclinic phase and acid sites.

temperature led to smaller surface area. In line with this reason, the catalytic activity, the fraction of tetragonal phase of sulfated zirconia, sulfur content on the catalyst, and the acidity of sulfated zirconia were directly proportional. In addition, the isobutene selectivity, the percentage of monoclinic phase of sulfated zirconia, the amount of base sites, and Zr^{3+} intensity related one another.

4. Conclusion

In order to develop more efficient raw materials for octane enhancer production, the improvement of catalyst characteristics for isosynthesis was investigated. In this present work, the effect of calcination temperature on characteristics of sulfated zirconia and its catalytic performance on isosynthesis was investigated. It was demonstrated that the changing in calcination temperature from 450 to 750 °C strongly affects the phase composition, acid–base properties, and surface properties. The results also indicated that for the commercial sulfated zirconia, CO conversion and reaction rate decreased with increasing calcination temperatures, whereas the isobutene selectivity increased. On the other hand, for synthesized sulfated zirconia (0.75% SZ (ZrO_2–N)), the isobutene selectivity decreased with increasing calcination temperature, while the CO conversion and reaction rate firstly increased when the calcination temperature increased from 450 °C to 600 °C, then they decreased at higher calcination temperature (750 °C). Importantly, the commercial sulfated zirconia exhibited higher catalytic activity than the 0.75% SZ (ZrO_2–N). However, the 0.75% SZ (ZrO_2–N) achieved higher selectivity of isobutene in hydrocarbons than the commercial ones due to larger amount of Zr^{3+} being present.

Acknowledgements

The financial support from the National Research Council of Thailand (NRCT) is greatly appreciated. The authors also would like to acknowledge the supports from Professor Shigeo Goto, the Thailand Research Fund and Commission on Higher Education.

References

[1] H. Pichler, KH. Ziesecke, The Isosynthesis, Bulletin 488, Bureau of Mines, Washington, DC, 1950.
[2] I. Wender, Fuel Process. Technol. 48 (1996) 189.
[3] H. Pichler, K.H. Ziesecke, Brennst. Chem. 30 (1949) 13.
[4] H. Pichler, K.H. Ziesecke, B. Traeger, Brennst. Chem. 30 (1949) 333.
[5] C. Su, J. Li, D. He, Z. Cheng, Q. Zhu, Appl. Catal. A Gen. 202 (2000) 81.
[6] C. Su, D. He, J. Li, Z. Chen, Q. Zhu, J. Mol. Catal. A Chem. 153 (2000) 139.
[7] K. Maruya, T. Komiya, T. Hayakawa, L. Lu, M. Yashima, J. Mol. Catal. A Chem. 159 (2000) 97.
[8] Y. Li, D. He, Z. Zhu, Q. Zhu, B. Xu, Appl. Catal. A Gen. 319 (2007) 119.
[9] Z. Zhu, D. He, Fuel 87 (2008) 2229.
[10] Y. Li, D. He, Z. Cheng, C. Su, J. Li, Q. Zhu, J. Mol. Catal. A Chem. 175 (2001) 267.
[11] W. Khaodee, B. Jongsomjit, S. Assabumrungrat, P. Praserthdam, S. Goto, Catal. Commun. 8 (2007) 548.
[12] W. Khaodee, B. Jongsomjit, P. Praserthdam, S. Goto, S. Assabumrungrat, J. Mol. Catal. A Chem. 280 (2008) 35.
[13] W. Khaodee, N. Tangchupong, B. Jongsomjit, S. Assabumrungrat, P. Praserthdam, S. Goto, Catal. Commun. 10 (2009) 494.
[14] W. Khaodee, N. Tangchupong, B. Jongsomjit, N. Laosiripojana, P. Praserthdam, S. Assabumrungrat, J. Ind. Eng. Chem., under revision.
[15] D. Fărcaşiu, J.Q. Li, S. Cameron, Appl. Catal. A Gen. 154 (1997) 173.
[16] E. Tani, M. Yoshimura, S. Somiya, J. Am. Ceram. Soc. 66 (1982) 11.
[17] M.I. Osendi, J.S. Moya, C.J. Sena, J. Soria, J. Am. Ceram. Soc. 68 (1985) 135.
[18] D. Fărcaşiu, J.Q. Li, Appl. Catal. A Gen. 175 (1998) 1.
[19] X. Li, K. Nagaoka, R. Olindo, J.A. Lercher, J. Catal. 238 (2006) 39.
[20] M. Hino, M. Kurashige, H. Matsuhashi, K. Arata, Thermochimica. 441 (2006) 35.
[21] Y. Li, D. He, Y. Yuan, Z. Cheng, Q. Zhu, Fuel 81 (2002) 1611.
[22] Y. Li, D. He, Q. Zhu, X. Zhang, B. Xu, J. Catal. 221 (2004) 584.

ภาคผนวก 11

AIChE

Alternative Concept for SOFC with Direct Internal Reforming Operation: Benefits from Inserting Catalyst Rod

Pannipha Dokamaingam and Navadol Laosiripojana
Energy Division, The Joint Graduate School of Energy and Environment, King Mongkut's University of Technology Thonburi, Bangkok 10140, Thailand

Apinan Soottitantawat and Suttichai Assabumrungrat
Dept. of Chemical Engineering, Faculty of Engineering, Chulalongkorn University, Bangkok 10330, Thailand

DOI 10.1002/aic.12091
Published online October 20, 2009 in Wiley InterScience (www.interscience.wiley.com).

Mathematical models of direct internal reforming solid oxide fuel cell (DIR-SOFC) fueled by methane are developed using COMSOL® software. The benefits of inserting Ni-catalyst rod in the middle of tubular-SOFC are simulated and compared to conventional DIR-SOFC. It reveals that DIR-SOFC with inserted catalyst provides smoother temperature gradient along the system and gains higher power density and electrochemical efficiency with less carbon deposition. Sensitivity analyses are performed. By increasing inlet fuel flow rate, the temperature gradient and power density improve, but less electrical efficiency with higher carbon deposition is predicted. The feed with low inlet steam/carbon ratio enhances good system performances but also results in high potential for carbon formation; this gains great benefit of DIR-SOFC with inserted catalyst because the rate of carbon deposition is remarkably low. Compared between counter- and co-flow patterns, the latter provides smoother temperature distribution with higher efficiency; thus, it is the better option for practical applications.
 AIChE J, 56: 1639–1650, 2010
Keywords: direct internal reforming, solid oxide fuel cell, catalyst

Introduction

Solid oxide fuel cell (SOFC) is an electrochemical device that typically operated at high temperature (973–1373 K)[1,2]; this technology is expected to be applied for energy generation in the near future. SOFC offers several advantages, e.g., the ability to use CO (along with H_2) as fuel and the high level of exhaust heat, which can be efficiently used in combined heat and power and combined cycle gas turbine applications. Importantly, because of its high operating temperature, several hydrocarbon compounds could be applied as primary fuels when it is operated as internal reforming (IR-SOFC). Currently, methane (as a major component in natural gas) is the most common primary fuel for IR-SOFC.

According to the internal reforming, this operation is referred to as the utilization of heat generated from exothermic electrochemical reaction to endothermic (steam) reforming of hydrocarbons.[2–5] Theoretically, there are two approaches for IR-SOFC, i.e., direct internal reforming (DIR-SOFC) and indirect internal reforming (IIR-SOFC). For DIR-SOFC approach, along with electrochemical reaction, the reforming reaction occurs simultaneously at the anode side of SOFC. Thus, high heat transfer and fuel conversion can be achieved from this operation; nevertheless, anode material must be optimized for both reactions and could be easily poisoned by carbon deposition from the reforming

Correspondence concerning this article should be addressed to N. Laosiripojana at navadol_l@jgsee.kmutt.ac.th.

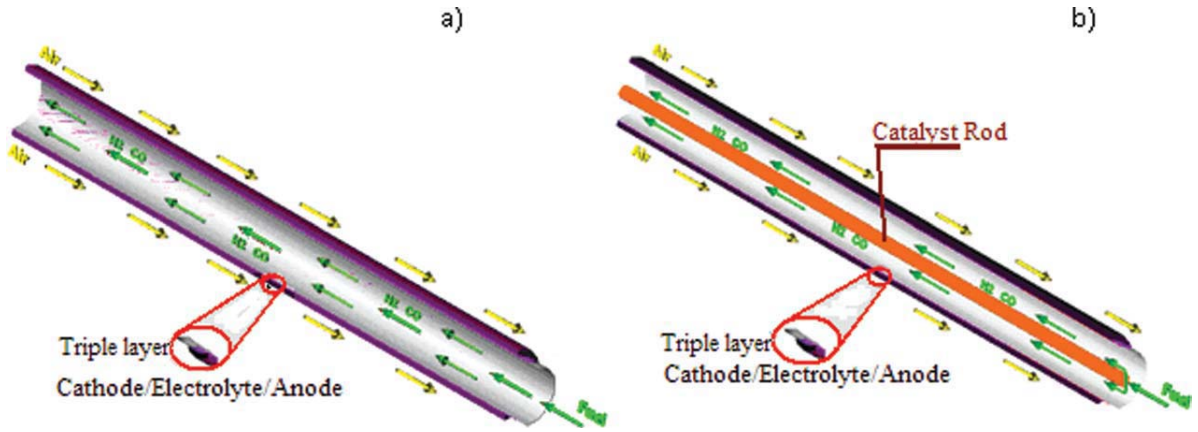

Figure 1. Tubular-designed DIR-SOFC systems in this work.

(a) Conventional DIR-SOFC and (b) inserted catalyst rod DIR-SOFC. [Color figure can be viewed in the online issue, which is available at www.interscience.wiley.com.]

of hydrocarbons. As for IIR-SOFC, the endothermic reforming reaction takes place at a reformer, which is in close thermal contact with the anode side of SOFC where exothermic electrochemical reaction occurs. IIR-SOFC gives advantage in terms of eliminating the requirement of separate fuel reformer and preventing anode material from carbon deposition. Nevertheless, IIR-SOFC offers less fuel conversion and also requires complex configuration compared to DIR-SOFC. Importantly, another major drawback of both DIR and IIR operation is the possible mismatch between rates of endothermic and exothermic reactions, which leads to significant local temperature reduction particularly near the entrance of the anode channel (for DIR) or reformer channel (for IIR) and consequently results in mechanical failure due to thermally induced stresses.[3–7]

In this work, a set of mathematical models was developed to predict the behaviors of tubular-designed DIR-SOFC fueled by methane, i.e., cell performance, temperature gradient, and amount of carbon deposition along the cell. The developed model was coded in COMSOL® program within 2D axial dimension application with an aim of determining the effect of operating conditions, i.e., inlet steam to carbon ratio and gas flow pattern on the system performance. Importantly, as the main scope of this study, we proposed one alternative concept for DIR-SOFC by investigating the benefits of inserting catalyst rod in the middle of the fuel channel. This configuration can be called as a hybrid system between DIR and IIR operations because the reforming reaction takes place simultaneously with the electrochemical reaction at the anode (as DIR operation) and also occurs on separate internal reforming catalyst (as IIR operation). It is noted that the intrinsic rate equations of methane steam reforming and the rate of carbon formation over Ni-based material as reported by Xu and Froment[8] and Zavarukhin and Kuvshinov[9] were applied integrally with DIR-SOFC model to predict the reforming characteristics of "Ni-based" catalyst rod and anode along with the electrochemical behavior of SOFC system. Details of these mathematical models are presented in the next section.

From the simulation, the system performances (i.e., electrical efficiency, temperature gradient along the cell, and amount of carbon formation at anode surface) of this DIR-SOFC with catalyst rod were determined. The effects of inlet steam to carbon ratio and gas flow patterns on the performance of this DIR-SOFC were also investigated and compared to conventional DIR-SOFC. Lastly, the suitable operating conditions of DIR-SOFC system fueled by methane were identified.

Mathematical Models

Model geometry

The schematic diagram of a tubular-designed DIR-SOFC applied in this work is shown in Figure 1. As described, two configurations, i.e., conventional tubular DIR-SOFC (Figure 1a) and DIR-SOFC with inserted catalyst rod (Figure 1b) were considered. For both configurations, methane and steam are fed to the anode channel of SOFC, where they were simultaneously converted to hydrogen-rich gas along with consumed electrochemically to generate electricity. Simultaneously, air is fed with the opposite flow direction through the air channel. It is noted that anode/electrolyte/cathode compositions of SOFC system considered here are Ni-YSZ/YSZ/LSM. All dimensions and physical properties of this SOFC system, which are based on the previous report from literatures,[10–14] are summarized in Table 1.

Model assumption and equations

The model was developed as the smallest single unit cell taking into account the effect of temperature on gas distribution, reactant conversion, and charge transfer. Our developed models were based on these assumptions: (1) each section is considered as nonisothermal steady-state conditions, (2) ideal gas behavior is applied for all gas components, (3) pressure drop in SOFC stack was neglected, (4) fuel utilization was fixed constantly at 80%, and (5) the reforming reaction and carbon formation occurred at the surface of Ni particles on the catalyst rod and SOFC anode. It is noted that the well-established methane steam reforming rate expressions proposed by Xu and Forment[8] were applied to predict the reforming rate for both sections; the difference in steam

Table 1. Constant Parameter Values of a Tubular IIR-SOFC System

Parameter	Value	Reference
Fuel cell length	0.60 m	10
Inserted catalyst rod	2×10^{-3} m	–
Inside radius of the cell	5.4×10^{-3} m	10
Anode thickness	1×10^{-3} m	10
Electrolyte thickness	4×10^{-5} m	10
Cathode thickness	5×10^{-5} m	10
Anode permeability	1×10^{-12}	11
Cathode permeability	1×10^{-12}	11
Average density of triple phase	633.73 kg m^{-3}	14
Average specific heat of triple phase	574.3 J kg^{-1} K^{-1}	14
Anode thermal conductivity	6.23 W m^{-1} K^{-1}	14
Electrolyte conductivity	2.7 W m^{-1} K^{-1}	14
Cathode thermal conductivity	9.6 W m^{-1} K^{-1}	14
Convection coefficient in the fuel channel	2987 W m^{-2} K^{-1}	14
Convection coefficient in the air channel	1322.8 W m^{-2} K^{-1}	14

reforming reactivity between them is related to the dissimilarity of their Ni-active surface area. In our modeling, the dimensions of SOFC system were modified to dimensionless application (with the full scale of 1.0), and the active areas of catalyst rod and anode were normalized as relative active area. The relative active surface area of anode is 0.07, whereas that of catalyst rod is 0.36. A number of equations were applied to predict concentration and temperature gradients along this tubular DIR-SOFC system. Details for these sets of equations are presented in the following sections and summarized in Table 2.

Gas Distribution. The combination of Brinkman equation and Navier-Stokes equation[15] (Eq. 1) was applied to predict gases distribution behavior in this work:

$$\nabla \cdot (\rho u u) = -\nabla p + \nabla \cdot (\nabla \mu u) - \frac{\mu}{k_p}(\varepsilon u), \tag{1}$$

where u is the fluid velocity, ρ the density, p the pressure, μ the viscosity, ε the porosity, and k_p is the permeability. It is noted that the influences of pressure and velocity gradient on gas diffusion properties were also took into account by applying molecular diffusion and binary diffusion equations (Eqs. 2 and 3, respectively).[16]

$$D_{i,\mathrm{mix}} = (1 - y_i) \Big/ \sum_{j,j \neq 1} (y_j / D_{ij}) \tag{2}$$

$$D_{i,j} = (0.00143) T^{1.75} / p M_{i,j}^{1/2} [\gamma_i^{1/3} + \gamma_j^{1/3}]^2, \tag{3}$$

where $D_{i,\mathrm{mix}}$ and $D_{i,j}$ are molecular diffusion and binary diffusion flux of species i in mixed gas (m^2 s^{-1}), y_i is mole fraction of species i, p is pressure, $M_{i,j} = 2/(1/M_i + 1/M_j$ in which M_i is molecular weight of component i, and γ is the special diffusion volume as reported by Fuller et al.[17] It is noted that, in the case of porous media, the diffusion behavior was corrected by applying porosity (ε) and tortuosity (τ), so-called effective diffusivity coefficient $D^{\mathrm{e}}_{i,\mathrm{pmix}}$ (Eq. 4). Furthermore, gas diffusion through porous media, $D_{i,\mathrm{pmix}}$, was explained by two mechanisms, i.e., molecular diffusion ($D_{i,\mathrm{mix}}$) (Eq. 5) and Knudsen diffusion ($D_{i,\mathrm{ku}}$) (Eq. 6) depending on the relation between pore diameter (d_p) and mean free path of molecular species.

$$D^{\mathrm{e}}_{i,\mathrm{pmix}} = \frac{\varepsilon}{\tau} D_{i,\mathrm{pmix}} \tag{4}$$

$$\frac{1}{D_{i,\mathrm{pmix}}} = \frac{1}{D_{i,\mathrm{mix}}} + \frac{1}{D_{i,\mathrm{ku}}} \tag{5}$$

$$D_{i,\mathrm{ku}} = \frac{1}{3} d_\mathrm{p} \sqrt{\frac{8RT}{\pi M_i}}, \tag{6}$$

where R is universal gas constant.

Energy Transfer. Heat transfer phenomena considered in this system involve the conduction along stack materials and convection from heat flow though the system. Furthermore, the effect of heat radiation between the catalyst rod and SOFC was also concerned for the case of DIR-SOFC with inserted catalyst rod. The calculated gas properties were referred as a function of temperature; thus, momentum, mass, and energy balances were integrated. It should be noted that, in all gas flow channels, both conduction and convection heat transfers were considered, and the heat capacity and conductivity of gas species were set as the function of temperature.[16]

Reforming Model. As mentioned earlier, methane steam reforming reaction over Ni-based catalyst rod and SOFC anode was simulated based on the intrinsic rate equations and parameters reported by Xu and Froment,[8] whereas the amount of carbon deposition was predicted based on the equations proposed by Zavarukhin and Kuvshinov.[9] It is noted that the developed model for predicting the rate of carbon formation, which was coded in COMSOL® program in this work, was first validated with the results reported by Zavarukhin and Kuvshinov[9] at the same operating conditions. As shown in Figure 2a, both results are in good agreement with the error less than 5%.

Importantly, the effects of heat convection in gas stream, heat of reactions, and conductive heat transfers from fuel channel were taken into account in the reforming model. Furthermore, in the case of DIR-SOFC with inserted catalyst rod, the radiation between the catalyst rod and the solid cell was also considered. We made the assumption here that the reforming reactions occurred only at the catalyst surface, and no gas was diffused into the catalyst rod.

SOFC Model. All momentum, mass, heat, and charge balance equations for SOFC systems in this work are given in Table 2. In detail, all electrochemical reactions take place at electrodes and electrolyte interface to generate electricity from both H_2 and CO. Here, the cell voltage is theoretically calculated from Nernst equation. It is noted that the actual voltage is always less than the theoretical value because of the presence of activation, concentration, and ohmic overpotentials.[1,2]

Activation loss

Activation loss, η_{act}, is the activation barrier of electrochemical reaction at electrode, which is significant at low current density.[2] This overpotential is determined from Butler-Volmer equation, Eq. 7. The relations of current density with H_2 and O_2 concentrations at electrodes are given in

Eqs. 8 and 9.[18] As the expression of activation loss from CO oxidation is not well ascertained, the current density from CO is assumed to be three times lower than that from H_2 (Eq. 10).[19] It is noted that all parameter values related to these equations are reported in Table 3.

$$j = j_0\left[\exp\left(\alpha\frac{n_e F}{RT}\eta_{act}\right) - \exp\left((1-(1-\alpha)\frac{n_e F}{RT}\eta_{act}\right)\right] \quad (7)$$

$$j_{0,H_2} = \vartheta_{anode}\left(\frac{p_{H_2}}{p_{ref}}\right)\left(\frac{p_{H_2O}}{p_{ref}}\right)\exp\left(-\frac{E_{act,anode}}{RT}\right) \quad (8)$$

$$j_{0,O_2} = \vartheta_{cathode}\left(\frac{p_{O_2}}{p_{ref}}\right)^{0.25}\exp\left(-\frac{E_{act,cathode}}{RT}\right) \quad (9)$$

$$j_{0,CO} = \frac{1}{3}j_{0,H_2}, \quad (10)$$

where j_0 is the exchange current density, j the current density, ϑ the exchange current density constant, α the charge transfer coefficient, n_e the number of electron, F the Faraday's constant and E_{act} is the activation energy.

Concentration overpotential

This overpotential, η_{con}, is caused by the dropping of pressure or partial pressure of reactant gases along porous electrodes at reaction sites.[2] It is normally reduced at high current density. The diffusion at bulk zone as defined in term of concentration overpotential is given in Eq. 11.[20,21] According to Suwanwarangkul et al.[22] and Hernández-Pacheco et al.,[23] the dusty gas model was applied to calculate concentration at active site.

$$\eta_{con} = \frac{RT}{2F}\ln\left(\frac{p^*_{H_2}p_{H_2O}}{p_{H_2}p^*_{H_2O}}\right) + \frac{RT}{2F}\ln\left(\frac{p^*_{CO}p_{CO_2}}{p_{CO}p^*_{CO_2}}\right) + \frac{RT}{4F}\ln\left(\frac{p^*_{O_2}}{p_{O_2}}\right), \quad (11)$$

where * represents gas partial pressure at active site.

Ohmic overpotential

This overpotential, η_{ohm}, occurs from the ion transport across the cell, which mainly depends on ionic conductivity of cell material. By applying ohm's law, the relation of ohmic overpotential and material resistivity is given in Eqs. 12 and 13,[12] in which the resistivity is determined from Eq. 14 based on the data in Table 4.

$$\eta_{ohm} = jR_{ohm} \quad (12)$$

$$R_{ohm} = \frac{\omega\delta}{A_{elec}} \quad (13)$$

$$\omega = a\cdot\exp(b/T), \quad (14)$$

where R_{ohm} is the ohmic resistance, ω the ionic conductivity, δ the thickness of electrode or electrolyte layer, and *a,b* are the constant property of material. It is noted that the transmission-line model as reported by Stiller et al.[24] can also apply to estimate the ohmic overpotential with comparable results to these equations. By applying the operating conditions (e.g., pressure, air, and fuel flow rates, inlet fuel temperature, fuel utilization, and inlet fuel composition) based on the work of Stiller et al.,[24] the deviations of observed ohmic overpotential between both models are in the range of $\pm 6\%$ (within the operating temperature range of 1250–1350 K).

Considering all polarizations, the cell performance was determined in terms of the electrical efficiency. It is noted that the anodic current was calculated from both H_2 and CO conversion rates, whereas the cell efficiency, η_{elec}, was calculated from the ratio between output power density (P) and the energy of all input fluids, Eq. 15.

$$\eta_{elec} = \frac{P.A_{act}}{\sum y_i^{in}\mathrm{LHV}_{i,1173K}}, \quad (15)$$

where A_{act} is the activation area, (m^2), $\mathrm{LHV}_{i,1173k}$ the lower heating value of component i at 1173 K., P the power density (W cm^{-2}), and y_i^{in} is the mole fraction of inlet gas, i. The governing equations for mass and heat transfers of SOFC anode are summarized in Table 2. It should be noted that *I–V* curve obtained from developed model in this work was validated with the previous work of Leng et al., [13] as shown in Figure 2b. Clearly, both the results are in good agreement.

Results and Discussion

Modeling of conventional DIR-SOFC and DIR-SOFC with inserted catalyst rod

The tubular DIR-SOFC model (with and without inserted catalyst rod) was first simulated at 1173 K and 1 bar. The inlet fuel (methane and steam) with inlet steam to carbon (*S/C*) ratio of 2 was fed to the fuel channel with a total flow rate of 24.8 $cm^3\ s^{-1}$; simultaneously, air was introduced to the cathode channel with the flow rate of 94.24 $cm^3\ s^{-1}$ (theoretical oxygen ratio). Table 3 presents all related parameters of these DIR-SOFC systems. It is noted that the consumption rate of H_2 and CO (U_f) at the anode channel was fixed constant at 80% for both configurations. Under these conditions, characteristic results of these two DIR-SOFC configurations, i.e., methane conversion, product gas distribution, and temperature gradient along SOFC channels (both fuel and air channels) are shown in Figures 3 and 4.

Figures 3a,b present the mole profiles of methane and hydrogen along the fuel channel of conventional DIR-SOFC (without inserted catalyst rod). It can be seen that the concentration of methane decreased along the length of fuel channel particularly at the surface of the anode (on the right-hand side of the channel); nevertheless, it is clear that significant amount of methane remains unreacted and presented at the outlet of the fuel channel. As for hydrogen concentration profile, oppositely, it increased along the length of fuel channel particularly at the surface of the anode, and considerable amount of hydrogen was presented in the gas products at the exit of the fuel channel. Both figures indicated that, under conventional DIR-SOFC conditions, methane incompletely reformed and hydrogen was inefficiently used by electrochemical reaction.

Figures 3c,d show the mole profiles of methane and hydrogen along the fuel channel of DIR-SOFC with inserted catalyst rod. Clearly, significant improvements in methane conversion and hydrogen utilization can be achieved. In detail,

Table 2. Steady-State 2D Dimensional Model's for Tubular DIR-SOFC

Fuel channel for conventional DIR-SOFC

$$\text{Mass balance } \nabla.(-D_i\nabla_{c_i} + c_i\vec{v}) = 0 \tag{17}$$

$$\text{Energy balance } \nabla.(\vec{v}\rho c_p T) - \sum \nabla.(\lambda_i \nabla T) = 0 \tag{18}$$

Boundary

$$z = L;\ r \geq 0;\ u_f = u_{in},$$
$$v_f = v_{in}, p_f = p_r, c_{i,f} = c_{i,in}, T_f = T_{in}$$

Fuel/anode interface and

$$z \geq 0; \quad \mathbf{n}\cdot N_{CH_4,f} = -\sum R_{reform} - R_{c-from},$$
$$\mathbf{n}\cdot N_{H_2O,f} = -\sum R_{reform}$$
$$\mathbf{n}\cdot N_{H_2,f} = \sum R_{reform} + R_{c-from},$$
$$\mathbf{n}\cdot N_{CO,f} = -\sum R_{reform}$$
$$\mathbf{n}\cdot N_{CO_2} = \sum R_{reform}$$
$$\mathbf{n}\cdot(k\nabla T) = h(T_f - T_s) + \sum \nabla H_{reform} R_{reform}$$

Anode/electrolyte 1 interface

$$z \geq 0;\ \mathbf{n}\cdot N_{H_2,f} = -J_{H_2}/2F,$$
$$\mathbf{n}\cdot N_{H_2O,f} = J_{H_2}/2F$$
$$\mathbf{n}\cdot N_{CO,f} = -J_{CO}/2F,,$$
$$\mathbf{n}\cdot N_{CO_2,f} = J_{CO}/2F$$
$$\mathbf{n}\cdot(k\nabla T) = \sum \Delta H_{elec} R_{elec} + J(E - \eta_{total})$$

Fuel channel for inserted catalyst rod DIR-SOFC

$$\text{Mass balance} \quad \nabla.(-D_i\nabla c_i + c_i\vec{v}) = 0 \tag{19}$$

$$\text{Energy balance } \nabla.(\vec{v}\rho c_p T) - \sum \nabla.(\lambda_i \nabla T) = 0 \tag{20}$$

Boundary

$$z = L;\ r \geq 0;\ u_f = u_{in}, v_f = v_{in},$$
$$p_f = p_r, c_{i,f} = c_{i,in}, T_f = T_{in}, T_{rod} = T_{in}$$

Fuel/catalyst rod interface and fuel/anode interface

$$z \geq 0; \quad \mathbf{n}\cdot N_{CH_4,f} = -\sum R_{reform} - R_{c-from},$$
$$\mathbf{n}\cdot N_{H_2O,f} = -\sum R_{reform}$$
$$\mathbf{n}\cdot N_{H_2,f} = \sum R_{reform} + R_{c-from},$$
$$\mathbf{n}\cdot N_{CO,f} = -\sum R_{reform}$$
$$\mathbf{n}\cdot N_{CO_2} = \sum R_{reform}$$

(*Continued*)

Table 2. (Continued)

Fuel/catalyst rod interface

$$\mathbf{n}\cdot(k\nabla T) = h_f(T_{rod} - T_f) + \sum \Delta H_{reform} R_{reform} + \frac{\sigma A_s (T_r^4 - T_s^4)}{\frac{1}{\varepsilon_r} + \frac{A_r}{A_s}\left(\frac{1}{\varepsilon_s} - 1\right)}$$

Fuel/anode interface

$$\mathbf{n}\cdot(k\nabla T) = h(T_f - T_s) + \sum \Delta H_{reform} R_{reform}$$

Anode/electrolyte 1 interface

$$z \geq 0; \quad \mathbf{n}\cdot N_{H_2,f} = -J_{H_2}/2F,$$
$$\mathbf{n}\cdot N_{H_2O,f} = J_{H_2}/2F$$
$$\mathbf{n}\cdot N_{CO,f} = -J_{CO}/2F,$$
$$\mathbf{n}\cdot N_{CO_2,f} = J_{CO}/2F$$
$$\mathbf{n}\cdot(k\nabla T) = \sum \Delta H_{elec} R_{elec} + J\eta_{total}$$

Solid cell

$$\text{Energy balance } \nabla.(\vec{v}\rho c_p T) - \nabla.(\lambda_s \nabla T) + \sum \Delta H_{elec} + \frac{\sigma A_s (T_r^4 - T_s^4)}{\frac{1}{\varepsilon_r} + \frac{A_r}{A_s}\left(\frac{1}{\varepsilon_s} - 1\right)} = 0 \tag{21}$$

Boundary

$$z = L;\ r \geq 0;\ T_s = T_{in}$$

Air channel

$$\text{Mass balance } \nabla.(-D_i\nabla c_i + c_i\vec{v}) = 0 \tag{22}$$

$$\nabla.(\vec{v}\rho c_p T) - \Sigma\nabla.(\lambda_i \nabla T) = 0 \tag{23}$$

Boundary

$$z = 0;\ r \geq 0; \quad u_a = 0, v_a = v_{a,in}, c_{i,a} = c_{a,in},\ T_a = T_{a,in}$$

Air/cathode interface

$$z \geq 0; \quad \mathbf{n}\cdot N_{O_2,f} = -J_{O_2}/2F$$
$$\mathbf{n}\cdot(k\nabla T) = h(T_s - T_a)$$

Outer layer

$$z \geq 0 \quad \mathbf{n}\cdot(k\nabla T) = 0$$

as seen in Figure 3c, the concentration of methane decreased along the length of fuel channel particularly near the anode and catalyst rod with greater rate than conventional DIR-SOFC because of the promotion of reforming reactivity by inserting the catalyst rod. Importantly, as shown in Figure 3d, hydrogen generated from the steam reforming reaction was

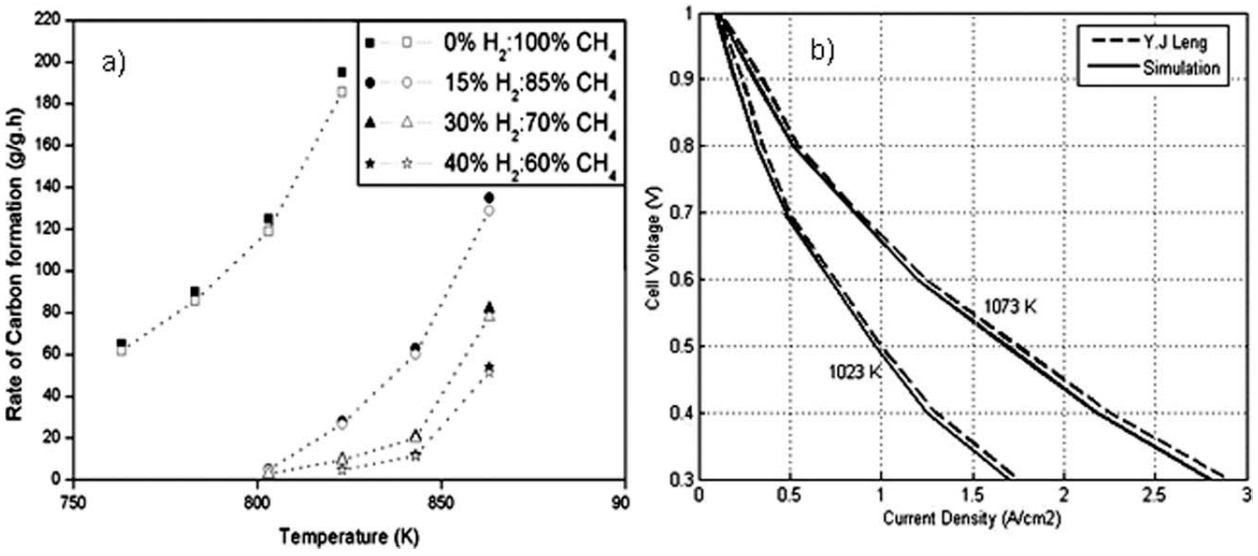

Figure 2. Validations of simulation results in this work with the literature.[9,13]

(a) Rate of carbon formation at various conditions (our simulation: blank symbols and the results from the literature[9]: black symbols); (b) *I–V* curve validation between our simulation results with the experimental results from literatures.[13]

efficiently used along the channel, thus significantly lower amount of hydrogen left the system compared to the conventional DIR-SOFC system. The results from Figures 3a–d can be summarize that, without catalyst rod, the anode alone inefficiently reforms methane, thus significant amount of methane remains presented in the system; under methane-rich gas condition, hydrogen generated from the reforming reaction cannot be well utilized electrochemically. By inserting the catalyst rod, the steam reforming of methane was promoted; with less methane presented in the system, hydrogen can be efficiently used via electrochemical reaction.

Figure 4 presents the temperature profiles along the fuel and air channels of both DIR-SOFC systems. Obviously, the local temperature reduction at the entrance of the fuel channel was reduced, and smoother temperature profiles along both channels can be achieved when the catalyst rod was inserted into the fuel channel. The temperature of DIR-SOFC with inserted catalyst rod decreases only 50 K (from 1173 K to the lowest 1123 K), whereas the temperature gradient dropped by 180 K in the case of conventional DIR-SOFC. From the calculation, the average temperature difference along the DIR-SOFC with inserted catalyst rod was within 8.3 K cm^{-1}, which is lower than the critical point (10 K) as previously reported,[25] whereas the average temperature difference along conventional DIR-SOFC was higher than 20 K. Under these inlet conditions, the output voltage from DIR-SOFC with inserted catalyst rod was 0.74 V, which is higher than that achieved from the conventional DIR-SOFC (0.69 V); furthermore, the electrical efficiency and power density significantly improved (from 45.3 to 63.5% and 0.32 to 0.45 A cm^{-2}). Importantly, the amount of carbon deposition on the anode of DIR-SOFC with inserted catalyst rod was predicted to be significantly less than that of the conventional DIR-SOFC (9.82×10^{-7} g g^{-1} h^{-1} for DIR-SOFC with inserted catalyst rod compared to 3.43×10^{-3} g g^{-1} h^{-1} for conventional DIR-SOFC).

It can be seen that all observed results indicated the great benefit of DIR-SOFC with inserted catalyst rod compared to conventional DIR-SOFC in terms of primary fuel conversion, temperature distribution along the system, electrical efficiency, output power density, and the potential amount of carbon deposition at the anode of SOFC. We suggested that these improvements are mainly related to the presence of higher amount of active nickel in the system, which helps to promote the steam reforming and generate more hydrogen for electrochemical reaction. The reason for better temperature distribution for DIR-SOFC with inserting catalyst rod is also related to the promotion of the endothermic steam reforming of methane to hydrogen, which is simultaneously consumed efficiently by the exothermic electrochemical reaction at SOFC anode. We indicated here that, at steady-state condition where the heat generated from the electrochemical reaction was continuously supplied to the system, the occurring of simultaneous high endothermic steam reforming and exothermic electrochemical reactions results in their good energy exchange coupling, which eventually enhances the great autothermal operation. Regarding the benefit on the reducing of potential carbon deposition at the anode of SOFC, although it was observed from the simulation that some carbon could be formed on the catalyst rod (6.83×10^{-4} g g^{-1} h^{-1}) during operation, this problem can be

Table 3. Constant Parameters for Predicting Activation Loss

ϑ_{anode} (A m^{-2})	5.5×10^8
$\vartheta_{cathode}$ (A m^{-2})	7.0×10^8
$E_{act,anode}$ (kJ $kmol^{-1}$)	1.1×10^5
$E_{act,cathode}$ (kJ $kmol^{-1}$)	1.2×10^5

Table 4. Resistivity of Cell Components, Ni-YSZ/YSZ/LSM[12]

Anode resistance constant	$a = 0.0000298$, $b = -1392$
Cathode resistance constant	$a = 0.0000811$, $b = 600$
Electrolyte resistance constant	$a = 0.0000294$, $b = 10{,}350$

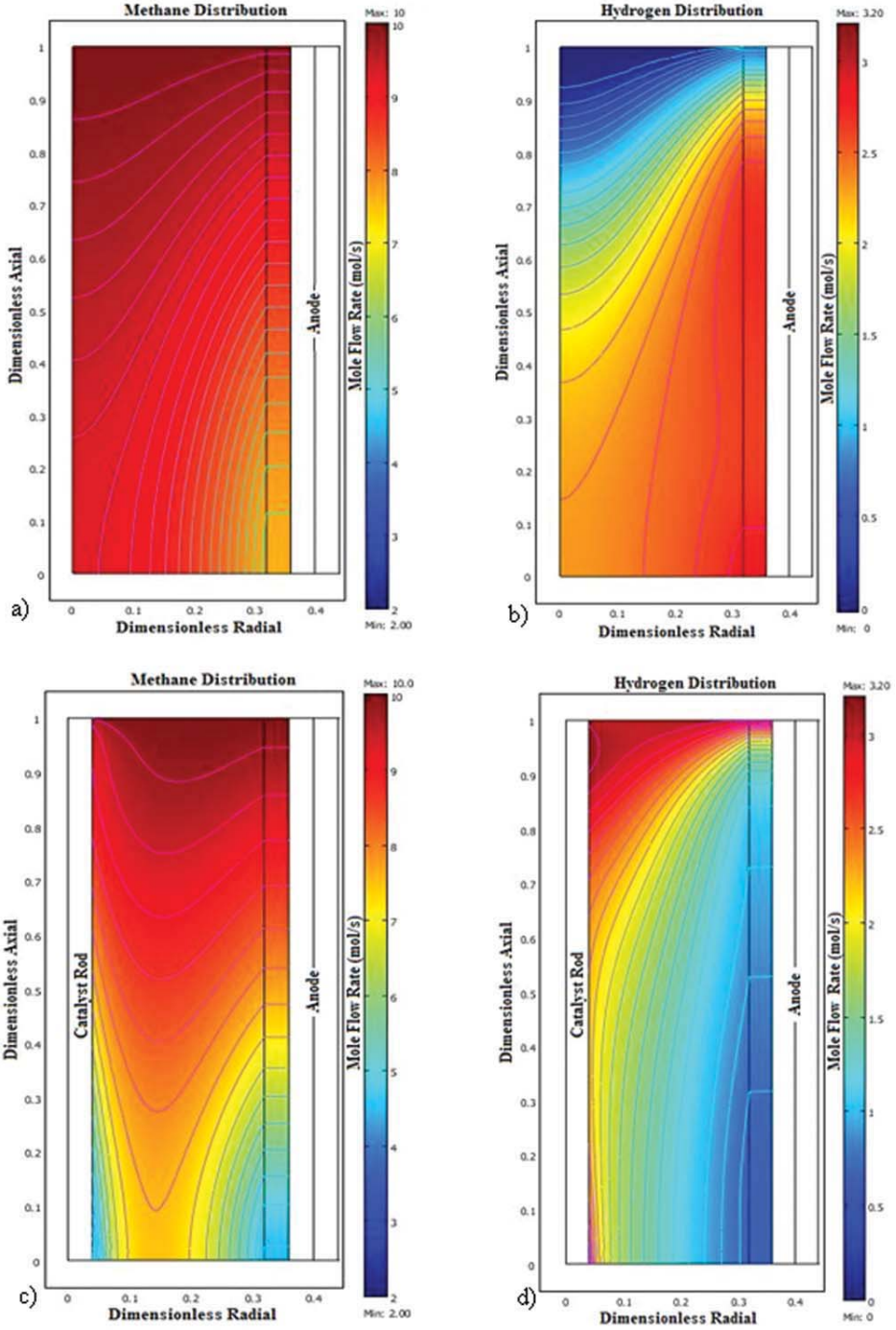

Figure 3. Results from COMSOL® represented the concentration profiles in the fuel channel of DIR-SOFC systems (simulated at 1 bar with inlet *S/C* ratio of 2).

Concentration profiles of (a) methane and (b) hydrogen in the fuel channel in the conventional DIR-SOFC. Concentration profiles of (c) methane and (d) hydrogen in the fuel channel in the inserted catalyst rod DIR-SOFC. [Color figure can be viewed in the online issue, which is available at www.interscience.wiley.com.]

practically minimized by applying alternative reforming catalyst with higher resistance toward carbon deposition (e.g., Rh-based catalysts) without any changing of SOFC anode required; this highlights another beneficial of DIR-SOFC with inserting catalyst rod in terms of catalyst flexibility.

As the next step, the effects of important operating conditions, i.e., inlet fuel flow rate, inlet steam to carbon ratio, and gas flow pattern on the system performance were studied to optimize the suitable operating conditions for these DIR-SOFC systems. It is noted that the effects of other operating

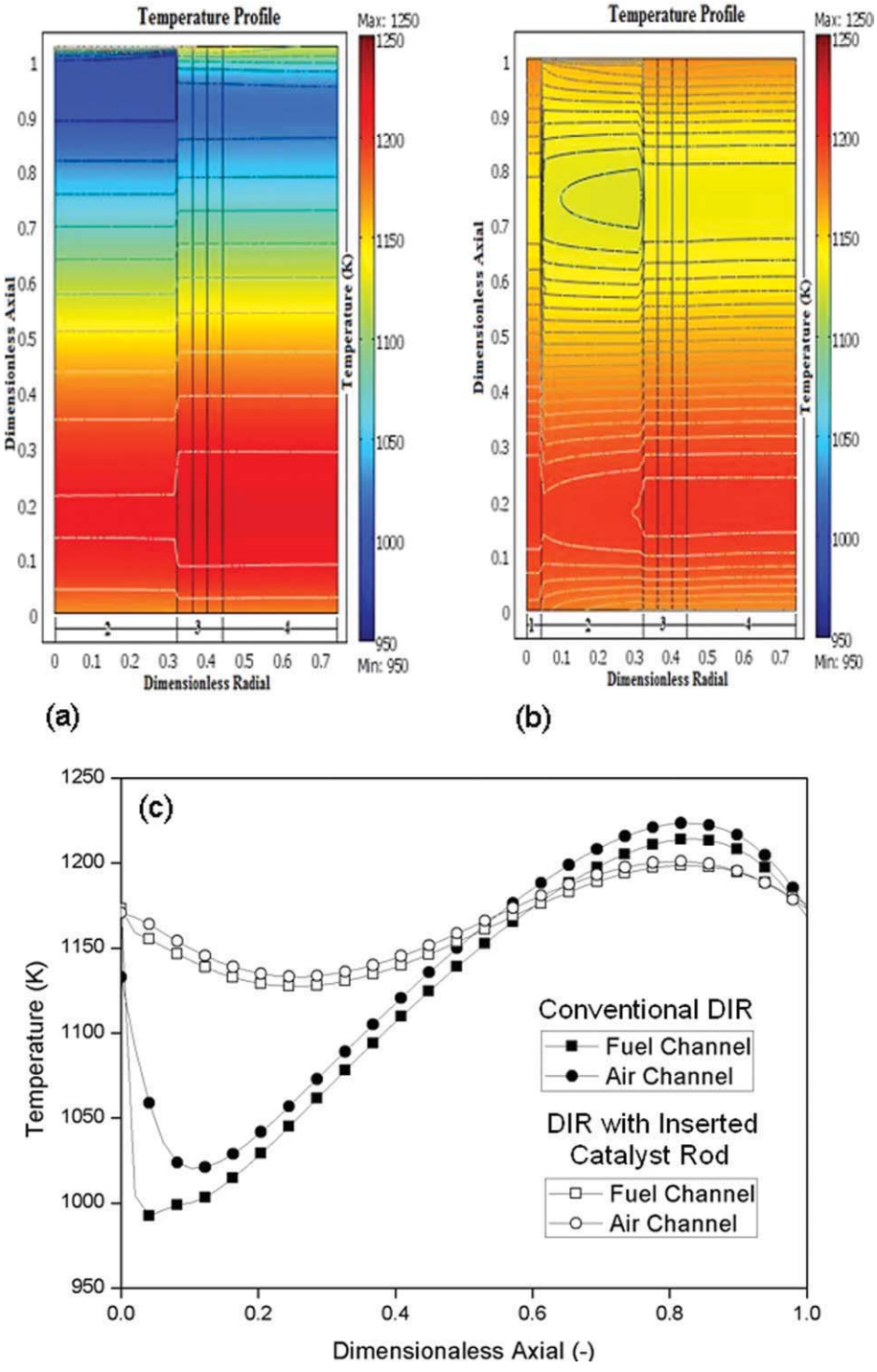

Figure 4. Results from COMSOL® represented the temperature gradient in the fuel and air channels of DIR-SOFC systems (simulated at 1 bar with inlet *S/C* ratio of 2).

Temperature gradients of the fuel and air channels (T_f and T_a, respectively) for (a) conventional DIR-SOFC and (b) inserted catalyst rod DIR-SOFC; (c) comparison of temperature profiles at each channel of both systems. [Color figure can be viewed in the online issue, which is available at www.interscience.wiley.com.]

conditions, e.g., fuel inlet temperature and operating pressure were also carried out. Nevertheless, we found insignificant impact of these operating parameters on the system performance, thus they are not reported here.

Effect of inlet fuel flow rate

The inlet fuel flow rate was found to be one of the major parameters that strongly affects the performance of DIR-SOFC system. Here, the effect of inlet fuel flow rate on the

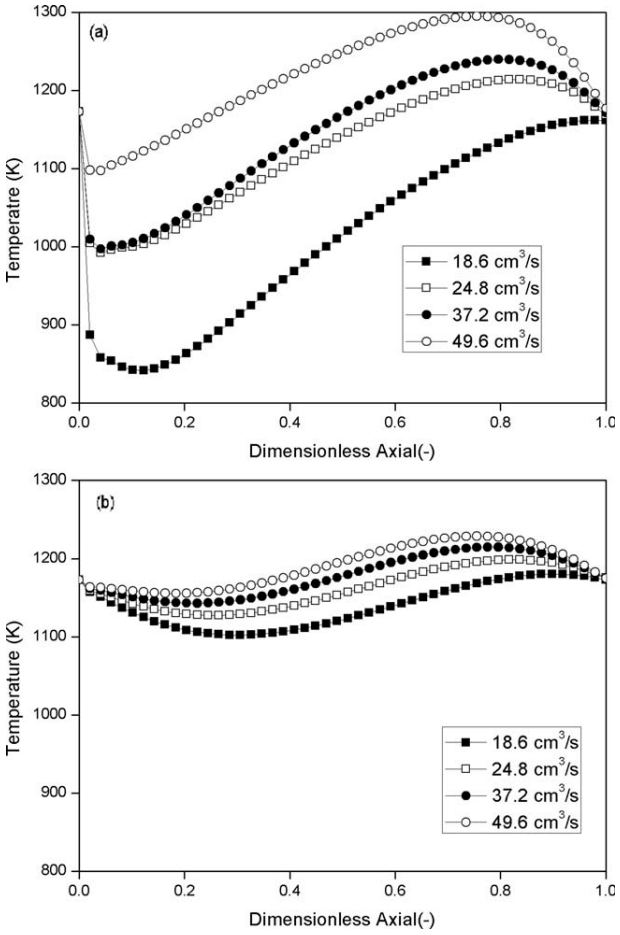

Figure 5. Effect of inlet fuel flow rate on the temperature gradient in the fuel channel of DIR-SOFC systems (simulated at 1 bar with inlet *S/C* ratio of 2).

Temperature profiles in the fuel channel of (a) conventional DIR-SOFC and (b) inserted catalyst rod DIR-SOFC at various inlet fuel flow rates.

temperature gradient, power density, electrical efficiency, and amount of carbon formation for both DIR-SOFC systems was studied by varying the inlet fuel flow rate from 18.6 to 24.8, 37.2, and 49.6 $cm^3\ s^{-1}$. Figure 5a and Table 5 indicate that the cooling effect and power density of conventional DIR-SOFC system can be improved by increasing the inlet fuel flow rate; nevertheless, the electrical efficiency significantly reduced (because of the lower rate of methane conversion at higher fuel flow rate), and the amount of carbon deposition increased considerably. Similar trends were observed for DIR-SOFC with inserted catalyst rod, Figure 5b and Table 5.

Effect of inlet S/C ratio

As possible carbon deposited on the surface of SOFC anode is one of the major problems for DIR-SOFC and it strongly depends on the ratio of steam to carbon in the system, we here aimed at the determination of suitable inlet *S/C* ratio to minimize the potential for carbon deposition in the

Table 5. Effect of Inlet Fuel Flow Rate on the Electrical Efficiency and Power Density of DIR-SOFC Systems (Simulated at 1 bar with Inlet *S/C* Ratio of 2)

	Power Density (A cm^{-2})		Electrical Efficiency (%)	
Inlet Velocity ($cm^3\ s^{-1}$)	Conventional DIR	DIR with Inserted Catalyst	Conventional DIR	DIR with Inserted Catalyst
18.6	0.27	0.42	49.67	78.98
24.8	0.32	0.45	45.25	63.53
37.2	0.36	0.47	33.3	44.64
49.6	0.46	0.51	22.7	35.57

cell and maximize the performance of the system. It is well established that the amount of carbon formation can be efficiently reduced by adding excess steam at the feed; nevertheless, too high steam content can reduce the overall system efficiency because high energy is required to vaporize water to steam. As for the typical methane steam reforming over Ni-based catalysts, it has been reported that the steam to carbon ratio should be in the range of 1.4–3.0.[26] Here, the effect of inlet steam content on the amount of carbon deposition and performance of both DIR-SOFC systems were investigated by varying the inlet steam to carbon (*S/C*) ratios from 1.5 to 4.0.

Figures 6 and 7 and Table 6 present the effect of inlet *S/C* ratio on the temperature gradient along the fuel channel, the electrical efficiency achieved, and the amount of carbon deposition for both DIR-SOFC systems. It can be seen that the amount of carbon formation decreased with increasing inlet *S/C* ratio (Figure 7) because the excess steam can prevent the formation of carbon species from the methane cracking reaction. Nevertheless, considering the temperature gradient and electrical efficiency, it was found that the cooling spot increased with increasing the inlet *S/C* ratio (Figure 6), whereas the electrical efficiency decreased (Table 6). This could be due to the fact that the presence of excess steam diluted hydrogen concentration in the fuel channel and

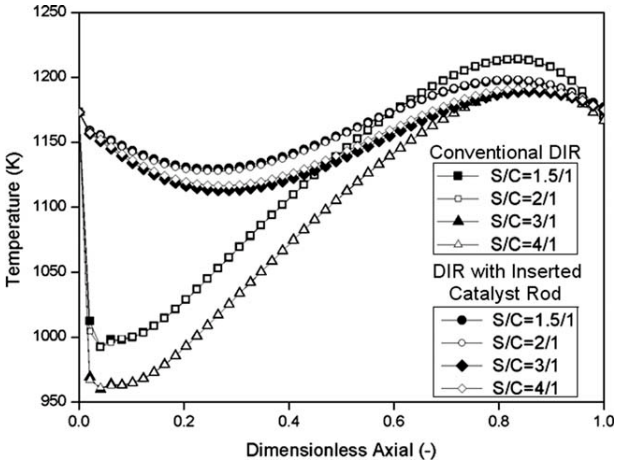

Figure 6. Effect of *S/C* ratio on the temperature gradient in the fuel channel of DIR-SOFC systems (simulated at 1 bar).

Temperature profiles in the fuel channel of conventional DIR-SOFC and inserted catalyst rod DIR-SOFC at various *S/C* ratios.

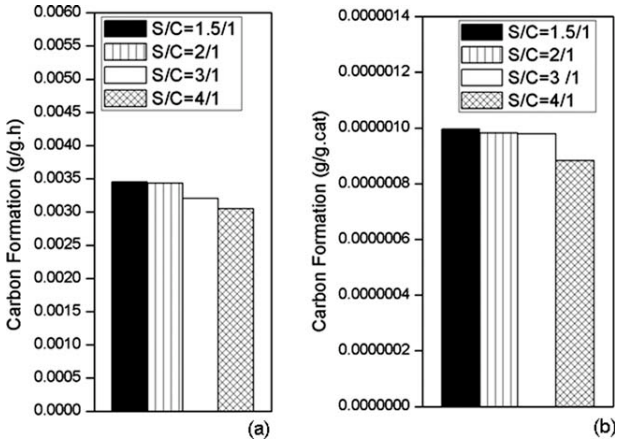

Figure 7. Effect of *S/C* ratio on the predicted carbon formation at the anode of DIR-SOFC systems.

Predicted amount of carbon formation at the anode of (a) conventional DIR-SOFC and (b) inserted catalyst rod DIR-SOFC at various *S/C* ratios.

resulted in lower the exothermic electrochemical reaction; thus, the temperature drops down because of the strong endothermic steam reforming reaction occurred. Hence, we concluded that, to maximize the performance of DIR-SOFC, low inlet *S/C* ratio must be applied; nevertheless, high potential for carbon deposition must be aware. This gains the great benefits of DIR-SOFC with inserted catalyst rod because the rate of carbon deposition was remarkably lower than the conventional DIR-SOFC even at a lower inlet *S/C* ratio (Figure 7b).

The modeling of DIR-SOFC with inserted catalyst rod at particularly low inlet *S/C* ratio (from 2:1 to 0.5:1) was also carried out to determine the optimum operating condition for this system. As shown in Figure 8, the electrical efficiency increased with decreasing inlet *S/C* ratio from 2:1 to 1.1:1, then it rapidly reduced at lower inlet *S/C* ratio; furthermore, significant amount of carbon deposition was observed. These strong negative effects could be due to the incomplete reforming of methane with steam and the occurring of methane cracking instead. Hence, the suitable inlet *S/C* ratio for DIR-SOFC with inserted catalyst rod should be slightly higher than the stoichiometric value (1/1).

Effect of flow direction

For typical autothermal application, e.g., heat exchanging system, flow direction of exchanged fluids strongly affects

Table 6. Effect of Inlet *S/C* Ratio on the Electrical Efficiency and Power Density of DIR-SOFC Systems (Simulated at 1 bar)

	Power Density (A cm^{-2})		Electrical Efficiency (%)	
Steam/ Carbon	Conventional DIR	DIR with Inserted Catalyst	Conventional DIR	DIR with Inserted Catalyst
1.5:1	0.37	0.48	45.95	64.25
2:1	0.32	0.45	45.25	63.53
3:1	0.32	0.41	38.88	47.10
4:1	0.31	0.39	33.99	44.96

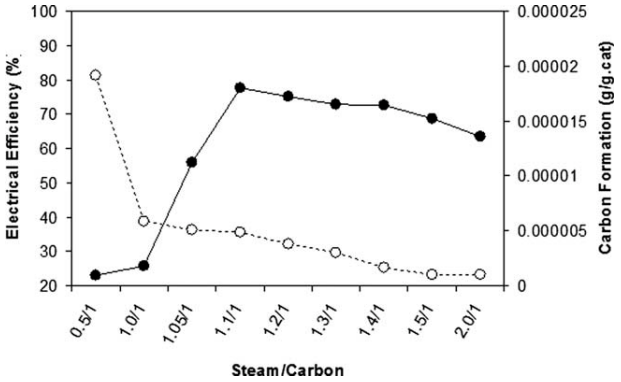

Figure 8. Effect of inlet *S/C* ratio (at lower range) on the electrical efficiency and predicted carbon formation of inserted catalyst rod DIR-SOFC (simulated at 1 bar).

Estimated electrical efficiency and predicted carbon formation at the anode of inserted catalyst rod DIR-SOFC at various *S/C* ratios.

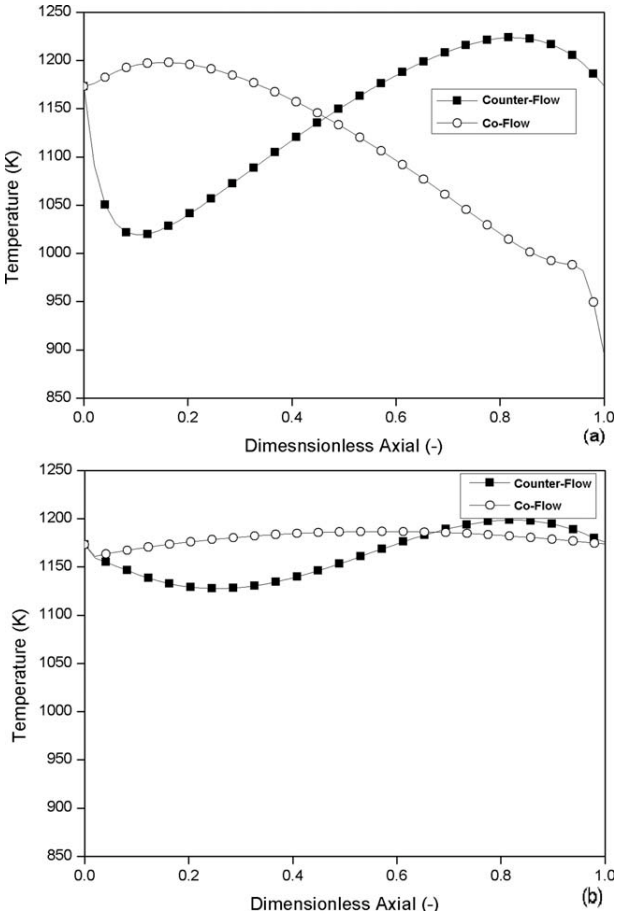

Figure 9. Effect of flow pattern on the temperature gradient in the fuel channel of DIR-SOFC systems (simulated at 1 bar with inlet *S/C* ratio of 2).

Temperature profiles in the fuel channel of (a) conventional DIR-SOFC with co-flow and counter-flow patterns and (b) inserted catalyst rod DIR-SOFC with co-flow and counter-flow patterns.

Table 7. Effect of Flow Pattern on the Electrical Efficiency, Power Density, and Predicted Carbon Formation of DIR-SOFC Systems (Simulated at 1 bar)

Flow Direction	Power Density (A cm^{-2})		Electrical Efficiency (%)		Carbon Formation (g g_{cat}^{-1})	
	Conventional DIR	DIR with Inserted Catalyst	Conventional DIR	DIR with Inserted Catalyst	Conventional DIR	DIR with Inserted Catalyst
Counter-flow	0.32	0.45	45.25	63.53	3.43×10^{-3}	9.82×10^{-7}
Co-flow	0.25	0.51	34.7	71.44	2.83×10^{-3}	9.83×10^{-7}

the heat transfer and reaction behavior in the fluid stream, thus the effect of fuel and oxidant flow direction on the DIR-SOFC performance was also considered here. In the previous sections, air flow is counter-flow to fuel flow in the fuel channel. As an alternative option, the system behavior was analyzed as co-flow pattern by changing mass and energy balances in air channel along with their corresponding boundary conditions while keeping all other operating conditions identical to those of counter-flow pattern. Figures 9a,b show the effect of these two gas flow patterns on the temperature profiles along the fuel channels. It can be seen that the flow directions of fuel gases and air strongly affect the temperature gradient along the system.

In the case of conventional DIR-SOFC configuration with co-flow pattern, no local cooling temperature occurred at the entrance of the fuel channel because the electrochemical reaction occurred rapidly at the entrance of the channel due to the oxygen-rich condition in the air channel, which resulted in sufficient heat for endothermic steam reforming reaction. Nevertheless, this flow pattern caused significant temperature drop at the second half of the channel as most of oxygen was electrochemically consumed, and the required heat for the steam reforming reaction is larger than the generated heat from electrochemical reaction. Under co-flow pattern, the average solid cell temperature was lower than that of the counter-flow pattern and resulted in the increase in cell resistance, which eventually reduced the electrical efficiency (Table 7) and output voltage (reduced by 34.7% to 0.65 V). According to the potential for carbon deposition, it was observed that lower amount of carbon deposition occurred for DIR-SOFC with co-flow pattern, Table 7. This is due to the presence of higher hydrogen content in the fuel channel for DIR-SOFC with co-flow pattern, which reduces the potential for carbon deposition, according to the carbon formation rate expression.[9]

Figure 9b presents the temperature distribution in the fuel channel for DIR-SOFC with inserted catalyst rod under counter- and co-flow patterns. Clearly, DIR-SOFC with co-flow pattern provided smoother temperature distribution with higher average cell temperature. These result in the reducing of cell overpotentials and consequently gain higher output voltage (0.77 V) and electrical efficiency (71.4%, Table 7). It is noted that the flow direction showed insignificant impact on the amount of carbon deposition for DIR-SOFC with inserted catalyst rod (Table 7). We summarized that the high efficiency of DIR-SOFC with inserted catalyst rod under co-flow pattern is due to the good matching between the heat exothermically supplied from the electrochemical reaction and the heat required for the endothermic steam reforming reaction along the fuel cell system, thus concluded here that DIR-SOFC with co-flow pattern is more satisfactory than that with counter-flow pattern.

Conclusions

The simulation indicated that DIR-SOFC with inserted catalyst rod provides smoother temperature gradient along SOFC system with significantly lower local cooling at the entrance of the fuel channel. In addition, higher power density and electrochemical efficiency with less carbon deposition can be achieved compared to the conventional DIR-SOFC.

By increasing the inlet fuel flow rate, the cooling effect and power density of both DIR-SOFC systems can be improved; nevertheless, less electrical efficiency with higher amount of carbon deposition was predicted. It was then found that, to maximize the performance of DIR-SOFC, low inlet *S/C* ratio must be applied; nevertheless, high potential for carbon deposition must be aware. According to the simulation result, the most suitable inlet *S/C* ratio for DIR-SOFC with inserted catalyst rod was 1.1, whereas that of conventional DIR-SOFC should not be less than 1.5. DIR-SOFC with counter-flow pattern was then compared to that with co-flow pattern. In the case of conventional DIR-SOFC, although the local cooling temperature at the entrance of the fuel channel and the amount of carbon deposition can be minimized, this flow pattern caused significant temperature drop at the second half of the channel; furthermore, the average solid cell temperature was lower than that of the counter-flow pattern, which resulted in the increase in cell resistant and eventually reduced the electrical efficient and output voltage. As for DIR-SOFC with inserted catalyst rod, the co-flow pattern provided smoother temperature distribution with higher average cell temperature, which leads to reduced cell overpotentials and consequently higher output voltage and electrical efficiency.

Acknowledgments

The financial support from the Thailand Research Fund (TRF) and Commission on Higher Education, and the Thailand Graduate Institute of Science and Technology (TGIST) program, Thailand's National Science and Technology Development Agency (NSTDA), grant no. TG-55-20-50-058D throughout this project is gratefully acknowledged.

Notation

C_p = specific heat of the gas streams, kJ mol^{-1} K^{-1}
A_{act} = external catalyst surface area = $\frac{\pi(d_t-2\tau_{cat})L}{\pi\left(d_t^2-(d_t-2\tau_{cat})^2\right)L}$
c_i = concentration, mol m^{-3}
$D_{i,j}$ = binary diffusion, m^2 s^{-1}
$D_{i,mix}^e$ = the effective molecular diffusivity, m^2 s^{-1}
$D_{i,ku}$ = the Kundsen diffusivity, m^2 s^{-1}

D_p = pore diameter, m
E = open circuit voltage, V
E_{act} = activation energy, kJ mol^{-1}
F = Faraday's constant, 96,487 C mol^{-1}
ΔH = the change of heat of reaction, kJ mol^{-1}
j_0 = exchange current density, mA cm^{-2}
j = current density, mA cm^{-2}
j_{H_2} = current density from hydrogen oxidation reaction, mA cm^{-2}
h = heat transfer coefficient, kJ m^{-1} s^{-1} K^{-1}
k = thermal conductivity, kJ m^{-1} s^{-1} K^{-1}
N_i^D = the bulk molar diffusive flux of gas component, mol m^{-1} s^{-1}
p^o = standard partial pressure, bar
p_i = partial pressure of species i,
R = universal gas constant; 8.314 J mol^{-1} K^{-1}.
R_{elect} = the hydrogen oxidation reaction rate, mol m^{-2} s^{-1}
q_{rad} = the heat flux from radiation, W m^{-2}
S_{act} = specific surface area of catalyst
T = temperature, K
u = fluid velocity, m s^{-1}
y_i = the mole fraction of gas

Greek letters

ρ = density, kg m^{-3}
γ = special Fuller et al.[17] diffusion volume
ϑ = exchange current density constant, mA cm^{-2}
$\alpha_{a,c}$ = charge transfer coefficient of anode and cathode
σ = Stefan-Boltzmann coefficient
ε = porosity
τ = tortuosity
η_{cell} = voltage drop of the whole cell, Volts
λ = thermal conductivity (kJ m^{-1} s^{-1} K^{-1})

Superscripts

* = active site

Subscripts

a = air channel
c-form = carbon formation
i = component (methanol, water, hydrogen, etc.)
j = reaction (SRM, WGS, etc.)
f = fuel channel
s = solid oxide fuel cell
Act = activation losses
cell = cell stack
con = concentration losses
ohm = ohmic losses
elec = electrochemical reactions
rod = catalyst rod
reform = reforming

Literature Cited

1. Hooger G. *Fuel Cell Technologies Handbook*. Boca Raton, FL: CRC Press, 2003.
2. Larminie J, Dicks A. *Fuel Cell Systems Explained*. Chichester: Wiley, 2000.
3. Angular P, Adjiman CS, Brandon NP. Anode-supported intermediate temperature direct internal reforming solid oxide fuel cell. I. Model-based steady-state performance. *J Power Sources*. 2004;138:120–138.
4. Iora P, Angular P, Adjiman CS, Brandon NP. Comparison of two IT DIR-SOFC models: impact of variable thermodynamic, physical, and flow properties. Steady-state and dynamic analysis. *Chem Eng Sci*. 2005;60:2963–2975.
5. Nikooyeh K, Jeje AA, Hill JM. 3D modeling of anode-supported planar SOFC with internal reforming of methane. *J Power Sources*. 2007;17:601–609.
6. Achenbach E, Riensche E. Methane/steam reforming kinetics for solid oxide fuel cells. *J Power Sources*. 1994;52:283–288.
7. Kandepu R, Imsland L, Foss BA, Stiller C, Thorud B, Bolland O. Modeling and control of a SOFC-GT-based autonomous power system. *Energy*. 2007;32:406–417.
8. Xu J, Froment GF. Methane steam reforming, methanation and water-gas shift. I. Intrinsic kinetics. *AIChE J*. 1989;35:88–96.
9. Zavarukhin SG, Kuvshinov GG. Mathematic modeling of the process of production of nanofibrous carbon from methane in an isothermal reactor with a fixed bed of the Ni-Al_2O_3 catalyst. *Chem Eng J*. 2006;120:139–147.
10. Zhu H, Colclasure AM, Kee RJ, Lin Y, Barnett SA. Anode barrier layers for tubular solid-oxide fuel cells with methane fuel streams. *J Power Sources*. 2006;161:413–419.
11. Costamagna P, Selimovic A, Borghi MD, Agnew G. Electrical model of the integrated planar solid fuel cell (IP-SOFC). *Chem Eng J*. 2004;102:61–69.
12. Chan SH, Khor KA, Xia ZT. A complete polarization model of a solid oxide fuel cell and its sensitivity to the change of cell component thickness. *J Power Sources*. 2001;93:130–140.
13. Leng YJ, Chan SH, Khor KA, Jiang SP. Performance evaluation of anode-supported solid oxide fuel cells with thin film YSZ electrolyte. *Int J Hydrogen Energy*. 2004;29:1025–1033.
14. Xue X, Tang J, Sammes N, Du Y. Dynamic modeling of single tubular SOFC combining heat/mass transfer and electrochemical reaction effects. *J Power Sources*. 2005;142:211–222.
15. Mauri R. A new application of the reciprocity relations to the study of fluid flows through fixed beds. *J Eng Math*. 1998;33:103–112.
16. Todd B, Young JB. Thermodynamic and transport properties of gases for use in solid oxide fuel cell modeling. *J Power Sources*. 2002;110:186–200.
17. Fuller EN, Schettler PD, Giddings JC. A new method for prediction of binary gas-phase diffusion coefficients. *Ind Eng Chem*. 1966;58:19–27.
18. Ramakrishna PA, Yang S, Sohn CH. Innovative design to improve the power density of a solid oxide fuel cell. *J Power Sources*. 2006;158:378–348.
19. Matsuzaki Y, Yasuda I. Relationship between the steady-state polarization of the SOFC air electrode, La0.6Sr0.4MnO3+δ/YSZ, and its complex impedance measured at the equilibrium potential. *Solid State Ionics*. 1999;126:307–313.
20. Zhu H, Kee RJ. A general mathematical model for analyzing the performance of fuel-cell membrane-electrode assemblies. *J Power Sources*. 2003;117:61–74.
21. Zhao F, Virkar AV. Dependence of polarization in anode-supported solid oxide fuel cells on various cell parameters. *J Power Sources*. 2005;141:61–74.
22. Suwanwarangkul R, Croiset E, Fowler MW, Douglas PL, Entche E, Douglas MA. Performance comparison of Fick's, dusty-gas and Stefan-Maxwell models to predict the concentration overpotential of a SOFC anode. *J Power Sources*. 2003;122:9–18.
23. Hernandez-Pacheco E, Singha D, Huttonb PN, Patelb N, Manna MD. A macro-level model for determining the performance characteristics of solid oxide fuel cells. *J Power Sources*. 2004;138:174–186.
24. Stiller C, Thorud B, Seljebø S, Mathisen Ø, Karoliussen H, Bolland O. Finite-volume modeling and hybrid-cycle performance of planar and tubular solid oxide fuel cells. *J Power Sources*. 2005;141:227–240.
25. Lim LT, Chadwick D, Kershenbaum L. Achieving autothermal operation in internally reformed solid oxide fuel cells: simulation studies. *Ind Eng Chem Res*. 2005;44:9609–9618.
26. Yamazaki O, Tomishige K, Fujimoto K. Development of highly stable nickel catalyst for methane-steam reaction under low steam to carbon ratio. *Appl Catal A*. 1996;136:49–56.

Manuscript received Mar. 25, 2009, and revision received Sept. 1, 2009.

ภาคผนวก 12

Chemical Engineering Communications
Publication details, including instructions for authors and subscription information:
http://www.informaworld.com/smpp/title~content=t713454788

A REACTION-EXTRACTION-REGENERATION SYSTEM FOR HIGHLY SELECTIVE OXIDATION OF BENZENE TO PHENOL

Garun Tanarungsun[a]; Hiroshi Yamada[b]; Tomohiko Tagawa[b]; Worapon Kiatkittipong[c]; Piyasan Praserthdam[a]; Suttichai Assabumrungrat[a]
[a] Center of Excellence in Catalysis and Catalytic Reaction Engineering, Department of Chemical Engineering, Faculty of Engineering, Chulalongkorn University, Bangkok, Thailand [b] Department of Chemical Engineering, Nagoya University, Nagoya, Japan [c] Department of Chemical Engineering, Faculty of Engineering and Industrial Technology, Silpakorn University, Nakhon Pathom, Thailand

Online publication date: 08 February 2010

To cite this Article Tanarungsun, Garun , Yamada, Hiroshi , Tagawa, Tomohiko , Kiatkittipong, Worapon , Praserthdam, Piyasan and Assabumrungrat, Suttichai(2010) 'A REACTION-EXTRACTION-REGENERATION SYSTEM FOR HIGHLY SELECTIVE OXIDATION OF BENZENE TO PHENOL', Chemical Engineering Communications, 197: 8, 1140 — 1151
To link to this Article: DOI: 10.1080/00986440903412894
URL: http://dx.doi.org/10.1080/00986440903412894

Chem. Eng. Comm., 197:1140–1151, 2010

ISSN: 0098-6445 print/1563-5201 online
DOI: 10.1080/00986440903412894

A Reaction-Extraction-Regeneration System for Highly Selective Oxidation of Benzene to Phenol

GARUN TANARUNGSUN,[1] HIROSHI YAMADA,[2]
TOMOHIKO TAGAWA,[2]
WORAPON KIATKITTIPONG,[3]
PIYASAN PRASERTHDAM,[1] AND
SUTTICHAI ASSABUMRUNGRAT[1]

[1]Center of Excellence in Catalysis and Catalytic Reaction Engineering, Department of Chemical Engineering, Faculty of Engineering, Chulalongkorn University, Bangkok, Thailand
[2]Department of Chemical Engineering, Nagoya University, Nagoya, Japan
[3]Department of Chemical Engineering, Faculty of Engineering and Industrial Technology, Silpakorn University, Nakhon Pathom, Thailand

The reaction-extraction-regeneration system for the liquid-phase oxidation of benzene to phenol in the benzene-water-oxygen system was investigated. Phenol was extracted in the extractor to reduce the concentration of phenol in the benzene phase. As vanadium catalyst was oxidized to inactive species after the oxidation reaction, the regenerator was installed in the system to reduce the oxidation state of vanadium catalyst from V^{4+} or VO^{2+} to the active V^{3+} under H_2 flow. The effects of various operating parameters including concentration of VCl_3 catalyst, O_2 and H_2 flow rates, benzene bubble size, pH, surface area of Pt regeneration catalyst, the metal species, and amount of ascorbic acid were investigated. Ascorbic acid was employed as a reducing agent for helping reduce the V^{4+} form to the active form and therefore improving the activity of vanadium catalyst. VCl_3 catalyst concentration of 10 mol/m^3 with pH of 3–4 in the reactor and Pt surface area of 0.05 m^2 in the regenerator showed optimal conditions for the system.

Keywords Benzene; Biphasic system; Hydroxylation; Partial oxidation; Reaction-extraction-regeneration system

Introduction

Phenol is an important chemical for the production of antioxidants, agrochemicals, and polymers. More than 90% of the world production of phenol has been obtained by the cumene process. In the cumene process, the cost of phenol is directly related to the effective usage of acetone, which is equimolarly produced (Schmidt, 2005). Therefore, many researchers are working on the development of a new route to phenol synthesis by a one-step process through the direct oxidation of benzene.

Address correspondence to Hiroshi Yamada, Department of Chemical Engineering, Nagoya University, Chikusa, Nagoya 464-8603, Japan. E-mail: yamada@nuce.nagoya-u.ac.jp

Hydrogen peroxide and nitrous oxide are currently too expensive to allow an economically viable process for direct oxidation of benzene. Molecular oxygen (O_2) is considered to be the best oxidant due to its low cost and significant advantages for the environment.

New processes for phenol production without acetone by-product and with high selectivity have been studied (Seo et al., 1997). Battistel et al. (2003) studied hydroxylation of benzene to phenol with molecular oxygen catalyzed by vanadium chloride. The efficiency of the reaction is related to the ability of the reductant to reduce vanadium without being inactivated by the presence of oxygen. The interaction of vanadium chloride and ascorbic acid influences the valence of vanadium species in the reaction. Since V^{5+} tends to increase as a function of time, the oxidation of benzene by O_2 usually gives quite low conversion and selectivity to phenol.

Miyake et al. (2002) studied hydroxylation of benzene to phenol with the addition of oxygen and hydrogen over platinum catalyst with transition metal salts. Vanadium salt offered the highest catalytic performance for phenol production. H_2O_2 was formed on platinum catalyst, and this H_2O_2 was homolytically decomposed to hydroxyl radical on the platinum. Remias et al. (2003) studied hydroxylation of benzene to phenol by coupling palladium-catalyzed in situ hydrogen peroxide generation from dihydrogen and dioxygen. It was reported that the vanadium catalyst gave higher activity than iron catalyst. The metal salt halides species in the reaction mixture showed reactivity in the order: $Cl^- < Br^- < I^-$.

Reis et al. (2004) studied the peroxidative oxidation of benzene catalyzed by various vanadium catalysts such as V_2O_5, $VOSO_4 \cdot 5H_2O$, and V_2O_4. V_2O_5 showed the highest activity for phenol production. With high acid excess, the activity decreased abruptly, probably as a consequence of decomposition of the catalyst. Mizuno et al. (2005) studied the biphase system of partial oxidation of benzene to phenol. The extractor helped improve the selectivity of phenol in the reaction system. However, Fe-H_2O_2 and V-O_2 system still provided low phenol yield and cannot be operated in the long term. Masumoto et al. (2002) studied the hydroxylation of benzene to phenol by a supported vanadium catalyst in an aqueous acetic acid solvent. During the reaction, the color changed from light blue (V^{4+}) at the initial stage to yellowish-brown (V^{5+}). In the initial stage the ascorbic acid reduced the oxidation state of vanadium ion from V^{5+} to V^{4+}. Liu et al. (2005) studied a micro-emulsion catalytic system for highly selective hydroxylation of benzene to phenol with hydrogen peroxide. The result showed high conversion of benzene but moderate selectivity of around 50%. Increasing the amount of water in the reaction increased the benzene conversion and phenol selectivity.

Jian et al. (2006) reported the homogeneous liquid phase oxidation of benzene to phenol by sodium metavanadate with hydrogen peroxide. The solvent and pH have an effect on vanadium species in the solution. The form of vanadium ion depended on pH. The order of oxidative ability of the complex in different solvents is acetonitrile > acetone > alcohol. VO^{2+} was found to be the catalytic precursor. Diperoxovanadate species and monoperoxovanadate species were formed with the addition of hydrogen peroxide. After the reaction, vanadium catalyst was returned to VO^{2+} to the catalytic cycle (Jian et al., 2006).

The hydroxylation of benzene with H_2O_2 using various transition metal catalysts (Cu, V, Fe) supported on TiO_2 support was studied in our previous work (Tanarungsun et al., 2007a, b). For a single metal catalyst, Fe showed highest yield because of highest conversion. Vanadium gave a comparable yield while phenol selectivity was

significantly higher (Tanarungsun et al., 2007a). $FeVCu/TiO_2$ tri-metal catalyst showed higher benzene conversion; however, selectivity and turnover frequency (TOF) were slightly decreased (Tanarungsun et al., 2007c). The ratio of Cu, V, and Fe influenced the acid properties of the catalyst, and therefore affected phenol yield and phenol selectivity (Tanarungsun et al., 2008a). The use of Pt or Pd as second metal catalyst can also improve the activity of Fe catalysts and improve the phenol selectivity (Tanarungsun et al., 2008b). Recently, our previous study (Yamada et al., 2008) introduced the regeneration unit to regenerate the deactivated catalyst since the system could not be run continuously without the regeneration unit. First, Pd/Al_2O_3 was employed as a regeneration catalyst, which was fixed by ZrO_2 balls on the top of the regenerator. However, Pd/Al_2O_3 preferentially adsorbed vanadium ions and ZrO_2 balls slightly adsorbed vanadium ions. Therefore, palladium metal bulk catalyst was employed instead to avoid the adsorption of active vanadium species.

In this article, the effect of the operation of the reaction-extraction-regeneration system on the phenol production rate was investigated intensively. The effects of various operating parameters in the reactor, i.e., the species of metal catalyst, concentration of VCl_3 catalyst, benzene bubble size, pH, feed flow rate of oxygen, amount of ascorbic acid, and in the regenerator, i.e., feed flow rate of H_2 and surface area of Pt regeneration catalyst, were investigated. The reaction system in this study was quite similar to that in our previous work (Yamada et al., 2008); however, the reaction and extraction were carried out in bubble columns instead of the stirred tanks in the previous work to further improve the performance.

Experimental Section

Three bubble jacket columns were used as the reactor, the extractor, and the regenerator (Figure 1).

Standard Condition for Reaction-Extraction System

In this study, benzene was reacted with water and oxygen to generate phenol in the semi-batch reaction-extraction-regeneration system. The details of each section follow.

Reactor
The reactor was operated in a three-phase system consisting of oxygen bubble, organic phase, and aqueous phase. The vanadium ion acting as a catalyst for the reaction was dissolved in the aqueous phase.

Extractor
The organic phase from the reactor was pumped to the extractor containing aqueous solution of NaOH in order to extract the reaction product, phenol. Phenol was extracted in the phenoxide form. Then the organic phase was fed back to the reactor.

Regenerator
The aqueous solution containing catalyst was pumped to the regenerator in order to regenerate the deactivated catalyst solution. The regenerator was packed with a Pt sheet, which acts as the catalyst for the regeneration process. Hydrogen gas

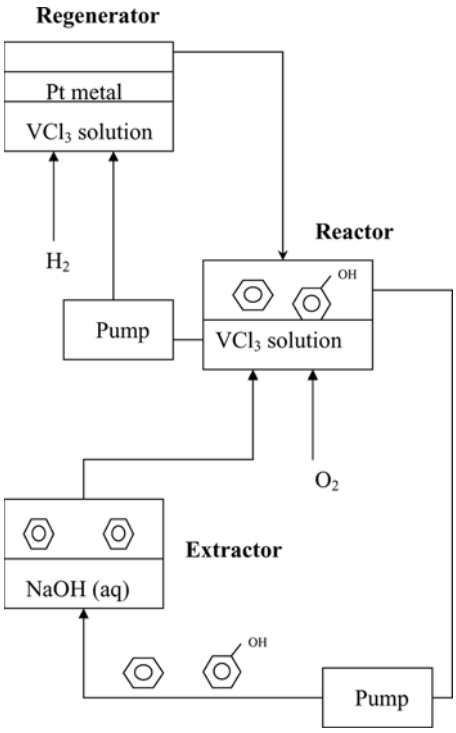

Figure 1. Schematic diagram of the reaction-extraction-regeneration system.

(30 mL/min) was fed in the regenerator to regenerate the deactivated catalyst in the aqueous solution.

Reaction Conditions

Reactor Condition

Benzene (150 mL) and catalyst solution (300 mL of 10 mol VCl_3/m^3-aq) were placed in a reactor where pure oxygen gas with a bubble size of 1 mm was continuously introduced into the reactor at a flow rate of 30 mL/min. Benzene was circulated from the reactor to the extractor by using a circulation pump operated at a constant flow rate of 30 mL/min. The other circulation pump was used to circulate the aqueous solution between the reactor and the regenerator at a flow rate of 50 mL/min. The reactor was operated at a temperature of 40°C using a circulating water bath equipped with a temperature controller. The vapor in the exit gas was trapped using a condenser operated at 2°C to control the amount of benzene evaporation from the system. In this system, the reaction occurs in the tri-phase reaction system.

Extractor Condition

Benzene (50 mL) and alkaline solution (125 mL of 172 mol $NaOH/m^3$-aq) were placed in an extractor that was operated with a controlled temperature of 50°C. An injector was used to distribute benzene bubbles in the alkaline solution. In this system, the reaction took place in the biphase reaction system.

Regenerator Condition

The aqueous VCl_3 catalyst solution (300 mL) was continuously fed with hydrogen (30 mL/min) in order to regenerate the catalyst. In a standard condition, a Pt metal sheet with surface area of 470 cm^2 (35 g) was used as a regeneration catalyst to reduce the oxidized vanadium ion catalyst in the aqueous solution. The regenerator was operated at a temperature of 60°C controlled by the water circulating system. The vapor in the exit gas was trapped using a condenser operated at 2°C to control the loss of the aqueous solution from the system. In this system, the reaction occurs in the tri-phase reaction system.

All chemicals used in this study were purchased from Wako Pure Chemical Industries, Ltd. No further purification was carried out. A small amount of organic phase was periodically sampled and analyzed with a gas chromatograph (GC-353B, GL Sciences, Inc.) equipped with a 25 m column (CP-Sil 8CB, J&W Scientific, Inc.) and operated at 383 K.

Characterization

Electron spin configuration was detected by using electron spin resonance spectroscopy (ESR) (JEOL model JES-RE2X) with the frequency of 8.8–9.6 GHz. The sample was operated in TE_{011} mode with the ES-TPRIT program. Fourier transform-infrared (FT-IR) spectra were recorded in a Nicolet impact 6700 instrument, using the range of 650–4000 cm^{-1}.

Results and Discussion

Effects of Operating Parameters on System Performance

The reactions taking place in the reaction-extraction-regeneration system in this study can be summarized as follows:

Reactor:

$$\text{Benzene} + \text{OH}^\circ \rightarrow \text{Phenol} \tag{1}$$

$$2V^{3+} + 1/2O_2 + H_2O \rightarrow 2V^{4+} + 2OH^\circ \tag{2}$$

$$V^{3+} + HO^\circ \rightarrow VO^{2+} + H^+ \tag{3}$$

Extractor:

$$\text{Phenol} + \text{NaOH} \rightarrow \text{Sodium phenoxide} + H_2O \tag{4}$$

Regenerator:

$$VO^{2+} + 0.5H_2 + H^+ \rightarrow V^{3+} + H_2O \tag{5}$$

$$V^{4+} + 0.5H_2 \rightarrow V^{3+} + H^+ \tag{6}$$

Without other states, the performance of the system was evaluated in term of phenol production rate at reaction time of 30 h.

Effect of Concentration of VCl_3 Catalyst

Figure 2 shows the effect of the catalyst concentration on the production rate of phenol in the range of 0–40 mol/m^3 of VCl_3 catalyst solution. The phenol production rate increased along with the increase of catalyst concentration. The phenol production rate was very low when the concentration of VCl_3 catalyst was lower than 0.5 mol/m^3. The optimum of catalyst concentration is approximately 10 mol/m^3. The effect of VCl_3 concentration on dissolved ability of O_2 and H_2 was investigated by using gas chromatography. The amounts of O_2 and H_2 dissolved in the catalyst phase in the reactor and the regenerator increased with increasing VCl_3 concentration. Therefore, the reaction and regeneration performance could be also enhanced.

Effect of O_2 Flow Rate in the Reactor

Oxygen as an oxidizing agent was fed to the bottom of the reactor via a gas injector. The effect of O_2 flow rate on the production rate of phenol is shown in Figure 3. The phenol production rate increased along with the increase of O_2 flow rate. This is likely due to the increase of interface area of catalyst and benzene by better mixing in the reactor and the increase of the hydroxyl radical in the reaction, which is a major oxidant in the reaction. Increasing O_2 flow rate from 30 mL/min to 120 mL/min increases phenol production rate about 50%. However, a disadvantage of using high O_2 gas flow rate in the system is the possible evaporation of benzene from the system.

Effect of H_2 Flow Rate in the Regenerator

Hydrogen was fed to the bottom of the regenerator via a gas injector for regenerating the catalyst. The effect of H_2 flow rate on the phenol production rate is shown in Figure 4. The reduction of used catalyst in the regenerator takes place with the presence of Pt metal and H_2. It was found that the phenol production rate can be improved around 25% with increasing the flow rate of H_2 gas from 30 to 120 mL/min. H_2 gas was employed for catalyst regeneration in the regenerator by reducing the vanadium ions from VO^{2+} and V^{4+} after the oxidation reaction to active V^{3+}.

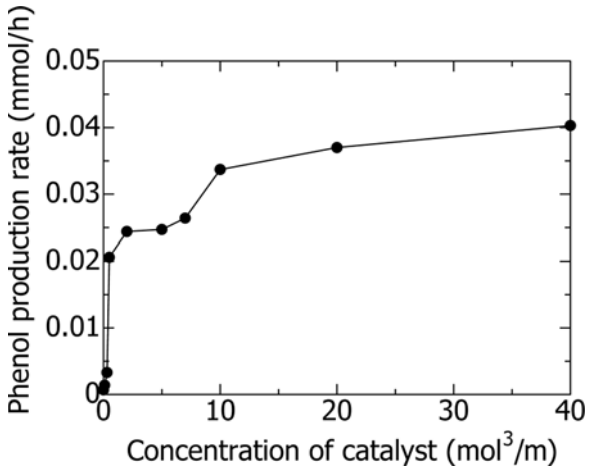

Figure 2. Influence of catalyst concentration on phenol production rate.

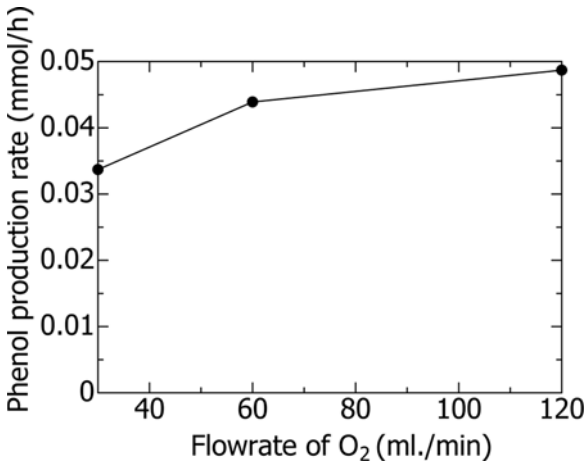

Figure 3. Influence of flow rate of O_2 on phenol production rate.

The further reduction from V^{3+} to V^{2+} could hardly occur because V^{3+} is a more stable species. The change of the oxidation state of vanadium ions becomes better when more hydrogen is fed to the regenerator. The efficiency of the reaction is related to the ability of the reducing agent to reduce vanadium without being deactivated by the presence of oxygen.

Effect of Benzene Bubble Size

Bubble size of liquid benzene was varied by using injectors of different sizes. The size of benzene bubble has an effect on the surface area of benzene for contacting with catalyst solution phase and mixing condition at the same benzene feed flow rate. The use of small-size benzene bubbles (2 mm diameter) shows a higher production rate than that of the large ones (5 mm diameter), with approximately 20% improvement (results not shown here). The smaller benzene bubbles allowed good contact with the aqueous catalyst solution.

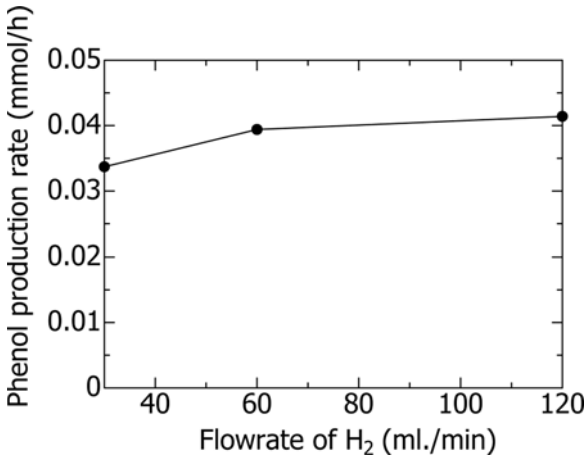

Figure 4. Influence of the flow rate of H_2 on phenol production rate.

Effect of pH in the Reactor on Phenol Production

The pH has an influence on the oxidation state of vanadium ions in the catalyst solution. It should be noted that catalyst cannot dissolve at a pH greater than 8. The pH controlled the species of vanadium ions in the aqueous solution. When VCl_3 dissolved in water with a concentration of 10 mol/m^3, the pH changed from 7 to 4 and brown color of solution was observed. HCl was added to adjust the pH from 4 to 3 and 1, and the color changed to green and then blue. When the pH changed from 4 to 6 by adding NaOH, the color changed to greenish-brown. The oxidation state of vanadium is very important for the reaction. The results show that at pH of 1 with a catalyst solution of blue color (V^{4+} and VO^{2+}), the oxidation reaction of benzene to phenol cannot occur, as observed by no phenol production. As shown in Figure 5, the suitable pH in the reactor for phenol production is in the range of 3–4.

Effect of Surface Area of Pt Regeneration Catalyst

The Pt metal reduced the oxidation state of vanadium ions from VO^{2+}, V^{4+} to V^{3+}. The Pt regeneration catalyst used in the study was in a sheet form. The surface area of the Pt metal sheet was varied by using different amounts of Pt. As shown in Figure 6, by increasing the surface area of Pt metal, phenol production rate was increased. At 0.157 m^2 of Pt metal the phenol production rate was increased only 10% from the case with 0.057 m^2 because Pt metal was excessive for regenerating the catalyst. The catalyst deactivation was found to be a major problem in the operation (formation of V^{4+}, V^{5+}) because it provided low activity for oxidation reaction.

Effects of Metal Catalyst Species and Amount of Ascorbic Acid on the Phenol Production Rate

Ascorbic acid was also added in the reactor to act as a reducing agent in the reaction system. The reactions that occurred by ascorbic acid are as follows:

$$2V^{3+} + \text{ascorbic acid} + 0.5O_2 \longrightarrow 2V^{2+} + \text{dehydroascorbic acid} + H_2O \qquad (7)$$

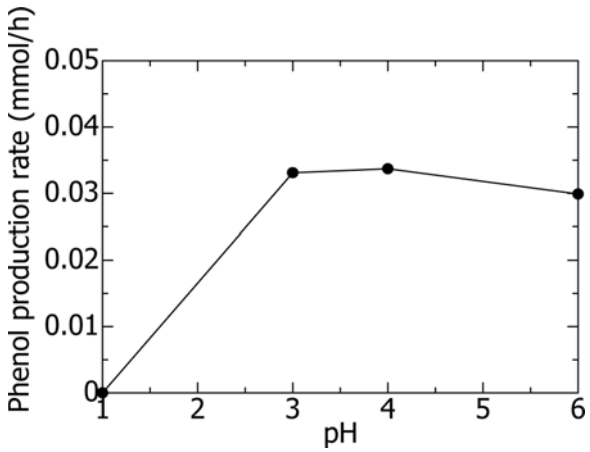

Figure 5. Influence of pH on phenol production rate.

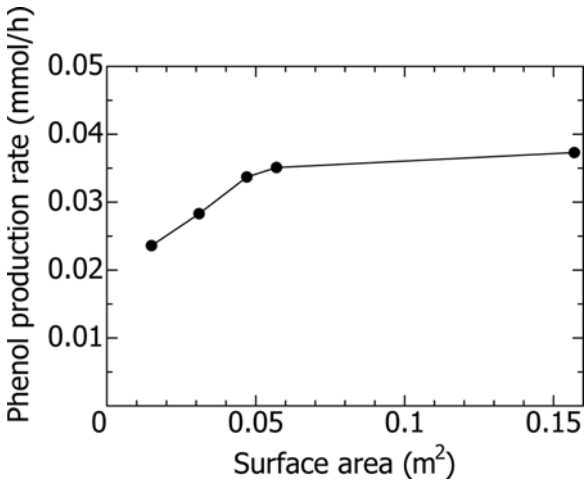

Figure 6. Influence of the surface area of Pt regeneration catalyst on phenol production rate.

$$2V^{2+} + O_2 + 2H^+ \longrightarrow 2V^{3+} + H_2O_2 \quad (8)$$

$$V^{2+} + H_2O_2 + H^+ \longrightarrow V^{3+} + OH^\circ + H_2O \quad (9)$$

$$V^{3+} + H_2O_2 \longrightarrow VO^{2+} + HO^\circ + H^+ \quad (10)$$

$$2V^{3+} + O_2 + 2H^+ \longrightarrow 2V^{4+} + 2OH^\circ \quad (11)$$

$$2V^{4+} + \text{ascorbic acid} + 0.5O_2 \rightarrow 2V^{3+} + \text{dehydroascorbic acid} + H_2O \quad (12)$$

$$2VO^{2+} + \text{ascorbic acid} \rightarrow 2V^{3+} + \text{dehydroascorbic acid} + H_2O \quad (13)$$

The amount of ascorbic acid influences the oxidation state of transition metal ion in the catalyst solution. The ascorbic acid changed V^{3+} to V^{2+} and Fe^{3+} to Fe^{2+} ion in the startup. Figure 7 shows the influence of the metal compound species and the amount of ascorbic acid on phenol production rate. Increasing the amount of ascorbic acid increased the phenol production rate for all metal species, i.e., VCl_3, $FeCl_3$, and $FeCl_2$. The efficiency of the reaction is related to the ability of the reducing agent to reduce VO^{2+} without being deactivated by the presence of oxygen. As a matter of fact, ascorbic acid undergoes autooxidation catalyzed by metal ions in the presence of oxygen. The ascorbic acid was able to interact as a chelating agent with several metal ions including vanadyl (VO_2^+) and metavanadate (VO_3^+) (Jian et al., 2006). However, it should be noted that without ascorbic acid added in the reactor as a normal operating condition, the reaction could proceed well for at least 30 h with the regenerator continuously fed with H_2.

As shown in Figure 7, compared among various metal species, VCl_3 catalyst showed the highest phenol production rate over $FeCl_3$ and $FeCl_2$ catalyst. Therefore, the catalytic activity depended on the kinds of metal and also their counter ions.

The species of vanadium ions were further analyzed by electron spin resonance (ESR). The ESR spectra of the reaction solution are presented in Figure 8 at startup

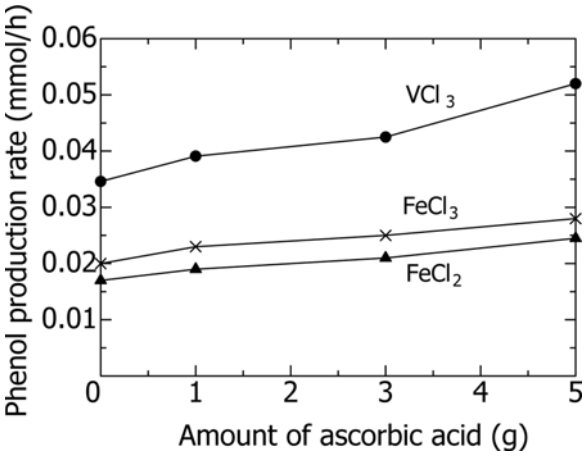

Figure 7. Influence of metal compound species and amount of ascorbic acid on phenol production rate.

time and after 8 h of reaction with and without ascorbic acid. The observed eight-line spectrum is a characteristics of vanadyl V(IV)O species (^{51}V, $I = 7/2$), and, in particular, it can be assigned to the $VOCl_2$ species (Battistel et al., 2003). Note that V^{3+} and V^{5+} ions are ESR silent. The V^{3+} was not a stable form of vanadium ion in the reaction, and it was changed to V^{4+} and VO^{2+} after the oxidation reaction, as illustrated in the increasing of ESR intensity shown in Figure 8. However, comparing the ESR after 8 h of reaction time between the systems with and without ascorbic acid (Figures 9(d) and 9(b), respectively), the increase of ESR intensity was less pronounced with the presence of ascorbic acid.

The ascorbic acid reduced the oxidized VO^{2+} by changing the oxidation state from VO^{2+}, V^{4+} to V^{3+}. At high concentration of ascorbic acid, the excessive

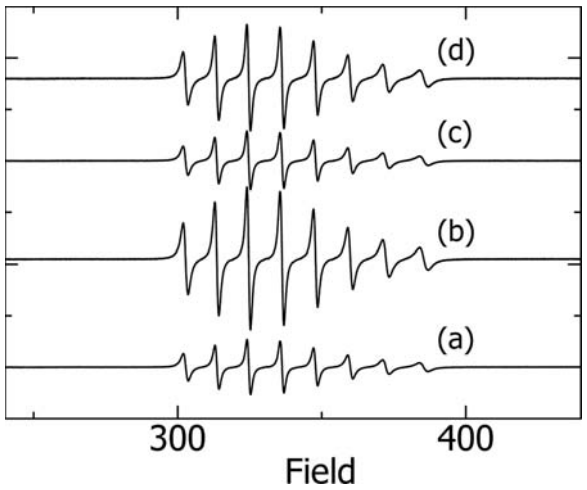

Figure 8. ESR spectra of vanadium (III) chloride: (a) on startup, (b) after 8 h, (c) on startup for the system with the addition of ascorbic acid, and (d) after 8 h for the system with the addition of ascorbic acid.

amount of ascorbic acid reduced VO^{2+} ions in the reaction system to V^{3+} ions while the oxidation reaction was taking place. Therefore, the ascorbic acid could regenerate catalyst similar to the case of using the regenerator.

Conclusion

The reaction-extraction-regeneration system was proposed in this study for the liquid-phase oxidation of benzene to phenol. The phenol was extracted from the reaction mixture as sodium phenoxide in the extraction phase. Aqueous catalyst was deactivated by O_2 to inactive forms. The regenerator was required to reduce the deactivated catalyst for the extended operation. The reaction could proceed well for at least 30 h with Pt metal sheet regeneration catalyst and continuous feeding of H_2 to the regenerator. Among metal catalyst species, i.e., VCl_3, $FeCl_3$, and VCl_2, VCl_3 showed the highest phenol production rate. The optimum condition for the system is VCl_3 catalyst concentration of 10 mol/m^3 and pH in range of 3–4 with oxygen feed rate of 60 mL/min in the reactor and Pt surface area of 0.05 m^2 with hydrogen feed rate of 60 mL/min in the regenerator. The ascorbic acid helped improve the phenol production by changing the oxidation state of vanadium catalyst. It was demonstrated that the reaction-extraction-regeneration system offered high phenol selectivity, long-time operation, and ease of startup and shutdown.

Acknowledgments

The support from Mitsubishi Chemical Corp, the Thailand Research Fund, and the Commission on Higher Education is gratefully acknowledged.

References

Battistel, E., Tassinari, R., Fornaroli, M., and Bonoldi, L. (2003). Oxidation of benzene by molecular oxygen catalysed by vanadium, *J. Mol. Catal. A*, **202**(1–2), 107–115.

Jian, M., Zhu, L., Wang, J., Zhang, J., Li, G., and Hu, C. (2006). Sodium metavanadate catalyzed direct hydroxylation of benzene to phenol with hydrogen peroxide in acetonitrile medium, *J. Mol. Catal. A*, **253**(1–2), 1–7.

Liu, H., Fu, Z., Yin, D., Yin, D., and Liao, H. (2005). A novel micro-emulsion catalytic system for highly selective hydroxylation of benzene to phenol with hydrogen peroxide, *Catal.Commun.*, **6**(9), 638–643.

Masumoto, Y., Hamada, R., Yokota, K., Nishiyama, S., and Tsuruya, S. (2002). Liquid-phase oxidation of benzene to phenol by vanadium catalysts in aqueous solvent with high acetic acid concentration, *J. Mol. Catal. A*, **184**(1–2), 215–222.

Miyake, T., Hamada, M., Niwa, H., Nishizuka, M., and Oguri, M. (2002). Effect of vanadium compound on the synthesis of phenol by hydroxylation of benzene with oxygen and hydrogen on platinum catalyst, *J. Mol. Catal. A*, **178**(1–2), 199–204.

Mizuno, T., Yamada, H., Tagawa, T., and Goto, S. (2005). Partial oxidation of benzene in benzene–water bi-phase system, *J. Chem. Eng. Jpn.*, **38**(10), 849–853.

Reis, P. M., Silva, J. A. L., Frausto da Silva, J. J. R., and Pombeiro, A. J. L. (2004). Peroxidative oxidation of benzene and mesitylene by vanadium catalysts, *J. Mol. Catal. A*, **224**(1–2), 189–195.

Remias, J. E., Pavlosky, T. A., and Sen, A. (2003). Catalytic hydroxylation of benzene and cyclohexane using in situ generated hydrogen peroxide: New mechanistic insights and comparison with hydrogen peroxide added directly, *J. Mol. Catal. A*, **203**(1–2), 179–192.

Schmidt, R. J. (2005). Industrial catalytic processes—Phenol production, *Appl. Catal. A*, **280**(1), 89–103.

Seo, Y. J., Mukai, Y., Tagawa, T., and Goto, S. (1997). Phenol synthesis by liquid-phase oxidation of benzene with molecular oxygen over iron-heteropoly acid, *J. Mol. Catal. A*, **120**(1–3), 149–154.

Tanarungsun, G., Kiatkittipong, W., Assabumrungrat, S., Yamada, H., Tagawa, T., and Praserthdam, P. (2007a). Fe (III), Cu (II), V (V)/TiO_2 for hydroxylation of benzene to phenol with hydrogen peroxide at room temperature, *J. Chem. Eng. Jpn.*, **40**(5), 415–421.

Tanarungsun, G., Kiatkittipong, W., Assabumrungrat, S., Yamada, H., Tagawa, T., and Praserthdam, P. (2007b). Liquid phase hydroxylation of benzene to phenol with hydrogen peroxide catalyzed by Fe(III)/TiO_2 catalysts at room temperature, *J. Ind. Eng. Chem.*, **13**(3), 444–451.

Tanarungsun, G., Kiatkittipong, W., Assabumrungrat, S., Yamada, H., Tagawa, T., and Praserthdam, P. (2007c). Multi transition metal catalysts supported on TiO_2 for hydroxylation of benzene to phenol with hydrogen peroxide, *J. Ind. Eng. Chem.*, **13**(5), 870–877.

Tanarungsun, G., Kiatkittipong, W., Praserthdam, P., Yamada, H., Tagawa, T., and Assabumrungrat, S. (2008a). Ternary metal oxide catalysts for selective oxidation of benzene to phenol, *J. Ind. Eng. Chem.*, **14**(5), 596–601.

Tanarungsun, G., Kiatkittipong, W., Praserthdam, P., Yamada, H., Tagawa, T., and Assabumrungrat, S. (2008b). Hydroxylation of benzene to phenol on Fe/TiO_2 catalysts loaded with different types of second metal, *Catal. Commun.*, **9**(9), 1886–1990.

Yamada, H., Mizuno, T., Tagawa, T., Tanarungsun, G., Praserthdam, P., and Assabumrungrat, S. (2008). Catalyst regeneration for partial oxidation of benzene in reaction-extraction system, *J. Jpn. Petrol. Inst.*, **51**(2), 114–117.

ภาคผนวก 13

Journal of Industrial and Engineering Chemistry 16 (2010) 411–418

Contents lists available at ScienceDirect

Journal of Industrial and Engineering Chemistry

journal homepage: www.elsevier.com/locate/jiec

Isosynthesis via CO hydrogenation over SO_4–ZrO_2 catalysts

Watcharapong Khaodee [a], Nicha Tangchupong [a], Bunjerd Jongsomjit [a], Navadol Laosiripojana [b], Piyasan Praserthdam [a], Suttichai Assabumrungrat [a,*]

[a] Center of Excellence in Catalysis and Catalytic Reaction Engineering, Department of Chemical Engineering, Faculty of Engineering, Chulalongkorn University, Bangkok 10330, Thailand

[b] The Joint Graduate School of Energy and Environment, King Mongkut's University of Technology Thonburi, Bangkok 10140, Thailand

ARTICLE INFO

Article history:
Received 8 April 2009
Accepted 7 October 2009

Keywords:
CO hydrogenation
Isobutene
Isosynthesis
Sulfated zirconia
Synthesis gas

ABSTRACT

Catalytic performances of sulfated zirconia catalysts with various contents of sulfur (from 0.1 to 0.75%) on isosynthesis were studied. It was firstly found that undoped-zirconia synthesized from zirconyl nitrate provided higher activity towards isosynthesis reaction (106 μmol kg-cat^{-1} s^{-1}) compared to that synthesized from zirconyl chloride (84.9 μmol kg-cat^{-1} s^{-1}). Nevertheless, the selectivity of isobutene in hydrocarbons was relatively lower. It was then observed that the catalytic reactivity and selectivity significantly improved by sulfur loading. The most suitable sulfur loading content seems to be at 0.1%, which gave the highest reaction rate and selectivity of isobutene. By applying several characterization techniques, i.e. BET, XRD, NH_3- and CO_2-TPD and SEM, it was revealed that the high reaction rate and selectivity towards isosynthesis reaction of sulfated zirconia catalysts are related to the acid–base properties, Zr^{3+} quantity and phase composition.

1. Introduction

Isobutene is an important feedstock for the production of oxygenated compounds. Currently, it is mainly produced from the extraction of petroleum feedstock. However, as the petroleum supply is becoming limited due to the progressive increase of fuel consumption, alternative route for isobutene production is of interest. Isosynthesis is a reaction that catalytically converts synthesis gas predominantly to branched chain hydrocarbons, especially isobutane and isobutene. Among various catalysts studied, zirconia and ceria have been reported as selective catalysts for isosynthesis in many studies [1–7]. It was further demonstrated that cerium coprecipated with zirconia, as called ceria–zirconia, can improve the catalytic activity [8]. A number of research efforts have focused on determining the relation between catalyst characteristics and their catalytic performance. As reported by Postula et al. [8], zirconias prepared by precipitation method and hydrothermal method were tested over isosynthesis reaction. The precipitated ones showed higher activity, whereas the hydrothermal ones offered greater selectivity of isobutene in C_4 hydrocarbons with corresponding to the high basicity on surface of zirconia. Su et al. [3] investigated the catalytic performance towards isosynthesis of various nanoscale zirconias synthesized by several techniques, such as precipitation method, supercritical fluid drying method and freeze-drying method. They concluded that better formation of isobutene is resulted from higher ratios of base to acid sites on catalyst surface. The results were in good agreement with those reported by Feng et al. [9], even they synthesized zirconia by different techniques (i.e. calcination of zirconyl salt and modified sol–gel method). The effect of the crystal phase such as monoclinic phase in zirconia on the catalytic performance was also investigated by Maruya et al. [5]. Due to the bifunctionality of zirconia, the acid–base properties could play an important role on the catalytic performance [3,10–13]. Several researches have proposed that catalytic activity is dependent on acid sites, while base sites or ratio of base sites to acid sites affect the selectivity of isobutene. Nevertheless, Lu et al. [14] revealed differently that the catalytic activity is dependent on strong basic site.

In our previous works, micron- and nanoscale zirconia and ceria were tested for the isosynthesis [15,16]. We reported that not only the acid–base properties, but the crystallite size and crystal phase also essentially influence the catalytic performance. At the same crystallite size, ceria shows higher activity than zirconia [15]. The effect of temperature ramping rate during calcination on characteristics of nanoscale zirconia and its catalytic performance for isosynthesis was investigated [16]. It was found that both tetragonal phase in zirconia and intensity of Zr^{3+} influence the selectivity to isobutene. In addition, the isosynthesis over ZrO_2–CeO_2 mixed oxide catalysts synthesized by coprecipitation and physical mixing methods with various contents of CeO_2 was also

* Corresponding author. Tel.: +66 2 218 6868; fax: +66 2 218 6877.
E-mail address: Suttichai.A@chula.ac.th (S. Assabumrungrat).

1226-086X/$ – see front matter © 2010 The Korean Society of Industrial and Engineering Chemistry. Published by Elsevier B.V. All rights reserved.
doi:10.1016/j.jiec.2009.10.005

studied [17]. We reported that catalysts prepared by physical mixing method offer higher catalytic activity than those prepared by coprecipitation method. In addition, the change in the selectivity of isobutene in hydrocarbons of the catalysts was well-correlated with the change in intensity of Zr^{3+}.

Metal oxides, such as ZrO_2, Al_2O_3, and TiO_2, are acid catalysts; their acidity could be enhanced by sulfation. Previously, several sulfated acid catalysts have been tested [18–23]. Among those acid catalysts, sulfated zirconia (SO_4–ZrO_2 abbreviated as SZ) has been the subject of extensive research work since its ability to catalyze isomerization of linear to branched light hydrocarbons. This catalyst is known as solid super acid and was reported to be active for *n*-butene isomerization even at low temperature, giving relatively high selectivity [23]. This catalyst may be a good choice for isosynthesis and, therefore, in this paper, the catalytic performances of sulfated zirconia on isosynthesis via CO hydrogenation were investigated. The catalysts were prepared by incipient wetness impregnation method using H_2SO_4 as a sulfating species. It is noted that two different zirconia salt precursors were employed for synthesizing zirconia via precipitation method. The catalytic performances of synthesized catalysts with different sulfur contents were then tested. In addition, various physical characteristics of synthesized catalysts, i.e. acid–base properties and surface properties including quantity of Zr^{3+} on the catalyst surface were determined in order to relate these properties with the catalytic performance.

2. Experimental

2.1. Catalyst preparation

2.1.1. Preparation of zirconia

Zirconia (ZrO_2) was synthesized via the precipitation method. A solution of zirconium salt precursors such as zirconyl chloride ($ZrOCl_2$) or zirconyl nitrate [$ZrO(NO_3)_2$] (0.15 M) was slowly dropped into a well-stirred precipitating solution of ammonium hydroxide (NH_4OH) (2.5 wt%) at room temperature. The solution was controlled at pH of 10. The obtained precipitate was removed, and then washed with deionized water until Cl^- was not detected by a silver nitrate ($AgNO_3$) solution. Then, the solid sample was dried overnight at 110 °C and calcined at 450 °C for 3 h with a temperature ramping rate of 5 °C/min.

2.1.2. Preparation of sulfated zirconia

Sulfated zirconia was prepared by the incipient wetness impregnation method. Different amounts of sulfuric acid were doped on zirconia (having sulfur contents of 0.1, 0.25, 0.5 and 0.75%) at room temperature. The obtained sample was then dried overnight at 110 °C and calcined at 450 °C for 3 h with a temperature ramping rate of 5 °C/min.

2.2. Catalyst characterizations

2.2.1. N_2 physisorption

Measurements of BET surface area, cumulative pore volume and average pore diameter were performed by N_2 physisorption technique using Micromeritics ASAP 2020 surface area and porosity analyzer.

2.2.2. X-ray diffraction (XRD)

The X-ray diffraction (XRD) patterns of powder were performed by X-ray diffractometer. The crystallite size was estimated from line broadening according to the Scherrer equation and α-Al_2O_3 was used as a standard. In addition, the characteristic peaks of crystal phase from XRD spectra were used to calculate the fraction of crystal phase in catalyst.

2.2.3. Electron spin resonance spectroscopy (ESR)

Electron spin configuration was detected by using electron spin resonance spectroscopy (ESR) with JEOL model JES-RE2X. The sample was degassed before measurement at room temperature.

2.2.4. Scanning electron microscopy (SEM)

Scanning electron microscopy (SEM) was used to determine the catalyst granule morphology. The model is JEOL JSM-5800LV and operated using the back scattering electron (BSE) mode at 20 kV.

2.2.5. Temperature-programmed desorption (TPD)

Temperature-programmed desorption techniques with ammonia and carbon dioxide (NH_3- and CO_2-TPD) were used to determine the acid–base properties of catalysts. TPD experiments were carried out using a flow apparatus. The catalyst sample (0.1 g) was treated at its calcination temperature (450 °C) in helium flow for 1 h and then saturated with 15% NH_3/He mixture or pure CO_2 flow after cooling to 100 °C. After purging with helium at 100 °C for 1 h to remove weakly physisorbed NH_3 or CO_2, the sample was heated to 450 °C at a rate of 20 °C/min in a helium flow of 50 cm^3/min. The amount of acid–base sites on the catalyst surface was calculated from the desorption amount of NH_3 and CO_2 by measuring the areas of the desorption profiles under the desorption temperature range of 100–450 °C. For the broad peak of desorption curve, it was deconvoluted to sub-peaks by peak fitting program equipped with the Micromeritics ChemiSorb 2750 pulse chemisorption system analyzer, and then converted to the amount of desorbed NH_3 or CO_2 by calibration curve of each desorbed gas.

2.3. Reaction study

Isosynthesis was carried out at 400 °C and atmospheric pressure in a fixed-bed quartz reactor packed with 2 g of catalyst. The inlet feed was a mixture of $CO/H_2/N_2$ (10/10/5 cm^3/min). The compositions of carbon monoxide and hydrogen in the feed and product streams were analyzed by a gas chromatography (Shimadzu model 8A (GC-8A)) equipped with thermal conductivity detector (TCD) and molecular sieve column, while carbon dioxide in the product stream was analyzed by the same GC with Poropak-Q column. Hydrocarbons in the product stream were analyzed by a gas chromatography Shimadzu model 14B (GC-14B) equipped with flame ionization detector (FID) with VZ-10 column.

3. Results and discussion

In this work, ZrO_2 and SO_4–ZrO_2 catalysts were used and tested for the catalytic performance on isosynthesis. The synthesized ZrO_2 obtained from $ZrOCl_2$ and $ZrO(NO_3)_2$ were denoted as ZrO_2–Cl and ZrO_2–N, respectively. The SO_4–ZrO_2 catalysts prepared by impregnating of various sulfur contents (i.e. 0.1, 0.25, 0.5 and 0.75 wt%) over ZrO_2 and denoted as w%SZ (ZrO_2–N) and w%SZ (ZrO_2–Cl).

3.1. Catalyst characterization

3.1.1. X-ray diffraction (XRD) and scanning electron microscopy (SEM)

The XRD patterns of ZrO_2 and sulfated zirconia (SO_4–ZrO_2) catalysts synthesized from $ZrOCl_2$ are shown in Fig. 1, whereas those synthesized from $ZrO(NO_3)_2$ are shown in Fig. 2. Clearly, both ZrO_2 and SO_4–ZrO_2 catalysts exhibited the similar XRD peaks at $2\theta = 28.2^\circ$ and 31.5°, indicating the presence of the monoclinic phase. Besides the monoclinic characteristic peaks, they also exhibited the XRD characteristic peaks at 2θ of 30.2°, 35.3°, 50.2° and 60.2°, which indicate the presence of tetragonal crystalline

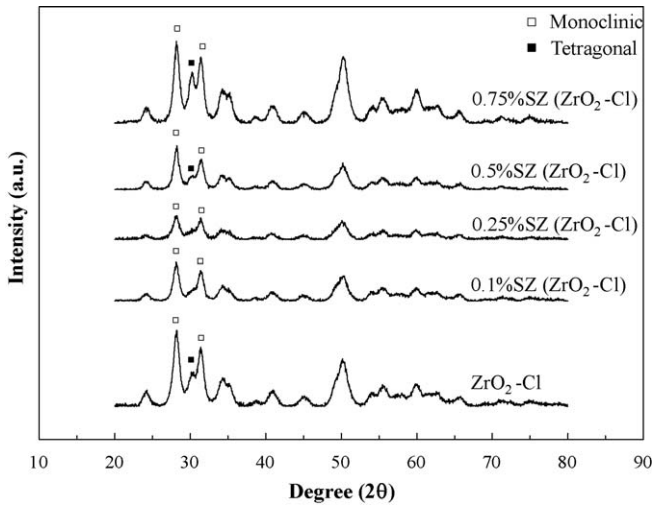

Fig. 1. XRD patterns of ZrO_2 and SO_4–ZrO_2 catalysts synthesized from $ZrOCl_2$.

phase. The crystallite size of the tetragonal phase of sulfated zirconia was determined from the peak at $2\theta = 30.2^\circ$ for 1 1 1 plane. For all catalysts, the contents of different phases are listed in Table 1. Typically, the monoclinic phase is stable up to ca. 1170 °C and then, transforms into the tetragonal phase at higher temperature, while the tetragonal phase is stable up to ca. 2370 °C and finally transforms into the cubic phase at higher temperature [24]. However, the metastable tetragonal phase in zirconia can usually be observed when the precipitation method from an aqueous salt solution is employed as also observed in this work or when the thermal decomposition of zirconium salts is used. As seen in Figs. 1 and 2, all catalysts obviously show the predominant crystal phase of monoclinic. Difference in precursor resulted in forming ZrO_2 with different phase compositions between monoclinic and tetragonal phases. The ZrO_2 prepared by $Zr(SO_4)_2$ showed tetragonal phase with amorphous, but ZrO_2 obtained from other zirconium salt precursors, such as $Zr(NO_3)_4$, $ZrCl_4$ and $ZrOCl_2$ exhibited the mixed phase of monoclinic/tetragonal phase [4,25,26]. Sulfated zirconia prepared from zirconium hydroxide precursor was entirely occupied by the tetragonal phase [27]. In this work, SZ (ZrO_2–Cl) contained more tetragonal phase compared with ZrO_2–Cl, but the opposite behavior was found in the SZ (ZrO_2–N) compared with the ZrO_2–N. Various previous studies [28–31] revealed that sulfation affected crystallization and phase transformation from tetragonal

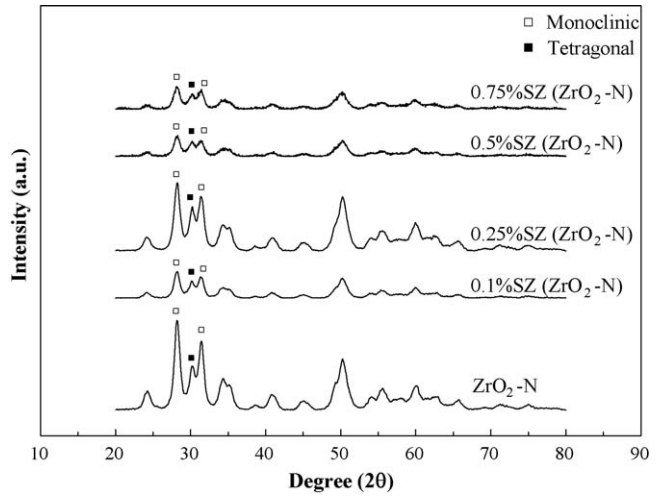

Fig. 2. XRD patterns of ZrO_2 and SO_4–ZrO_2 catalysts synthesized from $ZrO(NO_3)_2$.

Table 1
Summary of catalyst characteristics obtained from XRD measurement.

Catalysts	Crystal size (nm)[a]		% M
	M[b]	T[c]	
ZrO_2–N	8.7	4.7	67.3
0.1%SZ (ZrO_2–N)	10.0	5.5	76.1
0.25%SZ (ZrO_2–N)	10.2	13.8	84.1
0.5%SZ (ZrO_2–N)	10.0	6.1	75.4
0.75%SZ (ZrO_2–N)	9.1	9.5	71.1
ZrO_2–Cl	9.5	7.5	73.2
0.1%SZ (ZrO_2–Cl)	9.1	8.1	72.5
0.25%SZ (ZrO_2–Cl)	8.9	7.5	70.3
0.5%SZ (ZrO_2–Cl)	8.9	7.0	63.4
0.75%SZ (ZrO_2–Cl)	8.7	7.0	67.5

[a] Based on XRD line broadening.
[b] Monoclinic phase in ZrO_2.
[c] Tetragonal phase in ZrO_2.

to monoclinic of zirconia support. From the results in Table 1, only SZ (ZrO_2–N) behaved similar to the previous reports; this could be presumed that the different starting zirconium precursor can affect the phase composition of sulfated zirconia. Table 1 also illustrates the crystallite size of pure zirconia and sulfated zirconia. Based on the mainly monoclinic phase, the crystallite sizes were distributed in the low range of 8–11 nm. TEM images of pure zirconia (not shown) were similar to those in our previous work [15]. It was displayed that the particle size estimated from TEM image was insignificantly larger than the crystallite size calculated by means of XRD technique. Thus, the latter could be possibly representative for each catalyst size. Moreover, the morphologies of zirconia and sulfated zirconia were studied by SEM technique. The SEM

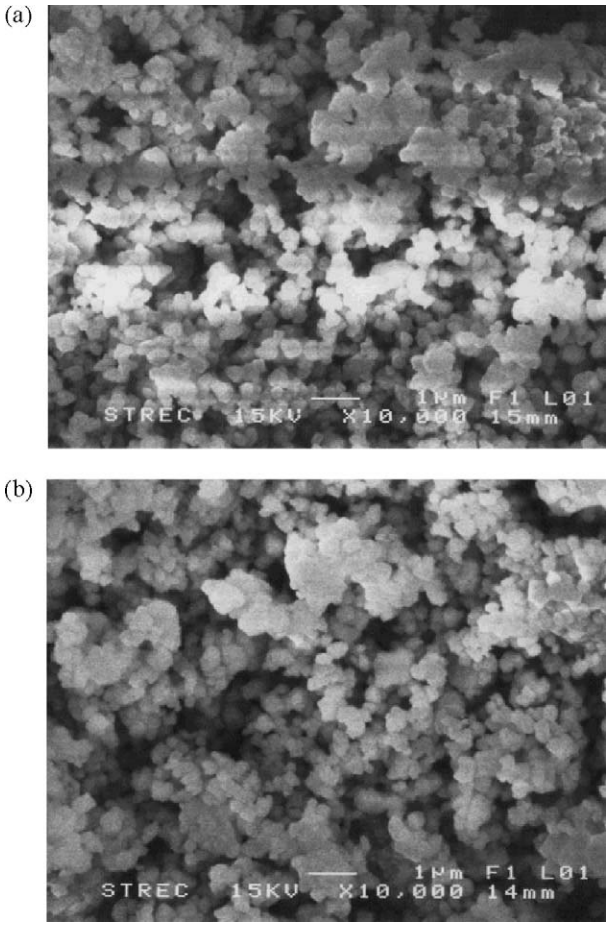

Fig. 3. SEM micrograph of (a) ZrO_2Cl and (b) 0.75% SZ (ZrO_2–Cl).

Table 2
N_2 physisorption results.

Catalysts	BET surface area[a] (m^2/g)	Cumulative pore volume[b] (cm^3/g)	Average pore diameter[c] (nm)
ZrO_2–N	76.2	0.198	5.5
0.1%SZ (ZrO_2–N)	222.7	0.345	4.9
0.25%SZ (ZrO_2–N)	243.3	0.361	4.8
0.5%SZ (ZrO_2–N)	227.3	0.336	4.8
0.75%SZ (ZrO_2–N)	232.3	0.351	4.8
ZrO_2–Cl	89.8	0.194	5.0
0.1%SZ (ZrO_2–Cl)	89.2	0.205	5.4
0.25%SZ (ZrO_2–Cl)	236.6	0.380	4.5
0.5%SZ (ZrO_2–Cl)	239.2	0.388	5.0
0.75%SZ (ZrO_2–Cl)	238.1	0.372	4.4

[a] Error of measurement = ± 5%.
[b] BJH desorption cumulative volume of pores between 1.7 and 300 nm diameter.
[c] BJH desorption average pore diameter.

micrographs of ZrO_2–Cl and 0.75% SZ (ZrO_2–Cl), for instance, at high resolution are shown in Fig. 3. It can be seen that there is inappreciable change in morphology after modifying the zirconia with sulfate.

3.1.2. N_2 physisorption

The specific surface area, cumulative pore volume, average pore diameter and pore size distribution of all synthesized catalysts were determined by N_2 physisorption using Micromeritics ASAP 2020 surface area and porosity analyzer. These parameters are summarized in Table 2. It was revealed that sulfated zirconia exhibited higher BET surface area than pure zirconia. These results were supported by N_2 adsorption–desorption isotherm plots of zirconia and sulfated zirconia catalysts as shown in Figs. 4 and 5, in which the lower N_2 adsorbed–desorbed quantities of zirconia subsequently indicate their lesser BET surface area. In addition, especially for ZrO_2–N, ZrO_2–Cl and 0.1%SZ (ZrO_2–Cl), isotherm plots of these catalysts were considerably less than those of other catalysts indicated their significant low surface area. As reported in Fărcaşiu et al. [27], the surface area of sulfated zirconia was dependent on the quantity of sulfuric acid added. However, its value began to drop after adding sulfuric acid more than 3 ml/g of zirconium hydroxide. At higher sulfur contents, the surface area suddenly decreased due to the alteration of crystal structure and sulfate migration into the bulk phase of zirconia support. Considering pore size distribution of zirconia and sulfated zirconia catalysts as shown in Figs. 6 and 7, no significant change in profile was observed for those regarding pore size distribution. However,

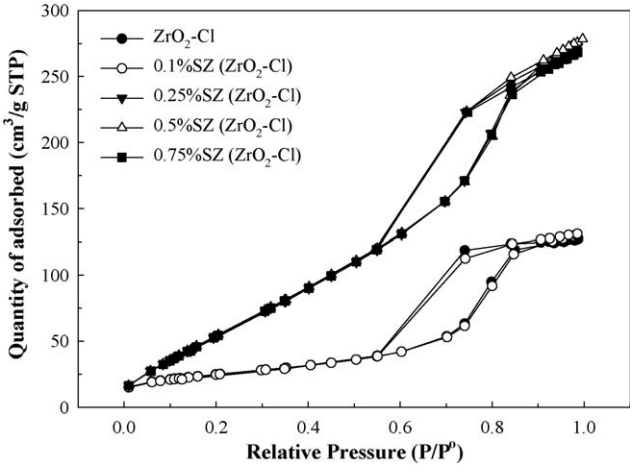

Fig. 4. N_2 adsorption–desorption isotherm plots of ZrO_2 and SO_4–ZrO_2 catalysts synthesized from $ZrOCl_2$.

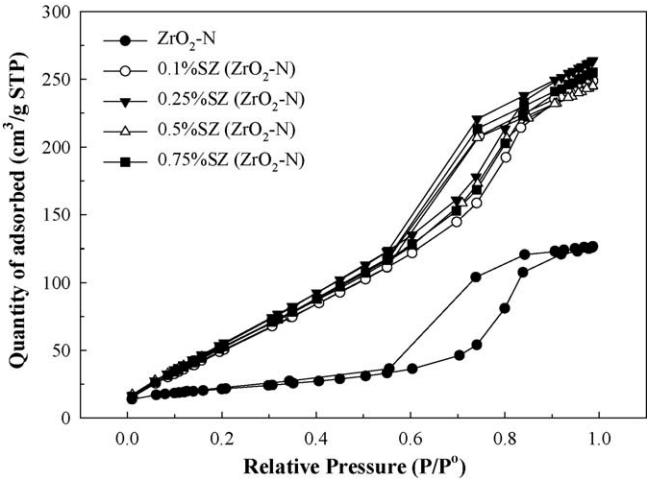

Fig. 5. N_2 adsorption–desorption isotherm plots of ZrO_2 and SO_4–ZrO_2 catalysts synthesized from $ZrO(NO_3)_2$.

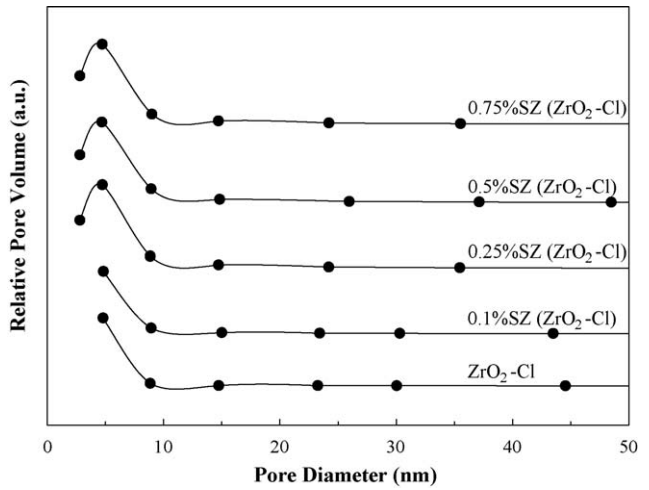

Fig. 6. Pore size distribution of ZrO_2 and SO_4–ZrO_2 catalysts synthesized from $ZrOCl_2$.

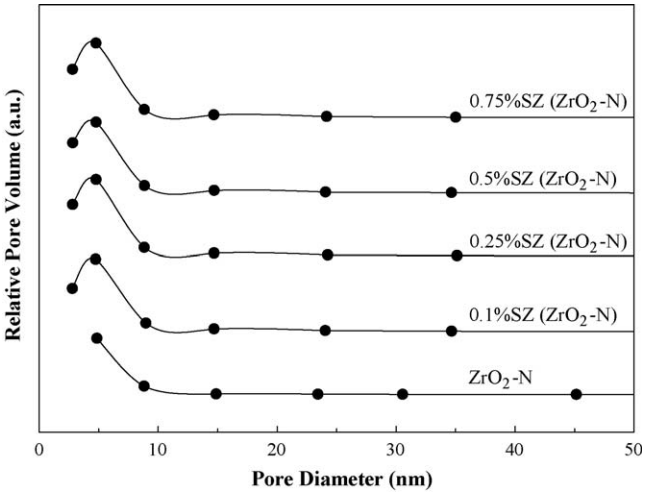

Fig. 7. Pore size distribution of ZrO_2 and SO_4–ZrO_2 catalysts synthesized from $ZrO(NO_3)_2$.

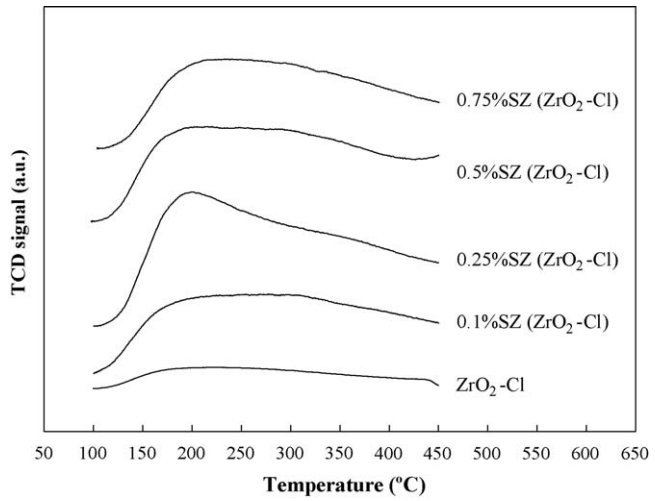

Fig. 8. NH_3-TPD profiles of ZrO_2 and SO_4–ZrO_2 catalysts synthesized from $ZrOCl_2$.

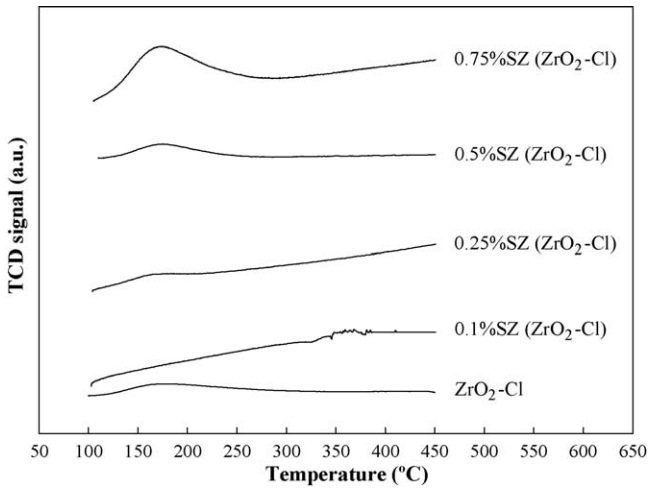

Fig. 10. CO_2-TPD profiles of ZrO_2 and SO_4–ZrO_2 catalysts synthesized from $ZrOCl_2$.

as the pore diameter at the peak of pore size distribution could refer to an average pore diameter; it was found that average pore diameters of ZrO_2–N, ZrO_2–Cl and 0.1%SZ (ZrO_2–Cl) catalysts are larger than those of the others. Nonetheless, it was noticed that no pore size below 5 nm appeared in pore size distribution plot for those three catalysts. There is an explanation from isotherm plots in Figs. 4 and 5. At low relative pressure (<0.5), the changes in the volume of N_2 desorption over these three catalysts were relatively low, compared to other catalysts. The N_2 desorption at low relative pressure was responsible for a very small pore size of catalyst. It presumably implied that no opened pore in very small size (in the range of 2–4 nm) was revealed for these three catalysts. For cumulative pore volume, these three catalysts exhibited smaller volume than others due to their less surface area and larger average pore diameter.

3.1.3. Temperature programmed-desorption (TPD)

The NH_3- and CO_2-TPD techniques were used to measure the acid–base properties of the catalysts, respectively. The NH_3- and CO_2-TPD profiles of zirconia and sulfated zirconia synthesized from $ZrOCl_2$ and $ZrO(NO_3)_2$ precursors are shown in Figs. 8–11. It is noted that the amounts of acid and base sites, which were calculated from the area below curves of these TPD profiles, are listed in Table 3. The characteristic peaks of these profiles are

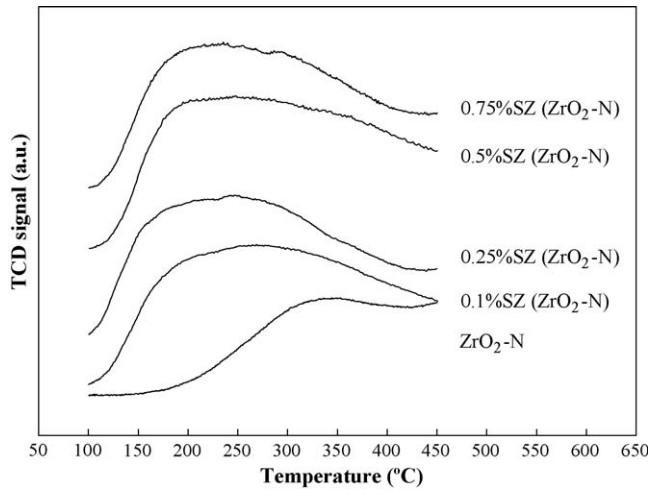

Fig. 9. NH_3-TPD profiles of ZrO_2 and SO_4–ZrO_2 catalysts synthesized from $ZrO(NO_3)_2$.

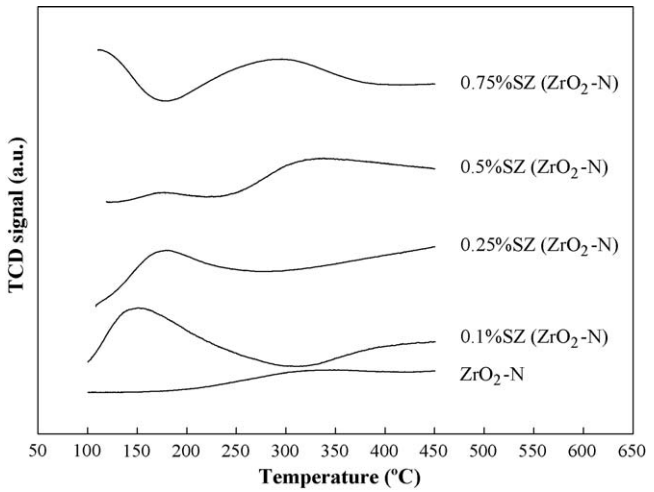

Fig. 11. CO_2-TPD profiles of ZrO_2 and SO_4–ZrO_2 catalysts synthesized from $ZrO(NO_3)_2$.

assigned to their desorption temperatures indicating the strength of Lewis acid sites on the surface. Ma et al. [32] indicated that NH_3 desorption peaks located at ca. 200 and 300 °C for ZrO_2 catalysts were corresponding to weak acid sites and moderate acid sites, respectively. Moreover, both peaks of monoclinic ZrO_2 exhibited slightly higher amount of acid sites compared to the tetragonal ZrO_2. The previous report from Li et al. [33] also indicated that the sulfated group on monoclinic SO_4–ZrO_2 should be more stable than

Table 3
Results from NH_3- and CO_2-TPD measurements.

Catalysts	Total sites (μmol/g)	
	Acid sites[a]	Base sites[b]
ZrO_2–N	197	257
0.1%SZ (ZrO_2–N)	959	76
0.25%SZ (ZrO_2–N)	1014	50
0.5%SZ (ZrO_2–N)	993	46
0.75%SZ (ZrO_2–N)	917	39
ZrO_2–Cl	594	55
0.1%SZ (ZrO_2–Cl)	978	25
0.25%SZ (ZrO_2–Cl)	1290	26
0.5%SZ (ZrO_2–Cl)	926	19
0.75%SZ (ZrO_2–Cl)	993	15

[a] From NH_3-TPD.
[b] From CO_2-TPD.

sulfated group on tetragonal SO_4–ZrO_2. According to NH_3 desorption peaks in this work (Figs. 8 and 9), not only ZrO_2 contained weak acid sites, but the moderate acid sites were also evident for SO_4–ZrO_2. In addition, the adsorption of sulfur group has some effect on acid site by being responsible for the presence of more acid sites with higher sulfur content. The model of generating acid sites by adding the sulfuric acid has been developed by several researchers [34–38]. The well-recognized model for the structure of the active site was proposed by Arata [34], wherein the sulfate bridges across two zirconium atoms. Their model takes into account the formation of Bronsted acid sites as a result of the uptake of water molecules as a weak Lewis base on the Lewis acid sites. The weak, moderate and strong base sites can be identified by CO_2 desorption peaks [32]. It was indicated that all kinds of base sites were presented in the tetragonal ZrO_2, whereas only weak and moderate base sites were observed on the monoclinic ZrO_2. From CO_2-TPD profiles in Fig. 10, ZrO_2–Cl exhibited higher desorption temperature than other catalysts due to more tetragonal phase and without sulfur loading. As for catalysts prepared from $ZrO(NO_3)_2$ precursor, they contained only the weak base sites and moderate base sites. The results in Fig. 11 and Table 3 indicate that ZrO_2–N exhibited higher base sites than sulfated zirconia. Furthermore, zirconia and sulfated zirconia prepared from $ZrO(NO_3)_2$ precursor had higher amount of CO_2 desorption peaks. This can be attributed to higher contents of monoclinic phase resulting in increased basicity of monoclinic SO_4–ZrO_2 over tetragonal SO_4–ZrO_2 as described in Li et al. [33]. It should be mentioned that acid sites of ZrO_2–Cl and ZrO_2–N were less than those of sulfated zirconia due to sulfated group on surface catalysts. It was suggested that differences in both acid and base sites can be attributed to the various fractions of crystal phases. In order to give a better understanding, the relationship between acid–base sites and percent of sulfur content in ZrO_2 is illustrated in Figs. 12 and 13. It was found that the amount of acid sites increased with increased percents of sulfur content in ZrO_2 up to the maximum at 0.25% of sulfur content, and then decreased with more sulfur loading. Considering the base sites, the amount of base sites decreased proportional sulfur content in ZrO_2.

3.1.4. Electron spin resonance (ESR) spectroscopy

A spin of unpaired electron was detected by means of ESR to identify defect center of zirconia considerably assumed as the existence of Zr^{3+} sites. Zr^{3+} signals represented at $g_{\perp} \sim 1.97$ and $g_{\parallel} \sim 1.95$ were very close to the positions of Zr^{3+} on ZrO_2 surface

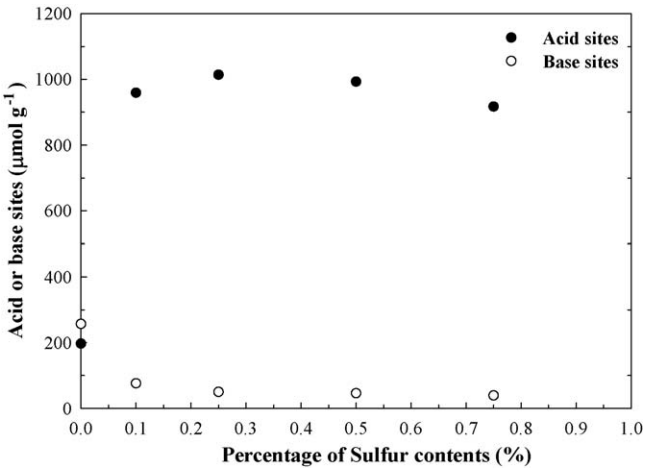

Fig. 13. Relationship between amount of acid and base sites and percent of sulfur content in ZrO_2 and SO_4–ZrO_2 catalysts synthesized from $ZrO(NO_3)_2$.

observed by many researchers [39–45]. Only $g_{\perp}$ was considered in this work due to the apparent signal. The relative ESR intensity of various zirconia and sulfated zirconia is shown in Fig. 14. It was found that quantity of Zr^{3+} ascended on amount of sulfuric acid during sulfation step. The result of ESR showed that the *g*-value of zirconia and sulfated zirconia were different. For ZrO_2–Cl, the Zr^{3+} quantity swiftly increased with increased sulfur content during the incipient wetness impregnation step. The highest intensity was observed at 0.25% of sulfur content, and then rapidly decreased beyond that value. The other zirconium salt precursor also exhibited the similar trend. Firstly, the relative intensity of Zr^{3+} gradually increased with more sulfur contents presented. The optimum point of Zr^{3+} intensity is 0.5%SZ (ZrO_2–N) after that the value decreased. From the early researches [44,45], it reasonably suggested that the Zr^{3+} center can be described as the oxygen coordinatively unsaturated zirconium sites on ZrO_2 surface. In addition, they proposed that the removal of the surface hydroxyl accounted for the formation of the new Zr^{3+} sites. However, the generation of Zr^{3+} sites should occur from another pathway. It was proposed that the surface structure of SO_4 combined with Zr elements in the bridging bidentate state. The S=O double bond nature in the sulfate complex is much stronger than that of a simple metal sulfate, thus the Lewis acid strength of Zr^{3+} becomes

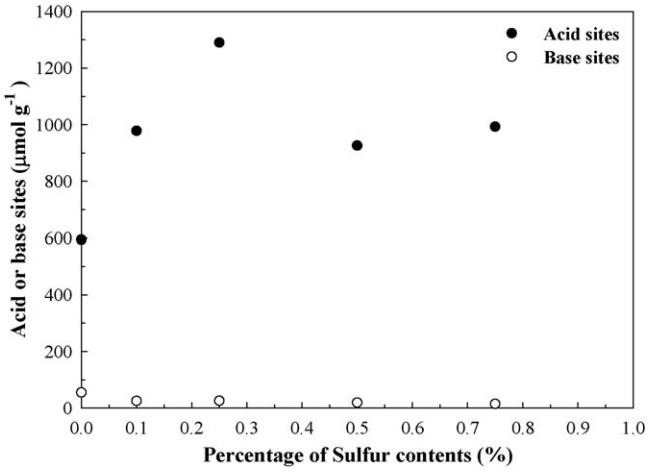

Fig. 12. Relationship between amount of acid and base sites and percent of sulfur content in ZrO_2 and SO_4–ZrO_2 catalysts synthesized from $ZrOCl_2$.

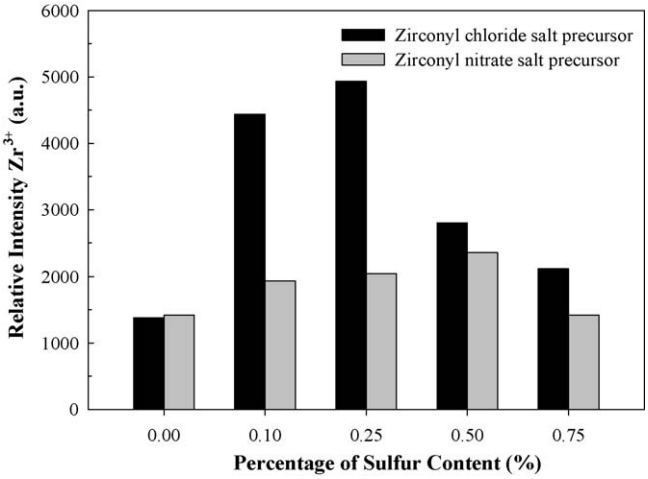

Fig. 14. Relative ESR intensity of various ZrO_2 catalysts.

Table 4
Catalytic activities and product selectivities from isosynthesis.

Catalysts	CO conversion (%)	Reaction rate (μmol kg-cat^{-1} s^{-1})	Product selectivity in hydrocarbons[a] (mol%)			
			C_1	C_2	C_3	i-C_4H_8
ZrO_2–N	3.16	106.0	11.0	5.5 (95.6)	10.1 (96.8)	73.4
0.1%SZ (ZrO_2–N)	3.49	117.0	1.1	0.5 (77.3)	8.0 (99.6)	90.4
0.25%SZ (ZrO_2–N)	2.65	88.8	0.7	0.7 (85.7)	8.2 (99.5)	90.4
0.5%SZ (ZrO_2–N)	2.72	91.1	0.3	0.4 (82.7)	8.1 (99.6)	91.1
0.75%SZ (ZrO_2–N)	2.70	90.5	0.7	0.5 (78.5)	8.1 (99.5)	90.6
ZrO_2–Cl	2.53	84.9	5.5	3.9 (75.3)	8.6 (95.9)	82.0
0.1%SZ (ZrO_2–Cl)	3.97	133.1	0.4	0.5 (89.1)	8.1 (99.7)	91.0
0.25%SZ (ZrO_2–Cl)	3.51	117.7	1.5	0.8 (85.1)	8.2 (99.5)	89.5
0.5%SZ (ZrO_2–Cl)	3.63	121.7	0.8	0.6 (81.2)	8.2 (99.5)	90.3
0.75%SZ (ZrO_2–Cl)	3.85	129.2	1.6	0.9 (75.7)	8.2 (99.2)	89.3

[a] Parentheses are the selectivity of olefin.

remarkably greater by the inductive effect of S=O in the complex. Moreover, it was revealed that there is the approximate linear relationship between Zr^{3+} quantity and the amount of acid sites.

3.2. Catalytic performance of isosynthesis over zirconia and sulfated zirconia catalysts

The reactivity and selectivity towards isosynthesis over synthesized ZrO_2 and SO_4–ZrO_2 catalysts were tested at 400 °C and atmospheric pressure with the inlet CO/H_2 ratio of 1.0. A previous study [15] reported the testing of catalytic stability with time-on-stream and showed that the steady-state rate was reached after 20 h. Table 4 presents the catalytic activity in terms of CO conversion and product selectivity from reaction. CO conversion and reaction rate were calculated from the product formation as expressed in the equations in the previous work [17]. The C_1–C_3 hydrocarbons and isobutene were mostly produced via CO hydrogenation, but only trace amount of other C_4 hydrocarbons and C_5^+ hydrocarbons was detected. Therefore, products in hydrocarbons listed in Table 4 comprise of C_1–C_3 hydrocarbons and isobutene. As seen in Table 4, it was found that undoped-zirconia synthesized from $ZrO(NO_3)_2$ provided higher activity towards isosynthesis reaction (106 μmol kg-cat^{-1} s^{-1}) than that synthesized from $ZrOCl_2$ (84.9 μmol kg-cat^{-1} s^{-1}), but the selectivity of isobutene in hydrocarbons was relatively lower (73.4% for ZrO_2–N and 82.0% for ZrO_2–Cl). In addition, the catalytic performance significantly improved by sulfur loading.

The catalytic activities of zirconia and sulfated zirconia synthesized from $ZrO(NO_3)_2$ or $ZrOCl_2$ were influenced by the

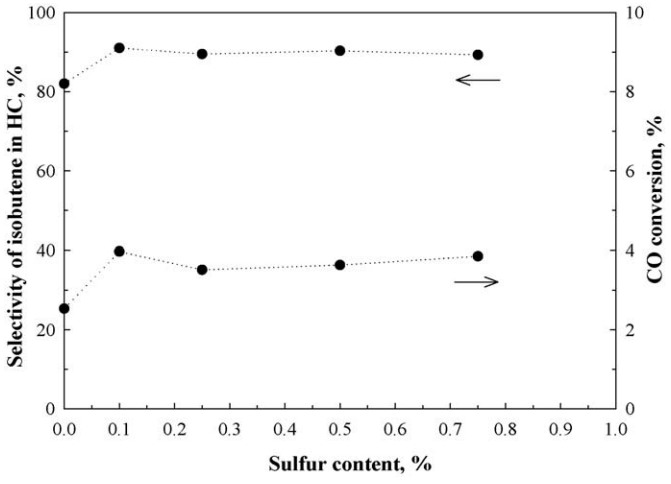

Fig. 15. Relationship between CO conversion and selectivity of isobutene with sulfur content in SO_4/ZrO_2–Cl.

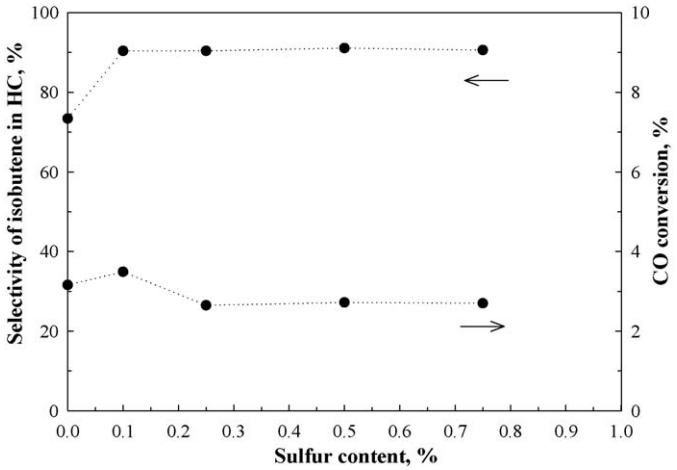

Fig. 16. Relationship between CO conversion and selectivity of isobutene with sulfur content in SO_4/ZrO_2–N.

Zr^{3+} quantity and amount of acid sites. Moreover, sulfur loading and surface area of catalysts also rendered higher activity. The small range of crystallite size or particle size does not show any effects on the catalytic reactivity, but the relative intensity of Zr^{3+} and acidity governed the catalytic selectivity of isobutene. The paraffins of C_1–C_3 hydrocarbons produced significantly decreased with increased sulfur loading. Considered the relationship between catalytic performance and sulfur content as shown in Figs. 15 and 16, it was possibly concluded that the most suitable sulfur loading content seems to be at 0.1%, which gave the reaction rate of 117 and 133.1 μmol kg-cat^{-1} s^{-1} for SZ (ZrO_2–N) and SZ (ZrO_2–Cl), respectively, and gave the selectivity of isobutene at 90.4 and 91.0%.

As mentioned, the acid sites and Zr^{3+} intensity affected the catalytic performance, but the peak of acid sites or Zr^{3+} quantity appeared at 0.25% of sulfur contents. It was observed that the ratio of base sites per acid sites at 0.1% is more than that of 0.25% for both SZ (ZrO_2–Cl) and SZ (ZrO_2–N) catalysts. Therefore, it reasonably postulated that it is necessary to have base sites even at low quantity to assist the improvement of catalytic performance. In addition, the base sites also related with the percentage of monoclinic phase in the catalyst.

4. Conclusions

Sulfated zirconia obtained from different precursors with sulfur loading in the range of 0.1–0.75% exhibited better catalytic activity and selectivity of isobutene in hydrocarbons than the undoped-zirconia. The sulfur loading, the amount of acid sites and relative

intensity of Zr^{3+} in sulfated zirconia affected the catalytic properties. In addition, the ratio of base sites per acid sites and phase composition of zirconia also influenced the catalytic performance. It was found that the 0.1%SZ (ZrO_2–Cl) was the suitable catalyst for isosynthesis at 400 °C, in which provides the reaction rate of 117 μmol kg-cat^{-1} s^{-1} [for SZ (ZrO_2–N)] and 133.1 μmol kg-cat^{-1} s^{-1} [for SZ (ZrO_2–Cl)] and gave the selectivity of isobutene at 90.4 and 91.0%, respectively.

Acknowledgements

The financial support from the National Research Council of Thailand (NRCT) is greatly appreciated. The authors also would like to acknowledge the supports from Professor Shigeo Goto, the Thailand Research Fund (TRF) and Commission on Higher Education (CHE).

References

[1] H. Pichler, K.H. Ziesecke, Brennst. Chem. 30 (1949) 13.
[2] H. Pichler, K.H. Ziesecke, B. Traeger, Brennst. Chem. 30 (1949) 333.
[3] C. Su, J. Li, D. He, Z. Cheng, Q. Zhu, Appl. Catal. A: Gen. 202 (2000) 81.
[4] C. Su, D. He, J. Li, Z. Chen, Q. Zhu, J. Mol. Catal. A: Chem. 153 (2000) 139.
[5] K. Maruya, T. Komiya, T. Hayakawa, L. Lu, M. Yashima, J. Mol. Catal. A: Chem. 159 (2000) 97.
[6] T. Maehashi, K. Maruya, K. Omen, K. Aika, T. Onishi, Chem. Lett. (1984) 747.
[7] K. Maruya, K. Ito, K. Kushihashi, Y. Kishida, K. Domen, T. Onishi, Catal. Lett. 14 (1992) 123.
[8] W.S. Postula, Z. Feng, C.V. Philip, A. Akgerman, R.G. Anthony, J. Catal. 145 (1994) 126.
[9] Z. Feng, W.S. Postula, A. Akgerman, R.G. Anthony, Ind. Eng. Chem. Res. 34 (1995) 78.
[10] (a) Y. Li, D. He, Z. Cheng, C. Su, J. Li, Q. Zhu, J. Mol. Catal. A: Chem. 175 (2001) 267; (b) D. Zhang, H. Yin, C. Ge, J. Xue, T. Jiang, L. Yu, Y. Shen, J. Ind. Eng. Chem. 15 (2009) 537.
[11] Y. Li, D. He, Y. Yuan, Z. Cheng, Q. Zhu, Fuel 81 (2002) 1611.
[12] Y. Li, D. He, Q. Zhu, X. Zhang, B. Xu, J. Catal. 221 (2004) 584.
[13] Y. Li, D. He, Y. Yuan, Z. Cheng, Q. Zhu, Energy Fuels 15 (2001) 1434.
[14] L. Lu, T. Hayakawa, T. Ueda, M. Hara, K. Domen, K. Maruya, Chem. Lett. (1998) 65.
[15] W. Khaodee, B. Jongsomjit, S. Assabumrungrat, P. Praserthdam, S. Goto, Catal. Commun. 8 (2007) 548.
[16] W. Khaodee, B. Jongsomjit, P. Praserthdam, S. Goto, S. Assabumrungrat, J. Mol. Catal. A: Chem. 280 (2008) 35.
[17] W. Khaodee, N. Tangchupong, B. Jongsomjit, S. Assabumrungrat, P. Praserthdam, S. Goto, Catal. Commun. 10 (2009) 494.
[18] J.R. Sohn, E.H. Park, J. Ind. Eng. Chem. 4 (1998) 197.
[19] J.R. Sohn, E.H. Park, H.W. Kim, J. Ind. Eng. Chem. 5 (1999) 253.
[20] J.R. Sohn, E.H. Park, J. Ind. Eng. Chem. 6 (2000) 297.
[21] J.R. Sohn, E.H. Park, J. Ind. Eng. Chem. 6 (2000) 312.
[22] J.R. Sohn, T.-D. Kwon, S.-B. Kim, J. Ind. Eng. Chem. 7 (2001) 441.
[23] Y.W. Suh, J.W. Lee, H.K. Rhee, Appl. Catal. A 274 (2004) 159.
[24] P.D.L. Mercera, J.G. Ommen, E.B.M. Doesburg, A.J. Burggraaf, J.R.H. Roes, Appl. Catal. A 71 (1991) 363.
[25] R. Srinivasan, B.H. Davis, Catal. Lett. 14 (1992) 165.
[26] F.C. Wu, S.C. Yu, J. Mater. Sci. 25 (1990) 970.
[27] D. Fărcaşiu, J.Q. Li, S. Cameron, Appl. Catal. A 154 (1997) 173.
[28] K. Arata, M. Hino, Mater. Chem. Phys. 26 (1990) 213.
[29] T. Yamaguchi, K. Tanabe, Y. Kung, Mater. Chem. Phys. 16 (1986) 67.
[30] M.S. Scurrell, Appl. Catal. 34 (1987) 109.
[31] R. Srinivasan, B.H. Davis, Prep. Am. Chem. Soc. Petrol. Chem. Div. 36 (1991) 635.
[32] Z.-Y. Ma, C. Yang, W. Wei, W.-H. Li, Y.-H. Sun, J. Mol. Catal. A: Chem. 227 (2005) 119.
[33] X. Li, K. Nagaoka, R. Olindo, J.A. Lercher, J. Catal. 238 (2006) 39.
[34] K. Arata, Adv. Catal. 37 (1990) 165.
[35] V. Bolis, G. Magnacca, G. Cerrato, C. Morterra, Langmuir 13 (1997) 888.
[36] C. Morterra, G. Cerrato, F. Pinna, M. Signoretto, J. Phys. Chem. 98 (1994) 12373.
[37] L.M. Kustov, V.B. Kazansky, F. Figueras, D. Tichit, J. Catal. 150 (1994) 143.
[38] V. Adeeva, J.W. de Haan, J. Janchen, G.D. Lei, V. Schunemann, L.J.M. van de Ven, W.M.H. Sachtler, R.A. van Santen, J. Catal. 151 (1995) 364.
[39] M.J. Torralvo, M.A. Alario, J. Soria, J. Catal. 68 (1984) 473.
[40] C. Moterra, E. Giamello, L. Orio, M. Volante, J. Phys. Chem. 94 (1990) 3111.
[41] F.R. Chen, G. Coudurier, J.F. Joly, J.C. Vedrine, J. Catal. 143 (1993) 616.
[42] H. Liu, X. Zhang, Q. Xue, J. Phys. Chem. 99 (1995) 332.
[43] C.R. Vera, C.L. Pieck, K. Shimizu, C.A. Querini, J.M. Parera, J. Catal. 187 (1999) 39.
[44] Q. Zhao, X. Wang, T. Cai, Appl. Surf. Sci. 225 (2004) 7.
[45] M. Anpo, T. Nomura, Res. Chem. Intermed. 13 (1990) 195.

ภาคผนวก 14

doi:10.4186/ej.2010.13.4.1

PERFORMANCE ASSESSMENT OF SOFC SYSTEMS INTEGRATED WITH BIO-ETHANOL PRODUCTION AND PURIFICATION PROCESSES

Issara Choedkiatsakul[1], Kanokporn Sintawarayan[1], Tanya Prawpipat[1], Apinan Soottitantawat[1], Wisitsree Wiyaratn[2], Worapon Kiatkittipong[3], Amornchai Arpornwichanop[1], Navadol Laosiripojana[4], Sumittra Charojrochkul[5] and Suttichai Assabumrungrat[1*]

[1] Department of Chemical Engineering, Faculty of Engineering, Chulalongkorn University, Bangkok, Thailand 10330
[2] Department of Production Technology Education, Faculty of Industrial Education and Technology, King Mongkut's University of Technology Thonburi, Bangkok, Thailand 10140
[3] Department of Chemical Engineering, Faculty of Engineering and Industrial Technology, Silpakorn University, Nakhon Pathom, Thailand 73000
[4] The Joint Graduate School of Energy and Environment, King Mongkut's University of Technology Thonburi, Bangkok, Thailand 10140
[5] National Metal and Materials Technology Center (MTEC), Pathumthani, Thailand 12120

Email: muay_iss@hotmail.com[1], cheenae@hotmail.com[1], nanana_nan@hotmail.com[1], Apinan.S@chula.ac.th[1], wisitsree@gmail.com[2], kworapon@su.ac.th[3], amornchai.a@chula.ac.th[1], navadol_l@gsee.kmutt.ac.th[4] sumittrc@mtec.or.th[5] and Suttichai.a@chula.ac.th[1*]

ABSTRACT

The overall electrical efficiencies of the integrated systems of solid oxide fuel cell (SOFC) with bio-ethanol production and purification processes at different levels of heat integration were investigated. The simulation studies were based on the condition with zero net energy (no external heat required). It was found that the most suitable operating condition of SOFC is at voltage between 0.7 and 0.85 V and temperature between 973 and 1173 K. Regarding the effect of percent ethanol recovery, the optimum percent ethanol recovery is observed at 95%. The SOFC integrated with bio-ethanol production and purification processes with reforming of biogas for producing extra hydrogen is found to be the most efficient system, offering the overall electrical efficiency of 36.17%. However, additional equipments such as biogas reformer and heat exchangers are required, resulting in increased investment cost.

KEYWORDS

solid oxide fuel cell, bioethanol, electrical efficiency, heat integration

doi:10.4186/ej.2009.13.4.1

I . Introduction

Nowadays, energy crisis is the crucial issue due to the increasing energy demand with the limiting of fossil fuels sources. Therefore, renewable energy has become an interesting topic for many researchers. Bio-ethanol is one of the attractive resources of renewable energy. It has extra advantages in term of production because it can be easily produced from biomass such as cassava, molasses and bagasse. Bio-ethanol can be further reformed to hydrogen which is a major fuel for solid oxide fuel cell (SOFC) to generate useful electricity and heat.

In this study, performance assessment of SOFC systems integrated with bio-ethanol production and purification processes was investigated. Bio-ethanol produced from cassava was considered. The energy consumption required at different unit operations were reported elsewhere [1], [2]. Biogas, a byproduct from bio-ethanol production, was also considered in this work as an additional fuel for generating heat or extra hydrogen for the system [1], [3]. The purification process of bio-ethanol to a higher ethanol concentration before being reformed to hydrogen for use in SOFC was studied by simulation using Aspen Plus™ program [4], [5]. The optimal conditions for the purification process are the conditions that provide the minimum required energy. For the SOFC system, Microsoft visual basic program was used to simulate and find the appropriate operating conditions [6], [7]. The work compares performance of various SOFC systems at different levels of heat integration in order to find a suitable system.

II. Modeling System

2.1 Energy consumption in ethanol production process

Bio-ethanol production process composes of milling, mixing, liquefaction, saccharification, fermentation, distillation, post-treatment and rectification [1]. The energy consumption per ton of ethanol produced for each unit of the process is shown in Table 1.

Stage	Electricity (kWh)	Heat (kWh)
Milling and mixing	30.24	-
Liquefaction and Saccharification	12.96	875.91
Fermentation	41.9	-
Distillation	24.24	2,802.92
Post-treatment	70.47	963.5
supplementary equipment	19.8	87.59
Biogas cogeneration (self supply)	-204.73	-822.49
Net Energy use (kWh)	-5.12	3,907.43
Overall energy use (kWh)	3,902.31	-

Table 1
Energy consumption in ethanol production process (per ton of 95.6%w/w ethanol) [2]

2.2 Distillation Modeling

The schematic diagram of the purification process is shown in Fig.1. Low ethanol concentration was purified to a desired level of ethanol concentration by the distillation column. The Radfrac rigorous equilibrium stage distillation module in Aspen™ plus program was used to simulate the process. The distillate stream from the distillation column was heated to the reformer temperature (1023 K) by Heater 1. The bottom stream containing mostly water was partially removed and heated by Heater 2 in order to mix with the distillate stream to get the 25 mol% ethanol concentration before being fed to the reformer.

doi:10.4186/ej.2009.13.4.1

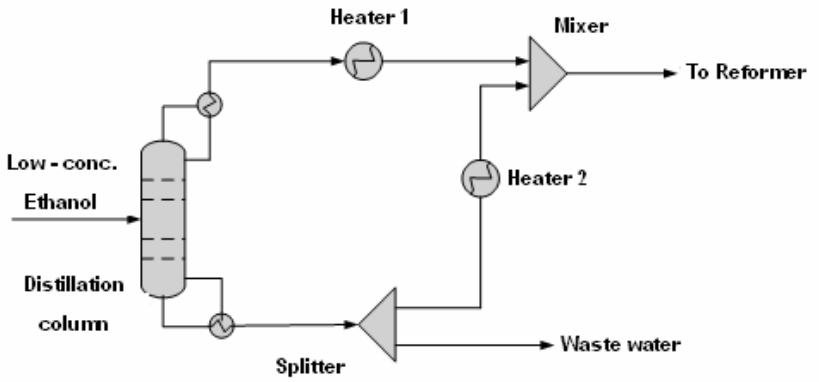

Figure 1
Schematic diagram of the purification process

2.3 SOFC Modeling

Fig. 2 shows the schematic diagram of SOFC system. The 25 mol% ethanol concentration was fed to the external reformer. The calculation was based on phase and chemical equilibrium. Excess air (500%) was preheated and fed to the cathode chamber of the SOFC stack. Generally, biogas which is a byproduct from the ethanol production process could be collected in order to produce steam and electricity or fed to the reformer to produce additional hydrogen gas for feeding to SOFC. Table 2 shows the amount and compositions of biogas.

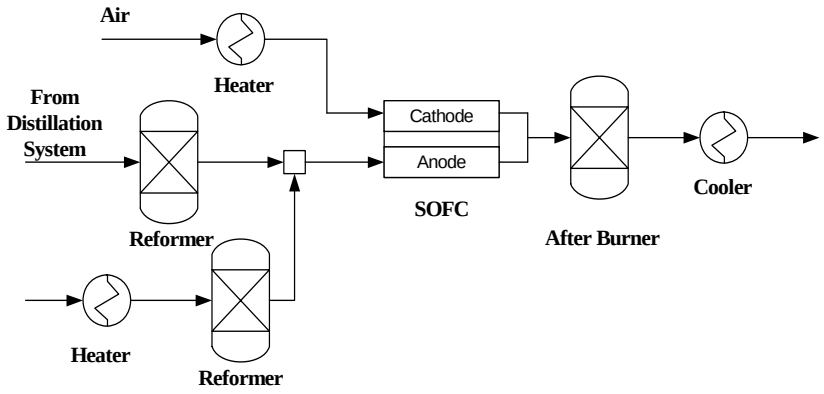

Figure 2
Schematic diagram of SOFC system

Component	Amount (mol)
CH_4	7,466
CO_2	1,014
O_2	197
N_2	740

Table 2
The amount and composition of biogas per ton of ethanol produced

In order to simplify the calculations, the reformer was assumed to operate isothermally and the outlet gas reached its equilibrium composition. The main reaction of biogas reforming is the steam reforming reaction (Eq. (1)) and the other reaction is water gas shift reaction (Eq. (2)) [5-6].

$$CH_4 + H_2O \longrightarrow 3H_2 + CO \quad (1)$$

$$CO + H_2O \longrightarrow CO_2 + H_2 \quad (2)$$

In SOFC stack, the electrochemical reaction takes place. Oxygen from air is reduced to oxygenions (Eq. (3)) at the cathode side and passes through the electrolyte to react with the hydrogen gas at the anode side (Eq. (4)). It was reported that H_2 electro-oxidation is much faster than CO electro-oxidation and the rate of water gas shift reaction is very fast at high temperatures. Therefore, it is assumed that only hydrogen ions react with oxygen ions.

$$1/2O_2 + 2e^- \longrightarrow O^{2-} \quad (3)$$

$$H_2 + O^{2-} \longrightarrow H_2O + 2e^- \quad (4)$$

The open circuit voltage (*E*) can be calculated by using the Nernst equation below

$$E = E_0 + \frac{RT}{2F}\ln\left(\frac{P_{H_2}P_{O_2}^{1/2}}{P_{H_2O}}\right) \quad (5)$$

where E_0 is the reversible potential (V), *R* is the gas constant (8.3145 J /mol.K), *T* is the SOFC temperature (K), *F* is the Faraday constant (9.6495104 C/mol) and P_i is partial pressure of species *i* (Pa).

The actual cell potential (*V*) is always less than the open circuit voltage (*E*) owing to the existence of the overpotentials as shown by Eq. (6).

$$V = E - \eta_{act} - \eta_{ohmic} - \eta_{conc} \quad (6)$$

The overpotentials are divided into three types: ohmic overpotential (η_{ohmic}), activation overpotential (η_{act}) and concentration overpotential (η_{conc}) which can be explained as below [6]:

2.3.1 Ohmic Overpotential

The ohmic overpotential is the resistance of the electron to flow through the electrodes, interconnections and electrolyte. This overpotential is the major loss of the SOFC stack which can be calculated from Eq. (7).

$$\eta_{ohmic} = 2.99x10^{-11} iL \exp\left(\frac{10300}{T}\right) \quad (7)$$

where *i* is the current density (A/cm^2) and *L* is the thickness of the electrolyte (μm).

2.3.2 Activation Overpotential

The activation overpotential occurs from the electrochemical reaction at the electrodes. Normally, the activation overpotential dominates at low current density but at high temperature, the reaction rate is very fast then this value is small. This overpotential can be expressed by the Butler-Volmer equation.

$$i = i_0\left[\exp\left(\frac{\alpha zF\eta_{act}}{RT}\right) - \exp\left(-\frac{(1-\alpha)zF\eta_{act}}{RT}\right)\right] \quad (8)$$

doi:10.4186/ej.2009.13.4.1

where i_0 is the exchange current density (A/cm^2), α is the symmetrical factor and z is the number of electrons that involve in the reaction. In case of SOFC, the value of α and z are 0.5 and 2 respectively. Consequently, the activation overpotential at anode and cathode side can be written as:

$$\eta_{act,j} = \frac{RT}{F}\sinh^{-1}\left(\frac{i}{2i_0}\right) \qquad j = a, c \tag{9}$$

The exchange current density (i_0) for the cathode and anode sides can be calculated from the following equations:

$$i_{0,a} = \gamma_a\left(\frac{P_{H_2}}{P_{ref}}\right)\left(\frac{P_{H_2O}}{P_{ref}}\right)\exp\left(-\frac{E_{act,a}}{RT}\right) \tag{10}$$

$$i_{0,c} = \gamma_c\left(\frac{P_{O_2}}{P_{ref}}\right)^{0.25}\exp\left(-\frac{E_{act,c}}{RT}\right) \tag{11}$$

where γ_i is the pre-exponential factor for electrode exchange current density (A/cm^2), $E_{act,i}$ is the activation energy of electrode (J/mol), subscripts a and c represent anode and cathode, respectively.

2.3.3 Concentration Overpotential

The concentration overpotential is the loss due to the difference in concentration of gas between the bulk and the reaction site. It can be estimated by Eqs. (12) and (13)

$$\eta_{conc,a} = \frac{RT}{2F}\ln\left[\frac{\left(1+\left(RT/2F\right)\left(l_a/D_{a(eff)}p^l_{H_2O}\right)i\right)}{\left(1-\left(RT/2F\right)\left(l_a/D_{a(eff)}p^l_{H_2}\right)i\right)}\right] \tag{12}$$

$$\eta_{conc,c} = \frac{RT}{4F}\ln\left[\frac{p^l_{O_2}}{\left(p_c-\delta_{O_2}\right)-\left(\left(p_c-\delta_{O_2}\right)-p^l_{O_2}\right)\exp\left[\left(RT/4F\right)\left(\delta_{O_2}l_c/D_{c(eff)}p_c\right)i\right]}\right] \tag{13}$$

where l_a , l_c are the thicknesses of anode and cathode (μm), p^l_i is the inlet pressure of species i (Pa), $D_{a(eff)}$ and $D_{c(eff)}$ are the effective diffusion coefficient of the anode and cathode (cm^2/s) and p_a, p_c are the operating pressure of SOFC at the anode and cathode sides (Pa). δ_{O2} , $D_{a(eff)}$ and $D_{c(eff)}$ can be expressed by:

$$\delta_{O_2} = \frac{D_{O_2,k(eff)}}{D_{O_2,k(eff)}+D_{O_2-N_2(eff)}} \tag{14}$$

$$D_{a(eff)} = \left(\frac{p_{H_2O}}{p_a}\right)D_{H_2(eff)}+\left(\frac{p_{H_2}}{p_a}\right)D_{H_2O(eff)} \tag{15}$$

$$D_{c(eff)} = \frac{\xi}{n}\left(\frac{1}{D_{O_2,k}}+\frac{1}{D_{O_2-N_2}}\right) \tag{16}$$

$$\frac{1}{D_{H_2(eff)}} = \frac{\xi}{n}\left(\frac{1}{D_{H_2,k}}+\frac{1}{D_{H_2-H_2O}}\right) \tag{17}$$

doi:10.4186/ej.2009.13.4.1

$$\frac{1}{D_{H_2O(eff)}} = \frac{\xi}{n}\left(\frac{1}{D_{H_2O,k}} + \frac{1}{D_{H_2-H_2O}}\right) \quad (18)$$

where $D_{i,\ k(eff)}$ is the effective Knudsen diffusivity of gas i (cm^2 /s), $D_{A-B(eff)}$ is the effective ordinary diffusivity of gas A versus gas B (cm^2 /s), $D_{i,\ k}$ is the Knudsen diffusivity of gas i (cm^2 /s), D_{A-B} is the ordinary diffusivity of gas A versus gas B (cm^2 /s) and ξ is the electrode tortuosity (μm).

Eq. (19) shows the relationship between effective parameter ($D_{(eff)}$) and nominal parameter (D):

$$D_{(eff)} = \frac{n}{\xi}D \quad (19)$$

The correlation below is used to calculate the Knudsen diffusivity:

$$D_{A,k} = 9700\sqrt{\frac{T}{M_A}} \quad (20)$$

where M_A is the molecular weight of gas A (g).

The Chapman-Enskog equation is used for calculating the ordinary diffusivity:

$$D_{A-B} = 1.8583x10^{-3}\left(\frac{T^{3/2}\left((1/M_A)+(1/M_B)\right)^{1/2}}{P\sigma_{AB}^2\Omega_D}\right) \quad (21)$$

where σ_{AB} is collision diameter (A°) which is equal to $(\sigma_A+\sigma_B)/2$ and Ω_D is the collision integral which can be calculated from the following equation.

$$\Omega_D = \frac{A}{T_k^B} + \frac{C}{\exp(DT_k)} + \frac{E}{\exp(FT_k)} + \frac{G}{\exp(HT_k)} \quad (22)$$

where T_k is equal to T/ε_{AB}, ε_{AB} is the Lennard-Jones energy interaction parameter scaled with respect to the Boltzman constant and A, C, E and G are constants for each gas.

The overall parameters used in this model are summarized in Table 3.

Parameters	Value	Parameters	Value
L (μm)	50	σ_{H_2} (Å)	2.827
$E_{act,a}$ (J/mol)	1.0 x 10^5	σ_{H_2O} (Å)	2.641
$E_{act,c}$ (J/mol)	1.2 x 10^5	σ_{N_2} (Å)	3.798
γ_a (A/m^2)	1.344 x 10^{10}	σ_{O_2} (Å)	3.467
γ_c (A/m^2)	2.051 x 10^9	ε_{H_2}	59.7
l_a (μm)	750	ε_{H_2O}	809.1
l_c (μm)	50	ε_{N_2}	71.4
ξ (μm)	5.4	ε_{O_2}	106.7
n	0.48		

Table 3
Summary of model parameters [6]

doi:10.4186/ej.2009.13.4.1

The effluents from the cathode and anode sides were fed to the afterburner. The complete combustion was assumed to occur in the afterburner; therefore the exit gas from the afterburner consists of nitrogen, oxygen, water and carbon dioxide. The exhaust gas temperature was reduced to 403 K and it was assumed to operate without heat loss.

The overall electrical efficiency of the system can be computed by Eq. (23):

$$\%\text{Overall Eff.} = \frac{W_{e,net}}{n_{EtOH} \cdot LHV_{EtOH} + n_{Biogas} \cdot LHV_{Biogas} + \text{Required External Heat}} \quad (23)$$

where $W_{e,net}$ is the net electrical power (MW), n_i is the flow_rate of component i (mol/s) and LHV_i is the lower heating value of component i (kJ/kg).

In this work we divided the case studies into four systems in order to compare performance of the system with different levels of heat integration. The details of each system are shown below:

System 1: SOFC system fed by high concentration ethanol. High concentration ethanol (95.6 wt.%) was used as a feed for this system. It was diluted with water to 25 mol% ethanol solution and fed to the reformer, generating hydrogen for use in the SOFC system.

System 2: SOFC system fed by bio-ethanol pre-purified to 25mol% of ethanol concentration.

System 3: Integrated system of SOFC and bio-ethanol purification process. In this case, bio-ethanol was purified to an optimal concentration of ethanol and diluted to 25 mol% ethanol before being fed to the reformer and later to the SOFC system. Heat integration between the SOFC and the bio-ethanol purification process was allowed. For example, heat from the SOFC system was recovered to use for preheating the bio-ethanol feed and for the supplying energy to the reboiler of the distillation column.

System 4: Integrated system of SOFC and bio-ethanol production and purification processes. Heat integration between the SOFC and bio-ethanol production and purification processes was allowed. As biogas is a byproduct in the bio-ethanol production process, two systems with different ways of biogas utilization were considered.

- **4.1** Biogas for cogeneration: biogas generated during the bio-ethanol production was burnt to generate heat for use in the integrated system.
- **4.2** Biogas for hydrogen production for SOFC: the system is similar to **4-1** but biogas was fed to the reforming process to produce extra hydrogen gas as a fuel for SOFC.

III. Results and discussion

3.1 Effect of ethanol concentration on energy requirement in distillation system

The minimum energy consumption in the distillation system can be obtained by varying the parameters, *i.e.* purity of ethanol in the distillate, percent ethanol recovery, the number of the column stages and the feed stage. The appropriate operating conditions from the simulation are listed in Table 4 for different values of ethanol recovery.

doi:10.4186/ej.2009.13.4.1

Parameters	Ethanol Recovery				
	80%	85%	90%	95%	99%
Ethanol purity	40	35	35	35	35
No. of stages	5	5	6	6	6
Feed stage	2	2	3	2	2
Net Heat Duty (MJ/ton EtOH)	8,973	9,065	9,552	9,790	11,048

Table 4
The appropriate operating conditions for distillation

3.2 Effects of SOFC operating voltage and fuel utilization on the SOFC performance

The system becomes more efficient when operated at the conditions at which the net useful heat (Q_{net}) is equal to zero because it achieves the maximum electricity for the overall system without requiring the external heat source. The value of Q_{net} is equal to zero means that the exothermic energy is exactly capable to supply to the required energy demanding units. However, the value of Q_{net} can also be positive or negative. A positive value of Q_{net} means that there is some heat left from the overall process and the negative value indicates that the external heat source is required to supply for the energy consuming units.

At a higher fuel utilization (U_f), the higher net useful electrical power ($W_{e,net}$) was obtained when operated at higher voltages because the lower heat loss was emitted from the SOFC stack. As a result of the higher $W_{e,net}$, the lower net useful heat (Q_{net}) was obtained. The appropriate voltages at which Q_{net} equals to zero for U_f = 70, 80 and 90% were 0.75, 0.65 and 0.575 V, respectively. The corresponding values of power density (P) were equaled to 3,000, 3,700 and 4,200 W/m^2.

3.3 Appropriate operating conditions for SOFC system

From Fig 3a), $W_{e,net}$ and overall efficiency increased with the increase of ethanol recovery up to 95%. Although at the higher ethanol recovery, the required energy for distillation system increased, the amount of ethanol provided to SOFC system increased. Consequently, the overall efficiency was higher when increasing the percent ethanol recovery to 95%. However, when percent ethanol recovery was between 95% and 99%, the performance started to decrease gradually and dramatically reduced at the percent ethanol recovery greater than 99% because the significantly higher energy required in the distillation system caused the SOFC system to operate at a lower fuel utilization in order to leave more un-reacted fuel to burn and compensate the higher heat demanded. This led to the reduction of the overall efficiency. The optimal percent ethanol recovery which obtained the maximum $W_{e,net}$ and overall efficiency was observed at 95% which was used to determine the appropriate operating voltage and temperature of SOFC as in Figs.3b) and 3c), respectively.

Fig.3b) indicates that the SOFC stack area increased with increasing the operating voltage while Q_{stack} decreased. The appropriate operating voltage should not be too low because it may cause the excessive heat generated in the stack which can directly damage the thermophysical property of the cell components. The most suitable operating voltage was in the range from 0.7 to 0.85 V. As the same reason as operating voltage, the operating temperature should not be too high. Therefore the suitable operating temperature for SOFC was in the range from 973 to 1173 K as shown in Fig. 3c).

doi:10.4186/ej.2009.13.4.1

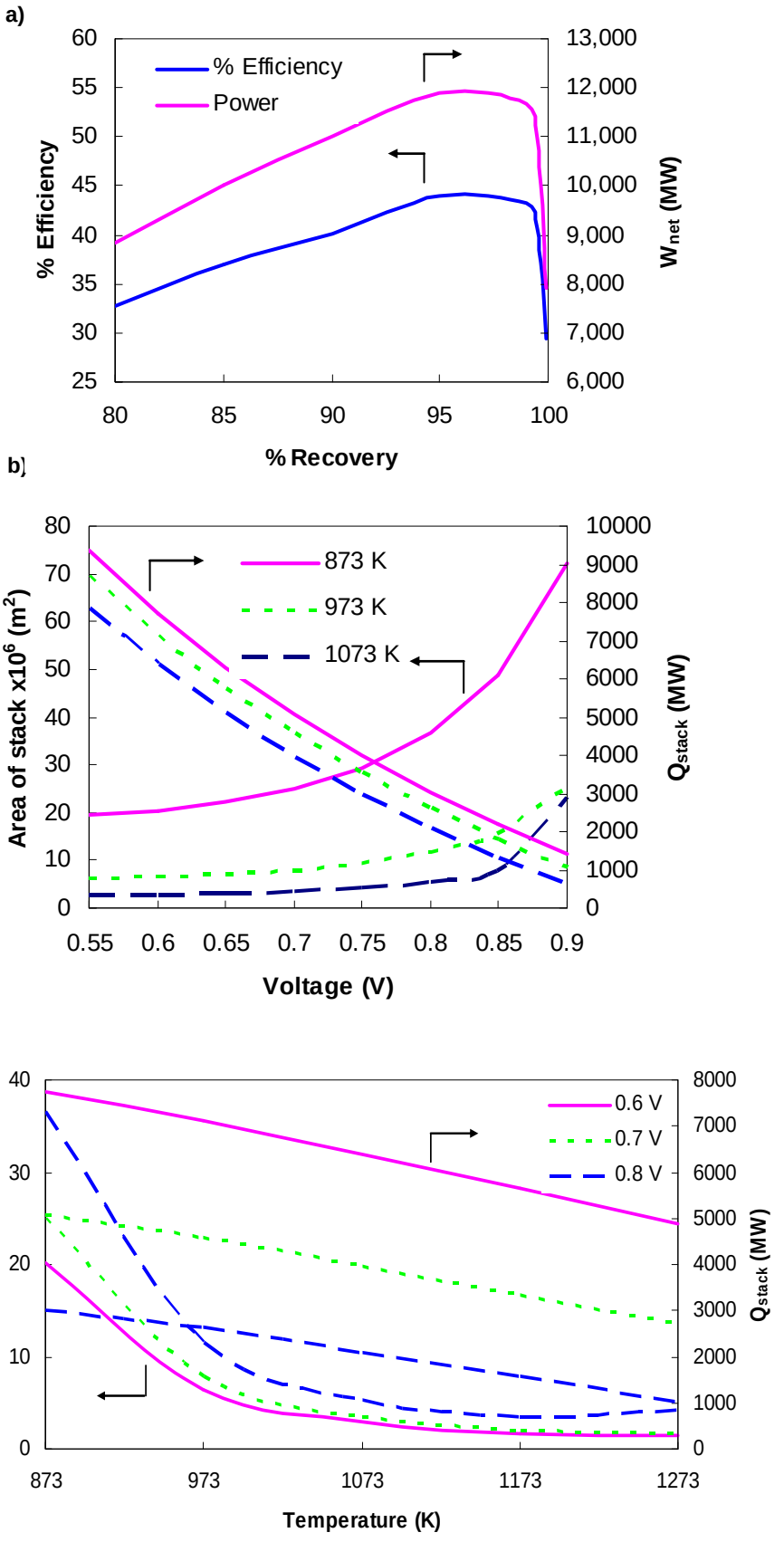

Figure 3
The effect of a) % ethanol recovery on the $W_{e,net}$ and the overall efficiency b) and c) operating voltage and operating temperature on SOFC stack area and Q_{stack}

doi:10.4186/ej.2009.13.4.1

3.4 Efficiency comparison among different systems.

3.4.1 Efficiency comparison in case of equal SOFC power density

In this section, the performance of different SOFC systems is compared to determine a suitable system for operation. Table 5 shows the net electrical power, the required external heat source and the overall electrical efficiency of each system. It can be seen that for the systems No.1, 2 and 3, the external heat source was required since the ethanol production process and/or the distillation system were not integrated with the SOFC system and therefore the heat released from the SOFC system can not be provided to the other systems. Consequently, the values of overall electrical efficiency are low. In contrast, the system no. 4 was the combination of all three systems; therefore the external heat source was not required. The simulation results indicated that the system 4-2 offered the highest overall efficiency with no external heat required.

System	$W_{e,net}$ (MW)	External Heat Required (MW)	%Overall Electrical Efficiency
1	10,643	14,067	22.64
2	10,135	9,871	23.67
3	10,135	3,976	27.45
4.1	10,135	0	30.76
4.2	11,908	0	36.14

Table 5 Efficiency comparison in case of equal SOFC power density (Ethanol Recovery = 95%, Operating voltage = 0.7 V, Temperature =1073 K, P = 3,619 W/m^2)

3.4.2 Efficiency comparison in case of equal SOFC stack area

The simulation results are shown in Table 6. It was found that the most attractive system is system no. 4. As the systems 4-1 and 4-2 had the competitive efficiency; hence, further study was necessary.

System	$W_{e,net}$ (MW)	External Heat (MW)	%Efficiency
1	11,354	14,067	24.15
2	11,224	9,871	26.21
3	11,224	3,976	30.40
4.1	11,224	0	34.06
4.2	11,046	0	33.52

Table 6 Efficiency comparison in case of equal SOFC stack area (Ethanol Recovery = 95%, Operating voltage = 0.7 V, Temperature =1073 K, *P* = 3,619 W/m^2)

3.5 Effects of SOFC operating conditions on SOFC performance: comparison between biogas cogeneration and biogas reforming for hydrogen production

3.5.1 Comparison on net useful heat and overall electrical efficiency

Table 7 shows the results for both systems. It can be seen that both systems offered comparable overall electrical efficiency and $W_{e,net}$. In fact, system 4-2 should give the higher efficiency and electricity than system 4-1 because the extra amount of hydrogen fuel was fed to SOFC system. However, the operation required the extra

doi:10.4186/ej.2009.13.4.1

heat to increase biogas temperature and for biogas reforming; therefore SOFC has to operate at a lower value of fuel utilization in order to leave enough fuel for combustion to compensate the additional heat required. Consequently, the overall efficiency decreased.

Table 7
Net useful heat and overall efficiency of two systems (95% ethanol recovery)

System	$W_{e,net}$ (MW)	%Efficiency
4-1	11,885	36.07
4-2	11,917	36.17

3.5.2 Comparison on power density and SOFC stack area

The effects of operating voltage and temperature on the power density and SOFC stack area are illustrated on Figs.4a-4b

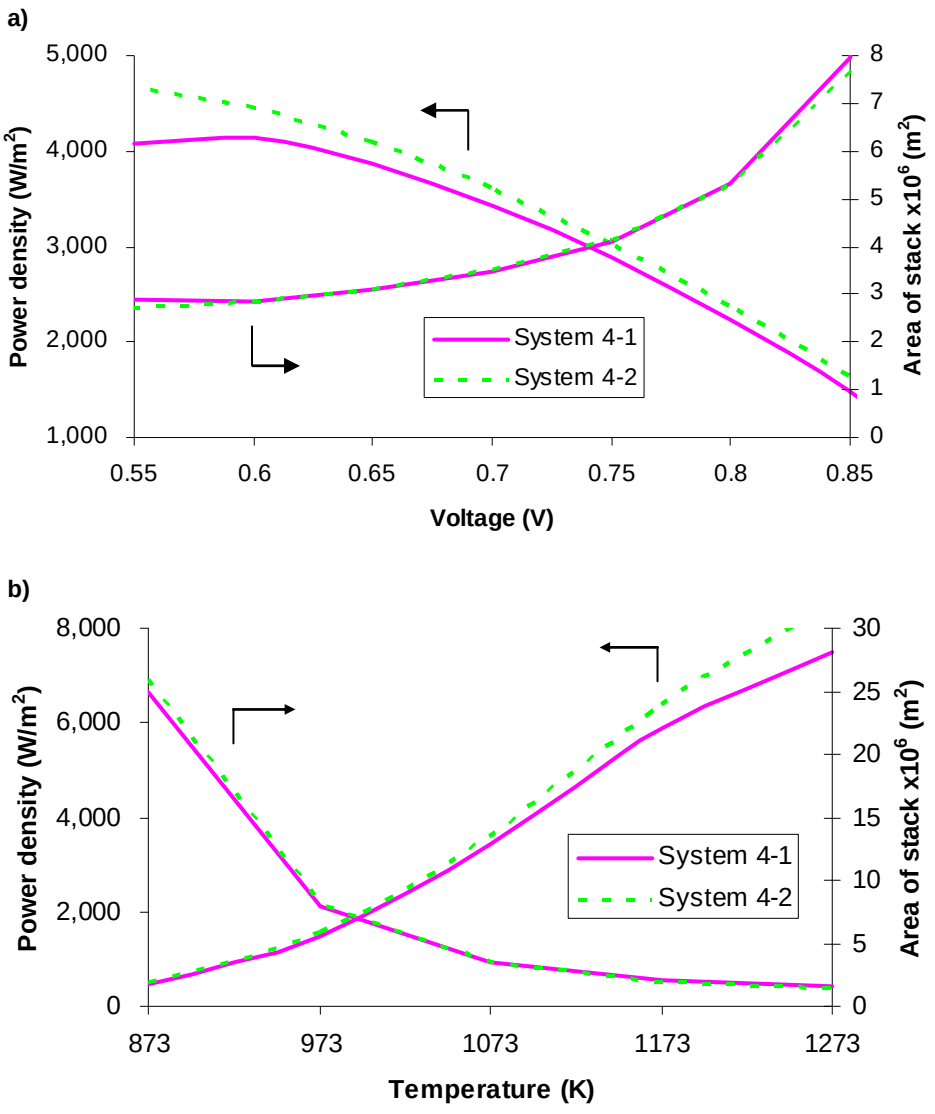

Figure 4
(a) Effects of operating voltage on the power density and SOFC stack area (95% ethanol recovery, T_{SOFC} = 1073 K)
(b) Effects of operating temperature on the power density and SOFC stack area (95% ethanol recovery, V = 0.7 V)

From Fig.4a) when the operating voltage increased, the power density decreased and thus the required stack area increased. For the effect of operating temperature as shown in Fig.4b), increasing operating temperature can improve power density and thus reduce the stack area. In addition, it can be seen that the power density in the system No.4-2 was about 5% greater than the other system while the SOFC stack area for both systems was almost the same. It should be noted that even though the system No.4-2 had the advantages of higher net electrical power and power density but it requires more unit operations such as biogas reformer and heat exchangers, leading to higher cost of investment and complicated system. Therefore, further study is recommended to compare the two systems in term of economic analysis.

IV. Conclusion

The SOFC system integrated with the bio-ethanol production and bio-ethanol purification was studied. The effects of operating parameters at Q_{net} equal to zero on the SOFC performance were presented. The results showed that the system can be operated in an energy self-sufficient mode by adjusting the operating parameters. It was found that the most suitable operating voltage was between 0.7 and 0.85 V and the operating temperature was in the range from 973 to 1173 K. Moreover the maximum overall efficiency and net electrical power were obtained when the percent ethanol recovery was equal to 95%. The results also indicated that the integrated system of SOFC and bio-ethanol production and purification processes with heat integration was possible and offered high overall electrical efficiency. The biogas for hydrogen production to SOFC had the slightly higher efficiency than the biogas for cogeneration but more unit operations and equipment are required which leads to higher cost of investment and complicated system. Consequently, the further study is recommended that the economic evaluation should be done to compare among both systems

doi:10.4186/ej.2009.13.4.1

V. Acknowledgement

This work is supported by the Thailand Research Fund and Commission on Higher Education and MTEC.

REFERENCES

[1] S. Yu and J. Tao, "Energy efficiency assessment by life cycle simulation of cassava-based fuel ethanol for automotive use in Chinese Guangxi context," *Energy*, vol. 34, no. 1, pp. 22–31, 2009.

[2] R. Leng, C. Wang, C. Zhang and D. Dai, "Life cycle inventory and energy analysis of cassava-based Fuel ethanol in China," *Journal of Cleaner Production*, vol. 16, no. 3, pp. 374-384, 2008.

[3] N. Chaisadtra, W. Nasomja and U. Hainghai, "A use of biogas produced from cassava's plant use water," (ME2004-58) Senior Project, Department of Mechanical Engineering, Faculty of Engineering, Khon Kaen University, Khon Kaen, 2005.

[4] W. Jamsak, et al., "Thermodynamic assessment of solid oxide fuel cell system integrated with bioethanol purification unit," *Journal of Power Sources,* vol. 174, no. 1, pp. 191-198, 2007.

[5] W. Jamsak, et al., "Design of a thermally integrated bioethanol-fuelled solid oxide fuel cell system integrated with a distillated column," *Journal of Power Sources*, vol. 187, no. 1, pp. 190-203, 2009.

[6] P. Piroonlerkgul, S. Assabumrungrat, N. Laosiripojana and A. A. Adesina, "Selection of appropriate fuel processor for biogas-fuelled SOFC system," *Chemical Engineering Journal*, vol. 140, no. 1-3, pp. 341-351, 2008.

[7] P. Piroonlerkgul, N. Laosiripojana, A. A. Adesina and S. Assabumrungrat, "Performance of biogas-fed solid oxide fuel cell systems integrated with membrane module for CO_2 removal," *Chemical Engineering and Processing: Process Intensification*, vol. 48, no. 2, pp. 672-682, 2009.

ภาคผนวก 15

Chemical Engineering and Processing 49 (2010) 1006–1016

Contents lists available at ScienceDirect

Chemical Engineering and Processing: Process Intensification

journal homepage: www.elsevier.com/locate/cep

Technical and economic study of integrated system of solid oxide fuel cell, palladium membrane reactor, and CO_2 sorption enhancement unit

P. Piroonlerkgul[a], W. Kiatkittipong[b], A. Arpornwichanop[a], A. Soottitantawat[a], W. Wiyaratn[c], N. Laosiripojana[d], A.A. Adesina[e], S. Assabumrungrat[a,*]

[a] Department of Chemical Engineering, Faculty of Engineering, Chulalongkorn University, Bangkok 10330, Thailand
[b] Department of Chemical Engineering, Faculty of Engineering and Industrial Technology, Silpakorn University, Nakhon Pathom 73000, Thailand
[c] Department of Production Technology Education, Faculty of Industrial Education and Technology, King Mongkut's University of Technology Thonburi, Bangkok 10140, Thailand
[d] The Joint Graduate School of Energy and Environment, King Mongkut's University of Technology Thonburi, Bangkok 10140, Thailand
[e] Reactor Engineering & Technology Group, School of Chemical Sciences & Engineering, University of New South Wales, Sydney, NSW 2052, Australia

ARTICLE INFO

Article history:
Received 15 June 2009
Received in revised form 10 January 2010
Accepted 12 July 2010
Available online 18 July 2010

Keywords:
Biogas
CO_2 capture
Solid oxide fuel cell
Palladium membrane

ABSTRACT

This paper deals with the integrated system of solid oxide fuel cell (SOFC), palladium membrane reactor (PMR), and CO_2 sorption enhancement (SE) unit. Three configurations of the SOFC systems fed by biogas are considered, i.e., PMR–SOFC, SE–PMR–SOFC, and SE–PMR–SOFC with a retentate gas recycling (SER–PMR–SOFC). The SOFC system equipped with a conventional reformer (CON–SOFC) is considered as a base case. The simulation results show that the capture of CO_2 in biogas before being fed to PMR (SE–PMR–SOFC) can improve H_2 recovery. The performance of SE–PMR–SOFC can be further enhanced by recycling retentate gas from PMR to CO_2 sorption enhancement unit (SER–PMR–SOFC). Compared to CON–SOFC, both SE–PMR–SOFC and SER–PMR–SOFC give higher power density and thus require smaller stack size (the stack size reduction of 1.55% and 8.27% are observed for SE–PMR–SOFC and SER–PMR–SOFC, respectively). The economic analysis is performed to identify the potential benefits of each SOFC configuration. The results indicate that SE–PMR–SOFC and SER–PMR–SOFC are not cost-effective systems compared with CON–SOFC; however, the capture of CO_2 in these SOFC systems offers an environmental benefit. High %total CO_2 capture and low cost of CO_2 capture are achieved under these SOFC systems.

1. Introduction

Solid oxide fuel cell (SOFC) is regarded as a promising electricity generation technology due to its high performance and environmental friendliness. Due to its high operating temperature (1073–1273 K), various types of fuel, e.g., methane, methanol, ethanol, natural gas, and oil derivatives, can be directly used without primary treatment [1,2]. Biogas is an attractive fuel for SOFC since it can be renewably used via photosynthesis process of plant and contains only trace amount of non-methane hydrocarbons. It composes of approximately 40–65 mol% of methane and 30–40 mol% of CO_2. Biogas can be directly fed to SOFC anode (internal reforming); however, the presence of CH_4 in biogas decreases the SOFC performance due to the carbon deposition and partial blocking of anode pore [3]. Large temperature gradient in SOFC stack caused by fast reforming reaction of methane is also a main problem of the internal reforming operation [4]. To overcome such difficulties, a fuel processor is required to convert methane in biogas into syngas prior to feeding into SOFC anode. Steam reforming is found to be the promising fuel processor for biogas-fuelled SOFC system [5]. However, the syngas obtained from the steam reforming reaction contains large amounts of CO and CO_2. Due to an increase in activation and concentration polarizations, SOFC performance decreases as the amount of CO in anode feed gas (syngas) increases [3,6]. In addition, the presence of CO_2 in syngas dwindles the SOFC performance because of the effect of the reverse water–gas shift reaction (RWGS) [7]. Suwanwarangkul et al. [7] also found that the use of pure-H_2 as fuel instead of reformed gas can improve the SOFC performance. For these reasons, the transformation of biogas to produce pure-H_2 is found to be suitable for the SOFC system.

Combining a H_2-selective membrane with steam reformers is one of the interesting technologies in pure-H_2 generation. Palladium membrane is an attractive membrane since it can achieve infinite selectivity for hydrogen over other gas species [8]. A number of researchers have focused on the integration of palladium membrane and reformers to produce pure-H_2 [9–11]. Under this operation, methane conversions higher than 80% can be achieved at

* Corresponding author. Tel.: +662 218 6868; fax: +662 218 6877.
E-mail address: Suttichai.A@chula.ac.th (S. Assabumrungrat).

0255-2701/$ – see front matter © 2010 Elsevier B.V. All rights reserved.
doi:10.1016/j.cep.2010.07.008

Nomenclature

$A_{\text{single cell}}$	active area of SOFC single cell (m^2)
A_{cell}	total active area of SOFC (m^2)
C_{cell}	capital cost of SOFC single cell ($)
$C_{\text{compressor}}$	capital cost of compressor ($)
C_p	heat capacity ($J\,mol^{-1}\,K^{-1}$)
C_{stack}	capital cost of SOFC stack ($)
d	diameter of inner tube of membrane reactor (mm)
d_p	CaO sorbent particle size (μm)
D	carbonator bed diameter (m)
D_p	catalyst pore diameter (μm)
$e_{\max}$	maximum thickness of the layer of $CaCO_3$ on the pore wall (50 nm)
E	theoretical open-circuit voltage of the cell (V)
E^0	theoretical open-circuit voltage of the cell at standard pressure (V)
E_{carb}	CO_2 capture efficiency (–)
E_p	activation energy for hydrogen permeation ($J\,mol^{-1}$)
f_0	inlet molar fraction of CO_2 (–)
f_a	volumetric fraction of CaO that reacts in the carbonator (–)
f_e	molar fraction of CO_2 at equilibrium of carbonation reaction (–)
f_f	gas friction factor [24] (–)
f_P	solid friction factor [24] (–)
F	Faraday constant ($9.6495 \times 10^4\,C\,mol^{-1}$)
F_0	Fresh CaO supplying rate ($mol\,s^{-1}$)
F_R	CaO-circulating rate ($mol\,s^{-1}$)
F_{CO_2}	CO_2 flow rate in gas mixture ($mol\,s^{-1}$)
g	gravity acceleration ($m\,s^{-2}$)
HP	power consumption in compressor (HP)
k_S	kinetic constant of carbonation reaction ($mol\,m^4\,s^{-1}$)
l_a	thickness of anode (μm)
l_c	thickness of cathode (μm)
L	thickness of electrolyte (μm)
L_b	carbonator bed height (m)
$\dot{m}$	molar flow rate ($mol\,s^{-1}$)
M_{CaO}	molecular weight of CaO ($g\,mol^{-1}$)
n	electrode porosity (–)
N	number of carbonation–calcination cycle (–)
N_k	permeation flux of component k ($mol\,m^{-2}\,s^{-1}$)
N_{cell}	number of SOFC single cell (–)
N_{stack}	number of SOFC stack (–)
P	pressure (Pa)
ΔP	pressure drop (Pa)
p_k	partial pressure of component k (Pa)
$p_{H_2,P}$	partial pressure of hydrogen in permeate side of membrane reactor (Pa)
$p_{H_2,R}$	partial pressure of hydrogen in retentate side of membrane reactor (Pa)
Q_0	pre-exponential factor for hydrogen permeation ($mol\,m^{-1}\,Pa^{-0.5}\,s^{-1}$)
Q_{NET}	difference between heat demand and heat generated in SOFC system (kW)
r_N	mass fraction of solid that have circulated N times (–)
R	gas constant ($8.3145\,J\,mol^{-1}\,K^{-1}$)
S_{ave}	maximum average reaction surface (m^{-1})
T	temperature (K)
u_f	gas velocity ($m\,s^{-1}$)
u_p	particle velocity ($m\,s^{-1}$)
U_f	fuel utilization (–)
v_t	gas terminal velocity ($m\,s^{-1}$)
V	cell voltage (V)
$V_{M,CaCO_3}$	molar volume of $CaCO_3$ ($m^3\,mol^{-1}$)
$\dot{W}_{\text{comp}}$	electricity consumed in the compressor (kW)
W_S	CaO inventory in carbonator (kg)
X_{ave}	average maximum carbonation conversion (–)
X_N	carbonation conversion after N cycle of carbonation–calcination (–)

Greek symbols

ε	bed void fraction (dimensionless)
ξ	electrode tortuosity (dimensionless)
δ	membrane thickness (μm)
ζ	hydrogen recovery (dimensionless)
η_{act}	activation loss (V)
η_{conc}	concentration loss (V)
η_{com}	compressor or pump efficiency (dimensionless)
η_{ohm}	ohmic loss (V)
ρ_c	catalyst density ($kg\,m^{-3}$)
ρ_f	gas density ($kg\,m^{-3}$)
ρ_{CaO}	CaO density ($kg\,m^{-3}$)
$\rho_{M,g}$	molar density of gas ($mol\,m^{-3}$)
μ	gas viscosity ($kg\,m^{-1}\,s^{-2}$)

Subscripts

f	fluid
k	component
p	particle
in	input
out	output

823 K compared with 1123 K in case of the conventional fixed-bed reactor [12].

The performance of a methanol-fuelled SOFC equipped with a palladium membrane reactor was investigated in our previous study [13]. The results showed that, under the same net electricity efficiency, the SOFC integrated with the membrane reactor needs smaller SOFC stack size compared to that with the conventional reformer. However, this operation is not cost-effective since extra cost on palladium membrane and high-pressure compressor is required. A further study was performed on methane-fed SOFC systems considering three operation modes of palladium membrane reactors, i.e., high pressure compressor, combined low pressure compressor and vacuum pump, and combined high pressure compressor and vacuum pump [14]. The SOFC system with a conventional reformer was considered as a base case for technical and economic analyses. The results revealed that the performance of SOFC is dependent on hydrogen recovery and operation mode. Moreover, the results demonstrate that the replacement of the conventional reformer with the membrane reactor becomes attractive and the combined high pressure compressor and vacuum pump is the best operation mode for integrating the membrane reactor with the SOFC stack. However, thermal management was not taken into account within the integrated systems.

Thermal management of methane-fuelled and biogas-fuelled SOFC systems operating in three different modes of membrane reactor was also recently investigated [15]. The system performance at an energy self-sustainable condition was evaluated. The investigation reported that the high pressure compressor mode is the best operation mode. It was also demonstrated that the replacement of the conventional reformer by the membrane reactor can improve system performance for both the methane-fuelled and biogas-fuelled SOFC systems. However, economic analysis revealed

that the integrated membrane reactor and SOFC system fuelled by either methane or biogas is not viable due to its high operating pressure at the retentate section of the membrane reactor, resulting in a high investment cost of high-pressure compressors. Furthermore, it became evident that the biogas-fuelled SOFC operating with a membrane reactor may be economically feasible when CO_2 in biogas is removed before feeding into membrane reactor. Among CO_2 capture technologies, a CaO–CO_2 acceptor (CaO carbonation) is one of attractive options. The use of CaO–CO_2 acceptor does not only minimize water–gas shift (WGS) reaction in membrane reactor [16–18] but also reduces the amount of CO_2 released to the environment. However, make-up CaO is required for the CaO–CO_2 acceptor due to the sintering effect of CaO sorbent after several cycles of carbonation–calcination [19,20]. This causes an increase in the operating cost. Vivanpatarakij et al. [21] studied the use of a CaO–CO_2 acceptor in a methane-fuelled SOFC system. It was found that the removal of CO_2 from syngas prior to feeding into SOFC stack can improve the SOFC performance. Nevertheless, this system configuration is not suitable from an environmental standpoint of view since CO_2 generated in SOFC stack via WGS reaction cannot be captured and must be released to the environment.

In this study, the performances of biogas-fuelled SOFC systems with different configurations are investigated. Four systems are considered, i.e., SOFC with conventional reformer (CON–SOFC), SOFC with palladium membrane reactor (PMR–SOFC, SOFC with palladium membrane reactor and CO_2 sorption enhancement (SE) unit by using a CaO–CO_2 acceptor (SE–PMR–SOFC), and SOFC with palladium membrane reactor and CaO–CO_2 acceptor with recycling a retentate gas from the membrane reactor (SER–PMR–SOFC). Technical and economic analyses are carried out to find out an appropriate configuration for the biogas-fuelled SOFC system.

2. Modeling of integrated SOFC systems

2.1. Palladium membrane reactor (PMR)

A palladium membrane reactor (PMR) is divided into two sections: permeate side (low pressure operation) and retentate side (high pressure operation). Steam which has proven to be the most suitable reforming agent for the SOFC system [5] is fed simultaneously with fuel gas (biogas) to the PMR. H_2 generated permeates through the palladium membrane to the permeate section and the rate of permeation depends on the difference of H_2 partial pressure between permeate and retentate sections. According to Xu and Froment's work [22], the main chemical reactions taking place in the reactor consist of methane steam reforming (Eq. (1)), water–gas shift reaction (Eq. (2)) and reverse carbon dioxide methanation (Eq. (3)).

$$CH_4 + H_2O \rightarrow 3H_2 + CO \quad (1)$$

$$CO + H_2O \rightarrow H_2 + CO_2 \quad (2)$$

$$CH_4 + 2H_2O \rightarrow CO_2 + 4H_2 \quad (3)$$

The feed molar ratio of H_2O to CH_4 is always set to 2.5 to inhibit the carbon formation [23]. The kinetic rate expressions used in the calculation are derived from the experimental results on $Ni/MgAl_2O_4$ catalyst of Xu and Froment [22]. The hydrogen permeation flux is inversely proportional to the membrane thickness and also varies with the operating temperature. It can be calculated by the correlation given in Eq. (4).

$$N_{H_2} = \frac{Q_0}{\delta} \exp\left(\frac{-E_P}{RT}\right)\left(p_{H_2,R}^{0.5} - p_{H_2,P}^{0.5}\right) \quad (4)$$

The value of the pre-exponential factor (Q_0) and the activation energy (E_P) are 6.33×10^{-7} mol/(m $Pa^{1/2}$ s) and 15,700 J/mol, respectively [10]. The membrane thickness (δ) is set to be 4.5 μm [10].

Table 1
Summary of model parameters.

Parameters	Value
SOFC stack [37]	
n	0.48
ξ	5.4
D_p	3 μm
l_a	750 μm
l_c	50 μm
L	50 μm
T	1073 K
P	1 bar
Palladium membrane reactor	
T	823 K
P	1 bar
ρ_c	2355 kg/m^3
ε	0.5
d	10 mm
Reactor tube length	0.15 m
Number of reactor tube	1000
Conventional reformer	
T	973 K
P	1 bar
CaO–CO_2 acceptor (carbonator) [20,38]	
T	973 K
M_{CaO}	56 g/mol
d_p	0.3 mm
ρ_{CaO}	3313.6 kg/m^3
$V_{M,CaCO_3}$	36.9 cm^3/mol
e_{max}	50 nm
k_S	4×10^{-10} m^4/(mol s)
ε	0.6

To simplify the calculations, pressure drop in the PMR is assumed to be zero. The governing ordinary differential equations are solved using finite difference method. More details and correlations used in the calculation for PMR are given in our previous work [15]. H_2 recovery (ζ) defined in Eq. (5) is employed as a PMR performance indicator. The parameters used in the calculations are given in Table 1. Thermodynamic equilibrium is assumed for the fuel processor in CON–SOFC. It should be noted that the chemical equilibrium model used for the conventional reformer represents the best hydrogen production achieved by CON–SOFC. Therefore, the potential benefits of applying the palladium membrane and the CaO acceptor in the SOFC system are analyzed compared to the best hydrogen production from the CON–SOFC.

$$H_2 \text{ recovery } (\zeta) = \frac{H_2 \text{ production rate}}{\text{Theoretical } H_2 \text{ production rate}} \quad (5)$$

2.2. CaO–CO_2 acceptor system

In this study, a CaO–CO_2 acceptor system is considered as the CO_2 capture technology. As described in Fig. 1, CO_2-rich gas is fed simultaneously with circulating CaO at the bottom of the carbonator in which CaO solid is fluidized and reacts with CO_2 in gas phase (Eq. (6)). Gas–solid mixture is discharged at the top of the bed and separated in the cyclone. Lean-CO_2 gas exits the CaO–CO_2 acceptor system and the reacted CaO is heated and then fed into the calciner bed. The calcination reaction which is the reverse of the carbonation reaction (Eq. (6)) takes place in the calcination bed to regenerate CaO. Make-up CaO is also fed to the system in order to keep the efficiency of CO_2 capture reasonably high. The mixture of CO_2 and regenerated CaO are released from the calciner and then fed into cyclone in which CaO solid is removed from gas stream.

$$CaO + CO_2 \rightarrow CaCO_3 \quad (6)$$

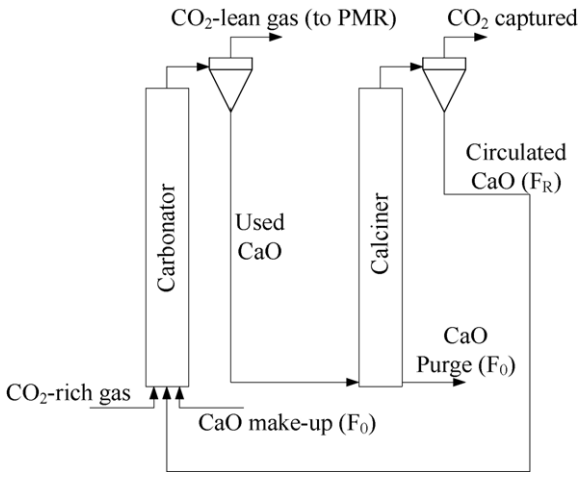

Fig. 1. The scheme showing the basic working of the CaO–CO_2 acceptor.

The efficiency of CO_2 capture is determined as the system performance indicator and defined as:

$$E_{carb} = \frac{CO_2 \text{ reacting with CaO in the bed}}{CO_2 \text{ entering the bed in the } CO_2\text{-rich gas}} \quad (7)$$

It depends on the CaO-circulating flow (F_R), CaO-make up flow (F_0) and CaO inventory (W_S) in the carbonation bed [20]. In this study, F_R/F_{CO_2} and W_S are kept constant at 10 (the utilization ratio of CaO in the carbonation bed is 0.1) and 50 kg, respectively. The calculation focuses on the estimation of F_0 to achieve the determined capture efficiency. In the calculation, a plug flow model of gas through perfectly mixed CaO bed is assumed. The average maximum carbonation conversion (X_{ave}) is initially determined from Eqs. (8)–(10).

$$X_N = \frac{1}{1/(1-X_r) + Nk} + X_r \quad (8)$$

$$r_N = \frac{F_0 F_R^{N-1}}{(F_0 + F_R)^N} \quad (9)$$

$$X_{ave} = \sum_{N=1}^{\infty} r_N X_N \quad (10)$$

The values of k and X_r are 0.52 and 0.075, respectively [19]. The capture efficiency can then be calculated using Eqs. (11)–(13) [20].

$$E_{carb} = \frac{F_R}{F_{CO_2}} X_{ave} \frac{f_a}{\ln(1/(1-f_a))} \quad (11)$$

$$\frac{F_{CO_2} \cdot M_{CaO}}{W_S \cdot k_S \cdot S_{ave} \cdot \rho_{M,g} \cdot f_a} \left[\frac{-f_0}{f_0 f_e - f_0} E_{carb} + \frac{f_0 (f_0 - 1)}{(f_0 f_e - f_0)^2} \ln\left(\frac{(f_0 - f_e) + (f_0 f_e - f_0) E_{carb}}{(f_0 - f_e)} \right) \right] = 1 \quad (12)$$

$$S_{ave} = \frac{V_{M,CaCO_3} X_{ave}}{M_{CaO} e_{max}} \rho_{CaO} \quad (13)$$

Mole fraction of CO_2 at equilibrium condition (f_e) is calculated using Eq. (14) [17]. For Eqs. (11) and (12), two unknown variables, i.e., f_a and E_{carb}, can be estimated. The CO_2-rich gas velocity is always controlled to be higher than the terminal settling velocity of CaO particle (v_t). CaO particle terminal settling velocity and pressure drop along the carbonation fluidized bed can be calculated employing Eq. (15) and (16), respectively [24].

$$f_e = \frac{4.137 \times 10^7 e^{-20{,}474/T}}{P} \quad (14)$$

$$v_t = \frac{0.153 \times g^{0.71} \times d_p^{1.14} \times (\rho_{CaO} - \rho_f)^{0.71}}{\rho_f^{0.29} \times \mu^{0.43}} \quad (15)$$

$$\frac{\Delta P}{L_b} = \rho_{CaO}(1-\varepsilon)g + \rho_f \varepsilon g + \frac{2 f_f \rho_f \varepsilon u_f^2}{D} + \frac{2 f_P \rho_{CaO}(1-\varepsilon) u_P^2}{D} \quad (16)$$

2.3. SOFC stack model and calculation procedure

In SOFC, the reaction between fuel (H_2 and CO) and oxidizing agent (air or O_2) called "Electrochemical reaction" takes place to generate electrical energy. Oxygen is reduced in the cathode section to oxygen ions (Eq. (17)) permeates through the solid electrolyte to the anode section. In this section, oxygen ions react with the hydrogen fuel (Eq. (18)) and steam is produced. Ni-YSZ, YSZ and LSM-YSZ are chosen as the materials in the anode, electrolyte and cathode of the SOFC cell, respectively.

$$\frac{1}{2}O_2 + 2e^- \rightarrow O^{2-} \quad (17)$$

$$H_2 + 2O^{2-} \rightarrow H_2O + 2e^- \quad (18)$$

The open circuit voltage (E) of the cell depends on temperatures and gas composition. It can be calculated from the Nernst equation, namely;

$$E = E^0 + \frac{RT}{2F} \ln\left(\frac{p_{H_2} p_{O_2}^{1/2}}{p_{H_2O}} \right) \quad (19)$$

The actual cell potential (V) is less than the open circuit voltage (E) due to the existence of overpotentials as shown in Eq. (20). The overpotentials can be categorized into three main sources: ohmic overpotential (η_{ohm}), activation overpotential (η_{act}) and concentration overpotential (η_{conc}). More details of the equations used in describing these overpotentials are given in our recent study [25].

$$V = E - \eta_{act} - \eta_{ohm} - \eta_{conc} \quad (20)$$

Assumptions made to simplify the calculation for the assessment of the SOFC stack include, (i) a constant operating voltage along the cell length is assumed as the current collector usually has high electrical conductivity, (ii) CO electro-oxidation is neglected as it was reported that its reaction rate is greatly lower compared with that of H_2 electro-oxidation [26], (iii) the equilibrium conversion of CO via WGS reaction is assumed in the anode section since the rate of WGS reaction is fast at high temperatures [27–29], (iv) the anode compositions always reach their equilibrium along the cell length due to the fast kinetics at high temperature. Large amounts of air (five times of theoretical air required to combust the methane fuel (biogas)) are fed into the SOFC cathode as the oxidant so as to minimize the temperature gradient in stack. The calculation takes place for each small fuel utilization region employing the mathematical model given in our recent work [5]. In each region, the open circuit voltage, overpotentials, equilibrium composition of anode fuel, stack area and current density are calculated. The stack areas calculated in each region are added up to yield the total stack area. Finally, the current calculated from the fuel utilized in the stack is divided by the total stack area to obtain the average current density and hence, the average power density may be determined. Fuel utilization (U_f) is computed by Eq. (21).

$$U_f = \frac{\text{total } H_2 \text{ consumed in SOFC stack}}{H_2 \text{ molar flow rate} + \text{CO molar flow rate}} \quad (21)$$

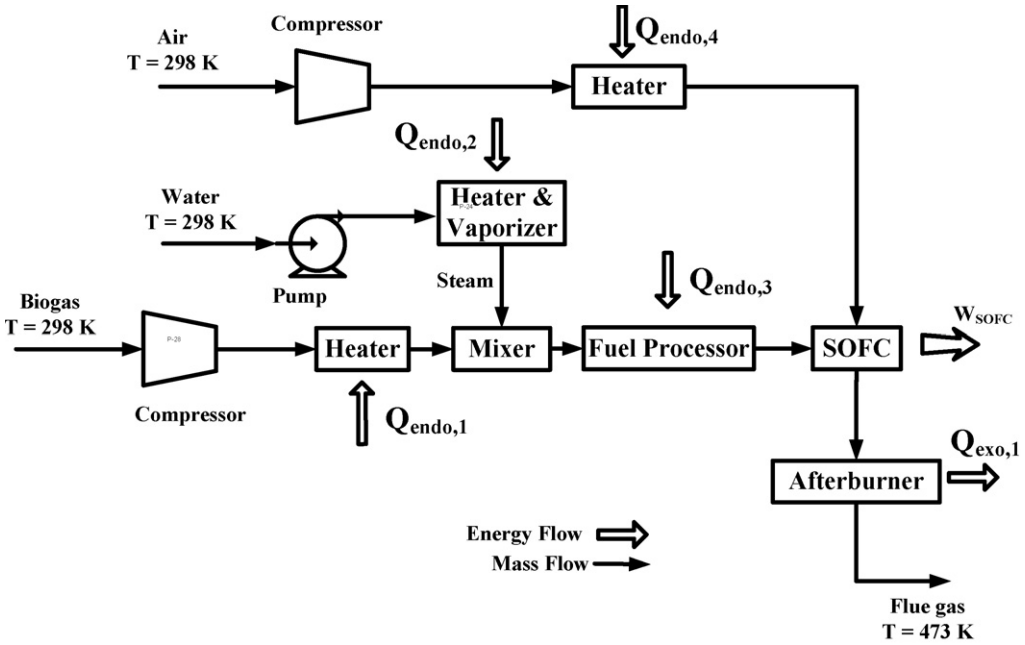

Fig. 2. The plant configuration of the CON–SOFC.

2.4. Afterburner and heat exchanger

The SOFC anode outlet gas and cathode outlet gas are mixed for post combustion. Total combustion is presumed in the afterburner hence, methane, carbon monoxide and hydrogen contents in the flue gas are taken as zero with the heat exchanger operating adiabatically.

2.5. Vacuum pump and compressor

For the calculation of vacuum pump and compressor, their outlet gas temperature and power consumption can be estimated employing Eqs. (22) and (23), respectively while the compressor efficiency is taken as 75% [30].

$$T_{out} = T_{in}\left(1 + \frac{1}{\eta_{com}}\left(\left(\frac{P_{out}}{P_{in}}\right)^{(\gamma-1)/\gamma} - 1\right)\right) \quad (22)$$

$$\dot{W}_{comp} = -\dot{m}\int_{T_{in}}^{T_{out}} C_p dT \quad (23)$$

$$\gamma = \frac{C_p}{C_p - R}. \quad (24)$$

2.6. SOFC system configurations

The use of a CaO–CO_2 acceptor in the SOFC system coupled to the PMR (SE–PMR–SOFC and SER–PMR–SOFC) is investigated in this study. To evaluate the feasibility of these configurations, the performance of the SOFC working with the conventional fuel processor (CON–SOFC) and the PMR (PMR–SOFC) is computed as base cases. The plant configuration for the CON–SOFC is illustrated in Fig. 2. Several units are included in the system that consists of a pre-reformer, an SOFC stack, an afterburner, a mixer, a vaporizer, and preheaters. Initially, the mixture of preheated steam and biogas is fed into the fuel processor so as to produce syngas via three chemical reactions (Eqs. (1)–(3)). Chemical equilibrium is assumed in the calculation of the conventional fuel processor. Syngas produced in the fuel processor is fed into the SOFC stack where the electrical energy is generated. To simplify the computation, the isothermal operation is assumed for the SOFC stack. The heat generated from the irreversibility in SOFC stack is utilized in air and syngas preheating. To achieve a desired temperature of the SOFC stack, an oxidizing agent (air) temperature is tuned up based on the energy balance in the SOFC stack. The residue fuel gas released from the SOFC stack is burned up in the afterburner in order to supply heat to the other parts of system. Temperature of flue gas released from the system is set to be 473 K. We remark that all the SOFC systems considered operate under "thermally self-sustaining" – condition for which external heat supplementation is not required. To achieve such a condition, a fuel utilization of SOFC stack is tuned up until the heat consumption and generation within the SOFC system are equivalent ($Q_{NET} = 0$).

Considering PMR–SOFC, SE–PMR–SOFC and SER–PMR–SOFC (Fig. 3), the conventional fuel processor is replaced by different fuel processing systems. Prior to feeding to the fuel processing system, biogas and steam is firstly compressed to achieve the operating pressure of retentate section. Pure H_2 obtained from each fuel processing system is preheated and fed to SOFC in which the electrochemical reaction takes place, while high-pressure retentate gas is fed into the afterburner.

For the fuel processing system in PMR–SOFC (Fig. 4a), the mixture of compressed biogas and steam is fed directly to the retentate section of PMR. Pure-H_2 and retentate gas is obtained at the permeate section and retentate section of PMR, respectively. Considering the fuel processing system in SE–PMR–SOFC (Fig. 4b), compressed biogas and steam are initially fed to the CaO–CO_2 acceptor in which CO_2 in biogas is removed. The CO_2-removed gas is subsequently cooled down and fed to PMR. In case of SER–PMR–SOFC (Fig. 4c), some retentate gas is recycled, mixed with biogas and steam, and subsequently fed to the CaO–CO_2 acceptor. It is noted that CO_2 is captured in the CaO–CO_2 acceptor until reaching the equilibrium value.

3. Results and discussion

Computer programs for solving all mathematical models describing the integrated SOFC systems proposed in this study are written in Visual Basic and the values of all parameters used in

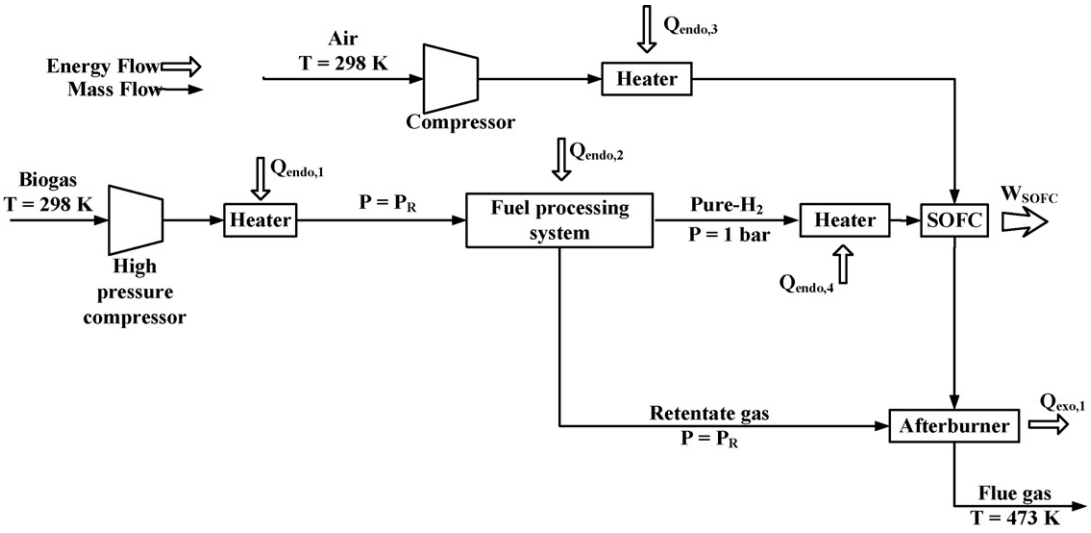

Fig. 3. The plant configuration of the PMR–SOFC, SE–PMR–SOFC and SER–PMR–SOFC.

the calculations are summarized in Table 1. As described in our previous works, the SOFC model employed in the calculation can well predict the experimental results of Zhao and Virkar [31] for the mixture of hydrogen (97%) and water (3%) [5] and shows good agreement with the simulation results of Petruzzi et al. [32] for SOFC feed gas with a low concentration of hydrogen [25]. The kinetic model and H_2 permeation model were verified in our recent work [15] and the results indicate that these models can well envisage the experimental results reported in the literature [11,33]. It should be noted that the kinetic data [22] was derived using relatively low pressures (3–15 bar); however, it was assumed that the models can be used for predicting the reaction rates throughout the range of pressures considered in this study (10–30 bar).

The effect of the extent of CO_2 captured and the retentate pressure on H_2 recovery of PMR in the case of SE–PMR–SOFC system is firstly investigated as illustrated in Fig. 5a. The improvement of H_2 recovery is obvious when the CO_2 content in PMR feed decreases due to the shift of the equilibrium of WGS reaction. An increase in retentate pressure can also improve H_2 recovery. It should be noted that the retentate pressure in the range of 10–30 bar is investigated in this study. Our previous study [15] showed that the operation of PMR–SOFC at excessively high retentate pressure (>40 bar) is not economically feasible; nevertheless, with low retentate pressure, H_2 recovery may not be adequately high. With the retentate pressure of 30 bar, PMR without CO_2 removal offers H_2 recovery of 0.896 which is significantly lower than that obtained from PMR with CO_2 removal rate at equilibrium value which is equal to 0.952. Even if the removal of CO_2 can improve the H_2 recovery of PMR, large amount of fresh CaO sorbent is required to achieve high extent of CO_2 removal. As described in Fig. 5b, a fresh CaO supplying rate of 0.021 mol/s is required to achieve CO_2 removal rate at the equilibrium value.

With SE–PMR–SOFC configuration, CO_2 removal rate is limited at 0.667 mol/s (the amount of CO_2 presented in biogas at the feed rate of 1.667 mol/s) and large amounts of CO_2 and CO generated in PMR cannot be captured. Moreover, methane conversion and H_2 recovery in PMR is inhibited by the presence of CO_2 and CO in retentate gas. To solve these problems, SER–PMR–SOFC configuration is proposed. With this configuration, some retentate gas is recycled and mixed with biogas prior to feeding to the CaO–CO_2 acceptor where CO_2 is captured until reaching equilibrium.

The influence of the recycle ratio and retentate pressure on H_2 recovery and CO_2 removal rate of SER–PMR–SOFC is illustrated in Fig. 6a. An increase in the recycle ratio can significantly improve both H_2 recovery and CO_2 removal rate, especially at low retentate pressure. At the retentate pressure of 10 bar and the recycle ratio of 0.9, the H_2 recovery of 0.967 and the CO_2 removal rate of 1.55 mol/s can be achieved. These values are extremely higher compared with the case that the recycle ratio is zero (H_2 recovery = 0.761, CO_2 removal rate = 0.664 mol/s). Furthermore, H_2 recovery can reach 0.994 as the retentate pressure and recycle ratio are 30 bar and 0.9, respectively. At high recycle ratio, an increase in retentate pressure does not significantly improve H_2 recovery, therefore, the operation at high retentate pressure (>17.5 bar) may not be superior due to the waste of high-pressure compressor load. Although the increase in recycle ratio can improve both H_2 recovery and CO_2 removal rate, the supplying rate of fresh CaO for SER–PMR–SOFC raises as well. As shown in Fig. 6b, for the operation at the recycle ratio of 0.9, fresh CaO supplying rate is three times higher than the operation without recycle of the retentate gas. Moreover, the increase in recycle ratio may cause high velocity of retentate gas and also the generation of pressure drop in PMR which is not considered in this study.

The effect of fuel utilization and CO_2 removal rate on the power density under energetically self-sustaining condition for SE–PMR–SOFC system is illustrated in Fig. 7. With high CO_2 removal rate, high fuel utilization is required for SE–PMR–SOFC to attain thermally self-sustaining operation. In this mode of operation, the increase in CO_2 removal rate improves the SOFC power density due to the increase in H_2 recovery. However, the improvement of power density with CO_2 removal rate becomes less pronounced high CO_2 removal rates. Fig. 8 shows the energy self-sufficient operation of SE–PMR–SOFC with equilibrium CO_2 removal rate at each operating voltage and retentate pressure. At each retentate pressure, an optimum operating voltage is found. Higher fuel utilization is required as the operating voltage decreases to achieve energy self-sustainable operation. The decrease in operating voltage can improve the power density, however, at excessive low operating voltage that fuel utilization close to 1 is required to achieve energy self-sustainable operation, the reduction in power density is found as the operating voltage decreases due to low value of H_2 concentration particularly near the exit of SOFC stack. The power density is improved as the retentate pressure increases owing to the improvement in H_2 recovery. With good operating condition is selected, SE–PMR–SOFC can offer higher power density compared with PMR–SOFC and CON–SOFC. The operation of SE–PMR–SOFC with equilibrium CO_2 capture at operating voltage and retentate pressure of 0.626 V and 30 bar, respectively, offers

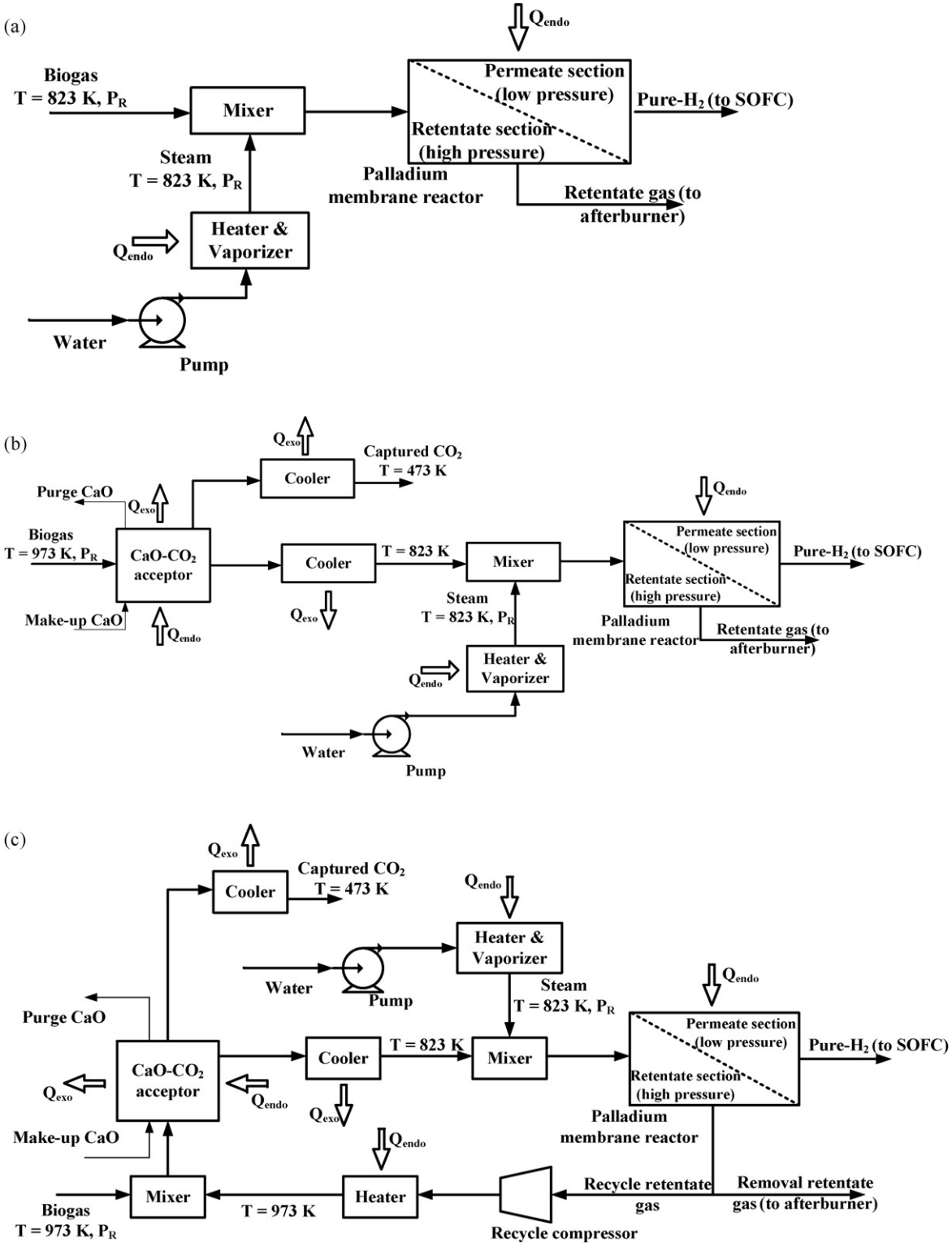

Fig. 4. Fuel processing system of (a) PMR–SOFC, (b) SE–PMR–SOFC and (c) SER–PMR–SOFC.

a power density of 0.431 W/cm^2, whereas the power densities of PMR–SOFC (retentate pressure = 51.24 bar) and CON–SOFC are 0.421 and 0.398 W/cm^2, respectively.

Considering SER–PMR–SOFC configuration, the effect of its recycle ratio and fuel utilization on the power density and thermally self-sustainable operation is illustrated in Fig. 9. High fuel utilization is required to achieve the energy self-sustainable operation for SER–PMR–SOFC operating at high recycle ratios. In this situation, the increase in recycle rate can improve the power density. These operating characteristics are similar to those of SE–PMR–SOFC since the operation at high recycle ratio offers high CO_2 removal rate. The study on the effect of permeate pressure and operating pressure on the power density for SER–PMR–SOFC operated at a recycle ratio of 0.5 is depicted in Fig. 10a. Similar to SE–PMR–SOFC, the increase in the retentate pressure can improve the power density due to the increase in H_2 recovery. Also, the optimum operating voltage is

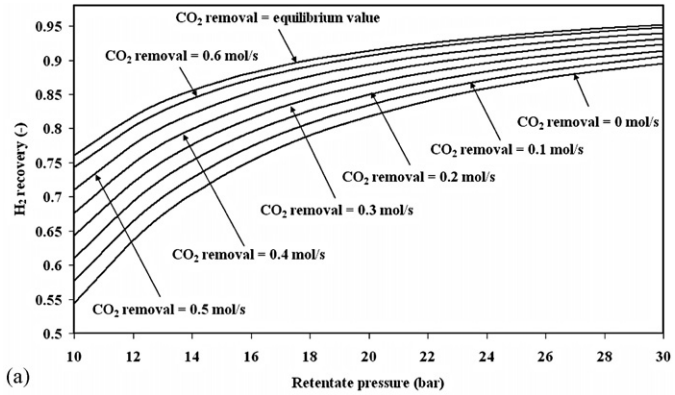

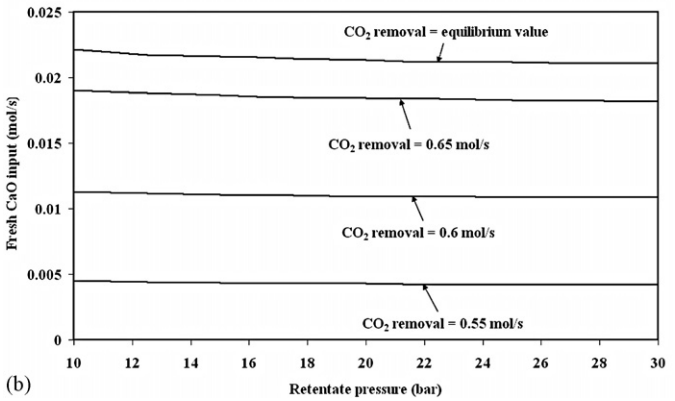

Fig. 5. The effect of the extent of CO_2 removal and retentate pressure on (a) H_2 recovery and (b) fresh CaO feed rate in case of SE–PMR–SOFC system.

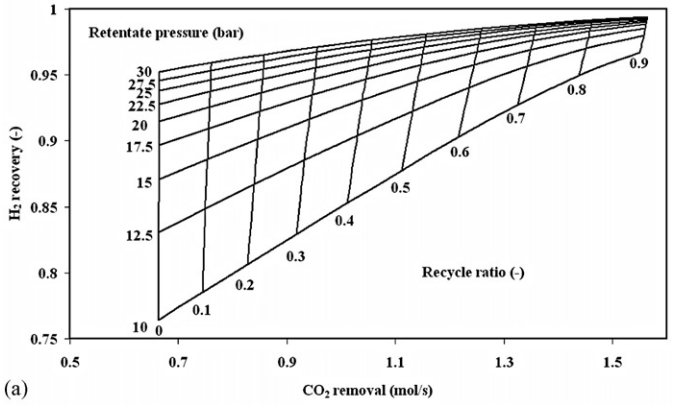

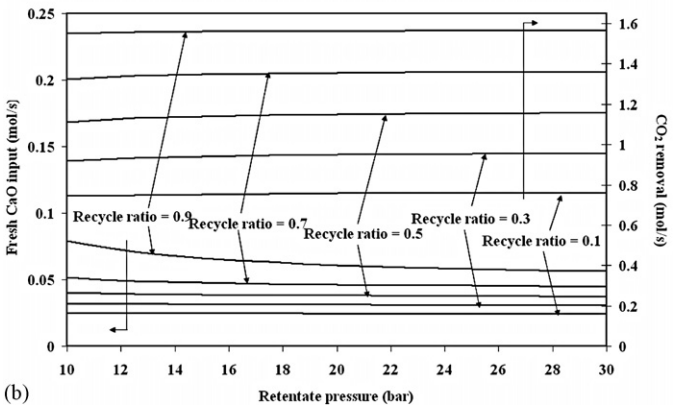

Fig. 6. The effect of the recycle ratio and retentate pressure on (a) H_2 recovery, CO_2 removal rate and (b) fresh CaO feed rate, CO_2 removal rate in case of SER–PMR–SOFC system.

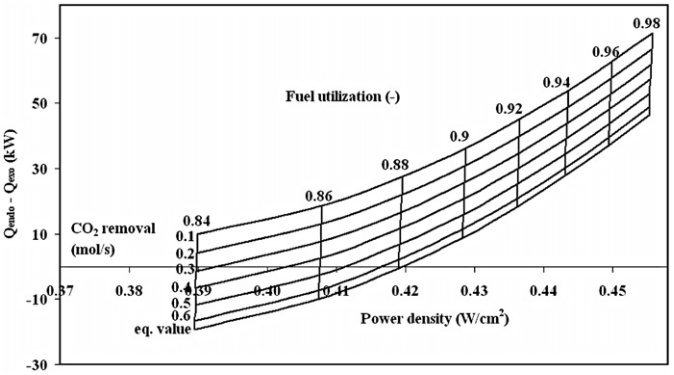

Fig. 7. The effect of fuel utilization and CO_2 removal rate on the power density and energy self-sufficient point for SE–PMR–SOFC system (P_R = 25 bar).

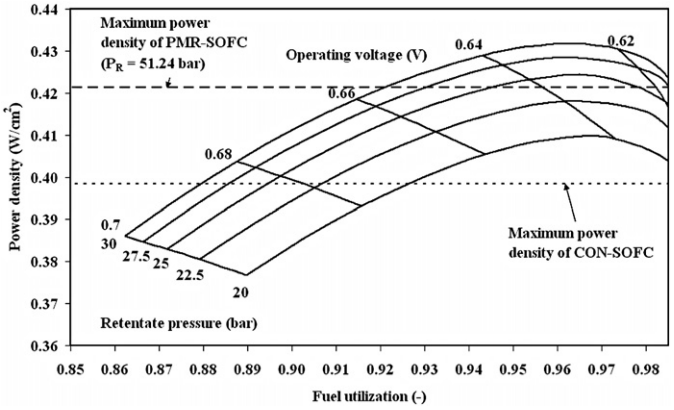

Fig. 8. The power density of SE–PMR–SOFC system with equilibrium CO_2 removal rate operating at energy self-sufficient point at each operating voltage and retentate pressure.

found. As shown in Fig. 10a, with the recycle ratio of 0.5, the optimum operating voltage is around 0.61–0.62 V and the maximum power density SER–PMR–SOFC is about 0.45 W/cm^2. As illustrated in Fig. 10b, operating voltage of PMR–SOFC at the recycle ratio of 0.5 is higher than 0.6 V which is the condition that the fuel utilization is close to 1. The results in Fig. 10a and b also indicate that the intermediate fuel utilization (around 0.94–0.96) is preferred for the operation of SOFC system. For the operation at the recycle ratio of 0.9, the optimum operating voltage is observed at around 0.6–0.61 V. Moreover, the optimum retentate pressure is also found at around 15 bar as illustrated in Fig. 11a. Even if the increase in the retentate pressure can improve H_2 recovery and also SOFC power

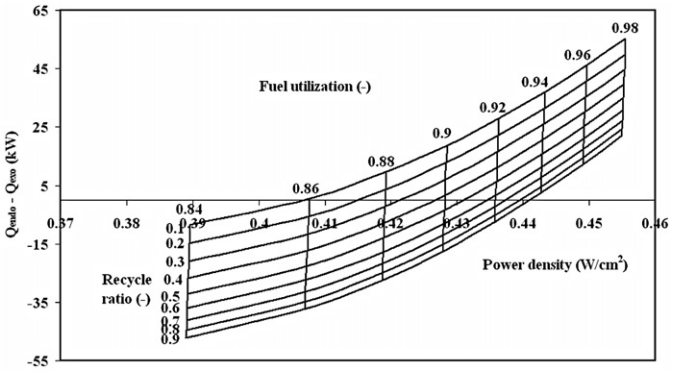

Fig. 9. The effect of fuel utilization and recycle ratio on the power density and energy self-sufficient point for SER–PMR–SOFC system (P_R = 17.5 bar).

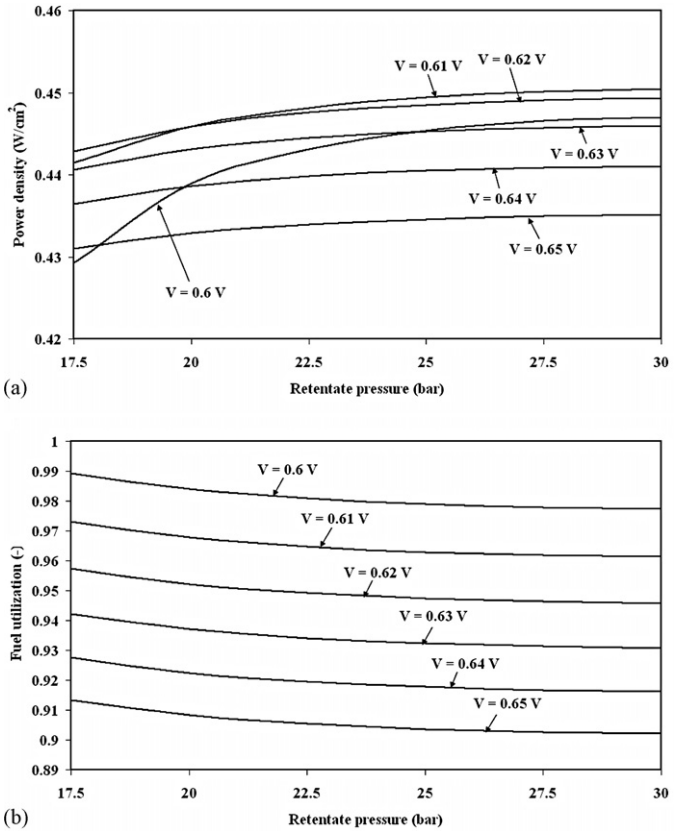

Fig. 10. The effect of permeate pressure and operating pressure on (a) the power density and (b) fuel utilization for SER–PMR–SOFC system operating at energy self-sufficient point and recycle ratio of 0.5.

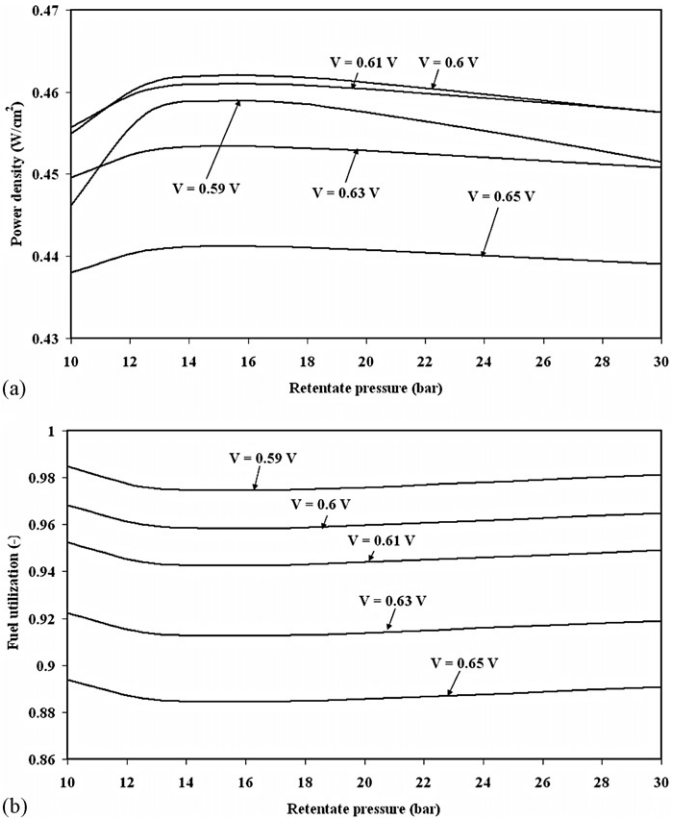

Fig. 11. The effect of permeate pressure and operating pressure on a) the power density and b) fuel utilization for SER–PMR–SOFC system operating at energy self-sufficient point and recycle ratio of 0.9.

density, the reduction in power density caused by the increase in electricity consumed by high-pressure compressor may attenuate this benefit especially at high recycle ratio where H_2 recovery is not improved significantly with increase in the retentate pressure as described in Fig. 6a. Similar to the case of operation at the recycle ratio of 0.5, the intermediate fuel utilization (around 0.94–0.96) is also preferred for SER–PMR–SOFC system with the recycle ratio of 0.9 as shown in Fig. 11b. When SER–PMR–SOFC system is operated at the recycle ratio of 0.9, the power density of 0.462 W/cm^2 can be achieved, which is higher than that of PMR–SOFC (0.421 W/cm^2) and CON–SOFC (0.398 W/cm^2).

Fig. 12 demonstrates the maximum power density, SOFC stack size, and the fresh CaO supplying rate at each recycle ratio of SER–PMR–SOFC. The stack size of SER–PMR–SOFC is always smaller than those of PMR–SOFC and CON–SOFC for all the values of recycle ratio. The increase in recycle ratio can improve the power density; however, the amount of fresh CaO used in the CaO–CO_2 acceptor also increases. It can be concluded that both the SE–PMR–SOFC and SER–PMR–SOFC systems can significantly improve the power density and also reduce the size of SOFC stack. However, in order to determine the potential benefits of PMR–SOFC, SE–PMR–SOFC and SER–PMR–SOFC systems, an economic analysis of the proposed systems compared to CON–SOFC as a base case should be performed, considering the use of large amount of fresh CaO sorbent. The influence of the recycle ratio on the potential benefit of SER–PMR–SOFC is also examined. In this analysis, the biogas feed rate was kept at 1.667 mol/s for all cases and therefore fuel feed cost is neglected. Furthermore, since the SOFC systems considered are operating as thermally self-sustainable units, additional heat or electricity from the outside of the system is not necessary. Therefore, only the capital costs of SOFC stack, PMR, and high-pressure compressor (HPC) coupled with the operating cost of fresh CaO sorbent are considered. Net cost saving is determined as an economical index and can be calculated as:

$$\begin{aligned}\text{Net cost saving} = {} & \text{Saving in capital cost of SOFC stack} \\ & - \text{Additional capital cost of PMR and HPC} \\ & - \text{Additional operating cost of fresh CaO sorbent}\end{aligned} \quad (25)$$

For the calculation of the operating cost of fresh CaO sorbent, project life time and the interest rate are assumed to be 5 years and 0%, respectively. The cost of fresh CaO sorbent is computed from

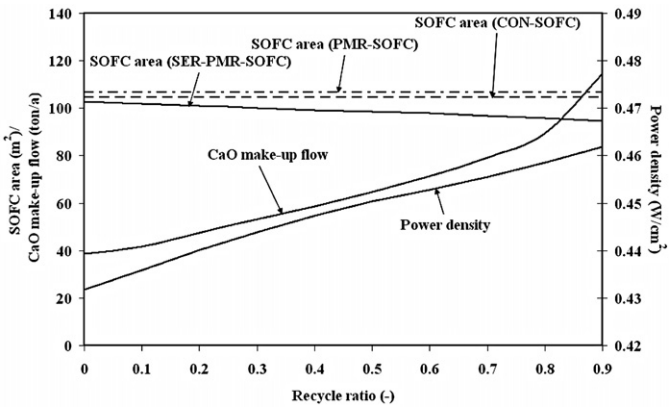

Fig. 12. The maximum power density SER–PMR–SOFC can achieve, SOFC stack size and the fresh CaO supplying rate at each recycle ratio in case that $Q_{NET} = 0$.

Table 2
Costing models of SOFC [34], palladium membrane [35], compressor [29] and CaO sorbent [21], and the price of carbon credit [36].

Costing model	
Cell cost ($)	$C_{cell} = A_{single\ cell} \times 0.1442$[a]
Number of cells	$N_{cell} = A_{cell}/A_{single\ cell}$
Number of stacks	$N_{stack} = N_{cell}/100$
Fuel cell stacks cost ($)	$C_{stack} = 2.7 \times (C_{cell} \times N_{cell} + 2 \times N_{stack} \times A_{single\ cell} \times 0.46425)$
Palladium membrane cost ($/kg)	6700
Compressor ($)	$C_{compressor} = 1.49 \times HP^{0.71} \times 10^3$
Project life time (year)	5
CaO sorbent ($/ton)	60

[a] A single cell area is fixed at 200 cm^2.

the total cost of fresh CaO used in the life time. All parameters used in capital cost estimation and economic study are summarized in Table 2. The additional benefit obtained from CO_2 capture is also considered in this study. Two indicators; i.e. %total CO_2 captured and cost of CO_2 capture and are defined as;

$$\%\text{total } CO_2 \text{ capture} = \frac{\text{Rate of } CO_2 \text{ capture (ton/}a\text{)}}{\text{Total } CO_2 \text{ in flue gas in case of CON} - \text{SOFC (ton/}a\text{)}} \times 100 \quad (26)$$

$$\text{Cost of } CO_2 \text{ capture (\$/ton)} = -\frac{\text{Net cost saving (\$)}}{\text{Rate of } CO_2 \text{ capture (ton/}a\text{)} \times \text{Plant life time (year)}} \quad (27)$$

%Total CO_2 capture represents the CO_2 capture efficiency of SER–PMR–SOFC configuration, whereas cost of CO_2 capture stands for the additional cost (relative to CON–SOFC) used in CO_2 capture per unit of CO_2 capture.

As illustrated in Fig. 13, PMR–SOFC configuration is not an attractive SOFC system due to high retentate pressure and also high electricity consumption in HPC. The use of SE–PMR–SOFC configuration in SOFC system (equilibrium CO_2 capture) is more economically beneficial compared with PMR–SOFC since it can yield high H_2 recovery with low retentate pressure. However, the negative net cost saving of the former indicates that its potential benefit is not equivalent to that of CON–SOFC. For SER–PMR–SOFC, maximum net cost saving is observed at the recycle ratio of 0.8. The operation at the recycle ratio of 0.9 is not favored even if high

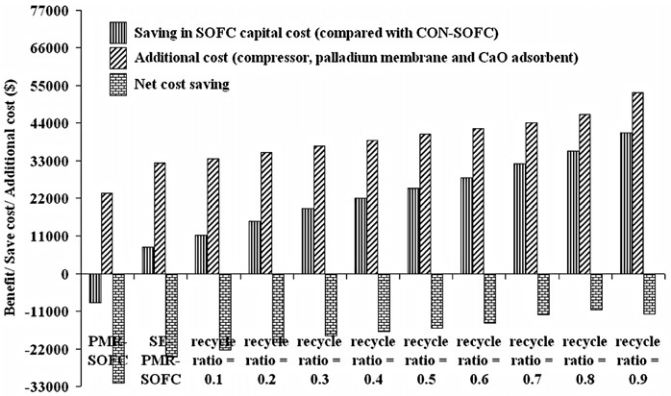

Fig. 13. Saving in SOFC stack cost, additional cost, net cost saving, benefit of carbon credit and total benefit of PMR–SOFC, SE–PMR–SOFC with equilibrium CO_2 capture and SER–PMR–SOFC operating at different recycle ratio.

power density is achieved since its CaO cost is higher compared to low recycle ratio as illustrated in Fig. 12. Although the net cost saving of SER–PMR–SOFC is superior to SE–PMR–SOFC, it is a negative value which indicates that both SE–PMR–SOFC and SER–PMR–SOFC are not good configurations for SOFC system. The additional study on the benefit of CO_2 capture takes place as shown in Fig. 14. The operation at high recycle ratio is preferred if high total CO_2 capture efficiency is required. Moreover, cost of CO_2 capture is reduced as the recycle ratio increases. Considering SER–PMR–SOFC operating at the recycle ratio of 0.9, its cost of CO_2 capture is $20.4/ton CO_2 capture at %total CO_2 capture of 93. With the identical %total CO_2 capture, this cost of CO_2 capture is far lower than the $228/ton CO_2 capture reported in the literature [21] which studied the cost of CO_2 capture from the flue gas of methane fuelled CON–SOFC system. It should be noted that according to the analysis in this literature [21], methane feed rate is kept at 1 mol/s and CaO acceptor is equipped in the system to capture CO_2 in flue gas. Hence, with the same production scale and technology, the result from this literature [21] is suitable to be used as benchmark in this study. The results of the technical and economical study for all SOFC configurations are summarized in Table 3. On the basis of a similar biogas feed rate of 1.667 mol/s with net electricity production of 416.79 kW, the improvement in power densities relative to CON–SOFC are 8.21%

Table 3
The technical and economical comparison of each configuration of SOFC system.

	CON–SOFC	PMR–SOFC	SE–PMR–SOFC	SER–PMR–SOFC	
			(equilibrium CO_2 capture)	Recycle ratio = 0.5	Recycle ratio = 0.8
Feed rate (mol/s)	1.667	1.667	1.667	1.667	1.667
Retentate pressure (bar)	–	51.24	30	30	20
H_2 recovery (–)	–	0.95	0.959	0.981	0.986
The amount of CO_2 capture (ton/a)	–	–	903.38	1575.13	1987.26
Fresh CaO feed rate (ton/a)	–	–	36.5	64.7	89.4
Power density (W/cm^2)	0.3984	0.4213	0.4311	0.4503	0.4586
%Improvement in power density	–	5.75	8.21	13.03	15.11
Electricity produced in SOFC (kW)	416.79	449.30	444.04	444.11	440.12
Net electricity produced (kW)	416.79	416.79	416.79	416.79	416.79
Electricity consumed in compressor (kW)	–	32.46	27.25	27.32	23.33
SOFC active area (m^2)	104.62	106.66	103	98.62	95.97
%Improvement in SOFC area	–	−1.95	1.55	5.74	8.27
Palladium membrane area (m^2)	–	4.71	4.71	4.71	4.71
Capital cost of SOFC ($)	433,559.29	442,000.46	426,842.12	408,698.58	397,703.18
Capital cost of Pd membrane ($)	–	1,716.37	1,716.37	1,716.37	1,716.37
Capital cost of compressor ($)	–	21,712.84	19,112.23	19,698.13	17,959.49
Cost of fresh CaO sorbent in life time ($)	–	–	10,957.36	19,413.52	26,811.97
Saving cost on SOFC ($)	–	−8,441.17	6,717.18	24,860.72	35,856.11
Net cost saving ($)	–	−31,870.37	−25,068.78	−15,967.30	−10,631.73
%Total CO2 capture (%)	–	–	39.79	69.38	87.53
Cost of CO_2 capture ($/ton CO_2 capture)	–	–	137.27	49.35	23.79

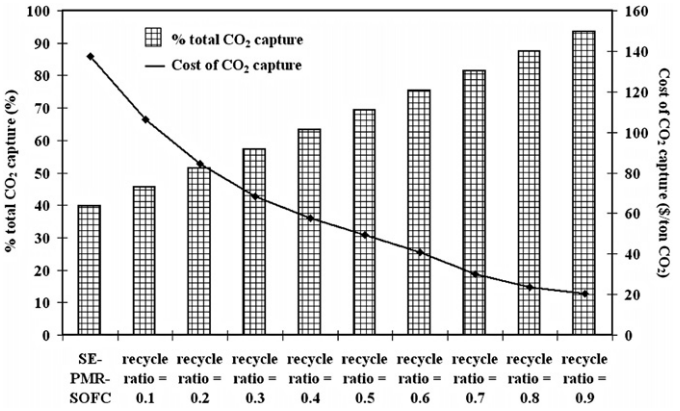

Fig. 14. %Total CO_2 capture and cost of CO_2 capture of SE–PMR–SOFC with equilibrium CO_2 capture and SER–PMR–SOFC operating at different recycle ratio.

and 15.11% for SE–PMR–SOFC and SER–PMR–SOFC with recycle ratio of 0.8, respectively. Also, the decreases in SOFC stack size of SE–PMR–SOFC and SER–PMR–SOFC with recycle ratio of 0.8 compared with CON–SOFC are about 1.55% and 8.27%, respectively. Even if SE–PMR–SOFC and SER–PMR–SOFC can offer higher performance compared with CON–SOFC, the operation of SOFC with these configurations is not economically feasible since the net cost savings are negative (−$25,068.78 for SE–PMR–SOFC and −$10,631.73 for SER–PMR–SOFC). However, these two configurations have the additional benefit of CO_2 capture. Their CO_2 capture costs are very low ($137.27 for SE–PMR–SOFC and $23.79 for SER–PMR–SOFC) especially for SER–PMR–SOFC configuration with high recycle ratio. It should be noted that the analyses in this study did not consider the effect of scale economy and therefore when considering this effect, the obtained results may deviate at different ranges of throughputs and thus power outputs.

4. Conclusions

The concept of the integration of an SOFC, a palladium membrane reactor (PMR), and a $CaO–CO_2$ acceptor is proposed in this study. With this concept, the $CaO–CO_2$ acceptor is employed to capture CO_2 in biogas prior to feeding to PMR where pure-H_2 is generated. Three configurations of SOFC system; i.e., PMR–SOFC, SE–PMR–SOFC, and SER–PMR–SOFC are considered. CON–SOFC is determined as a base case in the analysis. The concept of energetically self-sustaining operation ($Q_{NET} = 0$) is also employed to evaluate the real performance of SOFC systems. Technical analysis revealed that an operation at low value of retentate pressure (<30 bar) is sufficient to achieve high H_2 recovery (>0.95) as $CaO–CO_2$ acceptor is included in SOFC system. An increase in CO_2 removal rate of SE–PMR–SOFC can improve the power density of SOFC; however, the supply of fresh CaO sorbent is required. The recycle of retentate gas in case of SER–PMR–SOFC can improve CO_2 capture rate, H_2 recovery and also SOFC power density. Compared with CON–SOFC, the stack size of SE–PMR–SOFC and SER–PMR–SOFC with the recycle ratio of 0.8 is reduced by 1.55% and 8.27%, respectively. However, this benefit is not found in PMR–SOFC configuration. The economic study is performed to evaluate the potential benefit of each configuration of SOFC system. It is found that PMR–SOFC, SE–PMR–SOFC, and SER–PMR–SOFC are not attractive configurations due to their negative net cost saving relative to CON–SOFC. Nevertheless, SE–PMR–SOFC and SER–PMR–SOFC can offer high %total CO_2 capture and low cost of CO_2 capture. For SER–PMR–SOFC with the recycle ratio of 0.8, its cost of CO_2 capture is $23.79/ton CO_2 capture which is significantly lower than the estimate of $228/ton CO_2 capture reported in the literature which studied the cost of CO_2 removal from the flue gas of CON–SOFC system fed by methane.

Acknowledgements

This research is financially supported by the Thailand Research Fund and Commission on Higher Education.

References

[1] E. Achenbach, E. Riensche, J. Power Sources 52 (1994) 283.
[2] P. Aguiar, D. Chadwick, L. Kershenbaum, Chem. Eng. Sci. 57 (2002) 1665.
[3] S. Baron, N. Brandon, A. Atkinson, B. Steele, R. Rudkin, J. Power Sources 126 (2004) 58.
[4] J. Meusinger, E. Riensche, U. Stimming, J. Power Sources 71 (1998) 315.
[5] P. Piroonlerkgul, S. Assabumrungrat, N. Laosiripojana, A.A. Adesina, Chem. Eng. J. 140 (2008) 341.
[6] K. Eguchi, H. Kojo, T. Takeguchi, R. Kikuchi, K. Sasaki, Solid State Ionics 152–153 (2002) 411.
[7] R. Suwanwarangkul, E. Croiset, E. Entchev, S. Charojrochkul, M.D. Pritzker, M.W. Fowler, P.L. Douglas, S. Chewathanakup, H. Mahaudom, J. Power Sources 161 (2006) 308.
[8] G.Q. Lu, J.C. Diniz da Costa, M. Duke, S. Giessler, R. Socolow, R.H. Williams, T. Kreutz, J. Colloid Interface Sci. 314 (2007) 589.
[9] A. Basile, L. Paturzo, F. Gallucci, Catal. Today 82 (2003) 275.
[10] K.S. Patel, A.K. Sunol, Int. J. Hydrogen Energy 32 (2007) 2344.
[11] F. Gallucci, L. Paturzo, A. Basile, Int. J. Hydrogen Energy 29 (2004) 611.
[12] Y.M. Lin, S.L. Liu, C.H. Chuang, Y.T. Chu, Catal. Today 82 (2003) 127.
[13] W. Sangtongkitcharoen, S. Vivanpatarakij, N. Laosiripojana, A. Arpornwichanop, S. Assabumrungrat, Chem. Eng. J. 138 (2008) 436.
[14] S. Vivanpatarakij, N. Laosiripojana, A. Arpornwichanop, S. Assabumrungrat, Chem. Eng. J. 146 (2009) 112.
[15] P. Piroonlerkgul, W. Kiatkittipong, A. Arpornwichanop, A. Soottitantawat, W. Wiyratn, N. Laosiripojana, A.A. Adesina, S. Assabumrungrat, Int. J. Hydrogen Energy 34 (2009) 3894–3907.
[16] B. Balasubramanian, A. Lopez Ortiz, S. Kaytakoglu, D.P. Harrison, Chem. Eng. Sci. 54 (1999) 3543.
[17] D.K. Lee, I.H. Baek, W.L. Yoon, Int. J. Hydrogen Energy 31 (2006) 649.
[18] Z. Wang, J. Zhou, Q. Wang, J. Fan, K. Cen, Int. J. Hydrogen Energy 31 (2006) 945.
[19] J.C. Abanades, Chem. Eng. J. 90 (2002) 303.
[20] G.S. Grasa, J.C. Abanades, M. Alonso, B. Gonzalez, Chem. Eng. J. 137 (2008) 561.
[21] S. Vivanpatarakij, N. Laosiripojana, W. Kiatkittipong, A. Arpornwichanop, A. Soottitantawat, S. Assabumrungrat, Chem. Eng. J. 147 (2008) 336.
[22] J. Xu, G.F. Froment, AIChE J. 35 (1989) 88.
[23] S. Assabumrungrat, N. Laosiripojana, P. Piroonlerkgul, J. Power Sources 159 (2006) 1274.
[24] S.M. Walas, Chemical Process Equipment Selection and Design, Butterworth, Inc., USA, 1988.
[25] P. Piroonlerkgul, S. Assabumrungrat, N. Laosiripojana, A.A. Adesina, Chem. Eng. Process. 48 (2009) 672.
[26] M.A. Khaleel, Z. Lin, P. Singh, W. Surdoval, D. Collin, J. Power Sources 130 (2004) 136.
[27] R. Blom, I.M. Dahl, A. Slagtem, B. Sortland, A. Spjelkavik, E. Tangstad, Catal. Today 21 (1994) 535.
[28] M.C.J. Bradford, M.A. Vannice, Appl. Catal. A: Gen. 142 (1996) 97.
[29] H.M. Swaan, V.C.H. Kroll, G.A. Martin, C. Mirodatos, Catal. Today 21 (1994) 571.
[30] T. Kaneko, J. Brouwer, G.S. Samuelsen, J. Power Sources 160 (2006) 316.
[31] F. Zhao, A.V. Virkar, J. Power Sources 141 (2005) 79.
[32] L. Petruzzi, S. Cocchi, F. Fineschi, J. Power Sources 118 (2003) 96.
[33] J. Shu, B.P.A. Grandjean, S. Kaliaguine, Catal. Today 25 (1995) 327.
[34] F. Palazzi, N. Autissier, F.M.A. Marechal, D. Favrat, Appl. Therm. Eng. 27 (2007) 2703.
[35] M. Amelio, P. Morrone, F. Gallucci, A. Basile, Energy Convers. Manage. 48 (2007) 2680.
[36] B.T. Wong, K.Y. Show, D.J. Lee, J.Y. Lai, Bioresour. Technol. 100 (2009) 1734.
[37] M. Ni, M.K.H. Leung, D.Y.C. Leung, Energy Convers. Manage. 48 (2007) 1525.
[38] D. Alvarez, J.C. Abanades, Ind. Eng. Chem. Res. 44 (2005) 5608.

ภาคผนวก 16

INTERNATIONAL JOURNAL OF HYDROGEN ENERGY 35 (2010) 10257–10270

Available at www.sciencedirect.com

ScienceDirect

journal homepage: www.elsevier.com/locate/he

Effect of mode of operation on hydrogen production from glycerol at thermal neutral conditions: Thermodynamic analysis

Thirasak Pairojpiriyakul [a], *Worapon Kiatkittipong* [b], *Wisitsree Wiyaratn* [c], *Apinan Soottitantawat* [a], *Amornchai Arpornwichanop* [a], *Navadol Laosiripojana* [d], *Eric Croiset* [e], *Suttichai Assabumrungrat* [a,*]

[a] *Department of Chemical Engineering, Faculty of Engineering, Chulalongkorn University, Thailand*
[b] *Department of Chemical Engineering, Faculty of Engineering and Industrial Technology, Silpakorn University, Thailand*
[c] *Department of Production Technology Education, Faculty of Industrial Education and Technology, King Mongkut's University of Technology Thonburi, Thailand*
[d] *The Joint Graduate School of Energy and Environment, King Mongkut's University of Technology Thonburi, Thailand*
[e] *Department of Chemical Engineering, University of Waterloo, Canada*

ARTICLE INFO

Article history:
Received 4 May 2010
Received in revised form
11 July 2010
Accepted 23 July 2010
Available online 25 August 2010

Keywords:
Hydrogen production
Glycerol reforming
Thermodynamic analysis
Thermal neutral condition

ABSTRACT

Thermodynamic analysis of hydrogen production from glycerol under thermal neutral conditions is studied in this work. Heat requirement from the process can be achieved from the exothermic reaction of glycerol with oxygen in air fed to the system. Two modes of operation for air feeding are considered including (i) *Single-feed* mode in which air is fed in combination with water and glycerol to the reformer, and (ii) *Split-feed* mode in which air and part of glycerol is fed to a combustor in order to generate heat. The thermal neutral conditions are considered for two levels including *Reformer* and *System* levels. It was found that the H_2 yield from both modes is not significantly different at the *Reformer* level. In contrast, the difference becomes more pronounced at the *System* level. *Single-feed* and *Split-feed* modes offer high H_2 yield in low (600–900 K) and high (900–1200 K) temperature ranges, respectively. The maximum H_2 yields are 5.67 (water to glycerol ratio, $WGR = 12$, oxygen to glycerol ratio, $OGR = 0.37$, $T = 900$ K, *Split-feed* mode), and 3.28 ($WGR = 3$, $OGR = 1.40$, $T = 900$ K, *Single-feed* mode), for the *Reformer* and *System* levels, respectively. The difference between H_2 yields in both levels mainly arises from the huge heat demand for preheating feeds in the *System* level, and therefore, a higher amount of air is needed to achieve the thermal neutral condition. *Split-feed* mode is a favorable choice in term of H_2 purity because the gas product is not diluted with N_2 from the air. The use of pure O_2 and afterburner products (ABP) stream were also considered at the *System* level. The maximum H_2 yield becomes 3.75 ($WGR = 5.21$, $OGR = 1.28$, $T = 900$ K, *Split-feed* mode) at thermal neutral condition when utilizing heat from the ABP stream. Finally comparisons between the different modes and levels are addressed in terms of yield of by-products, and carbon formation.

* *Corresponding author*. Fax: +66 2 218 6877.
E-mail address: Suttichai.A@chula.ac.th (S. Assabumrungrat).
0360-3199/$ – see front matter © 2010 Professor T. Nejat Veziroglu. Published by Elsevier Ltd. All rights reserved.
doi:10.1016/j.ijhydene.2010.07.133

1. Introduction

Energy is absolutely essential for the prosperity of mankind. At present, the energy sources are mainly based on fossil fuels, such as petroleum, natural gas, and coal. Due to the limited availability and environmental problems with fossil fuels, in the near future, renewable and sustainable energy are poised to replace the present energy sources.

Biodiesel is a promising renewable fuel as it is produced from agricultural products. Biodiesel is nontoxic and environmentally friendly because of its low carbon monoxide, sulfur, particulate matter levels and absence of petroleum residuals. However, the use of biodiesel is currently rather limited due to high price barrier when compared with conventional diesel petroleum products. The cost of biodiesel can decrease drastically if its by-products can be utilized as feedstock to produce value-added products, such as hydrogen. One of the main by-products is glycerol ($C_3H_8O_3$), representing approximately 10% of biodiesel yields [1,2]. It could be used for the production of value-added chemical products such as propylene glycol ($C_3H_8O_2$) [2–5], glyceric acid ($C_3H_6O_4$) [2,6], lactic acid ($C_3H_6O_3$) [2,6,7], tartronic acid ($C_3H_4O_5$) [2,6], acrolein (C_3H_4O) [2,7], ethylene glycol ($C_2H_6O_2$) [2,5], glycolic acid ($C_2H_4O_3$) [6], oxalic acid ($C_2H_2O_4$) [2,7], and formaldehyde (CH_2O) [2]. Nevertheless, the economic analysis of the process needs to take into account the purification of glycerol from biodiesel production because the impurities in the mixture can easily deactivate catalysts or produce other undesired products.

Hydrogen production is another promising choice to manage the large excess of glycerol because the impurities content in glycerol always include methanol and water, both being reactants in the reforming process [8,9]. Hydrogen, the main fuel in most fuel cell applications, can always be produced via steam reforming reaction (SR) [10–14]. SR is, actually, the most commonly used process, providing high yields of H_2 production (theoretically 7 mol of H_2 per mole of glycerol reacted). However, it requires a large amount of external heat source, especially at high water to glycerol ratio (*WGR*). Currently, some alternative processes such as autothermal reforming (ATR) process are considered to decrease the demand for external heat source [15,16]. ATR combines steam reforming and partial oxidation reactions to operate at the thermal neutral point, that is with a net reactor heat duty of zero ($Q = 0$).

Most of the research works in hydrogen production from glycerol feedstock can be classified into two major areas which include catalysts development and thermodynamic analysis. A number of catalysts have been developed and tested to enhance the hydrogen production and also to suppress undesired by-products in the reforming process, for examples, Ni/Al_2O_3 [9,10,17,18], Ni/MgO [11,19,20] Ni/CeO_2 [10,20], Ni/TiO_2 [10,20], Pd/Ni/Cu/K [21,22], $Ni/CeO_2/Al_2O_3$ [18,20,23], $La_{1-x}Ce_xNiO_3$ [12], Ru/Y_2O_3 [11], Ir, Co/CeO_2 [10], Rh, Pt, Pd, Ir, Ru, Ce/Al_2O_3 [18] for steam reforming (SR), Raney-NiSn [24], Pt/Al_2O_3 [24–26], Ni/Al_2O_3 [26,27] for aqueous phase reforming (APR), $RhCeWc/Al_2O_3$ [16], Pd/Ni/Cu/K [21,22] for autothermal reforming (ATR), and Ru/Al_2O_3 [28] for supercritical water reforming (SWR).

All reported thermodynamic analysis has always focused on the effect of operating conditions, i.e. temperature, pressure, feed flow rate of water to glycerol ratio (*WGR*), and oxygen to glycerol ratio (*OGR*) to find suitable conditions for maximum H_2 production or to optimize energies in the reforming process without carbon formation. Equations of state such as SRK (Soave-Redlich-Kwong equation) [1,15,29] and PR (Peng-Robinson equation) [30] have been employed to estimate the amount of products. The thermodynamic analysis always considered only the primary products from the C, H, O system, including H_2, CO, CO_2 and CH_4 in gas phase and C in solid phase. Adhikari et al. [31] and Wang et al. [1] reported that the number of moles of H_2 increased with increasing temperature until 960 K and 925 K, respectively, with *WGR* of 9–12 for glycerol steam reforming. The lower temperatures result in a decrease in H_2 accompanied by an increase in CH_4 [8]. The number of moles of H_2 also increased with increasing *WGR* [1,15,19,31] but its effect seems to be small at *WGR* greater than 9 [32]. Rossi et al. [33] reported that insufficient *WGR* caused carbon formation because of CH_4 decomposition and that undesired products can also be produced by catalyst deactivation. The work of Rossi et al. [33] agrees with the results obtained by Adhikari et al. [31] at similar conditions. However, excess *WGR* must be of concern as it has a negative effect on the energy consumption [34]. Increasing pressure leads to a decrease in the moles of H_2 but increase the formation of CH_4 [1,31,33]. It is clear that CH_4 competes against H_2 in the steam reforming process. Moreover, CO and CO_2 are considered to be the main impurities to dilute H_2. Increasing the temperature increases CO via reforming and reverse water gas shift reactions but the maximum number of moles of CO_2 occurs at temperature around 850 K [31,32].

Luo et al. [35] investigated the effect of *OGR* in low temperature autothermal reforming and they reported a value of *OGR* that slightly decreases when increasing the temperature, e.g. *OGR* of 0.44 and 0.42 for temperature of 290 and 500 K, respectively. They concluded that methanation caused dramatic reduction in the H_2 mole fraction. Wang et al. [15] concluded that *OGR* around 0–0.4 must be fed with $WGR = 1–12$ in order to reach thermal neutral conditions, but the H_2 yield was decreased from 6.1 (steam reforming) to 5.62 at $WGR = 12$, $OGR = 0.36$, and $T = 900$ K. When air is co-fed to a reformer, H_2 production during the reforming process is reduced by the partial oxidation of glycerol. However, Swami and Abraham [21] reported that the moles of H_2 from ATR were always more than from SR when using of Pd/Ni/Cu/K catalyst.

Regarding the autothermal reforming process, all works have always focused only on the "*Reformer* level" [15,16,36] at which thermal neutral ($Q = 0$) occurs around the reformer, but the whole process still needs a significant amount of energy (heat sources), especially for preheating feeds. Wang et al. [15] reported that the maximum moles of H_2 in ATR of glycerol is always attained at $WGR = 12$ for *WGR* in the range of 1–12. It is clear that thermal neutral condition occurs around the reformer, but a large amount of energy is still required for generating steam to reach $WGR = 12$. So, it might be worth operating at a lower *WGR* from an overall energy saving point of view. However, there has been no work that considers the H_2 production at the thermal neutral condition for the "*System* level" where heat requirements in both feeds preheating and reforming are taken into account.

Therefore, the scope of this work focuses on glycerol reforming at both levels of consideration (i.e. *Reformer* and *System* levels) at thermal neutral conditions. H_2 concentration in the gas product is another important issue in H_2 production. SR and ATR processes offer different H_2 concentrations [15,21]. Therefore, the mode of supplying heat energy for the endothermic steam reforming becomes important. It is possible to supply oxygen or air directly into the steam reforming feed as ATR operation or to carry out combustion of fuel with oxygen or air in a separate chamber adjacent to the reformer to provide sufficient heat for operating the system at thermal neutral conditions. Hence, this work also investigates the effect of operation modes including i) *Single-feed* mode and ii) *Split-feed* mode for comparison between SR and ATR processes under thermal neutral conditions. The *Single-feed* mode represents an ATR, in which all reactants, consisting of glycerol, water, and air, are fed into the reactor while the *Split-feed* mode involves separated operation of a steam reformer fed by glycerol and water and a combustor fed by part of glycerol and air. It should be noted that both modes at thermal neutral conditions do not require any additional fuel other than glycerol. In order to compare performances between the two modes, the amounts of glycerol feed must be equal so that the comparison is on the same basis.

In this work, the effects of water to glycerol ratio (*WGR*), oxygen to glycerol ratio (*OGR*), and operating temperature (T) on the reaction performances are investigated over these two operation modes with two levels of consideration including *Reformer* and *System* levels. Suitable operating conditions for the H_2 production from glycerol of different modes and levels under thermal neutral conditions are determined and the obtained results on H_2 yield and concentrations of H_2 and by-products are compared.

2. Theory

The reactions taking place in H_2 production from glycerol can be summarized as follows:

Glycerol Steam Reforming (SR):

$$C_3H_8O_3 + 3H_2O \leftrightarrow 3CO_2 + 7H_2;\ \Delta H_{298\,K} = +127.67\ \mathrm{kJ\,mol^{-1}} \quad (1)$$

Partial Oxidations (POX):

$$C_3H_8O_3 + 0.5O_2 \leftrightarrow 2CO + CO_2 + 4H_2;\quad \Delta H_{298\,K} = -31.79\ \mathrm{kJ\,mol^{-1}} \quad (2)$$

$$C_3H_8O_3 + O_2 \leftrightarrow CO + 2CO_2 + 4H_2;\ \Delta H_{298\,K} = -314.76\ \mathrm{kJ\,mol^{-1}} \quad (3)$$

$$C_3H_8O_3 + 1.5O_2 \leftrightarrow 3CO_2 + 4H_2;\ \Delta H_{298\,K} = -579.73\ \mathrm{kJ\,mol^{-1}} \quad (4)$$

Oxidation or Combustion (OX):

$$C_3H_8O_3 + 3.5O_2 \leftrightarrow 3CO_2 + 4H_2O;\ \Delta H_{298\,K} = -1564.93\ \mathrm{kJ\,mol^{-1}} \quad (5)$$

Water Gas Shift (WGS):

$$CO + H_2O \leftrightarrow CO_2 + H_2;\quad \Delta H_{298\ K} = -41.17\ \mathrm{kJ\,mol^{-1}} \quad (6)$$

Thermodynamic analysis in this work was done following a non-stoichiometric approach. Possible species in the equilibrium products include glycerol ($C_3H_8O_3$), water (H_2O), hydrogen (H_2), carbon monoxide (CO), carbon dioxide (CO_2), methane (CH_4), carbon ($C_{(s)}$), oxygen (O_2) and nitrogen (N_2). Eq. (7) is provided for consideration of solid carbon-gas system [1,15].

$$\sum_{i=1}^{N-1} n_i \left(\Delta G^0_{f_i} + \mathrm{RT ln}\frac{\widehat{\phi}_i y_i P}{P^0} + \sum_j \lambda_j a_{ij} \right) + n_C G_{C_{(s)}}(T,P) = 0 \quad (7)$$

Aspen Plus program was employed for calculating equilibrium compositions and the corresponding overall heat of reactions while minimizing the Gibbs free energy. The Soave–Redlich–Kwong equation was selected as the method for estimating thermodynamic properties of the reaction systems [1,15,29].

Fig. 1 shows two levels of energy balance consideration including *Reformer* (dash line around reformer) and *System* levels (outside dash line) for *Single-feed* mode. At the *Reformer* level, the energy balance equation around the reformer unit can be expressed by Eq. (8) while Eq. (9) shows the energy balance equation at the *System* level. It should be noted that at the *System* level, apart from the energy involved in the reformer, the heat demands for feeds preheating are also taken into account, and therefore, in order to achieve a thermal neutral operation, it inevitably requires higher extent of exothermic reactions in order to supply enough energy to the system.

$$Q_{\textit{Reformer}\ \text{level (net)}} = \sum_{i=1}^{N} n_{i,\,\text{out}} H_{i,\,\text{out}} - \sum_{i=1}^{N} n_{i,\,\text{in}} H_{i,\,\text{in}} \quad (8)$$

$$\begin{aligned} Q_{\textit{System}\ \text{level (net)}} &= Q_{\text{heater (net)}} + Q_{\text{evaporator}} + Q_{\text{reformer}} \\ &= \sum_{i=1}^{N} n_{i,\,\text{out}} H_{i,\,\text{out}} - \sum_{i=1}^{N} n_{i,\,0} H_{i,\,0} \end{aligned} \quad (9)$$

Fig. 2 shows two levels of energy balance consideration including *Reformer* level (dash line around reformer) and *System* level (outside dash line) for the *Split-feed* mode of H_2 production from glycerol. Instead of co-feeding air with the reactants as in the *Single-feed* mode, air and part of the glycerol are fed to a combustor which generates heat for the units in the *Split-feed* mode. Glycerol is split into two fractions; first one (x) is for H_2 production inside reformer and the other one ($1 - x$) is for generating heat under combustion reaction in the combustor. At the *Reformer* level, the heat duty involves only that of the reformer; however, at the *System* level, it involves the duties of the reformer, heater, and evaporator units. Eqs. (10)–(12) and Eq. (13) show the energy balance equations for the *Reformer* and *System* levels, respectively. It should be noted that comparison between the two operation modes is based on the same amount of glycerol fed to the system.

$$\begin{aligned} Q_{\text{reformer}} &= \left(\sum_{i=1}^{N} n_{i,\,\text{out}} H_{i,\,\text{out}} - \sum_{i=1}^{N} n_{i,\,\text{in}} H_{i,\,\text{in}} \right)_{\text{reformer}} : n_{C_3H_8O_3,\,\text{in}} \\ &= x\,\text{mol} \end{aligned} \quad (10)$$

$$\begin{aligned} Q_{\text{combustor}} &= \left(\sum_{i=1}^{N} n_{i,\,\text{out}} H_{i,\,\text{out}} - \sum_{i=1}^{N} n_{i,\,\text{in}} H_{i,\,\text{in}} \right)_{\text{combustor}} : n_{C_3H_8O_3,\,\text{in}} \\ &= 1 - x\,\text{mol} \end{aligned} \quad (11)$$

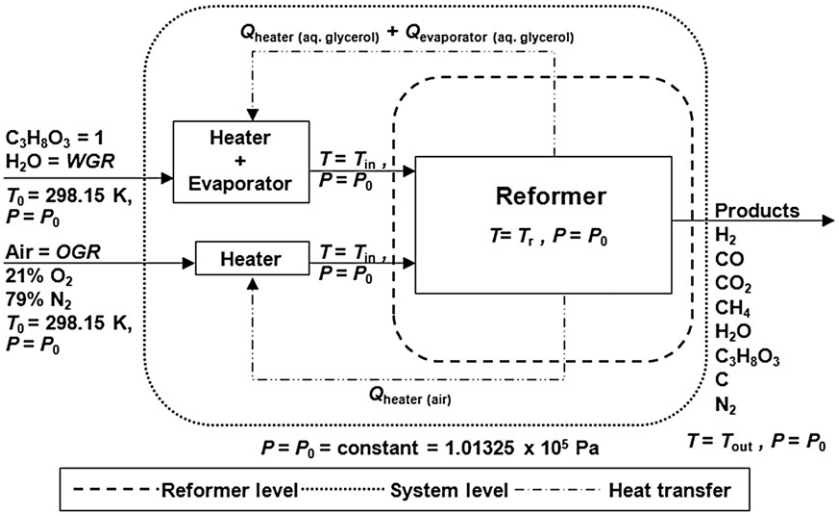

Fig. 1 – Schematic diagram of energy balances in *Single-feed* mode for *Reformer* and *System* levels (for isothermal condition in Reformer level, T_{in}, T_r, and T_{out} are equal).

$$Q_{Reformer\ level\ (net)} = Q_{reformer} + Q_{combustor} \tag{12}$$

$$Q_{System\ level\ (net)} = Q_{heater(net)} + Q_{evaporator} + Q_{reformer} + Q_{combustor} = \sum_{i=1}^{N} n_{i,\,out} H_{i,\,out} - \sum_{i=1}^{N} n_{i,\,0} H_{i,\,0} \tag{13}$$

The total net heat energy can be positive (endothermic), negative (exothermic) and zero (thermal neutral). $Q_{combustor\ (net)}$ is always negative because of the exothermic combustion reactions, while Q_{heater} and $Q_{evaporator}$ are always positive. The thermal neutral condition can be found by setting Eqs. (8)–(9) and Eqs. (12)–(13) equal to zero for the *Single-feed* and *Split-feed* modes, respectively.

The reaction performances are expressed in terms of yield of product *i* (Eq. (14)), and mole fraction of product *i* (dry basis) (Eq. (15)). In all simulations the glycerol feed rate and operating pressure are kept at 1 mol s^{-1} and 1.01325 × 10^5 Pa, respectively.

$$\text{Product } i \text{ yield } (-) = \frac{n_{i,\,out}}{n_{glycerol,\,0}} \tag{14}$$

$$\text{Product } i \text{ mol fraction (dry basis)} = \frac{n_{i,\,out}}{\sum_{i=1}^{N} n_{i,\,out} - n_{H_2O}} \tag{15}$$

3. Results and discussion

In this study, simulations were carried out at temperatures ranging from 600 to 1200 K. Based on the thermodynamic equilibrium, all of the glycerol was totally consumed in the reactions. This is also reported by other researchers [1,15,31].

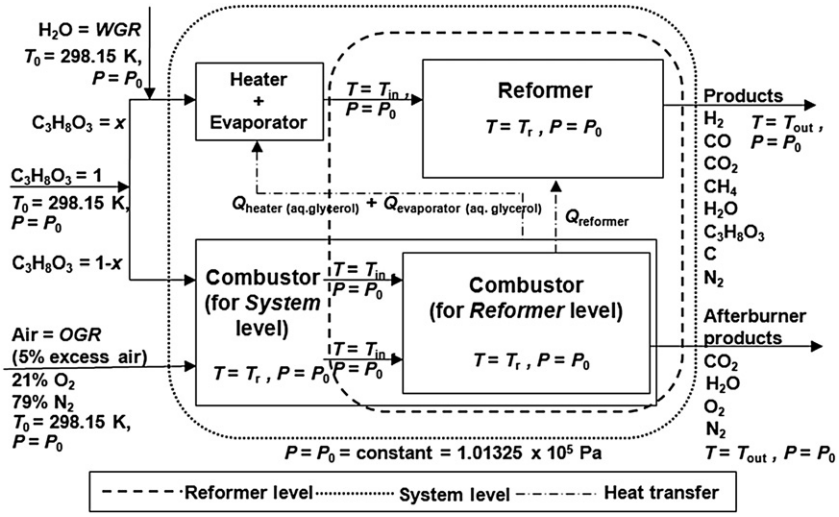

Fig. 2 – Schematic diagram of energy balances in *Split-feed* mode for *Reformer* and *System* levels (for isothermal condition in *Reformer* level, T_{in}, T_r, and T_{out} are equal).

3.1. *Effect of operating conditions on the energy requirement*

The effect of operating conditions, including temperature (*T*), water to glycerol ratios (*WGR*), and oxygen to glycerol ratios (*OGR*), on the net heat energy requirement (Q_{net}) was first investigated at constant atmospheric pressure (*P*) in order to determine ranges of variables that are possible for thermal neutral conditions. Energies from the two operation modes (*Single-feed* and *Split-feed*) at two levels (*Reformer* and *System*) were determined in order to determine the effect of all variables. Then, the operating conditions to achieve thermal neutral conditions were considered.

At the *Reformer* level, the net heat energy only involves heats of reactions. Steam reforming reaction (Eq. (1)) is an endothermic reaction but it can possibly be at thermal neutral conditions by adding oxygen to the reformer [13,16,36]. For the *Single-feed* mode, Fig. 3 shows that at *OGR* = 0–0.36 the reformer can be operated at thermal neutral conditions for *WGR* = 0–12 and *T* = 900 K. Increasing *WGR* increases the net heat energy until *WGR* greater than 8, then it becomes almost constant until *WGR* = 12. Dash-lines in Fig. 3 show the results of previous work [15] at similar conditions with *T* = 900 K, *WGR* = 1–12 and *OGR* = 0.2 and 0.4. Our simulation results are in good agreement with them, especially at high *WGR*s (*WGR* = 6, 9, 12). However, some discrepancies are observed at low *WGR*s. This is because their work used pure oxygen as an oxidant while air is considered in our study.

From Fig. 3, it is clear that at *T* = 900 K, *OGR* = 0.35 offers thermal neutral condition at *WGR* around 6. The operating temperature is another variable which influences the net energy. Fig. 4 indicates that the net heat energy surface is changed for *WGR* in the range of 0–12 and operating temperature in the range of 600–1200 K. From the results, increasing *WGR* affects only slightly the net energy. In contrast, operating temperature can significantly change the net heat energy from −300 at 600 K to 100 kJ/mol-glycerol at 1200 K. Increasing temperature between 600 and 900 K sharply increases the net heat energy but between 900 and 1200 K the change in net heat energy is not as significant. It should be noted that the energy neutral condition occurs only within a certain range of temperature: 900–960 for *WGR* between 0 and 12.

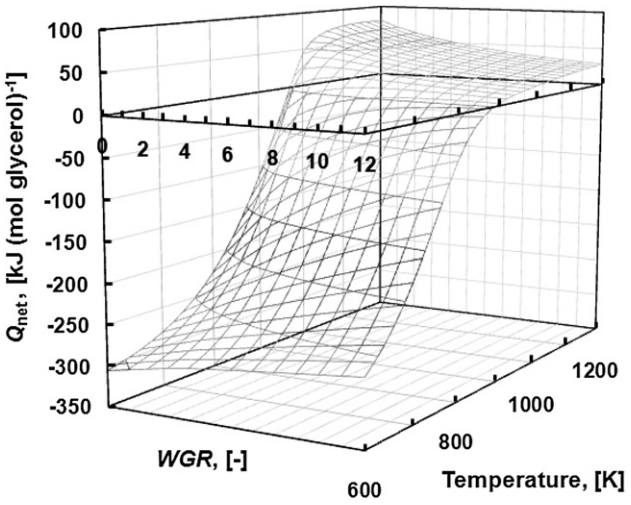

Fig. 4 – Net heat energies (Q_{net}) of *Reformer* level in *Single-feed* mode at different values of *WGR* and *T* (*OGR* = 0.35, *P* = 1.01325 × 10^5 Pa).

For the *Split-feed* mode, the net energy depends on the fractions of glycerol to be fed to the reformer and the combustor. Fig. 5 shows that increasing the fraction of glycerol to the reformer increases the net energy. It should be noted that the net energy for the combustor is always negative because of the oxidation reaction (Eq. (5)) which increases when increasing the number of moles of glycerol to the reformer. In order to provide sufficient heat to the reformer for *WGR* between 0 and 12, the fraction of glycerol to be fed to the combustor is between 0 and 0.11. Hence, more than 0.89 mol of glycerol is still always fed to the reformer. The reformer can be operated at thermal neutral conditions when *OGR* is between 0 and 0.37, which is close to that of the *Single-feed* mode. However one should expect, at least a slightly higher value of *OGR* in the *Split-feed* mode since the combustor

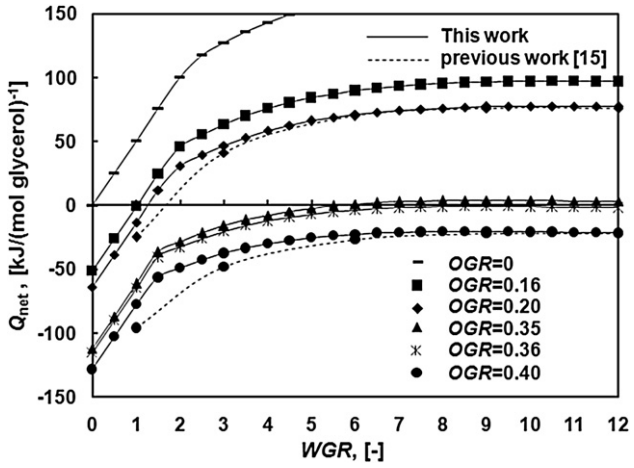

Fig. 3 – Net heat energies (Q_{net}) of *Reformer* level in *Single-feed* mode at different values of *WGR* and *OGR* (*P* = 1.01325 × 10^5 Pa, T_r = 900 K).

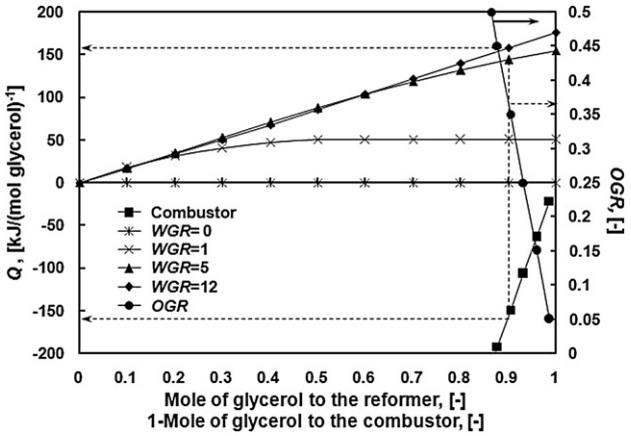

Fig. 5 – Heat energy (in the reformer and combustor) and *OGR* of *Reformer* level in *Split-feed* mode at different values of Mole of glycerol to the reformer and *WGR* (*P* = 1.01325 × 10^5 Pa, T_r = 900 K).

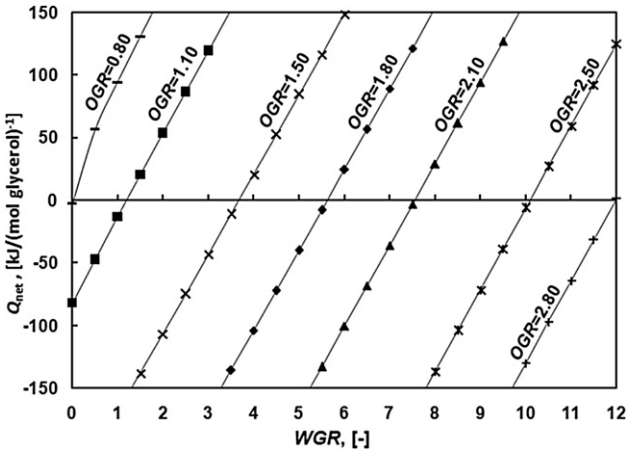

Fig. 6 – Net heat energies (Q_{net}) of *System* level in *Single-feed* mode at different values of *WGR* and *OGR* ($P = 1.01325 \times 10^5$ Pa, $T_r = 900$ K).

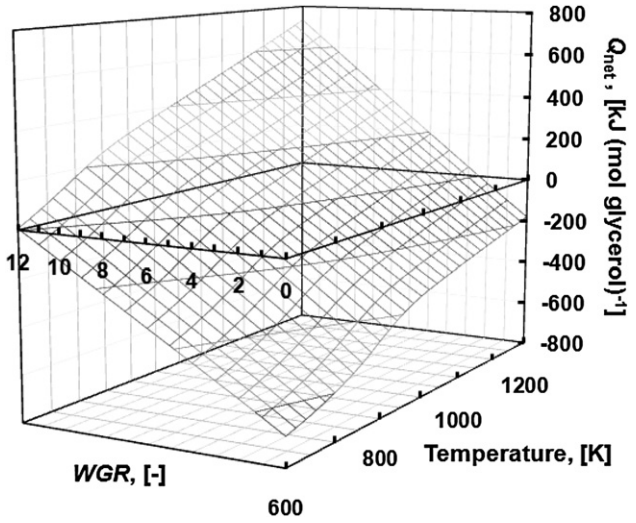

Fig. 7 – Net heat energies (Q_{net}) of *System* level in *Single-feed* mode at different values of *WGR* and *T* (*OGR* = 1.80, $P = 1.01325 \times 10^5$ Pa).

operates with 5% excess air. Furthermore, O_2 disappears in the product stream of the *Single-feed* mode but still appears in afterburner product stream in the *Split-feed* mode.

Considering the *System* level, the net energy includes preheating energy for heating up all feeds from room temperature (298.15 K) to the desired temperature, and heat of reactions in the reformer and combustor. For the *Single-feed* mode, Fig. 6 shows that increasing *WGR* increases the net heat energy for all *OGR*s. For providing thermal neutral conditions for *WGR* between 0 and 12, *OGR* has to be in the range of 0.80–2.80. The values of *OGR* at the *System* level are much higher than those at the *Reformer* level. This can be explained by the fact that the heat of reaction inside the reformer is only a small part of the net heat energy at the *System* level. Thus, much higher *OGR* is required to provide sufficient exothermic heat for the system. The high values of *OGR* can directly affect the H_2 production. However, *OGR* at the thermal neutral conditions at the *System* level is more sensitive to *WGR* than at the *Reformer* level; for examples, *OGR* = 1.8 with *WGR* = 5.60, *OGR* = 2.10 with *WGR* = 7.60, etc. The value of *WGR* was found to significantly influence the *OGR* requirement. Fig. 7 shows the net energy surface plot at different *WGR* and operating temperatures for *OGR* = 1.80. The operating temperature at the thermal neutral condition varies as *WGR* changes, for example, at *WGR* = 6, *T* = 860 K and at *WGR* = 7, *T* = 800 K. For *OGR* = 1.80 and *T* between 630 and 1120 K, the value of *WGR* to attain the thermal neutral condition will be between 3 and 11, depending on the value of temperature.

For the *Split-feed* mode at the *System* level, Fig. 8 shows that increasing *WGR* still increases the net heat energy but it is more pronounced than at the *Reformer* level. The fractions of glycerol to the reformer are 0.85–0.19 for *WGR* of 0–12. Increasing *WGR* rapidly decreases the fraction of glycerol to the reformer because the increase in energy demand requires glycerol fuel to be burnt in the combustor for decreasing the net heat energy from positive to zero via the combustion reaction (Eq. (5)). From the increase in the fraction of glycerol fed to the combustor, *OGR* has to increase from 0.51 to 3.00 to satisfy the combustion reaction with 5% excess air, when *WGR* increases from 0 to 12.

At the *System* level and for the *Single-feed* mode, the value of *WGR* strongly influences the value of *OGR* and the range of operating temperatures at thermal neutral conditions. However, operating temperature has the most influence at the *Reformer* level. It can be concluded that the net energy at the *System* level is considerably greater than that at the *Reformer* level due to the heat requirement for preheating the feeds. Apart from the selection of suitable conditions for operating the reformer or the system at thermal neutral conditions, the resulting products of H_2 and other gases as well as H_2 concentration are important information required to evaluate suitable operation modes for H_2 production from glycerol.

3.2. *Effect of operating conditions at the thermal neutral conditions*

Appropriate operating conditions should be selected to achieve the thermal neutral conditions and to enhance H_2

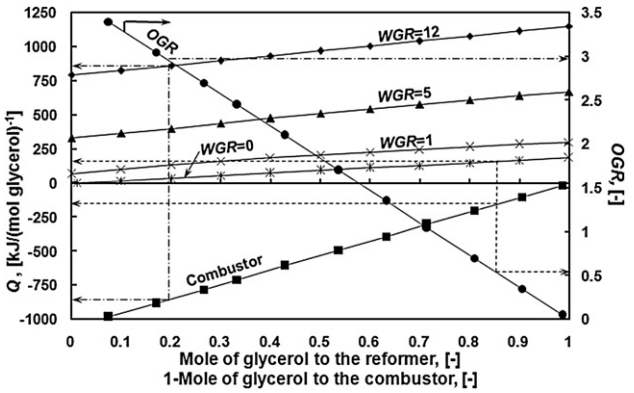

Fig. 8 – Heat energy (in the reformer and combustor) and *OGR* of *System* level in *Split-feed* mode at different values of Mole of glycerol to the reformer and *WGR* ($P = 1.01325 \times 10^5$ Pa, $T_r = 900$ K).

production as well as to suppress undesired by-products. In the H_2 production process, not only the steam reforming of glycerol (Eq. (1)) but also other reactions are involved in the reaction system, leading to formation of carbon and other by-products that might directly affect the stability of the system and the concentration of H_2 in the final product. All of them have been investigated from thermodynamic analysis and will be discussed in the following sections.

3.2.1. *Carbon formation*

The main reactions leading to carbon formation during reforming are the following reactions:

Boudouard reaction:

$$2CO \leftrightarrow CO_2 + C_{(S)}\ ; \quad \Delta H_{298K} = -172.43\ \text{kJ/mol} \tag{16}$$

Methane cracking:

$$CH_4 \leftrightarrow 2H_2 + C_{(S)}; \quad \Delta H_{298\ K} = +74.85\ \text{kJ/mol} \tag{17}$$

Reduction of CO:

$$CO + H_2 \leftrightarrow H_2O + C_{(S)}\ ; \quad \Delta H_{298\ K} = -131.26\ \text{kJ/mol} \tag{18}$$

Carbon formation is a major problem that causes blockage of the catalyst pores and that potentially can lead to break down of the reactor [8]. It can occur via several undesired reactions (Eqs. (16)–(18)) [15,31]. Wang et al. [15] reported that the Boudouard reaction (Eq.(16)) plays a significant role at temperatures below 915 K, whereas CH_4 cracking (Eq. (17)) becomes predominant at temperatures higher than 915 K. Fig. 9 shows the yield of solid carbon in two modes for WGR between 0 and 12 and T between 800 and 1200 K, at the *Reformer* level. It is shown that low WGRs tend to form solid carbon [36] but it does not appear at 800 K in both modes because a thermal neutral condition cannot occur at WGR lower than 4.5 (At 800 K, the thermal neutral condition for both modes start at WGR = 4.5). WGR of 4.5 is high enough to eliminate carbon in the reformer. However, the solid carbon appears in both modes at 900 K but the *Single-feed* mode shows less carbon than the *Split-feed* mode. This is because oxygen in the *Single-feed* mode facilitates operation above carbon boundary condition due to the presence of oxidation reactions (Eqs. (2)–(5)). No carbon formation is observed at T = 1000, 1100 and 1200 K. In the *Split-feed* mode, solid carbon is still formed even at temperatures higher than 900 K because water (Eq. (18)) is the only component that suppresses carbon formation unlike the case of *Single-feed* mode where oxygen is also present in the reformer. It can be concluded that carbon formation can be decreased by increasing WGR, OGR, and operating temperature in the *Single-feed* mode, but only WGR and operating temperature in the *Split-feed* mode. However, at WGR greater than 2, it is clear that no carbon is formed to the point of breaking down the reactor at the *Reformer* level. This is in agreement with Wang et al. [15] who reported that no carbon occurred at temperature above 1000 K, and WGR higher than 2.

At the *System* level, there is a huge energy requirement, requiring higher OGR for operating at the thermal neutral condition. Fig. 10 shows the carbon formation from both modes at the *System* level. Clearly, the results are very different than those obtained at the *Reformer* level. Within ranges of operating temperatures of 600–1200 K and WGR of 0–12, carbon formation is decreased when increasing the operating temperature and WGR. At 600 and 700 K, carbon formation is nearly equivalent between *Single-feed* and *Split-feed* modes. However, the difference between them starts at 800 K at which the *Split-feed* mode leads to higher carbon formation than the *Single-feed* mode. The *Single-feed* mode can operate without carbon formation at operating temperatures higher than 900 K, similar to the *Reformer* level. In contrast, the *Split-feed* mode still shows carbon formation above 900 K and it requires higher temperature (T = 1100–1200 K) to suppress carbon formation. From these results, it is clear that water (WGR) and oxygen to glycerol ratio (OGR) are the most important variables to manipulate in order to operate the

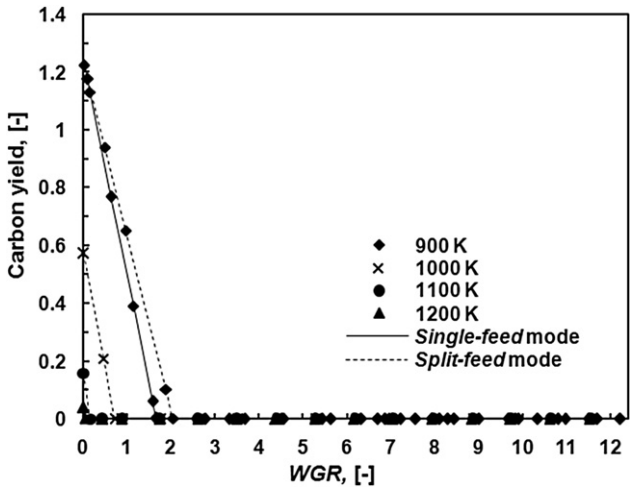

Fig. 9 – Carbon yield of *Reformer* level at different values of WGR and operating temperature (Q_{net} = 0, P = 1.01325 × 10^5 Pa).

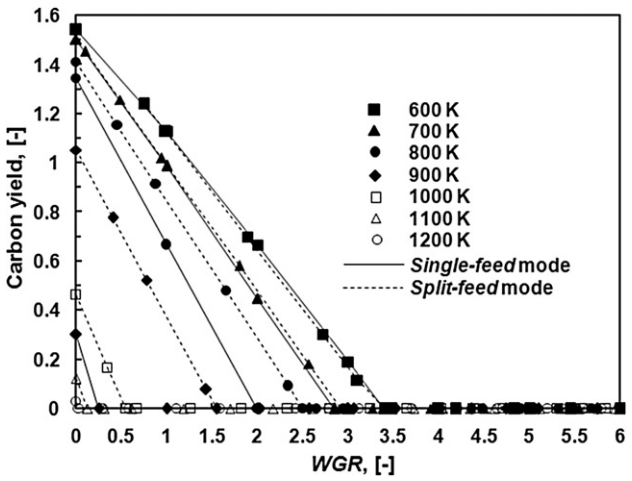

Fig. 10 – Carbon yield of *System* level at different values of WGR and operating temperature (Q_{net} = 0, P = 1.01325 × 10^5 Pa).

system without carbon formation. However, *OGR* does not directly affect the carbon formation in the *Split-feed* mode because oxygen is only used in the combustor. At thermal neutral conditions, *WGR* greater than 3.5 is sufficient to avoid carbon formation at the *System* level for *T* between 600 and 1200 K in both modes.

3.2.2. *Hydrogen production*

3.2.2.1. Hydrogen yield. Fig. 11(a) shows that the H_2 yield increases with increasing *WGR* at the *Reformer* level. The maximum H_2 yield is obtained at an operating temperature around 900 K. An optimum temperature is observed because the endothermic steam reforming is favorable at high temperature but the exothermic WGS reaction (Eq. (6)) is favorable at low temperature. Optimum temperatures were reported by other researchers to be at 925 K [1] and 960 K [31]. The *Split-feed* mode always offers a slightly higher H_2 yield than the *Single-feed* mode, except at low temperature (800 K) or small *WGR*s (0–7). This is because the small amount of oxygen fed to the reformer decreases the H_2 yield in the *Single-feed* mode. Fig. 11(b) shows the amount of *OGR* in both modes. Increasing *WGR* increases *OGR* at low temperatures (800, 900 K) but it slightly decreases *OGR* at high temperatures (1200 K). Although not shown in Fig. 11(b), the curves at 1000 K and above follow the same trend as that at 1200 K, that continuous decrease of *OGR* when increasing *WGR*. As seen in the previous section, to suppress carbon formation, increasing of *OGR* at small *WGR* for all temperatures, especially for the *Split-feed* mode, is required. However, the value of *OGR* does not strongly influence the H_2 production at the *Reformer* level because the amount of *OGR*s is quite small (0–0.51). It should be noted that the differences between *Single-feed* and *Split-feed* modes are not significant at the *Reformer* level – the maximum H_2 yields at *WGR* of 12, and operating temperature of 900 K are 5.67, and 5.64 for *Split-feed* and *Single-feed* modes, respectively. It agrees with the value of 5.62 at *WGR* of 12 determined by Wang et al. [15].

Considering the thermal neutral condition at the *System* level, as more heat requirement is involved, more glycerol is consumed to generate sufficient heat via partial oxidation or combustion for the system. Fig. 12(a) shows the H_2 yield at the *System* level for different operating temperatures, *WGR*s, and operation modes. It can be seen that the H_2 yield increases

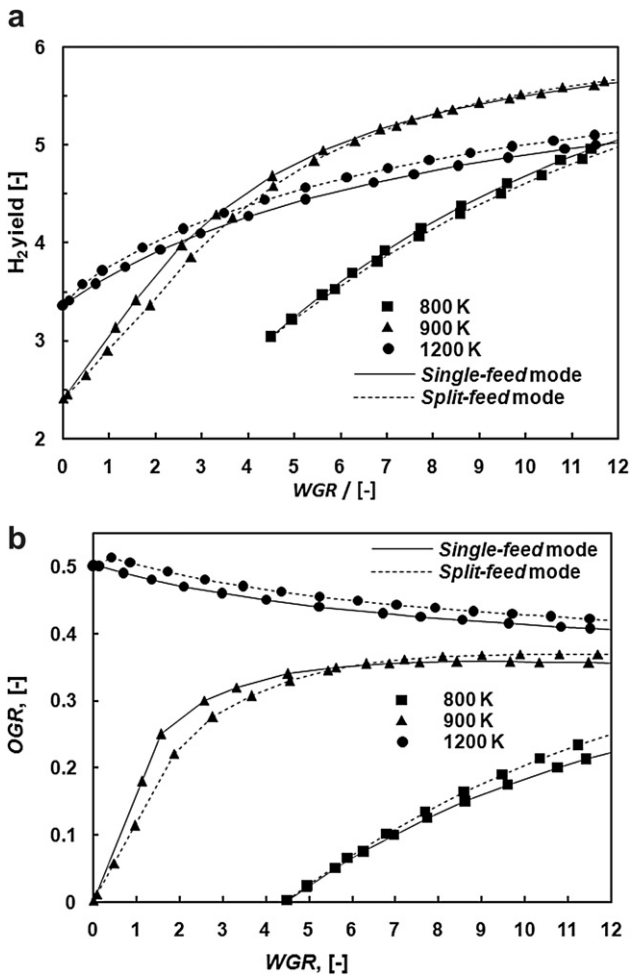

Fig. 11 – (a) H_2 yield and (b) *OGR* of *Reformer* level at different values of *WGR* and operating temperature (Q_{net} = 0, $P = 1.01325 \times 10^5$ Pa).

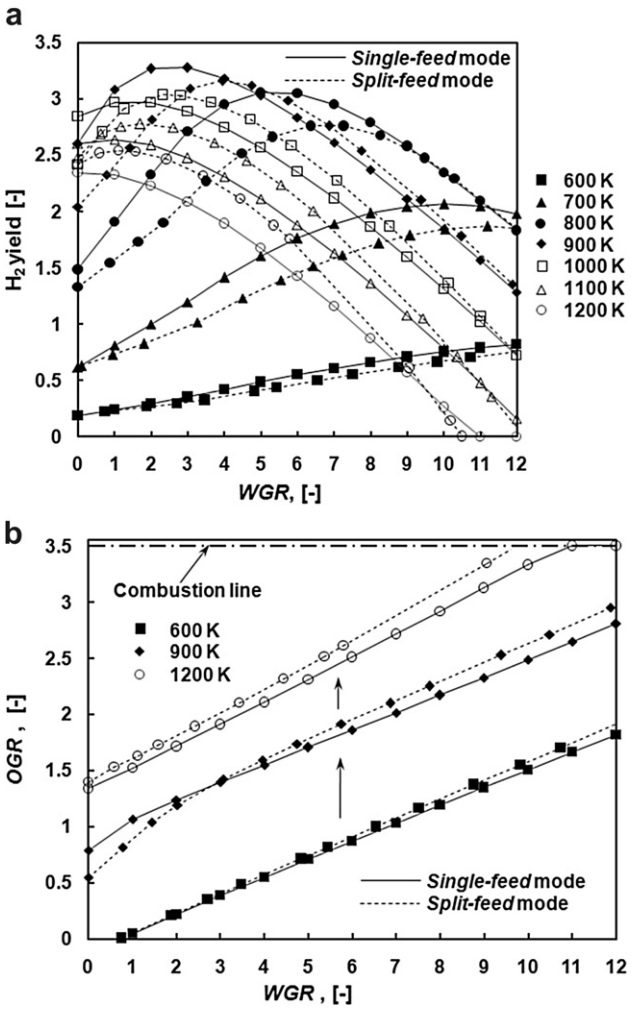

Fig. 12 – (a) H_2 yield, and (b) *OGR* of *System* level at different values of *WGR* and operating temperature (Q_{net} = 0, $P = 1.01325 \times 10^5$ Pa).

with increasing WGR at low operating temperatures (600 and 700 K). On the other hand, at higher operating temperatures (800, 900, 1000, 1100, and 1200 K), the H_2 yield increases only at low range of WGR; then it drops at high WGR. Moreover, increasing the temperature increases the H_2 yield until 900 K, above which it decreases because of the reverse water gas shift (Reverse WGS) effect (Eq. (6)), as discussed in the previous section on the *Reformer* level. At low temperatures (600, 700 K) within all ranges of WGR, it is observed that the *Single-feed* mode always offers higher H_2 yield than the *Split-feed* mode, likely due to the requirement of lower OGRs (Fig. 12(b)) which could promote H_2 production. However, at higher temperatures when WGR is high enough, it appears that the *Split-feed* mode becomes more favorable than the *Single-feed* mode. The values of WGR at this turning point vary with temperature; for examples, WGR = 9 at 800 K, WGR = 4 at 900 K, WGR = 2 at 1000 K, WGR = 0.5 at 1100 K, and WGR = 0 at 1200 K. These observations can be explained by the difference in characteristics among the two operation modes. For the *Single-feed* mode, all glycerol in the feed is fed to the reformer and therefore hydrogen atoms in glycerol reacting with oxygen could possibly be converted to additional H_2 unlike in the *Split-feed* mode where part of glycerol is totally combusted to CO_2 and H_2O which appear in the combustor effluent or afterburner products stream. Consequently, the *Single-feed* mode is likely to offer higher H_2 yield. However, at higher temperatures where the WGS reaction (Eq. (6)) becomes unfavorable, the presence of additional glycerol and oxygen for generating exothermic heat in the reformer in the *Single-feed* mode becomes less significant for improving H_2 production. The influence of WGS on H_2 production becomes important particularly at high temperature as evidenced by the lower value of transition WGR at higher temperature. Based on the simulation results, a maximum H_2 yield of 3.28 can be achieved at WGR = 3, OGR = 1.40, T = 900 K and *Single-feed* mode. At the same temperature, the *Split-feed* mode offers a slightly lower H_2 yield of 3.16 at a higher WGR of 3.96. It should be noted that the large amount of energy requirement at the *System* level decreases the H_2 yield from 5.67 at the *Reformer* level to 3.28 at the *System* level.

3.2.2.2. *Hydrogen mole fraction*. From the previous part concerning the H_2 yield at the *Reformer* level, it is shown that operation at T = 900 K and WGR = 12 offers the highest H_2 yield in both modes. Another important issue of concern is the H_2 concentration in the gas product. Fig. 13 shows the H_2 mole fraction (dry basis) at various operating temperatures for two values of WGR (WGR = 5 and 12). It is obvious that at the *Reformer* level, the *Split-feed* mode outperforms the *Single-feed* mode in term of H_2 concentration for both values of WGRs. In the *Split-feed* mode, air and part of glycerol are combusted in the combustor, and thus by-products including CO_2 and H_2O or N_2 (non-reacted substance) are not mixed with the H_2 product in the reformer unlike in the *Single-feed* mode. This is the main advantage of the *Split-feed* mode. WGR = 12 offers higher H_2 mole fraction (dry basis) than WGR = 5 in both modes due to the higher H_2 yield. Increasing the operating temperature (800–900 K) increases the H_2 mole fraction initially, and then decreases due to the effect of the reverse WGS (Eq. (6)), except at WGR = 12 in *Single-feed* mode. This is because the effect of N_2 dilution might hide the reverse WGS effect in the *Single-feed* mode. It can be concluded that the *Split-feed* mode is a preferable mode at the *Reformer* level as it offers higher H_2 mole fraction without lowering the H_2 yield compared to the *Single-feed* mode. The maximum H_2 mole fraction is 0.68 at WGR = 12 and T = 900 K for *Split-feed* mode, at the *Reformer* level.

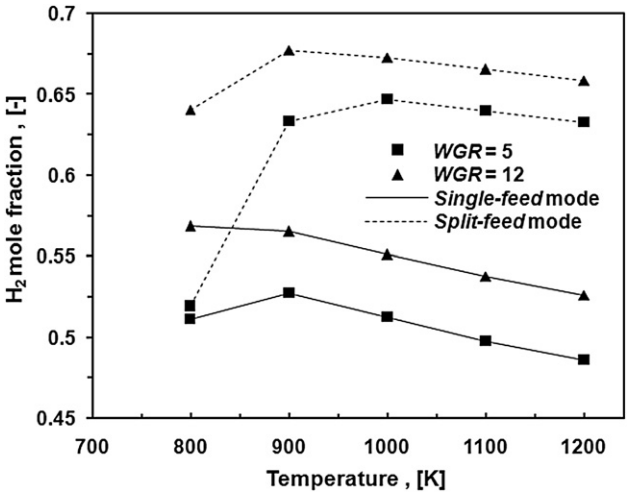

Fig. 13 – H_2 mole fraction (dry basis) of *Reformer* level at different values of WGR and operating temperature (Q_{net} = 0, P = 1.01325 × 10^5 Pa).

Considering the *System* level, WGR = 3 and 4 are the conditions that provide maximum H_2 yields in the *Single-feed* and *Split-feed* modes, respectively. Fig. 14 shows the H_2 mole fraction at both WGRs and at various operating temperatures (600–1200 K) for both modes. It is obvious that the *Split-feed* mode is still a superior choice than the *Single-feed* mode at both WGR = 3 and 4 because the exothermic reactions occur outside the reformer and the by-products from the reactions do not dilute H_2 in this mode. Increasing the temperature up to around 900 K increases the H_2 mole fraction, which then remains constant for temperatures between 900 and 1200 K, in

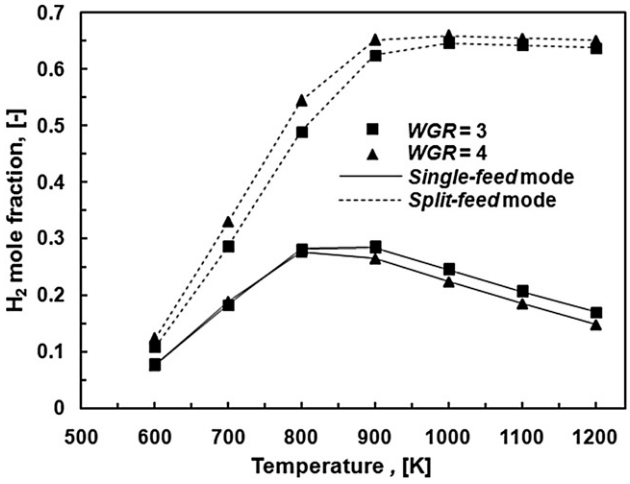

Fig. 14 – H_2 mole fraction (dry basis) of *System* level at different values of WGR and operating temperature (Q_{net} = 0, P = 1.01325 × 10^5 Pa).

the *Split-feed* mode. It is the opposite of the H_2 yield case. H_2 production is actually constant in the steam reforming process at high temperatures [36]. In the *Split-feed* mode, some of the glycerol must be separated and fed to the combustor which causes the H_2 yield to decrease, but it does not affect to the H_2 concentration. Similar to the trend of H_2 yield, $WGR = 4$ offers higher H_2 mole fraction than $WGR = 3$. In contrast, increasing the temperature up to 850 K increases the H_2 mole fraction; above 850 K, the H_2 mole fraction then decreases when increasing the temperature in the *Single-feed* mode. It is clear that the reverse WGS and nitrogen (N_2) from air influence H_2 dilution in the reformer. The maximum H_2 mole fraction is 0.66 at $WGR = 4$ and temperature of 900–1000 K for the *Split-feed* mode at the *System* level.

3.2.3. *By-products*.

From the previous part on H_2 mole fraction (dry basis), it is known that some by-products and unreacted reactants dilute H_2 concentration. Considering all the reactions in this system, the possible by-products include CO, CO_2, and CH_4, whereas the unreacted reactants are $C_3H_8O_3$, O_2. The thermodynamic analysis studies showed that, at all operating conditions chosen here, the glycerol conversion is 100% [1,15,31]. Therefore, the main obstruction to dilute H_2 must be N_2. Figs. 15 and 16 show the by-products and unreacted reactants at $T = 900$ K, $WGR = 0$–12, and both modes at the *Reformer* and *System* levels, respectively. It is observed that the trends of the by-products are quite similar at both levels, as will be discussed in the following.

The amount of nitrogen gas is the major problem in term of H_2 dilution. It is directly dependent on the value of *OGR* in the *Single-feed* mode. However, N_2 is not present in the reforming product in the *Split-feed* mode. Consequently, it does not affect the mole fraction of H_2. N_2 at the *Reformer* level is almost constant at *WGR* above 5 as *OGR* is almost constant in this range. In contrast, N_2 at the *System* level varies more significantly due to the strong dependency of *OGR* on *WGR*.

CO and CO_2 are the impurities that do not compete against H_2 production [31]. At the *Reformer* level, CO_2 increases when increasing *WGR* in both modes; however the *Split-feed* mode

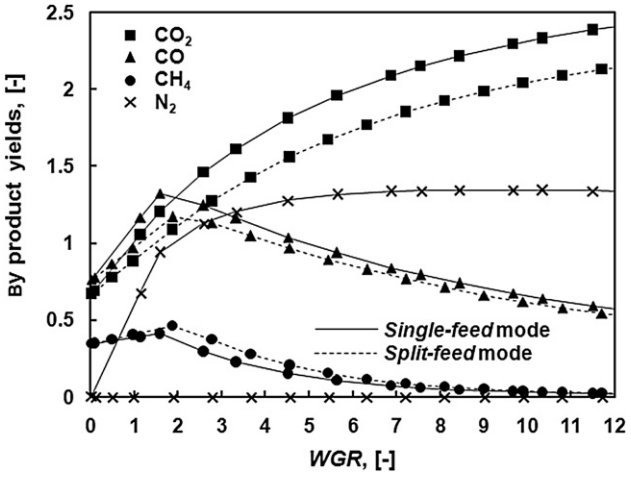

Fig. 15 – By-product yields including CO_2, CO, CH_4 and non-reacted substance N_2 of *Reformer* level as a function of *WGR* ($Q_{net} = 0$, $T_r = 900$ K, $P = 1.01325 \times 10^5$ Pa).

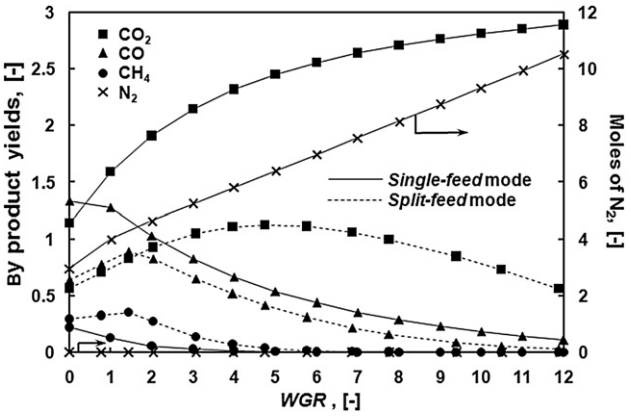

Fig. 16 – By-product yields including CO_2, CO, CH_4 and non-reacted substance N_2 of *System* level as a function of *WGR* ($Q_{net} = 0$, $T_r = 900$ K, $P = 1.01325 \times 10^5$ Pa).

offers lower CO_2 yield than the *Single-feed* mode where air is fed outside the reformer. Nevertheless, it is different at the *System* level because CO_2 is lower for *WGR* in the range of 6–12 in the case of *Split-feed* mode. This is because a larger amount of glycerol is diverted to the combustor to supply higher heat requirement. It is also the reason why CO_2 in the *Split-feed* mode is always less than in the *Single-feed* mode. Considering CO, the same tends are observed for both modes and levels. CO decreases when increasing *WGR* above 2 (Eq. (6)) [31]. The *Split-feed* mode still offers lower CO yield than the *Single-feed* mode, similar to CO_2. Even though the amount of CO is not large, it remains an issue if the product gas is to be used in low-temperature fuel cells (such as proton exchange membrane fuel cells (PEMFCs), CO being a poison for the platinum electrode of polymer electrolyte fuel cells (PEFCs)) [1,37]. Another undesired by-product is CH_4 [15,31]. CH_4 is almost suppressed when *WGR* is between 0 and 12 at 900 K in both modes and at both levels. The CH_4 yield decreases when increasing *WGR*. It is noted that the CH_4 yield initially increases at small values of *WGR* (0–2) due to the methanation reaction (Eq. (19)) but the reaction becomes unfavorable in the presence of high H_2O at higher *WGR*. Moreover, CH_4 is not favor in a system that involves oxygen in feed (*Single-feed* mode) because the products become CO or CO_2 rather than CH_4. The conditions that favor CH_4 formation are low ranges of temperature and low *WGR* [31]. It is the reason why CH_4 is always observed in higher amount in *Split-feed* mode than *Single-feed* mode at both levels. However, the CH_4 yield can be neglected in this range.

Methanation:

$$CO + 3H_2 \leftrightarrow CH_4 + H_2O\,; \quad \Delta H_{298\,K} = -206.11\ \text{kJ/mol} \tag{19}$$

It can be concluded that N_2 and CO_2 are the main impurities to dilute H_2 in the product. *Split-feed* mode is a promising operating mode to avoid this problem by feeding air as oxidizing agent outside the reformer and consequently higher mole fractions of H_2 are achieved in the gas product.

3.3. *Effect of oxidizing agent at thermal neutral conditions*

In the previous section, air was the oxidizing agent used in glycerol reforming at thermal neutral conditions; however, air contains significant amount of N_2. It is an interesting issue to determine whether using pure O_2 instead of air could improve H_2 production although it is well known that pure O_2 increases production costs. As it was concluded that the *Single-feed* and *Split-feed* modes at the *Reformer* level are not significantly different due to the low energy requirement, only the *System* level is investigated for determining the effect of the type of oxidizing agent. The calculations were based on the thermal neutral condition and at a temperature of 900 K which provides the highest H_2 yield. Fig. 17(a) compares the H_2 yield and the fraction of glycerol sent to the reformer for the cases using air and pure O_2 at different WGRs. Pure O_2 leads to higher H_2 yield than air for all values of WGR (0–12) in the *Split-feed* mode. This is because using pure O_2 reduces the demand of heat energy for heating N_2, and therefore, less glycerol is split to the combustor. The use of pure O_2 also increases the highest H_2 yield from 3.15 (air) to 3.45 (pure O_2) in the *Split-feed* mode at WGR of 4.00 (air) to 4.80 (pure O_2), respectively. However, for the *Single-feed* mode at low values of WGR (0–2), the H_2 yield in the air case is higher than that in the pure O_2 case. This can be explained from the fact that the difference of moles in the products and the reactants is positive for glycerol reforming and, therefore, the H_2 yield is favored at low operating pressures according to Le Chatelier's principle [31]. The presence of N_2 in air case provides similar effects as decreasing the pressure in the reformer. However, at higher WGRs (2–12) the use of pure O_2 offers higher H_2 yield. The H_2 yield can also be improved from 3.28 (air at WGR of 3) to 3.45 (pure O_2 at WGR of 4) in the *Single-feed* mode. Considering the maximum H_2 yield, both modes can provide a maximum yield of around 3.45 when using pure O_2 but at different WGRs. It is also observed that the fraction of glycerol to the reformer in the *Split-feed* mode strongly depends on the oxidizing agent. This is the reason that why pure O_2 also offers a higher H_2 yield than air.

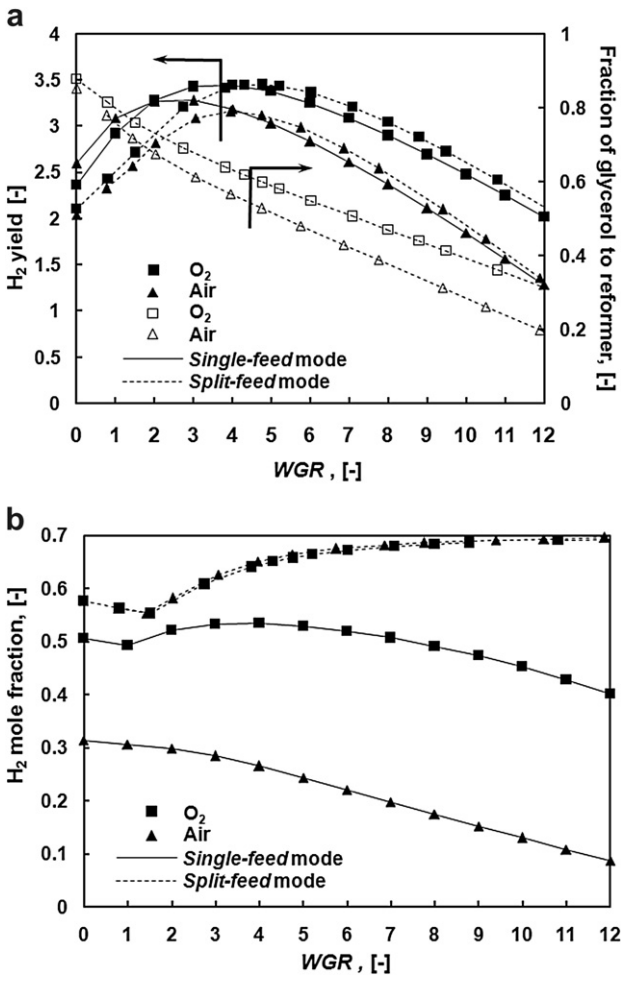

Fig. 17 – (a) H_2 yield and fraction of glycerol to reformer, (b) H_2 mole fraction (dry basis) of *System* level as a function of WGR for cases with different oxidizing agents (air or pure O_2) and operation modes (*Single-feed* or *Split-feed*) ($Q_{net} = 0$, $T_r = 900$ K, $P = 1.01325 \times 10^5$ Pa).

Fig. 17(b) shows the effect of oxidizing agent on the H_2 mole fraction when increasing WGR. The *Split-feed* mode shows much higher mole fractions of H_2 than that of the *Single-feed* mode in both air and pure O_2 cases. For the *Split-feed* mode, air and pure O_2 are not significantly different. Increasing WGR decreases the H_2 mole fraction for WGR in the range of 0–1.5, and then continuously increases to a H_2 mole fraction of 0.70. In contrast, pure O_2 in the *Single-feed* mode highly enhances the mole fraction of H_2 because the reformer does not have N_2 to dilute H_2. However, increasing WGR in the range of 1–4 increases the H_2 mole fraction similar to the *Split-feed* mode, and then at WGR = 4–12 decreases the mole fraction of H_2 similar to using air in *Single-feed* mode.

3.4. *Effect of using afterburner products as heat supply*

The afterburner products (ABP) stream in the *Split-feed* mode is at a high temperature (T_r), and thus is a potential heat source.

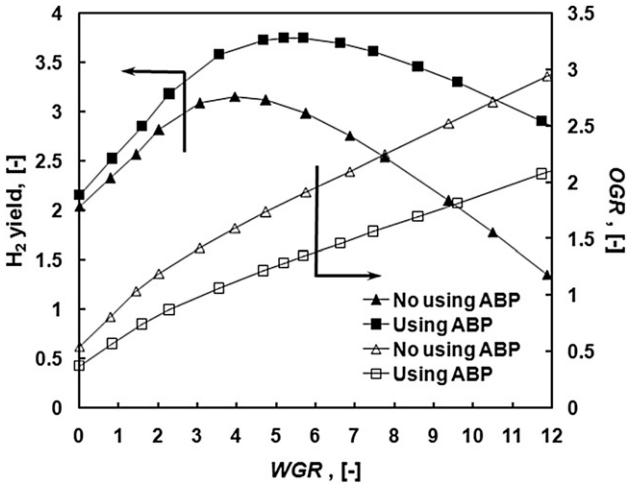

Fig. 18 – H_2 yield and OGR of *Split-feed* mode in *System* level as a function of WGR for cases with/without utilizing heat energy from Afterburner products (ABP) stream ($Q_{net} = 0$, $T_r = 900$ K, $P = 1.01325 \times 10^5$ Pa).

Table 1 – Summary of operating conditions at maximum H_2 yields, product yields and product distribution for different cases ($Q_{net} = 0$, $P = 1.01325 \times 10^5$ Pa).

Level	*Reformer*		*System*				
Mode	*Single-feed*	*Split-feed*	*Single-feed*	*Single-feed* + pure O_2	*Split-feed*	*Split-feed* + pure O_2	*Split-feed* + ABP
Conditions							
WGR, [–]	12	12	3	4	4.37	4.78	5.21
OGR, [–]	0.36	0.37	1.40	1.32	1.60	1.48	1.28
T, [K]	900	900	900	900	900	900	900
Yield, [–]							
H_2	5.64	5.67	3.28	3.45	3.16	3.45	3.75
CO	0.57	0.53	0.83	0.74	0.46	0.51	0.55
CO_2	2.41	2.14	2.15	2.22	1.12	1.23	1.34
CH_4	0.02	0.02	0.03	0.04	0.05	0.06	0.06
C	–	–	–	–	–	–	–
Mole fraction (dry basis), [–]							
H_2	0.57	0.68	0.28	0.54	0.66	0.66	0.66
CO	0.06	0.06	0.07	0.12	0.10	0.10	0.10
CO_2	0.24	0.26	0.19	0.34	0.23	0.23	0.23
CH_4	~0	~0	~0	0.01	0.01	0.01	0.01

It should be noted that for the *Split-feed* mode, as part of glycerol is split and combusted to supply heat for the reforming and evaporating processes outside the main reforming zone, the ABP from the combustion are unable to be further contributed on the hydrogen production, resulting in the decrease of H_2 yield from appearing of O_2. In addition, although it is possible to recycle part of the ABP to the reforming section, the presence of inert N_2 in the ABP stream would decrease the H_2 mole fraction in the final product. When the ABP recycle ratio increases close to 1, the performances of the *Split-feed* mode becomes similar to those of the *Single-feed* mode. Hence, only heat energy from ABP should be transferred to the heat demanding units including heater, evaporator, and reformer. With additional heat from ABP at the *System* level, Eq. (13) can be modified to Eq. (20) as shown below.

$$Q_{System\ level\ (net)} = Q_{heater(net)} + Q_{evaporator} + Q_{reformer} + Q_{combustor} + Q_{cooler\ (ABP)} = \sum_{i=1}^{N} n_{i,\,out} H_{i,\,out} - \sum_{i=1}^{N} n_{i,\,0} H_{i,\,0} \qquad (20)$$

It should be noted that the use of ABP stream for heat supply is not considered at the *Reformer* level.

As shown in Fig. 18, the H_2 yield increases from 3.16 ($WGR = 4.37$, $OGR = 1.60$, $T = 900$ K) to 3.75 ($WGR = 5.21$, $OGR = 1.28$, $T = 900$ K) when recovering heat from the ABP stream. In addition, the value of *OGR* also decreases because a lower amount of glycerol has to be split to the combustor. The operating conditions, product yields and product concentrations at maximum H_2 yields are summarized in Table 1 for different modes and at different levels. It is clear that the operating mode at the *Reformer* level does not significantly affect the H_2 yield, but the *Split-feed* mode enhances the H_2 mole fraction. At the *System* level, the H_2 yield in the *Single-feed* mode is higher than the *Split-feed* mode, but it leads to a lower H_2 mole fraction in the final products. However, the use of pure O_2 can increase the H_2 mole fraction in the *Single-feed* mode and the use of ABP in the *Split-feed* mode can further improve the H_2 yield while keeping a H_2 concentration. Moreover, no solid carbon is detected at the conditions which offer the highest H_2 yields.

4. Conclusion

A thermodynamic analysis was performed to investigate H_2 production from glycerol reforming at thermal neutral conditions. This work considers two modes of air feeding; i.e. *Single-feed* and *Split-feed* modes and at two levels, including *Reformer* and *System* levels. The H_2 yield from both modes is not significantly different at the *Reformer* level due to the small energy requirement from the heat of reactions. In contrast, it is observed at the *System* level that the *Single-feed* is favorable to H_2 generation at low temperatures (600–900 K), whereas in the *Split-feed* mode, more H_2 are generated at high temperatures (900–1200 K). The maximum H_2 yields are 5.67 ($WGR = 12$, $OGR = 0.37$, $T = 900$ K, *Split-feed* mode), and 3.28 ($WGR = 3$, $OGR = 1.40$, $T = 900$ K, *Single-feed* mode), at the *Reformer* and *System* levels, respectively. The *Single-feed* mode is a superior mode in term of suppressing carbon formation – no carbon formation is observed when operating at temperature above 900 K. However, carbon formation from both modes is totally inhibited at *WGR* higher than 2, and 3.5 at *Reformer* and *System* levels, respectively. Other by-products including CO, CO_2 and CH_4 were determined. The *Split-feed* mode offers higher H_2 concentration in the product gas because N_2 from air and part of CO_2 are not present in the gas product in the *Split-feed* mode unlike in the *Single-feed* mode. The use of pure O_2 instead of air is also considered in both modes at the *System* level. Use of pure O_2 in the *Single-feed* mode can increase the H_2 mole fraction in the product and H_2 yield from 0.28 to 0.54 and from 3.28 to 3.45, respectively. Moreover, the H_2 yield in the *Split-feed* mode is also enhanced when replacing air by pure O_2 (from 3.16 with air to 3.45 with pure O_2). However, using air or pure O_2 does not make a significant difference in term of H_2 mole fraction. Using pure O_2 is considered to be a good choice for H_2 production from glycerol at the thermal neutral conditions especially in the *Single-feed* mode. In addition, using the ABP stream to supply heat is beneficial to increase the H_2 yield in the *Split-feed* mode as it decreases the fuel requirement (glycerol and air). The maximum H_2 yield after recovering the ABP heat is 3.75

(*WGR* = 5.21, *OGR* = 1.28, *T* = 900 K, *Split-feed* mode) at thermal neutral condition.

Acknowledgements

This research is financially supported by the Thailand Research Fund and Commission on Higher Education.

Nomenclatures

a_{ij}	number of atoms of the *j*-th element present in each molecule of *i*-th species –
f_i^0	standard-state fugacity of the *i*-th species –
$\Delta G_{f_i}^0$	standard Gibbs function of formation of the *i*-th species, J mol^{-1}
$G_{C_{(s)}}$	molar Gibbs free energy of solid carbon, J mol^{-1}
H_i	enthalpy of the *i*-th species, J mol^{-1}
M	the total number of elements –
N	total species –
n_i	mole of the *i*-th species, mol
OGR	oxygen/glycerol ratio –
P	pressure, Pa
P^0	standard-state pressure, Pa
$Q_{combustor}$	heat energy of combustor, kJ mol^{-1}
$Q_{cooler\ (ABP)}$	heat energy of cooler from afterburner products stream, kJ mol^{-1}
$Q_{evaporator}$	heat energy of evaporator, kJ mol^{-1}
$Q_{heater\ (net)}$	net heat energy of heaters, kJ mol^{-1}
$Q_{R\ eformer\ level\ (net)}$	net heat energy of the *Reformer* level, kJ mol^{-1}
$Q_{reformer}$	heat energy of reformer, kJ mol^{-1}
$Q_{System\ level\ (net)}$	net heat energy of the *System* level, kJ mol^{-1}
R	ideal gas constant 8.314472, J mol^{-1} K^{-1}
T, T_r	operating temperature, K
WGR	water/glycerol ratio –
x	mole of glycerol for feeding to the reformer, mol
y_i	mole fraction of each substance in gas products –

Greek letters

λ_j	Lagrange multiplier –
$\widehat{\phi}_i$	fugacity coefficient of species *i* –

Subscripts

0	inlet stream to the *System* level
in	inlet stream to the reformer
out	outlet stream from the reformer

REFERENCES

[1] Wang X, Li S, Wang H, Liu B, Ma X. Thermodynamic analysis of glycerin steam reforming. Energy Fuels 2008;22(6): 4285–91.

[2] Rennard DC, Kruger JS, Schmidt LD. Autothermal catalytic partial oxidation of glycerol to syngas and to non-equilibrium products. Chem Sus Chem 2009;2(1):89–98.

[3] Dasari MA, Kiatsimkul P, Sutterlin WR, Suppes GJ. Low-pressure hydrogenolysis of glycerol to propylene glycol. Appl Catal A 2005;281(1–2):225–31.

[4] Deutsch J, Martin A, Lieske H. Investigations on heterogeneously catalysed condensations of glycerol to cyclic acetals. J Catal 2007;245(2):428–35.

[5] Maris EP, Davis RJ. Hydrogenolysis of glycerol over carbon-supported Ru and Pt catalysts. J Catal 2007;249(2): 328–37.

[6] Ketchie WC, Murayama M, Davis RJ. Selective oxidation of glycerol over carbon-supported AuPd catalysts. J Catal 2007; 250(2):264–73.

[7] Yang L, Joo JB, Kim YJ, Oh S, Kim ND, Yi J. Synthesis of superacidic mesoporous alumina and its application in the dehydration of glycerol. Kor J Chem Eng 2008;25(5): 1014–7.

[8] Slinn M, Kendall K, Mallon C, Andrews J. Steam reforming of biodiesel by-product to make renewable hydrogen. Bioresour Technol 2008;99(13):5851–8.

[9] Valliyappan T, Ferdous D, Bakhshi NN, Dalai AK. Production of hydrogen and syngas via steam gasification of glycerol in a fixed-bed reactor. Top Catal 2008;49(1–2):59–67.

[10] Zhang B, Tang X, Li Y, Xu Y, Shen W. Hydrogen production from steam reforming of ethanol and glycerol over ceria-supported metal catalysts. Int J Hydrogen Energy 2007;32(13):2367–73.

[11] Hirai T, Ikenaga N, Miyake T, Suzuki T. Production of hydrogen by steam reforming of glycerin on ruthenium catalyst. Energy Fuels 2005;19(4):1761–2.

[12] Cui Y, Galvita V, Rihko-Struckmann L, Lorenz H, Sundmacher K. Steam reforming of glycerol: the experimental activity of $La_{1-x}Ce_xNiO_3$ catalyst in comparison to the thermodynamic reaction equilibrium. Appl Catal B 2009;90(1–2):29–37.

[13] Adhikari S, Fernando SD, Haryanto A. Hydrogen production from glycerol: an update. Energy Convers Manage 2009;50 (10):2600–4.

[14] Fishtik I, Alexander A, Datta R, Geana D. A thermodynamic analysis of hydrogen production by steam reforming of ethanol via response reactions. Int J Hydrogen Energy 2000; 25(1):31–45.

[15] Wang H, Wang X, Li M, Li S, Wang S, Ma X. Thermodynamic analysis of hydrogen production from glycerol autothermal reforming. Int J Hydrogen Energy 2009;34(14):5683–90.

[16] Dauenhauer PJ, Salge JR, Schmidt LD. Renewable hydrogen by autothermal steam reforming of volatile carbohydrates. J Catal 2006;244(2):238–47.

[17] Czernik S, French R, Feik C, Chornet E. Hydrogen by catalytic steam reforming of liquid byproducts from biomass thermoconversion processes. Ind Eng Chem Res 2002;41(17): 4209–15.

[18] Adhikari S, Fernando S, Haryanto A. Production of hydrogen by steam reforming of glycerin over alumina-supported metal catalysts. Catal Today 2007;129(3–4):355–64.

[19] Adhikari S, Fernando S, Haryanto A. A comparative thermodynamic and experimental analysis on hydrogen production by steam reforming of glycerin. Energy Fuels 2007;21(4):2306–10.

[20] Adhikari S, Fernando SD, To SDF, Bricka RM, Steele PH, Haryanto A. Conversion of glycerol to hydrogen via a steam reforming process over nickel catalysts. Energy Fuels 2008;22 (2):1220–6.

[21] Swami SM, Abraham MA. Integrated catalytic process for conversion of biomass to hydrogen. Energy Fuels 2006;20(6): 2616–22.

[22] Sharma PO, Swami S, Goud S, Abraham MA. Catalyst development for stable hydrogen generation during steam reforming of renewable and nonrenewable resources. Environ Prog 2008;27(1):22–9.

[23] Profeti LPR, Ticianelli EA, Assaf EM. Production of hydrogen via steam reforming of biofuels on Ni/CeO_2–Al_2O_3 catalysts promoted by noble metals. Int J Hydrogen Energy 2009;34(12):5049–60.

[24] Shabaker JW, Huber GW, Dumesic JA. Aqueous-phase reforming of oxygenated hydrocarbons over Sn-modified Ni catalysts. J Catal 2004;222(1):180–91.
[25] Lehnert K, Claus P. Influence of Pt particle size and support type on the aqueous-phase reforming of glycerol. Catal Commun 2008;9(15):2543–6.
[26] Wen G, Xu Y, Ma H, Xu Z, Tian Z. Production of hydrogen by aqueous-phase reforming of glycerol. Int J Hydrogen Energy 2008;33(22):6657–66.
[27] Iriondo A, Barrio VL, Cambra JF, Arias PL, Guemez MB, Navarro RM, et al. Hydrogen production from glycerol over nickel catalysts supported on Al_2O_3 modified by Mg, Zr, Ce or La. Top Catal 2008;49(1–2):46–58.
[28] Byrd AJ, Pant KK, Gupta RB. Hydrogen production from glycerol by reforming in supercritical water over Ru/Al_2O_3 catalyst. Fuel 2008;87(13–14):2956–60.
[29] Li Y, Wang Y, Zhang X, Mi Z. Thermodynamic analysis of autothermal steam and CO_2 reforming of methane. Int J Hydrogen Energy 2008;33(10):2507–14.
[30] Tang H, Kitagawa K. Supercritical water gasification of biomass: thermodynamic analysis with direct Gibbs free energy minimization. Chem Eng J 2005;106(3):261–7.
[31] Adhikari S, Fernando S, Gwaltney SR, To SDF, Bricka RM, Steele PH, et al. A thermodynamic analysis of hydrogen production by steam reforming of glycerol. Int J Hydrogen Energy 2007;32(14):2875–80.
[32] Chen H, Zhang T, Dou B, Dupont V, Williams P, Ghadiri M, et al. Thermodynamic analyses of adsorption-enhanced steam reforming of glycerol for hydrogen production. Int J Hydrogen Energy 2009;34(17):7208–22.
[33] Rossi CCRS, Alonso CG, Antunes OAC, Guirardello R, Cardozo-Filho L. Thermodynamic analysis of steam reforming of ethanol and glycerine for hydrogen production. Int J Hydrogen Energy 2009;34(1):323–32.
[34] Dieuzeide ML, Amadeo N. Thermodynamic analysis of glycerol steam reforming. Chem Eng Technol 2010;33(1): 89–96.
[35] Luo N, Zhao X, Cao F, Xiao T, Fang D. Thermodynamic study on hydrogen generation from different glycerol reforming processes. Energy Fuels 2007;21(6):3505–12.
[36] Rabenstein G, Hacker V. Hydrogen for fuel cells from ethanol by steam-reforming, partial-oxidation and combined auto-thermal reforming: a thermodynamic analysis. J Power Sources 2008;185(2):1293–304.
[37] Hernandez L, Kafarov V. Thermodynamic evaluation of hydrogen production for fuel cells by using bio-ethanol steam reforming: effect of carrier gas addition. J Power Sources 2009;192(1):195–9.

ภาคผนวก 17

Solid State Ionics 181 (2010) 1568–1576

Contents lists available at ScienceDirect

Solid State Ionics

journal homepage: www.elsevier.com/locate/ssi

Analysis of planar solid oxide fuel cells based on proton-conducting electrolyte

Yaneeporn Patcharavorachot [a], N.P. Brandon [b], Woranee Paengjuntuek [c], Suttichai Assabumrungrat [a], Amornchai Arpornwichanop [a,*]

[a] Department of Chemical Engineering, Faculty of Engineering, Chulalongkorn University, Bangkok 10330, Thailand
[b] Department of Earth Science and Engineering, Imperial College London, London SW7 2AZ, United Kingdom
[c] Department of Chemical Engineering, Faculty of Engineering, Thammasat University, Patumthani 12120, Thailand

ARTICLE INFO

Article history:
Received 15 April 2009
Received in revised form 22 July 2010
Accepted 3 September 2010

Keywords:
Planar solid oxide fuel cell
Proton-conducting electrolyte
Electrochemical model
Fick's Model
Performance analysis

ABSTRACT

A solid oxide fuel cell based on a proton-conducting electrolyte (SOFC-H^+) is an attractive fuel cell technology because of its high theoretical efficiency. This study deals with the performance analysis of a planar SOFC-H^+ using a detailed electrochemical model, which takes into account all cell voltage losses, i.e., ohmic, activation, and concentration losses. The Fick's Model was used to explain gas diffusion in porous electrodes. The reliability of the developed SOFC-H^+ model was verified by comparison with experimental data reported in the literature. The effects of cell design (e.g., the use of anode, cathode, and electrolyte supports), geometry (e.g., thickness of cell components), and operating parameters (e.g., temperature, pressure, and gas composition) on the electrical characteristics of SOFC-H^+ were examined. The results indicate that an anode-supported SOFC-H^+ shows the best performance under the operating temperature of 1073 K and pressure of 1 atm. Ohmic loss is the major voltage loss in an anode-supported SOFC-H^+ due to the relatively low proton conductivity of the electrolyte. Furthermore, the performance of a SOFC-H^+ can be improved by decreasing the thickness of electrolyte and cathode, and the content of water in the oxidant, as well as by increasing the operating temperature and pressure.

1. Introduction

Fuel cells are regarded as a high-efficiency, low-environmental impact technology for electrical power generation. They can directly convert chemical energy into electricity through an electrochemical process. Among the different types of fuel cells, the solid oxide fuel cell (SOFC) has received much attention due to its high-temperature operation (1073–1273 K) which results in a high electrochemical reaction rate, the flexibility to use various fuel types (e.g., natural gas, propane, and bio-gas), and the possibility to develop heat and power cogeneration systems [1,2]. Another important feature of the SOFC is its all-solid-state construction using ceramics and metals; there is no liquid electrolyte with its attendant material corrosion and water management problems.

In general, there are two types of electrolyte (i.e., oxygen-ion and proton-conducting electrolytes) possible for use in a SOFC. To date, many studies have focused on SOFC technology using oxygen-ion conducting electrolytes (SOFC-O^{2-}) because of the chemical stability and low electrical resistance of oxygen-ion conductors, e.g., stabilized zirconia and doped ceria [1–10]. However, as solid oxides with proton conduction have been discovered and developed [11–17], a number of the studies related to the use of such proton-conducting SOFCs (SOFC-H^+) have been reported [11,18–25]. When a proton-conducting electrolyte is used, water vapor is produced at the cathode side. Higher hydrogen partial pressure at the anode side can enable a higher fuel utilization of hydrogen [21], offering increased system efficiency. More complete hydrogen utilization in a SOFC-H^+ further simplifies the overall system design by eliminating the need of the afterburner [22]. In addition, the SOFC-H^+ exhibits proton conductivity down to temperatures as low as 300 °C which offers the prospect of a wide range for applications, for example in transport [21,22].

In recent years, many researchers have studied the synthesis and characterization of proton-conducting materials for the SOFC-H^+ [11–21]. However, there are currently limited studies related to the modeling and analysis of SOFC-H^+ stacks and systems [22–25]. Further, most studies investigate the theoretical performance of the SOFC-H^+ without fully considering the irreversible losses found in actual fuel cell operations [22–24]. An electrochemical model is therefore required to predict the performance of SOFC-H^+ to enable the improved analysis and design of fuel cell systems based on this technology [3,6,7]. Recently, Ni et al. [25] analyzed the theoretical performance of CH_4-fed SOFC-H^+ by considering detailed voltage losses. However, in their work, the gas transport inside porous electrodes was developed based on the dusty gas model, which is more complicated and involves various physical and diffusion

* Corresponding author. Tel.: +66 2 2186878; fax: +66 2 2186877.
E-mail address: Amornchai.A@chula.ac.th (A. Arpornwichanop).

0167-2738/$ – see front matter © 2010 Elsevier B.V. All rights reserved.
doi:10.1016/j.ssi.2010.09.002

parameters. Apart from the dusty gas model, the Fick's Model in which the explicit analytical expression used to determine gaseous components at the electrode/electrolyte interface can be derived with acceptable accuracy, has been widely used to describe mass transport in porous SOFC electrodes [6,26]. This reduces the complexity of the model to describe mass transfer within the electrodes, leading to less computational time.

In this study, the performance of a planar SOFC-H^+ fueled on H_2 was investigated using a detailed electrochemical model of a cell model which takes into account the voltage losses, i.e., ohmic, activation and concentration losses. The Butler–Volmer Equation was employed to calculate the activation loss instead of using the Achenbach's Correlation [6]. Fickian diffusion through the porous electrodes was considered to determine the concentration losses. The ohmic loss was calculated from the electrolyte ionic conductivity. The results from the model were compared with experimental data in the literature. Using the developed model, the electrochemical performance of SOFC-H^+ was then analyzed with respect to different design, structural and operational parameters.

2. Theoretical model

A single planar SOFC-H^+ consists of an anode and cathode separated by an electrolyte, as shown in Fig. 1. The most common materials used for the electrodes and electrolyte of the SOFC-H^+ are Pt and $SrCe_{0.95}Yb_{0.05}O_{3-\alpha}$ (SCY), respectively. In general, porous platinum can be used for both the cathode and anode because of its high catalytic activity and stability in oxidative and reductive atmosphere. Furthermore, it is a pure electronic conductor [27,28]. As a result, the use of platinum-cermet as a support structure with a proton-conducting electrolyte has been reported in the literature [28,29], though the cost of this approach is likely to preclude commercial application. The SCY electrolyte is established as a proton-conducting material with relatively high proton conductivity [15] and has been used in several studies [13,16,18–20]. It is noted that, although $BaCeO_3$-based ceramics, e.g., $BaCe_{0.9}Y_{0.1}O_{3-\alpha}$ exhibit the highest ionic conductivity, the transport number of protons is lower than that of the $SrCeO_3$-based ceramics under the same operating conditions [16], which reduces the SOFC theoretical efficiency [30].

In H_2-fueled SOFC-H^+ operation, hydrogen molecules in the fuel are oxidized to form protons, releasing electrons at the anode side. The electrons flow in the external circuit from the anode to the cathode, while protons are transported through the electrolyte to the cathode/electrolyte interface where they react with oxygen at the cathode to produce water. The electrochemical reactions in the SOFC-H^+ are shown as [13,23]:

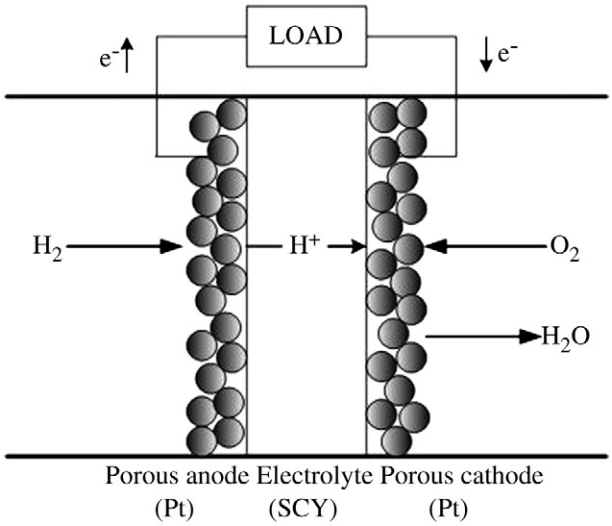

Fig. 1. The schematic of a solid oxide fuel cell based on a proton-conducting electrolyte.

$$\text{Anode}: H_2 \leftrightarrow 2H^+ + 2e^- \tag{1}$$

$$\text{Cathode}: 0.5O_2 + 2H^+ + 2e^- \leftrightarrow H_2O \tag{2}$$

$$\text{Overall}: H_2 + 0.5O_2 \leftrightarrow H_2O \tag{3}$$

The open-circuit voltage (E^{OCV}) generated by a fuel cell can be described by the Nernst equation as:

$$E^{OCV} = E^0 - \frac{RT}{2F}\ln\left(\frac{p_{H_2O(c)}}{p_{H_2(a)}p_{O_2(c)}^{0.5}}\right) \tag{4}$$

where "a" and "c" stand for anode and cathode, respectively, E^0 is the open-circuit voltage for a pure ionic conductor at standard pressure and can be determined as [7]:

$$E^0 = 1.253 - 2.4516 \times 10^{-4}T \tag{5}$$

Due to the internal cell resistances and overpotential losses, the operation voltage (V) is always less than the open-circuit voltage and can be expressed as:

$$V = E^{OCV} - iR_{ohm} - \eta_{act} - \eta_{conc} \tag{6}$$

where iR_{ohm} is the internal cell resistance referred to the ohmic loss and η_{act} and η_{conc} represent the activation and concentration overpotentials, respectively.

Activation overpotential is the loss caused by electrochemical reactions at the electrode surfaces. In this study, the Butler–Volmer Equation (Eq. (7)) was used to determine the activation overpotential:

$$i = i_{0,electrode}\left[\exp\left(\frac{\alpha nF}{RT}\eta_{act,electrode}\right) - \exp\left(-\frac{(1-\alpha)nF}{RT}\eta_{act,electrode}\right)\right] \tag{7}$$

where α is the transfer coefficient (=0.5), n is the number of electrons transferred in a rate-limiting reaction step, and $i_{0,electrode}$ is the electrode exchange current density.

Ohmic loss occurs due to the area specific resistance (R_{ohm}) to the flow of ions in the electrolyte, which depends on the thickness and ionic conductivity of electrolyte. By applying Ohm's law, the relation of the ohmic area specific resistance and electrolyte property can be expressed as:

$$R_{ohm} = \frac{\tau_{electrolyte}}{\sigma_{electrolyte}} \tag{8}$$

where τ and σ are the thickness and ionic conductivity of electrolyte, respectively. It is noted that as the electronic conductivity of the electrodes is high, the ohmic loss due to current collection at the electrodes was taken to be negligible.

Concentration overpotential is caused by a large reduction in the concentration of fuel and/or oxidant at the electrode/electrolyte interfaces. This loss is most pronounced when fuel or oxidant gases is fed to a fuel cell stack at lower partial pressure. η_{conc} is determined from the difference in the open-circuit voltage calculated based on the reactant and product concentrations at the electrode/electrolyte

interfaces (I) and that based on the bulk concentrations. According to its definition, the concentration overpotentials of the SOFC-H^+ can be derived as:

$$\eta_{\text{conc,anode}} = \frac{RT}{2F}\ln\left(\frac{p_{H_2(a)}}{p^{I}_{H_2(a)}}\right) \tag{9}$$

$$\eta_{\text{conc,cathode}} = \frac{RT}{2F}\ln\left(\left(\frac{p_{O_2(c)}}{p^{I}_{O_2(c)}}\right)^{0.5}\frac{p^{I}_{H_2O(c)}}{p_{H_2O(c)}}\right) \tag{10}$$

where $p^{I}_{H_2}$, $p^{I}_{O_2}$ and $p^{I}_{H_2O}$ represent the partial pressure of hydrogen at the anode/electrolyte interfaces and the partial pressures of oxygen and water vapor at the cathode/electrolyte interfaces, respectively.

To calculate the concentration overpotential, the partial pressures of H_2, H_2O and O_2 at the electrode/electrolyte interfaces need to be known. The partial pressures of H_2 at the anode/electrolyte interfaces (Eq. (11)) can be determined from self-diffusion mechanisms since H_2 is transported from the anode surface to the interface, and no product is generated in the anode side [3]. For the cathode side, the partial pressures of O_2 and H_2O at the cathode/electrolyte interfaces (Eqs. (12)–(13)) can be derived from the mass transport through the porous electrodes based on Fickian diffusion, assuming that the electrochemical reaction occurs at the electrode/electrolyte interface and that the diffusion rate of reactants to the interface is equal to the rate of electrochemical reaction [3,6,8,26,31].

$$p^{I}_{H_2} = P - \left(P - p_{H_2(a)}\right)\exp\left(\frac{iRT\tau_{\text{anode}}}{2FD_{a,\text{eff}}P}\right) \tag{11}$$

$$p^{I}_{O_2} = p_{O_2(c)} - \frac{iRT\tau_{\text{cathode}}}{2FD_{c,\text{eff}}} \tag{12}$$

$$p^{I}_{H_2O} = p_{H_2O(c)} + \frac{iRT\tau_{\text{cathode}}}{4FD_{c,\text{eff}}} \tag{13}$$

where τ_{anode} and τ_{cathode} are the thickness of anode and cathode, respectively. $D_{a,\text{eff}}$ and $D_{c,\text{eff}}$ represent the effective diffusion coefficients of the gas mixtures at the anode and cathode sides that can be explained by ordinary and Knudsen diffusions [3,31]. The calculation of the effective diffusion coefficients depend on the microstructure of the porous electrodes (porosity, pore size and tortuosity), the composition of the gas mixture, and the operating conditions (temperature and pressure), and is reported in Appendix A. It is noted that $D_{a,\text{eff}}$ is calculated from the effective diffusion coefficient of H_2 (Eq. (14)), whereas $D_{c,\text{eff}}$ is calculated from the effective ternary diffusion coefficient of O_2, N_2, and H_2O (Eq. (15)). Mass transfer on the cathode side is more complex as three components, i.e., O_2, H_2O and N_2 are considered within the porous cathode, and thus, the overall effective diffusion coefficient for the ternary component system is derived from the Stefan–Maxwell relation [26], as shown in Eqs. (16)–(17). Table 1 presents the value of $D_{a,\text{eff}}$ and $D_{c,\text{eff}}$ at initial condition ($T=1073$ K, $P=1$ atm, $\varepsilon=0.4$, $r=0.5$ μm and $\tau=5$).

$$\frac{1}{D_{a,\text{eff}}} = \frac{1}{D_{H_2-H_2O,\text{eff}}} + \frac{1}{D_{H_2k,\text{eff}}} \tag{14}$$

$$D_{c,\text{eff}} = \left(\frac{p_{H_2O}}{P}\right)D_{O_2,\text{eff}} + \left(\frac{p_{O_2}}{P}\right)D_{H_2O,\text{eff}} \tag{15}$$

where

$$\frac{1}{D_{O_2,\text{eff}}} = \frac{1}{D_{O_2k,\text{eff}}} + \frac{1}{D_{O_2-N_2,\text{eff}}} + \left(\frac{1}{D_{O_2-H_2O,\text{eff}}} - \frac{1}{D_{O_2-N_2,\text{eff}}}\right)(1-y_{N_2}) \tag{16}$$

Table 1
Values of input parameters used in the present study.

Parameter	Value
Operating temperature, T (K)	1073
Operating pressure, P (atm)	1.0
Molar flow rate of fuel, F_{fuel} (mol s^{-1})	2.27×10^{-5}
Molar flow rate of air, F_{air} (mol s^{-1})	2.27×10^{-5}
Cell length, L (m)	0.04
Cell width, W (m)	0.01
Electrode porosity, ε	0.4
Electrode pore radius, r (μm)	0.5
Electrode tortuosity, ξ	5.0
Electrolyte conductivity, $\sigma_{\text{electrolyte}}$ (Ω^{-1} m^{-1}) [20]	$225.92\exp(-6.3\times10^3/T)$
Effective diffusion coefficient at the anode side, $D_{a,\text{eff}}$ (m^2 s^{-1})	8.98×10^{-5}
Effective diffusion coefficient at the cathode side, $D_{c,\text{eff}}$ (m^2 s^{-1})	6.31×10^{-6}
Electrolyte-supported: ES-SOFC-H^+	
Thickness of anode, τ_{anode} (μm)	50
Thickness of electrolyte, $\tau_{\text{electrolyte}}$ (μm)	500
Thickness of cathode, τ_{cathode} (μm)	50
Anode-supported: AS-SOFC-H^+	
Thickness of anode, τ_{anode} (μm)	500
Thickness of electrolyte, $\tau_{\text{electrolyte}}$ (μm)	50
Thickness of cathode, τ_{cathode} (μm)	50
Cathode-supported: CS-SOFC-H^+	
Thickness of anode, τ_{anode} (μm)	50
Thickness of electrolyte, $\tau_{\text{electrolyte}}$ (μm)	50
Thickness of cathode, τ_{cathode} (μm)	500

$$\frac{1}{D_{H_2O,\text{eff}}} = \frac{1}{D_{H_2Ok,\text{eff}}} + \frac{1}{D_{H_2O-N_2,\text{eff}}} + \left(\frac{1}{D_{O_2-H_2O,\text{eff}}} - \frac{1}{D_{H_2O-N_2,\text{eff}}}\right)(1-y_{N_2}) \tag{17}$$

and where, in turn, $D_{O2,\text{eff}}$ and $D_{H2O,\text{eff}}$ are the effective binary diffusion coefficients of O_2 and H_2O in nitrogen, respectively, and y_{N2} represents the mole fraction of nitrogen present in the gaseous mixtures.

2.1. Model validation

The electrochemical model was numerically solved in Matlab to predict the characteristic performance of SOFC-H^+. The developed model was validated with the experimental data of Iwahara [18]. In this experiment, the materials used for anode, electrolyte and cathode were Pt|SCY|Pt, with a thickness of 50 μm, 500 μm, and 50 μm, respectively. The inlet fuel and oxidant consisted of 10% H_2 (~3% H_2O) and dry air (<0.1% H_2O), respectively. In the simulation, the exchange current densities of electrodes (i_0) were estimated and the proton conductivity of the electrolyte was obtained from Potter and Baker [20] (Table 1). Fig. 2 shows a model prediction of the I–V characteristics of the SOFC-H^+ cell operated at three temperatures (1073 K, 1173 K, and 1273 K) and a pressure of 1 atm in comparison with experimental data. It was found that the proposed model based on the exchange current densities of 800 A m^{-2} gave a good prediction of the experimental data.

3. Results and discussion

In this section, a performance analysis of the planar SOFC-H^+ with respect to key operating parameters under isothermal conditions is presented. Since planar SOFCs can generally be designed with different configurations, i.e., both electrolyte and electrode-supported structures, the impact of the design parameters is taken into account to find an optimal structure of the SOFC-H^+. Table 1 shows the standard values of the operating conditions and cell geometry and material properties of the SOFC-H^+ used in the present study. Humidified hydrogen (~3% H_2O) and dry air (<0.1% H_2O) are used

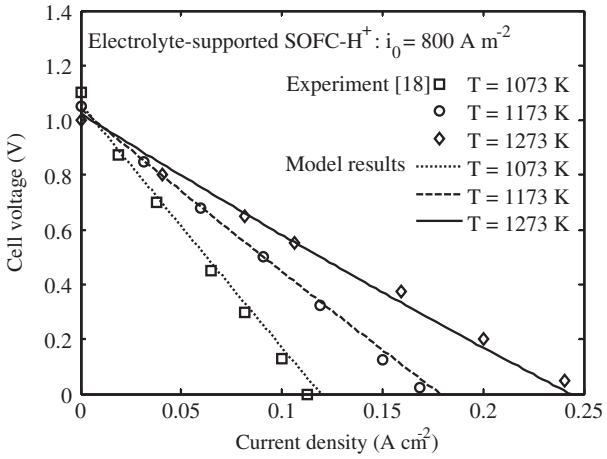

Fig. 2. Comparison between theoretical modeling results and experimental data by Iwahara [18].

as fuel and oxidant for fuel cell. The proton conductivity of the electrolyte was estimated from Potter and Baker [20]. To date, several methods have been proposed for manufacturing dense electrolyte with thin films on porous substrates. These include the preparation of proton-conducting electrolyte thin films using spin coating [32,33], pulsed laser deposition [34,35] and co-pressing and sintering processes [36,37]. Although differences in electrode porosity may occur during SOFC-H^+ fabrication, it was assumed in this study that the porosity of electrodes remain independent of processing route.

3.1. Role of support structures

The electrical characteristics of an anode-supported SOFC-H^+ are shown in Fig. 3. The cell voltage decreases with increasing current density due to the irreversible voltage losses. As seen in Fig. 3a, the power density reaches its maximum value of 0.26 W cm^{-2} at a current density of 0.48 A cm^{-2}. When the fuel cell is operated at a current density of 1.00 A cm^{-2}, the voltage and power density drop to zero and the fuel cell efficiency at this condition is 51%. From the simulation results, the ohmic loss represents the major loss in the fuel cell, followed by the cathode and anode activation overpotentials (Fig. 3b) and thus the development of electrolytes with higher ionic conductivity would improve performance. It is noted that at the current density of 1.00 A cm^{-2} the cell performance is not controlled by the concentration loss as a rapid voltage drop is not observed. The results show that although the anode-supported SOFC is considered, the concentration overpotential at the anode is negligible because H_2 can be transported quickly through the anode. Unlike the cathode side, higher molecular weights of O_2 and H_2O result in lower effective diffusion coefficients that result in higher concentration overpotentials at the cathode side.

Fig. 4a presents the performance of a SOFC-H^+ cell with different support structures (i.e., anode, cathode and electrolyte supports). It clearly indicates that the electrode-supported SOFC-H^+ provides as higher performance compared with the electrolyte-supported SOFC-H^+, not surprising given the impact of electrolyte resistance on cell behavior. Individual ohmic and concentration overpotentials of the SOFC-H^+ are given in Fig. 4b and c, respectively. A plot of the activation overpotential is not given as it is assumed to be independent of electrode thickness. As shown in Fig. 4b, ohmic loss dominates the electrolyte-supported SOFC-H^+ performance due to its higher electrolyte thickness, coupled with the relatively low ionic conductivity of the proton-conducting electrolyte. To reduce ohmic loss in the electrolyte-supported SOFC-H^+, higher operating temperatures and/or alternative electrolyte materials are required. Fig. 4c shows the difference of cathode concentration overpotential in the anode- and cathode-supported SOFC-H^+. Since

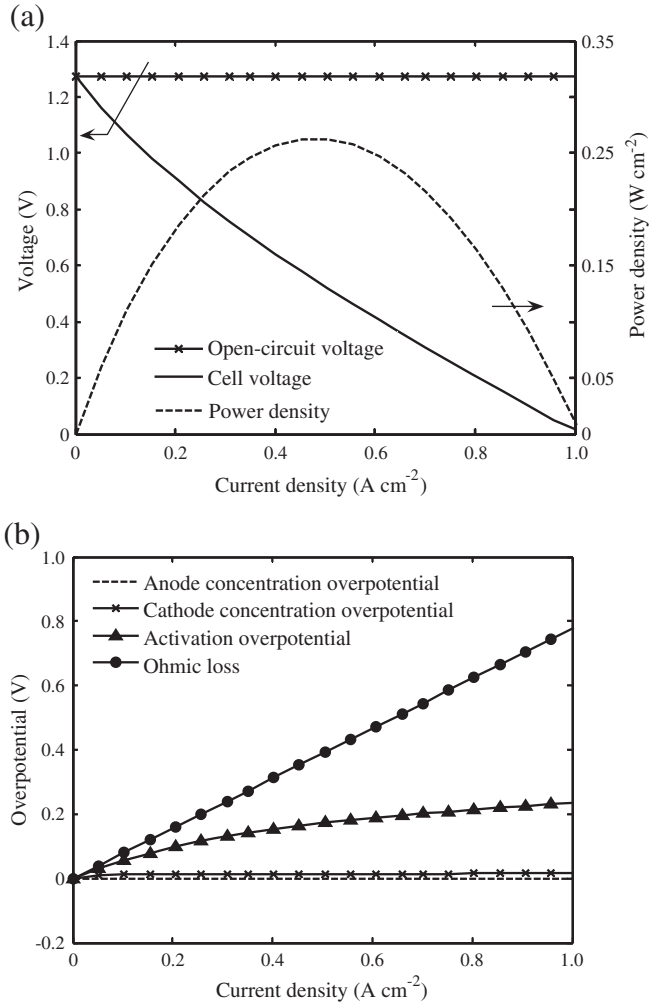

Fig. 3. The electrical characteristics of an anode-supported SOFC-H^+ cell at different current densities under isothermal conditions ($T = 1073$ K) and constant gas composition across the cell: (a) open-circuit voltage, cell voltage and power density and (b) overpotentials within the cell.

the transport of H_2 as a single component in the porous anode is quick, the anode concentration overpotential in both the anode- and cathode-supported SOFC-H^+ is relatively small. From Fig. 4c, it can be seen that the cathode concentration overpotential in the cathode-supported SOFC-H^+ is higher than that in the anode-supported SOFC-H^+. The use of a thicker cathode can hinder the transport of O_2 and H_2O, resulting in higher concentration overpotentials at the cathode side. Due to the difference in concentration overpotentials, the anode-supported SOFC-H^+ shows better performance than the cathode-supported SOFC-H^+; the anode-supported SOFC-H^+ can be operated at higher current densities and power densities. Therefore, the anode-supported SOFC-H^+ was selected as the basis to investigate the effects of structural and operational parameters on SOFC-H^+ performance in the next section.

3.2. Effect of electrolyte thickness

In order to further explore the performance of anode-supported SOFC-H^+s, the effect of operating current densities on cell power density at different electrolyte thicknesses was analyzed, as shown in Fig. 5a. Considering the present technology of fabricating a thinner electrolyte in a SOFC, it shows that in order to avoid an increase risk of breakage causing a gas leak, the minimum of the electrolyte thickness is about 10 μm [15,32–37]. Therefore, the effect of the electrolyte

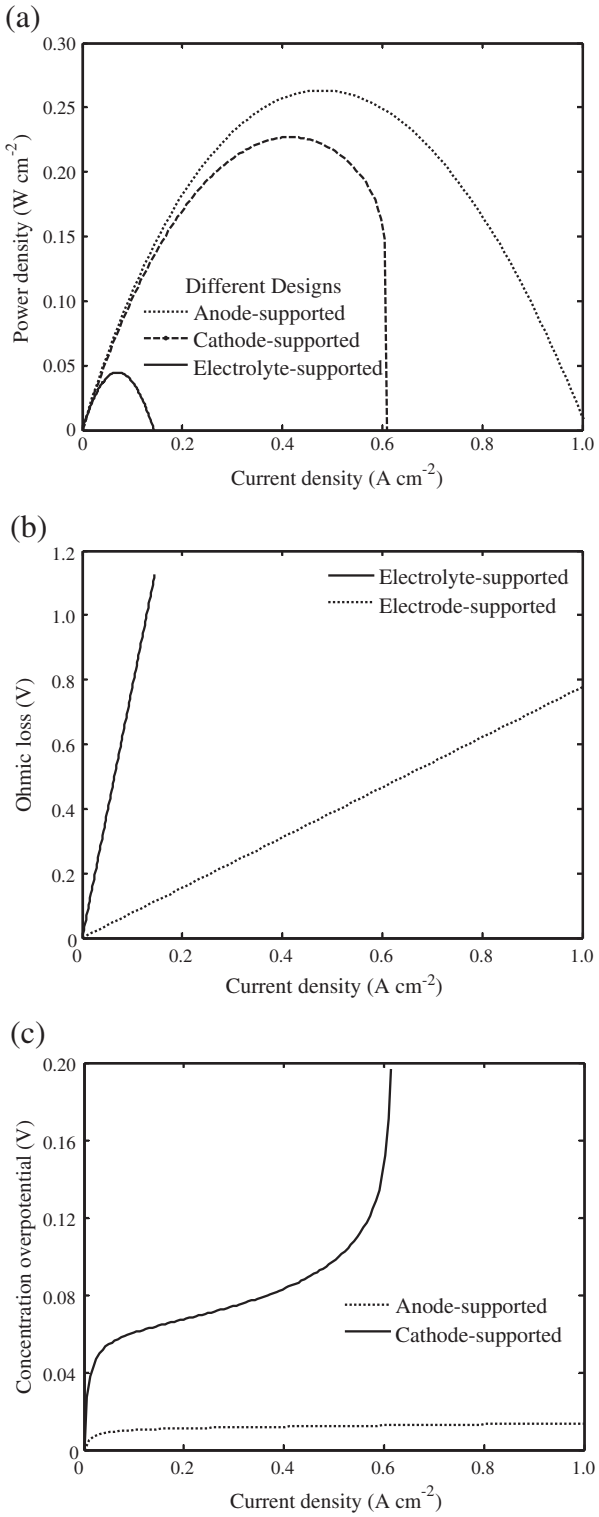

Fig. 4. Comparison of SOFC-H^+ with different support structures: (a) power density, (b) ohmic loss and (c) concentration overpotential.

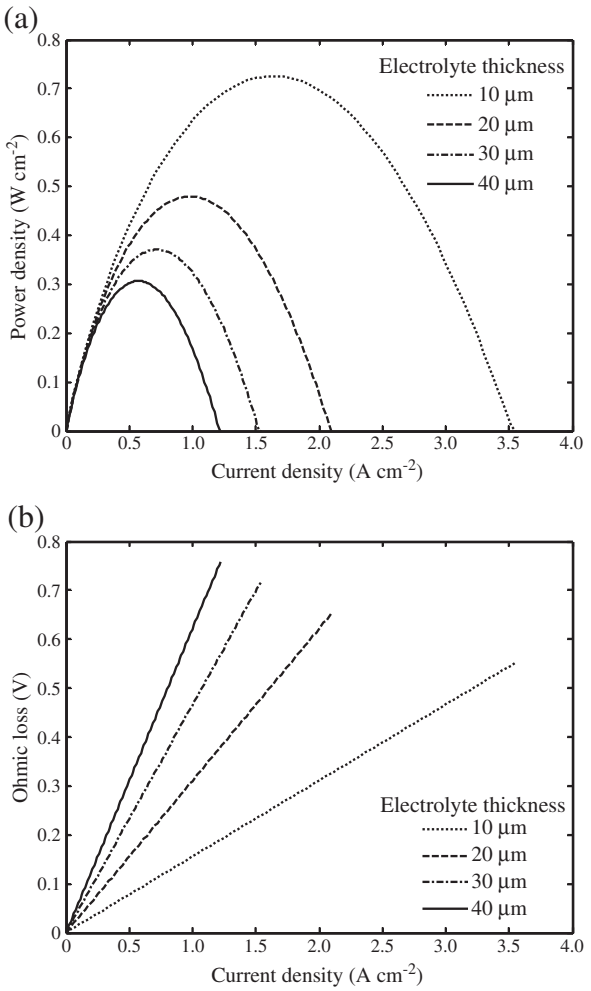

Fig. 5. Effect of electrolyte thickness at different current densities on (a) power density, and (b) ohmic loss.

thickness varying in the range 10–40 μm on the SOFC-H^+ performance was studied. It is noted that the anode and cathode thickness was fixed at 500 and 50 μm, respectively. At each value of electrolyte thickness, there is an optimum current density to achieve the maximum power density. As expected, the cell performance increases dramatically when the electrolyte thickness decreases, because of the decreases in electrolyte ohmic loss, as shown in Fig. 5b.

3.3. Effect of cathode thickness

Fig. 6a presents the characteristic curve of the anode-supported SOFC-H^+ at different cathode thicknesses (25, 50, 100 and 150 μm), with the electrolyte and anode thickness fixed at 10 and 500 μm, respectively. The simulation results show that the cell performance slightly decreased when the cathode thickness increased. As expected, the increased cathode thickness hinders the transport of O_2 from the surface to the cathode/electrolyte interface, and the transport of H_2O from the porous cathode to the air channel. These results lead to an increase in the concentration overpotential, as demonstrated in Fig. 6b. Considering the durability of an anode-supported SOFC-H^+, it has been reported that it should be fabricated with a cathode thickness of at least 50 μm [3,4,7,18,25]. It is noted that the anode, electrolyte and cathode thickness of 500, 10 and 50 μm are set as the standard cell geometry for a performance analysis of the SOFC-H^+ in subsequent sections.

3.4. Effect of operating temperature

Fig. 7a shows the cell power density as a function of operating current densities for the anode-supported SOFC-H^+ at different operating temperatures (873, 1073 and 1273 K). The individual overpotentials are shown in Fig. 7b–d. As shown in Fig. 7a, the cell performance increases significantly with increasing operating

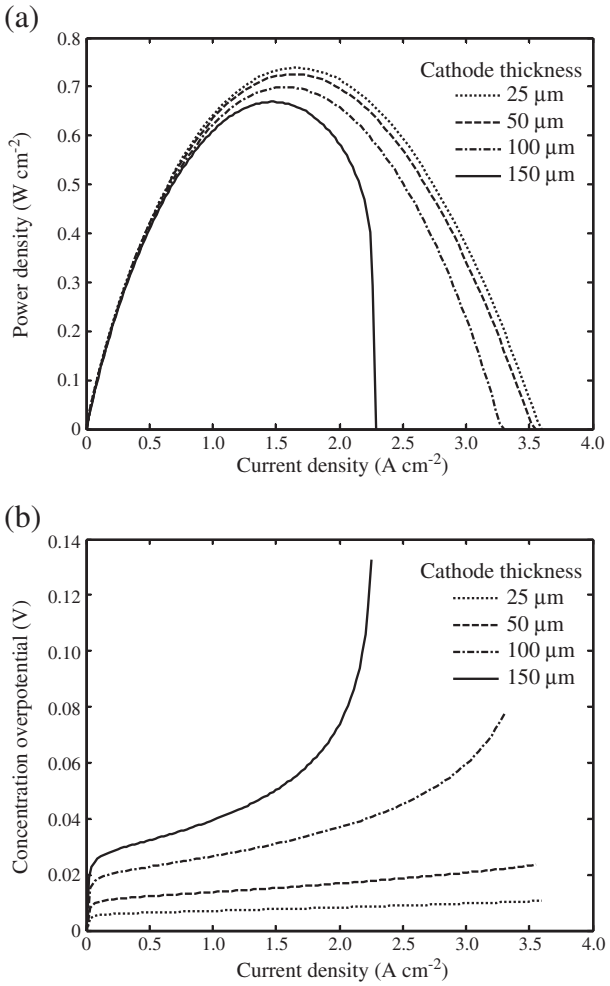

Fig. 6. Effect of cathode thickness at different current densities on (a) power density, and (b) concentration overpotential.

temperature. This is due to the fact that the ohmic loss is highly sensitive to operating temperatures; it greatly decreases with an increased temperature as illustrated in Fig. 7b. Conversely, the activation overpotential (Fig. 7c) and concentration overpotential (Fig. 7d) increase with an increase in operating temperature. It is noted that the effect of operating temperatures on the performance of SOFC was analyzed without the consideration of the degradation effect of electrodes. The result indicates that although the activation and concentration overpotentials increase with increasing temperatures, the SOFC-H^+ performance is improved. This is because of a remarkably decreased ohmic loss at high-temperature operation. It is noted that in general, the proton transport number decreases while oxide-ion transport number increases with increasing operating temperature. However, the proton transport number of pure SCY (larger than 0.9) decreases only slightly as the temperature increases over a wide temperature range [38,39].

3.5. Effect of operating pressure

The effect of operating pressure on the characteristic curve of the anode-supported SOFC-H^+ cell is shown in Fig. 8a. It can be seen that cell performance can be slightly improved when the operating pressure is changed from 1 atm to 10 atm. This is because O_2 can easily diffuse to the electrode/electrolyte interface when the SOFC-H^+ is operated under high pressure operation; the concentration overpotential is reduced as can be seen in Fig. 8b. It is noted that although the performance of SOFC-H^+ is improved due to the high pressure operation, it may result in the brittleness of the SOFC materials [5]. Therefore, a choice of operating pressure should be carefully selected.

3.6. Effect of water content

Unlike conventional oxide based SOFC, here it is necessary to explore the impact of water content on the cathode side of the fuel cell. Fig. 9a and b show that increasing water content in the oxidant from 0.1 to 12.0% decreases the cell performance. Even though, increasing water content results in a reduction of the concentration overpotential (Fig. 9c), higher water content in oxidant also decreases the concentration of O_2 required for the electrochemical reaction that causes a reduced open-circuit voltage. This leads to the deterioration of the cell performance. It is noted that the overall effective diffusion coefficients on the cathode side are based on three components (O_2, H_2O and N_2). Although the effective binary diffusion coefficients of O_2 and H_2O in N_2 are almost constant when water content increases, the difference in the mole fraction of O_2 and H_2O results in an increase in the effective diffusion coefficients and thus, the concentration overpotential is decreased.

4. Conclusions

A detailed electrochemical model of a SOFC-H^+ was presented in this study. The analysis of gas diffusion through the porous electrodes was developed based on Fickian diffusion to determine the concentration overpotential. The developed SOFC-H^+ model shows a good agreement with experimental data reported in the literature. Based on the developed model, the electrochemical performance of a planar SOFC-H^+ was analyzed with respect to different design, structural and operational parameters. Under the standard operating conditions ($T=1073$ K and $P=1$ atm), it was found that an anode-supported SOFC-H^+ provides the best performance in terms of an achievable power density across a wider range of operating current density. This is because an ohmic loss in the anode-supported SOFC-H^+ is lower than the electrolyte-supported SOFC-H^+. Concentration overpotentials become more significant for a cathode-supported cell. Considering the anode-supported SOFC-H^+, the ohmic loss is still a major loss due to the relatively low proton conductivity of electrolyte. The performance analysis of the anode-supported SOFC-H^+ shows that a decrease in electrolyte thickness and an increase in operating temperature can significantly reduce the ohmic loss. Further, it is found that the anode-supported SOFC-H^+ performance can be improved by decreasing cathode thickness and water content and by increasing operating pressure.

Nomenclature

$D_{a,eff}$	effective diffusion coefficient in the anode side ($m^2\ s^{-1}$)
$D_{c,eff}$	effective diffusion coefficient in the cathode side ($m^2\ s^{-1}$)
E^{OCV}	open-circuit voltage (OCV) (V)
E^0	OCV for standard temperature and pressure and pure reactants for the H_2 oxidation reaction (V)
F	Faraday's constant ($C\ mol^{-1}$)
F_{air}	molar flow rate of air ($mol\ s^{-1}$)
F_{fuel}	molar flow rate of the fuel ($mol\ s^{-1}$)
i	current density ($A\ m^{-2}$)
$i_{0,electrode}$	electrode exchange current density ($A\ m^{-2}$)
L	cell length (m)
n	number of electrons participating in the electrochemical reaction
P	pressure (atm)
p_i	partial pressure of component i (atm)
R_{ohm}	ohmic area specific resistance ($\Omega\ m^2$)
R	gas constant ($kJ\ mol^{-1}\ K^{-1}$)
r	electrode pore radius (μm)

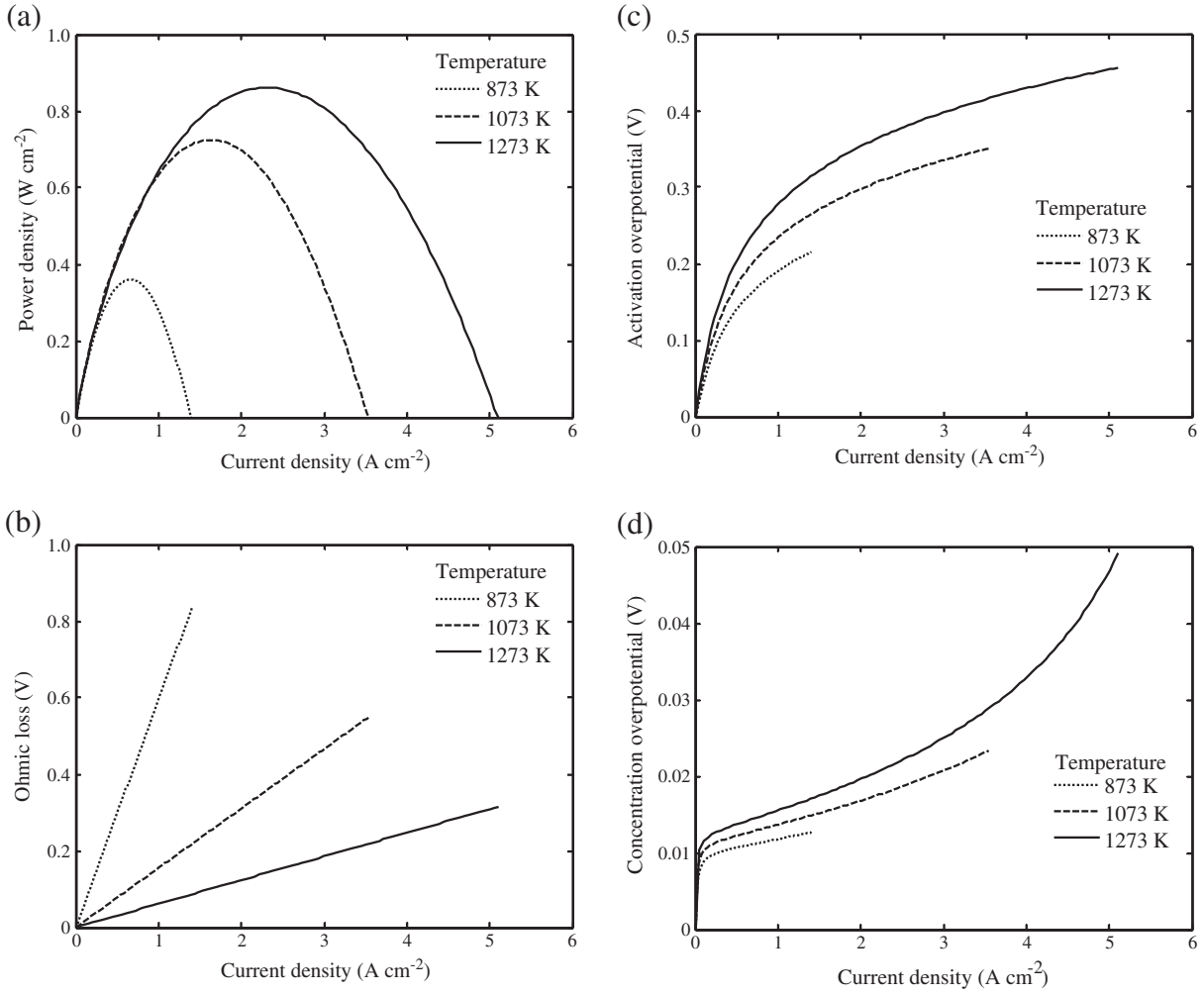

Fig. 7. Effect of operating temperature at different current densities on (a) power density, (b) ohmic loss, (c) activation loss, and (d) concentration overpotential.

T	temperature (K)
V	operation voltage (V)
W	cell width (m)

Greek symbols

α	transfer coefficient
ε	electrode porosity
η_{act}	activation overpotential (V)
η_{con}	concentration overpotential (V)
$\sigma_{electrolyte}$	ionic conductivity of electrolyte (Ω^{-1} m^{-1})
τ_{anode}	anode thickness (m)
$\tau_{cathode}$	cathode thickness (m)
$\tau_{electrolyte}$	electrolyte thickness (m)
ξ	electrode tortuosity

Superscripts

I	electrode/electrolyte interface

Acknowledgements

Y. Patcharavorachot thanks the Thailand's Commission on Higher Education for granting an exchange-program fellowship under the program "Strategic Scholarships for Frontier Research Network."

Support from the Thailand Research Fund, Commission on Higher Education, and Chulalongkorn University is gratefully acknowledged.

Appendix A. Effective diffusivity coefficient

Gas diffusion in a porous material is mainly described by two mechanisms; namely, ordinary diffusion and Knudsen diffusion. Ordinary diffusion occurs when the pore diameter of material is larger in comparison to the mean free path of the gas molecules. On the other hand, when the pore diameter is much smaller than the mean free path of the gas molecules, Knudsen diffusion becomes an important mechanism. The Knudsen diffusion coefficient can be predicted using the kinetic theory by relating the diameter of the pore and the mean free path of the gas [3,6,7].

For straight and round pores [3], the diffusion coefficient of the gaseous component A becomes:

$$D_{Ak} = 97\overline{r}\sqrt{\frac{T}{M_A}} \tag{A.1}$$

$$\overline{r} = \frac{2\varepsilon}{S_A \rho_B} \tag{A.2}$$

where S_A is the surface area of the porous solid (m^2 kg^{-1}), ρ_B is the bulk density of the solid particle (kg m^{-3}), ε is the porosity material, and M is the molecular mass (kg kmol^{-1}).

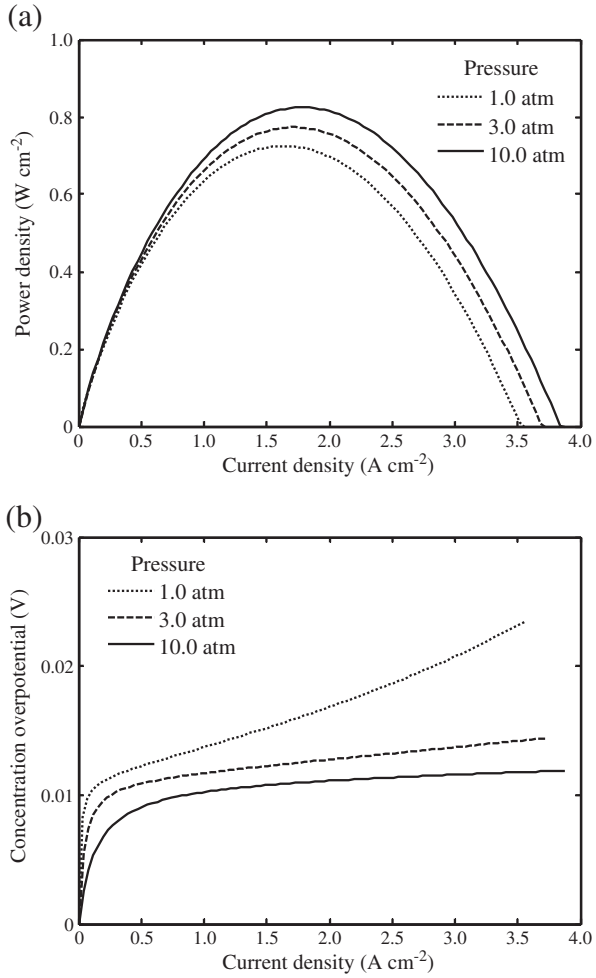

Fig. 8. Effect of operating pressure at different current densities on (a) power density, and (b) concentration overpotential.

To account for the tortuosity of the material, the Knudsen coefficient has to be modified in terms of an effective coefficient [3,6]:

$$D_{\mathrm{Ak,eff}} = D_{\mathrm{Ak}}\left(\frac{\varepsilon}{\xi}\right) \tag{A.3}$$

where ε and ξ represent the porosity and the tortuosity, respectively.

The binary ordinary diffusion coefficient in the gas phase can be determined by using the Chapman–Enskog theory [31] as follows:

$$D_{\mathrm{AB}} = 0.0018583\left(\frac{1}{M_{\mathrm{A}}} + \frac{1}{M_{\mathrm{B}}}\right)^{1/2}\frac{T^{3/2}}{p\sigma_{\mathrm{AB}}^2\Omega_{\mathrm{DAB}}} \tag{A.4}$$

$$\sigma_{\mathrm{AB}} = \frac{\sigma_{\mathrm{A}} + \sigma_{\mathrm{B}}}{2} \tag{A.5}$$

$$\Omega_{\mathrm{DAB}} = \frac{A}{\tau^B} + \frac{C}{\exp(D\tau)} + \frac{E}{\exp(F\tau)} + \frac{G}{H\tau} \tag{A.6}$$

$$\tau = \frac{kT}{\varepsilon_{\mathrm{AB}}} \tag{A.7}$$

$$\varepsilon_{\mathrm{AB}} = \left(\varepsilon_{\mathrm{A}}\varepsilon_{\mathrm{B}}\right)^{1/2} \tag{A.8}$$

where p is the total pressure (atm), k is the Boltzmann's constant, σ_{AB} (A°) is the characteristic length, and Ω_{DAB} is the collision integral based on the Lennard–Jones potential which can be obtained from $\varepsilon_{\mathrm{AB}}$.

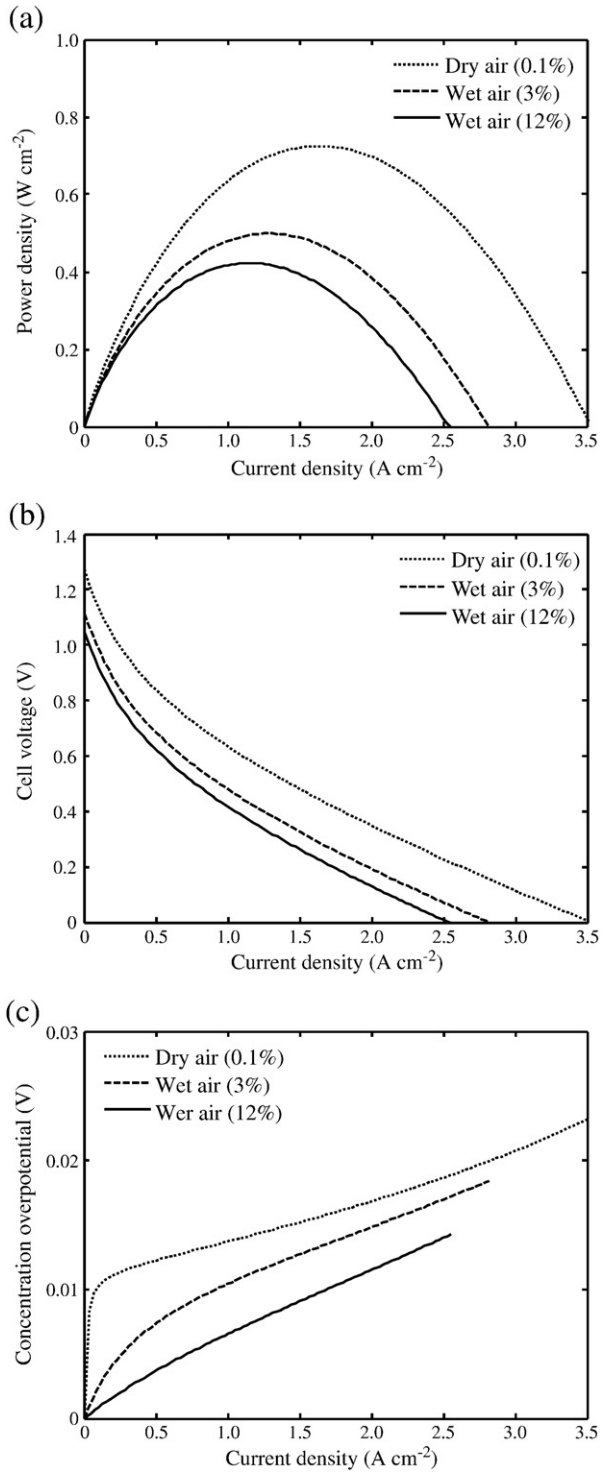

Fig. 9. Effect of water content at different current densities on (a) power density, (b) cell voltage, and (c) concentration overpotential.

$\varepsilon_{\mathrm{AB}}$ (K) is the characteristic Lennard–Jones length. The values for the characteristic lengths and the constants appearing in the collision integral are reported in Tables A.1 and A.2.

Similar to the Knudsen diffusion, the effective diffusion coefficient for the binary diffusion has to be modified in order to account for the tortuosity of the material:

$$D_{\mathrm{AB,eff}} = D_{\mathrm{AB}}\left(\frac{\varepsilon}{\xi}\right) \tag{A.9}$$

Table A.1
Lennard–Jones potential.

	N_2	O_2	H_2O	H_2
σ_i	3.798	3.467	2.641	2.827
ε_i/k	71.400	106.700	809.100	597.700

Table A.2
Collision integral constants.

A	B	C	D	E	F	G	H
1.06036	0.15610	0.19300	0.47635	1.03587	1.52996	1.76474	3.89411

Both ordinary diffusion and Knudsen diffusion may occur simultaneously. For self-diffusion transfer, the effective diffusion coefficient can be written as

$$\frac{1}{D_{A,eff}} = \frac{1}{D_{AB,eff}} + \frac{1}{D_{Ak,eff}} \quad (A.10)$$

References

[1] L. Petruzzi, S. Cocchi, F. Fineschi, J. Power Sources 118 (2003) 96.
[2] X. Xue, J. Tang, N. Sammes, Y. Du, J. Power Sources 142 (2005) 211.
[3] S.H. Chan, K.A. Khor, Z.T. Xia, J. Power Sources 93 (2001) 130.
[4] H. Zhu, R.J. Kee, J. Power Sources 117 (2003) 61.
[5] P. Costamagna, A. Selimovic, M.D. Borghi, G. Agnew, Chem. Eng. J. 102 (2004) 61.
[6] E. Hernandez-Pacheco, D. Singh, P.N. Hutton, N. Patel, M.D. Mann, J. Power Sources 138 (1–2) (2004) 174.
[7] M. Ni, M.K.H. Leung, D.Y.C. Leung, Energy Convers. Manage. 48 (2007) 1525.
[8] P. Aguiar, C.S. Adjiman, N.P. Brandon, J. Power Sources 138 (2004) 120.
[9] Y. Patcharavorachot, A. Arpornwichanop, A. Chuachuensuk, J. Power Sources 177 (2008) 254.
[10] A. Arpornwichanop, N. Chalermpanchai, Y. Patcharavorachot, S. Assabumrungrat, M. Tade, Int. J. Hydrogen Energy 34 (2009) 7780.
[11] P. Ranran, W. Yan, Y. Lizhai, M. Zongqiang, Solid State Ionics 177 (2006) 389.
[12] W.G. Coors, J. Power Sources 118 (2003) 150.
[13] H. Iwahara, H. Uchida, N. Maeda, J. Power Sources 7 (1982) 293.
[14] B. Zhu, B.E. Mellander, Solid State Ionics 70/71 (1994) 285.
[15] H. Iwahara, Solid State Ionics 86–88 (1996) 9.
[16] H. Iwahara, Y. Asakura, K. Katahira, M. Tanaka, Solid State Ionics 168 (2004) 299.
[17] G.Y. Meng, G.L. Ma, Q.L. Ma, R.R. Peng, X.Q. Liu, Solid State Ionics 178 (2007) 697.
[18] H. Iwahara, Solid State Ionics 28–30 (1988) 573.
[19] H. Taherparvar, J.A. Kilner, R.T. Baker, M. Sahibzada, Solid State Ionics 162–163 (2003) 297.
[20] A.R. Potter, R.T. Baker, Solid State Ionics 177 (2006) 1917.
[21] A. Epifanio, E. Fabbri, E. DiBartolomeo, S. Licoccia, E. Traversa, Fuel Cells 1 (2008) 69.
[22] C. Zamfirescu, I. Dincer, Thermochim. Acta 486 (2009) 32.
[23] A. Demin, P. Tsiakaras, Int. J. Hydrogen Energy 26 (2001) 1103.
[24] W. Jamsak, S. Assabumrungrat, P.L. Douglas, N. Laosiripojana, S. Charojrochkul, Chem. Eng. J. 119 (2006) 11.
[25] M. Ni, D.Y.C. Leung, M.K.H. Leung, J. Power Sources 183 (2008) 133.
[26] R. Suwanwarangkul, E. Croiset, M.W. Fowler, P.L. Douglas, E. Entchev, M.A. Douglas, J. Power Sources 122 (2003) 9.
[27] Y. Feng, J. Luo, K.T. Chuang, Fuel 86 (2007) 123.
[28] K. Sasaki, J. Tamura, M. Dokiya, Solid State Ionics 144 (2001) 223.
[29] A. Barbucci, R. Bozzo, G. Cerisola, P. Costamagna, Electrochim. Acta 47 (2002) 2183.
[30] A. Demin, P. Tsiakaras, E. Gorbova, S. Hramova, J. Power Sources 131 (2004) 231.
[31] R.B. Bird, W.E. Stewart, E.N. Lightfoot, Transport Phenomena, 2nd EdWiley, 2006.
[32] I. Kosacki, H.U. Anderson, Solid State Ionics 97 (1997) 429.
[33] S. Hamakawa, L. Li, A. Li, E. Iglesia, Solid State Ionics 48 (2002) 71.
[34] N. Ito, M. Iijima, K. Kimura, S. Iguchi, J. Power Sources 152 (2005) 200.
[35] H. Matsumoto, I. Nomura, S. Okada, T. Ishihara, Solid State Ionics 179 (2008) 1486.
[36] A. Essoumhi, G. Taillades, M. Taillades-Jacquin, D.J. Jones, J. Rozière, Solid State Ionics 179 (2008) 2155.
[37] G.C. Mather, F.M. Figueiredo, J.R. Jurado, J.R. Frade, Solid State Ionics 162–163 (2003) 115.
[38] M. Zheng, X. Chen, Solid State Ionics 70 (71) (1994) 595.
[39] M. Zheng, Bo. Zhu, Solid State Ionics 80 (1995) 59.

ภาคผนวก 18

Korean J. Chem. Eng., **28**(3), 649-655 (2011)
DOI: 10.1007/s11814-010-0440-z

Reactive distillation for biodiesel production from soybean oil

Lida Simasatitkul, Pimpatthar Siricharnsakunchai, Yaneeporn Patcharavorachot, Suttichai Assabumrungrat, and Amornchai Arpornwichanop†

Department of Chemical Engineering, Faculty of Engineering, Chulalongkorn University, Bangkok 10330, Thailand
(*Received 16 June 2010 • accepted 1 October 2010*)

Abstract−Biodiesel, which is regarded as a promising alternative to a conventional petroleum-based diesel fuel, can be produced from transesterification of vegetable oils and alcohol in conventional batch and continuous reactors. Since the transesterification is an equilibrium-limited reaction, a large excess of reactants is usually used to increase the production of biodiesel, thereby requiring more expensive separation of unreacted raw materials. This study proposed the use of a reactive distillation for transesterification of soybean oil and methanol catalyzed by sodium hydroxide to produce biodiesel. The simulation results showed that a suitable configuration of the reactive distillation column consists of three reactive stages. The optimal conditions for the reactive distillation operation are at the molar feed ratio of methanol and oil at 4.5 : 1, reflux ratio of 3, and reboiler duty of 1.6×10^7 kJ h^{-1}. Methanol and soybean oil should be fed into the column at the first stage. The effect of important operating and design parameters on the performance of reactive distillation was also presented.

Key words: Reactive Distillation, Biodiesel Production, Soybean Oil, Transesterification, Simulation

INTRODUCTION

Biodiesel as an alternative fuel has been presently receiving much attention due to the limited availability of conventional petroleum diesel and environmental concerns. It can be directly used to replace petroleum diesel without modifying diesel engines since their properties, e.g., specific gravity, cetane number, viscosity, cloud point, and flash point, are similar [1]. In general, biodiesel is derived from a transesterification reaction of triglycerides in vegetable oils or animal fats with alcohol (i.e., methanol and ethanol) under the presence of catalysts [2-4].

Various types of catalyst, which includes alkali and acid-based catalysts in both heterogeneous and homogeneous forms, and numerous feedstock based on available local vegetable oils can be employed for biodiesel production. As a result, there are a number of researches concerning the production of biodiesel from different vegetable oils and alcohols. An analysis of the effect of important operating conditions such as temperature, feed molar ratio, and type of catalyst, on the efficiency of a biodiesel production system is also the main topic of interest. For example, Narvaez et al. [5] investigated the kinetics of the transesterification of palm oil with methanol catalyzed by sodium hydroxide in a batch stirred reactor. Sharma et al. [6] studied the effect of key reaction parameters on the synthesis of biodiesel from various crude vegetable oils and determined optimal conditions for maximizing the biodiesel yield.

It has been known that the transesterification of vegetable oils to fatty acid ester as a biodiesel is an equilibrium-limited reaction. A large excess of alcohol over a stoichiometric ratio is usually employed in conventional reactors to achieve a high degree of the conversion of vegetable oils, thereby requiring the expensive separation of unreacted reactants from the biodiesel product [7]. As a consequence, potentially alternative processes to overcome such a difficulty should be explored. When considering the characteristics of the transesterification reaction, the use of reactive distillation, a multifunctional reactor combining chemical reaction and distillation in a single column, is a promising way. The simultaneous separation and reaction inside the column allow the equilibrium-limited reaction to take place more completely and reduce the separation cost of unreacted reactants [8-10]. Although a number of investigations have been reported on the implementation of a reactive distillation to biodiesel production, most of them focus on the utilization of free fatty acid extracted from vegetable oils as a reactant for an esterification process [11,12]. Matallana et al. [13] studied the production of biodiesel from lauric acid and 2-ethyl hexanol by using the reactive distillation. Kumar and Mahajani [12] applied the reactive distillation for the esterification of lactic acid with n-butanol catalyzed by Amberlyst-15. To date, few studies on reactive distillations have been performed for the transesterification of vegetable oils [7]. Recently, Silva et al. [14] preliminarily studied the synthesis of biodiesel from transesterification of soybean oil with ethanol by using reactive distillation. The effect of operating conditions such as catalyst concentration and ratio of ethanol and oil on the performance of biodiesel production was only studied without considering the impact of design parameters.

The aim of this work is concentrated on the analysis of a reactive distillation for biodiesel production from the transesterification of soybean oil with methanol. Pure soybean oil is considered to be a suitable feedstock due to its low content of free fatty acid (less than 0.3%), and thus a pretreatment of feedstock by removal of free fatty acid is unnecessary. A residue curve map is used as a tool to analyze a reactive distillation operation. Furthermore, the effect of various operating and design parameters on the performance of the reactive distillation for biodiesel production is investigated.

†To whom correspondence should be addressed.
E-mail: Amornchai.A@chula.ac.th

SIMULATION OF REACTIVE DISTILLATION FOR BIODIESEL PRODUCTION

Biodiesel is normally produced by a transesterification process of vegetable oils with methanol. The transesterification reaction consists of three-step reactions in series as shown below:

$$\begin{aligned} TG + CH_3OH &\underset{k_2}{\overset{k_1}{\longrightarrow}} DG + RCOOCH_3 \\ DG + CH_3OH &\underset{k_4}{\overset{k_3}{\longrightarrow}} MG + RCOOCH_3 \\ MG + CH_3OH &\underset{k_6}{\overset{k_5}{\longrightarrow}} GL + RCOOCH_3 \end{aligned} \quad (1)$$

From the above reaction scheme, triglyceride (TG), a major component in vegetable oils, reacts with methanol in the presence of catalyst to produce methyl esters ($RCOOCH_3$) as a biodiesel product and diglyceride (DG), monoglyceride (MG), and finally glycerol (GL) as a by-product. All the reactions are reversible and can be catalyzed by either alkali or acid catalysts; however, the alkali catalyst is preferable due to a higher reaction rate.

1. Kinetic Model of Soybean Oil

As mentioned earlier, the transesterification of triglyceride in vegetable oils and alcohol involves three reversible reactions (Eq. (1)). Kinetic expressions and rate constants for each reaction are necessary information for process simulations. This work was focused on the production of biodiesel from the transesterification of soybean oil and methanol with sodium hydroxide catalyst. Trilinolein, a major component in soybean oil, was represented as the triglyceride whereas dilinolein and monolinolein were referred to as the intermediate reactants. Methyl linoleate (methyl ester) was considered to be a major biodiesel product. The kinetic studies by Noureddini and Zhu [15] showed that the transesterification is a homogeneous liquid-phase and equilibrium-limited reaction and the kinetic parameters can be explained by the Arrhenius law. The rate expressions of each reaction are shown as follows:

$$\begin{aligned} r_{TG} &= -k_1[TG][A] + k_2[DG][A] \\ r_{DG} &= k_1[TG][A] - k_2[DG][E] - k_3[DG][A] + k_4[MG][E] \\ r_{MG} &= k_3[DG][A] - k4[MG][A] - k_5[MG][A] + k_6[GL][E] \\ r_E &= k_1[TG][A] - k_2[DG][E] + k_3[DG][A] \\ &\quad - k_4[MG][E] + k_5[MG][A] - k_6[GL][E] \\ r_{GL} &= k_5[MG][A] - k_6[GL][E] \end{aligned} \quad (2)$$

where TG, DG, MG, GL, A, and E denote the triglyceride, diglyceride, monoglyceride, glycerol, methanol, and methyl ester (biodiesel), respectively, and k_i is the rate constant of reaction i.

Table 1 shows the reaction constants of the transesterification reaction of soybean oil and methanol [15].

Table 1. Values of kinetic constant for transesterification of soybean oil and methanol

Rate constant	k_0 (L mol^{-1} s^{-1})	E_a (cal mol^{-1})
k_1	3.9×10^7	13,145
k_2	5.78×10^5	9,932
k_3	5.906×10^{12}	19,860
k_4	9.888×10^9	14,639
k_5	5.335×10^3	6,421
k_6	2.1×10^4	9,588

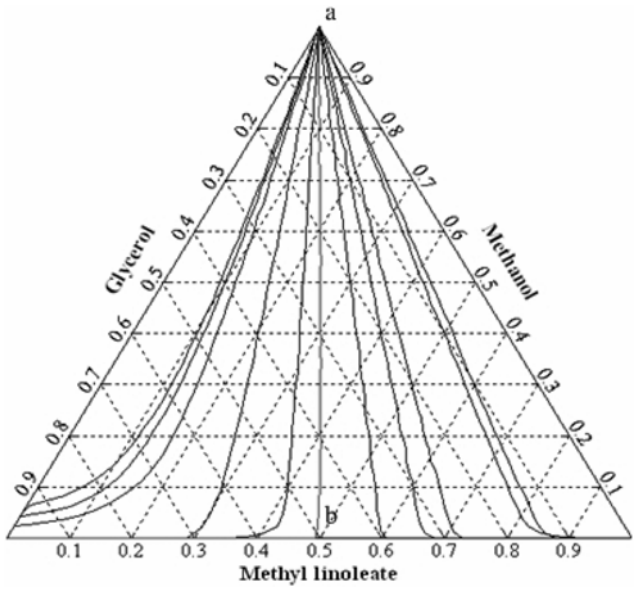

Fig. 1. Residue curve map for a ternary system in biodiesel production.

2. Phase Equilibrium

Fig. 1 shows the residue curve map of the tertiary system consisting of methanol, glycerol, methyl linoleate, in biodiesel production. There is a binary azeotrope (methyl linoleate and glycerol) at 229 °C. As glycerol and biodiesel can be decomposed at 150 °C and 250 °C, respectively, the reactive distillation should not be operated at higher reboiler temperatures. In addition, the composition of the products obtained from the transesterification reaction trends to be in the right-hand side of the distillation region (line ab in Fig. 1). Since the reactive distillation column cannot be operated across a distillation boundary, pure glycerol cannot be obtained. From Fig. 1, the binary azeotrope does not affect the separation because it is saddle node, and thus the distillate product stream of a reactive distillation is pure methanol while the bottom stream comprises methyl linoleate and glycerol.

3. Reactive Distillation for Biodiesel Production

The production of biodiesel from the transesterification of soybean oil with methanol in a reactive distillation was investigated in this study. Due to its low content of free fatty acid (less than 0.3 wt%), soybean oil can be directly used as the feedstock for biodiesel production without requiring a pretreatment unit. Simulations of the reactive distillation were performed by using HYSYS commercial software to analyze the effect of key operating and design parameters on its performance for biodiesel production. A rigorous equilibrium stage model and UNIQUAC model for describing thermodynamic properties and phase equilibriums were used. Methyl linoleate (biodiesel) was taken as the product of the transesterification reaction, whereas glycerol was considered to be the by-product. The following conditions were determined as the standard case study: the column was operated at atmospheric pressure and the pressure drop was negligible, soybean oil (trilinolein) and methanol were fed at the first stage of a reactive section, and total condenser and a stage efficiency of 100% were assumed.

Fig. 2 shows the configuration of the reactive distillation column used in this study. The column contains a total of 22 stages (includ-

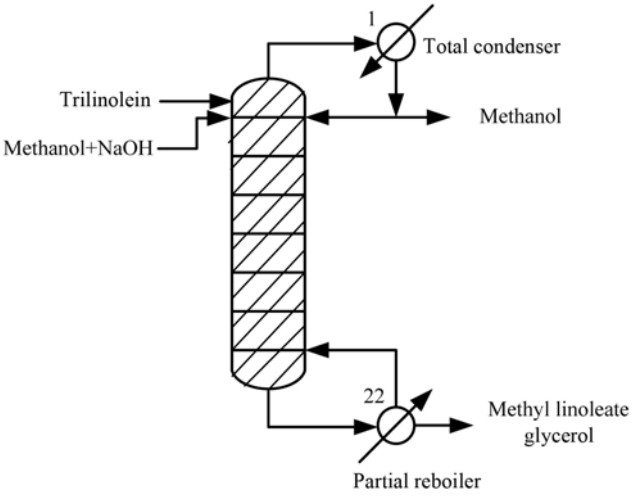

Fig. 2. Schematic diagram of reactive distillation for biodiesel production.

ing a condenser and a reboiler). Methyl linoleate and glycerol are produced in a reactive zone where the transesterification of trilinolein and methanol occurs. Since sodium hydroxide was used as a homogeneous catalyst, the reaction was assumed to occur over all the stages of the reactive distillation column.

To determine the performance of reactive distillation, the conversion of trilinolein in soybean oil and the yield of methyl linoleate as defined by Eqs. (3)-(4) was considered.

$$\text{Conversion} = \frac{F_{trilinolein,0} - F_{trilinoleion}}{F_{trilinolein,0}} \times 100\% \quad (3)$$

$$\text{Yield} = \frac{F_{methyl\ linoleate}}{3 \times F_{trilinolein,0}} \times 100\% \quad (4)$$

where $F_{trilinolein,0}$, $F_{trilinolein}$, and $F_{methyl\ linoleate}$ are the molar flow rates of trilinolein in feed and outlet streams, and methyl linoleate, respectively.

SIMULATION RESULTS

1. Standard Condition

At the standard condition, the feed streams consisting of trilinolein and methanol at the flow rates of 50 and 300 kmol/h, respectively, are separately fed to a reactive distillation column at the first stage. The column is operated at pressure of 1 atm with the reflux ratio of 3, feed temperature of 50 °C, and the reboiler duty of 1.2×10^7 kJ/h. Figs. 3(a) and 3(b) show, respectively, the composition and temperature profiles within the column under the standard condition. There is a large amount of methanol at the top of the column, whereas less trilinolein, dilinolein and monolinolein are observed. The bottom products consist of mostly methyl linoleate (biodiesel product) and slightly glycerol as a by-product. Under the standard condition, the conversion of trilinolein is 99% and the purity of methyl linoleate is 81%. The unreacted methanol, the lowest-boiling point substance, is withdrawn from the reactive distillation column as a distillate stream, whereas a mixture of methyl linoleate and glycerol is removed as a bottom stream as earlier stated in Section 2.2. The phase separation of methyl linoleate and glycerol in the product stream was not observed. It is noted that under low operating temperatures, glycerol cannot be separated from biodiesel product. To separate glycerol from biodiesel in the reactive distillation column, a higher temperature operation is required; however, this can result in a decreased amount of methanol in the reaction section, thus decreasing the conversion of trilinolein. In addition, this would make glycerol decompose.

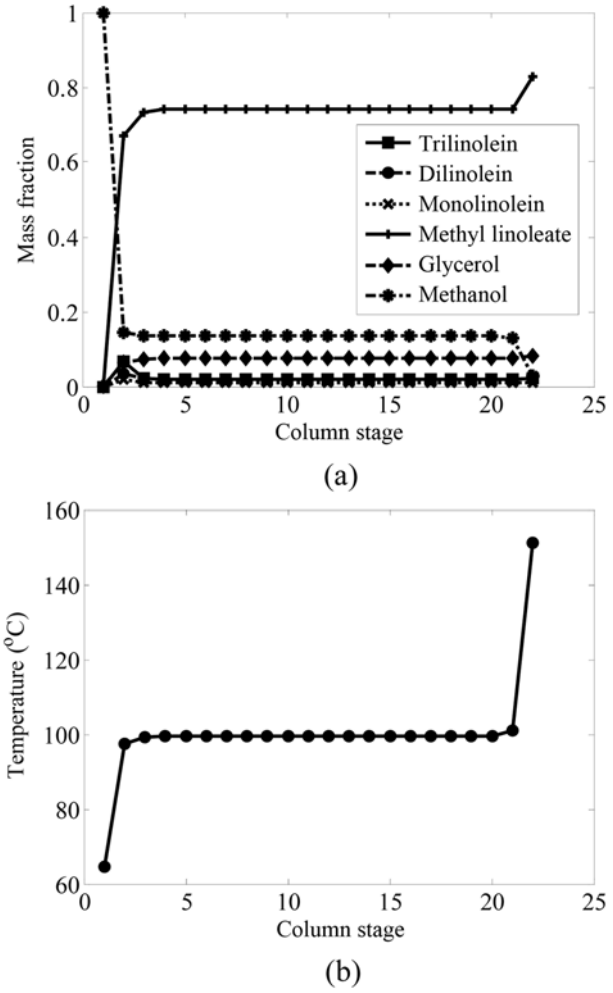

Fig. 3. (a) Composition and (b) temperature profiles in reactive distillation for biodiesel production at standard condition.

2. Effect of Feed Ratio of Methanol and Oil

The molar feed ratio of methanol and oil (trilinolein) is one of the key parameters on the performance of the reactive distillation. Fig. 4 shows the effect of molar feed ratio of methanol to oil on the conversion of trilinolein and the yield and purity of methyl linoleate. The simulation results demonstrate that the conversion of trilinolein and the yield of methyl linoleate increase with increasing feed molar ratio. The purity of methyl linoleate shows a decreasing trend at a higher ratio of methanol and oil due to the dilution effect of unreacted methanol. It is found that the feed streams of methanol and oil at the ratio of 4.5 is an optimal condition in terms of the product yield and purity. Fig. 4 also compares the performance of the reactive distillation with that of a conventional continuous reactor operated at 100 °C. It is clearly indicated that at the same feed ratio, the implementation of the reactive distillation to produce biodiesel gives

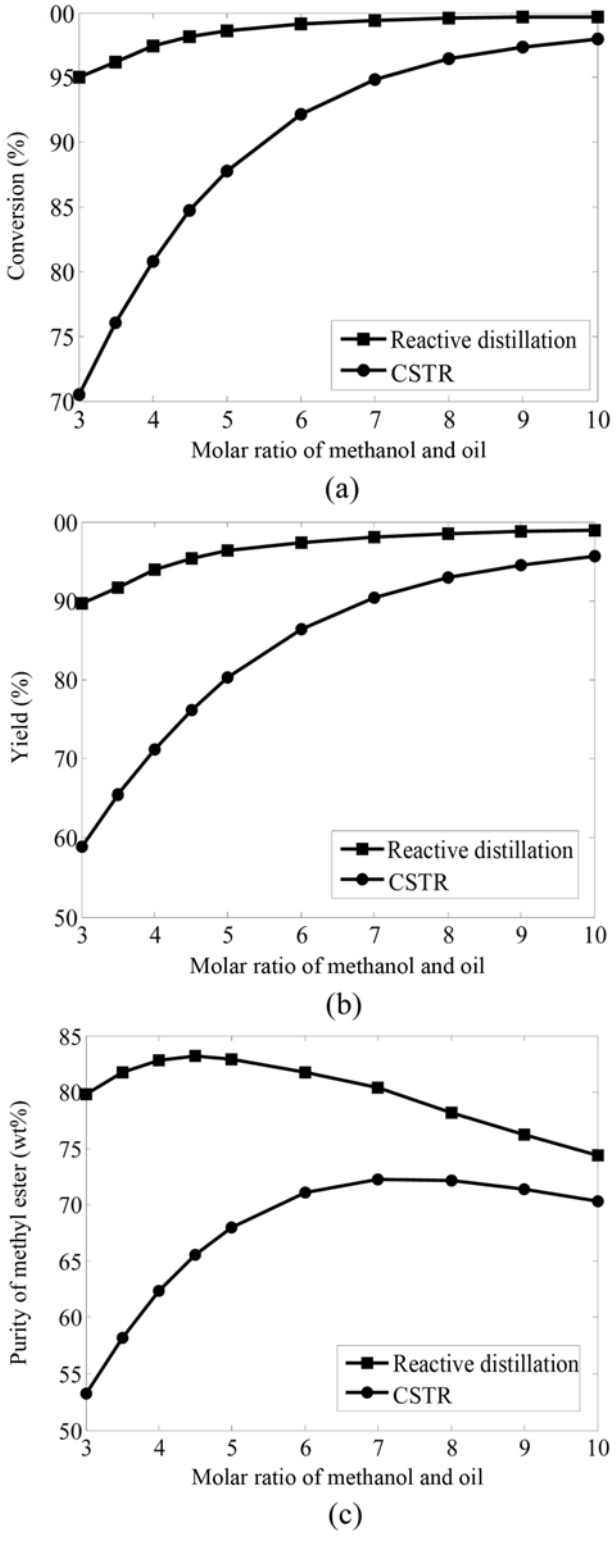

Fig. 4. Effect of molar feed ratio of methanol and oil on (a) conversion of trilinolein, (b) yield of methyl ester, and (c) purity of methyl ester.

a better performance because the removal of methyl linoleate and glycerol promotes the transesterification reaction.

3. Effect of Feed Temperature

The effect of feed temperatures on the performance of the reactive distillation in terms of the conversion of trilinolein and yield of methyl linoleate is studied. Fig. 5 indicates that when the feed temperature is increased from 25 ℃ to 90 ℃, the conversion of trilinolein and the yield of methyl linoleate are slightly decreased. An increase in feed temperatures decreases the amount of methanol in the reaction section of the column. This causes the reductions of trilinolein conversion and methyl linoleate yield in the reactive distillation. Since the feed temperature slightly affects the reactive distillation performance, the subsequent studies will be performed using the feed temperature of 25 ℃.

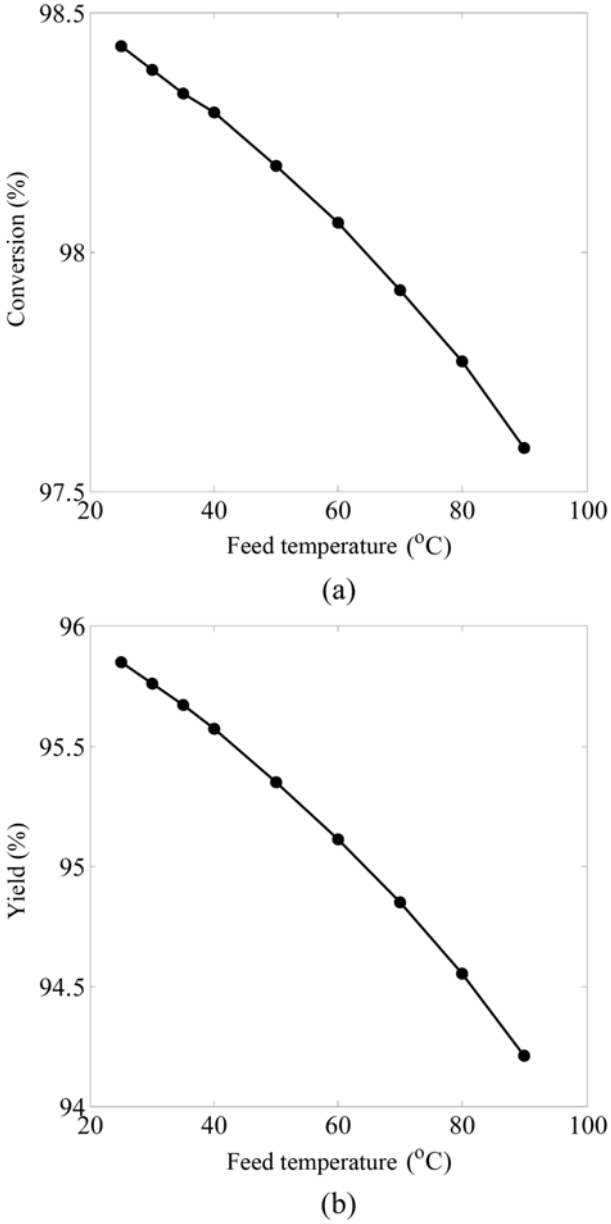

Fig. 5. Effect of feed temperature on (a) conversion of trilinolein and (b) yield of methyl ester.

4. Effect of Reboiler Heat Duty

The effect of reboiler heat duty on the performance of reactive distillation is shown in Fig. 6. Increased reboiler duty improves the conversion of trilinolein and the yield of methyl linoleate as the temperature in the reaction section increases. However, the performance

of reactive distillation for biodiesel production is degraded at high reboiler duty (>2×10^7 kJ/h). This is due to the large amount of methanol in the distillate stream being removed from the column. The result also shows that the reboiler duty increases the reboiler temperature (Fig. 6(a)). Fig. 6(c) shows an increase in the purity of biodiesel product with the increased reboiler duty since trilinolein highly reacts with methanol to produce methyl linoleate. Although the operation of reactive distillation at the reboiler duty of 2×10^7 kJ/h gives the highest trilinolein conversion, a high reboiler temperature may cause the decomposition of glycerol and biodiesel products. As a result, a suitable reboiler duty of the reactive distillation is 1.6×10^7 kJ/h.

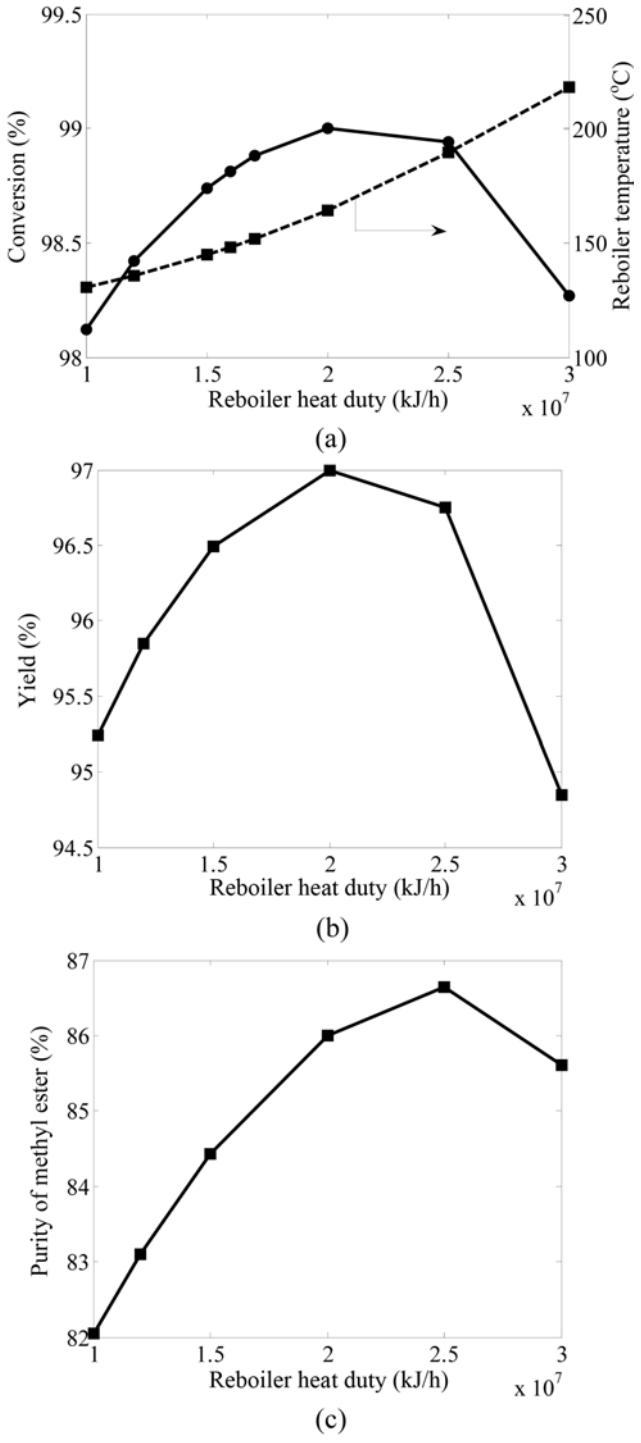

Fig. 6. Effect of reboiler duty on (a) conversion of trilinolein, (b) yield of methyl ester, and (c) purity of methyl ester at different reflux ratios (methanol to trilinolein molar ratio of 4.5 : 1, 20 reactive stages, feed location at the first stage of the column).

5. Effect of a Number of Reactive Stages

In this study, sodium hydroxide is considered as a homogeneous catalyst for the production of biodiesel from soybean oil. It is mixed with methanol before being fed into the reactive distillation column to react with trilinolein. As a result, the amount of catalyst is independent of a number of reactive stages in the column. Fig. 7 demonstrates the effect of changing the number of reactive stages on the reactive distillation performance when the feed ratio of methanol and trilinolein is 4.5 : 1. It is noted that the transesterification reaction is carried out at all the stages of the column. The results indicate that adding more reactive trays improves the system performance. Increasing the reactive stages causes trilinolein and metha-

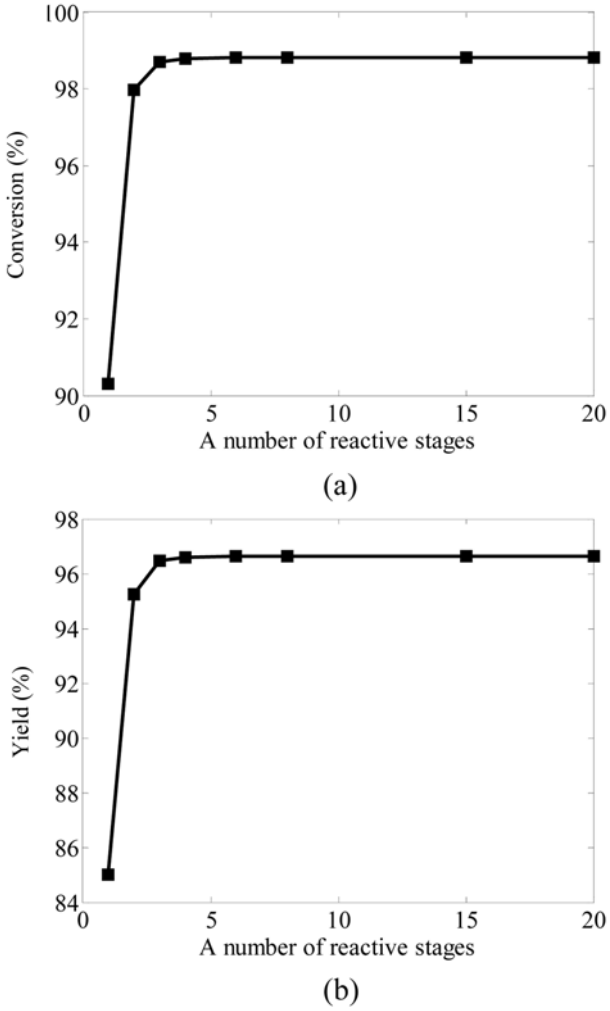

Fig. 7. Effect of a number of reactive stages on (a) conversion of trilinolein and (b) yield of methyl ester (methanol to trilinolein molar ratio of 4.5 : 1, reflux ratio of 3, reboiler duty of 1.6×10^7 kJ h^{-1}).

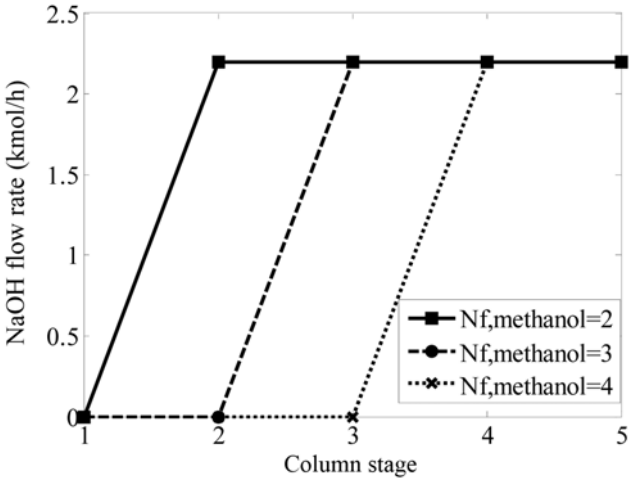

Fig. 8. Profile of NaOH at different feed locations of methanol when a number of the reactive stages are 3.

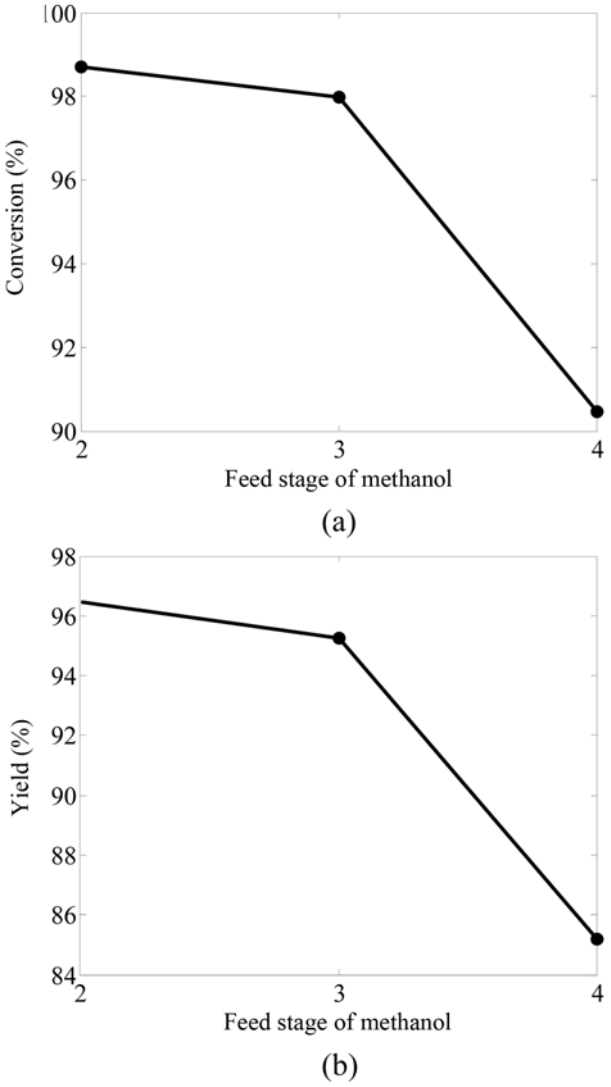

Fig. 9. Effect of feed location of methanol on (a) conversion of trilinolein and (b) yield of methyl ester (molar ratio of 4.5 : 1, reflux ratio of 3, reboiler duty of 1.6×10^7 kJ/h).

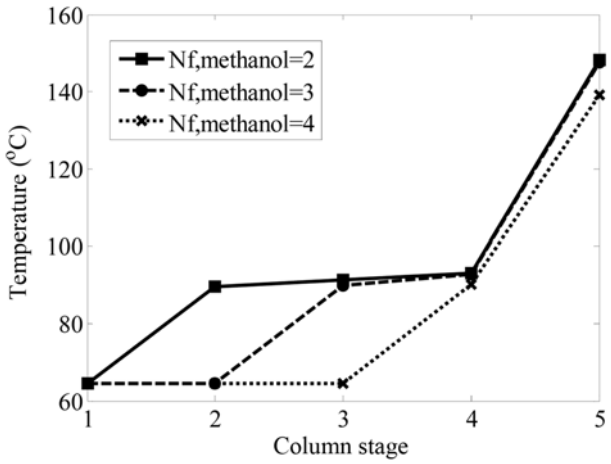

Fig. 10. Temperature profiles at different feed locations of methanol.

nol to have more contacting area, thereby enhancing the conversion of trilinolein. It is noticed that the performance of the reactive distillation is slightly improved when a number of the reactive stages are higher than 3.

6. Effect of Feed Location of Methanol

The location of a feed stream is an important design parameter having an effect on a reactive distillation performance. In general, a lighter reactant should be fed on the bottom stage of the reactive zone, whereas a heavier reactant is fed on the top stage of the reactive zone. However, for transesterification reaction of soybean oil and methanol, both the reactants are introduced to the column at the first reactive stage. Fig. 8 shows the distribution of sodium hydroxide within the column at different feed locations of methanol when the total number of reactive stages is 3. It is found that no catalyst exists above the feed stage of methanol. Therefore, moving the feed stage of methanol down to the bottom of the reactive distillation column decreases the conversion of trilinolein and the yield of methyl linoleate as shown in Fig. 9. Although a higher amount of methanol is observed at the upper stage of methanol feed location, the transesterification is less pronounced due to the absence of catalyst. Fig. 10 shows the profiles of the column temperature when methanol is fed to the column at different stages. The results show that introducing methanol at the top of the reactive distillation column can increase column temperatures, thus increasing the transesterification reaction.

From simulation studies, it is found that for biodiesel production from soybean oil, a suitable configuration of the reactive distillation column consists of only three reactive stages. The optimal conditions for the operation of the reactive distillation are at the molar feed ratio of methanol and oil at 4.5 : 1, reflux ratio of 3, and reboiler duty of 1.6×10^7 kJ h^{-1}. Methanol and soybean oil should be fed into the column at the first stage of the reactive distillation column. Fig. 11 shows the typical composition and temperature profiles of the reactive distillation at the optimal designed conditions. It can be seen that the compositions of the distillate product consist of only methanol, while the bottom product consists of mainly methyl linoleate.

CONCLUSIONS

We investigated the use of a reactive distillation for biodiesel pro-

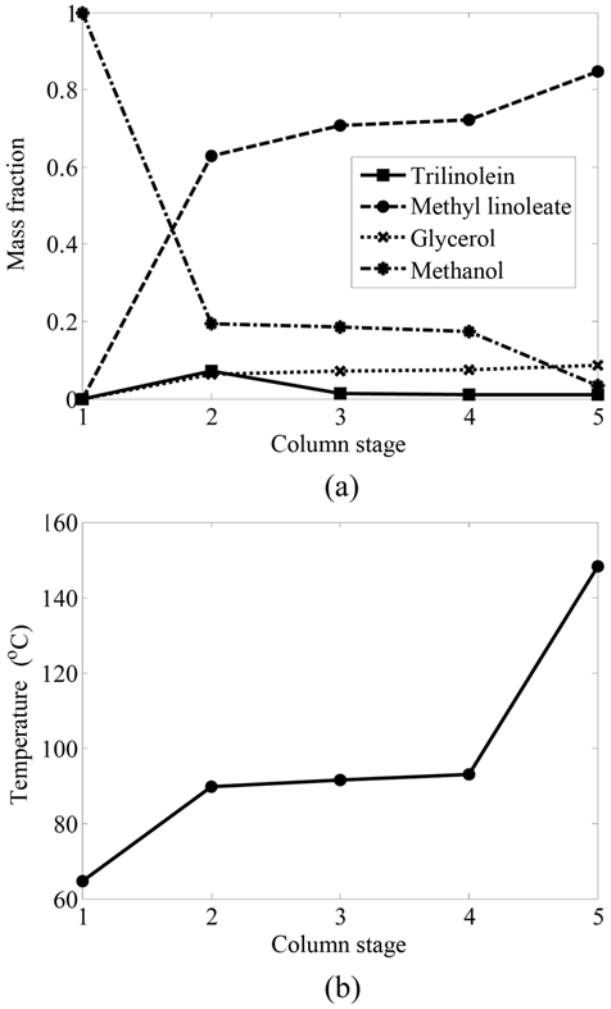

Fig. 11. (a) Composition and (b) temperature profiles in reactive distillation column (feed temperature of 25 °C, molar ratio of 4.5 : 1, reflux ratio of 3, reboiler duty of 1.6×10^7 kJ/h, reactive stage=3 and feed location of soybean oil and methanol at the first stage).

duction from transesterification of soybean oil (represented by trilinolein) and methanol catalyzed by sodium hydroxide. Effects of operating and design parameters of the reactive distillation, i.e., feed molar ratio, feed location, a number of reactive stages, on biodiesel production were analyzed to determine a suitable reactive distillation configuration. The results showed that increases in the molar feed ratio of methanol and oil and the reboiler duty enhance the performance of the reactive distillation in terms of the conversion of trilinolein, whereas the effect of feed temperature shows an opposite trend. The increased reactive stage also improves the performance of reactive distillation. To achieve a high conversion of trilinolein, soybean oil and methanol should be introduced at the first stage of column.

ACKNOWLEDGEMENT

The authors gratefully acknowledge support from The Thailand Research Fund, Commission of Higher Education, and Chulalongkorn University.

REFERENCES

1. T. Kalnes, T. Marker and D. R. Shonnard, *Int. J. Chem. React. Eng.*, **5**, A48 (2007).
2. J. M. Marchetti, V. U. Miguel and A. F. Errazu, *Renew. Sustain. Energy Rev.*, **11**, 1300 (2007).
3. G. Arzamendi, I. Campo, E. Arguinarena, M. Sanchez, M. Montes and L. M. Gandia, *Chem. Eng. J.*, **134**, 123 (2007).
4. Z. M. Wang, J. S. Lee, J. Y. Park, C. Z. Wu and Z. H. Yuan, *Korean J. Chem. Eng.*, **24**, 1027 (2007).
5. P. C. Narvaez, S. M. Rincon and F. J. Sanchez, *J. American Oil Chemists' Soc.*, **84**, 971 (2007).
6. Y. C. Sharma, B. Singh and S. N. Upadhyay, *Fuel*, **87**, 2355 (2008).
7. B. B. He, A. P. Singh and J. C. Thompson, Transactions of American Society of Agricultural and Biological Engineers, **49**, 107 (2006).
8. U. Sahapatsombud, A. Arpornwichanop, S. Assabumrungrat, P. Praserthdam and S. Goto, *Korean J. Chem. Eng.*, **22**, 387 (2005).
9. A. Arpornwichanop, K. Koomsup and S. Assabumrungrat, *J. Ind. Eng. Chem.*, **14**, 796 (2008).
10. A. Arpornwichanop, C. Wiwittanaporn, S. Authayanun and S. Assabumrungrat, *Korean J. Chem. Eng.*, **25**, 1252 (2008).
11. S. Bhatia, A. R. Mohamed, A. L. Ahmad and S. Y. Chin, *Comput. Chem. Eng.*, **31**, 1187 (2007).
12. R. Kumar and S. M. Mahajani, *Ind. Eng. Chem. Res.*, **46**, 6873 (2007).
13. L. G. Matallana, L. F. Gutierrez and C. A. Cardona, *Enpromer*, **64**, D2-O-5 (2005).
14. N. Silva, C. M. G. Santander, C. B. Batistella, R. M. Filho and M. R. W. Maciel, *Appl. Biochem. Biotechnol.*, **161**, 245 (2010).
15. H. Noureddini and D. Zhu, *J. American Oil Chemists' Soc.*, **74**, 1457 (1997).

ภาคผนวก 19

INTERNATIONAL JOURNAL OF HYDROGEN ENERGY 35 (2010) 13271–13279

Available at www.sciencedirect.com

ScienceDirect

journal homepage: www.elsevier.com/locate/he

Modeling of IT-SOFC with indirect internal reforming operation fueled by methane: Effect of oxygen adding as autothermal reforming

P. Dokmaingam [a], J.T.S. Irvine [b], S. Assabumrungrat [c], S. Charojrochkul [d], N. Laosiripojana [a,*]

[a] The Joint Graduate School of Energy and Environment, CHE Center for Energy Technology and Environment, King Mongkut's University of Technology Thonburi, Bangkok 10140, Thailand

[b] School of Chemistry, Purdie Building, University of St Andrews, St Andres, Fife KY16 9ST, UK

[c] Department of Chemical Engineering, Faculty of Engineering, Chulalongkorn University, Bangkok 10330, Thailand

[d] National Metal and Materials Technology Center (MTEC), Pathumthani, Thailand

ARTICLE INFO

Article history:
Received 20 July 2010
Received in revised form
9 September 2010
Accepted 14 September 2010
Available online 8 October 2010

Keywords:
SOFC
Autothermal reforming
Internal reforming

ABSTRACT

Mathematical models of an Intermediate Temperature Solid Oxide Fuel Cell (IT-SOFC) with indirect internal reforming operation (IIR-SOFC) fueled by methane were developed. The models were based on a steady-state heterogeneous two-dimensional tubular-design SOFC. The benefit in adding oxygen to methane and steam as the feed for autothermal reforming reaction on the thermal behavior and SOFC performance was simulated. The results indicated that smoother temperature gradient with lower local cooling at the entrance of the reformer channel can be achieved by adding a small amount of oxygen. However, the electrical efficiency noticeably decreased when too high oxygen content was added due to the loss of hydrogen generation from the oxidation reaction; hence, the inlet oxygen to carbon (O/C) molar ratio must be carefully controlled. Another benefit of adding oxygen is the reduction of excess steam requirement, which could reduce the quantity of heat required to generate the steam and eventually increases the overall system performance. It was also found that the operating temperature strongly affects the electrical efficiency achievement and temperature distribution along the SOFC system. By increasing the operating temperature, the system efficiency increases but a significant temperature gradient is also detected. The system with a counter-flow pattern was compared to that with a co-flow pattern. The co-flow pattern provided smoother temperature gradient along the system due to better matching between the heat supplied from the electrochemical reaction and the heat required for the steam reforming reaction. However, the electrical efficiency of the co-flow pattern is lower due to the higher cell polarization at a lower system temperature.

* *Corresponding author.*
E-mail address: navadol_l@jgsee.kmutt.ac.th (N. Laosiripojana).

0360-3199/$ – see front matter © 2010 Professor T. Nejat Veziroglu. Published by Elsevier Ltd. All rights reserved.
doi:10.1016/j.ijhydene.2010.09.045

1. Introduction

A Solid Oxide Fuel Cell (SOFC) is an electrochemical device which enables a conversion of chemical energy to electrical energy with high efficiency and low environmental impact. Typically, SOFC is operated at high temperature (between 700and1100 °C) under atmospheric or elevated pressures [1]. Under these operating conditions, the primary hydrocarbon fuels e.g. methane or natural gas can be internally reformed (internal reforming SOFC or IR-SOFC) to H_2 and CO which are sufficient fuels for SOFC. Theoretically, the promising reforming process for IR-SOFC operation is the endothermic steam reforming reaction, from which the required heat comes from the exothermic electrochemical reaction. According to IR-SOFC operation, there are 2 main approaches i.e. direct internal reforming (DIR-SOFC) and indirect internal reforming (IIR-SOFC). For DIR-SOFC approach, the reforming reaction occurred simultaneously with electrochemical reaction at the anode side of SOFC; thus a high heat transfer rate can be achieved from this operation. Nevertheless, the anode material for DIR-SOFC must be optimized for both reactions as it could be easily poisoned by carbon deposition from the reforming of hydrocarbons. As for IIR-SOFC, the endothermic reforming reaction takes place at the reformer, which is in close thermal contact with the anode side of SOFC where the exothermic electrochemical reaction occurs. IIR-SOFC provides advantages in terms of eliminating the requirement of a separate fuel reformer, enhancing a good heat transfer between the reformer and the fuel cell, and preventing the anode material from carbon deposition. However, the main drawback of IIR-SOFC is a possible mismatch between the rates of endothermic and exothermic reactions, which leads to a significant local temperature reduction particularly near to the entrance of the reformer and consequently results in a mechanical failure due to thermal induced stresses [1–3]. Several approaches for minimizing this mismatch problem have been proposed, e.g. applying the catalyst with low reforming reactivity or using the internal coated-wall designed reformer [1–3].

Recently, one promising approach for SOFC technology is to reduce the operating temperature of SOFC system, called as intermediate temperature SOFC (IT-SOFC). This operation provides the great benefit in terms of SOFC material component selection. To operate an IT-SOFC with internal reforming, a highly endothermic steam reforming reaction might not be a suitable option. On this basis, the combination of steam reforming and partial oxidation as called autothermal reforming could be a better choice since it can minimize the requirement of an external heat for the reaction. Nevertheless, the optimum inlet hydrocarbon, steam and oxygen ratios to operate this reaction efficiently have still been under investigation. For instance, Hoang et al., 2005 [4]; Ding et al., 2008 [5]; and Halabi et al., 2008 [6] studied the effect of several operating parameters e.g. pressure, and oxygen to carbon ratio (O/C) on the behavior of a packed bed designed autothermal reformer fueled by methane. They revealed that the hot spot usually occurs at the entrance of the reformer. The simulation results by Hoang et al., (2005) [4] indicated that the oxidation reaction generally occurs faster than the steam reforming; hence the system temperature initially increases due to the heat supply from the oxidation reaction before drops down due to the heat utilization by the steam reforming. Gudlavalleti et al., 2007 [7] presented that the temperature deviation occurred in the system strongly affects the service life of the reforming catalyst. Ding et al., (2008) [5] suggested that the steady state operation can be achieved rapidly when the radius of reactor is reduced but this parameter insignificantly influences the methane conversion and hydrogen yield. Previously, Lim et al., 2005 [8] applied the concept of autothermal reforming with high temperature IIR-SOFC modeling and indicated the benefit in term of temperature gradient reduction. Nevertheless, the effect of operating parameters on the system performance has not been considered in that study.

In the present work, a set of mathematical models was developed with an aim to predict the behaviors (i.e. cell performance and temperature gradient) of a tubular-design IT-SOFC with indirect internal reforming operation fueled by methane. The autothermal reforming was applied at the internal reformer and the operating temperature was maintained above 973 K since it was reported to be the minimum operating temperature of Ni/YSZ (SOFC anode) with expectable activity [9,10]. The developed model was coded in COMSOL® program within 2-D axial dimension application and the effect of operating conditions (i.e. inlet oxygen to carbon ratio, inlet steam to carbon ratio and gas flow pattern) on the system performance was determined. From the simulations, the suitable operating conditions of this SOFC system were identified.

2. Mathematical models

2.1. Kinetic equations of autothermal reforming reactions

In the present work, the autothermal reforming reaction of methane over Ni-based catalyst was applied. The reaction is based on the combination of 4 main reactions including (1) total oxidation, (2) methane steam reforming reaction, (3) reverse methanation and (4) water gas shift reaction.

$$CH_4 + 2O_2 \Leftrightarrow CO_2 + 2H_2O \quad (1)$$

$$CH_4 + H_2O \Leftrightarrow CO + 3H_2 \quad (2)$$

$$CH_4 + 2H_2O \Leftrightarrow CO_2 + H_2 \quad (3)$$

$$CO + H_2O \Leftrightarrow CO_2 + H_2 \quad (4)$$

The intrinsic rate equations and parameters of reaction (1) were reported by Ayabe et al. (2003) [11], while those of reaction (2)–(4) were reported by Xu and Froment (1989) [12]. Under non-isothermal condition, the effects of heat convection in gas stream, heat of reactions, conductive heat transfers in the packed bed catalyst and radiation heat transfer between the solid cell and the packed bed were taken into account in the reforming model.

2.2. Model geometry

The schematic diagram of a tubular IIR-SOFC for this investigation is presented in Fig. 1. Ni-based catalyst was used for

the autothermal reforming process. The anode/electrolyte/cathode compositions of the SOFC system considered here are Ni-YSZ/YSZ/LSM-YSZ. According to this configuration, methane, steam, and oxygen are fed to the internal reformer, where the autothermal reforming takes place. In the present work, the plug flow along the flow channels was assumed. At the end of the reformer, this reformate gas is continuously fed back to the fuel channel of SOFC. Simultaneously, air is fed to the opposite flow direction through the air channel. All dimensions and physical properties of this SOFC system are based on several of previous publications [13–15] as summarized in Table 1.

2.3. *Model assumption and equations*

The IIR-SOFC model was developed as the smallest single unit cell taking into account the effect of temperature on gas distribution, reactant conversion, and charge transfer. Our developed models were based on the assumptions of (1) each section is considered as non-isothermal steady state condition, and (2) ideal gas behavior is applied to all gas components. Several equations were applied to simulate the concentration and temperature gradients along this tubular IIR-SOFC system. The details for these sets of equations are given in Tables 2 and 3 and the entire developed mathematical model was coded in the COMSOL® program within 2-D axial dimension application.

3. Results and discussion

3.1. *Modeling of IIR-SOFC with autothermal reforming*

Firstly, the model was simulated at a reference condition, from which the feed temperature and operating pressure were fixed at 973 K and 1 bar while the proportion of methane, water and oxygen in the inlet fuel was 1.0:2.0:0.2. This total inlet feed of 14.2 $cm^3\ s^{-1}$ was introduced to the internal reformer. To maintain the oxygen utilization at 25% in the cathode side, the inlet air flow rate into the cathode was 94.24 $cm^3\ s^{-1}$. As a reference case, the gas stream in the fuel channel flows countercurrently to the gas stream in the air channel. Under these conditions, the characteristic results for the defined reference cases i.e. the methane conversion, product gas distribution and temperature gradient along the IIR-SOFC are calculated as shown in Figs. 2 and 3.

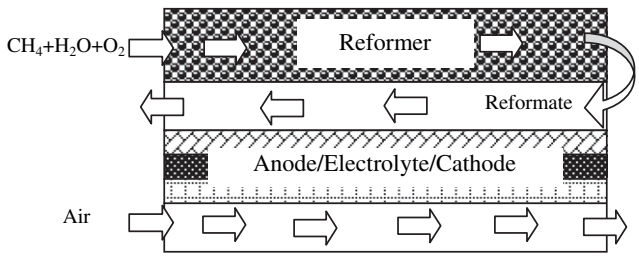

Fig. 1 – Schematic diagram of tubular-designed SOFC with indirect internal reforming operation.

Table 1 – Dimension and constant parameter values of a tubular IIR-SOFC system.

Parameters	Value	Reference
Fuel cell Length	0.60 m	[13]
Reformer radius	2×10^{-3} m	[13]
In side radius of the cell	5.4×10^{-3} m	[13]
Anode thickness	1×10^{-3} m	[13]
Electrolyte thickness	4×10^{-5} m	[13]
Cathode thickness	5×10^{-5} m	[13]
Anode permeability	1×10^{-12}	[14]
Cathode permeability	1×10^{-12}	[14]
Average density of triple phase	633.73 kg/m^3	[15]
Average specific heat of triple phase	574.3 J/kg/K	[15]
Anode thermal conductivity	6.23 W/m/K	[15]
Electrolyte conductivity	2.7 W/m/K	[15]
Cathode thermal conductivity	9.6 W/m/K	[15]
Convection coefficienct in the fuel channel	2987 $W/m^2/K$	[15]
Convection coefficienct in the air channel	1322.8 $W/m^2/K$	[15]

Fig. 2 presents the concentration profiles of methane, steam, hydrogen, carbon monoxide, carbon dioxide and oxygen in the reformer and the fuel channel. The concentration of oxygen decreases immediately at the entrance of the reformer whereas methane is slowly converted until it is completely consumed at the end of the reformer. Carbon dioxide is rapidly generated in the area of oxygen conversion due to the domination of methane oxidation reaction. Water is also generated and later consumed by the steam reforming reaction. As for the hydrogen concentration profile, it increases along the length of reformer owing to the existing of methane. At this operating condition, the outlet of reformer consists of 19.3% H_2O, 64.4% H_2, 12.8% CO and 3.5% CO_2. This gaseous product is continuously fed backward to the fuel channel. Then, H_2 and CO are consumed via electrochemical reaction at the anode and electrolyte interface, generating electricity along with H_2O and CO_2 as reaction by-products. It should be noted that the CO electro-oxidation is neglected in this study as it was reported that its reaction rate is much slower compared with that of H_2 electro-oxidation [16] and the rate of WGS reaction is fast particularly at high temperatures [17,18].

Fig. 3 shows the temperature profiles along the reformer, fuel and air channels of this IIR-SOFC system. It can be noticed that a slight local cold spot occurs at the entrance of the reformer with a temperature gradient along the system of 0.5 K cm^{-1}, within the acceptable range of temperature gradient as suggested by Lim et al., (2005) (10 K cm^{-1}) [8]. It is noted that the electrical efficiency predicted at this operating condition is 45.0%. For further investigation and improvement,

Table 2 – Steady state 2-D dimensional model for tubular packed bed reformer.

Mass Balance $\nabla\cdot(-D_i\nabla c_i + c_i\vec{v}) - \rho_B\sum\nu_i R_{reform} = 0$ (1)

Energy Balance $\nabla\cdot(\vec{v}\rho c_p T) - \nabla\cdot(\lambda_i\nabla T) + \sum\Delta H_{reform}R_{reform} = 0$ (2)

Boundary $z = 0; r \geq 0; U_r = 0, v_r = v_{r,in}, c_{i,r} = c_{r,in}, T_r = T_{r,in}$

$$r = r_r; z \geq 0; n\cdot(k\nabla T) = \lambda_{rf}(T_r - T_f) + \frac{\sigma A_s(T_r^4 - T_s^4)}{\frac{1}{\varepsilon_r} + \frac{A_r}{A_s}\left(\frac{1}{\varepsilon_s} - 1\right)}$$

Table 3 – Steady state 2-D dimensional model for tubular SOFC.

Fuel Channel

Mass balance $\nabla\cdot(-D_i\nabla c_i + c_i\vec{v}) - \sum \nu_i R_{elec} = 0$ (5)

Energy balance $\nabla\cdot(\vec{v}\rho c_p T) - \sum \nabla\cdot(\lambda_i \nabla T) = 0$ (6)

Boundary $z = L;\ r \geq 0;$ $U_f = U_r, v_f = v_r, p_f = p_r, c_{i,f} = c_{i,r}, T_f = T_r$

$r = r_r; z \geq 0;$ $n\cdot(k\nabla T) = h_{rf}(T_f - T_r)$

$r = r_f;\ z \geq 0;$ $n\cdot N_{H_2,f} = -J_{H_2}/2F,\quad n\cdot N_{H_2O,f} = J_{H_2}/2F,$

$n\cdot N_{CO,f} = -J_{CO}/2F,$

$n\cdot N_{CO_2,f} = J_{CO}/2F n\cdot(k\nabla T) = h_{fs}(T_s - T_f)$

Solid Cell

Energy balance $\nabla\cdot(\vec{v}\rho c_p T) - \nabla\cdot(\lambda_s\nabla T) + \sum \Delta H_{elec} + \frac{\sigma A_s(T_r^4 - T_s^4)}{\frac{1}{\varepsilon_r} + \frac{A_r}{A_s}(\frac{1}{\varepsilon_s} - 1)} = 0$ (7)

Boundary

Anode/electrolyte interface; $n\cdot(k\nabla T) = \sum \Delta H_{elec} R_{elec} + J(E - \eta_{total})$

$r = r_f; z \geq 0;$ $n\cdot(k\nabla T) = h_{fs}(T_s - T_f)$

$r = r_s; z \geq 0;$ $n\cdot(k_{sa}\nabla T) = \lambda_{sa}(T_a - T_s)$

Air channel

Mass balance $\nabla\cdot(-D_i\nabla c_i + c_i\vec{v}) = 0$ (8)

Energy balance $\nabla\cdot(\vec{v}\rho c_p T) - \sum \nabla\cdot(\lambda_i\nabla T) = 0$ (9)

Boundary $z = 0; r \geq 0;$ $u_a = 0, v_a = v_{a,in}, c_{i,a} = c_{a,in}, T_a = T_{a,in}$

$r = r_a; z \geq 0;$ $n\cdot N_{O_2,f} = -J_{O_2}/2F;\quad n\cdot(k\nabla T) = \lambda_{fs}(T_s - T_f)$

$r = r_a; z \geq 0$ $n\cdot(k\nabla T) = 0$

the effects of several operating parameters on the system performance were studied to optimize the suitable operating conditions for this IIR-SOFC system.

3.2. *Effect of oxygen to carbon (O/C) molar ratio*

Although an addition of oxygen along with methane and steam is beneficial for IT-SOFC system, the portion of inlet oxygen must be carefully concerned since it is well known that oxygen is a poisonous gas for anode material as well as the electrochemical reactions. Hence, it must be ensured that all added oxygen is completely converted in the internal reformer. In the present work, the effect of oxygen to carbon ratio on the thermal and electrochemical behaviors of this IIR-SOFC system was simulated by varying the O/C molar ratio from 0:1 to 1:1. The concentration profiles in the reformer and

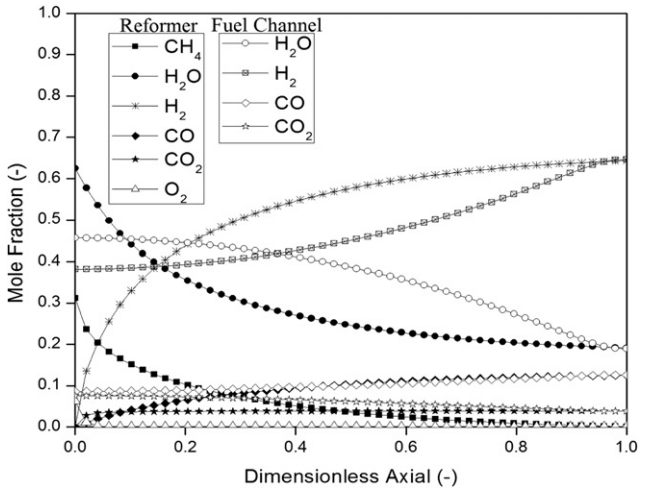

Fig. 2 – Concentration profile in the internal reformer of IIR-SOFC with autothermal operation (simulated at 1 bar with inlet C:S:O = 1.0:2.0:0.2).

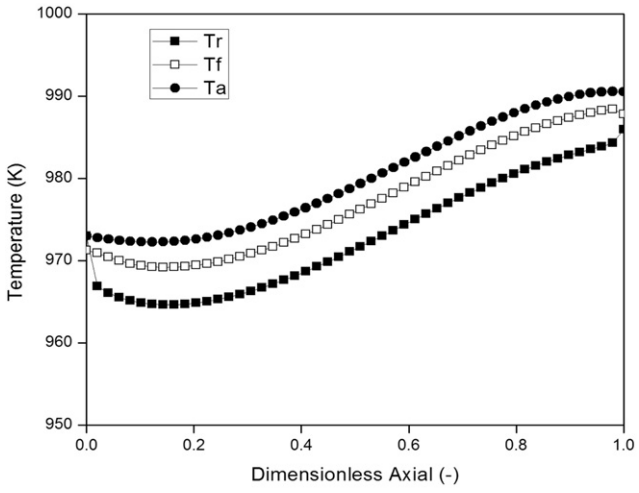

Fig. 3 – Temperature profiles in the internal reformer of IIR-SOFC (simulated at 1 bar with inlet CH_4:H_2O:O_2 = 1.0:2.0:0.2).

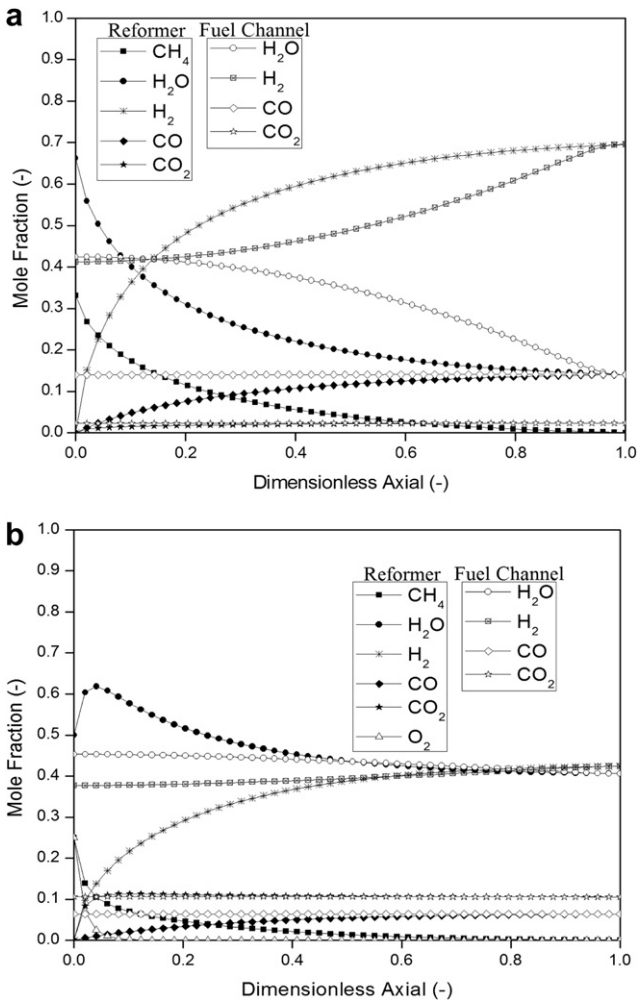

Fig. 4 – (a) Concentration profile in the reformer and fuel channel (CH_4:H_2O:O_2 = 1.0:2.0:0.0); and (b) Concentration profile in a reformer and a fuel channel (CH_4:H_2O:O_2 = 1.0:2.0:1.0).

the fuel channel at these O/C ratios are presented in Fig. 4 (a) and (b), respectively. Compared to Fig. 2 (reference case with O/C molar ratio of 0.2:1), it can be seen that the rate of methane conversion increases when oxygen is added. Nevertheless, the amount of hydrogen production oppositely decreased (particularly for the case with O/C molar ratio of 1:1, from which a significant amount of water is generated instead via the methane oxidation reaction). Fig. 5 presents the temperature distribution in the reformer at different O/C molar ratios (0:1, 0.2:1 and 1:1). Apparently, the local cooling temperature decreases with increasing O/C molar ratio since higher energy is supplied from the exothermic oxidation reaction. The maximum temperature gradient and the electrical efficiency achieved for each case are summarized in Fig. 6. Although the maximum temperature gradient is considerably low when a high amount of oxygen (O/C molar ratio of 1:1) is added, the electrical efficiency dramatically drops down to 20% due to the low hydrogen generated from the reformer. This result reveals that an addition of oxygen along with methane and steam is good for stabilizing the

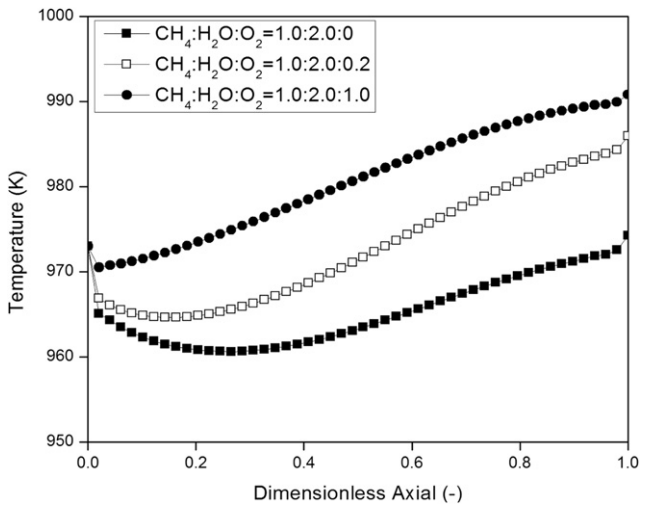

Fig. 5 – Effect of O/C on the temperature profile of reformer for IIR-SOFC with autothermal operation.

temperature of the system and preventing the SOFC stack cracking problem [7]; however, it also causes the reduction of electrical efficiency. Hence, it is suggested here that only a small amount of oxygen (i.e. with O/C molar ratio of 0.2:1) should be added along with the primary fuel to improve the temperature distribution of the system with a slight deactivation in electrical efficiency achievement.

3.3. *Effect of inlet steam to carbon (S/C) molar ratio*

Regarding the autothermal reforming operation, some inlet methane is reacted with oxygen; hence it is possible to reduce the amount of excess steam for the methane steam reforming reaction. Theoretically, the use of low inlet steam can reduce the quantity of heat required to generate steam via vaporizing and eventually increases the overall system performance. Therefore, the effect of inlet S/C molar ratio on the performance

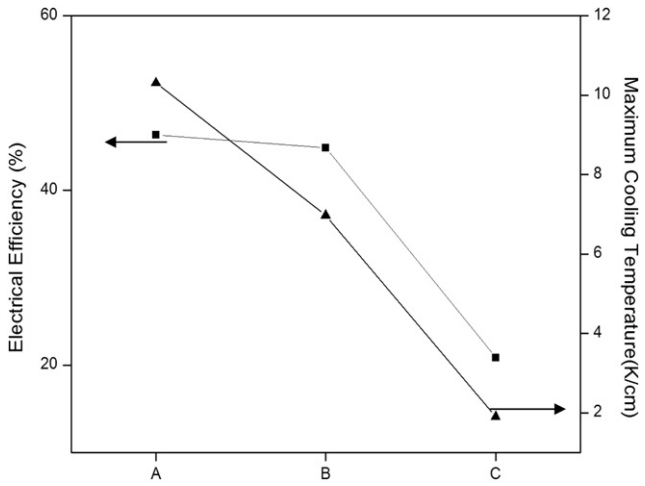

Fig. 6 – Effect of oxygen addition on electrical efficiency achieved from IIR-SOFC system (A: CH_4:H_2O:O_2 = 1.0:2.0:0.0, B: CH_4:H_2O:O_2 = 1.0:2.0:0.2, C: CH_4:H_2O:O_2 = 1.0:2.0:1.0).

of IIR-SOFC was simulated in the present work by varying the inlet S/C molar ratios (0.7:1, 1:1, 1.5:1 and 2:1) while keeping the inlet O/C molar ratio constant at 0.2:1. Fig. 7 presents the influence of inlet S/C molar ratio on the temperature behaviors of the reformer and the fuel channel (anode side), while Fig. 8 shows its effect on the electrical efficiency achievement. It was found that the cooling spot decreased when the low inlet S/C ratio was applied whereas the electrical efficiency oppositely increased particularly when decreasing the inlet S/C ratio from 2:1 to 1.5:1. This could be due to the fact that, in the presence of high steam content, the strong endothermic steam reforming reaction easily takes place, which leads to the occurrence of a cooling spot at the entrances of the reformer and fuel channel as well as the low temperature distribution along the system (particularly for the case with inlet S/C ratio of 2/1); this low temperature distribution can cause the higher polarizations of the SOFC. Furthermore, the presence of high steam content dilutes the hydrogen concentration generated from the reformer, which consequently reduces the exothermic electrochemical reaction and eventually decreases the electrical efficiency achievement. Therefore, we suggested that, to maximize the performance of this IIR-SOFC system, low inlet S/C ratio must be applied; nevertheless, possible carbon deposition from the cracking of methane must be carefully aware.

3.4. *Effect of operating temperature*

Since the methane oxidation is an exothermic reaction, it is thermodynamically favored at lower operating temperature. This is in contrast with the electrical properties of SOFC which prefers higher operating temperature in order to reduce the cell polarizations. Therefore, the effect of operating temperature was considered in this present work. Fig. 9 presents a temperature profile of the reformer while Fig. 10 shows the electrical efficiency achievement at different operating temperatures (973 K, 1073 K and 1173 K). It can be seen that, at lower operating temperature, the temperature distribution is smoother than that of high operating temperature. However, the electrical efficiency is relatively low.

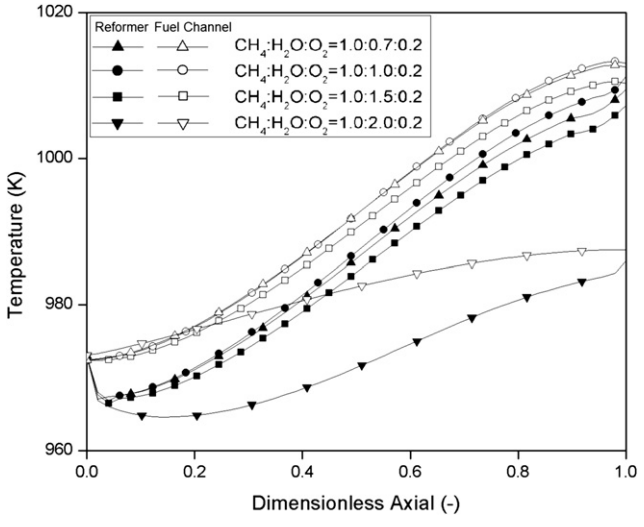

Fig. 7 – Effect of S/C on the temperature profiles of reformer and fuel channel for IIR-SOFC with autothermal operation.

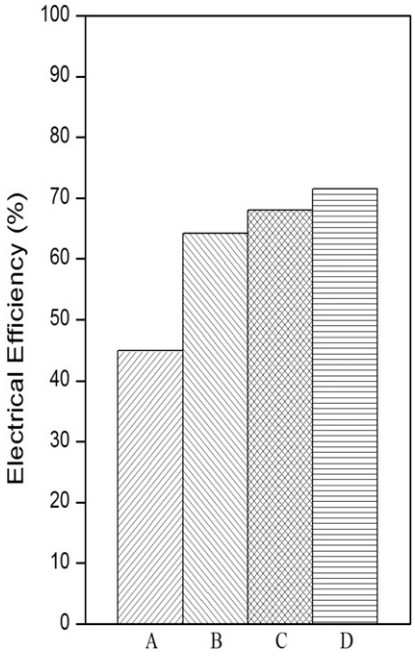

Fig. 8 – Effect S/C on electrical efficiency achieved from IIR-SOFC with autothermal operation (A: CH_4:H_2O:O_2 = 1.0:0.7:0.2, B: CH_4:H_2O:O_2 = 1.0:1.0:0.2, C: CH_4:H_2O:O_2 = 1.0:1.5:0.2, D: CH_4:H_2O:O_2 = 1.0:2.0:0.2).

3.5. *Effect of flow direction*

Theoretically, as for a typical heat exchanging system, the flow direction of exchanged fluids strongly affects the heat transfer and reaction behavior in the fluid stream, thus the effect of fuel gas and oxidant gas flow direction on the IIR-SOFC performance was also considered here. Alternatively to the reference case, the system behavior was analyzed as a co-flow pattern by changing the momentum, mass and energy balances in air channel together with their related boundary

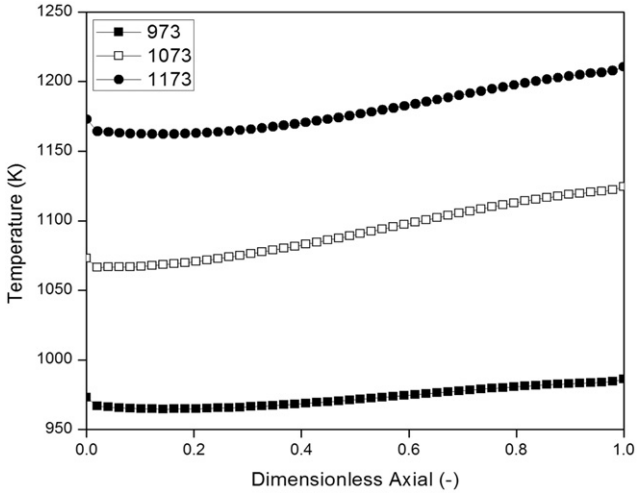

Fig. 9 – Effect of operating parameter on the temperature profile of reformer for IIR-SOFC with autothermal operation.

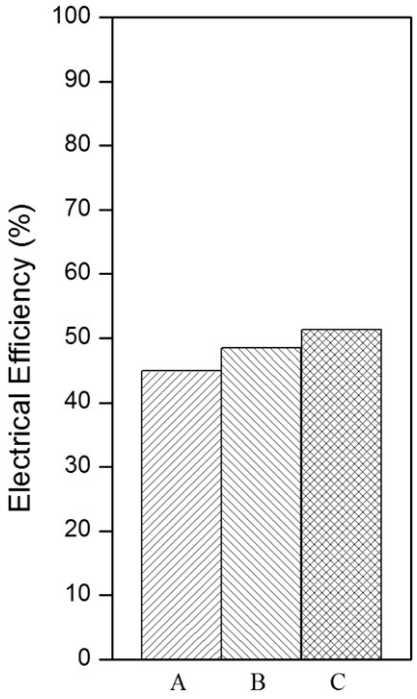

Fig. 10 – Effect of operating parameter on electrical efficiency achieved from IIR-SOFC with autothermal operation (A = 973 K, B = 1073 K, C = 1173 K).

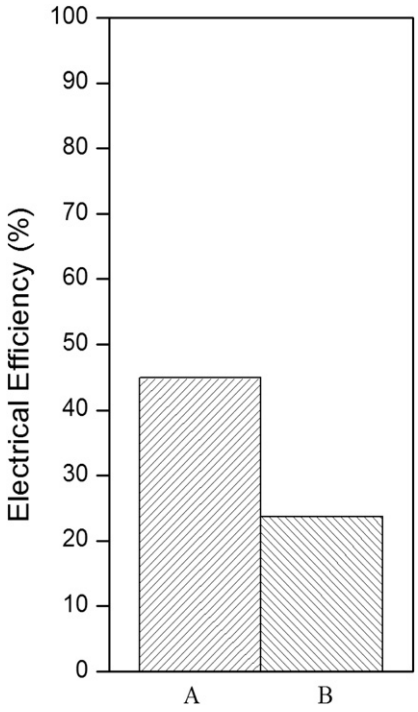

Fig. 12 – Comparison of electrical efficiency of IIR-SOFC with different gas flow pattern. (A = counter flow, B = Co-flow).

conditions while keeping all other operating conditions identical to those of the counter-flow pattern (reference case). Fig. 11 presents the temperature distribution in the reformer, fuel channel and air channels for this IIR-SOFC operated as a co-flow pattern across SOFC. It can be seen that the temperature increases until the approximate center of the system before dropping down at the second-half of the system. Compared with the counter-flow operation (Fig. 3), it is clear that the temperature distribution of these two gas flow patterns is dissimilar due to different initial heat generation

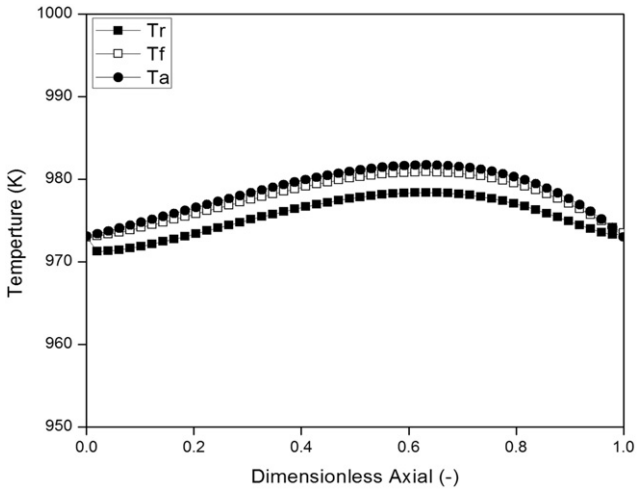

Fig. 11 – Temperature profiles in the internal reformer of IIR-SOFC reformer operated under co-flow pattern (simulated at 1 bar with inlet CH_4:H_2O:O_2 = 1.0:2.0:0.2).

positions which is strongly controlled by the oxidant flow direction. For the counter-flow operation, the temperature increases along the flow direction due to heat accumulation along SOFC and the maximum temperature presents at the end of the system. For the case of co-flow configuration, heat is generated as soon as the fuel gas is fed into the fuel channel ($z = 1$) and then accumulated along the air stream until reaching the entrance of the reformer ($z = 0$) where heat is extremely consumed. Therefore, the temperature at the two ends of IIR-SOFC is lower than that at the estimated center of the system. From the simulation, it was indicated that the average temperature of the co-flow configuration is lower than that of the counter-flow, which is not practical for electrical properties of the cell. Consequently, as shown in Fig. 12, the lower electrical efficiency can be obtained from the co-flow pattern.

4. Conclusions

The simulation of a tubular-design intermediate temperature IIR-SOFC indicated that the smoother temperature gradient with a slight drop in electrical efficiency can be achieved by adding a small amount of oxygen (with inlet oxygen to carbon (O/C) molar ratio of 0.2:1) along with methane and steam autothermal reforming. Another benefit of an oxygen addition is the reduction of excess steam requirement, which could reduce the quantity of heat required for the steam generation unit and eventually increases the overall system performance. By increasing the operating temperature, the system efficiency increases but a significant temperature gradient

also occurs. The SOFC system with counter-flow and co-flow patterns were compared, the later provided smoother temperature gradient along the system due to better matching between the heat supplied from the electrochemical reaction and the heat required for the steam reforming reaction; but the electrical efficiency achievement is lower due to the greater cell polarization at lower system temperature.

Acknowledgements

The financial support from the Thailand Research Fund (TRF) and Commission on Higher Education, and the Thailand Graduate Institute of Science and Technology (TGIST) program, Thailand's National Science and Technology Development Agency (NSTDA), grant no. TG-55-20-50-058D throughout this project is gratefully acknowledged. The authors would like to acknowledge Dr. John T.H. Pearce for the English correction of this manuscript.

REFERENCES

[1] Park H-K, Lee Y-R, Kim M-H, Chung G-Y, Nam S-W, Hong S-A, et al. Studies of the effects of the reforming in an internal-reforming molten carbonate fuel cell by mathematical modeling. J Power Sources 2002;104:140–7.
[2] Aguiar P, Chadwick D, Kershenbaum L. Modelling of an internal reforming solid oxide fuel cell. Chem Eng Sci 2002; 57:1665–77.
[3] Dokamaingam P, Assabumrungrat S, Soottitantawat A, Sramala I, Laosiripojana N. Modeling of SOFC with indirect internal reforming operation: comparison of conventional packed-bed and catalytic coated-wall internal reformer. Int J Hydrogen Energy 2009;34:410–21.
[4] Hoang DL, Chan SH, Ding OL. Kinetic and modelling study of methane steam reforming over sulfide nickel catalyst on a gamma alumina support. Chem Eng J 2005; 112:1–11.
[5] Ding OL, Chan SH. Autothermal reforming of methane gas–modelling and experiment validation. Int J Hydrogen Energy 2008;33:633–43.
[6] Halabi MH, Croon MHJM, Schaaf JVD, Cobden PD, Schoten JC. Modeling and autothermal reforming of methane to hydrogen in a fixed bed reformer. Chem Eng Sci 2008;137: 568–78.
[7] Gudlavalleti S, Ros T, Lieftink D. Thermal sintering studies of an autothermal reforming catalyst. Appl Catal B 2007;74: 251–60.
[8] Lim LT, Chadwick D, Kershenbaum L. Achieving autothermal operation in internally reformed solid oxide fuel cells: simulation studies. Ind Eng Chem Res 2005;44:9609–18.
[9] Kim SD, Moon H, Hyun SH, Moon J, Kim J, Lee HW. Performance and durability of Ni-coated YSZ anodes for intermediate temperature solid oxide fuel cells. Solid State Ionics 2006;177:931–8.
[10] Souza S, Visco SJ, Jonghe LCD. Thin-film solid oxide fuel cell with high performance at low-temperature. Solid State Ionics 1997;98:57–61.
[11] Ayabe A, Omoto H, Utaka T, Kikuchi R, Sasaki K, Teraoka Y, et al. Catalytic autothermal reforming of methane and propane over supported metal catalysts. Appl Catal A 2003; 241:261–9.
[12] Xu J, Froment GF. Methane steam reforming, methanation and water-gas shift: I. intrinsic kinetics. AIChE J 1989a;35: 88–96.
[13] Zhu H, Colclasure AM, Kee RJ, Lin Y, Barnett SA. Anode barrier layers for tubular solid-oxide fuel cells with methane fuel streams. J Power Sources 2006;161:413–9.
[14] Costamagna P, Selimovic A, Borghi MD, Agnew G. Electrochemical model of the integrated planar solid oxide fuel cell (IP-SOFC). Chem Eng J 2004;102:61–9.
[15] Xue X, Tang J. Dynamic modeling of single tubular SOFC combining heat/mass transfer and electrochemical reaction effects. J Power Sources 2005;142(1–2):211–21.
[16] Khaleel MA, Lin Z, Singh P, Surdoval W, Collin D. A finite element analysis modeling tool for solid oxide fuel cell development: coupled electrochemistry, thermal and flow analysis in MARC®. J Power Sources 2004;130:136–48.
[17] Blom R, Dahl IM, Slagtem A, Sortland B, Spjelkavik A, Tangstad E. Carbon dioxide reforming of methane over lanthanum-modified catalysts in a fluidized-bed reactor. Catal Today 1994;21:535–43.
[18] Bradford MCJ, Vannice MA. Catalytic reforming of methane with carbon dioxide over nickel catalysts II. Reaction kinetics. Appl Catal A Gen 1996;142:97–122.

Nomenclature

C_P: Specific heat of the gas streams, kJ/mol/K
A_{act}: external catalyst surface area $= \frac{\pi(d_r - 2\tau_{cat})L}{\pi(d_r^2 - (d_r - 2\tau_{cat})^2)L}$
c_i: Concentration, mol/m^3
$D_{i,j}$: Binary diffusion, m^2/s
$D^e_{i,mix}$: The effective molecular diffusivity, m^2/s
$D_{i,ku}$: The Kundsen diffusivity, m^2/s
d_p: Pore diameter, m
E: Open circuit voltage, V
E_{act}: Activation energy, kJ/mol
F: Faraday's constant, 96,487 C/mol
ΔH: The change of heat of reaction, kJ/mol
j_0: Exchange current density, mA/cm^2
j: Current density, mA/cm^2
j_{H_2}: Current density from hydrogen oxidation reaction, mA/cm^2
h: Heat transfer coefficient, kJ/m/s/K
k: Thermal conductivity, kJ/m/s/K
N_i^D: The bulk molar diffusive flux of gas component, mol/m s
p^o: Standard partial pressure, bar
p_i: Partial pressure of species i,
R: Universal gas constant; 8.314 J/mol K
R_{elect}: The hydrogen oxidation reaction rate, mol/m^2 s
q_{rad}: The heat flux from radiation,W/m^2
S_{act}: Specific surface area of catalyst
T: Temperature, K
u: Fluid velocity, m/s
y_i: The mole fraction of gas

Greek letters

ρ: Density, kg/m^3
γ: Special diffusion volume
ϑ: Exchange current density constant, mA/cm^2
$\alpha_{a,c}$: Charge transfer coefficient of anode and cathode
σ: Stefan-Boltzmann coefficient
ε: Porosity
τ: Tortuosity
η_{cell}: Voltage drop of the whole cell, Volts
λ: thermal conductivity (kJ/m/s/K),

Superscripts

*: Active site

Subscripts

a: Air channel
i: Component (methanol, water, hydrogen, etc.)
j: Reaction (SRM, WGS, etc.)
f: Fuel channel
s: Solid oxide fuel cell

Act: Activation losses
Cell: Cell stack
Con: Concentration losses
ohm: Ohmic losses
elec: Electrochemical reactions
reform: Reforming

ภาคผนวก 20

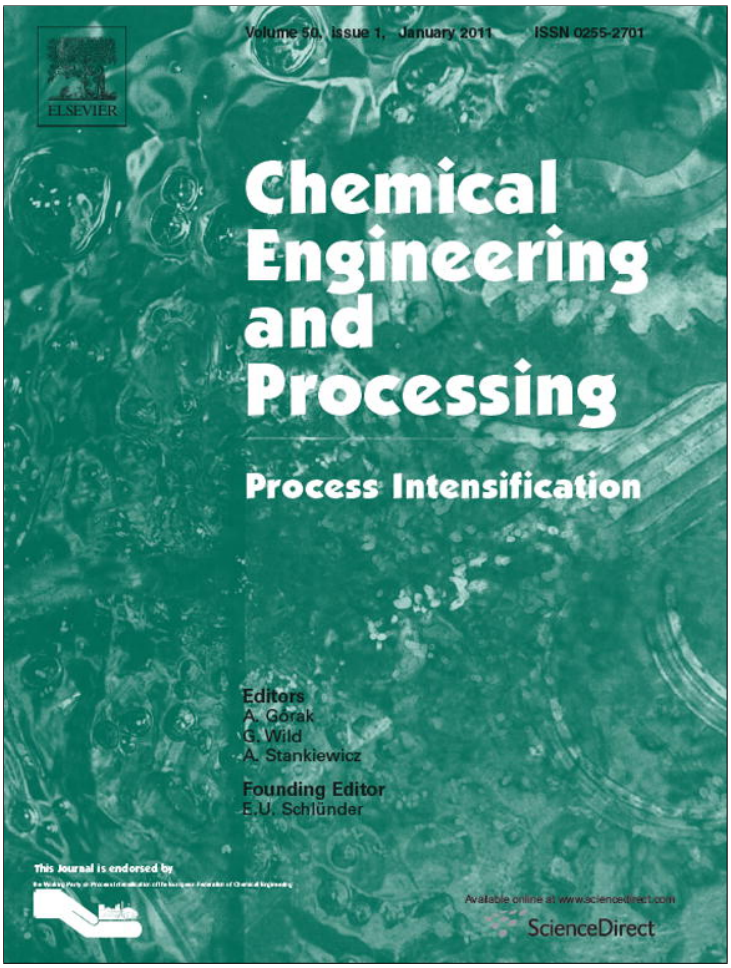

Chemical Engineering and Processing 50 (2011) 53–58

Contents lists available at ScienceDirect

Chemical Engineering and Processing: Process Intensification

journal homepage: www.elsevier.com/locate/cep

Partial oxidation of benzene catalyzed by vanadium chloride in novel reaction–extraction–regeneration system

Garun Tanarungsun[a], Hiroshi Yamada[b,*], Tomohiko Tagawa[b], Worapon Kiatkittipong[c], Piyasan Praserthdam[a], Suttichai Assabumrungrat[a]

[a] Center of Excellence in Catalysis and Catalytic Reaction Engineering, Department of Chemical Engineering, Faculty of Engineering, Chulalongkorn University, Bangkok 10330, Thailand
[b] Department of Chemical Engineering, Nagoya University, Chikusa, Nagoya 464-8603, Japan
[c] Department of Chemical Engineering, Faculty of Engineering and Industrial Technology, Silpakorn University, Nakhon Pathom 73000, Thailand

ARTICLE INFO

Article history:
Received 20 November 2009
Received in revised form
10 November 2010
Accepted 11 November 2010
Available online 19 November 2010

Keywords:
Benzene
Partial oxidation
Bi-phase system
Reaction–extraction–regeneration system
Hydroxylation

ABSTRACT

This paper investigates the liquid-phase partial oxidation of benzene to phenol in a novel system consisting of reactor, extractor and regenerator. Since vanadium catalyst (V^{3+}) is oxidized in the reactor and therefore deactivated, the regenerator with Pd or Pt catalyst and H_2 feed is employed to regenerate the deactivated vanadium. The V^{4+} ion can be reduced to V^{3+} and consequently the phenol production can be enhanced. Although the regenerator can regenerate vanadium catalyst and the reaction can proceed for over 100 h, some V^{4+} is still present. The feed position of benzene and catalyst solution have the influence on mixing condition in the reactor and interface area between benzene and catalyst solution. Counter current flow operation with the feeds of catalyst solution and benzene at the top and the bottom respectively shows the highest phenol production. The operating temperature of reactor, extractor and regenerator showed insignificant effect on phenol production rate.

1. Introduction

Phenol is commercially produced by the indirect-multistage cumene process which produces equimolar acetone as a by-product. Due to this disadvantage, the direct oxidation of benzene to phenol under mild conditions is desired. Many kinds of transition metal catalysts such as Cu, V, Fe, Pd and Pt have been investigated for the direct oxidation with molecular oxygen and hydrogen [1–7]. Vanadium is one of the most popular catalysts for hydroxylation of benzene to phenol.

Miyake et al. [6] investigated the influence of metal salts on hydroxylation of benzene to phenol with oxygen and hydrogen. Among several of cation metal species, most species retarded the reaction while only vanadium, iron, lanthanum, and yttrium vanadium enhanced the phenol production especially vanadium showed an outstanding performance. And vanadium acetylacetonate, $V(acac)_3$, showed the highest activity among the various vanadium compounds, i.e., $VO(acac)_2$, VCl_3, $VOCl_2$, NH_4VO_3, VOC_2O_4, $VOSO_4$, VCl_3. It was speculated that vanadium compounds having vanadyl group V=O was effective for the reaction. Ascorbic acid was a good reducing agent for this system. Masumoto et al. [2] employed $VO(C_5H_7O_2)_2$ supported on SiO_2, TiO_2 and Al_2O_3 for phenol production. The Al_2O_3 showed the best reaction performance and the lowest percent leaching of V. With ascorbic acid added, the oxidation state of vanadium was changed from V^{5+} to V^{4+}, improving the yield of phenol. Therefore it can be concluded that V^{4+} was more effective than V^{5+}. Among various vanadium catalysts studies, e.g., $VOSO_4{\cdot}5H_2O$, VCl_3, $VO(C_5H_7O_2)_2$, NH_4VO_3 and V_2O_5, $VO(C_5H_7O_2)_2$, NH_4VO_3 gave a maximum yield.

Murata et al. [8] used Pd and transition metal-modified ZrO_2, SiO_2 and Al_2O_3. The V with Pd showed the highest yield of phenol production. The study of various vanadium compounds on the Al_2O_3 showed that $VOCl_3$ and VCl_3 gave high yield of phenol but low selectivity. Vanadium oxide catalysts supported on clay showed high selectivity with a conversion of 14%. Comparing among various transition metal oxides, i.e. Cu, Cr, Fe, V, Mn, W, Mo, vanadium was most suitable for hydroxylation of benzene to phenol. V–O–Al and V–O–Si bridges in the catalyst may be responsible for the reaction [9]. Among the various reducing agents, e.g., ascorbic acid, dithiothreitol and 2-mercaptoethanol, ascorbic acid offered the highest selectivity and reactivity for phenol production. V^{4+} species was rapidly formed in the reaction medium after the initial addition of VCl_3 [10].

Tanarungsun et al. [11,12] studied the hydroxylation of benzene with H_2O_2 using various transition metal catalysts (Cu, V, Fe) supported on TiO_2 support. The results showed that the added

* Corresponding author. Tel.: +81 52 789 4529; fax: +81 52 789 3387.
E-mail address: yamada@nuce.nagoya-u.ac.jp (H. Yamada).

0255-2701/$ – see front matter © 2010 Elsevier B.V. All rights reserved.
doi:10.1016/j.cep.2010.11.006

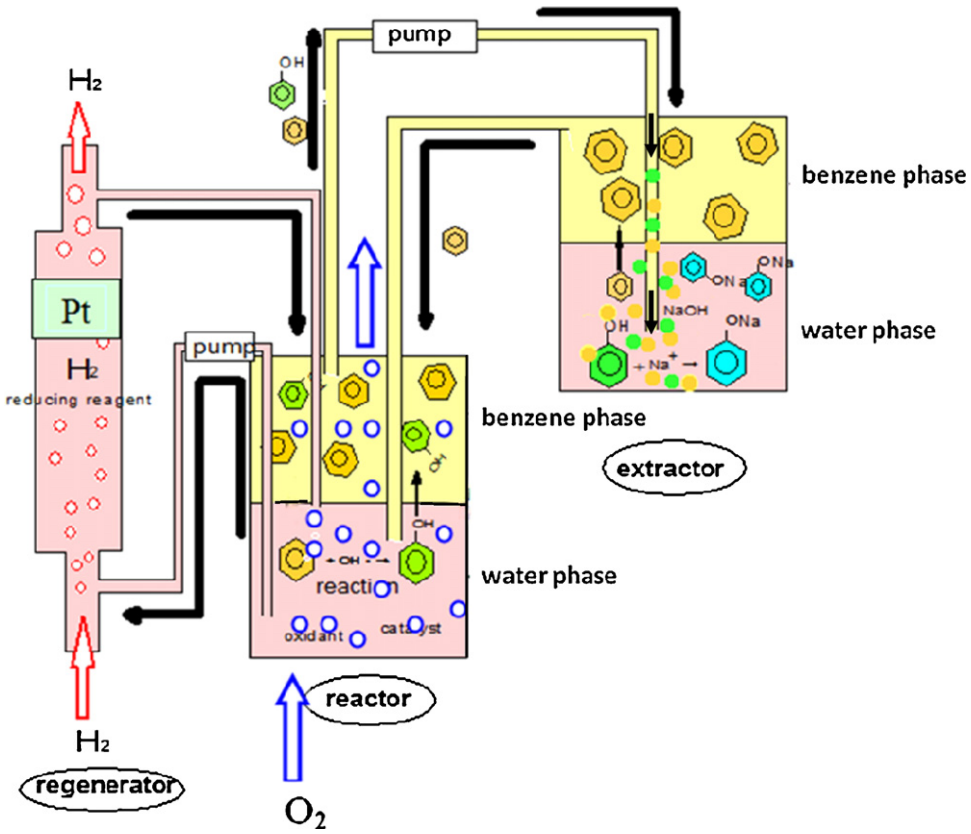

Fig. 1. The reaction–extraction–regeneration system.

vanadium in the Fe/TiO_2 can improve the activity of catalyst to produce phenol. The use of Pt or Pd second metal catalyst can also improve the activity of Fe catalysts and improve the phenol selectivity [13]. The ternary metal catalyst including Cu, V and Fe metal catalysts could improve the overall activity to phenol and the ratio of Cu, V and Fe showed the effect on phenol yield and phenol selectivity [14,15].

Mizuno et al. [16] studied the benzene–water bi-phase system with Fe–H_2O_2 and V–O_2 catalyst and compares the non-circulation and circulation by CSTR reactor. Benzene was oxidized to phenol in water. An extractor containing aqueous alkaline was used to separate phenol from the reactor. Installing an extractor into the reaction system improved the selectivity to phenol in both catalyst systems. Yamada et al. [17] studied the regeneration of vanadium catalyst by using H_2 reductant in the benzene–water bi-phase system operated in a CSTR reactor. The system can be operated with good stability and the phenol yield was increased depending on the operating time.

In this paper, the liquid-phase oxidation of benzene to phenol in the benzene–water bi-phase system is further improved by applying a novel three bubble column system. The influence of the position of benzene and catalyst solution feed in reactor, the type and the amount of regenerator catalyst, reaction time, feed flow rate of benzene and VCl_3 catalyst, the operating temperature of reactor, regenerator and extractor were investigated.

2. Experimental

2.1. Standard operating system

Three bubble jacket columns were used as reactor, extractor and regenerator as shown in Fig. 1. The standard conditions for operating the reaction–extraction–regeneration system were summarized as follows:

Reactor. Benzene (1.5×10^{-4} m^3) and aqueous catalyst solution (3×10^{-4} m^3 with a VCl_3 concentration of 10 mol/m^3) were placed in the reactor where oxygen gas with a bubble size of 1 mm (3×10^{-5} m^3/min) was continuously introduced into the reactor. The reactor was operated at a temperature of 40 °C.

Extractor. Benzene (5×10^{-5} m^3) and aqueous alkaline solution (1.25×10^{-4} m^3 with a NaOH concentration of 172 mol/m^3) were placed in an extractor. The extractor was operated at a temperature of 50 °C. Benzene was circulated from the extractor to the reactor by using a circulation pump with a constant flow rate of 3.0×10^{-5} m^3/min.

Regenerator. The aqueous VCl_3 catalyst solution (3.0×10^{-4} m^3) was continuously circulated with hydrogen gas (3.0×10^{-5} m^3/min). Pt metal (0.047 m^2) was used for regenerating the oxidized vanadium catalyst. The other circulation pump was used to circulate the aqueous solution between the reactor and the regenerator. The flow rate was set at 5.0×10^{-5} m^3/min. The regenerator was operated at a temperature of 60 °C.

It should be noted that there was no adding up of aqueous VCl_3 catalyst solution and NaOH solution during the performed experiment.

All chemicals used in this study were purchased from Wako Pure Chemical Industries, Ltd. No further purification was carried out.

2.2. Sample analysis

A small amount of organic phase mixture was periodically sampled and analyzed by gas chromatography (GC-353B, GL Sciences, Inc.) with hydrogen flame ionization detector. The analysis was performed by injecting 1 μl of sample in a CP-Sil 8CB capillary column of 25 m in length (J&W Scientific, Inc.). Helium was used as a carrier gas with a flow rate of 60 ml/min. The injector temperature and the detector temperature were set at 200 °C while the column temperature was 110 °C.

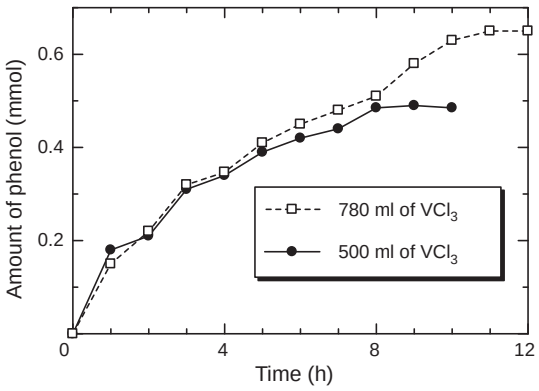

Fig. 2. Influence of the reaction time and amount of VCl_3 catalyst solution for the system without regeneration catalyst (●, 500 ml of VCl_3; □, 780 ml of VCl_3 catalyst solution).

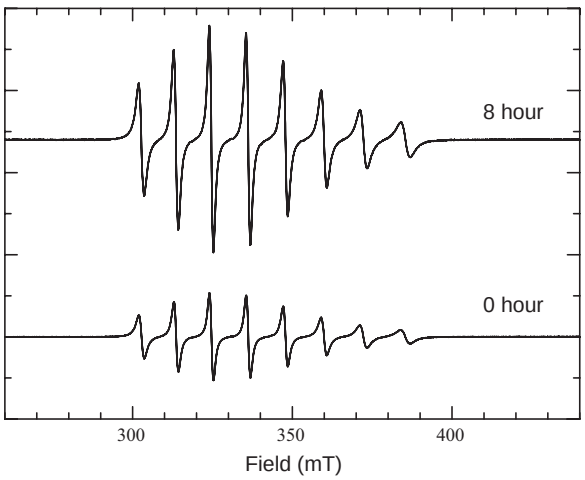

Fig. 3. ESR spectra of vanadium (III) chloride on the reaction.

2.3. Catalyst characterization

Electron spin configuration was detected by using electron spin resonance spectroscopy (ESR) (JEOL model JES-RE2X) with the frequency of 8.8–9.6 GHz. A sample was characterized in TE_{011} mode with ES-TPRIT program. FTIR spectra were recorded by a Nicolet impact 6700 instrument, using in the range of 650–4000 cm^{-1}.

3. Results and discussion

3.1. Effect of the amount of VCl_3 catalyst on phenol production of the system without regeneration catalyst

The reactions taking place in the reactor are summarized as follows:

$$\text{Benzene} + O_2 \rightarrow \text{Phenol} \quad (1)$$

$$2V^{3+} + O_2 + 2H^+ \rightarrow 2V^{4+} + 2OH^\bullet \quad (2)$$

$$V^{3+} + HO^\bullet \rightarrow VO^{2+} + H^+ \quad (3)$$

while the reaction in the extractor is as follow.

$$\text{Phenol} + \text{NaOH} \rightarrow \text{Sodium phenate} + H_2O \quad (4)$$

Sodium phenate could be converted back to phenol by reacting with sulfuric acid as industrialized by Sunoco/UOP process [18]. It should be noted that since sodium phenate could be converted to phenol with 100% yield, we prefer to use the term of "phenol" which is our desired product rather than "sodium phenate" in this study. The effects of amount of catalyst solution and circulation system were simultaneously investigated under the system configuration similar to Fig. 1 except that no Pt catalyst and H_2 gas feed to the regenerator. Therefore, in this part, the regenerator was used only as a circulation system without any reaction. Fig. 2 shows the amount of phenol production as a function of reaction time. The phenol production could not proceed after 8 h with 500 ml of VCl_3 solution. Phenol could be further produced with increasing the amount of VCl_3 solution i.e. 780 ml; however the phenol production was leveled off with 11 h of reaction time. The deactivated performance was due to the change of ion from V^{3+} to $V^{4+}$and VO^{2+} as observed by the change in color of the catalyst solution from green brown at start up to blue after 8 h and 11 h for 500 and 780 ml of VCl_3 catalyst solution respectively. This indicated that the regeneration unit for regenerating the deactivated catalyst is important for continuous operation of the system. It should be noted that vanadium ion has different colors for different oxidation states; i.e. V^{2+}, V^{3+}, V^{4+} and V^{5+} show purple, green, blue and yellow respectively [19].

Noted that VCl_3 dissolved in water is in a hexahydrate form, however, it does not exhibit the green color of V^{3+} because it changes the formula to $[VCl_2(H_2O)_4]Cl{\cdot}2H_2O$. Removal of the two bound chloride ligands from $[VCl_2(H_2O)_4]^+$ in aqueous solution gives the green ion $[V(H_2O)_6]^{3+}$ [19].

The vanadium ion species affect the oxidation reaction. Vanadium (III) which was not stable in the atmospheric pressure was oxidized to V^{4+} in the vanadyl form. V^{4+} vanadium species is particularly stable as the vanadyl ion (VO^{2+}) which is an isolated cation. This was confirmed by an additional ESR analysis. Note that V(III) and V(V) ions are ESR silent. The ESR spectra of the reaction mixture are presented in Fig. 3 at time zero and after 8 h of reaction. The observed eight-line spectrum is a characteristic of vanadyl V(IV)O species (^{51}V, $I = 7/2$) and in particular, it can be assigned to the $VOCl_2$ species [10]. The increase of ESR intensity at 8 h shows the increase in the amount of V^{4+}. FTIR results show the vanadyl complexes generally appearing at 985+/−50 $cm^{-1}$of the IR stretching frequency for the V=O which is corresponding well with that observed in this work at 1013 cm^{-1} (result was not shown here) [10].

3.2. Phenol production performance in the system with regeneration catalyst

As described in the previous section, V^{3+} of VCl_3 was oxidized to V^{4+} and VO^{2+} and the reaction was inferior. The reaction can be further extended by using Pt catalyst and a continuous flow of H_2 into the regenerator.

The reactions occurred in the regenerator are summarized as follows:

$$VO^{2+} + 0.5H_2 + H^+ \rightarrow V^{3+} + H_2O$$

$$V^{4+} + 0.5H_2 \rightarrow V^{3+} + H^+$$

As shown in Fig. 4, the reaction took place continuously without deterioration during 100 h. The system could be operated for more than 100 h as the amount of phenol increased progressively with the reaction time. With the use of Pt metal catalyst and H_2 feeding in the regenerator, the color of the catalyst solution was pale green-blue, which was different from the blue in the system with no regeneration. This might presume that VO^{2+}, V^{4+} and V^{3+} were always present in the reactor and the regenerator.

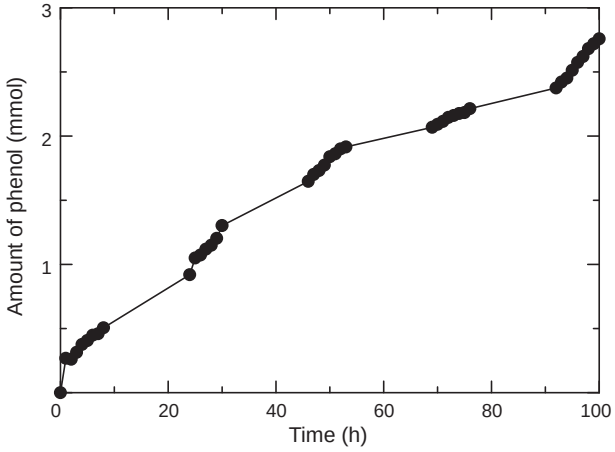

Fig. 4. Influence of the reaction time for the system with regenerator.

3.3. Effect of benzene and catalyst feed pattern on phenol production rate

Fig. 5 shows the effect of benzene and catalyst solution feed patterns on phenol production rate. Four feed patterns were investigated at the reaction time of 8 h.

1. Feed benzene and catalyst solution at the top of reactor (co-current operation).
2. Feed benzene bubble and catalyst solution at the bottom of reactor (co-current operation).
3. Feed benzene at the top of reactor and feed catalyst solution at the bottom of reactor (counter current operation).
4. Feed benzene bubble at the bottom of reactor and feed catalyst solution at the top of reactor (counter current operation).

As shown in Fig. 5, the counter current flow operation in case 4 showed the highest phenol production rate. This is because benzene and phenol products were the main components in the upper phase while VCl_3 catalyst solution was in the lower phase of the reactor. Therefore, feeding the benzene at the bottom and catalyst solution at the top of the reactor enhanced the mixing performance and reaction rate. In addition, in this case, benzene was possibly fed as small bubbles at the bottom of the column. This increased the surface area of contraction and, therefore, the reaction was pronounced.

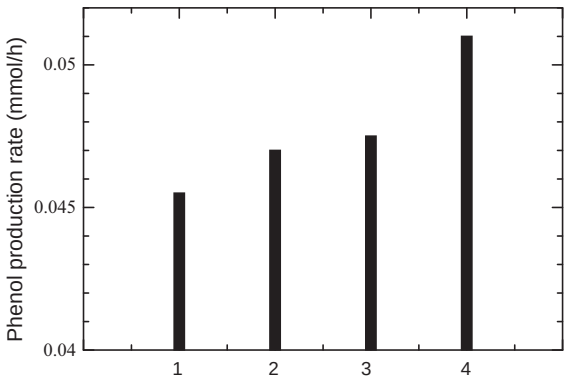

Fig. 5. Influence of the feed patterns on the phenol production rate.

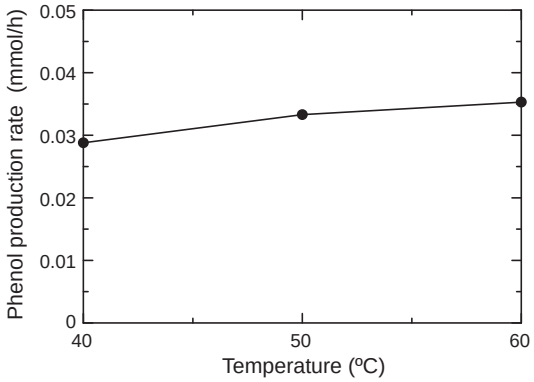

Fig. 6. Influence of the reactor temperature on the phenol production rate.

3.4. Effect of reactor temperature

To explore the effect of reactor temperature on the production rate of phenol, the temperature was varied from 40 to 60 °C while the other parameters were kept at the standard condition with a reaction time of 30 h. It should be noted that the change in the reactor temperature slightly affected the temperatures of regenerator and extractor. However, to investigate the effect of temperature of each section, the focus is therefore only on the section of the main contribution. The phenol production rate slightly increases with the increase of reactor temperature as shown in Fig. 6.

The reaction temperature influenced the amount of benzene dissolved in the catalyst solution phase and the amount of oxygen gas dissolved in the catalyst solution phase. As confirmed by gas chromatograph the increase of temperature from 40 to 60 °C increases the amount of benzene dissolved in the catalyst solution phase about 30%. However, the improvement of phenol production rate is just around 20%. This is because the amount of O_2 gas dissolved in the catalyst solution decreased with increasing temperature.

3.5. Effect of regenerator temperature

The phenol production rate was observed to increase around 7% after increasing temperature from 40 to 60 °C (Fig. 7). Although the regenerator temperature has a little effect on produced phenol, the regenerator is very important for the continuous system because it regenerates the deactivated catalyst in the system. At different Pt surface area, the phenol production rate could be improved but the phenol production rate was increased only 10% from 40 to 60 °C. The operating temperature of regenerator showed insignificant effect on the phenol production because the catalyst can be regenerated

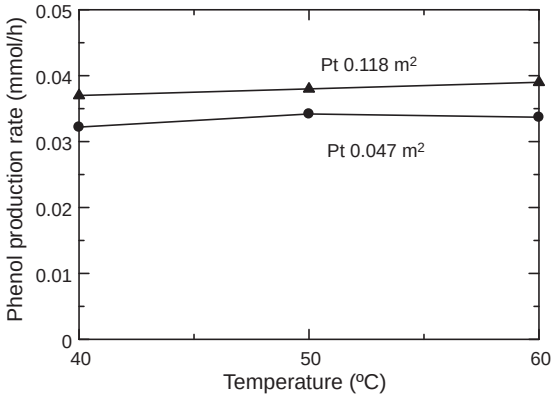

Fig. 7. Influence of the regenerator temperature on the phenol production rate with different surface areas of regeneration catalyst (●, 0.047 m^2 of Pt; ▲, 0.118 m^2 of Pt).

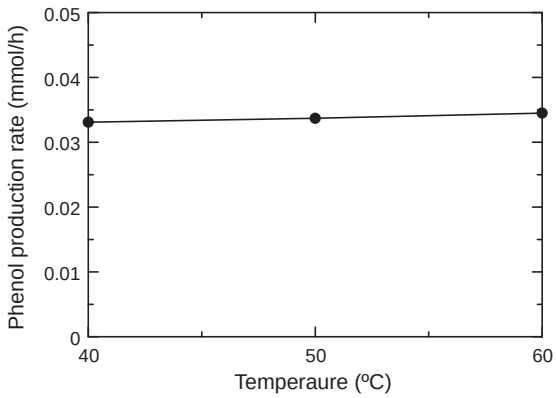

Fig. 8. Influence of the extractor temperature on the phenol production rate.

by Pt metal in short time at 40–60 °C.

3.6. Effect of extractor temperature

The influence of extractor temperature on the phenol production rate is shown in Fig. 8. The reaction in the extractor can be expressed as Phenol + NaOH = Sodium phenate + water. The extractor temperature did not have the pronounced effect on the phenol production as only 5% increase was observed when the temperature changes from 40 to 60 °C. The reaction limiting step should be the oxidation reaction because increasing the temperature increased the amount of phenol dissolved in the aqueous phase but the phenol production rate was constant.

3.7. Effect of the type of regenerator catalyst

Pt and Pd were well known catalysts for reducing the oxidation state of metal catalyst. Pt may give higher performance than Pd for hydroxylation of benzene to phenol because it can generate H_2O_2 from H_2 and O_2; however, Pt was more expensive than Pd. The activities of Pt and Pd for regenerating vanadium ion in the phenol production were shown in Fig. 9. The performance of Pd to regenerate vanadium catalyst may be comparable to that of Pt since similar phenol production rates were obtained. Noted that the colors of the catalyst solution were the same in all cases and this may imply that the vanadium states are merely the same. The surface area of regeneration catalyst has the effect of regeneration time for reduce catalyst. Increasing the metal surface area increased the phenol production rate.

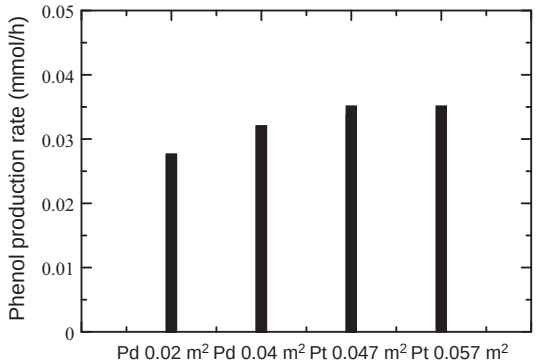

Fig. 9. Influence of the type of regeneration catalyst.

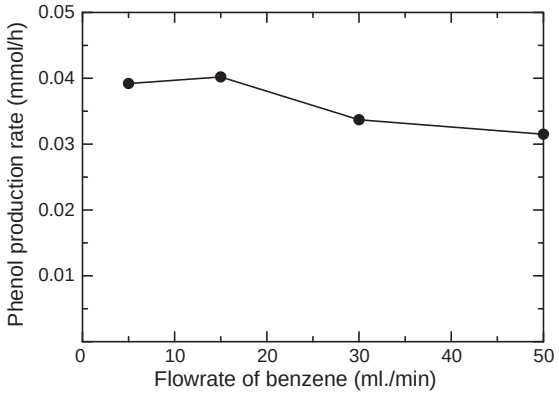

Fig. 10. Influence of the flow rate of benzene on the phenol production rate.

3.8. Effect of benzene flow rate

The dependence of the phenol production rate on the flow rate of benzene was investigated and the results are given in Fig. 10. The phenol production rate slightly decreased when the flow rate of benzene increased from 5 to 15 ml/min. Although the benzene was circulated within the reactor–extractor system and the residence time remained the same at different flow rates, the flow rate of benzene showed some influences on the overall reaction performance. It is likely that at a high flow rate of benzene, it became difficult to provide a good separation between NaOH aqueous solution and benzene within a short contact time within the extractor. Moreover, the benzene from the extractor when fed back to the reactor may be contaminated with NaOH and therefore resulted in the change in pH of the reaction mixture in the reactor.

3.9. Effect of catalyst solution flow rate

The phenol production rate versus catalyst flow rate is shown in Fig. 11. In the circulation system, the aqueous catalyst solution was circulated between the reactor and the regenerator. The flow rate of catalyst has the effect on mixing in the reactor. Because the reaction was carried out in a three phase system, degree of the mixing significantly influenced the interface area of the reaction. Increasing the catalyst flow rate increased the phenol production rate because it increased the interface area between benzene and catalyst solution. In addition, the deactivated catalyst can be efficiently regenerated in the regenerator.

In our previous work, the effects of O_2 and H_2 flow rates and benzene bubble size on the phenol production rate have been investigated [20]. The phenol production rate could be increased with

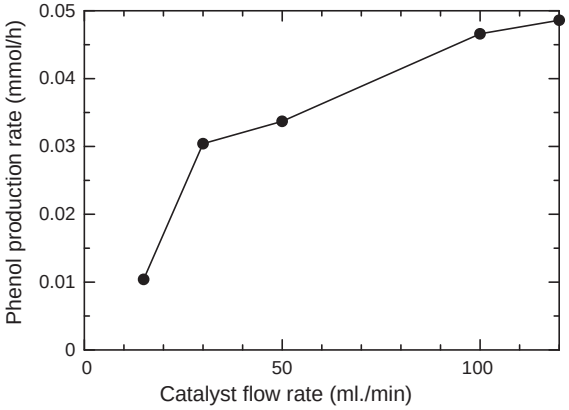

Fig. 11. Influence of the catalyst flow rate on the phenol production rate.

increasing O_2 and H_2 flow rates and/or decreasing benzene bubble size. In addition, as shown by the effect of benzene and catalyst solution flow rates in this study, it is obvious that there are mass transfer limitations in the reaction–extraction–regeneration system. Although the mass transfer limitation could not be totally eliminated, of course our study can suggest how to minimize them.

4. Conclusion

The combined system of reactor, extractor and regenerator was proposed in this study for the liquid-phase oxidation of benzene to phenol. Due to the catalyst deactivation, the regenerator was required for reducing the deactivated catalyst for the continuous operation. The regenerator was employed to regenerate the deactivated vanadium. The V^{4+} ion can be reduced to V^{3+} by using H_2 and Pt or Pd catalyst, as a result, phenol production could be enhanced. The feed position of benzene and catalyst solution have the influence on mixing condition in the reactor and interface area between benzene and catalyst solution. Counter current flow operation with the feeds of catalyst solution and benzene at the top and the bottom respectively showed the highest phenol production. The operating temperature of reactor, extractor and regenerator showed insignificantly effect on phenol product rate.

Acknowledgements

The supports from Mitsubishi Chemical Corp., The Thailand Research Fund and Commission on Higher Education are gratefully acknowledged.

References

[1] T. Miyahara, H. Kanzaki, R. Hamada, S. Kuroiwa, S. Nishiyama, S. Tsuruya, J. Mol. Catal. A 176 (2001) 141–150.
[2] Y. Masumoto, R. Hamada, K. Yokota, S. Nishiyama, S. Tsuruya, J. Mol. Catal. A 184 (2002) 215–222.
[3] K. Lemke, H. Ehrich, U. Lohse, H. Berndt, K. Jaehnisch, Appl. Catal. A 243 (2003) 41–51.
[4] H.A. Burton, I.V. Kozhevnikov, J. Catal. Mol. A 184 (2002) 285–290.
[5] N.I. Kuznetsova, L.I. Kuznetsova, V.A. Likholobov, G.P. Pez, Catal. Today 99 (2005) 193–198.
[6] T. Miyake, M. Hamada, H. Niwa, M. Nishizuka, M. Oguri, J. Mol. Catal. A 178 (2002) 199–204.
[7] Y. Liu, K. Murata, M. Inaba, Catal. Commun. 6 (2005) 679–683.
[8] K. Murata, R. Yanyong, M. Inaba, Catal. Lett. 102 (2005) 143–147.
[9] X. Gao, J. Xu, Appl. Clay. Sci. 33 (2006) 1–6.
[10] E. Battistel, R. Tassinari, M. Fornaroli, L. Bonoldi, J. Mol. Catal. A 202 (2003) 107–115.
[11] G. Tanarungsun, W. Kiatkittipong, S. Assabumrungrat, H. Yamada, T. Tagawa, P. Praserthdam, J. Chem. Eng. Jpn. 40 (2007) 415–421.
[12] G. Tanarungsun, W. Kiatkittipong, S. Assabumrungrat, H. Yamada, T. Tagawa, P. Praserthdam, J. Ind. Eng. Chem. 13 (2007) 444–451.
[13] G. Tanarungsun, W. Kiatkittipong, P. Praserthdam, H. Yamada, T. Tagawa, S. Assabumrungrat, Catal. Commun. 9 (2008) 1886–1890.
[14] G. Tanarungsun, W. Kiatkittipong, S. Assabumrungrat, H. Yamada, T. Tagawa, P. Praserthdam, J. Ind. Eng. Chem. 13 (2007) 870–877.
[15] G. Tanarungsun, W. Kiatkittipong, P. Praserthdam, H. Yamada, T. Tagawa, S. Assabumrungrat, J. Ind. Eng. Chem. 14 (2008) 596–601.
[16] T. Mizuno, H. Yamada, T. Tagawa, S. Goto, Partial oxidation of benzene in benzene–water bi-phase system, J. Chem. Eng. Jpn. 38 (2005) 849–853.
[17] H. Yamada, T. Mizuno, T. Tagawa, G. Tanarungsun, P. Praserthdam, S. Assabumrungrat, J. Jpn. Petro. Inst. 51 (2008) 114.
[18] R.J. Schmidt, Appl. Catal. A 280 (2005) 89.
[19] R.C. Young, M.E. Smith, Inorganic Syntheses, vol. IV, 1953, pp. 126.
[20] G. Tanarungsun, H. Yamada, T. Tagawa, W. Kiatkittipong, P. Praserthdam, S. Assabumrungrat, Chem. Eng. Commun. 197 (2010) 1140.

ภาคผนวก 21

INTERNATIONAL JOURNAL OF CHEMICAL REACTOR ENGINEERING

Volume 8 2010 *Article* A158

Thermodynamic Analysis for Gasification of Thailand Rice Husk with Air, Steam, and Mixed Air/Steam for Hydrogen-Rich Gas Production

Rajesh Kempegowda* Suttichai Assabumrungrat†

Navadol Laosiripojana‡

*King Mongkut's University of Technology Thonburi, rajeshsk76@gmail.com

†Chulalongkorn University, suttichai.a@chula.ac.th

‡King Mongkut's University of Technology Thonburi, navadol_l@jgsee.kmutt.ac.th

ISSN 1542-6580

Thermodynamic Analysis for Gasification of Thailand Rice Husk with Air, Steam, and Mixed Air/Steam for Hydrogen-Rich Gas Production*

Rajesh Kempegowda, Suttichai Assabumrungrat, and Navadol Laosiripojana

Abstract

Thermodynamic analysis of gasification with air, steam, and mixed air-steam was performed over rice husk to determine the optimum conditions (i.e., equivalence ratio (ER), steam to biomass ratio (SBR) and operating temperature) that can maximize the yield of hydrogen production with low energy consumption. It was found that for air gasification, H_2 production is always less than CO production and considerably decreased with increasing ER. For steam gasification, the simulation revealed that H_2 production is greater than CO, particularly at high SBR and low temperature; furthermore, H_2 yield increased steadily with increasing temperature and SBR until reaching SBR of 3.5-4.0, then the effect of steam on H_2 yield becomes less pronounced. As for the mixed steam/air gasification, H_2 production yield increased with increasing SBR, but decreased dramatically with increasing ER (up to 0.4). Among these three operations, the highest H_2 production yield can be achieved from the steam gasification with SBR of 4.0. Nevertheless, by considering the system efficiency, the combined air-steam gasification provided significant higher hydrogen production efficiency than the other two operations. The optimum condition for combined air-steam gasification can be achieved at 900°C with ER of 0.1 and SBR of 2.5, which provided the efficiency up to 66.5 percent.

KEYWORDS: gasification, biomass, hydrogen, thermodynamic analysis

*The financial support from the Thailand Research Fund (TRF) throughout this project is gratefully acknowledged.

1. Introduction

Energy and environment are currently the world's most concerns. Nowadays, it is known that the world energy consumption has been dominating by various types of fossil fuels e.g. natural gas, oil and coal. Eighty-two percent of this energy has been transformed into heat, electricity or movement by means of fossil fuel combustion processes, which has produced CO_2 emissions to the atmosphere equivalent to 7 Gton of carbon per year (Pacala & Socolow, 2004). The high utilization of these fossil fuels strongly accelerates the depletion of world fossil fuel resources as well as causing environmental damage in terms of climate change and global warming. Recently, there have been several attempts to minimize these energy and environmental problems. It is widely known that the development of clean alternative (and/or renewable) fuels to replace conventional oil is one of the important procedures; and among the clean alternative fuels, hydrogen is one of the promising fuels that is expected to be widely utilized in the near future.

Thailand has signed the Kyoto Protocol and has a commitment to reduce the level of greenhouse gas emissions (ONEP, 2002). Currently, although a per capita emission of Thailand is still below the world average, it has been rising up due to the growing of our fossil fuel consumption rate (EIA, 2006). Once, this value reaches or becomes higher than that of the world average, Thailand could possibly face the non-tariff trade barrier; therefore, Thai government has been currently attempting to promote the use of clean alternative fuels to replace conventional fossil fuels. On the basis of Thailand as an agricultural country, several types and numerous amount of lignocellulosic biomass are available. Thus, the uses of these biomasses as feedstock for clean alternative fuel production (i.e. hydrogen) would be a great option for Thailand to reduce the fuel import rate as well as decrease CO_2 emission rate from the combustion of conventional fossil fuels. It is noted that, recently, several research programs supported by Thailand government have been attempting to develop and promote the use of small to medium scale solid oxide fuel cell (SOFC) in remote areas, where numerous amount of lignocellulosic biomass are accessible. Furthermore, the research program on biomass to liquid (BTL) production via Fischer-Tropsch (FT) process is also of great interest.

Theoretically, gasification is known as a well-developed process for converting lignocellulosic biomass to synthesis gas, which can be later applied for SOFC and FT process. Generally, the main products from gasification of biomass are H_2, CO, CH_4 and CO_2 with various production ratios depending on the gasification co-agent (i.e. steam and air), type of biomass, and its operating conditions (i.e. temperature and pressure). Among these parameters, gasification agent is known as one important factor that strongly affects the product

distribution. Many researchers have developed models for biomass gasification (Zainal et al., 2001; Mathieu and Dubuisson, 2002; Di Blasi, 2002; Giltrap et al., 2003; Jayah et al., 2003; Babu and Sheth, 2005a; Sheth and Babu; 2005b). Zainal et al (2002) used the equilibrium model to predict the composition of producer gas. The effects of initial moisture content in the wood and the temperature in the gasification zone on the calorific value are investigated. Mathieu and Dubuisson (2002) have developed a model based on minimization of Gibbs free energy is performed in the ASPEN PLUS process simulator. The effects of the oxygen factor, the air temperature, operating pressure and the injection of steam were studied and they concluded that critical air temperature above which the preheating is no longer efficient, there is an optimum oxygen factor, the oxygen enrichment of air plays an efficient role under a certain value and the operating pressure has only a slight positive effect on the process efficiency. Giltrap et al (2003) developed models for the reduction zone of downdraft biomass gasifier to predict the composition of producer gas under steady state operation. The drawback of this model is that it over predicts the methane concentration. CH_4 products produced and temperature, and the variation of produced by pyrolysis is rapidly combusted with the char reactivity along the length of the gasifier bed and oxygen at the air inlets reduced the amount of CH_4 predicted. Jayah et al (2003) studied the downdraft gasifier performance by assuming two sub-models of the pyrolysis and gasification zones, respectively. The pyrolysis sub-model has been used to determine the maximum temperature and the composition of the gas entering the gasification zone. Model concludes that moisture content and heat loss have greater effects on reactor temperature and hence on the conversion efficiency. Babu and Sheth (2006) modified the Giltrap et al (2003) model by incorporating the variation of char reactivity factor (*CRF*) along the reduction zone of downdraft biomass gasifier. Increasing CRF exponentially along the reduction bed length in the model gave better prediction of temperature and composition profiles when compared with the experimental data and earlier models reported in literature. In addition, Mahishi et.al (2007) studied the thermodynamic analysis of hydrogen production from biomass. They studied the effects of temperature, pressure; steam biomass ratio (SBR) and equivalence ratio (ER) on the equilibrium hydrogen yield. Gibbs energy minimization (non-stoichiometric approach) approach which is based on commercially available open source software Stanjan (v.3.93L) was used to determine the product gas composition of wood (designated by $CH_{1.5}O_{0.7}$) gasification.

Nevertheless, the thermodynamic analysis of biomass gasification system (with various gasification agents) for hydrogen-rich gas production purpose has been limited. In this study, a set of mathematical model was developed in order to predict the behavior of biomass gasification with different gasification agents (i.e. air, steam, and mixed air/steam) in terms of hydrogen production yield and

system efficiency. The composition of lignocellulosic biomass in the present work is based on local rice husk since it is the major crop residue of Thailand. The model was developed by using bvp4c routine in MATLAB program. The bvp4c is a finite difference code that implements the three-stage Lobatto IIIa formula. This is a collocation formula and the collocation polynomial provides a C^1-continuous solution that is fourth-order accurate uniformly. Mesh selection and error control are based on the residual of the continuous solution. This routine is generally applied for solving the boundary condition equation with finite element method. Number of mesh points in each investigation was optimized between accuracy of results and time for calculation, (relative error tolerance is 1e-5). The effects of operating conditions (i.e. inlet oxidant/fuel ratio, steam/air ratio, and operating temperature) on yield of hydrogen production and system efficiency were determined. From this study, the optimum operating conditions of biomass gasification for hydrogen generation were identified.

2. Gasification modeling without char formation

2.1 Assumptions

A steady-state equilibrium model was developed to predict the product gas distribution from the biomass gasification with air, steam, and mixed air-steam. As described, rice husk was applied as biomass; the elemental compositions i.e. carbon, hydrogen, oxygen and nitrogen of rice husk (dry-ash free basis) are given in Table 1.

Table 1. Ultimate analysis of Rice Husk as received percentage by dry-ash free basis (W. Permchart & V. I. Kouprianov, 2004)

	C	H	N	O
% by weight dry ash free basis	48.7	6.96	.36	43.98

Starting from the ultimate analysis of biomass and mass fractions of all elements, the substitution fuel formula $C_nH_aO_bN_q$ can be calculated by assuming that n is equal to 1.0 by the following expressions:

$$a = \frac{mass\ fraction\ (H)\ \times\ Molecular\ weight\ (C)}{mass\ fraction\ (C)\ \times\ Molecular\ weight\ (H)} \quad (1)$$

$$b = \frac{mass\ fraction\ (O)\ \times\ Molecular\ weight\ (C)}{mass\ fraction\ (C)\ \times\ Molecular\ weight\ (O)} \quad (2)$$

Published by The Berkeley Electronic Press, 2010

$$q = \frac{mass\ fraction\ (N) \times Molecular\ weight\ (C)}{mass\ fraction\ (C) \times Molecular\ weight\ (N)} \quad (3)$$

From these expressions, the estimated molecular formula of rice husk in the present work is $CH_{1.703}O_{0.678}N_{0.007}$. The assumption used in this work is that the rice husk rapidly mixed with the bed material and almost instantaneously heated up to the bed temperature due to the intense gas-solid mixing facilitated with high heat transfer coefficient. Hence, the pyrolysis occurs rapidly and results in a component mix with a relative large amount of gaseous materials; then the gasification and tar conversion reactions take place in the gas phase. At equilibrium state, no solid char is presented in the product and the main composition of product gases are CO, CO_2, CH_4, H_2 and H_2O; the involved intermediate reactions takes place during the process are as follows:

Oxidation reaction

$$C + O_2 \Leftrightarrow CO_2 \quad (4)$$

Boudouard reaction

$$C + CO_2 \Leftrightarrow 2CO \quad (5)$$

Steam gasification

$$C + H_2O \Leftrightarrow CO + H_2 \quad (6)$$

Methanation reaction

$$C + 2\,H_2 \Leftrightarrow CH_4 \quad (+75{,}000\ J/mol) \quad (7)$$

Water gas shift reaction

$$CO + H_2O \Leftrightarrow CO_2 + H_2 \quad (+41{,}200\ J/mol) \quad (8)$$

Reaction 4 occurs rapidly, while the steam gasification, boudouard reaction, and methanation reaction are in equilibrium. The water gas shift reaction can be regarded as the subtraction of steam gasification and boudouard reactions, hence it can also be considered as equilibrium condition. Global reaction for the biomass gasification is given by:

$$CH_aO_b + wH_2O + mO_2 + 3.76mN_2 = x_1H_2 + x_2CO + x_3CO_2 + x_4H_2O + x_5CH_4 + 3.76mN_2 \quad (9)$$

Where m corresponds to the molar quantity of air used during the gasifying process and depends on the equivalence rate of the gasifying process and the stoichiometric air/fuel ratio of the biomass. X1, x_2, x_3, x_4 and x_5 are unknown compositions. The nitrogen content of biomass is neglected for simplicity of the global reaction. The overall equilibrium approach in this work is given in Fig. 1.

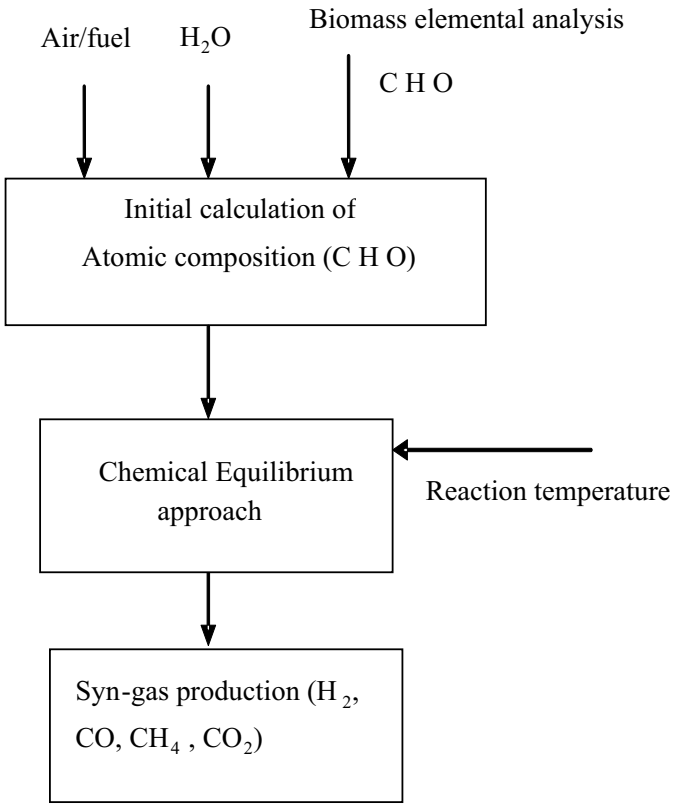

Figure 1. Structure of the simulation of equilibrium model

2.2 System efficiency analysis

Thermodynamic efficiency was estimated from the equilibrium model of biomass gasification with various inlet SBR (0.5-5.0), ER (0.2-0.4), and operating temperatures (750-900^{o}C). These ranges of operating were typically reported in several previous commercial and research pilot gasifiers (Turn et.al.,1998, Navraez,1997; Minkova, 2000 & Corella,1991). The first law analysis was carried out by assuming constant pressure in a steady state equilibrium gasifier; and the energy balance (as presented in Eq. 11) was applied.

$$H_{\text{Rice Husk}} + w\,(H_{H2O(l)} + H_{H2O(vap)}) + m\,(H_{O2}+3.76\,H_{N2}) + Q_{EG} = x_1H_{H2} + x_2H_{CO} + x_3H_{CO2} + x_4H_{H2O} + x_5H_{CH4} + 3.76mH_{N2} \quad (11)$$

H is the absolute enthalpy and Q_{EG} is the heat released (or supplied) to the air gasifier. The absolute enthalpy of each species is the sum of the standard enthalpy of formation of species and sensible enthalpy change due to temperature (Eq. 12). The moisture content of biomass tested here is about 10 %.

$$H = H^{o}_{f} + \Delta H \tag{12}$$

It is noted that the higher heating value of rice husk (in MJ/kg) was developed using the formula developed by Channiwala and Parikh (2002), where z_c, z_H, z_O, z_N, z_{ash} are the mass percentages on dry basis.

$$HHV_{Rice.Husk} = \left(0.3491 z_c + 1.1783 z_H - 0.103 z_O - 0.01051 z_N - 0.0211 z_{ash}\right) \tag{13}$$

The higher heating value can be converted into the LHV using the enthalpy of evaporation for the water formed during combustion, while the enthalpy of formation for solid fuel was determined following the work from Souza-Santos, (2009). Q_{EG} is negative value when the heat is liberated; this generally happens during partial oxidation of biomass (air gasification). A zero value for Q_{EG} is an interesting case which represents the adiabatic gasification and means a self-sustaining process (auto thermal gasification). We here assumed that the steam generator provides superheated steam at 427ºC and the air-preheater heats the air from ambient temperature to 77ºC before entering the gasifier. It is noted that the efficiency was calculated from the equations below:

$$\text{Efficiency} = \frac{\text{LHV of hydrogen in product gas}}{\text{LHV of biomass} + \text{all other input energies}} \tag{14}$$

$$\text{Efficiency} = \frac{\left(\text{Hydrogen produced in kg}\right) \text{x} \left(\text{LHV(kJ/kg)}\right)}{\text{LHV of biomass} + \text{Q}_{\text{EG}} + Q_{steam} + Q_{air}} \tag{15}$$

where Q_{steam} and Q_{air} can be calculated from the following equations:

$$\text{Q}_{\text{steam}} = \text{w}_{H_2O} \times \text{H}_{H_2O} \tag{15}$$

$$Q_{\text{air}} = m\,\text{O}_2 \times H_{\text{O2}} + 3.76\, m\text{N}_2 \times H_{\text{N2}} \tag{16}$$

3. Results and discussions

3.1 Model validation

Firstly, the developed air gasification model in the present work was validated with the previous air gasification model reported by Venkat et.al., (2008) who used cashew nut shell as feedstock. And also model values are compared with experimental values at various equivalence ratios for air gasification model and also for steam gasification results. The effect of equivalence ratio on product composition (dry basis) for both models was compared as shown in Figure 2 for H_2, CO, CO_2 and CH_4 gas production in molar compositions. Clearly, similar trends of all products with slight different in product compositions were observed. The different in product compositions could be due to the use of different feedstock composition since the chemical formula of cashew nut shell is $CH_{0.686}O_{0.32}N_{0.09}$.

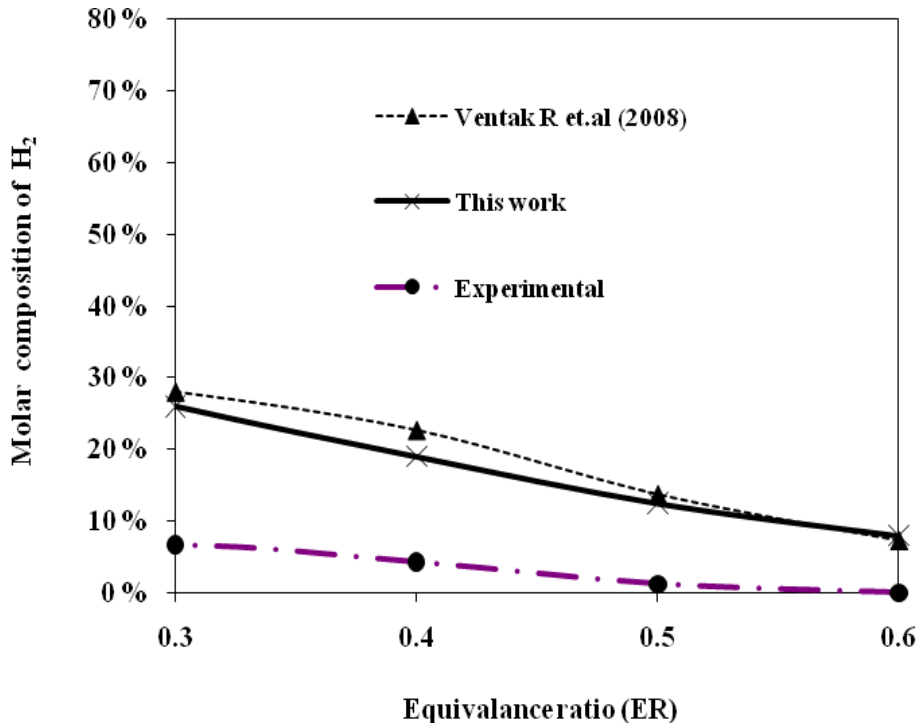

Figure 2. (a) H_2 produciton results from air gasiifcation

Published by The Berkeley Electronic Press, 2010

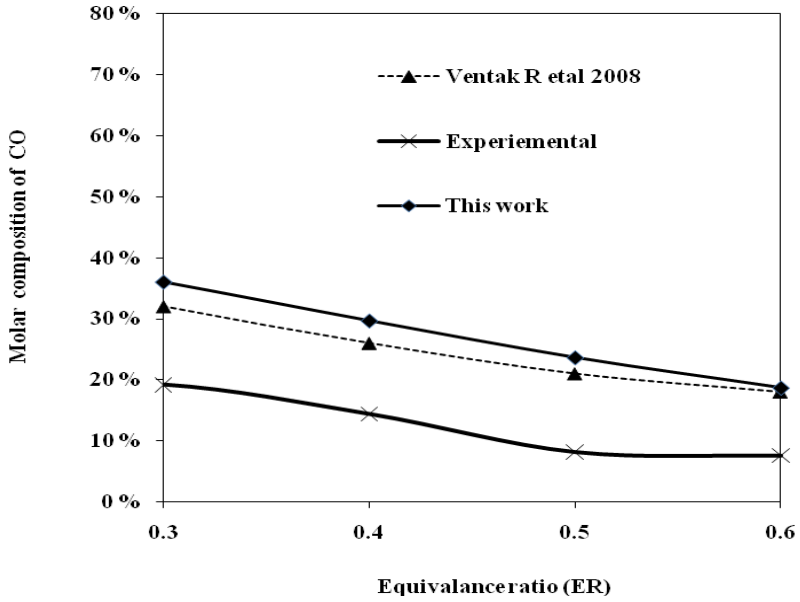

Figure 2.(b) CO produciton form air gasiifcation

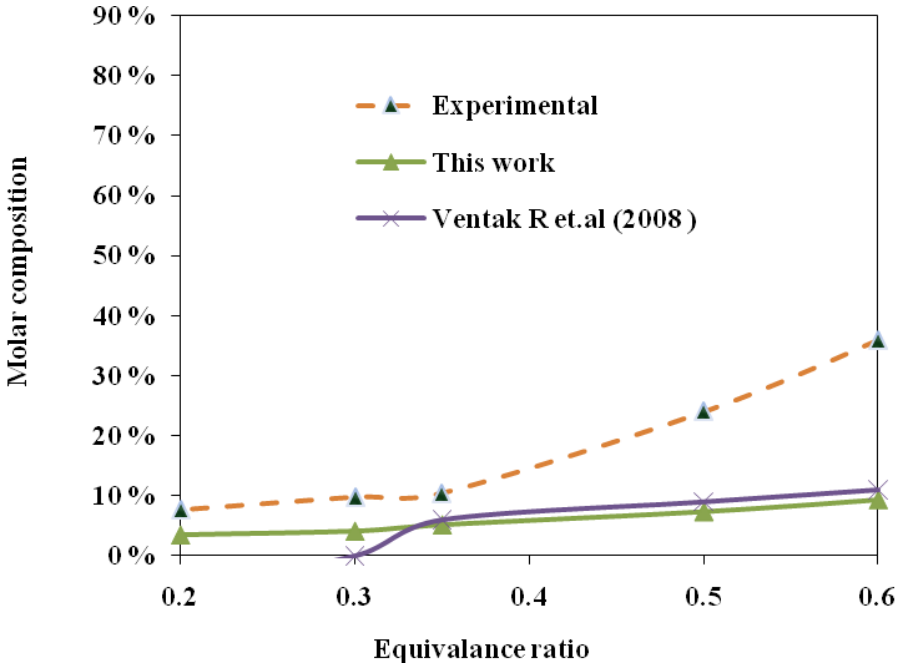

Figure 2. (c) CO_2 production from air gasificaiton

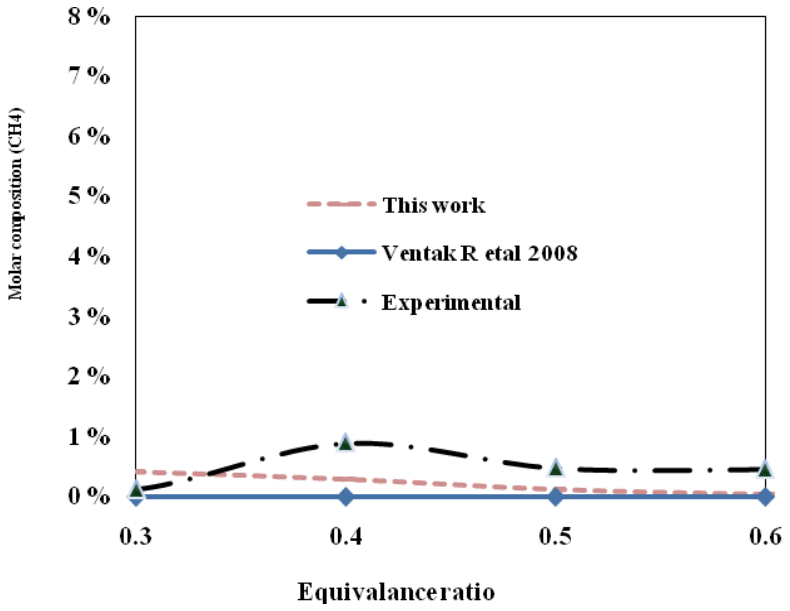

Figure 2.(d) *CH_4 production from air gasification*

Figure 2. Model validations for H_2,CO, CO_2 and CH_4 production from air gasification from this work compared to experiments and other works

The modeling also indicated that less than 0.1% of CH_4 is produced, which is also in good agreement with the previous modeling result from Li et al. (2004) who reported the methane concentration less than 1.0 for air blown gasification. Mansaray et al., (1999) inferred that increasing the ER lead to a decrease in the concentrations of methane and other light hydrocarbons, which have relatively large heating values. The modeling results validate the statement of a decreasing CH_4 concentration for increasing ER. Conversely, the prediction on CH_4 made by the model is lower than the actual experimental values as shown in Figure 2 (d). Luiz et al., (2007) experienced similar differences in CH_4 predicted by the model as against experimental results and referred the cause as a result of the sudden cease of gasification reactions at the bottom of the reactor. This cease could probably be attributed to the consequence of the temperatures at the bottom, which are too low to start the reactions. In chemical equilibrium modeling, it is assumed that all reactions achieve a steady-state condition; thus, no kinetic effects (such as sudden cease) are considered.

Published by The Berkeley Electronic Press, 2010

Importantly, our developed model was also compared with other developed models (i.e. the models of down draft gasifier developed by Jarungthammachote and Dutta **Error! Reference source not found.**); and Altafini et al (2003) as well as with the experimental results from the literature presented by Zhao et al (2009) and Wu et al 0. It is noted that the error from these comparisons was determined by the root-mean-square (RMSE), from which is defined as given in Eq. (17):

$$RMSE_j = \sqrt{\frac{\sum_i (OR_k - Mod_i)^2}{D}} \qquad (17)$$

where OR is the values from the literature for, Mod is the value predicted from the model in the present work, where subscript i represents the mole fraction values of the present work and subscript k represents the mole fraction values of product gases literatures and D is the number of data. These deviations are presented in Table 2 and 3.

Table 1. Comparison of simulation results in the present work with other models from the literatures (mole fraction) (at the temperature of 700 ºC)

	Gas composition on dry basis (mole fraction)						RMSE
	H_2	CO	CH_4	CO_2	N_2	m	
Simulation results from the present work	0.136	0.233	0.003	0.079	0.500	0.350	
Simulation results from Altafini et al (2003)	0.200	0.197	0.000	0.101	0.510	0.336	0.032
Simulation results from Jarungthammachote et al (2007)	0.182	0.234	0.016	0.098	0.510	0.336	0.022

Altafini et al (2003) used SYNGAS routine based on gibs minimization approach to produce syngas from saw dust of elemental compositions (C: 52 %, H_2: 6.07, O_2: 41.55 %, N_2: 0.28 %). The SYNGAS routine results refer to the condition of 10% sawdust moisture content and reaction temperature of 800^{o}C and equivalence ratio of 0.329. Jarungthammachote et al (2007) studied the modeling of gasifer based equilibrium modeling approach (stocihiometric) for

municipal solid waste as shown in Table 2 with a moisture content of 14.2 % and ER ratio of .3578, the model was modified with experimental data of different feed stock compositions(Zainal et al (2002), Altafini et al (2003) and Jayah et al. (2003). In addition, other experimental results of Wu et al (2009) for rice husk were compared as shown in Table 3; the ER ratio was varied between 0.22 to 0.28 for practical 1.2 MW gasifer as well as for the Zhao et al (2009) in the entrained flow gasifier. The differences in the results may come from the assumptions defined in simplifying the model, such as all gases are assumed to be ideal, no residue, absence of tar, feed stock compositions. The interesting points in the comparisons are the amount of H_2 and CH_4. The model predicted higher amounts of H_2, but the predicted amounts of CH_4 are lower than all experimental data. It is important to note that equilibrium models as stated by Bacon et al (1983), substantially higher CH_4 in the product gas than what was estimated from his equilibrium model calculation. A possible explanation to this is that the state of equilibrium was not met during the experiment. It is inferred from the validation that, the models need to be modified with respect to the practical results pertaining to the feed compositions.

Table 2. Comparison of simulation results in the present work with the experimental results from the literatures (at the temperature of 800 ºC)

	Gas composition on dry basis (mole fraction)						RMSE
	H_2	CO	CH_4	CO_2	N_2	m	
Simulation results from the present work	0.220	0.292	0.006	0.058	0.506	0.284	
Experimental results from Zhao et al (2009)	0.059	0.148	0.013	0.133	0.645	0.28	0.109
Experimental results of Wu et al (2009)	0.074	0.165	0.047	0.160	0.495	0.002	0.134

The results were also compared for the mixed air-steam gasification. Modeling of mixed air-steam gasification performed by introducing steam mixed with air to the system. Figure 3 presents the experimental and modeled results for various SBR ratios of 0.5, 1.5, 2.0, and 3.0 respectively at a constant equivalence ratio of .22.The experimental results of Pengmei Lv et al (2003) is used to compare the modeling results at same ER and SBR ratios. Obviously there is a significant deviation from the experimental values.

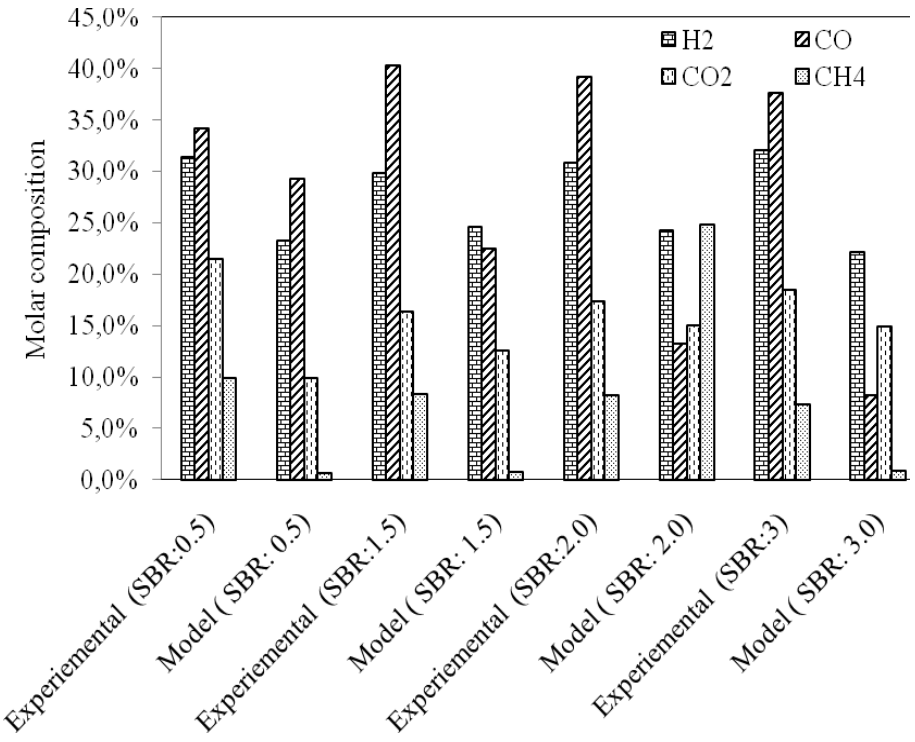

Figure 3. Model Validation results for steam gasification

3.2 Product analysis from gasification with various operating conditions

The product gas compositions in terms of hydrogen yield, and H_2/CO, CO/CO_2 and CH_4/H_2 molar ratios from the gasification of rice husk at different equivalence ratio (ER), steam to biomass ratio (SBR), operating temperature, and steam to air ratio were then determined. It is noted that ER is the measuring of the amount of external oxygen supplied to the system, which obtained by dividing the actual oxygen to biomass molar ratio to the stoichiometric oxygen to biomass molar ratio; while SBR is defined as the mole steam fed per mole of biomass. Figure 4 shows the H_2/CO, CO/CO_2 and CH_4/H_2 molar ratios produced from the air gasification of rice husk at various ER (from 0.2 to 0.6) and operating temperatures (750-900ºC). It can be seen that CO production is significantly higher than CO_2 production particularly at low ER and high operating temperature, while H_2 production is slightly lower than CO production at low ER but considerably decreased with increasing ER (H_2/CO reduced from 0.83 at ER of 0.2 to 0.41 at ER of 0.6). These modeling results are well supported by several previous experimental works, from which generally reported the molar

composition of H_2/CO production less than 1.0 in all operating conditions Li et al. (2004) as explained in the previous section.

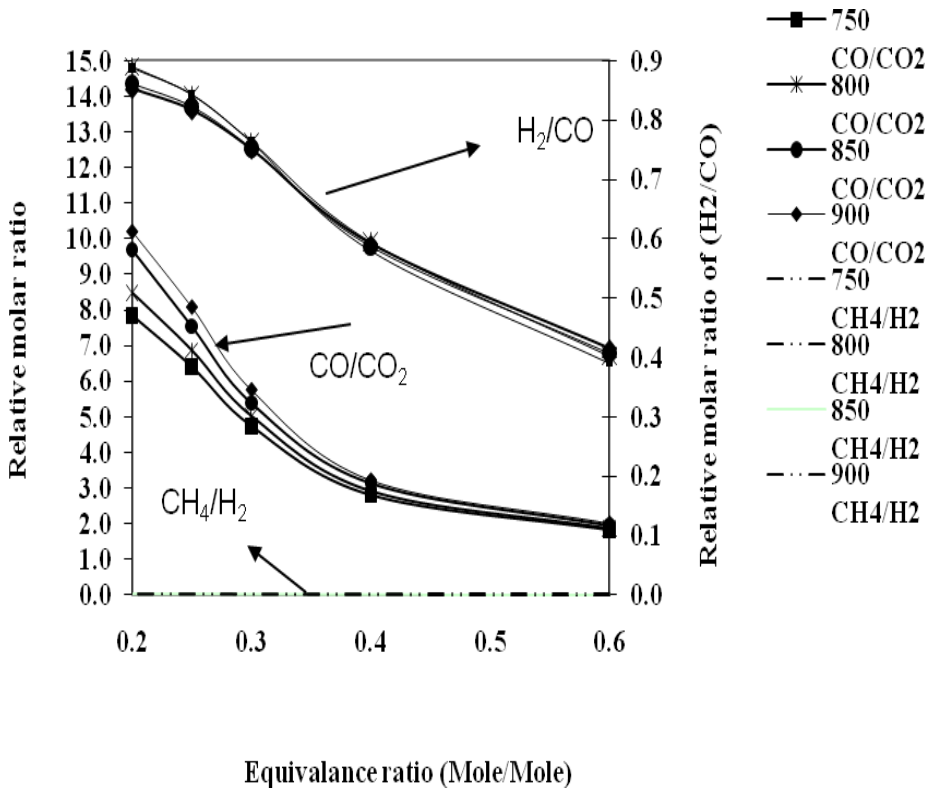

Figure 4. H_2/CO, CO/CO_2 and CH_4/H_2 molar ratios produced from the air gasification of rice husk at various ER (from 0.2 to 0.6) and operating temperatures (750-900ºC)

The modeling of steam gasification was then performed by introducing steam instead of air to the system. Figure 5 presents the effect of SBR on the H_2/CO, CO/CO_2 and CH_4/H_2 molar ratio productions at different temperatures. Clearly, H_2 production is always greater than CO production particularly at high SBR and low temperature (750ºC), while CO production is also higher than CO_2 production but significantly decreases with increasing SBR due to the effect of water gas shift reaction (Franco C et al., 2003). Small amount of CH_4 is observed from the system; it decreases with increasing temperature but slightly increases with increasing SBR.

As another concept, the modeling of biomass gasification with mixed steam/air was carried out for comparison. The product gas compositions from the gasification at various SBR, ER (0.2, 0.3 and 0.4), and operating temperatures are presented in Figure 6 (a)-(c). Compared to the air-alone gasification, higher amount of H_2 and CO_2 are produced at the same ER and operating temperature, due to the occurring of water gas shift and steam gasification reactions.

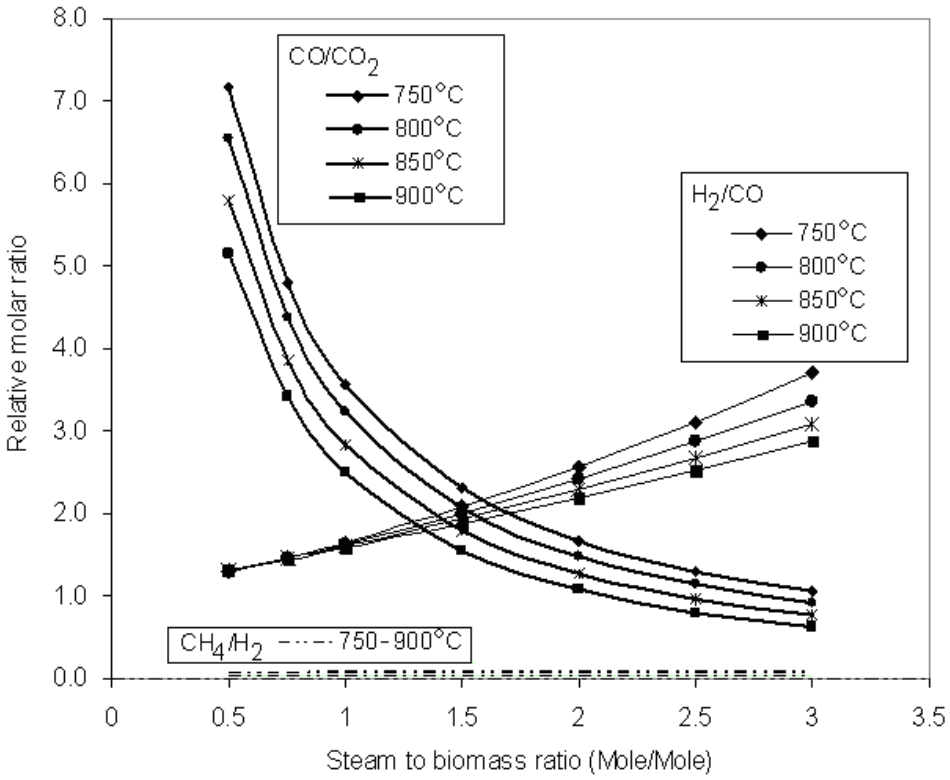

Figure 5. H_2/CO, CO/CO_2 and CH_4/H_2 molar ratio produced from steam gasification of rice husk at various SBR (from 0 to 3.0) and operating temperatures (750-900ºC)

.

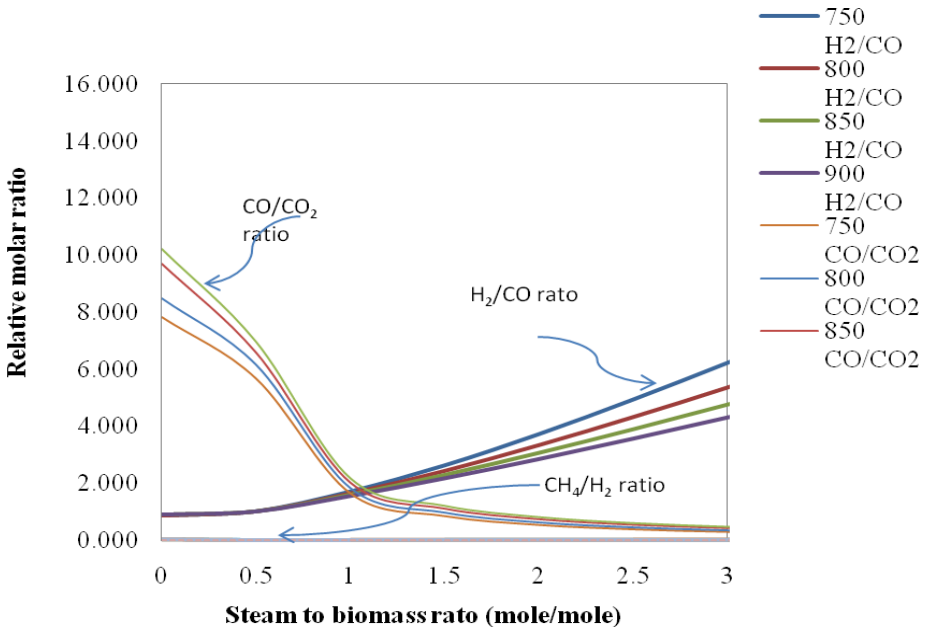

Figure 6 (a) *ER of 0.2*

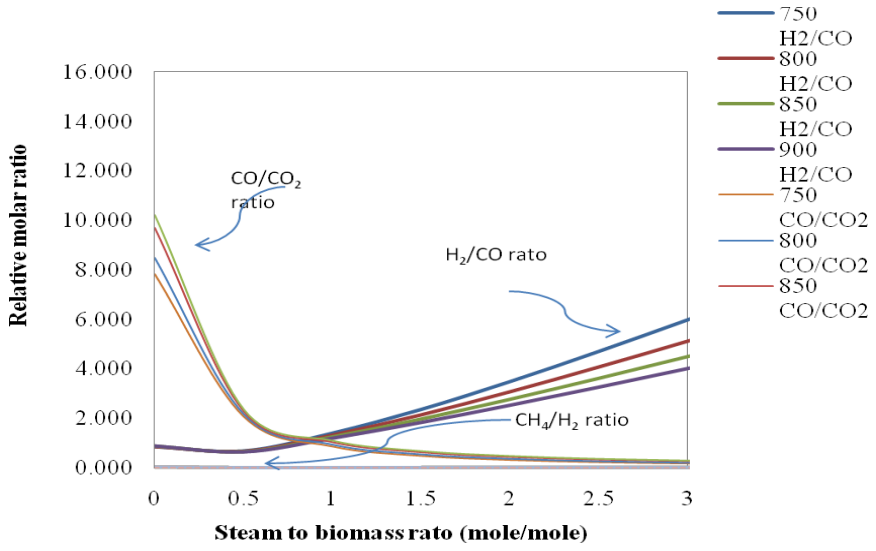

Figure 6 (b) *ER of 0.3*

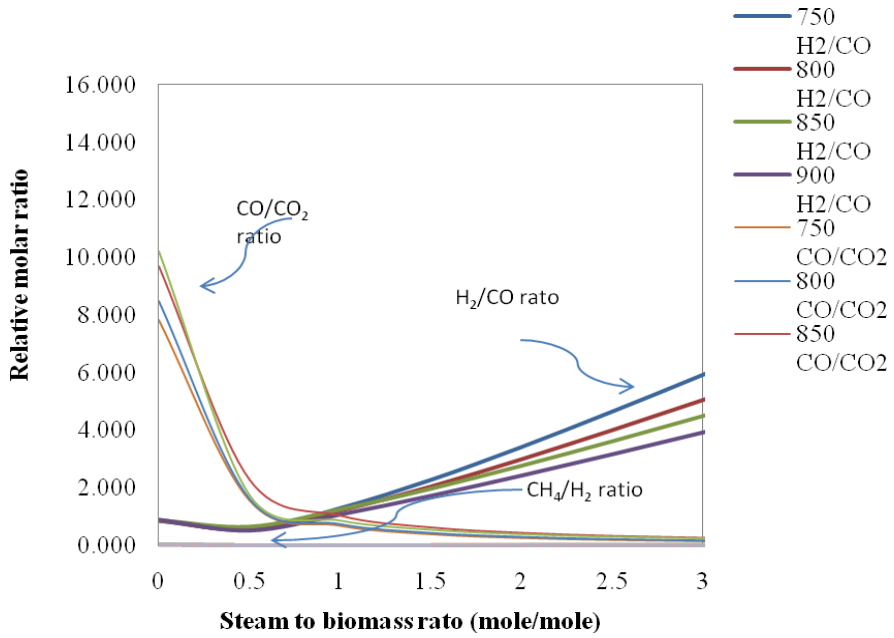

Figure 6 (c) *ER of 0.4*

Figure 6. Product gas compositions from the mixed steam/air gasification at various SBR, and ER ((a) 0.2, (b) 0.3 and (c) 0.4) at various temperatures

3.2 Effect of temperature, SBR and ER ratios on hydrogen yield

Figure 7 shows the yield of H_2 production from the steam gasification at wider range of SBR (from 0.2 to 10). It can be seen that H_2 yield increased steadily with increasing temperature and SBR until reaching SBR of 3.5-4.0; then the effect of steam on H_2 yield becomes less pronounce. Figure 8 shows the effects of SBR, ER on H_2 production yield for the mixed steam/air gasification at (a) 750ºC, (b) 800ºC, (c) 850ºC and (d) 900ºC

Figure 8 (a)-(d) shows the effects of SBR and ER on H_2 production yield at different temperatures. Similar to the steam gasification, H_2 yield initially increased with increasing SBR; then the effect of steam becomes less pronounce at higher SBR. It can also be seen that H_2 yield decreased dramatically with increasing ER (up to 0.4), which could be due to the impacts of air gasification along with reverse water gas shift reactions meaning oxidizing reaction.

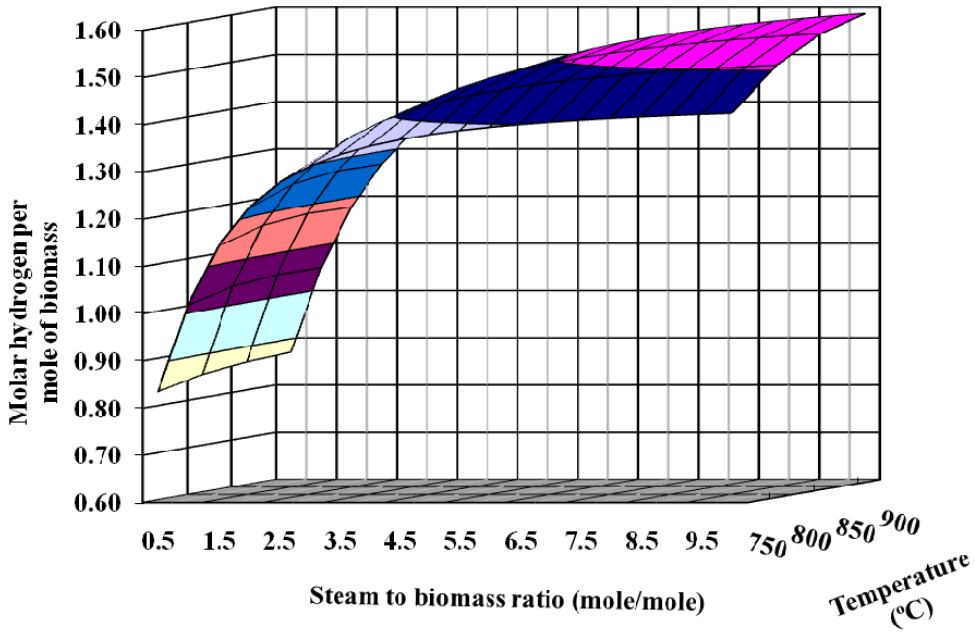

Figure 7. The yield of H_2 production from the steam gasification at various SBR (from 0.2 to 10)

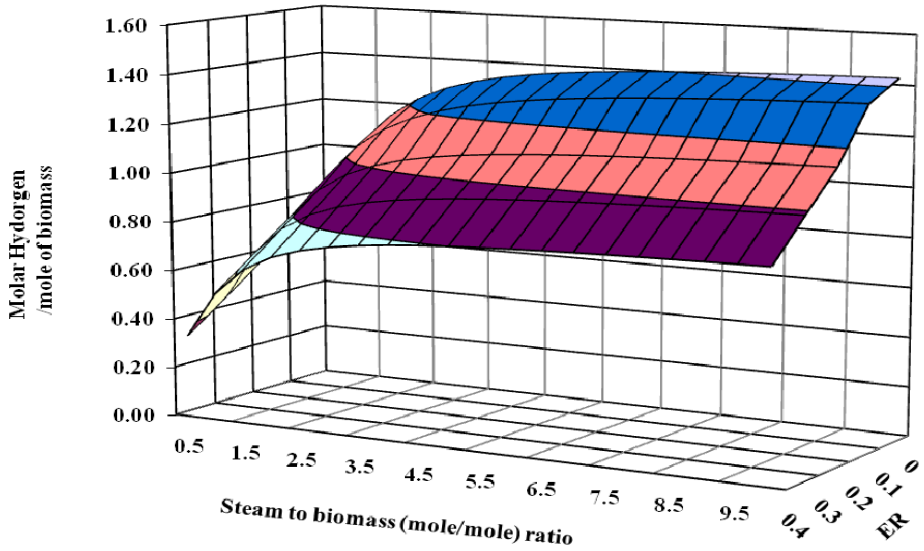

Figure 8 (a) 750°C

Published by The Berkeley Electronic Press, 2010

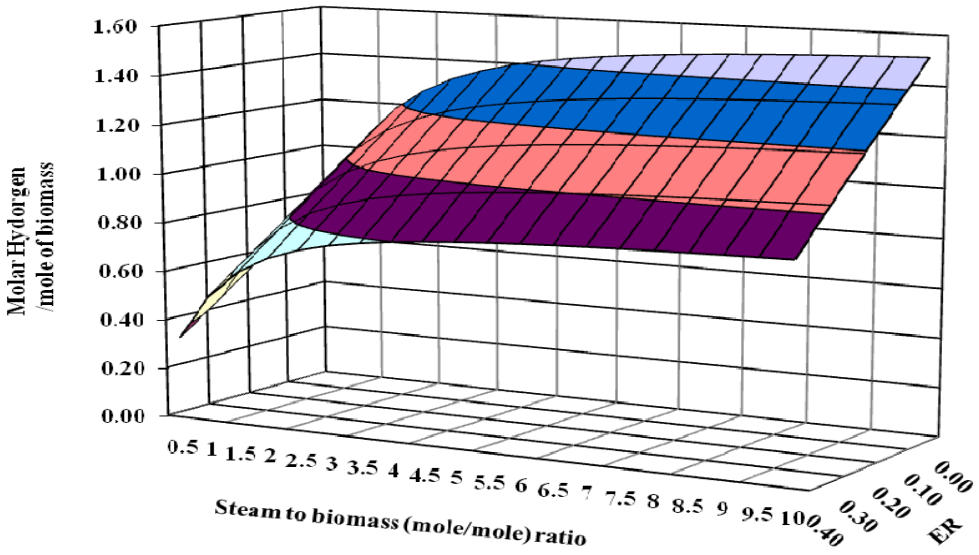

Figure 8 (b) 800°C

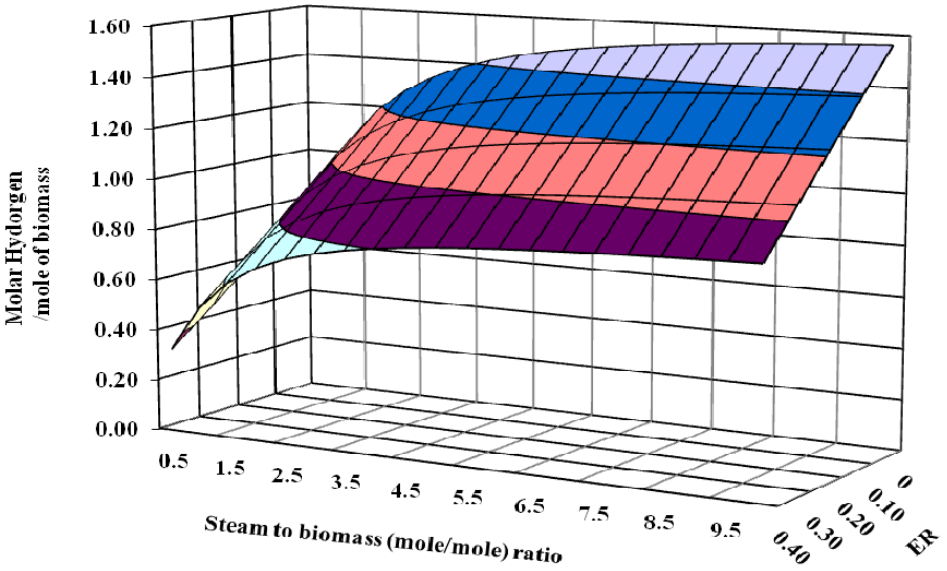

Figure 8 (c) 850°C

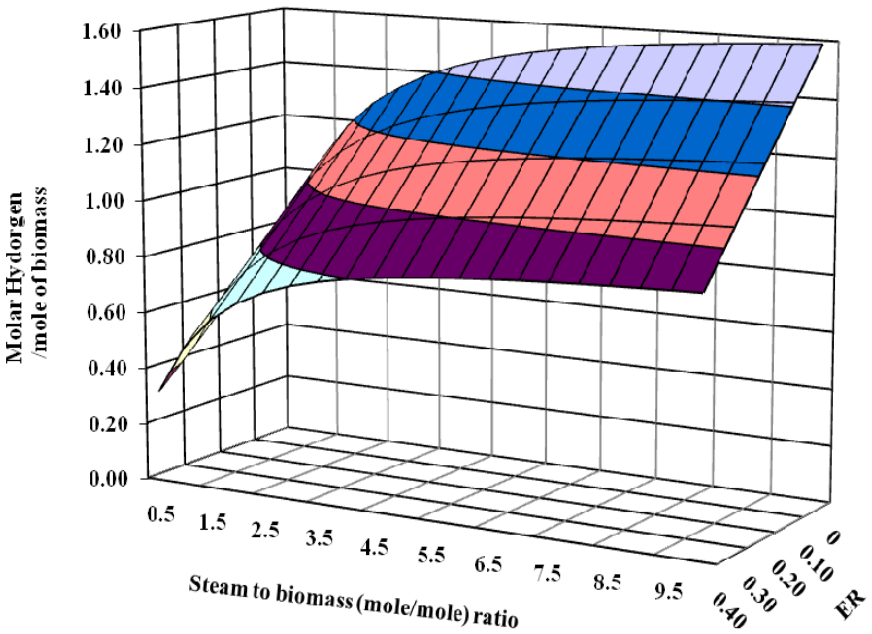

Figure 8 (d) 900ºC

Figure 8. The effects of SBR and ER on H_2 production yield from the mixed steam/air gasification at (a) 750ºC, (b) 800ºC, (c) 850ºC and (d) 900ºC

3.3 Efficiency analysis from gasification with various gasification agents

From the above studies, the highest hydrogen production can be achieved from the steam gasification with SBR of 4.0; nevertheless, the energy consumption for the system is also important concern. Hence, the thermodynamic efficiencies of these three processes were analyzed in order to determine the optimum operating conditions that can produce maximum amount of hydrogen with less energy consumption.

According to our thermodynamic analysis, in case of typical air gasification, the efficiency dramatically decreased with increasing ER in the range of temperatures studied (750-900ºC), Fig. 9. It was also found that the efficiency slightly increased with increasing temperature (from 35% at 750ºC to 42.5% at 900ºC with ER of 0.2).

Published by The Berkeley Electronic Press, 2010

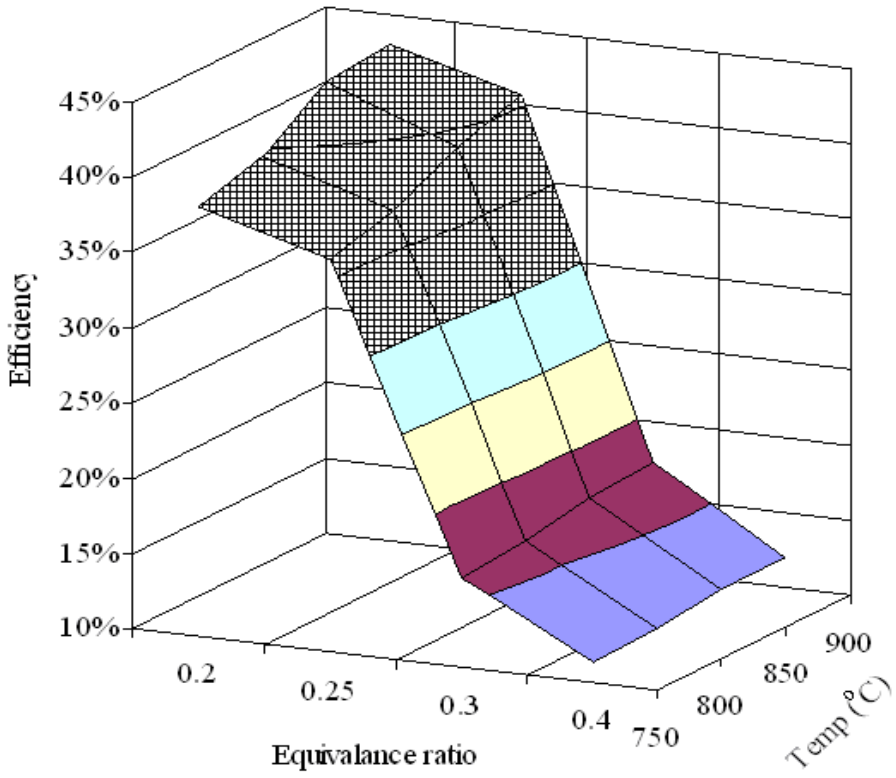

Figure 9. Thermodynamic efficiency of air gasification at various ER

As for the steam gasification, initially the efficiency increased with increasing SBR (from 26% at SBR of 0.5 to 32% at SBR of 2.5); then it decreased at higher SBR, Fig. 10. Similar to the air gasification, the efficiency increased (in the order of 5-10%) with increasing temperature over this range of SBR. Therefore, the optimum operating conditions for steam gasification are at 900ºC with inlet SBR of 0.5.

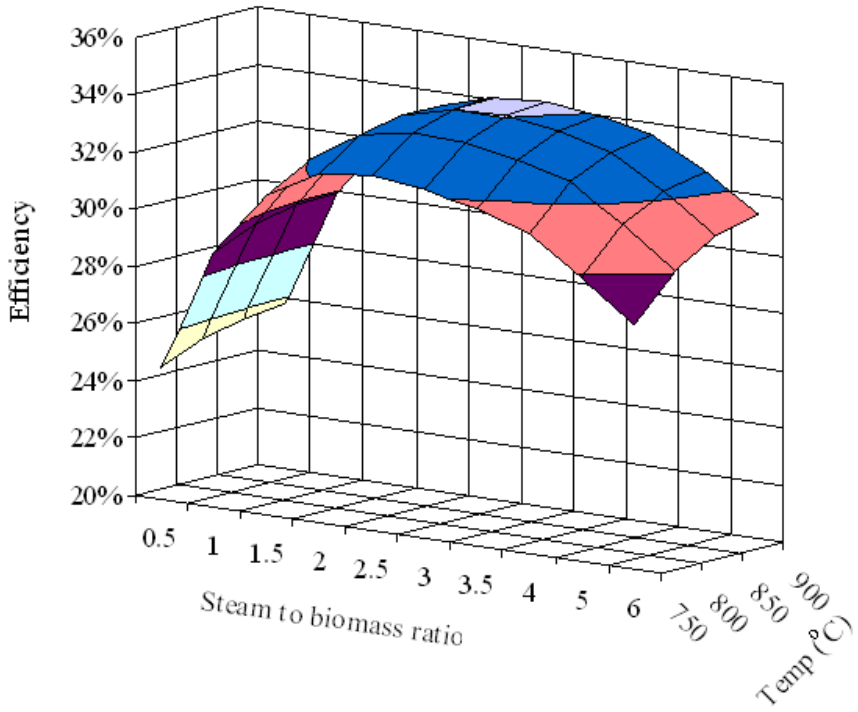

Figure 10. Thermodynamic efficiency of steam gasification at various SBR and operating temperatures

Lastly, for the case of mixed air-steam gasification, the effects of ER and SBR on the thermodynamic efficiencies were estimated at various temperatures (750, 800, 850 and 900^{o}C), as shown in Fig. 11 (a)-(d). Similar trends were observed in all range of operating temperatures, in which the efficiency increased as ER and SBR increased until reaching the optimum point and then reduced with further increasing of ER and SBR. The optimum condition for the mixed air-steam gasification seems to be at 900^{o}C with ER and SBR of 0.1 and 2.5, respectively, which could provide the efficiency up to 66.5%.

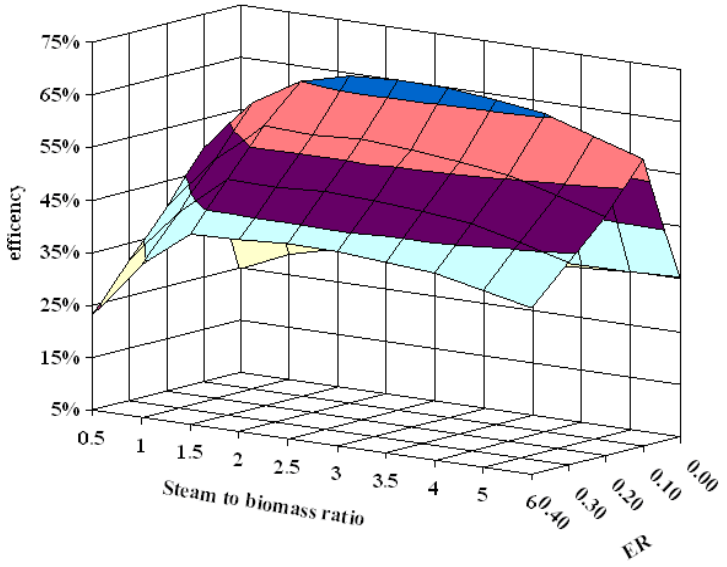

Figure 11(a)

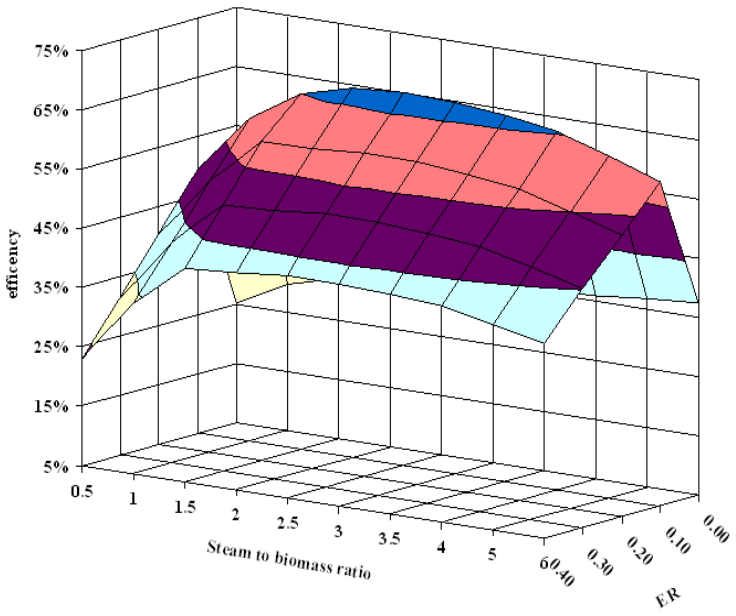

Figure 11 (b)

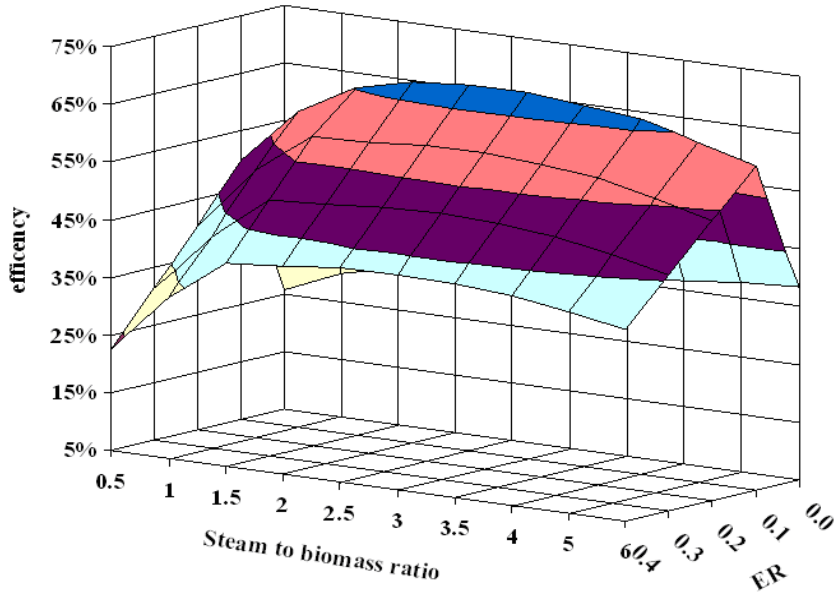

Figure 11 (c)

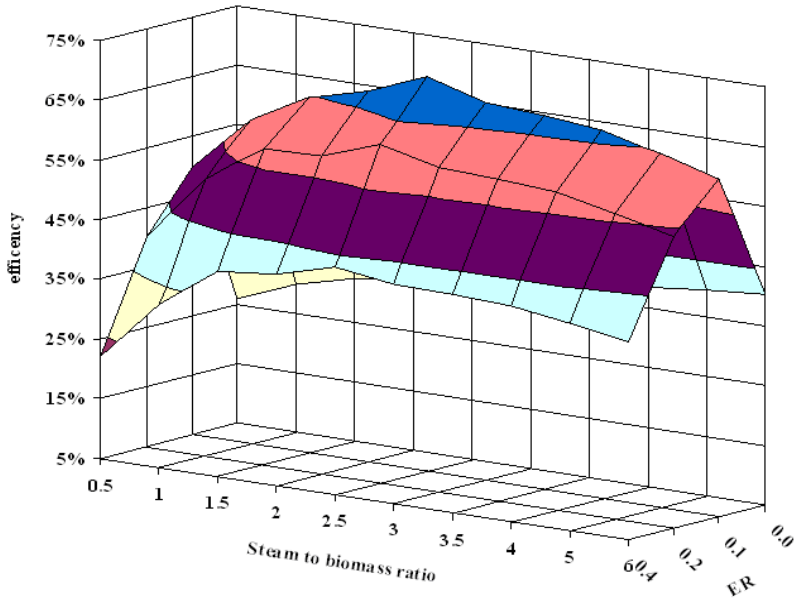

Figure 11 (d)

Figure 11. The effects of ER and SBR on the thermodynamic efficiencies of mixed steam/air gasification at (a) 750ºC, (b) 800ºC, (c) 850ºC and (d) 900ºC

In summary, according to our analysis, the mixed air-steam gasification is the good candidate to produce hydrogen-rich gas from Thailand rice husk with highest efficiency compared to air and steam alone gasification. The benefit of this operation is mainly due to the supplement of sufficient heat from the partial oxidation of biomass (with air), which is efficiently used for steam activation reaction providing the autothermal operation. Hence, this operation will be selected as biomass conversion process to produce hydrogen-rich gas for later utilization in SOFC and/or FT-process for BTL production.

4. Conclusion

The thermodynamic analysis of biomass gasification with various gasification agents (i.e. air, steam, and mixed air/steam) indicated that the highest hydrogen production yield can be achieved from the steam gasification with SBR of 4.0. Nevertheless, by considering the system efficiency, the combined air-steam gasification provided significant higher hydrogen production efficiency compared to air and/or steam gasification. The optimum condition can be achieved at 900^{o}C with ER and SBR of 0.1 and 2.5, respectively, which could provide the efficiency up to 66.5%. This selected optimum condition will be later applied for the integrated biomass gasification with SOFC for electrical generation and with FT-process for BTL production purposes.

Nomenclature

H_2/CO	Hydrogen to Carbon monoxide product molar ratio
CO/CO_2	Carbon monoxide to carbon dioxide product molar ratio
CH_4/H_2	Methane to Hydrogen product molar ratio
SBR	Steam to biomass ratio
ER	Equivalence ratio

REFERENCES

Alderucci, V. Alderucci, P.L. Antonucci, G. Maggio, N. Giordano, V. Antonucci, "Thermodynamic analysis of SOFC fuelled by biomass-derived gas", International Journal of Hydrogen Energy, Volume 19, Issue 4, , Pages 369-376 1994)

Altafini, C.R., Wander PR, Barreto RM. "Prediction of the working parameters of a wood waste gasifier through an equilibrium model". Energy Conversion and Management, 44: 2763–2777 (2003).

Bacon, D.W., Downie J, Hsu JC, Peters J. "Modelling of fluidized bed wood Gasifiers". In: Overend RP, Milne TA, Mudge KL, editors. *Fundamentals of thermochemical biomass conversion*. UK: Elsevier Applied Science Publishers; p. 717–32 (1982).

Babu, B.V., P. N. Sheth, "Modeling and Simulation of Reduction Zone of Downdraft Biomass Gasifier: Effect of Char Reactivity Factor", Energy Conversion and Management, 47 (2006) 2602-2611.

Blasi, C.D., "Modeling chemical and physical processes of wood and biomass pyrolysis", Progress in Energy and Combustion Science, 34: 47-90 (2008).

Corella J, Aznar MP, Delgado J, Aldea E. Steam gasification of cellulosic waste in a fluidized bed with downstream vessels, Ind Eng Chem Res 1991; 30: 2252–2262.

Channiwala, S.A, Parikh PP. A unified correlation for estimating HHV of solid, liquid and gaseous fuels. Fuel, 81: 1051–63 (2002).

Cairns, E.J, Tevebaugh AD. CHO gas phase composition in equilibrium with carbon and carbon deposition boundaries at one atmosphere, J Chem Eng Data 9: 453–62 (1964).

Devi, L.K., Ptasinski J, Janssen F, Paasen S, Bergman P, Kiel J, "Catalytic decomposition of biomass tars: use of dolomite and untreated olivine", Renewable Energy, 30: 565–587 (2005).

EIA, World Carbon Dioxide Emissions from the Use of Fossil Fuels, http://www.eia.doe.gov/iea/carbon.html, (2006)

Fock, F.; Thomsen, K. P. B. "Modelling a Biomass Gasification System by Means of EES" The Scandinavian Simulation Society, Technical University of Denmark: Lyngby, (2000).

Franco, C., Pinto F, Gulyurtlu I, Cabrita, "The Study of Reactions Influencing the Biomass Steam Gasification Process", Fuel, 82: 835–842 (2003).

Giltrap, D.L, McKibbin R, Barnes GRG "A steady state model of gas-char reactions in a downdraft biomass gasifier", Solar Energy, 74: 85-91 (2003).

Jayah, T.J., Lu Aye, R. J. Fuller, D. F. Stewart, "Computer simulation of a downdraft wood gasifier for tea drying", Biomass and Bioenergy, 25 (2003) 459-469.

Jarungthammachote, S., Dutta A. "Thermodynamic equilibrium model and second law analysis of a downdraft gasifier". Energy, 32:1660–1669 (2007).

Li, X.T., Grace JR, Lim CJ, Watkinson AP, Chen HP, Kim JR, Biomass Gasification in a Circulating Fluidized Bed, Biomass and Bioenergy, 26: 171-193 (2004).

Mahishi, M. R., and Goswami, D. Y., "Thermodynamic Optimization of Biomass Gasifier for Hydrogen Production," Int. J. Hydrogen Energy, 32(16), pp. 3831–3840 (2007).

Mansaray, K.G., Ghaly, A. E. Al-taweel, A. M.; Hamdullahpur,F.; Ugursal, V. I. Air gasification of rice husk in a dual distributor type fluidized bed gasifier , Biomass Bioenergy 17, 315–332 (1999).

Mathieu, P., Dubuisson R. Performance analysis of a biomass gasifier. Energy Conversion and Management, 43: 9-12 (2002).

Minkova, V., Marinov SP, Zanzi R, Bjornbom E, Budinova T, Stefanova M, Lakov L. "Thermochemical treatment of biomass in a flow of steam or in a mixture of steam and CO_2", Fuel Process Technol., 62: 45–52 (2000).

Navraez, I., Corella J, Orio A. "Fresh tar (from a biomass gasifier) elimination over a commercial steam reforming catalyst. Kinetics and effect of different variables of operation". Ind Eng Chem Res, 36: 317–27 (1997).

ONEP, Cabinet Resolutions dated 28th August 2002, http://www2.onep.go.th/CDM/en/unf_kyoto_motto.html#1, (2002)

Pacala, S., Socolow R. "Stabilization wedges: solving the climate problem for the next 50 years with current technologies Science" , 305: 968–72 (2004).

Pfeifer, C., Rauch R, Hofbauer H. "In-bed catalytic tar reduction in dual fluidized bed biomass steam gasifier", Ind. Eng. Chem. Res. 43: 1634–1640 (2004).

Pengmei Lv, Jie Chang,, Zuhong Xiong,, Haitao Huang, Chuangzhi Wu, and, Yong Chen, Jingxu Zhu Biomass Air−Steam Gasification in a Fluidized Bed to Produce Hydrogen-Rich Gas Energy & Fuels 17 *(3), 677-682,(* 2003**).**

Pellegrini and Oliveira, L.F. Pellegrini and S. Oliveira Jr., Exergy analysis of sugarcane bagasse gasification, *Energy* 32 pp. 314–327 (2007),

Souza-Santos, M.L., "CSFB applied to fluidized-bed gasification of special fuels", Fuel, 88: 826-833 (2009).

Turn, SQ, Kinoshita D, Zhang Z, Ishimura D, Zhou J. "An experimental investigation of hydrogen production from biomass gasification". Int J Hydrogen Energy , 23: 641–648 (1998).

Venkata, R.M., Lakshmanan E, Sethumadhavan R, Renganarayanan S. "Modeling and Experimental Validation of Cashew Nut Shell Char Gasification Adopting Chemical Equilibrium Approach", Energy & Fuels, 22: 2070–2078 (2008).

Wu, C.Z., Yin X, Ma L, Zhou Z, Chen H, "Operational characteristics of a 1.2-MW biomass gasification and power generation plant", Biotechnology Advances, 27: 588-592 (2009).

W. Permchart, V. I. Kouprianov, Emission performance and combustion efficiency of a conical fluidized-bed combustor firing various biomass fuels, Bioresource Technology, Volume 92, Issue 1, Pages 83-91 (2004).

Zainal, Z.A., Ali R, Quadir GA, Seetharamu KN. "Experimental investigation of a downdraft biomass gasifier". Biomass Bioenergy, 23:283–9 (2002).

Zhao, Y., Shaozeng S, Hongming T, Qian J, Su F, Ling F, "Characteristics of rice husk gasification in an entrained flow reactor", Bioresource Technology, 100: 6 (2009).

ภาคผนวก 22

INTERNATIONAL JOURNAL OF HYDROGEN ENERGY 36 (2011) 5067–5075

Available at www.sciencedirect.com

ScienceDirect

journal homepage: www.elsevier.com/locate/he

Performance improvement of bioethanol-fuelled solid oxide fuel cell system by using pervaporation

I. Choedkiatsakul [a], S. Charojrochkul [b], W. Kiatkittipong [c], W. Wiyaratn [d], A. Soottitantawat [a], A. Arpornwichanop [a], N. Laosiripojana [e], S. Assabumrungrat [a,*]

[a] Department of Chemical Engineering, Faculty of Engineering, Chulalongkorn University, Bangkok 10330, Thailand
[b] National Metal and Materials Technology Center (MTEC), Pathumthani 12120, Thailand
[c] Department of Chemical Engineering, Faculty of Engineering and Industrial Technology, Silpakorn University, Nakhon Pathom 73000, Thailand
[d] Department of Production Technology Education, Faculty of Industrial Education and Technology, King Mongkut's University of Technology Thonburi, Bangkok 10140, Thailand
[e] The Joint Graduate School of Energy and Environment, King Mongkut's University of Technology Thonburi, Bangkok 10140, Thailand

ARTICLE INFO

Article history:
Received 2 November 2010
Received in revised form
28 December 2010
Accepted 5 January 2011
Available online 12 February 2011

Keywords:
Solid oxide fuel cell
Bioethanol
Pervaporation
Process improvement

ABSTRACT

This work proposes an improvement in performance with respect to the electrical efficiency of a bioethanol-fuelled Solid Oxide Fuel Cell (SOFC) system by replacing a conventional distillation column by a pervaporation unit in the bioethanol purification process. The simulation study indicates that the membrane separation factor has a significant influence on the electrical power and heat energy required to generate a feed of 25 mol% ethanol in water to the reformer. The values of overall electrical efficiency of the SOFC systems with a distillation column and with a pervaporation unit are compared under the thermally self-sufficient condition ($Q_{net} = 0$) which offers their maximum electrical efficiency. At the base case, the SOFC system with a pervaporation unit provides an electrical efficiency of 42% compared with 34% achieved from the system with a distillation unit, indicating a significant improvement by using a pervaporation unit. An increase in ethanol recovery can further improve the overall electrical efficiency. The study also reveals that further improvement of the membrane selectivity can slightly enhance the overall efficiency of the SOFC system. Finally, an economic analysis of a bioethanol-fuelled SOFC system with pervaporation is suggested as the basis for further development.

1. Introduction

The Solid Oxide Fuel Cell (SOFC) is one of the most interesting power generation technologies nowadays because of its highly efficient and direct conversion of chemical energy to electricity. Fuel flexibility is the major advantage of SOFC since it can be fed with various primary fuels such as ammonia, methane, biogas, methanol and ethanol [1–5]. A number of researchers have investigated SOFC systems fuelled by bioethanol which is considered as a green renewable fuel [6–9]. However, most of the studies considered a feed of high purity ethanol rather than bioethanol. Several studies have been carried out to improve performance of SOFC systems fuelled by ethanol. Some electrolyte materials were proposed as a means of improving performance and stability of these systems [10–13]. Moreover, the effects of operating

* Corresponding author. Fax: +66 2 218 6877.
E-mail address: suttichai.a@chula.ac.th (S. Assabumrungrat).
0360-3199/$ – see front matter
doi:10.1016/j.ijhydene.2011.01.016

parameters on SOFC performance such as type of reforming process, operating temperature, operating voltage and fuel utilization were also investigated [14–16].

Recently, an SOFC system integrated with a distillation column for bioethanol purification was proposed [8]. The heat generated from the SOFC stack and the afterburner was supplied to the distillation column, reformer and heaters to preheat the feed. The system could be operated at an energy self-sufficient condition without relying on other external heat sources apart from the bioethanol feed. Jamsak et al. [9] designed a thermally integrated bioethanol-fuelled SOFC system with a distillation column using a heat exchanger network. The performance of the SOFC system integrated with bioethanol production and purification processes was investigated by considering the potential use of biogas co-generated in the bioethanol production as a primary fuel for hydrogen production in the SOFC system [17].

Regarding the technology for water/alcohol separation, apart from the conventional distillation, there are several potential technologies i.e. pervaporation [18–20], membrane distillation [21–23], adsorption [24–26] and extraction [27,28]. Among such technologies, pervaporation is considered to be promising particularly in terms of low energy requirement due to moderate temperature and pressure operation [29,30]. Moreover, it is an environmental-friendly technology and is independent of the vapor/liquid equilibrium characteristics of the substances to be separated. A number of membranes have been tested for separation of water/alcohol mixtures [31–36]. Due to the promising characteristics of pervaporation, it is interesting to investigate the possible improvement of the bioethanol-fuelled SOFC system by replacing a conventional distillation column with a pervaporation unit. Although it is likely that a SOFC system integrated with pervaporation offers higher electrical power than that with the distillation column due to the lower demand of heat energy, the requirement of extra electrical power for operating a vacuum pump may suppress the potential improvement.

The main objective of this work is to improve the overall efficiency of a bioethanol-fuelled SOFC system by integrating the SOFC system with a pervaporation unit to purify bioethanol prior to feeding to the SOFC system. The performance of the proposed SOFC system is compared with a conventional SOFC system integrated with a distillation column. In addition, the effects of operating parameters such as operating cell voltage, ethanol recovery and membrane selectivity on overall electrical efficiency of the SOFC system are investigated.

2. Process description and simulation

Fig. 1 shows a schematic diagram of the SOFC system. The system consists of a purification unit, a reformer, a SOFC stack and an afterburner. Bioethanol feed containing 3 mol% ethanol, which is derived from fermentation broth [37], is introduced to the purification unit to prepare a reformer feed at a desired concentration of ethanol (25 mol%). At the reformer, ethanol is converted to hydrogen rich gas via a steam reforming reaction ($C_2H_5OH + H_2O \leftrightarrow 2CO + 4H_2$). Carbon monoxide can further react with steam to generate more hydrogen and carbon dioxide via a water gas shift reaction ($CO + H_2O \leftrightarrow CO_2 + H_2$). It is assumed that the gas product is at its equilibrium composition. The reformed gas and air are fed to the anode and cathode of the SOFC stack, respectively, where the chemical energy of the fuel is directly converted to electricity. Exhaust gases from the stack are combusted in the afterburner. Heat released from the SOFC stack (Q_4) and the afterburner (Q_5) is supplied to the other energy-demanding units including the purification process (Q_1), reformer (Q_2), and air heater (Q_3). It is assumed that the hot gas is discharged to the environment at 403 K.

In this work, the performance of the SOFC system integrated with a purification unit is evaluated at the energy self-sufficient condition where the net energy (Q_{net}) defined as the difference between the exothermic heat (Q_4 and Q_5) and the endothermic heat (Q_1, Q_2 and Q_3) of the system (Eq. (1)) is equal to zero. Generally, the value Q_{net} can be positive, zero or negative. When Q_{net} is negative, the system requires more energy from an external heat source. The system can be energy self-sufficient when $Q_{net} \geq 0$. The best performance of

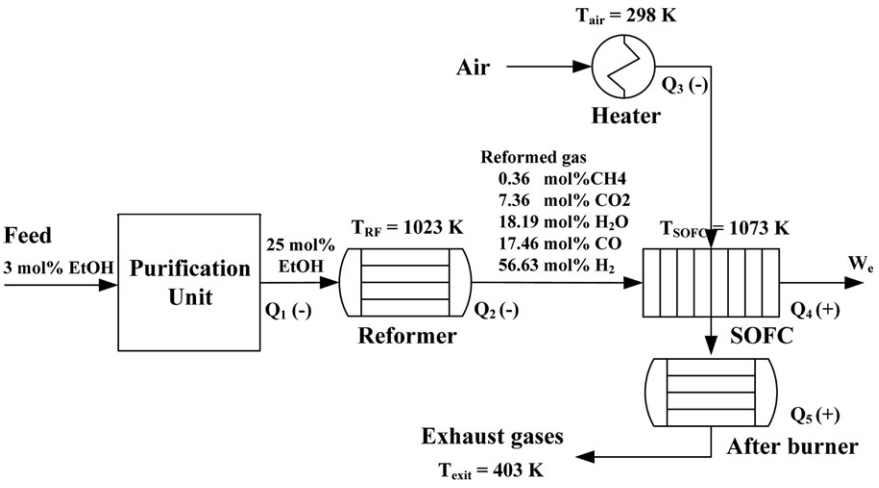

Fig. 1 – Schematic diagram of SOFC system integrated with purification unit.

the SOFC system in term of electrical efficiency can be achieved when $Q_{net} = 0$ [8]. It should be noted that in practice the values of the electrical efficiency are lower than those reported in this work as they are subjected to heat losses particularly for a system with a complicated heat exchanger network.

$$Q_{net} = (Q_4 + Q_5) - (Q_1 + Q_2 + Q_3) = 0 \quad (1)$$

Two bioethanol purification systems are considered in this study, i.e. pervaporation (Fig. 2(a)) and conventional distillation (Fig. 2(b)). For pervaporation, the membrane acts as a selective barrier which allows ethanol to selectively transport through it. The retentate stream may be partially mixed with the permeate stream to obtain 25 mol% ethanol based on the stoichiometric ratio of ethanol steam reforming. The obtained permeated composition is significantly dependent on the membrane selectivity. The relationship between the permeate composition (y) and the retentate composition (x) is assumed to be described by the membrane separation factor (α_{PV}).

$$\alpha_{PV} = \frac{y_P/(1-y_P)}{x_R/(1-x_R)} \quad (2)$$

Heat involved in the pervaporation process (Q_{PV}) includes the energy required to raise the temperature of the bioethanol feed to the pervaporation temperature ($T_{PV} = 333$ K), to vaporize all vapor permeating through the membrane, and to heat the permeate and part of the retentate to generate a feed of 25 mol% ethanol in water at the steam reforming temperature (T_{SR}) of 1023 K. The electrical power consumption of a vacuum pump in the pervaporation unit can be calculated from the following equations:

$$W_{e,PV} = -m_p \int_{T_{in}}^{T_{out}} C_p \, dT \quad (3)$$

$$T_{out} = T_{in}\left(1 + \frac{1}{\eta_{pump}}\left(\left(\frac{P_{out}}{P_{in}}\right)^{(\gamma-1)/\gamma} - 1\right)\right) \quad (4)$$

$$\gamma = \frac{C_p}{C_p - R} \quad (5)$$

The efficiency of the vacuum pump was assumed to be 75% [38]. It is noted that all of the variables are defined in the nomenclature.

With regard to the distillation column, a Radfrac rigorous equilibrium stage distillation module equipped with a partial condenser and a kettle boiler in Aspen™ plus program was set for the process simulation. Similar to the pervaporation process, the bottom stream in which the composition is mainly water may be partially mixed with the distillate stream to obtain the desired concentration of ethanol. The minimum reboiler heat duty, which could be obtained by adjusting the number of stages and reflux ratio, was used in the present study [8].

The computation of SOFC performance was based on our previous work [39]. For SOFC stack, the Ni-YSZ, YSZ and LSM-YSZ were used as the materials for the anode, electrolyte and cathode respectively. Since the H_2 electro-oxidation is much faster than CO electro-oxidation then it was assumed that only hydrogen ions reacted with oxygen ions as illustrated in Eqs. (6) and (7) [40]:

$$1/2O_2 \rightarrow O^{2-} \quad (6)$$

$$H_2 + O^{2-} \rightarrow H_2O + 2e^- \quad (7)$$

The open-circuit voltage (E) can be calculated from the Nernst equation as expressed in Eq. (8).

$$E = E_0 + \frac{RT}{2F}\ln\left(\frac{p_{H_2}p_{O_2}^{1/2}}{p_{H_2O}}\right) \quad (8)$$

The actual cell potential (V) is always less than the open-circuit voltage (E) owing to the existence of the overpotentials as shown by Eq. (9).

$$V = E - \eta_{act} - \eta_{ohmic} - \eta_{conc} \quad (9)$$

The ohmic overpotential (η_{ohmic}) is the resistance of the electron to flow through the electrodes, interconnections and electrolyte. This overpotential is the major loss of the SOFC stack which can be calculated from Eq. (10).

$$\eta_{ohmic} = 2.99 \times 10^{-11} iL \exp\left(\frac{10\,300}{T}\right) \quad (10)$$

The activation overpotential (η_{act}) occurs from the electrochemical reaction at the electrodes. Normally, the activation overpotential dominates at low current density but at high temperature, the reaction rate is very fast such that this value is small. This overpotential can be expressed by the Butler–Volmer equation.

$$i = i_0\left[\exp\left(\frac{\alpha z F \eta_{act}}{RT}\right) - \exp\left(-\frac{(1-\alpha)zF\eta_{act}}{RT}\right)\right] \quad (11)$$

In case of SOFC, the values of α and z are 0.5 and 2 respectively [41]. Consequently, the activation overpotential at anode and cathode side can be written as

$$\eta_{act} = \frac{RT}{F}\sinh^{-1}\left(\frac{i}{2i_0}\right) \quad (12)$$

The exchange current density (i_0) for the cathode and anode side can be calculated from these two equations:

$$i_{0,a} = \gamma_a\left(\frac{p_{H_2}}{P_{ref}}\right)\left(\frac{p_{H_2O}}{P_{ref}}\right)\exp\left(-\frac{E_{act,a}}{RT}\right) \quad (13)$$

$$i_{0,c} = \gamma_c\left(\frac{p_{O_2}}{P_{ref}}\right)^{0.25}\exp\left(-\frac{E_{act,c}}{RT}\right) \quad (14)$$

The concentration overpotential (η_{conc}) is the loss due to the difference concentration of gas between the bulk and the reaction site. It can be estimated by Eqs. (15) and (16).

$$\eta_{conc,a} = \frac{RT}{2F}\ln\left[\frac{\left(1 + \left(\frac{RT}{2F}\right)\left(\frac{l_a}{D_{a(eff)}p^l_{H_2O}}\right)i\right)}{\left(1 - \left(\frac{RT}{2F}\right)\left(\frac{l_a}{D_{a(eff)}p^l_{H_2}}\right)i\right)}\right] \quad (15)$$

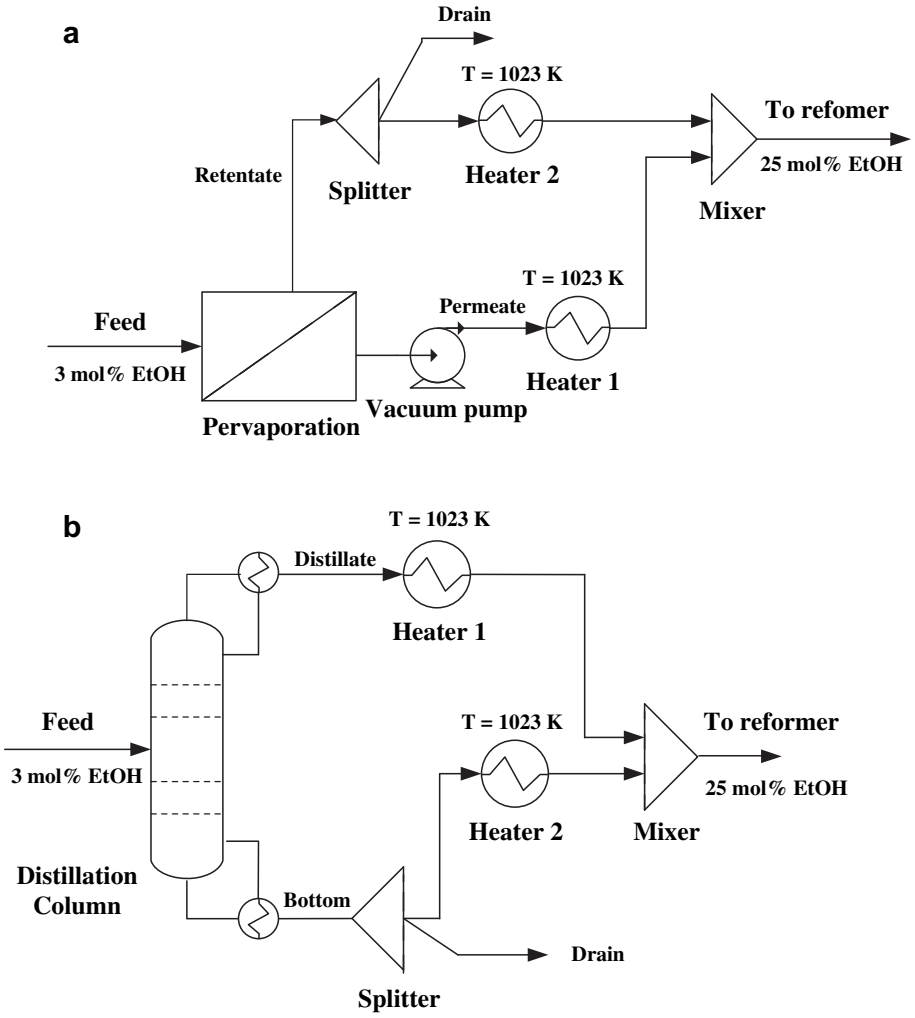

Fig. 2 – Schematic diagrams of bioethanol purification processes: (a) pervaporation and (b) distillation.

$$\eta_{\mathrm{conc,c}} = \frac{RT}{4F}\ln\left[\frac{p^{\mathrm{I}}_{\mathrm{O}_2}}{\left(\left(\mathrm{P_c}-\delta_{\mathrm{O}_2}\right)-\left(\left(\mathrm{P_c}-\delta_{\mathrm{O}_2}\right)-p^{\mathrm{I}}_{\mathrm{O}_2}\right)\exp\left[\left(\frac{RT}{4F}\right)\left(\frac{\delta_{\mathrm{O}_2} l_{\mathrm{c}}}{D_{\mathrm{c(eff)}}\mathrm{P_c}}\right)\mathrm{i}\right]\right)}\right] \tag{16}$$

δ_{O_2}, $D_{\mathrm{a(eff)}}$ and $D_{\mathrm{c(eff)}}$ can be expressed by

$$\delta_{\mathrm{O}_2} = \frac{D_{\mathrm{O}_2,\mathrm{k(eff)}}}{D_{\mathrm{O}_2,\mathrm{k(eff)}} + D_{\mathrm{O}_2-\mathrm{N}_2\mathrm{(eff)}}} \tag{17}$$

$$D_{\mathrm{a(eff)}} = \left(\frac{p_{\mathrm{H_2O}}}{\mathrm{P_a}}\right)D_{\mathrm{H_2(eff)}} + \left(\frac{p_{\mathrm{H_2}}}{\mathrm{P_a}}\right)D_{\mathrm{H_2O(eff)}} \tag{18}$$

$$\frac{1}{D_{\mathrm{c(eff)}}} = \frac{\xi}{n}\left(\frac{1}{D_{\mathrm{O_2,k}}} + \frac{1}{D_{\mathrm{O_2-N_2}}}\right) \tag{19}$$

$$\frac{1}{D_{\mathrm{H_2(eff)}}} = \frac{\xi}{n}\left(\frac{1}{D_{\mathrm{H_2,k}}} + \frac{1}{D_{\mathrm{H_2-H_2O}}}\right) \tag{20}$$

$$\frac{1}{D_{\mathrm{H_2O(eff)}}} = \frac{\xi}{n}\left(\frac{1}{D_{\mathrm{H_2O,k}}} + \frac{1}{D_{\mathrm{H_2-H_2O}}}\right) \tag{21}$$

Eq. (22) shows the relation between effective parameter ($D_{\mathrm{(eff)}}$) and nominal parameter (D):

$$D_{\mathrm{(eff)}} = \frac{n}{\xi}D \tag{22}$$

The correlation below is used to calculate the Knudsen diffusivity:

$$D_{\mathrm{i,K}} = 9700\sqrt{\frac{T}{M_{\mathrm{i}}}} \tag{23}$$

The Chapman–Enskog equation is used for calculating the ordinary diffusivity:

$$D_{A-B} = 1.8583 \times 10^{-3}\left(\frac{T^{3/2}\left(\left(\frac{1}{M_A}\right)+\left(\frac{1}{M_B}\right)\right)^{1/2}}{P\sigma_{AB}^2\Omega_D}\right) \quad (24)$$

where σ_{AB} and Ω_D can be calculated from the following equations:

$$\sigma_{AB} = \frac{\sigma_A + \sigma_B}{2} \quad (25)$$

$$\Omega_D = \frac{A}{T_k^B} + \frac{C}{\exp(D\cdot T_k)} + \frac{E}{\exp(F\cdot T_k)} + \frac{G}{\exp(H\cdot T_k)} \quad (26)$$

where T_k is equal to T/ϵ_{AB} and A, C, E and G are constants for each gas.

The overall efficiency of the system can be computed by Eq. (27). Only the electrical power required for operating a vacuum pump in the pervaporation operation is considered in the calculations of $W_{e,net}$.

$$\%\ \text{Overall electrical efficiency} = \frac{W_{e,net}}{n_{EtOH}LHV_{EtOH}} \times 100\% \quad (27)$$

The parameters used in the calculations are summarized in Table 1.

The SOFC model was validated with the previous experimental results of Zhao and Virkar [42] and Tao et al. [43] for high concentration of hydrogen in the feed and of Petruzzi et al. [44] for low concentration of hydrogen in the feed. Good agreement was observed.

3. Results and discussion

Fig. 3 shows the effect of the membrane separation factor on the heat (Q_{PV}) and electrical power ($W_{e,PV}$) required for operating the pervaporation process. When a membrane with higher selectivities is used, the purification process consumes less electrical power but greater amount of heat. This is due to the dependence of $W_{e,PV}$ on the flow rate of the permeate stream (Eq. (3)) which continuously decreases at higher separation factors due to the higher ethanol purity achieved. On the other hand, a greater amount of heat is demanded to preheat water in the retentate stream when mixing with the purified ethanol to obtain the reformer feed at the desired ethanol concentration (25 mol%). The results also indicate that when the pervaporation is operated at a higher ethanol recovery, the process requires higher electrical power and heat, and in addition, the minimum value of membrane separation factor to achieve the ethanol purity as low as 25 mol% in the permeate stream becomes higher.

To compare the performance of the systems with different purification processes, the electrical efficiencies were calculated based on the same operating conditions; i.e. ethanol recovery = 80%, T_{SR} = 1073 K and operating cell voltage = 0.7 V. For the pervaporation, the membrane separation factor of 49 which

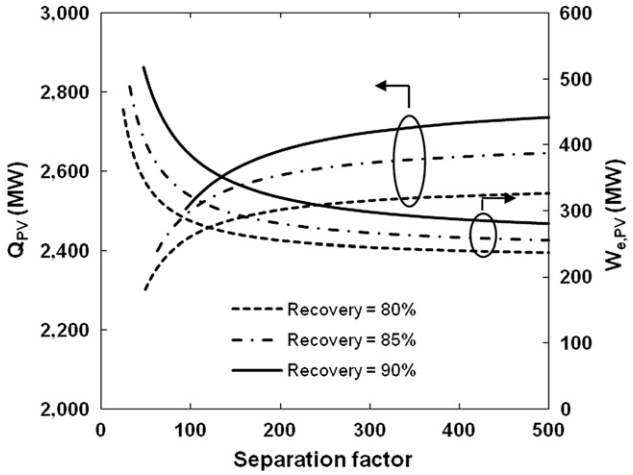

Fig. 3 – Effect of membrane separation factor on heat (Q_{PV}) and electrical power ($W_{e,PV}$) required for operating the pervaporation system (T_{PV} = 333 K, P_p = 0.1 atm).

Table 1 – Summary of SOFC model parameters [39].

Parameters	Value
l (μm)	50
$E_{act,a}$ (J/mol)	1.0×10^5
$E_{act,c}$ (J/mol)	1.2×10^5
γ_a (A/m^2)	1.344×10^{10}
γ_c (A/m^2)	2.051×10^9
l_a (μm)	750
l_c (μm)	50
ξ (μm)	5.4
n	0.48
σ_{H_2} (Å)	2.827
σ_{H_2O} (Å)	2.641
σ_{N_2} (Å)	3.798
σ_{O_2} (Å)	3.467
ϵ_{H_2}	59.7
ϵ_{H_2O}	809.1
ϵ_{N_2}	71.4
ϵ_{O_2}	106.7

Table 2 – Performance of SOFC systems integrated with different purification units which operate at thermally self-sufficient condition (ethanol recovery = 80%, operating voltage = 0.7 V, T_{SOFC} = 1073 K).

Parameters	Purification unit	
	Pervaporation	Distillation
1. Heat (MW)		
Purification	2301	3580
Reformer	417	421
Air heater	22,575	23,892
Afterburner	25,293	27,893
2. Electrical power (MW)		
Purification	453	0
Electricity	4920	3701
Net electrical power	4467	3701
3. Fuel utilization (%)	92	68
4. Overall electrical efficiency (%)	42	34

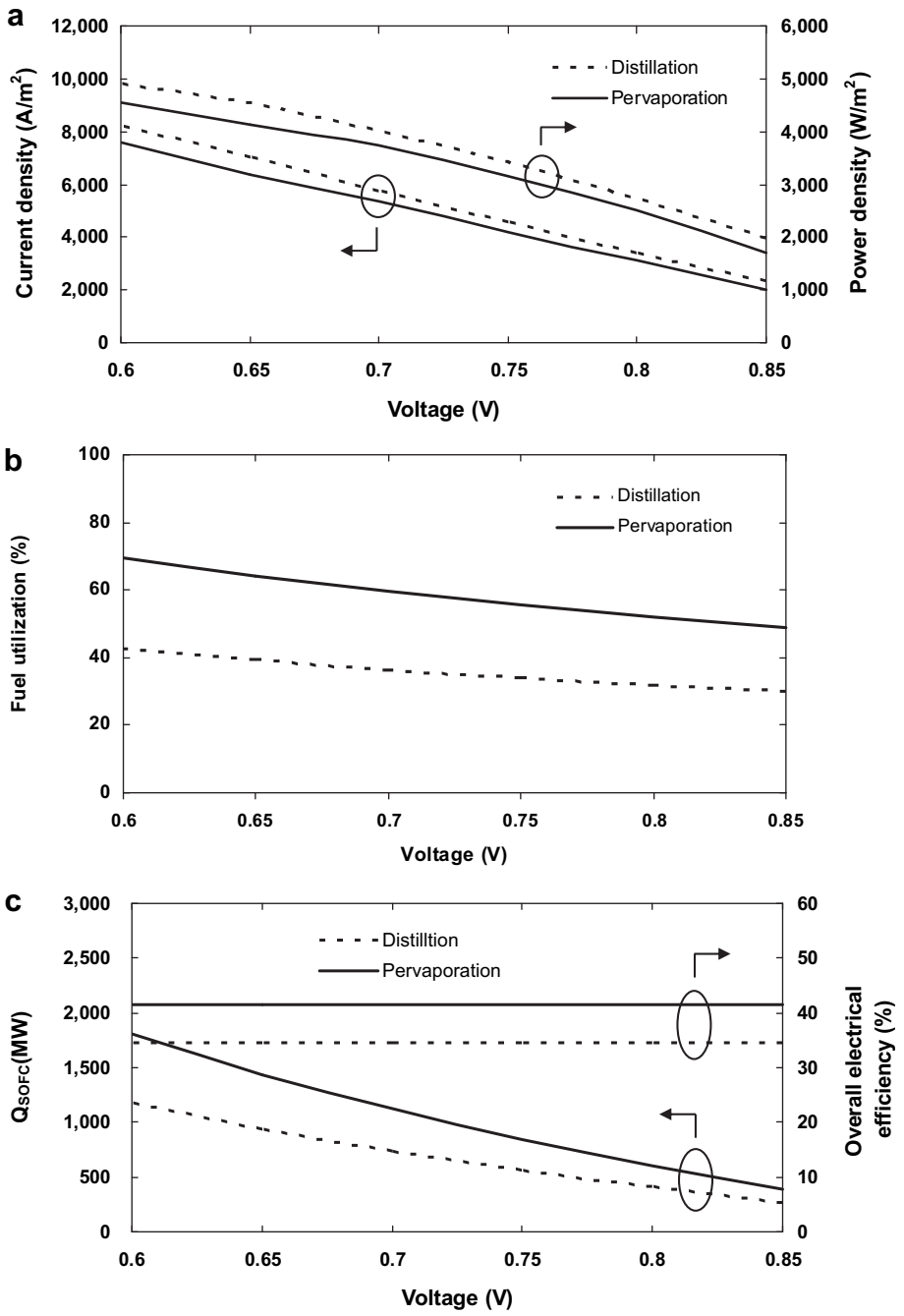

Fig. 4 – Effect of operating voltage on (a) current density and power density, (b) fuel utilization of SOFC stack and (c) heat of SOFC stack (Q_{SOFC}) and overall electrical efficiency of the SOFC system (ethanol recovery = 80%, T_{SOFC} = 1073 K, membrane separation factor = 49).

offers the ethanol purity of the permeate stream close to 25 mol % was considered. The results in Table 2 indicate that the overall electrical efficiency of the SOFC system integrated with pervaporation (42%) is much higher than that achieved from the use of a conventional distillation column (34%). The significant reduction of heat demand from the use of pervaporation allows the SOFC feed to be utilized more efficiently for electrical power generation as observed by the greater value of fuel utilization of 92% in the pervaporation system compared to that of 68% in the distillation system, even though part of the electrical power generated at the SOFC stack (4920 MW) is required to operate the vacuum pump of the pervaporation unit (453 MW). Apparently, the replacement of the distillation column by the pervaporation can remarkably improve the overall electrical efficiency of the system.

The effect of operating voltage on the current density and power density, the corresponding fuel utilization, the heat of SOFC stack (Q_{SOFC}) and the overall electrical efficiency at the energy self-sufficient condition ($Q_{net} = 0$) is shown in Fig. 4(a)–(c), respectively. It was found that the current

density, power density, fuel utilization and heat of SOFC stack (Q_{SOFC}) decrease with increasing the operating voltage. However, the overall electrical efficiency remains unchanged for all different operating voltages. At a higher operating voltage, the stack is operated at the voltage close to its theoretical electromotive force, resulting in smaller irreversible losses and consequently lower heat of SOFC stack (Q_{SOFC}) as well as the current density and the power density. To maintain the condition of $Q_{net} = 0$ at a smaller value of Q_{SOFC}, the stack needs to be operated at a lower fuel utilization thus a greater amount of the exhaust fuel is left for the afterburner to generate sufficient heat for the system. The sources of heat generation just alter between the heat of SOFC and heat from the afterburner for supplying the other heat consuming units in the system which does not vary with operating voltage. Therefore, the overall electrical efficiency achieved from the system does not vary with the operating voltage. It is noted that an appropriate voltage needs to be carefully selected as the operation of SOFC at too low voltage leads to a high heat level in the SOFC stack which may cause difficulty in heat removal from the stack while operation at too high voltage leads to a low cell power density and thus a large stack area is required.

When the effect of ethanol recovery is considered, the overall electrical efficiency of the SOFC systems can be further improved by increasing the ethanol recovery as shown in Fig. 5. Although, the required energy for the purification unit rises at higher ethanol recovery, the amount of ethanol provided to the SOFC system still increases. Consequently, the overall efficiency is higher when increasing the ethanol recovery. Again, it has been demonstrated that the SOFC system integration with a pervaporation unit provides higher overall electrical efficiency than that integrated with a distillation column. Importantly, economic analysis is essential in determining a suitable ethanol recovery as the operation at a higher ethanol recovery may result in significant increases in capital costs such as a distillation column with more trays or membrane with much larger area. The results shown in Fig. 5 also indicate that the minimum membrane separation factor significantly increases with increasing the ethanol recovery, indicating that a highly selective membrane is needed to enable operation at high ethanol recovery. Finally, the effect of membrane separation factor on the overall

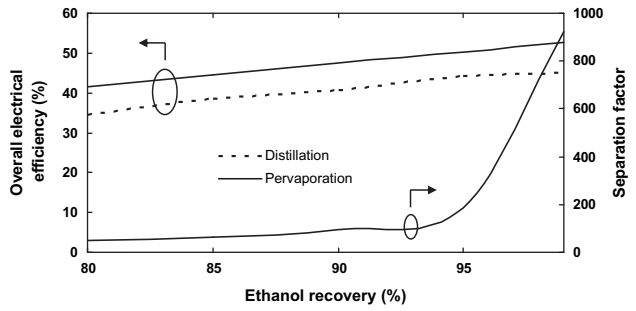

Fig. 5 – Effect of ethanol recovery on overall electrical efficiency of the SOFC system and the membrane separation factor (operating voltage = 0.7 V, T_{SOFC} = 1073 K).

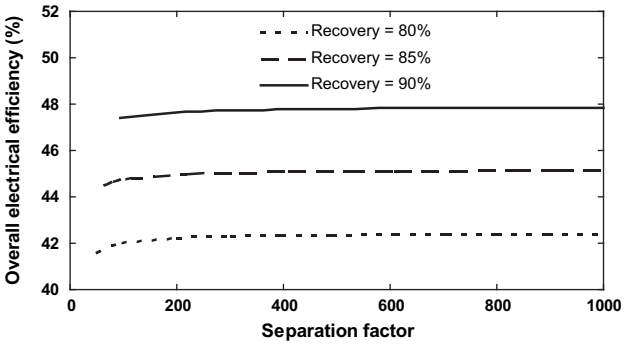

Fig. 6 – Effect of membrane separation factor on overall electrical efficiency of the SOFC system (operating voltage = 0.7 V, T_{SOFC} = 1073 K).

electrical efficiency is shown in Fig. 6. The overall electrical efficiency slightly increases at high separation factor, indicating that the use of a highly selective membrane may be unnecessary. It should be noted that the separation factors of membrane for ethanol/water recovery reported in the literatures are in the range from 10 to 125 [24–29]. Therefore, the use of the minimum value of membrane separation factor to achieve the 25 mol% of ethanol purity in the permeate stream is possible.

4. Conclusions

The performances of bioethanol-fuelled SOFC systems integrated with two different purification processes, i.e. distillation and pervaporation have been compared. The SOFC system integrated with a pervaporation unit has been demonstrated to be a promising choice over the SOFC system with conventional distillation unit since the replacement of distillation with pervaporation can reduce the energy demand in bioethanol purification. Therefore, the overall electrical efficiency of the SOFC system can be improved. The SOFC stack can be operated at different voltages and fuel utilization to achieve the thermally self-sufficient condition of the SOFC system, resulting in different power density and heat generation from the SOFC stack. Regarding the effect of ethanol recovery, the overall electrical efficiency increases with an increase of ethanol recovery but the pervaporation requires a membrane with a higher selectivity. It is also demonstrated that the development of membrane with superior selectivity may be unnecessary since it only gives a slight improvement in the overall electrical efficiency of the SOFC.

Acknowledgements

This research work is financially supported by the Thailand Research Fund, Commission on Higher Education, National Metal and Materials Technology Center (MTEC) and National Science and Technology Development Agency (NSTDA). The authors also would like to thank Dr. John Pearce for correcting the English and giving useful suggestions.

Nomenclature

C_p	heat capacity at constant pressure, kJ kmol^{-1} K^{-1}
$D_{i,K}$	Knudsen diffusivity of component i, cm^2 s^{-1}
D_{A-B}	ordinary diffusivity of gas A versus gas B, cm^2 s^{-1}
$D_{i(eff)}$	effective diffusion coefficient of electrode i, cm^2 s^{-1}
$D_{i,k(eff)}$	effective Knudsen diffusivity of component i, cm^2 s^{-1}
$D_{A-B(eff)}$	effective ordinary diffusivity of gas A versus gas B, cm^2 s^{-1}
E	theoretical open-circuit voltage of the cell, V
E_0	theoretical open-circuit voltage of the cell at standard pressure, V
E_{act}	activation energy, kJ mol^{-1}
F	Faraday constant (9.6495×10^4), C mol^{-1}
i	current density, A cm^{-2}
i_0	exchange current density, A cm^{-2}
l_a	thickness of anode, μm
l_c	thickness of cathode, μm
L	thickness of electrolyte, μm
LHV_{EtOH}	lower heating value of ethanol, kJ kmol^{-1}
m_p	permeate flow rate, mol s^{-1}
M_i	molecular weight of gas i, g
n	electrode porosity, dimensionless
n_{EtOH}	molar flow rate of ethanol, mol s^{-1}
p_i	partial pressure of component i, Pa
p_i^I	inlet pressure of component i, Pa
P	pressure, Pa
P_{ref}	reference pressure (10^5), Pa
Q_{net}	net useful heat, MW
Q_{PV}	heat generation at pervaporation purification unit, MW
Q_{SOFC}	heat generation at the SOFC stack, MW
R	gas constant (8.3145), J mol^{-1} K^{-1}
T	temperature, K
U_f	fuel utilization, %
V	cell voltage, V
$W_{e,net}$	net electrical power, MW
$W_{e,PV}$	electrical power consumption of a vacuum pump in pervaporation unit, MW
x_R	mole fraction of ethanol at retentate side of the membrane, dimensionless
y_P	mole fraction of ethanol at permeate side of the membrane, dimensionless
z	number of electron participating in the electrochemical reaction, dimensionless

Greek letters

α	charge transfer coefficient, dimensionless
α_{PV}	separation factor of membrane, dimensionless
ξ	electrode tortuosity, dimensionless
δ_i	coefficient used in concentration overpotential of component i, dimensionless
η_{act}	activation loss, V
η_{conc}	concentration loss, V
η_e	overall electrical efficiency, %
η_{ohmic}	ohmic loss, V
η_{pump}	pump efficiency, %
σ_{AB}	collision diameter, Å
Ω_D	collision integral, dimensionless
ϵ_{AB}	Lennard-Jones energy interaction parameter scaled with respect to the Boltzman constant, dimensionless
γ_a	pre-exponential factor for anode exchange current density, A m^{-2}
γ_c	pre-exponential factor for cathode exchange current density, A m^{-2}

Subscripts

a	anode
c	cathode
in	input
out	output

REFERENCES

[1] Zhang L, Yang W. Direct ammonia solid oxide fuel cell based on thin proton-conducting electrolyte. J Power Sources 2008; 179:92–5.

[2] Hao Y, Goodwin DG. Efficiency and fuel utilization of methane-powered single-chamber solid oxide fuel cells. J Power Sources 2008;183:157–63.

[3] Shiratori Y, Oshima T, Sasaki K. Feasibility of direct-biogas SOFC. Int J Hydrogen Energy 2008;33:6316–21.

[4] Liu M, Peng R, Dong D, Gao J, Liu X, Meng G. Liquid methanol-fueled solid oxide fuel cell. J Power Sources 2008;185:188–92.

[5] Laosiripojana N, Wiyratn W, Kiatkittipong W, Arpornwichanop A, Soottitantawat A, Assabumrungrat S. Reviews on solid oxide fuel cell technology. Eng J 2009;13: 73–90.

[6] Hernández L, Kafarov V. Use of bioethanol for sustainable electrical energy production. Int J Hydrogen Energy 2009;34: 7041–50.

[7] Arteaga LE, Peralta LM, Kafarov V, Casas Y, Gonzales E. Bioethanol steam reforming for ecological syngas and electricity production using a fuel cell SOFC system. Chem Eng J 2008;136:256–66.

[8] Jamsak W, Assabumrungrat S, Douglas PL, Croiset E, Laosiripojana N, Suwanwarangkul R, et al. Thermodynamic assessment of solid oxide fuel cell system integrated with bioethanol purification unit. J Power Sources 2007;174:191–8.

[9] Jamsak W, Douglas PL, Croiset E, Suwanwarangkul R, Laosiripojana N, Charojrochkul S, et al. Design of a thermally integrated bioethanol-fueled solid oxide fuel cell system integrated with a distillation column. J Power Sources 2009; 187:190–203.

[10] Huang B, Zhu XJ, Hu WQ, Yu QC, Tu HY. Characteristics and performance of lanthanum gallate electrolyte-supported SOFC under ethanol steam and hydrogen. J Power Sources 2009;186:29–36.

[11] Cimenti M, Hill JM. Direct utilization of ethanol on ceria-based anodes for solid oxide fuel cells. Asia Pac J Chem Eng 2009;4:45–54.

[12] Tapan N, Kok A. Characterization of cerium oxide and carbon supported Ag–Cu electro-catalysts for anode electrode in direct ethanol fuel cells. Chem Eng Comm 2009; 196:131–47.

[13] Ye XF, Wang SR, Hu Q, Wang ZR, Wen TL, Wen ZY. Improvement of multi-layer anode for direct ethanol solid oxide fuel cells. Electrochem Commun 2009;11:823–6.

[14] Diethelm S, Vanherle J. Ethanol internal steam reforming in intermediate temperature solid oxide fuel cell. J Power Sources; 2010.

[15] Arpornwichanop A, Chalermpanchai N, Patcharavorachot Y, Assabumrungrat S, Tade M. Performance of an anode-supported solid oxide fuel cell with direct-internal reforming of ethanol. Int J Hydrogen Energy 2009;3(4):7780–8.
[16] Cimenti M, Hill JM. Thermodynamic analysis of solid oxide fuel cells operated with methanol and ethanol under direct utilization, steam reforming, dry reforming or partial oxidation conditions. J Power Sources 2009;186:377–84.
[17] Choedkiatsakul I, Sintawarayan K, Prawpipat T, Soottitantawat A, Wirayatn W, Kiatkittipong W, et al. Performance assessment of SOFC systems integrated with bio-ethanol production and purification processes. Eng J 2010;13:1–14.
[18] Huang S, Hung W, Liaw D, Lo C, Chao W, Hu C, et al. Interfacially polymerized thin-film composite polyamide membranes: effects of annealing processes on pervaporative dehydration of aqueous alcohol solutions. Sep Purif Technol 2010;72:40–7.
[19] Khayet M, Cojocaru C, Zakrzewska-Trznadel G. Studies on pervaporation separation of acetone, acetonitrile and ethanol from aqueous solutions. Sep Purif Technol 2008;63: 303–10.
[20] Ma Y, Wang J, Tsuru T. Pervaporation of water/ethanol mixtures through microporous silica membranes. Sep Purif Technol 2009;66:479–85.
[21] Huang Y, Baker RW, Vane LM. Low energy distillation membrane separation process. Ind Eng Chem Res 2010;49: 3760–8.
[22] Boi C, Bandini S, Sarti GC. Pollutants removal from wastewaters through membrane distillation. Desalination 2005;183:383–94.
[23] Banat FA, Al-Shannag M. Recovery of dilute acetone–butanol–ethanol (ABE) solvents from aqueous solutions via membrane distillation. Bioprocess Eng 2000;23: 643–9.
[24] Oliveira JFG, Lucena IL, Saboya RMA, Rodrigues ML, Torres AEB, Fernandes FAN, et al. Biodiesel production from waste coconut oil by esterification with ethanol: the effect of water removal by adsorption. Renew Energy 2010;35: 2581–4.
[25] Wang Y, Gong C, Sun J, Gao H, Zheng S, Xu S. Separation of ethanol/water azeotrope using compound starch-based adsorbents. Bioresour Technol 2010;101:6170–6.
[26] Oudshoorn A, van der Wielen LAM, Straathof AJJ. Adsorption equilibria of bio-based butanol solutions using zeolite. Biochem Eng J 2009;48:99–103.
[27] Pfeuffer B, Kunz U, Hoffmann U, Turek T, Hoell D. Heterogeneous reactive extraction for an intensified alcohol production process. Catal Today 2009;147S:S357–61.
[28] Shao P, Kumar A. Recovery of 2,3-butanediol from water by a solvent extraction and pervaporation separation scheme. J Memb Sci 2009;329:160–8.
[29] Fernandez ES, Geerdink P, Goetheer ELV. Thermo pervap: the next step in energy efficient pervaporation. Desalination 2010;250:1053–5.
[30] Lipnizki F. Membrane process opportunities and challenges in the bioethanol industry. Desalination 2010;250:1067–9.
[31] Matsuda H, Yanagishita H, Negishi H, Kitamoto D, Ikegami T, Haraya K, et al. Improvement of ethanol selectivity of silicalite membrane in pervaporation by silicone rubber coating. J Memb Sci 2002;210:433–7.
[32] Zhan X, Li J, Huang J, Chen C. Enhanced pervaporation performance of multi-layer PDMS/PVDF composite membrane for ethanol recovery from aqueous solution. Appl Biochem Biotechnol; 2008:1–11.
[33] Chen H, Li Y, Zhu G, Liu J, Yang W. Synthesis and pervaporation performance of high-reproducibility silicalite-1 membranes. Chin Sci Bull 2008;53:3505–10.
[34] Chang CL, Chang MS. Preparation of multi-layer silicone/PVDF composite membranes for pervaporation of ethanol aqueous solutions. J Memb Sci 2004;238:117–22.
[35] Lia L, Xiao Z, Tan S, Pu L, Zhang Z. Composite PDMS membrane with high flux for the separation of organics from water by pervaporation. J Memb Sci 2004;243:177–87.
[36] Vane LM. A review of pervaporation for product recovery from biomass fermentation processes. J Chem Technol Biotechnol 2005;80:603–29.
[37] Leng R, Wang C, Zhang C, Dai D, Pu G. Life cycle inventory and energy analysis of cassava-based fuel ethanol in China. J Cleaner Prod 2008;16:374–84.
[38] Kaneko T, Brouwer J, Samuelsen GS. Power and temperature control of fluctuating biomass gas fueled solid oxide fuel cell and micro gas turbine hybrid system. J Power Sources 2006; 160:316–25.
[39] Piroonlerkgul P, Assabumrungrat S, Laosiripojana N, Adesina AA. Selection of appropriate fuel processor for biogas-fuelled SOFC system. Chem Eng J 2008;140:341–51.
[40] Khaleel MA, Lin Z, Singh P, Surdoval W, Collin D. A finite element analysis modeling tool for solid oxide fuel cell development: coupled electrochemistry, thermal and flow analysis in MARC®. J Power Sources 2004;130:136–48.
[41] Chan SH, Khor KA, Xia ZT. A complete polarization model of a solid oxide fuel cell and its sensitivity to the change of cell component thickness. J Power Sources 2001;93:130–40.
[42] Zhao F, Virkar AV. Dependence of polarization in anode-supported solid oxide fuel cells on various cell parameters. J Power Sources 2005;141:79–95.
[43] Tao G, Armstrong T, Virkar A. Intermediate temperature solid oxide fuel cell (IT-SOFC) research and development activities at MSRI. In: Nineteenth annual ACERC&ICES conference, Utah; 2005.
[44] Petruzzi L, Cocchi S, Fineschi F. A global thermo-electrochemical model for SOFC systems design and engineering. J Power Sources 2003;118:96–107.

ภาคผนวก 23

INTERNATIONAL JOURNAL OF HYDROGEN ENERGY 36 (2011) 267–275

Available at www.sciencedirect.com

ScienceDirect

journal homepage: www.elsevier.com/locate/he

Hydrogen production from glycerol steam reforming for low- and high-temperature PEMFCs

Suthida Authayanun [a], *Amornchai Arpornwichanop* [a,*], *Yaneeporn Patcharavorachot* [a], *Wisitsree Wiyaratn* [b], *Suttichai Assabumrungrat* [a]

[a] *Department of Chemical Engineering, Faculty of Engineering, Chulalongkorn University, Bangkok 10330, Thailand*
[b] *Department of Production Technology Education, Faculty of Industrial Education and Technology, King Mongkut's University of Technology Thonburi, Bangkok 10140, Thailand*

ARTICLE INFO

Article history:
Received 3 August 2010
Received in revised form
16 October 2010
Accepted 20 October 2010
Available online 20 November 2010

Keywords:
Glycerol
Steam reforming
PEMFC
Optimal condition
Thermodynamic analysis

ABSTRACT

This paper presents a thermodynamic study of a glycerol steam reforming process, with the aim of determining the optimal hydrogen production conditions for low- and high-temperature proton exchange membrane fuel cells (LT-PEMFCs and HT-PEMFCs). The results show that for LT-PEMFCs, the optimal temperature and steam to glycerol molar ratio of the glycerol reforming process (consisting of a steam reformer and a water gas shift reactor) are 1000 K and 6, respectively; under these conditions, the maximum hydrogen yield was obtained. Increasing the steam to glycerol ratio over its optimal value insignificantly enhanced the performance of the fuel processor. For HT-PEMFCs, to keep the CO content of the reformate gas within a desired range, the steam reformer can be operated at lower temperatures; however, a high steam to glycerol ratio is required. This requirement results in an increase in the energy consumption for steam generation. To determine the optimal conditions of glycerol steam reforming for HT-PEMFC, both the hydrogen yield and energy requirements were taken into consideration. The operational boundary of the glycerol steam reformer was also explored as a basic tool to design the reforming process for HT-PEMFC.

1. Introduction

A fuel cell is a promising source of electricity generation, due to its high efficiency and environmental friendliness. In principle, a fuel cell generates electricity via an electrochemical reaction of hydrogen and oxygen and produces only water and heat as by-products. But because hydrogen is not readily available, it is necessary to produce it from other sources. Most hydrogen is produced from reforming processes of natural gas. Although natural gas is a cost-effective feedstock, it is also a limited and nonrenewable resource [1,2]. For this reason, various studies have been conducted to develop the means to produce hydrogen from renewable resources to support the future use of fuel cells.

To date, glycerol is considered an alternative fuel for hydrogen production because it is a by-product of the production of biodiesel, which uses vegetable oils or fats as feedstock. Therefore, glycerol is a promising, renewable source of hydrogen production [3]. Typically, the main goal of hydrogen production is to maximize hydrogen yield, and thus, most of the previous investigations have identified the favorable conditions and methods to achieve this goal. Rabenstein et al. [4] studied the production of hydrogen from ethanol using three common methods, i.e., steam reforming,

* *Corresponding author*. Tel.: +66 2 2186878; fax: +66 2 2186877.
E-mail address: Amornchai.A@chula.ac.th (A. Arpornwichanop).
0360-3199/$ – see front matter © 2010 Professor T. Nejat Veziroglu. Published by Elsevier Ltd. All rights reserved.
doi:10.1016/j.ijhydene.2010.10.061

partial oxidation, and autothermal reforming. It was revealed that steam reforming provides the highest hydrogen yield and that coke formation can be eliminated by increasing the steam to ethanol molar ratio and the oxygen to ethanol molar ratio. Vagia et al. [5] analyzed the equilibrium product composition of reforming processes of an aqueous bio-oil fraction. They found that steam reforming gives a higher yield of hydrogen, compared to the autothermal reforming, because part of the fuel feed in autothermal reforming is consumed by the combustion reaction to supply heat to the system. The maximum hydrogen yield can be achieved at a temperature of 900 K, for both the steam reforming and autothermal reforming processes. A high steam to fuel ratio favors the hydrogen yield but also increases the energy requirements.

Considering glycerol reforming, various studies have relied on experiments [6–12] or simulations [13–19] to investigate the effects of key operating parameters on the various reforming processes and to identify the optimal conditions. Buffoni et al. [20] studied glycerol steam reforming based on a nickel catalyst. Their results indicated that the operating temperature strongly influences the activity of the nickel catalyst; the minimum temperature that provides high hydrogen selectivity is 823 K. Adhikari et al. [13] concluded from their simulation results that the optimal conditions for hydrogen production from glycerol are a temperature above 900 K, atmospheric pressure, and a steam to glycerol molar ratio of 9. Wang et al. [15] studied steam reforming of glycerol and found that the optimal temperature and steam to glycerol molar ratio were in the range of 925–975 K and 9–12, respectively. Low-temperature operation and a high steam to glycerol molar ratio are required to minimize CO formation. They suggested that while high-temperature operation is preferable for hydrogen production, CO removal is desired for applications in fuel cells. Recently, Chen et al. [21] conducted a thermodynamic analysis through an experiment of a glycerol steam reforming process. They found that the predicted results were in agreement with the experimental data and that the steam to glycerol ratio is a key factor for improving the conversion of glycerol.

Among the different types of fuel cell, the polymer electrolyte membrane, or proton exchange membrane, fuel cell (PEMFC) is one of the most attractive fuel cells for automobile, residential and portable applications because it operates at low temperatures (allowing it to start up and shut down very quickly) and provides a high current density [22,23]. Currently, PEMFCs can be divided into two types depending on the operating temperatures, low-temperature (LT-PEMFCs) and high-temperature (HT-PEMFCs) proton exchange membrane fuel cells. LT-PEMFCs can be operated at temperatures of approximately 333–353 K and are limited to sources of high hydrogen purity. The content of CO in the hydrogen feed for a LT-PEMFC can be no greater than 10 ppm to avoid catalyst poisoning [24]. Therefore, the obtained reformate gas needs to be treated using water gas shift and preferential oxidation processes before being fed to the LT-PEMFC. The HT-PEMFC was developed from a LT-PEMFC and operates at temperatures around 373–473 K. At higher temperatures, the extent of CO that adsorbs on Pt in a HT-PEMFC is reduced, resulting in a high tolerance for CO [25]. In fact, a HT-PEMFC can tolerate CO up to 2–5% at 453 K with a insignificant degradation in the cell performance [26]; thus, it is possible to use the reformate gas for a HT-PEMFC directly without prior purification. There have been few studies that have focused on determining the optimal conditions for the glycerol reforming process of LT-PEMFC, and based on our knowledge, no research has reported the optimal conditions of reforming processes for HT-PEMFC. It should be noted that the generation of hydrogen for each type of PEMFC has different requirements and limitations. Therefore, apart from maximizing the hydrogen yield, it is necessary to take these aspects into consideration in the production of hydrogen for PEMFC applications.

In this study, a steam reforming of glycerol to generate hydrogen for LT-PEMFCs and HT-PEMFCs is considered by taking into account different requirements for the CO content of the reformate gas. A thermodynamic analysis is performed to find suitable conditions for the glycerol steam reforming process that not only maximize the hydrogen yield but also provide a CO concentration that satisfies the operational constraints of LT-PEMFCs and HT-PEMFCs. For LT-PEMFCs, the optimal conditions for the glycerol steam reforming are examined. A water gas shift reactor is also included in the reforming process to remove CO. For the HT-PEMFC, this study aims to explore the possibility of using the reformate gas directly from the glycerol steam reforming. The operational boundary of the glycerol steam reforming for a HT-PEMFC is also examined.

2. Theory

2.1. Fuel processing for LT-PEMFC

LT-PEMFCs operate at low temperatures and require hydrogen fuel with low CO content to avoid catalyst poisoning. The content of CO in the hydrogen feed for a LT-PEMFC must be less than 10–50 ppm. However, the CO contamination in hydrogen-rich reformate gas exceeds this limit. To reduce CO to the required level, it is necessary to add water gas shift (WGS) and preferential oxidation (PROX) processes to the fuel reforming process. The typical fuel processing system for a LT-PEMFC is demonstrated in Fig. 1. The main reaction that occurs in the steam reformer is glycerol steam reforming (Eq. (1)), whereas the side reactions are water gas shift (Eq. (2)), methanation (Eq. (3)), and methane dry reforming (Eq. (4)). The reactions in the CO pretreating units are shown in Eqs. (5)–(7).

Steam reformer

$$C_3H_8O_3 + 3H_2O \leftrightarrow 7H_2 + 3CO_2 \quad (1)$$

$$CO + H_2O \leftrightarrow H_2 + CO_2 \quad (2)$$

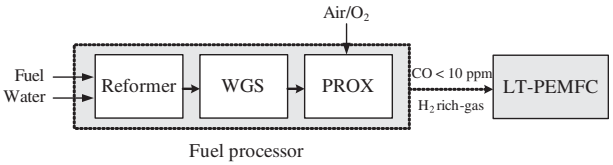

Fig. 1 – Fuel processor for LT-PEMFC.

$$CO + 3H_2 \leftrightarrow CH_4 + H_2O \quad (3)$$

$$CO_2 + CH_4 \leftrightarrow 2H_2 + 2CO \quad (4)$$

WGS reactor

$$CO + H_2O \leftrightarrow H_2 + CO_2 \quad (5)$$

PROX reactor

$$CO + 0.5O_2 \leftrightarrow CO_2 \quad (6)$$

$$H_2 + 0.5O_2 \leftrightarrow H_2O \quad (7)$$

In the WGS reactor, CO is removed and additional hydrogen is also generated at the same time. Nonetheless, the reformate gas obtained from this process still has a CO level that exceeds the acceptable level for LT-PEMFC. Therefore, the reformate gas is treated by a PROX process to reduce the concentration of CO to a satisfactory level. However, the oxygen fed into the PROX process not only reacts with CO (Eq. (6)) but also consumes hydrogen, as described by Eq. (7). The selectivity of CO oxidation in the PROX process is about 0.4–0.9 and is dependent on the catalyst and operating parameters [27–29]. It should be noted that when the effluent gas of the WGS process contains more CO, a higher amount of oxygen must be fed to the PROX process, resulting in a greater hydrogen loss due to the oxidation of hydrogen (Eq. (7)). This result indicates that the quality of the reformate gas obtained from the PROX process depends on the amount of CO and hydrogen from the WGS process when the maximum value of hydrogen content and the minimum value of CO content are required from this process. Therefore, the PROX process was not included in the fuel processor of the LT-PEMFC to find the optimal conditions of the glycerol steam reformer.

In practice, to increase the hydrogen yield of an endothermic steam reforming reaction, high-temperature operation and excess steam usage are required to shift the equilibrium toward the product side. As mentioned above, the reformate gas obtained from the steam reformer cannot be fed into the LT-PEMFC immediately and requires further CO removal, e.g., from a WGS reactor. This process changes the H_2 and CO content. The operating conditions that produce the highest hydrogen yield in the steam reformer may not be the optimal conditions for supplying reformate gas to the LT-PEMFC. As the quality of the reformate gas fed to the LT-PEMFC depends on the hydrogen and CO compositions coming out of the WGS reactor, determining the optimal conditions for the glycerol processor by considering the WGS process should be explored. Thus, the effects of the operating parameters (the reformer temperature and the steam to glycerol molar ratio) on the hydrogen and CO concentrations obtained from the WGS reactor are studied.

2.2. Fuel processing for HT-PEMFC

From a thermodynamic point of view, the adsorption of CO on the Pt surface can be reduced by increasing the temperature and/or decreasing the CO concentration [30]. As a result of the high operating temperature (in the range of 373–473 K), HT-PEMFCs can tolerate up to 5% CO, compared to LT-PEMFCs in which the CO content of the hydrogen feed must be less than 10–50 ppm. The adsorption of CO and H_2 on the Pt surface can be described by Langmuir adsorption isotherms, as shown in Eqs. (8) and (9). The CO molecule adsorbs associatively on Pt below 500 K, whereas H_2 is dissociatively adsorbed [24].

$$CO(g) + Pt \rightarrow Pt - CO \quad (8)$$

$$H_2(g) + 2Pt \rightarrow 2Pt - H \quad (9)$$

In general, CO coverage on Pt decreases at higher temperatures; because the adsorption of CO is an exothermic process, the Pt active sites for hydrogen adsorption increase. This result means that the possibility of hydrogen adsorption, which is less exothermic than CO adsorption, increases at high temperatures. Li et al. [25] reported the relative activity of a Pt catalyst for hydrogen oxidation as a function of temperature at different CO concentrations and found that the oxidation of hydrogen can be promoted at high-temperature operation. Other advantages of the high-temperature operation of PEMFCs (apart from the enhanced CO tolerance) include an increase in the electrochemical reaction rates, simplified water management, and improved heat management [31–33].

Due to the increased CO tolerance of HT-PEMFCs at high temperatures, it is possible to use the reformate gas directly from reformers without the use of CO removal processes. In addition, the higher operating temperature of PEMFCs also offers the efficient utilization of waste heat to preheat fuel or to supply the reforming processes. Jespersen et al. [34] claimed that a HT-PEMFC is more suitable than a LT-PEMFC to integrate with an on-board fuel processing unit. The overall system for the fuel processing of a HT-PEMFC is illustrated in Fig. 2. In this study, the reforming process is analyzed to determine its efficiency and the operational boundary that provides an appropriate reformate product to supply to the HT-PEMFC. The simulation results are presented while considering the constraint on CO content in the reformate gas.

2.3. Carbon formation

Carbon formation is a significant problem in fuel reforming processes because it causes deactivation of the catalyst. Many studies have proposed various methods to prevent the formation of carbon during the reforming process, including variations in the operating conditions, the development of new catalysts resisting on carbon, and the addition of oxygen and other promoters to inhibit carbon formation [35–39]. The main potential reactions for the formation of carbon are shown as follows:

Boudouard

$$2CO \leftrightarrow CO_2 + C \quad (10)$$

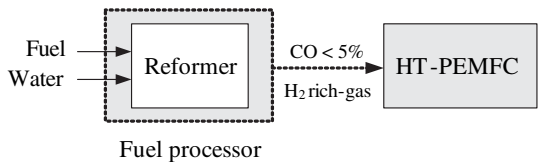

Fig. 2 – Fuel processor for HT-PEMFC.

Methane cracking

$$CH_4 \leftrightarrow 2H_2 + C \quad (11)$$

CO reduction

$$CO + H_2 \leftrightarrow H_2O + C \quad (12)$$

To avoid carbon formation, an appropriate temperature and steam to glycerol ratio should be determined. In this work, the boundaries of carbon formation during glycerol steam reforming are also presented to describe a carbon free region and a carbon formation region.

3. Methodology

The equilibrium composition of the reformate gas obtained from the steam reforming system of glycerol mentioned earlier was calculated using direct minimization of the Gibbs free energy. The primary components were $C_3H_8O_3$, H_2O, CO, CO_2, H_2, CH_4, and C. The other intermediate compounds of the glycerol steam reforming, such as ethane, propane, methanol and ethanol, can be neglected [21,40].

As the reaction proceeds, the total Gibbs free energy decreases; the equilibrium condition is reached when the total Gibbs free energy (G^t) attains its minimum value. Therefore, the equilibrium composition can be determined by solving the minimization problem as follows:

$$\min_{n_i}(G^t)_{T,P} = \sum_{i=1}^{C} n_i \overline{G}_i = \sum_{i=1}^{C} n_i \left(G_i^\circ + RT \ln \frac{\overline{f}_i}{f_i^\circ} \right) + n_S G_S \quad (13)$$

where G_i° is the Gibbs free energy of the species in standard conditions, C is the total number of components in the reaction system, n_i is the amount of each gaseous component, n_s is the number of carbon molecules involved in the carbon formation, and G_S is the Gibbs free energy of solid carbon.

According to the conservation of atomic species, n_i has to satisfy the following relationship:

$$\sum_{i=1}^{C} a_{ji} n_i = b_j, \quad \text{for } 1 \le j \le M \quad (14)$$

where a_{ji} is the number of atoms of element j in component i, b_j is the total number of atoms of element j in the reaction mixture, and M is the total number of elements. The solid component is also considered for element balances in Eq. (14). The thermodynamic characteristics of glycerol and the other products can be obtained from HYSYS's pure component library database [41].

In this study, the thermodynamic analysis of a steam reformer was performed by using the HYSYS simulator. Based on a Gibbs reactor module coupled with the Peng-Robinson Stryjek-Vera (PRSV) method for computing thermodynamic properties, the minimization problem of Gibbs free energy (as stated above) was solved to find the equilibrium composition of the reactive system. The prediction results were compared with the experiment data reported by Profeti et al. [11]. It was observed that the product distribution obtained from the HYSYS simulator and the experimental data were in agreement.

4. Results and discussion

To analyze the performance of a glycerol steam reforming process, it was assumed that the inlet temperature of the reactant feeds was 298 K and that a steam reformer is operated under isothermal conditions. As carbon formation is one of the most critical problems that can affect the catalyst activity in reforming processes, the operating conditions of the steam reformer should be carefully selected. Fig. 3 illustrates the effects of the steam to glycerol ratio (S/G) and the reformer temperature on carbon formation. It indicates the boundary of carbon formation for glycerol steam reforming, which is helpful for determining feasible conditions to avoid carbon formation. It is observed that carbon formation is thermodynamically inhibited at high temperatures and high steam to glycerol ratios.

4.1. Hydrogen production for LT-PEMFC

For LT-PEMFC, the reformate gas obtained from the steam reformer requires treatment from a WGS reactor to eliminate some of the CO and enhance the hydrogen content, after which it can be sent to a PROX reactor to further reduce the CO concentration to the desired level. The operating conditions of the steam reformer influence the hydrogen and CO levels obtained from the WGS reactor. Consequently, the effect of the reformer operating conditions on the product gases from the WGS unit was investigated for a given condition of the WGS reactor, to identify the optimal conditions for the glycerol steam reformer. However, the hydrogen content in the reformate gas obtained from the PROX reactor depends on the amount of CO and H_2 at the outlet of the WGS reactor. Thus, the fuel processor for a LT-PEMFC, consisting of only a steam reformer and a WGS unit, was considered in this study.

Figs. 4 and 5 show the simulation results of hydrogen production from glycerol for a LT-PEMFC. Fig. 4 indicates that the amount of hydrogen produced from the steam reformer increases with increased temperature and steam to glycerol molar ratio, whereas the %CO decreases at a high steam to glycerol molar ratio and low temperature. This is due to the

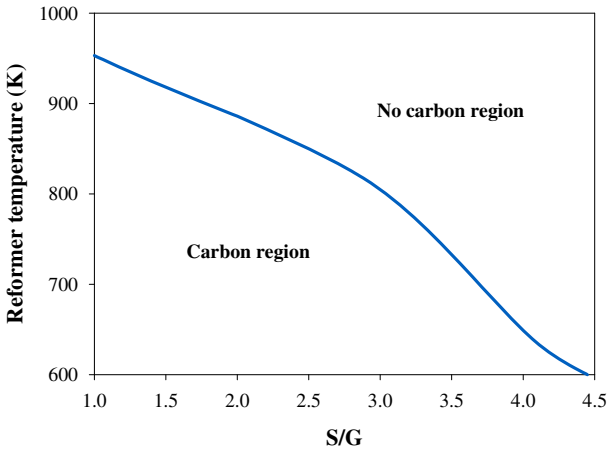

Fig. 3 – Boundary of carbon formation for a glycerol steam reformer at atmospheric pressure.

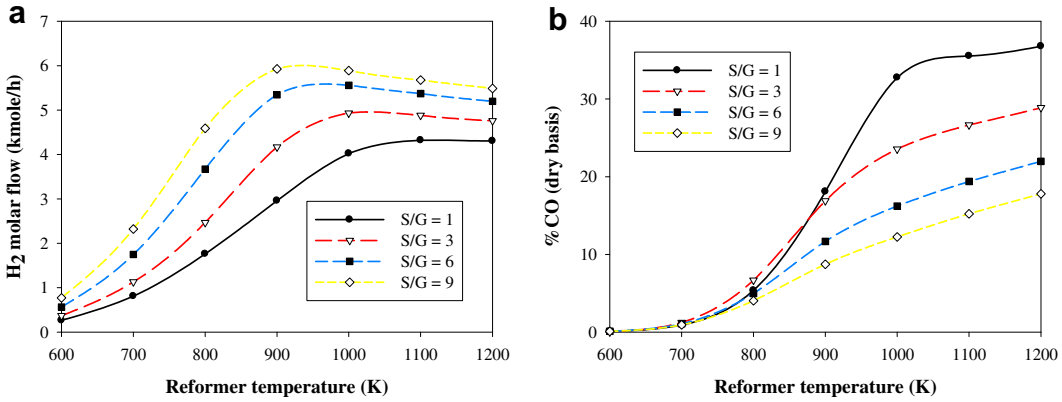

Fig. 4 – Compositions of reformate gas from a glycerol steam reformer: (a) H_2 molar flow and (b) %CO (dry basis).

endothermicity of the steam reforming reaction and the exothermicity of the water gas shift reaction. However, at each steam to glycerol ratio, there is an optimal temperature that provides the greatest hydrogen yield. These results are consistent with previous studies on glycerol reforming [6,7,13]. Although an increase in the steam to glycerol molar ratio offers the advantages of enhancing the hydrogen yield and reducing the CO concentration, it also increases the energy consumption of the reforming system.

Fig. 5 shows the compositions of H_2 and CO from the WGS unit operating at a temperature of 473 K at which the maximum conversion of CO is observed [42]. However, a higher temperature would improve the kinetics of the water gas shift reaction. The results clearly indicate that a steam to glycerol molar ratio of 6 is the most suitable for producing reformate gases with LT-PEMFC applications. It should be noted that previous studies claimed that a higher steam to glycerol ratio is required to enhance the hydrogen yield and decrease the CO concentration [13,15]. Although the addition of excess steam increases the amount of hydrogen and reduces CO concentration in the reformer and the water gas shift unit, using a steam to glycerol ratio higher than 6 insignificantly changes the hydrogen yield at temperatures above 1000 K. This operating point provides the highest hydrogen yield, as indicated by Fig. 5(a). A similar trend is also observed for the CO concentration, which is kept constant at steam to glycerol ratios higher than 6. In addition, the formation of carbon is suppressed at this operational range. Therefore, for LT-PEMFC, excess steam over the optimal ratio is not necessary for a glycerol steam reformer integrated with a LT-PEMFC.

4.2. *Hydrogen production for HT-PEMFC*

As mentioned above, the high CO tolerance of HT-PEMFCs makes it possible to use the reformate gas directly from the steam reformer. This type of PEMFC can withstand CO up to 5% with no significant loss of performance [26]. The quality of the reformate gas used in HT-PEMFCs differs from that used in LT-PEMFCs, and consequently, the optimal operating conditions of the reforming process would also be different. For HT-PEMFC, the concentration of CO in the reformate gas from the steam reformer was taken into consideration. To control the fraction of CO to an acceptable level, the reformer needs to operate at low temperatures and high steam to glycerol ratios. However, the low-temperature operation of the reformer causes a reduction in hydrogen content, which has a considerable effect on the fuel cell performance. To directly use the reformate gas obtained for HT-PEMFC, this study aims at finding optimal conditions that favor hydrogen yield while

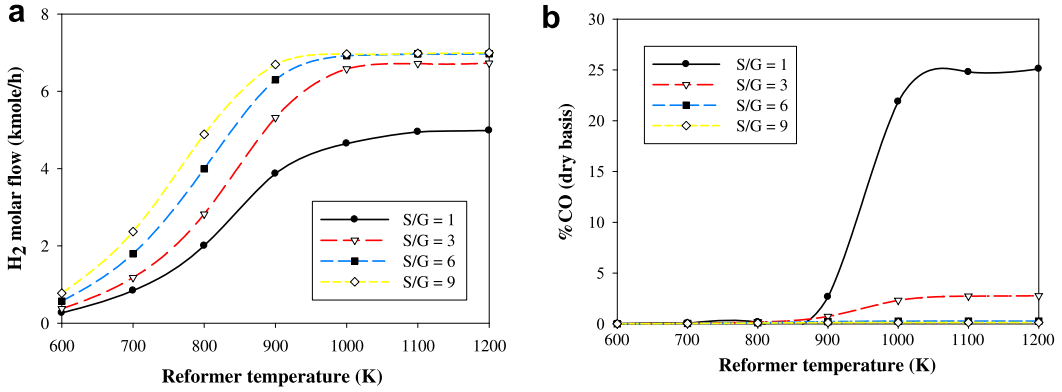

Fig. 5 – Compositions of reformate gas from a water gas shift reactor operating at a temperature of 473 K: (a) H_2 molar flow and (b) %CO (dry basis).

avoiding CO contamination levels in the reformate gas that surpass the tolerable level of HT-PEMFC.

Fig. 6 shows the relationship between the steam to glycerol ratio and the reformer temperature at different %CO tolerances of the HT-PEMFC. The results reveal that the reformer can be operated at higher temperatures when the steam to glycerol ratio is increased, at all %CO tolerances considered. In addition, the operating reformer temperature also increases with an increased CO tolerance level of HT-PEMFC. Several investigations have shown that temperature has a direct effect on hydrogen yield [43,44]. Therefore, the hydrogen yield increases with respect to the CO tolerance level and the steam to glycerol ratio, as shown in Fig. 7. For a 5% CO tolerance, hydrogen yield becomes constant when the steam to glycerol ratio is over 18.

Fig. 8 shows the compositions of hydrogen, methane and CO_2 at different %CO tolerances of a HT-PEMFC when the steam to glycerol ratio is fixed at 12. The reformer temperature is adjusted according to the %CO tolerance, and the relation of the steam to glycerol ratio and the reformer temperature for each %CO tolerance is shown in Fig. 6. The simulation results indicate that the hydrogen composition obtained from the steam reformer is higher when a high CO fraction in the reformate gas is allowed, compared to cases in which only a low CO fraction is allowed. Carbon dioxide and methane gradually decrease when increasing the content of CO in the reformate gas. Therefore, the hydrogen fraction (a key parameter affecting the fuel cell performance) is increased if the HT-PEMFC can tolerate more CO. It can be concluded from Figs. 7 and 8 that high steam to glycerol ratios and CO tolerance in the HT-PEMFC improves the performance of the reformer in terms of hydrogen content and concentration.

The extent of CO has a significant influence on the performance of the PEMFC when reformate gas is used as the reactant feed. Therefore, the appropriate reforming conditions need to be determined. Fig. 9 shows the boundary of the operating conditions for glycerol steam reforming that generate CO levels below 5%. The region above the solid line indicates the operating conditions in which the content of CO produced is in the acceptable level for HT-PEMFCs. If the

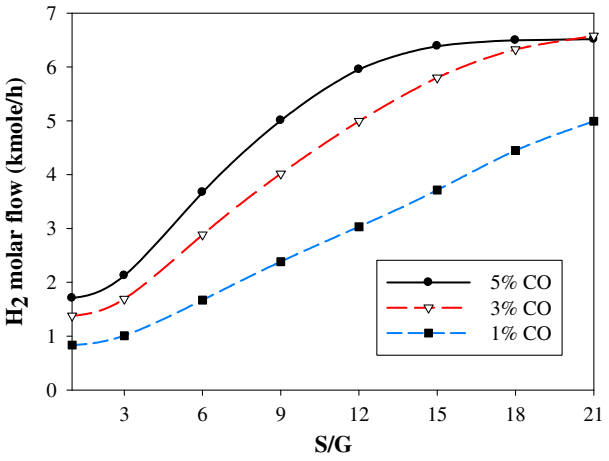

Fig. 7 – Effect of steam to glycerol molar ratio on hydrogen molar flow at different %CO tolerances of HT-PEMFC.

glycerol steam reformer is operated at conditions far away from the CO boundary line, the concentration of CO will decrease. However, the fraction of hydrogen, which has a direct effect on the PEMFC performance, also decreases. Fig. 9 also indicates the boundary of carbon formation (dashed line). At conditions above this boundary line, carbon formation is thermodynamically inhibited. As a result, the optimal condition of glycerol steam reforming for a HT-PEMFC is shown in the gray region. Within this region, there is no carbon formation and the CO level contaminating the hydrogen-rich reformate gas is lower than 5%.

4.2.1. *Energy analysis*

Fig. 10 shows the relation between the energy requirement for the glycerol steam reforming process and the operating temperature at different steam to glycerol ratios. Although increases in the temperature and steam to glycerol ratio enhance the hydrogen yield, the energy needed for reformer operation increases. To identify the actual optimal conditions of glycerol reforming for HT-PEMFCs, the efficiency of the

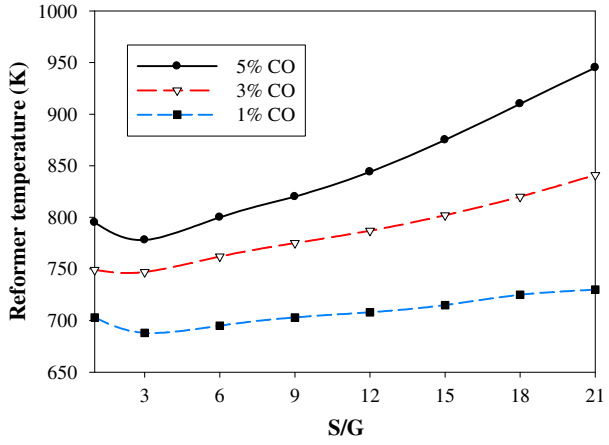

Fig. 6 – Relation of steam to glycerol molar ratio and reformer temperature at different %CO tolerances of HT-PEMFC.

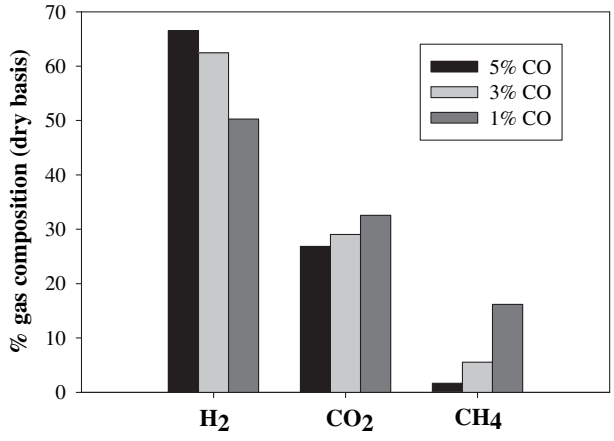

Fig. 8 – Product distributions of glycerol steam reforming (steam to glycerol ratio = 12) at different %CO tolerances of HT-PEMFC.

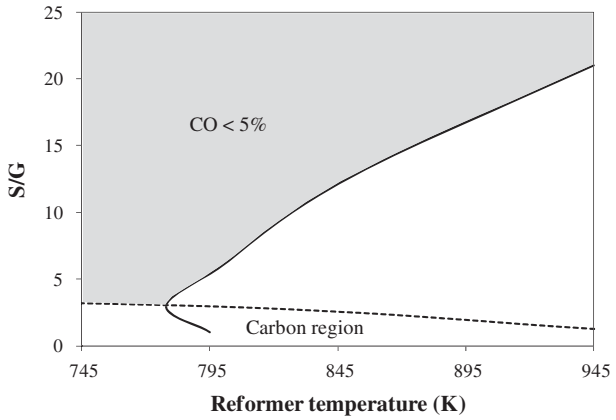

Fig. 9 – Operational boundary of glycerol steam reforming for HT-PEMFC.

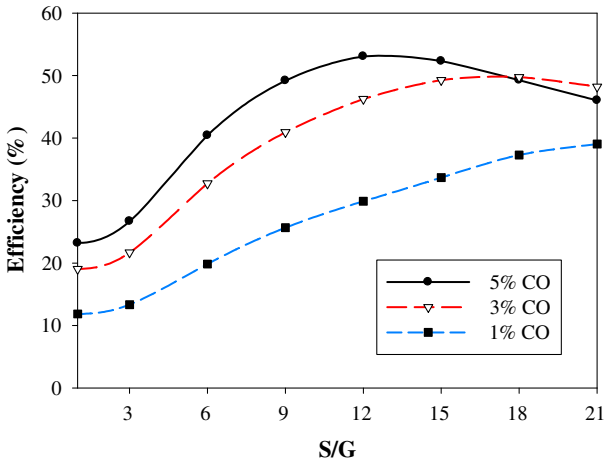

Fig. 11 – Efficiency of the glycerol steam reforming process at different %CO tolerances of HT-PEMFC.

reformer, taking into account the energy consumption as shown in Eq. (15), was used as the parameter to indicate performance.

$$\text{efficiency}\left(\%\right) = \frac{\text{LHV of hydrogen}\left(\dot{m}_{H_2}\right)}{\text{LHV of glycerol}\left(\dot{m}_{\text{glycerol}}\right) + \text{energy used for reforming process}} \times 100 \quad (15)$$

where LHV is the lower heating value. It should be noted that the energy required for the steam reforming process accounts for the heat of vaporization, sensible heat to heat up the reactants to the desired temperature and the heat needed for maintaining the reformer at an isothermal operation level.

Fig. 11 indicates that the efficiency of the reformer increases as the reformate gas is allowed to contain more CO. This effect is due to increased hydrogen production. In addition, the results reveal that increasing the steam to glycerol ratio also enhances the reformer process efficiency. Apart from the increased hydrogen yield, operation at a high steam to glycerol ratio also causes the reformer to operate at a high temperature until reaching the limiting level of CO. Moreover, the external heat required for vaporization is reduced because the waste heat in the product stream can be recovered to preheat the reactant feeds. This reduction enhances the total efficiency of the reforming process. From Fig. 11, the maximum efficiency of the reformer producing reformate gas with 5%CO is reached at a steam to glycerol ratio of 11–14. At this ratio, the operating temperature of the glycerol steam reformer is around 830–860 K (see Fig. 6). When more steam is added, the reformer efficiency decreases because the external heat required to sustain the reformer is higher than the energy obtained from the hydrogen produced. In the case of a 1% CO tolerance, the reformer can reach its maximum efficiency if it is operated at a higher steam to glycerol molar ratio.

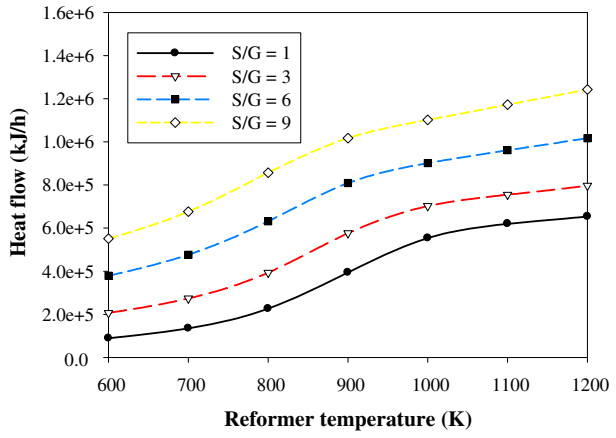

Fig. 10 – Heat flow of glycerol steam reforming at different steam to glycerol molar ratios.

5. Conclusions

Hydrogen production from a glycerol steam reforming process for LT-PEMFCs and HT-PEMFCs was investigated in this study. Due to the different requirements for the reformate gas in terms of the CO content, the reforming process for LT-PEMFCs requires a CO pretreating unit, whereas HT-PEMFCs can directly use the reformate gas as fuel. The simulation results showed that for LT-PEMFC, the optimal conditions for the glycerol steam reforming process integrated with a WGS reactor, which is operated at a temperature of 473 K, to maximize hydrogen yield and minimize CO are at a temperature of 1000 K and a steam to glycerol molar ratio of 6. For HT-PEMFCs with different %CO tolerances, it was found that the glycerol steam reformer can be operated at higher temperatures when a higher CO tolerance in the HT-PEMFC is allowed, resulting in an increased hydrogen yield. An increase in the steam to glycerol ratio also enhances hydrogen production, but requires more energy. Considering the performance of the glycerol steam reformer in terms of energy

efficiency, the operation of the reformer at a steam to glycerol ratio of 11–14 produces the highest reformer efficiency when reformate gas containing 5%CO is considered.

Acknowledgements

S. Authayanun would like to thank the Office of the Higher Education Commission, Thailand for their grant support under the program Strategic Scholarships for Frontier Research Network for the Joint Ph.D. Program Thai Doctoral degree for this research.

Support from the Thailand Research Fund, Commission of Higher Education and Chulalongkorn University is also gratefully acknowledged.

REFERENCES

[1] Halabi MH, de Croon MHJM, van der Schaaf J, Cobden PD, Schouten JC. Modeling and analysis of autothermal reforming of methane to hydrogen in a fixed bed reformer. Chemical Engineering Journal 2008;137:568–78.
[2] Levent M, Gunn DJ, El-Bousi MA. Production of hydrogen-rich gases from steam reforming of methane in an automatic catalytic microreactor. International Journal of Hydrogen Energy 2003;28:945–59.
[3] Byrd AJ, Pant KK, Gupta RB. Hydrogen production from glycerol by reforming in supercritical water over Ru/Al_2O_3 catalyst. Fuel 2008;87:2956–60.
[4] Rabenstein G, Hacker V. Hydrogen for fuel cells from ethanol by steam-reforming, partial-oxidation and combined auto-thermal reforming: a thermodynamic analysis. Journal of Power Sources 2008;185:1293–304.
[5] Vagia EC, Lemonidou AA. Thermodynamic analysis of hydrogen production via autothermal steam reforming of selected components of aqueous bio-oil fraction. International Journal of Hydrogen Energy 2008;33:2489–500.
[6] Dauenhauer PJ, Salge JR, Schmidt LD. Renewable hydrogen by autothermal steam reforming of volatile carbohydrates. Journal of Catalysis 2006;244:238–47.
[7] Slinn M, Kendall K, Mallon C, Andrews J. Steam reforming of biodiesel by-product to make renewable hydrogen. Bioresource Technology 2008;99:5851–8.
[8] Swami SM, Abraham MA. Integrated catalytic process for conversion of biomass to hydrogen. Energy & Fuels 2006; 20:2616–22.
[9] Zhang B, Tang X, Li Y, Xu Y, Shen W. Hydrogen production from steam reforming of ethanol and glycerol over ceria-supported metal catalysts. International Journal of Hydrogen Energy 2007;32:2367–73.
[10] Hirai T, Ikenaga N, Miyake T, Suzuki T. Production of hydrogen by steam reforming of glycerin on ruthenium catalyst. Energy & Fuels 2005;19:1761–2.
[11] Profeti LPR, Ticianelli EA, Assaf EM. Production of hydrogen via steam reforming of biofuels on $Ni/CeO_2–Al_2O_3$ catalysts promoted by noble metals. International Journal of Hydrogen Energy 2009;34:5049–60.
[12] Pompeo F, Santori G, Nichio NN. Hydrogen and/or syngas from steam reforming of glycerol. Study of platinum catalysts. International Journal of Hydrogen Energy 2010; 35:8912–20.
[13] Adhikari S, Fernando S, Gwaltney SR, To SD, Bricka RM, Steele PH, et al. A thermodynamic analysis of hydrogen production by steam reforming of glycerol. International Journal of Hydrogen Energy 2007;32:2875–80.
[14] Luo N, Cao F, Zhao X, Xiao T, Fang D. Thermodynamic analysis of aqueous-reforming of polylols for hydrogen generation. Fuel 2007;86:1727–36.
[15] Wang X, Li S, Wang H, Liu B, Ma X. Thermodynamic analysis of glycerin steam reforming. Energy & Fuels 2008;22:4285–91.
[16] Authayanun S, Arpornwichanop A, Paengjuntuek W, Assabumrungrat S. Thermodynamic study of hydrogen production from crude glycerol autothermal reforming for fuel cell applications. International Journal of Hydrogen Energy 2010;35:6617–23.
[17] Wang X, Li M, Wang M, Wang H, Li S, Wang S, et al. Thermodynamic analysis of glycerol dry reforming for hydrogen and synthesis gas production. Fuel 2009; 88:2148–53.
[18] Wang H, Wang X, Li M, Wang M, Li S, Wang S, et al. Thermodynamic analysis of hydrogen production from glycerol autothermal reforming. International Journal of Hydrogen Energy 2009;34:5683–90.
[19] Chen H, Zhang T, Dou B, Dupont V, Williams P, Ghadiri M, et al. Thermodynamic analyses of adsorption-enhanced steam reforming of glycerol for hydrogen production. International Journal of Hydrogen Energy 2009;34:7208–22.
[20] Buffoni IN, Pompeo F, Santori GF, Nichio NN. Nickel catalysts applied in steam reforming of glycerol for hydrogen production. Catalysis Communications 2009;10:1656–60.
[21] Chen H, Ding Y, Cong NT, Dou B, Dupont V, Ghadiri M, et al. A comparative study on hydrogen production from steam-glycerol reforming: thermodynamics and experimental. Renewable Energy 2011;36:779–88.
[22] Lin Y, Lin C, Chen Y, Yin K, Yang C. An analytical study of the PEM fuel cell with axial convection in the gas channel. International Journal of Hydrogen Energy 2007;32:4477–88.
[23] Dawes JE, Hanspal NS, Family OA, Turan A. Three-dimensional CFD modelling of PEM fuel cells: an investigation into the effects of water flooding. Chemical Engineering Science 2009;64:2781–94.
[24] Zhang J, Xie Z, Zhang J, Tang Y, Song C, Navessin T, et al. High temperature PEM fuel cells. Journal of Power Sources 2006;160:872–91.
[25] Li Q, He R, Jensen JO, Bjerrum NJ. Approaches and recent development of polymer electrolyte membranes for fuel cells operating above 100 °C. Chemistry of Material 2003; 15:4896–915.
[26] Das SK, Reis A, Berry KJ. Experimental evaluation of CO poisoning on the performance of a high temperature proton exchange membrane fuel cell. Journal of Power Sources 2009; 193:691–8.
[27] Ahluwalia RK, Zhang Q, Chmielewski DJ, Lauzze KC, Inbody MA. Performance of CO preferential oxidation reactor with noble-metal catalyst coated on ceramic monolith for on-board fuel processing applications. Catalysis Today 2005; 99:271–83.
[28] Cipiti F, Recupero V. Design of a CO preferential oxidation reactor for PEFC systems: a modelling approach. Chemical Engineering Journal 2009;146:128–35.
[29] Marino F, Descorme C, Duprez D. Supported base metal catalysts for the preferential oxidation of carbon monoxide in the presence of excess hydrogen (PROX). Applied Catalysis B: Environmental 2005;58:175–83.
[30] Bellows RJ, Marucchi-Soos EP, Buckley DT. Analysis of reaction kinetics for carbon monoxide and carbon dioxide on polycrystalline platinum relative to fuel cell operation. Industrial & Engineering Chemistry Research 1996;35:1235–42.
[31] Pan C, He R, Li Q, Jensen JO, Bjerrum JN, Hjulmand HA, et al. Integration of high temperature PEM fuel cells with a methanol reformer. Journal of Power Sources 2005;145:392–8.

[32] Shao Y, Yin G, Wang Z, Gao Y. Proton exchange membrane fuel cell from low temperature to high temperature: material challenges. Journal of Power Sources 2007; 167:235–42.
[33] Yang C, Costamagna P, Srinivasan S, Benziger J, Bocarsly AB. Approaches and technical challenges to high temperature operation of proton exchange membrane fuel cells. Journal of Power Sources 2001;103:1–9.
[34] Jespersen JL, Schaltz E, Kaer SK. Electrochemical characterization of a polybenzimidazole-based high temperature proton exchange membrane unit cell. Journal of Power Sources 2009;191:289–96.
[35] Pedernera MN, Pina J, Borio DO. Kinetic evaluation of carbon formation in a membrane reactor for methane reforming. Chemical Engineering Journal 2007;134:138–44.
[36] Parmar RD, Kundu A, Karan K. Thermodynamic analysis of diesel reforming process: mapping of carbon formation boundary and representative independent reactions. Journal of Power Sources 2009;194:1007–20.
[37] Laosiripojana N, Sutthisripok W, Assabumrungrat S. Synthesis gas production from dry reforming of methane over CeO_2 doped Ni/Al_2O_3: influence of the doping ceria on the resistance toward carbon formation. Chemical Engineering Journal 2005;112:13–22.
[38] Medrano JA, Oliva M, Ruiz J, Garcia L, Arauzo J. Catalytic steam reforming of acetic acid in a fluidized bed reactor with oxygen addition. International Journal of Hydrogen Energy 2008;33:4387–96.
[39] Parizotto NV, Rocha KO, Damyanova S, Passos FB, Zanchet D, Marques CMP, et al. Alumina-supported Ni catalysts modified with silver for the steam reforming of methane: effect of Ag on the control of coke formation. Applied Catalysis A: General 2007;330:12–22.
[40] Dou B, Rickett GL, Dupont V, Williams PT, Chen H, Ding Y, et al. Steam reforming of crude glycerol with in situ CO_2 sorption. Bioresource Technology 2010;101:2436–42.
[41] HYSYS Process Simulator Version 3.1, Hyprotech Ltd., Calgary, Canada.
[42] Chen WH, Hsieh TC, Jiang TL. An experimental study on carbon monoxide conversion and hydrogen generation from water gas shift reaction. Energy Conversion and Management 2008;49:2801–8.
[43] Faungnawakij K, Kikuchi R, Eguchi K. Thermodynamic evaluation of methanol steam reforming for hydrogen production. Journal of Power Sources 2006;161:87–94.
[44] Liu S, Zhang K, Fang L, Li Y. Thermodynamic analysis of hydrogen production from oxidative steam reforming of ethanol. Energy & Fuel 2008;22:1365–70.

ภาคผนวก 24

Thermodynamic Analysis of Hydrogen Production from Glycerol at Energy Self-Sufficient Conditions

Thirasak Pairojpiriyakul,[1] Worapon Kiatkittipong,[2] Apinan Soottitantawat,[1] Amornchai Arpornwichanop,[1] Navadol Laosiripojana,[3] Wisitsree Wiyaratn,[4] Eric Croiset[5] and Suttichai Assabumrungrat[1]*

1. *Department of Chemical Engineering, Faculty of Engineering, Chulalongkorn University, Phatumwan, Bangkok, Thailand*
2. *Department of Chemical Engineering, Faculty of Engineering and Industrial Technology, Silpakorn University, Nakhon Pathom, Thailand*
3. *The Joint Graduate School of Energy and Environment, King Mongkut's University of Technology Thonburi, Bangkok, Thailand*
4. *Department of Production Technology Education, Faculty of Industrial Education and Technology, King Mongkut's University of Technology Thonburi, Bangkok, Thailand*
5. *Department of Chemical Engineering, University of Waterloo, Waterloo, ON, Canada N2L 2G1*

A thermodynamic analysis based on the principle of minimising the Gibbs free energy is performed for hydrogen production from glycerol. When the operating parameters such as water/glycerol ratio (*WGR*), oxygen/glycerol ratio (*OGR*) and operating temperature (*T*) are carefully chosen, the energy self-sufficient conditions can be achieved. Two levels of energy self-sufficient, (i) within the reformer and (ii) within the overall system, are considered. Unlike the consideration in the reformer level reported in most works in literature, the consideration in the overall system level represents more realistic results based on the fact that some energy is required for heating up the feeds to a desired operating temperature. The obtained results demonstrate that the maximum hydrogen production significantly decreases from 5.65 mol H_2/mol glycerol for the reformer level to 3.31 mol H_2/mol glycerol for the system level, emphasising the significant demand of energy for feed preheating.

Keywords: hydrogen production, glycerol, autothermal, thermodynamic analysis

INTRODUCTION

Nowadays, humans are using an extravagant amount of energy in a non-sustainable manner. Therefore, demands for alternative energies are poised to grow substantially in the near future. Biodiesel is currently one of promising carbon neutral biofuels (Iriondo et al., 2008) whose part of the CO_2 emitted upon combustion can be absorbed by plants. Its production in the world has continuously increased every year from 2 to 11.1 million tons/year in the period 2004–2008—an increase of more than 500% in only 4 years (Biodiesel 2020, 2008). In biodiesel production, glycerol ($C_3H_8O_3$) is also present as a major by-product from the transesterification process. A large excess of glycerol or waste glycerol is thus brought down to much lower price in the world market. As a result, it is important to explore potential applications of glycerol resulting from the biodiesel production processes (Adhikari et al., 2007a). Two major approaches are: (i) purifying glycerol to synthetic glycerin for later applications in drug/pharmaceuticals industries (Bernesson et al., 2004; Wicke et al., 2008; Malca and Fausto, 2011). Moreover, synthetic glycerin from fossil sources is being gradually substituted by glycerol from natural sources in the market (Niederl-Schmidinger

*Author to whom correspondence may be addressed.
E-mail address: suttichai.a@chula.ac.th
Can. J. Chem. Eng. 9999:1–8, 2011

DOI 10.1002/cjce.20621
Published online in Wiley Online Library (wileyonlinelibrary.com).

and Narodoslawsky, 2008), and (ii) converting glycerol to high-value chemicals via different reactions such as condensation to [1,3]dioxan-5-ols and [1,3]dioxolan-4-yl-methanols (Deutsch et al., 2007), hydrogenolysis to propylene glycol (Dasari et al., 2005; Lechon et al., 2009; Anand et al., 2010), dehydration to acrolein (Yang et al., 2008), oxidation to glyceric acid, tartronic acid and, oxalic acid (Ketchie et al., 2007) and etherification to higher glycerol ethers used as oxygenate additives for fuels such as biodiesel and diesel petroleum (Klepacova et al., 2007; Kiatkittipong et al., 2011) or gasoline (Kiatkittipong et al., 2010). Sometimes, it is directly used as a fuel for heat generation (Soimakallio et al., 2009; Thamsiriroj and Murphy, 2010) or as animal feed in agricultural industry (Malca and Fausto, 2011).

Among all the applications of glycerol, hydrogen production has attracted a number of researches, especially considering the large potential for hydrogen demand in fuel cell applications for stationary power generator, portable power, micro power and transportation (Youn et al., 2008). Hydrogen production can be carried out via different reactions such as gasification, steam reforming (SR) (Faungnawakij et al., 2006; Adhikari et al., 2007b; Das et al., 2007; Rakib et al., 2008; Hernandez and Kafarov, 2009; Oliveira et al., 2009; Beaver et al., 2010), aqueous-phase reforming (APR) (Luo et al., 2007, 2008; Iriondo et al., 2008) and autothermal reforming (ATR) (Dauenhauer et al., 2006; Li et al., 2008a,b; Reese et al., 2009; Reese et al., 2010). SR is currently the most commonly used process for hydrogen production, which can be developed by investigating suitable operating conditions (pressure, temperature, water to fuel ratios), catalysts and heat transfer management (Yanbing et al., 2007). However, it requires a large amount of heat from an external heat source. On the other hand, considerably lower energy demand can be achieved when adding some oxygen in the reforming process. Therefore, ATR is considered as a process with lower demand of external heat sources.

A number of works on hydrogen production from glycerol have recently been studied. Adhikari et al. (2007a) exposed that temperatures higher than 900 K, atmospheric pressure and water/glycerol ratio (*WGR*) of 9 were suitable for hydrogen production via glycerol SR by using of Gibbs minimisation method. Under these conditions methane production and solid carbon are thermodynamically diminished. Dauenhauer et al. (2006) examined the ATR of glycerol. The best condition was found with Rhodium-Ceria-washcoat catalyst at *WGR* of 4.5, carbon to oxygen ratio of 0.9 and temperature of 1135 K, offering hydrogen selectivity of 79%. Furthermore, Slinn et al. (2008) reported the prediction of reformer performance by thermodynamic theory with the optimum conditions for glycerol reforming at 1133 K and *WGR* of 2.5.

In this study, a thermodynamic analysis based on the principle of minimising the Gibbs free energy is performed for hydrogen production from glycerol. The effect of operating parameters, i.e. water/glycerol ratio (*WGR*), oxygen/glycerol ratio (*OGR*) and operating temperature (*T*) on the hydrogen production, carbon formation and net energy were investigated. The operating conditions were carefully chosen to achieve the energy self-sufficient conditions for two system levels, that is the reformer level and the overall system level. Finally, the suitable conditions which offer the highest hydrogen production for both system levels are determined and the obtained hydrogen productions are compared.

THEORY

The reactions taking place in the hydrogen production from glycerol can be summarised as follows:

Glycerol Steam Reforming (SR):

$$C_3H_8O_3 + 3H_2O \leftrightarrow 3CO_2 + 7H_2; \quad \Delta H_{298\,K} = +127.67\,kJ/mol \quad (1)$$

Partial oxidations (POX):

$$C_3H_8O_3 + 0.5O_2 \leftrightarrow 2CO + CO_2 + 4H_2; \quad \Delta H_{298\,K} = -31.79\,kJ/mol \quad (2)$$

$$C_3H_8O_3 + O_2 \leftrightarrow CO + 2CO_2 + 4H_2; \quad \Delta H_{298\,K} = -314.76\,kJ/mol \quad (3)$$

$$C_3H_8O_3 + 1.5O_2 \leftrightarrow 3CO_2 + 4H_2; \quad \Delta H_{298\,K} = -579.73\,kJ/mol \quad (4)$$

Oxidation or combustion (OX):

$$C_3H_8O_3 + 3.5O_2 \leftrightarrow 3CO_2 + 4H_2O; \quad \Delta H_{298\,K} = -1564.93\,kJ/mol \quad (5)$$

Decomposition reaction (DR):

$$C_3H_8O_3 \leftrightarrow 3CO + 4H_2; \quad \Delta H_{298\,K} = +250\,kJ/mol \quad (6)$$

Methanations (MET):

$$CO + 3H_2 \leftrightarrow CH_4 + H_2O; \quad \Delta H_{298\,K} = -206.11\,kJ/mol \quad (7)$$

$$CO_2 + 4H_2 \leftrightarrow CH_4 + 2H_2O; \quad \Delta H_{298\,K} = -164.94\,kJ/mol \quad (8)$$

Methane CO_2 reforming (MCR):

$$CH_4 + CO_2 \leftrightarrow 2CO + 2H_2; \quad \Delta H_{298\,K} = +247.28\,kJ/mol \quad (9)$$

Water gas shift (WGR):

$$CO + H_2O \leftrightarrow CO_2 + H_2; \quad \Delta H_{298\,K} = -41.17\,kJ/mol \quad (10)$$

Carbon formations via:
Boudouard reaction:

$$2CO \leftrightarrow CO_2 + C_{(S)}; \quad \Delta H_{298\,K} = -172.43\,kJ/mol \quad (11)$$

Methane cracking:

$$CH_4 \leftrightarrow 2H_2 + C_{(S)}; \quad \Delta H_{298\,K} = +74.85\,kJ/mol \quad (12)$$

Reduction of CO:

$$CO + H_2 \leftrightarrow H_2O + C_{(S)}; \quad \Delta H_{298\,K} = -131.26\,kJ/mol \quad (13)$$

The minimisation of Gibbs free energy method has been used in this study for predicting the product compositions at equilibrium. G^t is the total Gibbs free energy. n_i is the number of moles of species i that minimises the value of Gibbs free energy. n_j indicates all the number of moles except the ith species. At constant

temperature and pressure, the equilibrium equation is given as follows:

$$dG^t = \sum_{i=1}^{N} \mu_i \, dn_i \tag{14}$$

The non-stoichiometric approach was calculated after a selection of possible products. Equation (14) can be expressed as:

$$G^t = \sum_{i=1}^{N} \mu_i \, n_i \tag{15}$$

$$G^t = \sum_{i=1}^{N} n_i G_i^0 + RT \sum_{i=1}^{N} n_i \ln \frac{\hat{f}_i}{f_i^0} \tag{16}$$

The reaction equilibrium in gas phase theory and Lagrange's undetermined multiplier method were used to derive Equations (17)–(19) from Equation (16)

$$\Delta G_{f_i}^0 + RT \ln \frac{\hat{\phi}_i y_i P}{P^0} + \sum_j \lambda_j a_{ij} = 0 \tag{17}$$

$$\sum_{i=1}^{N} n_i \left(\Delta G_{f_i}^0 + RT \ln \frac{\hat{\phi}_i y_i P}{P^0} + \sum_j \lambda_j a_{ij} \right) = 0 \tag{18}$$

$$\sum_{i=1}^{N} n_i a_{ij} = A_j \tag{19}$$

Equation (19) is the constraints of elemental balances. a_{ij} is the number of atoms of the jth element present in each molecule of species i and A_j is the total mass of jth element in the feed. Equation (20) is provided for consideration of solid carbon–gas system (Wang et al., 2008)

$$\sum_{i=1}^{N-1} n_i \left(\Delta G_{f_i}^0 + RT \ln \frac{\hat{\phi}_i y_i P}{P^0} + \sum_j \lambda_j a_{ij} \right) + n_C G_{C_{(s)}}(T, P) = 0 \tag{20}$$

Aspen Plus program (Aspen Plus® Version 2006) was employed for calculating equilibrium compositions and the corresponding overall heat of reactions under the conditions of minimisation of Gibbs free energy. Glycerol ($C_3H_8O_3$), water (H_2O), hydrogen (H_2), carbon monoxide (CO), carbon dioxide (CO_2), methane (CH_4), carbon ($C_{(s)}$), oxygen (O_2) and nitrogen (N_2) are identified as possible species in the equilibrium products. The Soave–Redlich–Kwong equation was selected as the method for estimating thermodynamic properties of the reaction systems (Li et al., 2008b; Wang et al., 2008, 2009).

Figure 1 shows the system of energy balance in the hydrogen production from glycerol. Two levels of energy balances; that is reformer and overall system levels, are considered. Equation (21) shows the energy balance equation around the reformer unit. However, depending on the amount of air supplied, the reformer duty might be relatively small in comparison of the overall system duty. Therefore, in the overall system level analysis, net energy including all heat required in the heater, evaporator and reformer are taken into account. The energy balance in the system level is shown in Equation (22):

$$Q_{\text{reformer(net)}} = \sum_{i=1}^{N} n_{i,\text{out}} H_{i,\text{out}} - \sum_{i=1}^{N} n_{i,\text{in}} H_{i,\text{in}} \tag{21}$$

$$\begin{aligned} Q_{\text{system(net)}} &= Q_{\text{heater(net)}} + Q_{\text{evaporator}} + Q_{\text{reformer}} \\ &= \sum_{i=1}^{N} n_{i,\text{out}} H_{i,\text{out}} - \sum_{i=1}^{N} n_{i,0} H_{i,0} \end{aligned} \tag{22}$$

The total net heat energy can be positive (endothermic), negative (exothermic) and zero (energy self-sufficient). The last one is the condition of interest in this study. The energy self-sufficient condition can be found by setting Equations (21) and (22) equal to zero for the reformer, and system cases, respectively. It should be noted that the results obtained from the calculations in this work represent the maximum achievable hydrogen production based on the energy self-sufficient system. In a real system, the values will

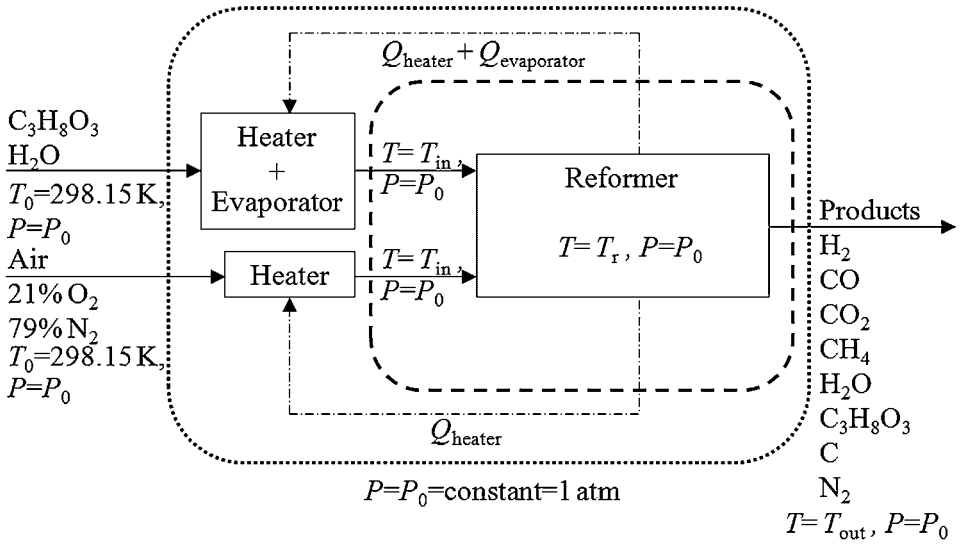

Figure 1. The schematic of energy boundary conditions ---- Reformer, ... System, and _.._. Heat transfer in system case. (If isothermal condition is considered in reformer level, T_{in}, T_r and T_{out} will be equivalent.)

be lower due to deviation from the thermodynamic equilibrium reactions and the presence of heat loss.

The reaction performances are expressed in terms of glycerol conversion (Equation 23), and yield of product i (Equation 24). In all simulations the glycerol feed rate and operating pressure are kept at 1 mol/s and 1 atm, respectively.

$$\text{Glycerol conversion (\%)} = \frac{n_{\text{Glycerol},0} - n_{\text{Glycerol,out}}}{n_{\text{Glycerol},0}} \times 100\ (\%) \quad (23)$$

$$\text{Yield of product } i = \frac{n_{i,\text{out}}}{n_{\text{Glycerol},0}} \quad (24)$$

RESULTS AND DISCUSSION

At the conditions chosen in this work, all simulations showed that the glycerol conversion from Equation (23) is 100%, which means that no glycerol appears in the products.

Hydrogen Production From Glycerol Under Isothermal Operation

Yield of hydrogen

Figure 2a shows the yield of H_2 at different values of *WGR* and *OGR*. The calculations are based on isothermal operation at $T = 940$ K. To verify the calculations, the results from previous published works (Adhikari et al., 2007a; Wang et al., 2008; Rossi et al., 2009) shown by symbols are compared with those from simulations in this work. The simulation results from this work show very good agreement with those from previous works with discrepancy within ±1.50%. It is clearly shown that they all are in good agreement.

At $OGR = 0$, SR (Reaction 1) is the main reaction. According to the reaction stoichiometry, three moles of H_2O ($WGR = 3$) are required to react with 1 mol of glycerol. It is obvious that the yield of H_2 increases with increasing *WGR* and the value as high as 6.20 could be achieved at $WGR = 12$ and $OGR = 0$. When *OGR* is greater than 0, hydrogen is also generated via POXs (Reactions 2–4). The use of oxidant (air) together with steam has been a promising strategy in hydrogen production technology as it can reduce the demand of energy requirement/transfer to the reaction system (Rabenstein and Hacker, 2008). However, the yield of H_2 obviously decreases with increasing *OGR*, and therefore, high levels of *OGR* should be avoided. It should be noted that at the same values of *WGR*, the yield of H_2 at $OGR = 0$ are generally higher than those at $OGR > 0$ except at $WGR < 2$. This is attributed to the presence of carbon formation which will be discussed in the following section.

Carbon formation

A major problem with the reforming processes is the formation of solid carbon or coke. When solid carbon occurs, it causes some disadvantages to the processes including blockage of the catalyst pores, and breakdown of the reactor in severe cases because of plugging (Reese et al., 2010). Solid carbon is an unfavoured product in hydrogen production. It can take place via several undesired reactions (Reactions 11–13), for example CO disproportionation (Reaction 11) or CH_4 cracking (Reaction 12) or the reaction of CO with H_2 (Reaction 13) (Wang et al., 2008). As shown in Figure 2b for $T = 940$ K, no carbon formation occurs when $WGR > 2$ or $OGR > 0.8$. The highest mole of carbon (1.01) appears at the most severe condition of $WGR = 0$ and $OGR = 0$. Carbon formation can be suppressed by increasing *WGR*, which retards the reduction

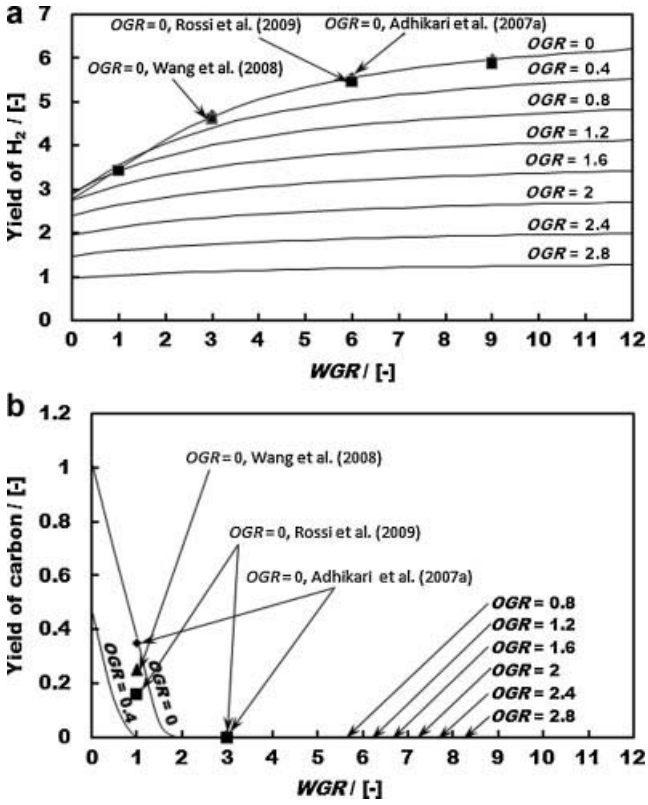

Figure 2. (a) Yield of H_2 and (b) Yield of carbon at different values of *WGR* and *OGR* at $P = 1$ atm, $T = 940$ K; ♦ at $OGR = 0$ (Adhikari et al., 2007a); ▲ at $OGR = 0$ (Wang et al., 2008); ■ at $OGR = 0$ (Rossi et al., 2009).

of CO (Reaction 13) and/or increasing *OGR* which promotes the POXs whose products could subsequently suppress carbon formation. Figure 2b also compares the values of the yield of carbon calculated from this work with those from literatures (Adhikari et al., 2007a; Rossi et al., 2009; Wang et al., 2008). Some discrepancy observed among the literature (Adhikari et al., 2007a; Wang et al., 2008; Rossi et al., 2009) and this work is due to the differences in equation of state and thermodynamic data sources.

Figure 3 shows the temperatures at boundary of carbon formation for wider ranges of *WGR* and *OGR*. For example, at $WGR = 0.5$ and $OGR = 0$, carbon formation starts to appear at $T = 1038.5$ K and a higher temperature than this value ($T > 1038.5$ K) is required to avoid the carbon formation. Again, it is clear that carbon formation becomes less severe when increasing *WGR* or *OGR*.

Net heat energy

Figure 4 shows the effects of *WGR* and *OGR* on the net heat energies of the reformer and the overall system at $T = 940$ K. For the reformer level, when increasing *WGR* from 0 to 1.5, the net heat energy sharply increases until reaching a maximum. After reaching its maximum value, the net heat energy gradually decreases. The increase of the net heat energy is mainly governed by the strong endothermic SR while the decrease of the net heat energy is likely from the exothermic WGS particularly at high excess amount of water. The net heat energy obviously decreases with increasing *OGR* as the exothermic POXs play a more important role. There are only some ranges of *OGR* (0.19–0.39) which provides the energy self-sufficient condition ($Q_{\text{net}} = 0$, dashed line). It should be noted that although two values of *WGR* are observed

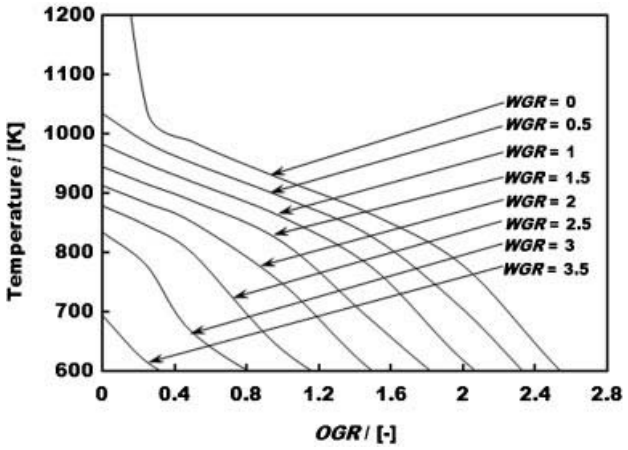

Figure 3. Boundary of carbon formation as a function of *WGR*, *OGR* and *T* at $P = 1$ atm.

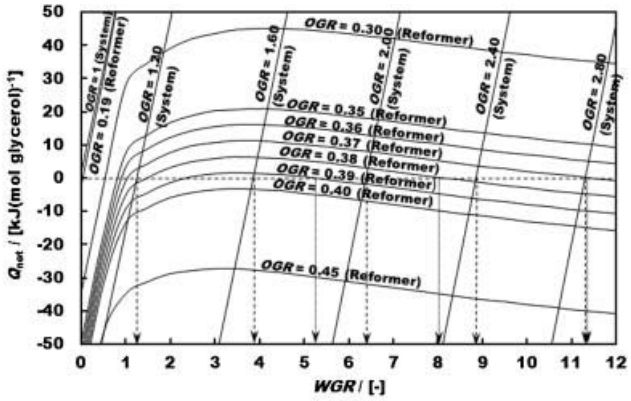

Figure 4. Net heat energies (Q_{net}) of Reformer and System as a function of *WGR* and *OGR* at $P = 1$ atm, $T_r = 940$ K.

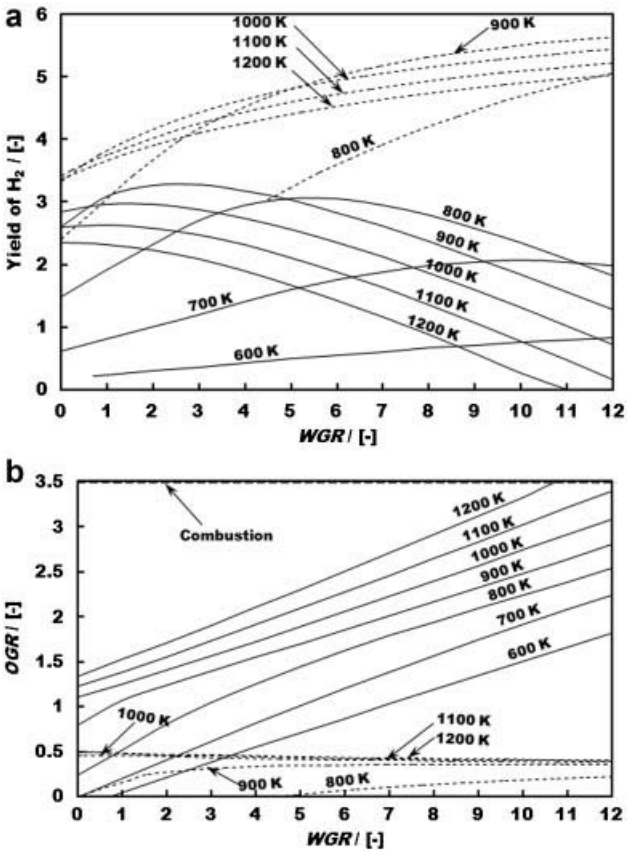

Figure 5. (a) Yield of H_2 and (b) *OGR* of Reformer and System as a function of *WGR* and operating temperature at energy self-sufficient condition; ..... Reformer, ____ System.

for a given value of *OGR*, the higher value *WGR* should be selected as it offers a higher hydrogen production.

Considering the energy balance on the system level, in contrast, energy self-sufficient condition of the system can occur in a wider range of *OGR* (1.0–2.8 for $T = 940$ K). At $OGR = 1$, it is the minimum *OGR* value to offer energy self-sufficient condition at $WGR = 0$, then increasing *WGR* increases energy requirement of the system. The relationship of *OGR* and *WGR* in the system at energy self-sufficient condition is quite different from that of the reformer case; namely, increasing *WGR* always requires higher *OGR*. The key reason is the huge energy requirement for heating liquid water at $T_0 = 298.15$ K to vapour at a high temperature. Thus, a relatively high value of *OGR* is necessary to generate sufficient energy for the system. However, hydrogen production greatly reduces when operating at higher values of *OGR* (Figure 2a). Therefore, *WGR* is a significant parameter to be selected for achieving high hydrogen production. In the following sections only the simulation results based on the energy self-sufficient condition will be reported.

Hydrogen Production From Glycerol Under Energy Self-Sufficient Condition

From the previous section, it is demonstrated that energy self-sufficient condition can be achieved by appropriate adjustment of operating parameters including *WGR*, *OGR* and the operating temperature. However, only two parameters can be specified and the other is to be determined. For example, when *WGR* and *OGR* are given, only some values of temperature are possible to offer the energy self-sufficient condition. It should be noted that although operating pressure can also influence the condition, the main SR is favourable at low pressure and therefore only the operation at atmospheric pressure is considered in this study. Figure 5a shows the yield of H_2 at different values of *WGR* and operating temperatures while their corresponding values of *OGR* are given in Figure 5b. For the reformer case (shown by dashed lines), the yield of H_2 always increases when increasing *WGR*. In contrast, for the system case, there is an optimum *WGR* that provides the highest mole of H_2 for each temperature. Figure 5b indicates that the corresponding values of *OGR* are not quite dependent on *WGR* for the reformer case unlike the overall system case (continuous lines). This is obviously because the feed temperature for the reformer case is assumed to be at the operating temperature of interest while it is at $T_0 = 298.15$ K for the system case. Therefore, the energy change within the reformer only arises from the change in heat of reaction which is quite small relatively to the high energy demanded for preheating the feeds (especially water). For the system case at low values of *WGR*, the yield of H_2 increases with increasing *WGR* according to the promotion of SR; however, the higher *OGR* required for generating sufficient energy for feed heating deteriorates the hydrogen production. It should be noted that for some operating temperatures, minimum values of *WGR* to achieve energy self-sufficient condition are observed for both the reformer and the system levels. The values appear at $OGR = 0$.

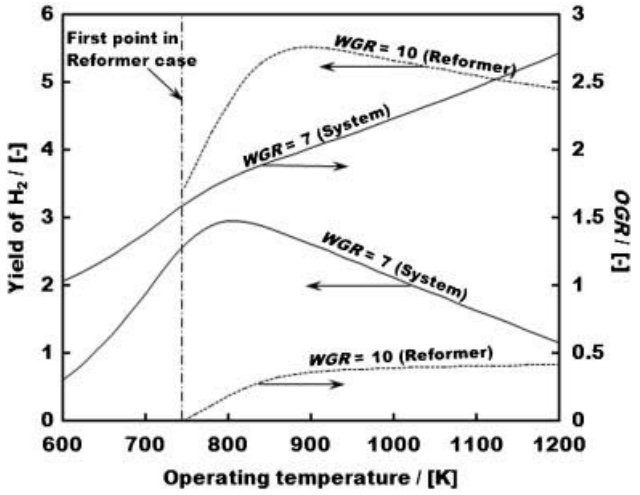

Figure 6. Yield of H_2 and *OGR* of Reformer ($WGR = 10$) and System ($WGR = 7$) as a function of operating temperature at energy self-sufficient condition; ..... Reformer, ____ System.

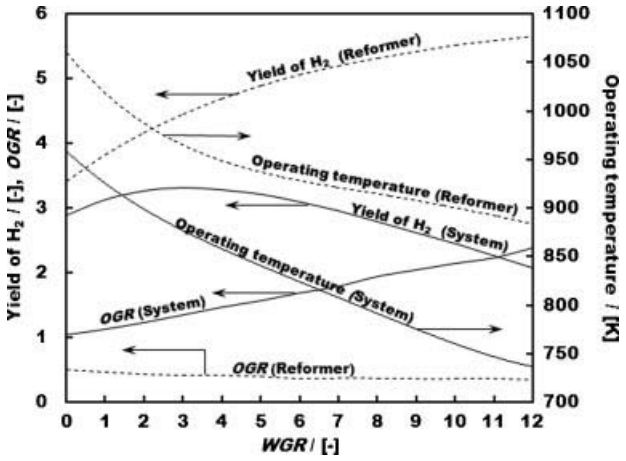

Figure 7. Maximum of yield of H_2, *OGR* and operating temperature of Reformer and System levels as a function of *WGR* at energy self-sufficient condition; ..... Reformer, ____ System.

The influence of operating temperature on the yield of H_2 and corresponding *OGR* at a specific value of *WGR* is demonstrated in Figure 6 ($WGR = 10$ for the reformer case and $WGR = 7$ for the system case). It is clear that the value of *OGR* always increases with increasing operating temperature; however, there is an optimum temperature which provides the highest yield of H_2 for a given *WGR*. As the strong endothermic SR is favourable at high temperature, the yield of H_2 increases significantly with operating temperature. However, the decrease of H_2 at higher temperatures results from both the reverse of WGS (Reaction 10) which is also favourable at high temperatures and from the demand of higher *OGR* which results in lowing hydrogen production (Figure 2a).

Maximum Hydrogen Production

From the previous section it is clear that there is an optimum operating temperature which provides the highest yield of H_2 for each *WGR*. In order to determine the maximum possible hydrogen production, the highest yield of H_2 together with their corresponding *OGR* and operating temperature are calculated at different values of *WGR* (Figure 7). In the reformer case, it was observed that the yield of H_2 always increase with increasing *WGR*. Within the range of $WGR = 0$–12, the maximum yield of H_2 is 5.65 at $WGR = 12$, $OGR = 0.35$ and $T = 880$ K. However, for the system case, the maximum value of 3.31 appears at $WGR = 3$, $OGR = 1.35$ and $T = 875$ K. Although the yield of H_2 increases at the beginning, the use of too much value of *WGR* causes detrimental effect on the hydrogen production as the system requires too much energy for heating the excessive water. Figure 7 also indicates that the value of *OGR* for the reformer case slightly changes with increasing *WGR*. As reported earlier, there is a small range of *OGR* which can offer energy self-sufficient condition. However, for the system case the energy requirement changes quite significantly with increasing *WGR* and therefore the *OGR* becomes more dependent on *WGR*. It should be noted that when operating the reformer or the system with higher *WGR*, the optimum temperature always decreases. This should be related to the exothermic WGS which becomes more favourable toward hydrogen production at a lower temperature.

From this study, it is demonstrated that when hydrogen production operates under energy self-sufficient condition, a maximum hydrogen production of 3.31 mol H_2/mol glycerol is achieved. In practice, the hydrogen production will be lower than this value because of the presence of inevitable heat losses in the system. The reported value is much lower compared with the case when the production is operated under the energy self-sufficient in the reformer. However, in this case additional heat sources are required for other unit operations.

CONCLUSION

A thermodynamic analysis of hydrogen production from glycerol reforming was carried out. The results from isothermal operation indicate that increasing *WGR* enhances the hydrogen production but also requires large extent of external heat source. However, an increase of *OGR* reduces the hydrogen production but decreases the energy requirement. The energy self-sufficient condition can be achieved when *WGR*, *OGR* and operating temperature are carefully selected. The energy self-sufficient for the reformer level shows that only a small amount of *OGR* is required in the operation. The maximum mole of H_2 in the range of study is 5.65 at $WGR = 12$, $OGR = 0.35$ and $T = 880$ K. Much higher *OGR* is required to provide sufficient energy especially for the feed preheating which is in contrast to the energy self-sufficient for the overall system level. At the system level, the maximum yield of H_2 is achievable under self-sufficient conditions 3.31, which corresponds $WGR = 3$, $OGR = 1.35$ and $T = 875$ K.

ACKNOWLEDGEMENTS

This work was supported by the Royal Golden Jubilee PhD program, the Thailand Research Fund and Commission on Higher Education. The authors also would like to acknowledge the support from the Higher Education Research Promotion and National Research University Project of Thailand, Office of the Higher Education Commission (EN278A).

NOMENCLATURE

A_j	the total number of atoms of *j*th element in the reaction mixture
a_{ij}	number of atoms of the *j*th element present in each molecule of *i*th species
f_i^0	standard-state fugacity of the *i*th species
$\hat{f}_i$	fugacity of the *i*th species

G^t	total Gibbs free energy (J/mol)
G_i^0	standard-state Gibbs free energy of the ith species (J/mol)
ΔG_{fi}^0	standard Gibbs function of formation of the ith species (J/mol)
$G_{C_{(s)}}$	molar Gibbs free energy of solid carbon (J/mol)
$H_{i,0}$	enthalpy of the ith species in feed in overall system case (J/mol)
$H_{i,\text{in}}$	enthalpy of the ith species in feed in reformer case (J/mol)
$H_{i,\text{out}}$	enthalpy of the ith species in products (J/mol)
M	the total number of elements
N	total species
n_i	mole of the ith species
$n_{i,0}$	mole of the ith species in feed in overall system case (mol)
$n_{i,in}$	mole of the ith species in reformer feed (mol)
$n_{i,out}$	mole of the ith species in products (mol)
n_j	mole of the jth species except ith specie (mol)
n_C	mole of solid carbon (mol)
$n_{\text{Glycerol, 0}}$	mole of glycerol in feed (mol)
$n_{\text{Glycerol, out}}$	mole of glycerol in products (mol)
n_{H_2O}	mole of water in products (mol)
OGR	oxygen/glycerol ratio
P	pressure (atm)
P^0	standard-state pressure (atm)
$Q_{\text{evaporter}}$	heat energy of evaporator (kJ/mol)
$Q_{\text{heater(net)}}$	net heat energy of heater (kJ/mol)
$Q_{\text{reformer(net)}}$	net heat energy of reformer (kJ/mol)
$Q_{\text{system(net)}}$	net heat energy of the overall system (kJ/mol)
R	ideal gas constant 8.314472 (J/mol/K)
T, T_r	operating temperature (K)
T_0	feed temperature in overall system case (K)
T_{in}	input temperature in reformer case (K)
T_{out}	output temperature in reformer and overall system cases (K)
WGR	water/glycerol ratio
y_i	mole fraction of each substance in gas products

Greek Letters

λ_j	Lagrange multiplier
μ_i	chemical potential of species i (J/mol)
$\hat{\phi}_i$	fugacity coefficient of species i

REFERENCES

Adhikari, S., S. Fernando, S. R. Gwaltney, S. D. F. To, R. M. Bricka, P. H. Steele and A. Haryanto, "A Thermodynamic Analysis of Hydrogen Production by Steam Reforming of Glycerol," Int. J. Hydrogen Energy **32**, 2875–2880 (2007a).

Adhikari, S., S. Fernando and A. Haryanto, "A Comparative Thermodynamic and Experimental Analysis on Hydrogen Production by Steam Reforming of Glycerin," Energy Fuels **21**, 2306–2310 (2007b).

Anand, K. A., K. S. Anisia, A. K. Agarwal and A. Kumar, "Hydrogenolysis of Glycerol With FeCo Macrocyclic Complex Bonded to Raney Nickel Support Under Mild Reaction Conditions," Can. J. Chem. Eng. **88**(2), 208–216 (2010).

Aspen Plus® Version 2006, Aspen Technology, Inc., Massachusetts, USA, Cambridge (2006).

Beaver, M. G., H. S. Caram and S. Sircar, "Sorption Enhanced Reaction Process for Direct Production of Fuel-Cell Grade Hydrogen by Low Temperature Catalytic Steam—Methane Reforming," J. Power Sources **195**, 1998–2002 (2010).

Bernesson, S., D. Nilsson and P. A. Hansson, "A Limited LCA Comparing Large- and Small-Scale Production of Rape Methyl Ester (RME) Under Swedish Conditions," Biomass Bioenergy **26**, 545–559 (2004).

Biodiesel 2020: Global Market Survey, Feedstock Trends and Forecasts. in: "Multi-Client Study," 2nd ed., Emerging Markets Online, Houston (2008).

Das, N. K., A. K. Dalai and R. Ranganathan, "Hydrogen Yield From Low Temperature Steam Reforming of Ethanol," Can. J. Chem. Eng. **85**(1), 92–100 (2007).

Dasari, M. A., P. Kiatsimkul, W. R. Sutterlin and G. J. Suppes, "Low-Pressure Hydrogenolysis of Glycerol to Propylene Glycol," Appl. Catal. A **281**, 225–231 (2005).

Dauenhauer, P. J., J. R. Salge and L. D. Schmidt, "Renewable Hydrogen by Autothermal Steam Reforming of Volatile Carbohydrates," J. Catal. **244**, 238–247 (2006).

Deutsch, J., A. Martin and H. Lieske, "Investigations on Heterogeneously Catalysed Condensations of Glycerol to Cyclic Acetals," J. Catal. **245**, 428–435 (2007).

Faungnawakij, K., R. Kikuchi and K. Eguchi, "Thermodynamic Evaluation of Methanol Steam Reforming for Hydrogen Production," J. Power Sources **161**, 87–94 (2006).

Hernandez, L. and V. Kafarov, "Thermodynamic Evaluation of Hydrogen Production for Fuel Cells by Using Bio-Ethanol Steam Reforming: Effect of Carrier Gas Addition," J. Power Sources **192**, 195–199 (2009).

Iriondo, A., V. L. Barrio, J. F. Cambra, P. L. Arias, M. B. Guemez, R. M. Navarro, M. C. Sanchez-Sanchez and J. L. G. Fierro, "Hydrogen Production From Glycerol Over Nickel Catalysts Supported on Al_2O_3 Modified by Mg, Zr, Ce or La," Top. Catal. **49**, 46–58 (2008).

Ketchie, W. C., M. Murayama and R. J. Davis, "Selective Oxidation of Glycerol Over Carbon-Supported AuPd Catalysts," J. Catal. **250**, 264–273 (2007).

Kiatkittipong, W., P. Intaracharoen, N. Laosiripojana, C. Chaisuk, P. Praserthdam and S. Assabumrungrat, "Glycerol Ethers Synthesis From Glycerol Etherification With tert-Butyl Alcohol in Reactive Distillation," JT Comput. Chem. Eng. In press (2011). DOI: 10.1016/j.compchemeng.2011.01.016.

Kiatkittipong, W., S. Suwanmanee, N. Laosiripojana and P. Praserthdam Suttichai Assabumrungrat, "Cleaner Gasoline Production by Using Glycerol as Fuel Extender," Fuel Process. Technol. **91**, 456–460 (2010).

Klepacova, K., D. Mravec, A. Kaszonyi and M. Bajus, "Etherification of Glycerol and Ethylene Glycol by Isobutylene," Appl. Catal. A **328**, 1–13 (2007).

Lechon, Y., H. Cabal, C. Rua, N. Caldes, M. Santamaria and R. Saez, "Energy and Greenhouse Gas Emission Savings of Biofuels in Spain's Transport Fuel. The Adoption of the EU Policy on Biofuels," Biomass Bioenergy **33**, 920–932 (2009).

Li, A., C. J. Lim, T. Boyd and J. R. Grace, "Simulation of Autothermal Reforming in a Stage-Separation Membrane Reactor for Pure Hydrogen Production," Can. J. Chem. Eng. **86**(3), 387–394 (2008a).

Li, Y., Y. Wang, X. Zhang and Z. Mi, "Thermodynamic Analysis of Autothermal Steam and CO_2 Reforming of Methane," Int. J. Hydrogen Energy **33**, 2507–2514 (2008b).

Luo, N., X. Zhao, F. Cao, T. Xiao and D. Fang, "Thermodynamic Study on Hydrogen Generation from Different Glycerol Reforming Processes," Energy Fuels **21**, 3505–3512 (2007).

Luo, N., X. Fu, F. Cao, T. Xiao and P. P. Edwards, "Glycerol Aqueous Phase Reforming for Hydrogen Generation Over Pt Catalyst—Effect of Catalyst Composition and Reaction Conditions," Fuel **87**, 3483–3489 (2008).
Malca, J. and F. Fausto, "Life-Cycle Studies of Biodiesel in Europe: A Review Addressing the Variability of Results and Modelling Issues," Renew Sust. Energy Rev. **15**, 338–351 (2011).
Niederl-Schmidinger, A. and M. Narodoslawsky, "Life Cycle Assessment as an Engineer's Tool?" J. Cleaner Prod. **16**, 245–252 (2008).
Oliveira, E. L. G., C. A. Grande and A. E. Rodrigues, "Steam Methane Reforming in a Ni/Al_2O_3 Catalyst: Kinetics and Diffusional Limitations in Extrudates," Can. J. Chem. Eng. **87**(6), 945–956 (2009).
Rabenstein, G. and V. Hacker, "Hydrogen for Fuel Cells From Ethanol by Steam-Reforming, Partial-Oxidation and Combined Auto-Thermal Reforming: A Thermodynamic Analysis," J. Power Sources **185**, 1293–1304 (2008).
Rakib, M. A., J. R. Grace, S. S. E. H. Elnashaie, C. J. Lim and Y. G. Bolkan, "Kinetic Simulation of a Compact Reactor System for Hydrogen Production by Steam Reforming of Higher Hydrocarbons," Can. J. Chem. Eng. **86**(3), 403–412 (2008).
Reese, M. A., S. Q. Turn and H. Cui, "High Pressure Autothermal Reforming in Low Oxygen Environments," J. Power Sources **187**, 544–554 (2009).
Reese, M. A., S. Q. Turn and H. Cui, "Kinetic Modelling of High Pressure Autothermal Reforming," J. Power Sources **195**, 553–558 (2010).
Rossi, C. C. R. S., C. G. Alonso, O. A. C. Antunes, R. Guirardello and L. Cardozo-Filho, "Thermodynamic Analysis of Steam Reforming of Ethanol and Glycerine for Hydrogen Production," Int. J. Hydrogen Energy **34**, 323–332 (2009).
Slinn, M., K. Kendall, C. Mallon and J. Andrews, "Steam Reforming of Biodiesel By-Product to Make Renewable Hydrogen," Bioresource Technol. **99**, 5851–5858 (2008).
Soimakallio, S., T. Makinen, T. Ekholm, K. Pahkala, H. Mikkola and T. Paappanen, "Greenhouse Gas Balances of Transportation Biofuels, Electricity and Heat Generation in Finland—Dealing With the Uncertainties," Energy Policy **37**, 80–90 (2009).
Thamsiriroj, T. and J. D. Murphy, "Can Rape Seed Biodiesel Meet the European Union Sustainability Criteria for Biofuels?" Energy Fuels **24**, 1720–1730 (2010).
Wang, X., S. Li, H. Wang, B. Liu and X. Ma, "Thermodynamic Analysis of Glycerin Steam Reforming," Energy Fuels **22**, 4285–4291 (2008).
Wang, H., X. Wang, M. Li, S. Li, S. Wang and X. Ma, "Thermodynamic Analysis of Hydrogen Production From Glycerol Autothermal Reforming," Int. J. Hydrogen Energy **34**, 5683–5690 (2009).
Wicke, B., V. Dornburg, M. Junginger and A. Faaij, "Different Palm Oil Production Systems for Energy Purposes and Their Greenhouse Gas Implications," Biomass Bioenergy **32**, 1322–1337 (2008).
Yanbing, L., J. Baosheng and X. Rui, "Carbon Dioxide Reforming of Methane With a Free Energy Minimisation Approach," Korean J. Chem. Eng. **24**, 688–692 (2007).
Yang, L., J. B. Joo, Y. J. Kim, S. Oh, N. D. Kim and J. Yi, "Synthesis of Superacidic Mesoporous Alumina and Its Application in the Dehydration of Glycerol," Korean J. Chem. Eng. **25**, 1014–1017 (2008).
Youn, M. H., J. G. Seo, K. M. Cho, J. C. Jung, H. Kim, K. W. La, D. R. Park, S. Park, S. H. Lee and I. K. Song, "Effect of Support on Hydrogen Production by Auto-Thermal Reforming of Ethanol Over Supported Nickel Catalysts," Korean J. Chem. Eng. **25**, 236–238 (2008).

Manuscript received February 10, 2011; revised manuscript received April 8, 2011; accepted for publication April 14, 2011.